

UNIVERSITÀ DEGLI STUDI DI PADOVA

DOCTORAL THESIS

Industrializing Vanadium Redox Flow Battery

Author:
Andrea TROVÒ

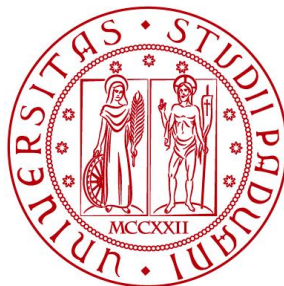
Supervisor:
Prof. Massimo GUARNIERI
Coordinator:
Prof. Roberto Turri

*A thesis submitted in fulfilment of the requirements
for the degree of Doctor of Philosophy*

in the

Energy Storage and Conversion Lab
Department of Industrial Engineering
Electrical Energy Engineering Curricula, XXXII cycle

November 29, 2019



**UNIVERSITÀ
DEGLI STUDI
DI PADOVA**

Declaration of Authorship

I, Andrea Trovò declare that this thesis titled, and the work presented in it are my own. I confirm that:

- This work was done wholly or mainly while in candidature for a PhD degree at the University of Padova.
- Where I have consulted the published work of others, this is always clearly attributed.
- Where I have quoted from the work of others, the source is always given. With the exception of such quotations, this thesis is entirely my own work.
- I have acknowledged all main sources of help.
- Where the thesis is based on work done by myself jointly with others, I have made clear exactly what was done by others and what I have contributed myself.

Signed:



Date: November 29, 2019

The energy of the universe is constant.

Rudolf Julius Emmanuel Clausius

Abstract

Electrical Energy Engineering Curricula, XXXII cycle
Department of Industrial Engineering

Doctor of Philosophy

Industrializing Vanadium Redox Flow Battery

by Andrea TROVÒ

Redox flow batteries (RFBs) have strong potential for providing future stationary energy storage, in view of the rapid expansion of renewable energy sources and smart grids. Their development and future success largely depend on the research on new materials mainly electrolytic solutions, membranes, and electrodes that are typically conducted on small single cells. Technological development plays a fundamental role in view of the successful application of RFBs in large plants, and while a quite vast literature on these topics already exists, very little research has been reported on the technology of large RFB systems.

This thesis presents the design, construction, and extensive experimental campaigns of a vanadium redox flow battery (VRFB) test facility of industrial size, referred to as IS-VRFB, where such technologies have been developed and tested.

The heart of the IS-VRFB is a 9 kW/27 kW h 40-cell 600 cm² stack, which is one of the very few VRFB plants of this size in the world. The polarization curve during charge and discharge has been performed showing superior performances in comparison to those normally reported in the literature for this type of battery, and a procedure for qualifying such performance has been developed, and is presented in this study.

Extensive numerical modeling has been carried out to gain a full understanding of the experimental data. Accordingly, this thesis reports on an original model capable of simulating the thermal behavior of a VRFB stack both in standby (i.e. without power and reactants flow), and in charge/discharge conditions, capable of computing the evolution of the temperature distribution in the cells (taking into account ions crossover through the membrane, and Joule loss due to shunt currents and inherent self-discharge effects). For the first time, a model is presented that is capable of simulating the cell temperature distribution in the stack and its time evolution considering all above effects, providing new results that can constitute the basis for advanced cooling strategies in future industrial RFB systems.

An analysis is also presented of the losses occurring in the system due to species crossover, shunt current, hydraulic pressure drops, and pumping, in addition to cell over potentials. Fast response analyses have been developed, achieving important information with regard to the dynamic response of the battery when connected to a grid. Preliminary impedance spectroscopy tests in a multichannel configuration are also reported showing the electrical behavior of such a VRFB system.

This study enables important drivelines to aid the designers of a compact VRFB stack to increase the battery efficiency. Similar analyses have been performed to obtain the optimal flow for each operating condition on such an industrial VRFB system. To the best of my knowledge, studies that offer detailed scrutiny of all major loss causes that are experimentally validated on a kW-class system are missing in the literature. In general, the results presented are new and aim to cover the lack of studies on IS-VRFB in view of widespread commercialization.

Acknowledgements

I would like to thank my supervisor Prof. Massimo Guarnieri for the support and motivation during these three years of PhD. His advices and knowledge have been precious in both research and writing activities.

My sincere thanks also go to Prof. Del Col, Dr. Angelo D'Anzi and Dr. Joseph Epoupa Mengou who provided me with skills before starting my PhD program and all graduating students who worked in the laboratory on their dissertation, helping me in many activities.

I thank my high school teacher Ferdinando Marinelli, who taught me the true method of study.

I would like to thank my family: my parents Pierpaolo and Stefania, my grandparents, and my girlfriend Elena for the patience and moral support.

Contents

Declaration of Authorship	iii
Abstract	vii
Acknowledgements	ix
List of Figures	xx
List of Tables	xxi
Abbreviations	xxiv
Constants	xxv
Symbols	xxx
1 Motivation	1
2 Introduction	5
2.1 Redox Flow Batteries	5
2.2 Electrochemical background	6
2.2.1 Nernst-equation	7
2.2.2 Cell overpotentials	8
2.2.3 RFB historical overview	11
2.2.4 Actual RFB technologies	11
Iron/Chromium	12
Bromine/polysulphide	12
Zinc-bromine	12
Vanadium-bromine	13
2.3 All-vanadium	13
2.3.1 Cell configuration	14
2.3.2 VRFB topologies	14
2.3.3 Circulation of the liquid electrolytes	14
Single stack flow circulation modes	14
Multiple stack flow circulation connections	15
Configuration of the storage tanks	15
2.3.4 Vanadium Redox Flow Batteries Components	16
Electrolytes	16
Electrodes	17
Bipolar plate	18
Membranes	19
2.3.5 Scale up process	20
2.3.6 VRFB management system and Power Electronics	21
2.4 Economic analyses	23
2.4.1 Cost distribution for VRFB	23
2.4.2 Reliability Metrics	25
2.4.3 Main VRFB plants installed	26
2.5 Standards for flow batteries (Information updated July 2019)	27

3	IS-VRFB stack	31
3.1	Bipolar plates	32
3.1.1	Flat graphite plates	32
3.1.2	Flow frames	33
	Flow frame design	33
	Flow frame manufacturing	34
	Bipolar plates assembly	35
3.1.3	Carbon felts	37
3.1.4	Gaskets	38
3.1.5	Current feeders	39
3.1.6	End-plates	39
3.1.7	SOC measuring	43
3.1.8	Stack assembly	45
3.1.9	Quality control	46
4	IS-VRFB test facility design	51
4.1	Hydraulic design	52
4.1.1	Piping	52
4.1.2	Tanks	53
4.1.3	Inert atmosphere and differential pressure gauge	54
4.1.4	Hydraulic pumps	54
4.1.5	Thermo fluid-dynamic sensors	55
4.1.6	Test facility assembly	58
4.2	Electrical design	61
4.2.1	Power management system (PMS)	61
4.3	Electromagnetic interference	62
4.4	Battery management system (BMS)	64
4.4.1	Surveillance system (SS)	65
4.4.2	Electrical schemes	66
4.4.3	Electrical sensors	66
4.4.4	Software development	66
4.4.5	Human Machine Interface (HMI)	71
5	IS-VRFB modeling	75
5.1	Hydraulic modeling	76
5.1.1	Head loss in pipes	76
	Major losses	76
	Minor losses	78
5.1.2	Stack pressure losses	81
5.2	Electric modeling	83
5.2.1	IS-VRFB shunt current model	84
5.3	Crossover modeling	88
5.4	Thermal modeling	88
5.4.1	Standby thermal modeling	89
	Standby mode development	90
	Mass balance	91
	Energy balance	92
	Thermal balance	93
5.4.2	Operation thermal modeling	94
	Mass balance	94
	Heat generation	95
	Energy balance	95
5.5	Thermal model implementation	96

6	Polarization curves	101
6.1	Theoretical background	101
6.2	Experimental method	102
6.3	Results	104
6.3.1	Fast mode measurement procedure	105
6.3.2	Steady-state mode measurement procedure	106
6.3.3	Experimental tests	107
6.3.4	Fast mode tests	107
6.3.5	Steady-state mode tests	107
6.3.6	Effect of concentration dynamics at start-up	109
6.3.7	Comparison between fast and steady state curves	109
6.4	Key points	111
7	Thermal analyses	115
7.1	Standby thermal analyses	115
7.1.1	Model validation	115
7.1.2	Model simulations and results	117
	Dynamic distributions of the cell species concentrations	119
	Effects of shunt currents on the temperature distribution	121
	Thermal effects of each loss term	122
7.1.3	Key points	122
7.2	Operation thermal analyses	123
7.2.1	Experimental validation	123
7.2.2	High-current simulations of a large VRFB	124
7.2.3	Key points	127
8	Maximizing VRFB efficiency	131
8.1	Energy losses distribution	131
8.1.1	Experimental method	132
	LabVIEW routines	132
	Energy computation	135
8.1.2	Numerical model	136
	Hydraulic losses	136
	Electrical losses	136
	Crossover losses	137
8.1.3	Energy efficiencies	137
8.1.4	Analysis of results	138
	Hydraulic model validation	138
	Hydraulic losses impact on the efficiency	139
8.1.5	Comparison of loss contributions	140
	Charge/discharge analyses	141
8.1.6	Key points	142
8.2	Optimization of flow rate management system	143
8.2.1	Experimental method	144
8.3	Analysis of mass transport losses	144
8.3.1	Optimal flow rate identification	149
8.3.2	Characterization at $\alpha \geq \alpha_k$	149
8.3.3	Comparison of the loss equivalent resistances	152
8.3.4	Stack hydraulic losses computation	153
8.4	Identifying optimal flow rate modulation	155
8.5	Implementation and validation	155
8.5.1	Implementing the control algorithm	155
8.5.2	Validation tests	157
8.5.3	Key points	157

9	Fast response analyses	161
9.1	Theoretical Background	161
9.2	Experimental method	162
9.3	Results and discussion	162
9.3.1	Cells voltage evolution	167
10	Aging Effects investigations	169
10.1	Disassembly and check operations	169
10.2	Stack reassembly	174
11	EIS tests	179
11.1	Theoretical background	179
11.2	EIS measurement tests	183
11.2.1	Experimental method	183
11.3	Calibration tests	186
11.4	Cabling optimization	186
11.5	Influence parameters	190
11.6	Preliminary results on IS-VRFB	190
12	Main results summary	195
13	Conclusion and future work	199
	Achievements	206
	Funding	209
	Appendix	211
A	Electrolyte properties investigations	211
A.1	Viscosity measurements	211
A.2	Electrical conductivity measurements	214
B	Standards Publication	217
	References	314

List of Figures

1.1	A power-duration diagram of existing electrochemical system. The blue dotted line encircles ECESs; TES: thermal ES; CAES: compressed air ES; A-CAES: adiabatic compressed air ES; PHES: pumped hydro ES; ZEBR A: Zeolite Battery Research Africa Project (Na-Ni-Cl battery); UPS: uninterruptible power supply ([19]).	2
2.1	Redox flow battery scheme: RFB stack and electrolyte tanks are separated.	6
2.2	Effect of overpotentials on the current (figure based on [53]).	10
2.3	Polarization curve of a redox flow battery for charge and discharge. The corresponding dominating loss mechanisms are highlighted.	11
2.4	Diagram of a Vanadium Redox Flow Battery.	13
2.5	VRFB topologies; left: conventional series stack (CSS), right: alternative parallel stack (APS).	15
2.6	Single stack flow circulation modes; top-left: parallel electrolyte circulation (mode A), top-right: parallel electrolyte circulation (mode B), bottom-left: sequence electrolyte circulation (countercurrent), bottom-right: sequence electrolyte circulation (equicurrent).	16
2.7	Embodiment of VRFB system illustrating a cross sectional illustration with electrolyte storage tanks including tank dividers.	17
2.8	Graphical representation of the mission of Energy Storage and Conversion Lab at UNIPD: a path from advanced laboratory tests to grid-scale VRFB systems such as the 200 MW/800 MWh VRFB system installed at Dalian (China) and realized by Rongke Power; actually the biggest battery in the world.	20
2.9	Left: phase shift Double Active Bridge; right: phase shift Double Active bridge with resonant tanks [19].	22
2.10	Component cost distribution for Gen-2 chemistry (PNNL's all-vanadium redox flow battery). Chemical costs are dominant for the 1-MW/4-MWh system at 48%, while membrane (separator) material costs are 22%. Conversely, for the 1-MW/0.25-MWh system, the stack costs are dominant, led by membrane costs at 42% [171].	24
2.11	Cost sharing of 250 kW VRFB stack with Nafion and SPEEK membrane [177].	25
2.12	Cumulative VRFB systems installation for stationary applications (2000 to 2015) and installed power in selected country [177].	27
3.1	IS-VRFB stack flow distribution.	32
3.2	Graphite flat plate: physical data (left), products (right).	33
3.3	Contours of velocity magnitude (m s^{-1}) of a poor flow frame geometry, $Q_c=0.8 \text{ L min}^{-1}$, $SOC=50\%$.	33
3.4	3D model used to compute the cell flow resistance including distribution channels and porous electrodes. Left: 3D mesh color map of the electric potential; right: φ in V produced by a 1 A shunt current.	34
3.5	Left: Molded flow frame (polypropylene with glass fibers); right: effects of bad reheating ($150 \text{ }^\circ\text{C}$ for 2 hours) in the tested cure.	35
3.6	Bipolar plate assembly phases.	36
3.7	GFE-1 carbon felt X-ray computed tomography reconstruction.	37
3.8	Carbon felt thermo-chemical treatment.	38
3.9	IS-VRFB EPDM gasket.	38
3.10	IS-VRFB current feeder realization.	39
3.11	Front-end plate representation.	40

3.12	Front-end plate representation, internal flow path.	41
3.13	Left: six-way motorized mixing valve (old system); right: two three-way mixing valves (new system).	43
3.14	Left: front end-plate; right: back end-plate.	44
3.15	Nerst equation representation Eq.2.16 (Sec.2.2.1)	44
3.16	IS-VRFB <i>OCV</i> cell.	45
3.17	Left: IS-VRFB half-cell assembly; right: preliminary IS-VRFB stack compression by means the hydraulic press.	46
3.18	IS-VRFB stack fastening procedure.	47
3.19	IS VRFB stack quality control by using nitrogen.	48
4.1	IS-VRFB simplified P&ID.	52
4.2	Main IS-VRFB hydraulic components.	53
4.3	IS-VRFB tanks.	53
4.4	Millibaric pressure safe control system in inert atmosphere for highly reactive liquid solutions.	54
4.5	Left: IS-VRFB pump, PMD-641 by Sanso, Japan; right: PMD-641 characteristic curve.	55
4.6	Left: IS-VRFB bigger pump, CM MAG – P06 by M Pumps Industry, Italy; right: CM MAG – P06 characteristic curve.	55
4.7	Volumetric flow-meters, Proline Promag by Endress+Hauser, Switzerland.	56
4.8	Differential pressure gougues (Deltabar PMD by Endress+Hauser).	57
4.9	Resistance Temperature Detectors (RTDs) Pt-100 (TR11 by Endress+Hauser).	57
4.10	Potentiometric type level sensors, (Val.Co S.r.l., Italy).	57
4.11	IS-VRFB 3D model.	59
4.12	IS-VRFB hydraulic plant assembly. Left: aluminum rack assembly; right: piping assembly.	60
4.13	Filling the tank with the electrolyte.	60
4.14	IS-VRFB test facility and the main components.	61
4.15	IS-VRFB power management system (PMS) with the power electrical scheme, including the PS, the PL, the user board and the power contactors (1, 2 and 3).	62
4.16	Inverter-motor cable section (courtesy of [246]).	63
4.17	Copper shielding pipes for motor-inverter cables.	63
4.18	Electromagnetic shields examples [247].	64
4.19	Shielding metal box.	64
4.20	Simplified electrical measurements scheme.	67
4.21	Simplified electrical power scheme.	68
4.22	IS-VRFB electrical sensors.	69
4.23	Software structure of IS-VRFB BMS.	70
4.24	IS-VRFB human-machine interface.	72
5.1	The Moody chart [265].	78
5.2	Entrance flow conditions and loss coefficient [265].	79
5.3	Exit flow conditions and loss coefficient [265].	80
5.4	Loss coefficient for a sudden contraction and a sudden expansion [265].	80
5.5	Loss coefficients of a 90° bend pipe [265].	80
5.6	Segments of hydraulic circuits (lumped representation).	82
5.7	Four conductive loops with shunt currents formed in the hydraulic segments of a two-cell stack.	83
5.8	IS-VRFB stack internal resistance profile vs. <i>SOC</i> during charge (<i>ch</i>) and discharge (<i>dh</i>).	84
5.9	Equivalent electric circuit of a 40-cell stack used in computing the shunt currents.	85
5.10	3D model used to compute the cell flow resistances $R_{c+,n}$, $R_{c-,n}$ including distribution channels and porous electrode. In this case, the IS-VRFB flow frame design with flat bipolar plates was considered. Top left: electrode and flow frame tessellation, top right: color map of the electric potential φ in V produced by a 1 A shunt current, bottom: resulting $R_{c+,n}$, $R_{c-,n}$ as functions of <i>SOC</i>	87

5.11	Due to the gaps caused by the gasket thickness, the stack lateral thermal exchange surface was modeled as a vertically oriented array of parallel flat fins.	94
5.12	Energy losses of the pumps (SANSO PMD-641) as a function of flow rate.	96
5.13	Thermal model algorithm for charge/discharge operation.	97
6.1	Flowchart of the automatic procedure to collect data for polarization curve computation.	103
6.2	Top: the Polarization case in the UI Handling loop; bottom-left: the window that allows the user to set the parameter for the polarization routine; bottom-right: the SubVI internal structure.	104
6.3	Time evolution of the stack current after connection at $SOC=40\%$ and at different values of flow rate Q and load resistance R_L	105
6.4	Reference current profile during data harvesting in steady-state condition controlled by the automatic LabVIEW routine to drive the PMS in both charge and discharge modes.	106
6.5	Fast mode tests. Top-left: Internal resistance during charge at different flow rates Q (i.e. specific flow rates q); top-right: internal resistance during discharge at different flow rates Q (and q); bottom-left: polarization curves at different $SOCs$ with $Q=29.5 \text{ L min}^{-1}$ ($q=20.5 \times 10^{-3} \text{ cm s}^{-1}$); bottom-right: power curves at different $SOCs$ with $Q=29.5 \text{ L min}^{-1}$ ($q=20.5 \times 10^{-3} \text{ cm s}^{-1}$).	108
6.6	Steady-state mode tests. Top-left: internal resistance during charge at different flow rates Q (i.e. specific flow rates q); top-right: internal resistance during discharge at different flow rates Q (and q); bottom-left: polarization curves at different $SOCs$ with $Q=29.5 \text{ L min}^{-1}$ ($q=20.5 \times 10^{-3} \text{ cm s}^{-1}$); bottom-right: power curves at different $SOCs$ with $Q=29.5 \text{ L min}^{-1}$ ($q=20.5 \times 10^{-3} \text{ cm s}^{-1}$).	110
6.7	Discharge power curve (on PMS and passive load) at $SOC=70\%$ and different flow rates Q	110
6.8	Comparison between discharge polarization (left) and power (right) curves at $SOC=30\%$ and $Q=10$ and 29.5 L min^{-1}	111
7.1	Validation of the stack thermal model on the IS-VRFB with initial $SOC=80\%$:. Top-left: computed evolutions of the average temperatures over the cell lateral surfaces; top-right: thermal imager measurements after 1.5 h; bottom: comparison of the average temperature distributions after 1.5 h.	116
7.2	Distributions of the computed shunt currents in the IS-VRFB stack after 15 min. Left: Shunt current I_{c+} and I_{c-} in the positive and negative cell compartments (where the electric resistances are higher); right: shunt current I_{m+} and I_{m-} in the positive and negative manifolds (where electric resistances are much lower). These distributions are responsible for the different cell temperature shown in Fig.7.1.	116
7.3	Comparison between the IS-VRFB experimental data and numerical results of two lateral cell temperatures over a period of 4 h (after which all loss events are exhausted). Left: T4 in the 4- <i>th</i> cell (hottest); right: and T20 in the 20- <i>th</i> cell (coldest). Discrepancies are below $3.1 \text{ }^\circ\text{C}$	117
7.4	Numerical results of the internal temperature evolution in the IS-VRFB stack obtained in the validation test conditions. Left: plot of numerical temperature distribution; right: temperature evolution of the 3- <i>rd</i> and 37- <i>th</i> cell (i.e. end and hottest) and 20- <i>th</i> cell (i.e. central and coldest).	119
7.5	Computed evolutions of ion concentrations in the IS-VRFB 40 cells over a 36 h with initial $SOC=95\%$. The cross represents the gradient from the external (1- <i>st</i> and 40- <i>th</i> cells) to the central cell (20- <i>th</i> cell). Top: with shunt currents thermal effects; bottom: neglecting shunt currents effects.	120
7.6	Evolutions of the temperatures in the IS-VRFB 40 cells during a 72 h simulation with initial $SOC=95\%$. Top: considering shunt currents; bottom: neglecting shunt currents.	121

7.7	Evolution during phase 1 of the Joule losses produce by the shunt current in the IS-VRFB cells ($n=1$ to 40) with initial $SOC=95\%$: a) cells (– and + together); b) manifolds (– and + together); c) internal equivalent resistances (representing over potential losses). Initial ($t=0$) distribution of Joule losses among: d) cells; e) manifolds; f) internal equivalent resistances.	122
7.8	Computed and measured electrolyte temperature evolutions at the inlet and outlet pipes during charge and discharge. $T_{ta\pm}$ = computed electrolyte temperatures in the positive/negative tank; $T_{ip\pm}$ = computed electrolyte temperatures in the positive/negative input pipes; $T_{op\pm}$ = computed electrolyte temperatures in the positive/negative output pipes; T1/3= measured electrolyte temperatures in the positive/negative input pipes; T2/4= measured electrolyte temperatures in the positive/negative output pipes.	124
7.9	Simulation of high-current (400 A) long-duration (8 h) discharge and charge: heat rate contributions and electrolyte temperature in cells $n= 1, 20$ and 40.	126
7.10	Simulation of high-current (400 A) long-duration (8 h) discharge (left) and charge (right): positive electrolyte temperature at stack inlet (ip) and outlet (op) piping, and in the tank (ta) (negative electrolyte has a similar evolution).	127
8.1	Flowchart of the routine for the efficiency evaluations. The whole process is complicated by the presence of several security layers. In fact, the high energy the device can store makes the charge and discharge process very long and delicate so there must be a way to keep it under control. Problems connected to the over-charging or over-discharging of the device can be the corruption of the electrodes or the formation of hydrogen that must be totally avoided [259].	133
8.2	Left: ancillary power losses composition; right: pump efficiency η_{pu} vs. vanadium solution flow rate Q as resulting from Eq.8.4. In order to obtain this diagram, the same flow rates were imposed in the positive and negative hydraulic circuits. . .	135
8.3	3D representation of IS-VRFB balance of plant.	137
8.4	Sankey diagram of the power flows and loss terms which affect the energy flows and on the energy efficiency.	138
8.5	Left: characteristic curve of the pump (PMD 641); right: pressure drop profiles in the negative electrolyte circuit vs. flow rate Q at $SOC=50\%$ (the positive electrolyte piping pressure has a similar profile).	139
8.6	Negative electrolyte piping pressure drop profile vs. flow rate with pie chart of its contribution in laminar and turbulent flow at $SOC=50\%$ (the positive electrolyte piping pressure has a similar profile).	139
8.7	Profiles of power losses for electrolyte circulation vs. flow rate at $SOC=50\%$ in both positive and negative compartments. The difference between the total value P_w measured by the wattmeter and the hydraulic circuit losses $P_h = P_s + P_{pi}$ is due to P_w in the pump impellers, electric motors and electronic inverters.	140
8.8	Battery energy losses contributions in charge/discharge cycles performed at stack currents of: a) 30 A, b) 50 A, c) 70 A in the SOC ranges shown in Tab.8.2. . .	142
8.9	Experimental polarization curves (V vs. I) during discharge obtained on the IS-VRFB test facility at different flow rates: $Q=10$ L min ⁻¹ , 20 L min ⁻¹ and 29.5 L min ⁻¹ and SOC s (10%, 20%, 30%, 40%, 50%, 60%, 70%, 80%, 90%).	145
8.10	Experimental polarization curves (V vs. I) during discharge obtained on the IS-VRFB test facility at different flow rates: $Q=10$ L min ⁻¹ ($q= 6.9 \cdot 10^{-3}$ cm s ⁻¹) and 29.5 L min ⁻¹ ($q= 20.5 \cdot 10^{-3}$ cm s ⁻¹): a) $SOC =10\%$, 20%, 30%; b) $SOC =40\%$, 50%, 60%; c) $SOC =70\%$, 80%, 90%.	147
8.11	Experimental polarization curves (V vs. I) during discharge obtained on the IS-VRFB test facility at fixed flow factors α ($\alpha=4, 6, 8, 10, 12, 14, 16, 18, 20$). .	148
8.12	Key flow factor α_k and corresponding key electrical resistance $R_o \simeq R_k$ vs. SOC	149
8.13	Relative difference between resistance R_i and R_k at different flow rate Q , different flow factor α and different SOC . Data point are code-colored as function of α , showing that as α increases this fraction Δr tends to a minimum value dependent on Q and independent of SOC	150

8.14	Flow-rate dependent losses P_Q by contours plotted for different current I and flow rate Q	154
8.15	P_w and P_s vs flow rate with different $SOCs$	156
9.1	Current and voltage trend over time in 0–20 ms and 0–120 s time range.	163
9.2	Current I_p/I_{ss} and power P_p/P_{ss} ratios evolution v.s. Q , SOC and load.	164
9.3	Power trend over time in 0–20 ms and 0–120 s time range.	165
9.4	Cell voltage evolution at different SOC and Q	166
9.5	Cell voltage evolution with voltage unbalance.	167
10.1	Aluminum rack and hydraulic pressure jack.	170
10.2	Top: plant after the first phase (OCV cell, LEM and horizontal upper profile removed); bottom: the removed objects accurately separated.	170
10.3	Second phase: the mixing valve is dismantled from the frontal panel.	170
10.4	Third phase: the stack's hung and moved with a crane and placed horizontally.	171
10.5	Fourth phase: the stack's turned vertically. Left: some electrolyte leakage is detected from the bottom part, center: clips are applied to avoid polypropylene plates to open completely as it can be noticed in right.	171
10.6	Fifth phase: membrane disassembled and preliminary visual check. In right: some manifold channels are blocked up by PVC shavings due to previous drilling maintenance operations on the head plate.	171
10.7	Sixth phase: PVC frontal plate is divided from its metal where more electrolyte leakage are detected.	172
10.8	Seventh phase: each membrane with two gaskets is divided and each bipolar plate is washed with bi-distilled water and accurately examined.	172
10.9	Some of the flaws found on the plates: a) a carbon felts hole, b) acetic silicon behavior in presence of corrosive environment and electric field, c) and d) imperfections on bi-polar plates surface, e) and f) carbon felts deposit close to the plate inlets.	173
10.10	Reassembly procedure's operations. Left: a final and accurate check on the manifold holes status. Center: first cells assembled on the designated aluminum rack. Right: all the cells reassembled and final operations on the head of the battery.	174
10.11	Voltage vs time graph of the stack's cells. Cell 16's behavior is pointed.	174
10.12	Stack measuring and pressing.	175
10.13	Single cells cabling.	175
10.14	The stack is repositioned horizontal.	176
10.15	The gas sealing test.	176
11.1	Application of small excitation amplitudes allows the signal to be linearized [380].	180
11.2	Angular offset between the voltage and current waves [380].	180
11.3	Nyquist diagram of a specific system [381].	181
11.4	Bode diagram of a specific system.	181
11.5	Randle's circuit (top) and the analogous Nyquist diagram (bottom) [382]	182
11.6	Physical meaning associated with a Randles circuit [383].	183
11.7	MMulty SP graphic interface.	184
11.8	Graphical interface for parameter monitoring of the MMulty SP program.	185
11.9	Schematic of electrical connections of the electronic plate (it has welded on both sides).	187
11.10	Final result of electrical connections of the electronic board.	188
11.11	Connection between each terminal of the electrochemical cells and the electronic board.	188
11.12	Connection between the data acquisition cards (terminal in red box) managed by LabVIEW software and its terminal on the electronic board b).	189
11.13	Front panel of indicator LEDs.	189
11.14	Connection between the data acquisition cards of the EIS measurement program and its corresponding terminal d) of the electronic board.	189
11.15	Final connection diagram of the electronic board.	190

11.16	Theoretical equivalent circuit of the battery	191
11.17	EIS diagrams: EIS measurements from cell $n=6, 12, 16$ and 20 (out of 40 cells) in the range $1-20.000$ Hz, at $SOC=60\%$, with a flow rate $Q=20$ L min^{-1} , $I=80$ A and modulated current= 0.8 A.	192
A.1	Left: withdrawal of electrolyte with a syringe; center: pycnometer on the scale; right: reverse flow U-tube viscometer.	212
A.2	Viscosimeter with sealed measuring tube to arrest the levels precisely at the start- ing marks.	212
A.3	Measured density ρ values of the positive and negative electrolyte.	213
A.4	Measured kinematic viscosity ν of the positive and negative electrolyte.	213
A.5	Four pole electrode for electric conductivity measurements.	214

List of Tables

2.1	Featured of electrochemical energy storage technologies for stationary services ([19])	26
3.1	Carbon felt Beijing Great Wall GFE-1 data sheet.	37
4.1	Measurement ranges and uncertainty of the thermo fluid-dynamic IS-VRFB sensors.	57
4.2	Measurement ranges and uncertainty of the electrical IS-VRFB sensors.	66
5.1	Equivalent roughness for new pipes [265].	78
5.2	Loss coefficients for pipe components.	81
7.1	IS-VRFB parameters used in validation and simulations of the thermal model.	118
8.1	Values of the empirical minor loss coefficients (concentrated) ζ used in calculating the concentrated pressure losses.	136
8.2	Numerical and experimental energy terms and system efficiencies during charge/discharge cycles. W_{ch} = converted electric energy in charge, W_{dh} = converted electric energy in discharge, $W_{w,rt}$ = round-trip total hydraulic losses (i.e. for electrolyte circulation), $W_{i,rt}$ = round-trip losses due to cell over potentials, $W_{sc,rt}$ = round-trip losses due to shunt currents, $W_{co,rt}$ = round-trip losses due to species crossover, SE = system efficiency; <i>exp</i> = experimental, <i>num</i> = numerical.	141
8.3	Stack components physical properties	152
8.4	Specifications of IS-VRFB stack for pressure drop computation.	153
8.5	Data fit of $P_s(Q)$.	155
8.6	Experimental campaign for optimal flow rate identification	157
8.7	Round trip efficiency (<i>RTTE</i>) at different <i>SOC</i> range and current I at fixed α and modulated α .	157
11.1	Technical data sheet MMulty SP	185
11.2	Equivalent electric scheme model parameters on 6-th, 12-th, 16-th, 20-th cells.	191
A.1	Empirical parameters in Eq.A.1 for the <i>SOC</i> -dependence of the kinematic viscosity of both electrolytes.	214

List of Abbreviations

ASR	A rea S pecific R esistance
APS	A lternative P arallel S tack
BMS	B attery M anagement S ystem
BP	B ipolar P late
CAES	C ompressed A ir E nergy S torage
CAPEX	C APital E Xpenditure
CE	C oulombic E fficiency
CFD	C omputational F luid D ynamics
CNC	C omputer N umerical C ontrol
CSS	C onventional S eries S tack
CSTR	C ontinuous-flow S tirred T ank R eactor
ECES	E le C trochemical E nergy S torage
EE	E nergy E fficiency
EIS	E lectrochemical I mpedance S pectroscopy
EPDM	E thylene P ropylene D iene M onomer
EPL	E qual P ath L ength
ESS	E nergy S torage
ESS	E nergy S torage S ystem
FC	F uel C ell
FES	F lywheel E nergy S torage
FKM	F orschungs K uratorium M aschinenbau
GHG	G reen H ouse G as
HDPE	H igh D ensity P oly E thylene
HMI	H uman M achine I nterface
IFBF	I nternational F low B attery F orum
IS-VRFB	I ndustrial S cale- V anadium R edox F low B attery
OCV	O pen C ircuit V oltage
P&ID	P iping & I nstrumentation D igram
PEM	P roton E xchange M embrane
PEMFC	P roton E xchange M embrane F uel C ell
PHES	P umped H ydroelectric E nergy S torage
PID	P roportional I ntegral D erivative
PE	P oly E thylene
PL	P assive L oad
PLC	P rogrammable L ogic C ontroller
PMS	P ower M anagement S ystem
PP	P oly P ropylene
PS	P ower S upply
PTFE	P oly T etra F luoro E thylene
PV	P hoto V oltaic
PVC	P oly V inyl C hloride
PVDF	P oly V inyl I dene F luoride
RE	R enewable E nergy
RFB	R edox F low B attery
RTD	R esistance T emperature D etector
RTE	R ound T rip E fficiency
SCADA	S upervisory C ontrol A nd D ata A cquisition
SE	S ystem E fficiency

SMES	S uperconducting M agnetic E nergy S torage
SNG	S ynthetic N atural G as
SOC	S tate O f C harge
SOH	S tate O f H ealth
SS	S urveillance S ystem
TES	T hermal E nergy S torage
VE	V oltage E fficiency
VRFB	V anadium R edox F low B attery
ZEBRA	Z elite B attery R esearch A frica

Physical Constants

Avogadro constant	$N_A = 6.02214086 \times 10^{23} \text{ mol}^{-1}$
Boltzmann constant	$k_B = 1.38064852 \times 10^{-23} \text{ J K}^{-1}$
Elementary charge	$q_e = 1.60217662 \times 10^{-19} \text{ C}$
Faraday constant	$F = 96,485 \text{ C mol}^{-1}$
Gravitational acceleration	$g = 9.8 \text{ m s}^{-2}$
Universal gas constant	$K = 8.314 \text{ J K}^{-1} \text{ mol}^{-1}$

List of Symbols

Full names

A	Membrane active area [m ²]
A_{cross}	Cross-sectional area of the electrolyte flow [m ²]
A_k	Cross-sectional area in the k -th direction/of k -th element [m ²]
C	Molar concentration [mol L ⁻¹]
C^0	Bulk concentration [mol L ⁻¹]
E'_0	Corrected standard potential = 1.37 V
C_P	Specific heat at constant pressure [J kg ⁻¹ K ⁻¹]
c_v	Vanadium molar concentration [mol L ⁻¹]
d	Membrane tickness [m]
D	Piping diameter [m]
d_f	Fiber diameter of the carbon felt [m]
E_a	Activation energy [J mol ⁻¹]
E_o	Open Circuit Voltage (OCV) [V]
exp	Experimental
f	Friction factor
h	Convection heat transfer coefficient [W m ⁻² K ⁻¹]
h_0	felt thickness before compression [mm]
h_{cr}	felt thickness after compression [mm]
hl	High load Chap.9
i	i -th
I	Stack current [A]
I_o	Exchange current [A]
j	Current density [A cm ⁻²]
j_o	Exchange current density [A mm ⁻²]
j_r	Reaction rate [mol m ⁻² s ⁻¹]
k	Diffusivity coefficient [cm ² s ⁻¹]
K_{kc}	Kozeny-Carman constant
l	Length of i -th element [m]
L_{fin}	Height of fin [m]
l'_x	Felt length (flow direction) Tab.8.4 [m]
l'_y	Felt length (width direction) Tab.8.4 [m]
l'_z	Felt length (thickness direction) Tab.8.4 [m]
M	Moles of crossover species [mol]
ml	Medium load Chap.9
N	Cell number
Nu	Nusselt number
num	Numerical
P	Power [W]
Q	Stack electrolyte flow rate [L min ⁻¹]
q	Stack specific flow rate [cm s ⁻¹]
R	Electrical resistance [Ω]
Ra	Rayleigh number
Re	Reynolds number
R_k	Key resistance [Ω]
s	State Of Charge
Sh	Dependents shares
sl	Small load Chap.9

T	Temperature [$^{\circ}\text{C}$] or [K]
t	Time [s]
u	Fluid speed [m s^{-1}]
U	Overall heat transfer coefficient [$\text{W m}^{-2} \text{K}^{-1}$]
V	Voltage [V]
v	Electric voltage drop [V]
V_c	Cell volume [m^3]
V_e	Electrode volume [m^3]
$V(j)$	j -th vanadium specie
V_{sy}	Volume of thermodynamic system [m^3]
V_{ta}	Tank volume [m^3]
W	Energy [J]
W_{el}	Electrical work [J]
W_{tot}	Mechanical and electrical work [J]
x -	x direction (Fig.5.11)
y -	y direction (Fig.5.11)
z -	z direction (Fig.5.11)
z	Number of electrons in the electrochemical reaction
Z	Impedance [Ω]

Subscripts

+	positive electrolyte
-	negative electrolyte
a	activation
air	air
an	ancillary
b	bipolar plate
c	cell
dl	double layer capacity
ch	charge
cn	concentrated (or localized or minor hydraulic losses)
cn,m	concentrated (or localized or minor hydraulic losses in meters)
co	crossover (irreversible)
dh	discharge
di	distributed (or major hydraulic losses)
di,m	distributed (or major hydraulic losses in meters)
e	electrode porous felt
el	electrolyte
$empty$	empty
end	end
eq	equivalent
fin	fin (heat exchange vertical surface)
fl	flux of electrolyte
gh	gross hydraulic
h	hydraulic
i	stack internal
il	irreversible losses (in load operation)
im	immaginary
in	inverter
ip	inlet pipe (from tank to stack)
k,n	electric circuit index for n -th cell
L	load
m	manifold
max	maximum
min	minimum
mo	motor
mol	number of moles

<i>n</i>	cell index
<i>o</i>	ohmic
<i>op</i>	outlet pipe (from stack to tank)
<i>opt</i>	optimal
<i>p</i>	peak
<i>P</i>	products
<i>pf</i>	pumping friction
<i>pi</i>	pipng
<i>PP</i>	polypropylene
<i>pu</i>	pump
<i>Q</i>	flow rate dependent
<i>R</i>	reactant
<i>re</i>	reversible entropic
<i>rea</i>	real
<i>rt</i>	along the duration of a whole cycle
<i>s</i>	stack
<i>sa</i>	sulfuric acid
<i>sc</i>	shunt current losses
<i>ss</i>	steady state
<i>sta</i>	standard
<i>sto</i>	stoichiometric
<i>sur</i>	superficial
<i>sy</i>	thermodynamic system
<i>t</i>	transport
<i>ta</i>	tank
<i>tr</i>	transferred
<i>w</i>	wattmeter
<i>war</i>	Warburg impedance
<i>x</i>	sum index

Greek Symbols

α	Flow factor
α_k	Key flow factor
β	Thermal expansion coefficient of air [$^{\circ}\text{C}^{-1}$]
δ	Thickness [m]
ΔG	Gibbs free energy change [J]
ΔH	Entalpy change [J]
Δp	Pressure drop [Pa]
ΔS	Entropy change [J K^{-1}]
Δ^R	Is used in thermodynamics to indicate reaction balance values
Δr	index of the incidence of $R_a + R_t$ [%]
ϵ	Porosity
ϵ_c	Porosity after compression
η	Efficiency
Γ_{wall}	Wall shear stress between the fluid and pipe surface [Pa]
ι	Electric charge [C]
λ	Thermal conductivity [$\text{W m}^{-1} \text{K}^{-1}$]
μ	Dynamic viscosity [Pa s]
ν	Kinematic viscosity [$\text{m}^2 \text{s}^{-1}$]
ρ	Density [kg m^{-3}]
σ	Electrical conductivity [S m^{-1}]
σ_{war}	Warburg diffusion coefficient
σ_f^{eff}	effective carbon felt conductivity [S m^{-1}]
σ_{el}^{eff}	effective electrolyte conductivity [S m^{-1}]
σ_s	conductivity of the solid carbon felt material [S m^{-1}]
τ	Integration time [s] or [h]
τ_a	Acquisition time [s], Chap.6

τ_{ci}	Idle time during charge [s], Chap.6
τ_{di}	Idle time during discharge [s], Chap.6
τ_{sb}	Waiting time during standby [s], Chap.6
θ	Heat exchange efficiency
Θ	Internal energy [J]
ξ	Roughness
Ξ	Thermodynamic species
ζ	Minor loss coefficient
φ	Electrical potential [V]
ϖ	Activity coefficient
ρ	Symmetric factor
ς	Felt compression ratio
\aleph	Permeability of the porous electrode

Chapter 1

Motivation

Energy underlies the economy, welfare and development state of societies with a direct link to the environmental issues.

The dominant primary energy sources today are fossil fuels (coal, oil, and gas), which supply $\approx 85\%$ of primary energy [1], [2]. Industrial development, population and economic growth lead to increasing energy demands, particularly in emerging large-population countries (especially China and India) [3].

A significant proportion of total energy produced is consumed by the power, industry, transportation, and construction sectors. Furthermore, the power sector alone is responsible for approximately 40% of total energy related emissions [4] and 25% of total greenhouse gas (GHG) emissions [5]. World energy demand is expected to more than double by 2050 and more than triple by the end of 2100 [6]. Incremental improvements to conventional approaches in existing energy networks will not be adequate to supply this demand in a sustainable way. Growing demand leads to environmental challenges such as climate change, global warming, and air pollution health impacts, with the risk of soil and water contamination [6], [7]. According to Boden and Andres [8] and Heard et al. [9] the atmospheric CO_2 concentration increased from ≈ 360 ppm to ≈ 400 ppm between 1995 and 2015, while fossil fuel CO_2 emissions rose from ≈ 6.4 Gt C yr $^{-1}$ in 1995 to ≈ 9.8 Gt C yr $^{-1}$ in 2013 [10]. Moreover, in the last 120 years, global temperatures have increased by 0.8 °C [11].

This has occurred mainly due to anthropogenic emissions [12]. If this trend continues, the temperature increase could be 6.5–8 °C by 2100. Renewable energy (RE), especially wind and solar energy, has been widely regarded as one of the most promising solutions regarding carbon emissions reductions, oil depletion, and the increasing energy consumption demand [13]. Policies for renewable energy development and strategies with incentives have been launched by various governments [14]. In addition, it is expected that by 2025, solar PV and onshore wind energy will experience a strong price reduction of 43% and 26%, respectively [15]. Large-scale energy storage (> 50 MW) is therefore of crucial importance for manage daily fluctuating power demands on large grids, and to cope with the intermittent nature of renewable sources as they grow, thus guaranteeing larger proportions of the energy required for grids [10]. Energy storage systems (ESSs) can be classified into five main groups [16]:

- chemical systems such as hydrogen storage technology with fuel cell/electrolyzer, or synthetic natural gas (SNG) with reversible chemical reactions;
- mechanical systems such as compressed air energy storage (CAES), pumped hydroelectric storage (PHES), falling weights, and flywheel energy storage (FES);
- electrical systems such as capacitors, supercapacitors, and superconducting magnetic energy storage (SMES);
- thermal systems such as latent heat storage, sensible heat storage, and thermal absorption and adsorption systems;
- electrochemical systems (ECES), including different types of batteries.

Generally, ESSs can be used for a wide range of applications with different time and magnitude scales [6]. A recent authoritative report by the Boston Consulting Group (USA) forecasted investments exceeding US\$10 billion per year on ESS technologies by 2020 [17]. ESSs must

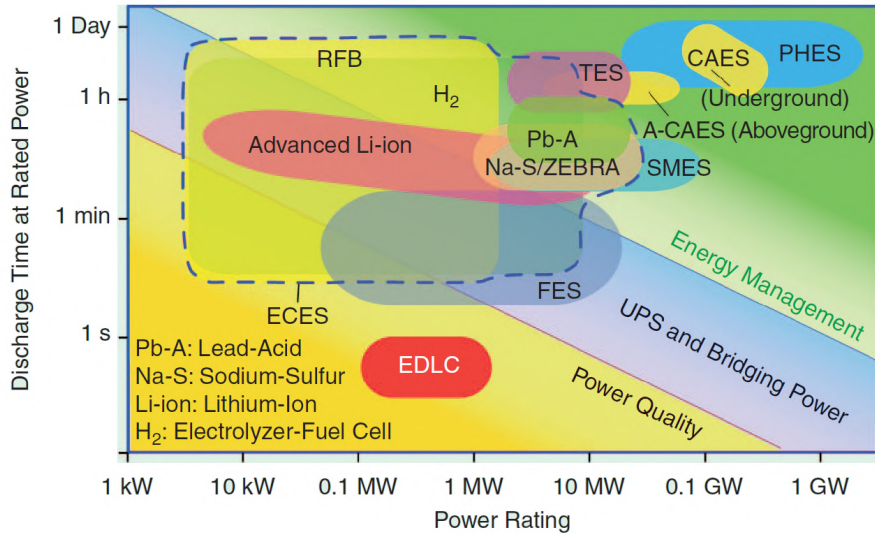


FIGURE 1.1: A power-duration diagram of existing electrochemical system. The blue dotted line encircles ECESs; TES: thermal ES; CAES: compressed air ES; A-CAES: adiabatic compressed air ES; PHEs: pumped hydro ES; ZEBR A: Zeolite Battery Research Africa Project (Na-Ni-Cl battery); UPS: uninterruptible power supply ([19]).

satisfy various criteria, such as storage costs, energy density rating, being stationary or portable, offering short or long-time storage, quick response time, security, end-use (e.g., grid connected or standalone), environmental impacts, and storage time limits [18]. In [10], some important characteristics among different ESSs have been compared. Moreover, different types of ESS based power and energy capital costs and operating and maintenance costs have been analysed.

ESSs have broad and various specifications, applications, and limitations. For example, flywheel energy storage systems (FES) present high efficiency, stability, and power density with a good fast response time [20], but have some disadvantages, including high self-discharge rates, low overall magnitude, safety concerns, and high costs. Another example, compressed-air energy storage (CAES) systems, present some advantages such as grid-scale potential, long life, flexibility with a relatively low operation and maintenance costs, and low self-discharge rates [21]. Nevertheless, the efficiency of these systems is moderate [22] and the geological suitability of the storage site is a key issue. Generally, electrochemical systems are efficient, convenient, easy to use, reliable, and need low maintenance, but generally can present environmental concerns, high cost (compared to utility power) and the need for critical materials (e.g., Li and Co), and low energy density presents a further limitation of some batteries [23]. Several surveys report that electrochemical energy storage systems are the solution for assisting intermittent renewable energy generators, with short-to long-time-scale energy storage, because of their site versatility, modularity that allows wide scalability, ease of operation, and static structure [24], [25], [26]. In fact, they are located in a wide area of the power/duration diagram beyond the capabilities of other storage technologies (Fig.1.1). Moreover, they are expected to have wide implementation in the coming years as distributed storage systems. Accordingly, substantial funds have already been allocated to guarantee their scientific and technological development. Forecasts indicate a growth to 150 GW in installed power, which corresponds to 10,000 times more than capacity in 2014 [27].

Among electrochemical systems, redox flow batteries (RFBs) represent one of the most recent technologies and a highly promising choice for stationary energy storage [28]. In contrast to conventional batteries, RFBs can provide multiple services, such as peak shaving and response for frequency and voltage regulation, for either solar or wind power generation and the power grid. For these reasons, they are now considered a safer alternative to Li-ion stationary systems (for example for indoor use in buildings) [29]. Moreover, because devices complying with local legislation on fire safety and with electrolyte management will have competitive advantages, the standardization of RFBs has been progressed via the International Electrotechnical Commission

[30] as an addition to updated grid storage standards (Sec.2.5).

The grid-scale deployment of RFBs in a multi device energy market with many service providers has been hindered by a perception that the technology is still in an early stage of development, and by the relatively high capital costs of the electrolytes (e.g. vanadium in the case of the present thesis) and ion exchange membranes. However, market conditions have become more profitable for RFB manufacturers. The rising cost of wind power curtailment has been incentivised by heavy investment in China [31], while the electrolyte leasing models have relieved the impact of vanadium costs [32]. In addition, the price of cobalt in Li-ion cell cathodes has more than doubled since 2016 [33], which is due to the "high-risk" status of its supply chain [34]. Work continues on the commercialization of other RFB systems, such as zinc-bromine [35], and the research for feasible organic chemistries continues [36], [37], [38].

The future success of such systems could overcome present limitations. Whilst the principles of this technology are well known and established, the path to scale-up and development has often been unclear to researchers [39], and the full potential of RFBs has yet to be realized. Actually, progress is currently restricted due to the scarcity of electrochemical engineering studies on cell design, reaction environment, and their relation to performance and efficiency [39]. Indeed, according to the recent authoritative review [40] "... the majority of publications have been restricted to short term studies of small electrodes in the laboratory; very few contributions have considered pilot-scale devices and the effect of cell design, electrode structure, reaction environment and operational conditions on performance. ...". The objective of this thesis is to contribute to filling this gap by reporting the experimental and numerical knowledge obtained on an industrial-size 9 kW/27 kW h vanadium redox flow battery. In fact, today the most researched and successful technology is the all-vanadium based RFB (VRFB), the only technology that has reached effective commercial fruition. The present thesis work is part of a project within the Department of Industrial Engineering (University of Padua), developed at the Energy Storage and Conversion Laboratory that aims to be a path from advanced laboratory tests (typically conducted at chemist laboratories) to grid-scale VRFB systems.

Chapter 2

Introduction

2.1 Redox Flow Batteries

A battery is an electrochemical device that is capable of storing chemical energy and generating electrical energy by a reaction of oxidation and reduction between two active materials. A redox flow battery (RFB) works on a similar principle, but with the distinction of having the active materials split from the region in which the electric current occurs (cell) [41]. RFBs are sometimes referred to as electrochemical regenerative fuel cells, because they involve the supply of an external stored fuel and oxidant in the form of two soluble redox couples by generating electrical energy [42]. This is due to the oxidation and reduction reactions at inert electrodes, which are separated by the ion exchange membrane in an electrochemical cell. However, RFBs are distinguished from fuel cells by the reversible nature of the electrochemical reactions; that is, they can generally be considered as a secondary battery and so they can be recharged many times without replacing the electroactive material.

A general RFB is comprised of two liquid electrolytes that are stored in two different tanks and pumped through the cell to produce energy, as shown in Fig.2.1. The oxidation at one electrode remove electrons and ions from one electrolyte, while the reduction at the other side recombines them into the other electrolyte. The ions migrate from the anode to the cathode through a solid electrolyte that is impermeable to electrons, which are forced through an external electric circuit providing the electric power exchange. As the detailed study in the following sections will show, a polymeric membrane constitutes the electrolyte and the electric power is delivered to a DC/AC converter and in turn to the grid [43]. A completely soluble redox couple and inert electrode avoid undesirable electrode processes, such as structural changes of the electrode, which affect other secondary battery systems. Energy storage capability is determined by the concentration of the reactants and the size of the storage tanks, while the power is determined by the number of individual cells and their electrode area [44].

This enables the independent sizing of energy and power, which is one of the most important advantages of these batteries. This feature provides RFBs with the unique ability to perform specific power and energy requirements for each practical application. In practical terms, the energy of existing plants is usually between 10^2 and 10^7 Wh, exceeding that of most electrochemical energy storage (ECES) by at least by one order of magnitude [43]. In this regard, RFBs and fuel cells (FCs) have more advantages than other electrochemical technologies, where storage times of longer than 4–6 h are required. Other important advances can be identified, as follows:

- no self-discharge appears because the two electrolytes are stored in two different tanks;
- the cell temperature can be easily monitored by regulating the electrolyte flow to avoid temperature rise (≥ 50 °C), compared with other batteries such as the sodium sulfur batteries;
- the *SOC* (state of charge) can be easily measured through an open cell voltage signal;
- RFBs are capable of fast response allowing them to be applied for the stable supply of renewable energy [45];
- short overload does not damage the cell.

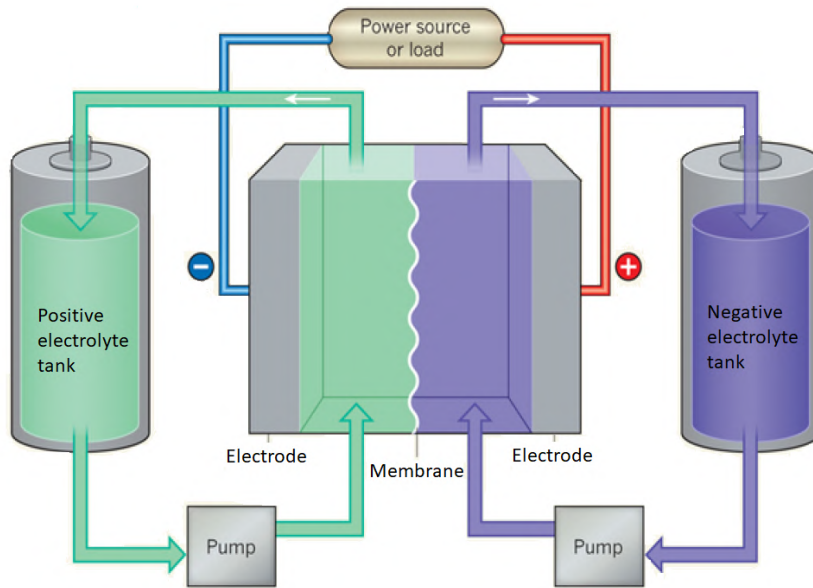


FIGURE 2.1: Redox flow battery scheme: RFB stack and electrolyte tanks are separated.

Conversely, some disadvantages are still present, as follows:

- the power and energy density are relatively low compared to other technologies, due different factors such as slow transport properties of the liquid electrolyte (transport losses), and relatively low current density and cell voltage due to the limited molar concentration of the reactant species into the electrolyte;
- Because electrolytes are conductive, parasitic shunt currents appear, i.e. electric currents along the flow channels, which produce losses and affect the overall battery efficiency.

It can therefore be inferred that the main problem is their size, especially the electrolyte storage tanks that can be quite cumbersome, and this could be a limitation where space is limited as in automotive field. For these reasons, RFBs are more attractive for stationary storage applications, load-leveilling, and stand-alone applications [46].

2.2 Electrochemical background

The usable thermodynamic potential of a system (like the chemical system discussed here) is described by the Gibbs free energy [47] that describes how much energy can be converted into an arbitrary other kind of energy. It is the difference between the total energy content H and the entropic (non-usable) term TS :

$$G = H - TS \quad (2.1)$$

differentiation gives

$$dG = dH - TdS - SdT \quad (2.2)$$

Derivatives of the enthalpy H and the entropy S are problematic because they cannot be measured directly. Therefore, the following steps aim to replace them with constant values (later called "enthalpy and entropy of reaction"). The enthalpy H is defined by the internal energy Θ and the mechanical work pV_{sy} as follows:

$$H = \Theta + pV_{sy} \quad (2.3)$$

$$dG = d\Theta - TdS - SdT + pdV_{sy} + Vdp \quad (2.4)$$

In a last step, $d\Theta$ can be further specified as

$$d\Theta = TdS - W_{tot} = TdS - (pdV_{sy} + W_{el}) \quad (2.5)$$

where the work W_{tot} comprises mechanical and electrical work [47]. Inserting Eq.2.5 into Eq.2.4 and cancelling out dS and dV_{sy} yields the final expression for the partial Gibbs free energy, as follows:

$$dG = -SdT + V_{sy}dp - dW_{el} \quad (2.6)$$

If the electrochemical energy conversion happens at constant temperature and pressure, the assumption that dT and dp are 0 can be made [47], and one obtains the theoretical maximum electrical work $W_{el} = -\Delta^R G$. The expression Δ^R is used in thermodynamics to indicate reaction balance values. It is useful to apply energetic values on molar quantities, which is will be labelled by the subscript "mol."

The electrical work W_{el} can be described as an electrical charge ι , which has moved against an electrical potential change $\Delta\varphi$:

$$W_{el} = \Delta\varphi\iota \quad (2.7)$$

As charge is quantized and consists of single elementary charges it can be expressed as follows:

$$\iota = n_{mol}Fz \quad (2.8)$$

where n_{mol} is the number of particles in mol and F the Faraday constant that describes the charge of one mole of particles. In equilibrium, i.e. without current, the sum of both electrodes' electrical potentials is referred to as the open circuit voltage E_0 of an electrochemical cell [47]. Combining Eqs.2.7 and 2.8 and inserting the molar energy [J mol^{-1}] yields:

$$\Delta\varphi = E_0 = -\frac{\Delta^R G_{mol}}{zF} \quad (2.9)$$

The variable z is the stoichiometric number of exchanged charges per reaction in mol_{e-}/mol_R .

The subscript E_0 is the open circuit voltage, equilibrium conditions without current flow. This voltage is characteristic for each individual electrochemical system and only depends on the thermodynamic state. As E_0 of most electrochemical cells amounts to approximately 1 V, which is too low for many applications, most practically used energy converters are assemblies of several cells in series. The molar Gibbs free energy $\Delta^R G_{mol}$ describes how much energy has to be expended or is released by the reaction. It is calculated by summarizing the reaction enthalpy $\Delta^R H_{mol}$ and entropy $\Delta^R S_{mol}$. As these values depend on the temperature and pressure conditions, the Gibbs energy is usually taken at (chemical) standard conditions of 1 bar and 298.15 K, indicated by the superscript 0. It can be derived from the reaction enthalpy $\Delta^R H_{mol}^0$ and the reaction entropy $\Delta^R S_{mol}^0$, which can be found in the literature for many species:

$$\Delta^R G_{mol}^0 = \Delta^R H_{mol}^0 - T\Delta^R S_{mol}^0 \quad (2.10)$$

To account for temperatures and pressures that differ from the standard state, $\Delta^R G_{mol}^0$ can be corrected by adding the temperature dependence of the heat capacity and the pressure dependence [48].

2.2.1 Nernst-equation

In the previous sections, the Gibbs free energy was considered a function of the two independent variables T and p . However, it also depends on the chemistry of the active species, i.e. their concentration and molecular interactions, as they are usually part of a mixture of different species. These properties are described by the chemical potential Υ , which defines how the free energy changes with the number of particles in the system. Every species i in each phase has

an individual chemical potential. It is the partial differential of G when temperature, pressure, and the molarities of all the other species $\Xi_{j \neq i}$ stay constant [49]:

$$\Upsilon(i) = \left(\frac{dG}{d\Xi(i)} \right)_{T,p,\Xi(j \neq i)} = G_{molar}(i)(T,p,\Xi(i)) \quad (2.11)$$

To obtain the Gibbs free energy of a redox reaction, the following reaction couple taking place at the cell electrodes is considered:



By using the Van 't Hoff equation,

$$\Delta^R G_{mol} = \Delta^R G_{mol}^0 + KT \frac{\alpha(M)^m \alpha(N)^n}{\alpha(A)^a \alpha(B)^b} \quad (2.13)$$

is the activity that takes all molecular interactions to all the other solution components into account [47], [49]. The activity is correlated to the so-called activity coefficient $\varpi(i)$ and the normalized concentration $c(i)/c(0)$ of the component with $c(0) = 1 \text{ mol l}^{-1} = 1$:

$$\alpha(i) = \varpi \frac{c(i)}{c(0)} \quad (2.14)$$

$$0 \leq \varpi \leq 1 \quad (2.15)$$

For ideal (i.e. very dilute) solutions ($\leq 0.01 \text{ M}$), the activity coefficient approaches the value 1 so that the activity equals the molar concentration.

In combination with Eq.2.9, the open circuit voltage can be expressed with the so called Nernst equation [49]:

$$E(\alpha_i) = E'_0 - \frac{KT}{zF} \ln \left(\frac{\alpha(M)^m \alpha(N)^n}{\alpha(A)^a \alpha(B)^b} \right) \quad (2.16)$$

To consider the temperature dependence, Eq.2.16 is coupled with Eq.2.10 resulting in:

$$E(T, \alpha(i)) = E'_T - \frac{KT}{zF} \ln \left(\frac{\alpha(M)^m \alpha(N)^n}{\alpha(A)^a \alpha(B)^b} \right) = E'_0 + \frac{\Delta^R S}{zF} (T - T_0) - \frac{KT}{zF} \ln \left(\frac{\alpha(M)^m \alpha(N)^n}{\alpha(A)^a \alpha(B)^b} \right) \quad (2.17)$$

Eqs.2.16 and 2.17 highlight that a potential difference can also appear with equal and opposite electrode reactions, due to the different concentrations of the same species at the two electrodes. The gradient of concentration in this case gives rise to a diffusion phenomenon of ions (ex. protons) that stabilizes when the voltage due to the charge separation balances the potential difference due to the concentration.

2.2.2 Cell overpotentials

One of the most important aspects of electrochemical devices is their reaction kinetics. On the one hand it governs the reaction rate and thereby the power exchanges, while on the other hand the kinetics is related to efficiency losses of the device. Current and reaction rate are usually described as densities per cell area, expressed with small characters. Following Eq.2.7, the current density at an electrode can be written as follows:

$$j = z \times F \times j_r \quad (2.18)$$

In this equation, j_r describes the reaction rate in $\text{mol m}^{-2} \text{ s}^{-1}$, while the quantity of moles per reaction and the Faraday constant convert this into a current density. During the state of thermodynamic equilibrium there is no net reaction and thus no visible current. However, the reaction and its reverse reaction still take place with an equal rate, thereby cancelling each other

out to 0 [49]:

$$j = j_1 - j_2 = 0 \quad (2.19)$$

In the above case, the current j_1 and j_2 are referred to as the exchange current I_0 . When the electrical circuit is closed and a net current is allowed to flow, the effect of polarization is observed. This is caused by different partial steps that form the total reaction, such as diffusion processes, adsorption, or current exchange. The result is a voltage change from the equilibrium potential by the so called overpotentials Υ at each electrode i , which changes to overcome these reaction limitations [49]. In the case of discharge, the overvoltage reduces the overall voltage E_o . When charging they combine to a voltage higher than E_o :

$$\Upsilon(i) = \Delta\phi(i) - \Delta\phi(i, 0) = |\Upsilon(i)| = |E_o| - |V| \quad (2.20)$$

The kinetics of an RFB is usually described by three different overpotentials: activation, ohmic, and concentration overpotentials. At low current densities, the distinctive voltage loss is caused by the activation overpotential Υ_a . This means that the reaction has to overcome a certain energetic barrier the activation energy to transfer an electron from the electrode to the electrolyte, and vice versa [49]. The fundamental equation describing the effect of activation overpotential on the actual current density is known as the Butler-Volmer equation:

$$j = j_0 \left\{ \exp \left[\frac{\rho z F \Upsilon_a}{K T} \right] - \exp \left[- \frac{(1 - \rho) z F \Upsilon_a}{K T} \right] \right\} \quad (2.21)$$

j_0 denotes the exchange current density while the two terms in brackets represent the anodic and cathodic reaction, respectively. The symmetry factor ρ describes how fast the forward reaction takes place in comparison to the backwards reaction; for an RFB its value is usually close to 0.5 [43]. The number of electrons per reaction is z . At low activation overpotentials the current density can be approximated as linear [50]:

$$j = \frac{j_0 z F \Upsilon_a}{K T} \quad (2.22)$$

As a linear function, this can also be expressed as an ohmic law having a charge-transfer resistance R_t [50]:

$$R_t = \frac{K T}{j_0 z F} \quad (2.23)$$

At high negative or positive overpotentials (depending on the reaction direction), one of the two terms of Eq.2.21 becomes very small and can be neglected. The resulting functions reduce to the Tafel equations and enable the following expression for Υ_a :

$$\Upsilon_a = \frac{K T}{\rho z F} \ln(j_0) - \frac{K T}{\rho z F} \ln(j) \quad (2.24)$$

The first part represents the constant activation overvoltage at the exchange current density, while the second part describes the logarithmic dependence of overvoltage of the actual current. In addition to activation overpotentials, every cell also has an ohmic loss contribution. This is mainly caused by charge transfer through the membrane and electrolytes, but also includes the resistive behavior of all the electrodes, plates, and other conducting parts. The ohmic overpotential Υ_o can be derived as [51]:

$$\Upsilon_o = \Sigma R j A \quad (2.25)$$

In this equation, the subscripts ΣR describes the sum of all ohmic resistance contributions, such as membrane, electrolytes, electrodes, current collector, and contact interfaces [50].

When the current density is further increased, the limited diffusion of species comes into account. As all the reactants and products have to move to/from the reaction sites, there is a rate-limiting effect due to the finite diffusion velocity of the ions [47].

This results in a depletion of reactant or an accumulation of products at the reaction sites,

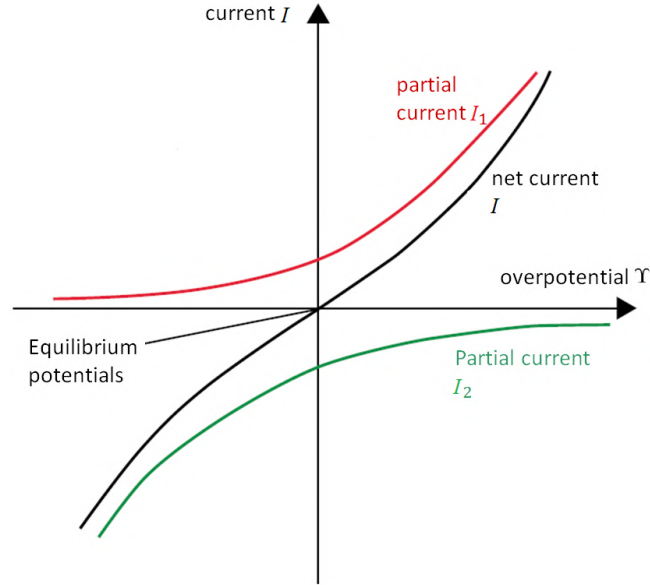


FIGURE 2.2: Effect of overpotentials on the current (figure based on [53]).

quantified by the concentration difference between the bulk concentration C^0 , and the concentration at the reaction site C . The effect is the so-called concentration overpotential. Three transport mechanisms influence this process: diffusion, migration, and convection. The former describes a movement driven by chemical potential, migration refers to transport driven by an electrical field, and convection is the macroscopic movement of fluid electrolyte that transports species. In general, the concentration overpotential can be quantified as [52]:

$$\Upsilon_t = \frac{KT}{\varrho z F} \ln\left(\frac{C_R C_P^0}{C_R^0 C_P}\right) \quad (2.26)$$

In this equation, C_R^0 and C_P^0 are the bulk concentrations of the corresponding rate-limiting reactant and product. The actual concentrations are denoted as C_R and C_P , respectively. In fact, all three mechanisms are physically present at every point of operation and only their influence on the electric circuit changes. Summarizing, the total overpotential of an RFB is as follows:

$$\Upsilon = \Upsilon_a + \Upsilon_t + \Upsilon_o \quad (2.27)$$

Inserting the concentration overpotential into the Butler-Volmer equation, one obtains a more complete description of the reaction kinetics, as follows:

$$j = j_0 \left\{ \frac{C_R}{C_R^0} \exp\left[\frac{\varrho z F \Upsilon_a}{KT}\right] - \frac{C_P}{C_P^0} \exp\left[-\frac{(1-\varrho) z F \Upsilon_a}{KT}\right] \right\} \quad (2.28)$$

A good overview of the current-overvoltage behavior is obtained by the visualization of the Butler-Volmer equation, displayed in Fig.2.2

At equilibrium state both current densities have the same value, thereby compensating each other. Examining higher negative or positive over voltages, a rising net current density is evident as one reaction direction dominates the other.

Around the equilibrium state the trend is nearly linear, while at sufficient high values of Υ it is of logarithmic shape. The three overpotential effects can be clearly identified in Fig.2.3, which shows the polarization curve of an RFB. Here, the dependency of cell voltage on the current density is displayed, which is an often-used instrument to understand the behavior of electrochemical energy converters.

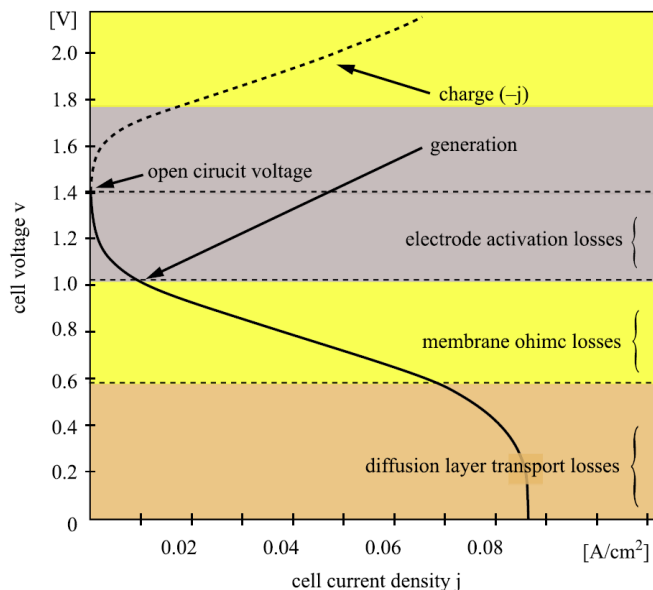


FIGURE 2.3: Polarization curve of a redox flow battery for charge and discharge. The corresponding dominating loss mechanisms are highlighted.

2.2.3 RFB historical overview

The RFB concept is relatively well-established, with the vanadium (V) redox couple first being mentioned in 1933 by P.A. Pissort, in France [54], and a patent on a titanium chloride redox flow cell being registered by Walter Kango (Germany) in 1954. It was firstly investigated by S. Ashimura et al. in Japan in 1971 [55]. Many potential redox couples (such as Fe-Cr) have been selected by NASA since the first effective proposal of the redox flow cell concept by Thaller, starting with Fe-Ti electrolyte [56]. However, significant development has only really ensued since the 1980s and 1990s, mainly in Japan, with the NEDO projects that aimed to complement pumped-hydro plants [57], [58].

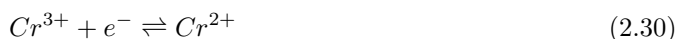
The all-vanadium RFB was developed in 1978 in Italy by A. Pellegri and P.M. Spaziante [59], but without further significant development. The first known commercial development of RFBs using vanadium in both half cells occurred at the University of New South Wales (UNSW), Australia, by Skyllas-Kazacos, who registered a patent in 1986 [60]. In the last decade, more attention was focused on RFB systems and more producers appeared in different countries. This is especially the case for VRFBs with minor importance in Zn-Br₂ and Br-polysulfate systems. A recent area of research in the RFB industry is the identification, synthesis, and modification of novel organic-based flow batteries [61], which use active materials based on organic molecules in at least one electrode reaction.

2.2.4 Actual RFB technologies

Here, a brief review focused on the main redox species for RFBs is presented, with a synthetic overview of different categories of redox couples, together with a brief consideration of future high-energy chemistries. The redox species are the most important component in RFBs, on which all performance depends, with power and energy density dependent on redox potential and solubility, respectively. The cell OCV is determined by the equilibrium potentials of the active species in the cathode and anode. The capacity depends on the effective concentration (i.e. the solubility) multiplied by the number of electrons transferred during the redox reactions (z) [62]. The first research on the RFB was mostly based on metal and halogen ions. In recent years, non-aqueous system has become a hotspot, providing a wider electrochemical range of various redox species [63], while molecular engineering is used to modify the redox couples to achieve higher solubility and higher redox potentials [64]. In addition, other approaches tend to combine RFBs with the Li-ion concept [65], [66].

Iron/Chromium

In this chemistry, the Fe^{3+}/Fe^{2+} and Cr^{3+}/Cr^{2+} redox couples are used as the cathodic and anodic electrolytes, with a small cell open circuit voltage of 1.18 V.



The Fe^{3+}/Fe^{2+} redox couple shows quite good reversibility and fast kinetics. However, the bad kinetics of Cr^{3+}/Cr^{2+} usually require a high operating temperature, which significantly increases the cost [67]. These features make Fe/Cr RFBs inferior to VRFBs, and they have therefore been abandoned in favor of others chemistries.

Bromine/polysulphide

In these RFBs, the electrolytes during the discharge cycle are constituted of sodium bromide in the positive side and sodium polysulfide in the negative [68]. These chemical species are quite abundant, inexpensive, and are very soluble in aqueous media. During charging the bromide ions are oxidized to bromine and complexed as tri-bromide ions. At the positive side the following reaction occurs:



At the negative half-cell, the sulfur presents as soluble polysulfide anion and is reduced to sulfide ion:



The electrolyte solutions are separated by a cation exchange membrane to prevent the sulfur anions reacting directly with the bromine, and the electrical balance is obtained by the transport of sodium ions through the membrane. In discharge, the sulfide ion is the reducing element and the tri-bromide ion is the oxidizing one. The *OCV* is approximately 1.5 V and varies depending on the *SOC* of the active species. The main difficulties with this system's redox couple are as follows:

- the different nature of the electrolytes causes cross-contamination of both electrolytes over time;
- the difficult maintained of electrolyte balance with a fixed composition;
- the possible deposition of sulfur ions in the membrane;
- the need to avoid $H_2S(g)$ and $Br_2(g)$ evolution.

These systems were successfully evaluated by the former Technologies Regenesys Ltd. [44], but in 2004 they stopped and the technology has since been replaced by VRFB.

Zinc-bromine

The $Zn - Br$ battery is another quite successful RFB system, which has been demonstrated for decades [69]. The cathodic reaction is the reduction of Br_2 and the oxidation of Br^- , while Zn strips and plates into the anode. The main electrochemical reactions are listed as follows:



in the cathodic and the anodic sides, respectively.

$ZnBr_2$ has a high solubility (higher than 2.0 M), but Br_2 is less miscible in aqueous solvent, which substantially limits the possible energy density of the $Zn - Br$ battery. In addition, the stability of Zn is affected by the corrosivity of Br_2 .

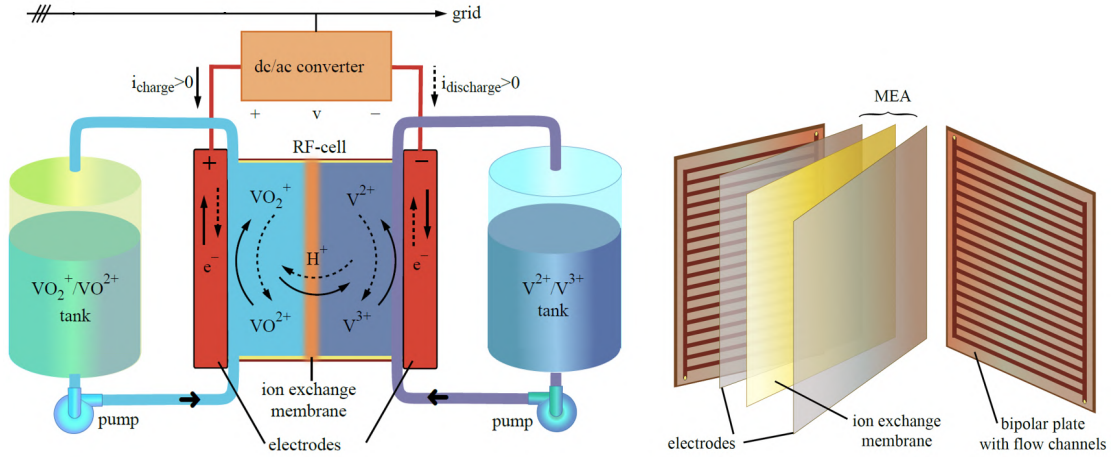
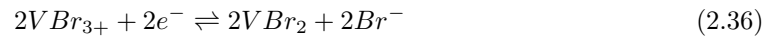


FIGURE 2.4: Diagram of a Vanadium Redox Flow Battery.

Vanadium-bromine

The vanadium-bromine technology employs VBr_3/VBr_2 and $Br^-/ClBr^-$ in the negative and positive electrolytes, respectively, with HBr and HCl as a supporting electrolyte [70]. The main electrochemical reactions are as follows:

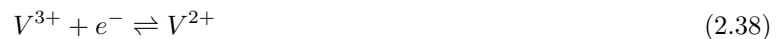


in the cathodic and the anodic sides, respectively. The relatively high solubility of vanadium bromine (between 1 and 3 M) compared with vanadium sulfate tends to increase the energy density. Conversely, in the vanadium/bromide system, Br_2 vapor emission constitutes the main disadvantage due to being corrosive and poisonous.

2.3 All-vanadium

The most researched and successful RFB is the all-vanadium RFB (VRFB), the only technology that has achieved an effective commercial use [71], and is the technology studied in this thesis.

It uses vanadium/vanadium dissolved in aqueous sulfuric acid (5 M). By using the same metal ions in both electrolytes, the electrodes and membrane are not contaminated and the cell capacity does not decrease with time, allowing for a longer duration of the battery. A VRFB cell is constituted by two half-cells, each with a solid electrode in contact with the liquid electrolyte. The separation between the half-cells is provided by a solid electrolyte membrane. Fig.2.4. Electrochemical half reactions of a VRFB are as follows:



The standard OCV of a VRFB cell is $E_o = 1.4$ V at 25 °C. During charging at the positive half-cell tetravalent vanadium $V(IV) = (VO^{2+})$ is oxidized to pentavalent vanadium $V(V) = VO_2^+$, while at the negative half-cell trivalent $V(III) = V^{3+}$ is reduced to bivalent $V(II) = V^{2+}$. The hydrogen ions $2H^+$ move through the solid electrolyte membrane to maintain the electrical neutrality of the electrolytes. Further explanation will be given in the following sections.

2.3.1 Cell configuration

With regard to the flow configuration of the cell, two designs are used: “flow-thorough” and “flow-by” configurations [72]. In the first case, the electrolytic solutions permeate directly into the porous electrodes from the frame borders, current collectors have no flow channels, and the electric current is perpendicular to the electrolyte flow [73], [74]. The flow-through configuration is only possible with a thick porous electrode. In the second case, the electrolytic solutions are fed into the porous electrode from flow channels grooved in the current collectors with an increment of the active surface area, by enhancing the mass transport in comparison to the planar electrodes, which are more commonly used.

Static, inert turbulence promoters can be placed in the flow channel to keep the separation between electrode and membrane uniform [40]. In this configuration, the overall direction of fluid flow in the cell is perpendicular to the current and parallel when it passes for a short distance across the porous electrode [75]. Similarly in fuel cells, this configuration has been applied to RFBs by milling interdigitated [76] and serpentine channels in the bipolar plates (BPs) [77]. These flow fields can also be cut from the electrodes [78]. Perforated electrode have also been proposed [79]. Some studies (in a small cell) have demonstrated that these configurations increase the flow across the porous electrode that results in a significant increase of performance and reduced pressure drop in the cell. Nevertheless, larger cell over potential losses are generated due to reduced electrical contact area and to a thick BP. In fact, the results with large electrodes remain to be investigated because those studies are usually performed in small-scale single cells.

2.3.2 VRFB topologies

In a VRFB, the cells are typically connected in series to form the cell stack (conventional configuration [74]), with the number of cells stacked depending on the nominal required output voltage. Each cell is separated from the adjacent one by interposing conductive BPs. Then, the BP is in touch with the negative electrode of one cell, while on the opposite face, it is in touch with the positive electrode of the next cell. The constitution of a typical cell stack is shown in Fig.2.5. An alternative approach, conceived some years ago, consists of the parallel electric connection of the cells forming small stacks. In this case, each current collector has the same polarity of two consecutive cells (monopolar plates) on both sides. In turn, several of these stacks are connected in series to increase the overall voltage, while external piping feed them in parallel. This configuration is an alternative VRFB topology Fig.2.5.

In [74], the group at Padua (where the author works), evaluated a performance model of the cell shunt current (Sec.5.2), and hydraulic losses (Sec.8.1.4) have been developed and assembled with the aim of analyzing their differences for both conventional and alternative stacks. Results demonstrated that alternative configuration can produce markedly lower losses than a conventional one, thus matching higher efficiency, reasonably by 10 %, which means that an overall battery efficiency of approximately 85% or more can be achieved. Conversely, the alternative configuration is more cumbersome, with more piping and requiring a larger space, compared to the conventional design in the case of a kW-scale system.

2.3.3 Circulation of the liquid electrolytes

Single stack flow circulation modes

The circulation of the liquid electrolytes through the cell stack can be performed in two modes: parallel and sequence modes (Fig.2.6). The first option is the most common and advantageous configuration, where the internal manifolds simultaneously feed the cells. The electrolyte flows from the bottom to the top to remove gas bubbles. However, this solution can become critical when made in high-voltage batteries, due to the presence of an electric by-pass current, known as the “shunt current” (Sec.5.2), along the electrolytes flow path in the manifolds. This would result in decreased efficiency of the battery. The parallel mode can be performed in two main modes, mode A (like IS-VRFB mode) and mode B (Fig.2.6). According to the author’s opinion, mode B can be preferable regarding the uniformity of feeding in each cell due to the uniform pressure drop along the cells. In the second mode, the positive and negative electrolytes flow subsequently

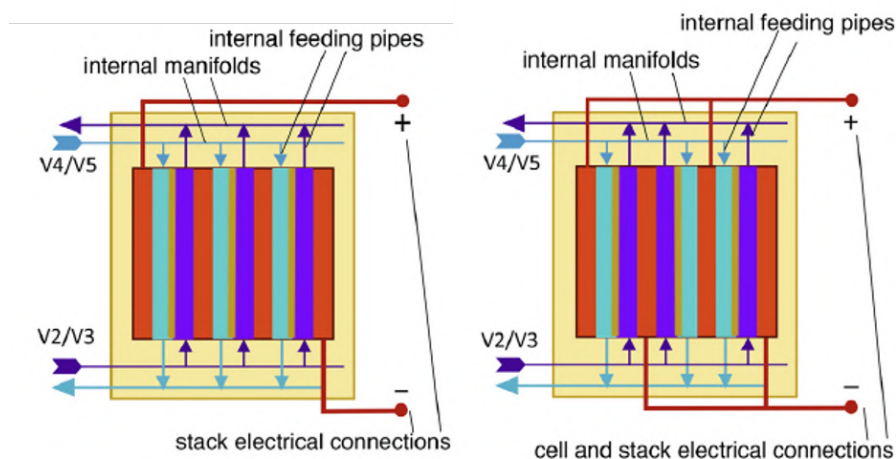


FIGURE 2.5: VRFB topologies; left: conventional series stack (CSS), right: alternative parallel stack (APS).

through all cells that flow from the end of one cell to the entrance of the subsequent cell. In this way, the electric by-pass currents are significantly reduced and only a residual current remains [80]. However this configuration is not recommended [81]; in fact, the electrolyte concentration gradually changes along the cells, appearing as a higher pressure drop and less uniform flow [40].

There are two possible modes for the circulation of the liquid electrolytes in sequence: the equicurrent and the countercurrent modes [82]. In the first case, the inlet and outlet of both electrolytes are at the same side. In the second case, the inlet of the positive side is at the same location as the outlet of the negative side. The countercurrent mode can be considered more advantageous than the equicurrent case because it can reduce cell voltage variation along the stack and water transfer between the cells, while increasing the charge efficiency [83].

Multiple stack flow circulation connections

Multiple stacks can mainly be connected in two ways in terms of their hydraulic connections: in parallel and in cascade. The first is the most common configuration, where the individual stacks in the system are connected to the tanks in parallel. All the stacks operate with the same inlet state of charge. This configuration is more commonly used in medium-sized RFBs [40]. In the cascade configuration, the stacks are connected hydraulically in series and the concentration of the active species is different from one stack to the others. This configuration is usually implemented in large systems with planar electrodes, to reduce the amount of piping, the electrical connections, and their relative cost [40].

Configuration of the storage tanks

For the configuration of the tanks, there are two possible options: “recirculation mode” and “batch mode.” In the first case, two tanks are used to store the electrolytes separately; one tank for the positive and the other for the negative, and each tank is provided with one circulation pump. This is the most common solution. Each electrolyte is pumped from the tank to the stack through a closed hydraulic circuit. In this mode, having only one tank for each electrolyte means it is possible to store more energy in a given volume, but there is a charge dilution over time. In fact, in this case a uniform concentration is maintained that changes gradually during charge and discharge. Conversely, the “batch mode” configuration works with four tanks, two for the positive electrolyte and two for the negative. The charged electrolyte is pumped from one tank to the stack where the electrochemical reactions occur, and then they come back to the second tank. Therefore, in this mode when switching from charging to discharging conditions (or vice versa), the direction of the liquid flow must be inverted. In this case, the volume occupied in each tank is an indicator of the state of charge, and the two electrolytes stored in the charged tanks are maintained during the whole discharge in a state of full charge.

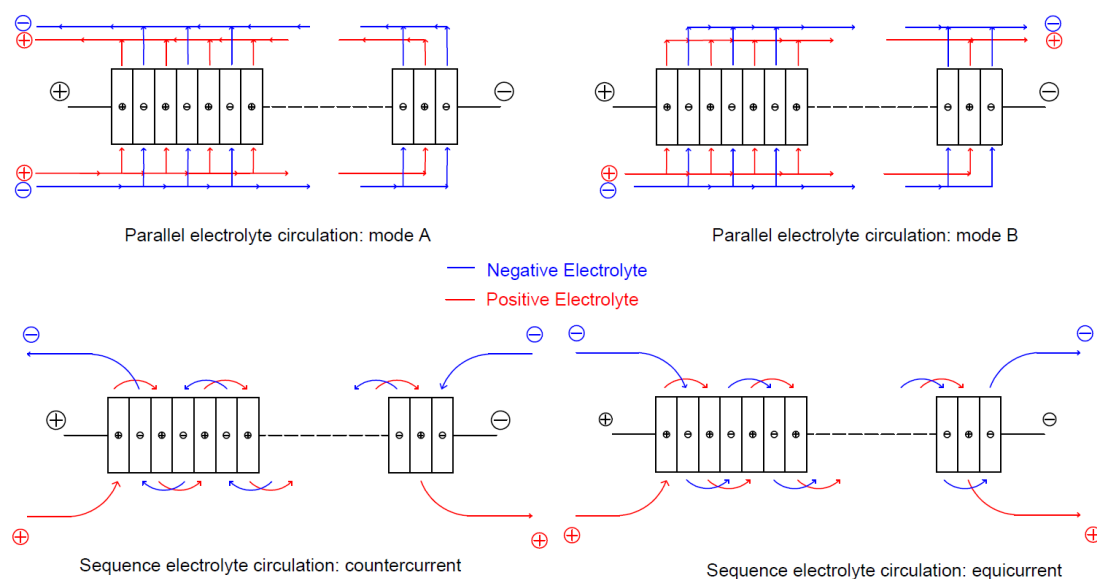


FIGURE 2.6: Single stack flow circulation modes; top-left: parallel electrolyte circulation (mode A), top-right: parallel electrolyte circulation (mode B), bottom-left: sequence electrolyte circulation (countercurrent), bottom-right: sequence electrolyte circulation (equicurrent).

An alternative configuration is constituted by some active and/or passive dividers within a single tank that allow the reduction of the electrolyte mixing of charged electrolyte with the discharged one [84].

2.3.4 Vanadium Redox Flow Batteries Components

Electrolytes

The electrolyte, which includes vanadium ions, acids, counter anions, and water, are key components for VRFBs because they are the most expensive components [85] and have a dominant influence on VRFB performance. Ideal electrolytes should have a high concentration of vanadium, a low viscosity, chemical and thermal stability, facility for chemical analysis to monitor the state of charge, a high ionic conductivity, low cost, quite high abundance, and be safe to use. Clearly, these properties are determined by the chemical properties of components and some compromise must be achieved at certain molar concentrations by using additives or acid mixtures that can enhance some of these features. In particular, the concentration, the electrochemical activity, and the stability of vanadium ions determine the energy density and the reliability of VRFBs [86]. Starting from the work of the pioneers of VRFBs, vanadium electrolyte technology has improved, and is evolving towards a more reliable and more cost-effective system. Some reviews on VRFB have been reported concerning recent issues on vanadium electrolytes [87], [88].

Generally, a high concentration of active species means higher energy capacity and higher volumetric energy density, and an increment of the current output by reducing secondary reactions. Saturated solutions can also be used in some systems, but in others care must be taken to prevent vanadium precipitation/crystallization. Accordingly, inhibitors can be employed to minimize the thermal precipitation of solids in electrolyte samples. In particular, low temperature stability of negative half-cell electrolytes is analyzed in [89]. Recently, Roe et al. [90] have suggested stabilizing a 3 M vanadium electrolyte by adding 1 wt% H_3PO_4 + 2 wt% ammonium sulfate at 30 °C. Kausar et al. [91] have demonstrated that the $V(V)$ mixed with 1 wt% H_3PO_4 + 2 wt% ammonium sulfate is more stable at 50 °C compared with sodium hexametaphosphate, ammonium sulfate, and ammonium phosphate additives. Zhang et al. [92] performed a detailed study on the effects of various organic and inorganic additives regarding the stability of $V(II)$, $V(III)$, $V(IV)$, and $V(V)$ ions in sulfuric acid solutions, showing that polyacrylic acid

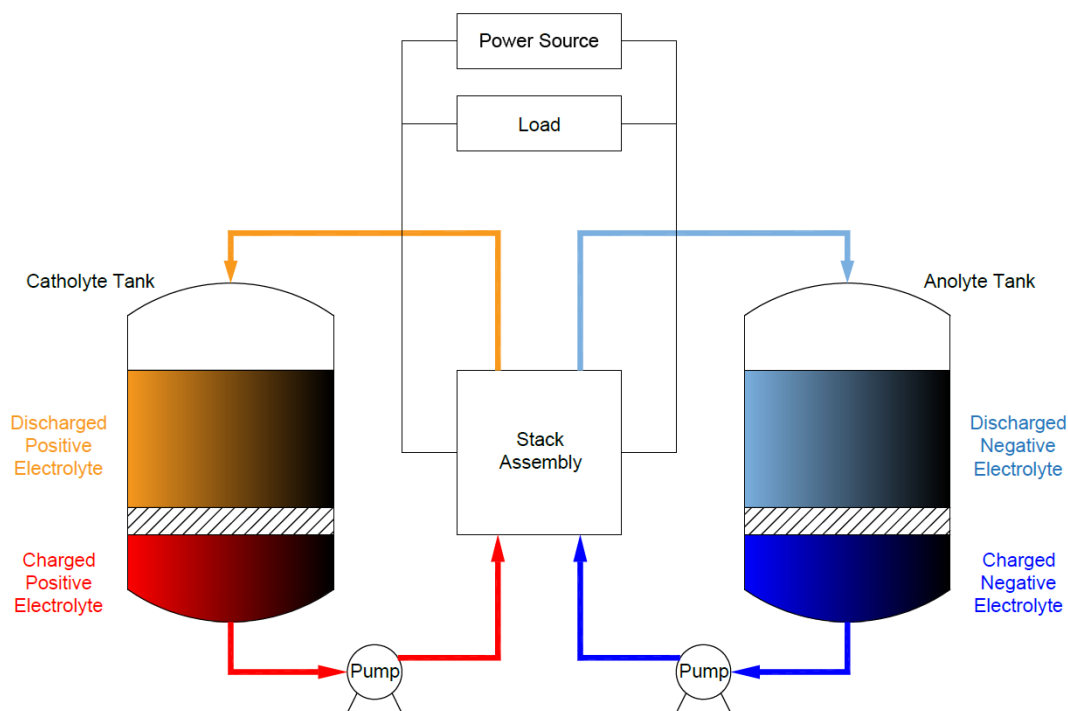


FIGURE 2.7: Embodiment of VRFB system illustrating a cross sectional illustration with electrolyte storage tanks including tank dividers.

and its mixture with CH_3SO_3H are one of the most promising candidates for VRFB electrolyte stabilizing agents.

In addition, as the properties of the electrolytes change with the SOC , it is important to consider the interactive effects of these changes. The importance of analyzing redox species in an electrolyte, preferably by an on-line, non-destructive technique, can be an important feature.

The electrolyte viscosity should be considered in the mass transport issue. As described by the Reynolds number, high mass transport rates are easier to achieve through low viscosity electrolyte. Moreover, the diffusion coefficient of vanadium species is related to the viscosity by means of the Einstein-Stokes relationship.

Electrolyte electrical conductivity affects the cell over potential, especially in saturated solutions, which can have relatively high resistivity. Moreover, the shunt currents are determined by the conductivity of electrolytes, as can be seen in Eqs.5.23, 5.24.

Vanadium electrolytes are usually based on H_2SO_4 solutions, sometimes with a small concentration of H_3PO_4 that allows the stability to increase [42]. Mixtures of sulfuric and methane sulfonic acids have also been proposed [93], as well as sulfuric-hydrochloric mixtures [94].

Complex electrolytes consisting of suspensions of percolating conductive particles have also been considered for VRFBs, for example for VO^{2+}/VO_2^+ redox couple [95].

Electrodes

The key components of all electrochemical cells are the electrodes coupled with separators and turbulence promoters. The electrodes provide the reaction sites and must possess high surface area, suitable porosity, low electronic resistance, and high electrochemical activity for the reactions [96]. In addition, VRFB electrodes should present chemical stability (usually in acidic or alkaline medium), resistance to oxidation, reasonable cost, the possibility of high current densities operation with an adequate mechanical strength and elastic modulus, coupled with a long cycling life. Generally, the electrode materials used in RFBs can be classified on the basis of structural geometry (two or three dimensional), flow mode (flow-by or flow-through), materials (carbon-based or metallic), electro catalyst coating (coated or uncoated), and thermal or chemical treatment (treated or untreated) [40]. The three-dimensional (3D) electrodes are

used to counteract the limitations of electrochemical cells with two-dimensional (2D) electrodes [97], [98]. However, 3D felts are preferred in VRFBs, due to the high surface area that facilitates fast reaction kinetics.

Several papers report the experimental characterization and modeling of reaction environments for different applications of electrodes [99], as well as their properties, performance, and characterization [100].

The most commonly used electrode material in VRFBs are graphitic or vitreous carbon materials [101].

Since the early days of VRFB development [102], graphite felt has been a favored material. Studies at the University of Southampton have reported the performance of a laboratory scale flow cell using graphite felt electrodes of 100 cm² active area [103]. In a 2013 review, Parasuraman et al. [104] described the materials for VRFB applications, particularly BPs, cloths, and felts made of graphite, for both the positive and negative half-cells. The surface of the graphite electrode used as an anode shows a slow disintegration due to the oxygen evolution during the overcharge as a result of a slow oxidation. Graphite felts demonstrate good stability as a cathode [105]. The graphite felt has also been used in VRFBs in both half-cell electrolytes [106]. Surface treatments of graphite electrodes are proposed to improve the reaction kinetics in RFBs [107], [108], [109], [110], [111] among which are: chemical etching [112], thermal treatment [113], chemical doping [114], and the addition of metallic catalyst sites to the carbon fibers [115]. Usually graphite fibers can be improved by treating them with sulfuric acid followed by heat treatment, increasing their chemical activity [116], [117], [118], [119]. Modified graphite felts have demonstrated their suitability to withstand oxidant environments, while maintaining a good electrical conductivity and a suitable electron-transfer surface [120], [121].

A marked trend in the use of graphite felt for VRFB applications is the incorporation of graphene flakes and carbon nanotubes, especially multi-walled carbon nanotubes into the electrodes, either as surface impregnations or as composites. Recent works include [122] and [123]. The VRFB incorporating graphite felt electrodes has been improved through the use of advanced electrode materials, and design to enhance their performance, for example by using a graphite felt electrode, which had received microwave treatment [124].

Wei et al. [125] reported the use of nanoparticles of copper deposited on the graphite felts in the VRFBs, which slightly improved the kinetics of the V^{3+}/V^{2+} redox reaction, obtaining higher energy efficiency in comparison with the battery without the copper catalyst.

Carbon cloth was also tested for the VRFB [126]. A disadvantage of these materials can be their oxidation and embrittlement after prolonged use. Thus, further investigations in RFBs are necessary, by using accelerated electrode degradation methods [127].

The hydrodynamics and mass transport characterization of graphite fibers, in addition to potential and current distributions, are a critical issue, as they play an important role in the kinetics of the desired electrochemical reactions, current efficiency, and energy consumption. Accordingly, advanced studies were performed by Maggiolo et al. [128], by using the Lattice Boltzmann method to obtain the optimal fiber orientation with regard to the diffusivity and the pressure drop minimization.

Bipolar plate

The BPs have two main functions in the VRFB: chemical separation of each cell and electrical connection between cells in series. They constitute the reversible cathodic and anodic compartment allowing the current to pass perpendicularly to the electrode active area. The BPs of a VRFB system are usually made from graphite and are vulnerable to breakage during battery operation [129]. Electrical contact to the felt is often achieved by mechanical pressure, which determines the electrical resistance of the inter phase. This can be a challenge regarding the uniformity of the felt materials for the long-term battery operation. Thermal bonding of the felt to the BPs can provide a solution to obtaining robust connections, but may compromise the electrode surface with regard to conductivity [40]. Another option can be represented by the adhesive conductive layer that connects the electrode with the graphite BP to form an assembly [130].

Recently, metal and composite BPs have been studied to solve these problems. However, metal BPs need a coating process (such as gold or titanium nitrate coating) to prevent corrosion

of metal in the electrolyte acid environment, which results in high cost and low productivity. In the case of the composite BPs, the problem of relatively low electrical conductivity should be reduced. In this regard, [131] reports the characteristics of the pyrolytic graphite and expanded flake graphite, focusing on the durability of the graphite coating and the carbon/epoxy composite BP in a sulfuric acid environment, with respect to the porosity of the felt. The electrical conductivity of the composite BPs can be improved using several methods. Lee et al. [132] suggested plasma superficial treatment on the carbon composites BP. In this case, the composite BP showed approximately a 70% increase of the electrical conductivity in comparison with the absence of the treatment. Despite this, it was not enough for the VRFB application due to the higher cost. They also suggested a coating method for the carbon composite BPs to reduce the superficial electrical contact resistance [133]. However, while this method is suitable for the PEMFC, it is not guaranteed for VRFB due to the sulfuric acid environment. In [134], a carbon composite BP for the VRFB has been realized considering its electrical and chemical stabilities against strong acids.

In [135], a corrugated carbon/epoxy composite BP for VRFBs was designed to increase the efficiency of the electrolyte flow by decreasing the area-specific resistance (ASR). The design and performance of a graphite-based polymer composite BP been studied by the compression molding method with different filler contents in [136]. Recently, [137] investigated a synthetic graphite and carbon nanotube filled with polyphenylene sulfide, by using a co-rotating twin-screw extruder and injection molding to obtain an injection-molded BP. The performance of RFBs using flow-by configurations can also be improved by placing inert "turbulence promoters" in the form of polymeric meshes or nets within the electrode channels [40]. This leads to an increment of the mass transport, mixing, and turbulence effects, that demonstrates a higher limiting current density with a uniform flow distribution at the electrode surface [138].

Membranes

The membrane is a key component in a vanadium redox flow cell. The function of the membrane is to prevent the mixing of the positive and negative electrolytes with the consequent short-circuiting of the two compartments, while allowing the transfer of ions to complete the electrical circuit during the passage of current. A great amount of work has been undertaken to select a proper membrane for a VRFB stack. In VRFB technology, an ideal membrane should offer the following features: resistance to the highly oxidizing environment, good chemical stability under acidic conditions, low permeability to the vanadium or polyhalide ions, low electrical resistance, high permeability to the charge carrying hydrogen ions, good mechanical resistance expressed by swelling ratio, and dimensional stability with low cost [139]. In addition, another important feature is the ability to avoid the preferential water transfer from one compartment to the other [140]. Generally, the membranes are expensive, comprising as much as 40% of the total VRFB cost [62].

The ion exchange membranes are very similar to ion exchange resins and the difference arises from the mechanical requirements. Ion exchange resins are geometrically unstable, for example, cation exchange resins are usually brittle and anion exchange resins are soft [141]. The ion exchange membranes consist of cross-linked linear polymer chains, which form a three-dimensional network. Without the cross-linking, the membranes tend to self-dissolve in water forming a polyelectrolyte solution. The ion exchange membranes and resins present fixed ion functional groups with oppositely charged counter ions to guarantee the ion migration. These ionic functional groups are the exchange sites capable of forming an electrostatic bond through an ion of opposite charge. The process of ion exchange occurs when the mobile counter ions are replaced by another, with the same charge from solution in a reversible and stoichiometric process. In general, the membrane in RFB technology can be classified into pore filled, perfluorinated, modified perfluorinated, partially per-fluorinated, and non-fluorinated [142].

Cationic membranes guarantee better ionic conductivity, chemical stability, and mechanical strength in comparison with the anionic membranes [143], although some anionic membranes have shown considerably lower permeability than vanadium species [144].

In a VRFB, the most widely investigated membranes are the perfluorosulfonic acid polymers, such as DuPont's Nafion, which presents good stability for the highly oxidizing $V(V)$ solution in the charged positive electrolyte [142]. Despite their high cost, Nafion cation-exchange membranes

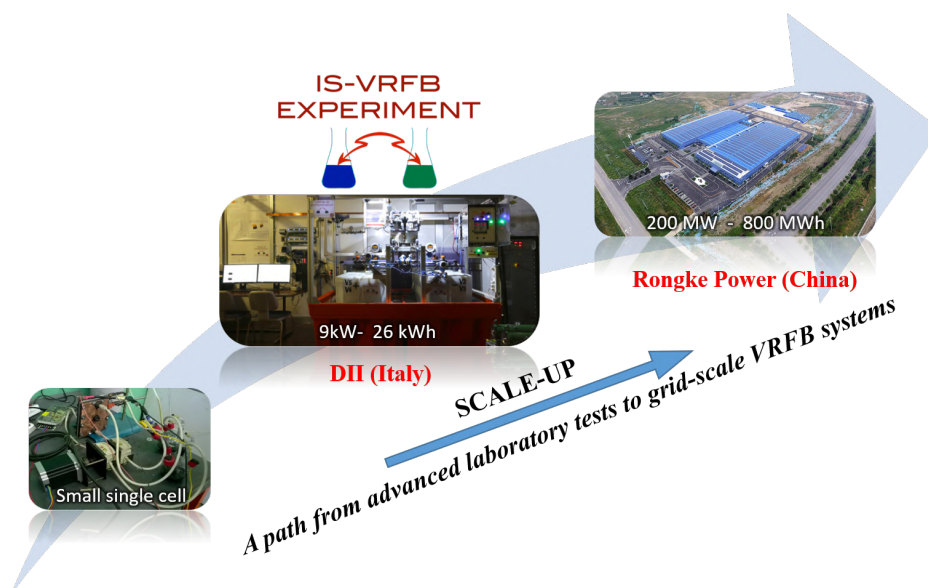


FIGURE 2.8: Graphical representation of the mission of Energy Storage and Conversion Lab at UNIPD: a path from advanced laboratory tests to grid-scale VRFB systems such as the 200 MW/800 MWh VRFB system installed at Dalian (China) and realized by Rongke Power; actually the biggest battery in the world.

are now the most commonly used membrane in VRFBs. These membranes are commercially available and widely used in fuel cells [145], consisting of perfluorocarbon membranes with high conductivity and chemical resistance being acceptable trade-offs.

However, reactive species and water have quite high diffusivity and permeability in Nafion materials [146] and electrolyte cross mixing remains an issue in most VRFBs. To reduce these problems and costs, several methods have been investigated [147], [148], [149], [150], [151], [152], [153], [154], [155].

Alternative solutions for ion exchange membranes include Aciplex1, Fumatech1, VANADion1, and Flemion1 [118], [156].

A low-cost alternative ion exchange membrane is constituted by the microporous separators that provide similar performance [157]. Most are based on polymer-ceramic composites, such as Daramic1. The major issue with microporous separators is their high permeability, which results in electrolyte cross-mixing, [158], and a consequent pressure balancing control or more frequent electrolyte rebalancing [146].

2.3.5 Scale up process

The scale-up process of a RFB is the path from laboratory concept through several stages of development, to an efficient and cost effective commercial device for grid scale applications. This process involves many stages of development to obtain such commercial system. Scale-up involves a dimensional analysis and simulation to ensure adequate electrode geometry, current distribution, reaction kinetics, fluid flow, etc. The realization of the IS-VRFB test facility, which is the core of this PhD thesis aims to give information for such process on VRFB (Fig.2.8). Scale-up can be carried out with three different approaches, based on the complexity and precision that reflect chronological developments in the field [40]: a) black box approach, b) parametric studies, c) modeling and simulation. Moreover, the process involves three main steps:

- 1° step: fundamental electrochemistry: include the study of electrode reactions by using a three-electrode cell, materials, and electrolyte composition by using cyclic and linear voltammetry. These studies provide a non-scalable configuration of the system. Preliminary kinetics information can be obtained by using a laminar flow rotary disc electrode [159]. Four-electrode cells can be used to study the electrode materials and membrane

properties;

- 2° step: electrochemical technology: the previous concept is tested in a laboratory and then scaled-up to pilot stacks, which are designed to take into account the effect of potential and current distribution as well as transport properties. This important stage determines whether the system is realizable. Some tests (such as polarization and charge/discharge curves) are usually performed in unit flow cells with at least 100 cm² active area electrodes (not smaller) and current over 10 A [40]. It is important to consider that over 40 years of experience have indicated the proper sizes of flow cells to manage electric and transport issues. After, the cell is increased to pilot scale, usually with an active area between 100 and 10,000 cm² with a current of between 100 and 1000 A [40], which allows a realistic figure of merit to be obtained. The design of flow distributors, cell flow frames, and transport issues can start at this point. Pilot scale stacks should be of easy accessibility with an open frame design. This is the case for the IS-VRFB test facility installed at the Energy Storage and Conversion Lab of the University of Padua, described in the next sections and that constitutes the core of this thesis. In this step, the main problems may include the dimension changes of the cell and components, flow distribution, and assembly problem, as is discussed in the following sections with regard to the IS-VRFB. Aging effects and *SOC* measuring methods are also evaluated and tested in this step, as well as the sealing problems that constitute one of the major challenges in VRFB stack engineering. Cost analyses can be performed in this step and constitute the basis of the last 3° Step;
- 3° step: commercial device plant: the design and construction of the commercial RFB starts with this step, including modules, ancillary systems, and the battery management system. In this step, the final prototype is tested and installed safely by means of maintenance and operating procedures. In this thesis, this step has been developed for some aspects, such as the battery management system and the stack engineering. Finally, marketing and education for customers are required to expand the market; attention must be given to constant improvements, customer satisfaction, performance monitoring, and failure analyses.

2.3.6 VRFB management system and Power Electronics

The current literature lacks specific studies dedicated to the VRFB management system, including its ancillaries, and power electronics solutions that can address the specific features of these kinds of electrochemical systems. A system supervisor, or battery management system (BMS), is needed to coordinate and control the fluid dynamic, electrical, and chemical process parameters, according to the electric input and output power grid requirements. The actual supervisors of commercial VRFBs are not always optimized, for example regarding the maximization of the overall round-trip efficiency. The VRFB BMS would need *SOC* and state of health (*SOH*) on-line data monitoring to ensure an optimized overall control that allows power exchange to the grid to be met together with increasing reliability and stack durability [103] by simultaneously improving dynamic performance. The *SOC* estimation (Sec.3.1.7) method can be integrated into the battery management system and can be based on Coulomb counting, Kalman filters, or *OCV* determination like the case of IS-VRFB. Conversely, the evaluation of VRFB *SOH* is more problematic. This is actually performed on lithium batteries [160] and fuel cells [161] through electrochemical impedance spectroscopy (*EIS*), which is now the subject of on-field applications through quite low cost and reliable electronics [162]. The *SOH* on line monitoring is usually performed by switching the bidirectional converter, as often happens for fuel cells [162]. Moreover, it interfaces the VRFB to the external grid. Its main features, which make it particular for VRFB applications, are the wide input voltage range, its suitability to cover charging and discharging operations, and its intrinsic bidirectionality.

For the fuel cell and lithium batteries, the topological solution results in a cascade of two stages (DC/DC and DC/AC), which allows flexibility to realize an interface with renewable energy sources, such as a photo voltaic panel and wind park, having a high voltage bus. The

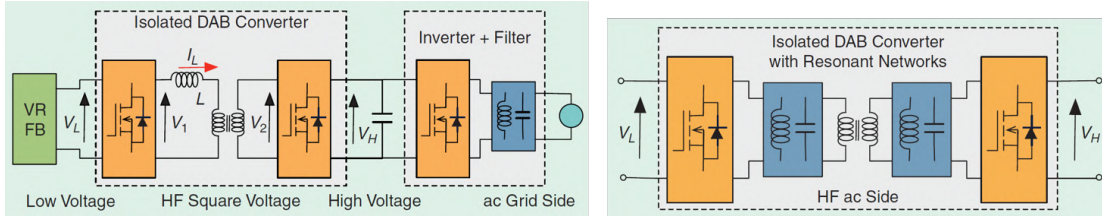


FIGURE 2.9: Left: phase shift Double Active Bridge; right: phase shift Double Active bridge with resonant tanks [19].

DC/AC bidirectional converter allows smart grid connection. The DC/AC topologies for grid connection of intermittent renewable sources is a common topic in the literature [163]. The more challenging are present in the DC/DC topology and control. The main features of the most promising solutions have been summarized in [19]. The phase-shift dual active bridge is a very good candidate for implementing the DC/DC power stage employed in VRFB systems [164] (Fig.2.9 (left)). Adopting a high-frequency transformer by means of the DC/DC converter topology allows galvanic isolation and simultaneously a corresponding high-voltage conversion ratio. Moreover, the phase-shift modulation allows a change to the current in the filter inductance (L), by changing the displacement between the square wave voltages appearing at the output of the left-part bridge and at the input of the right-part bridge. The magnitude and the sign of the phase-shift angle determine the amount and the direction of the transferred power, respectively. By referring to the AC side of the active bridges and by assuming operation of a sinusoidal system for the sake of simplicity, this results in the following:

$$P = \frac{V_1 V_2 \sin(\delta)}{X} \quad (2.39)$$

where V_1 and V_2 are the amplitude of the first harmonic of the line/line voltages at the both sides of the inductance, its reactance therefore being X , and δ being the angle of the displacement between the two sinusoidal voltage waves.

The dual active bridge can also have clamping circuits with resonant tanks to achieve reduced component stresses, soft-switching operation mode, and high conversion efficiency (Fig.2.9 (right)). Some examples of tank circuits are reported in [164], starting from the classic inductive capacitive type, revealing that the parasitic parameters can save additional components. In high-power applications, as in centralized VRFB storage systems for smart grids, the relatively low output voltage requires that the upstream bridge input is separated so that multiphase and interleaved configurations can manage currents as high as some hundreds of amperes. These solutions also offer the possibility of a smaller VRFB current ripple, so bulky and heavy filtering elements can be avoided and the electrolytic capacitors' duration will be higher. Three-phase dual active bridge topology reduces component stress, but requires the three-phase symmetrical transformer that has almost identical leakage inductances in each phase [165], [166].

Similar to the lithium batteries and fuel cell, VRFBs suffer the aging effect and behavior of the cell stack (Sec.10). Although high-power VRFBs systems are actually commercialized for centralized storage plants, much work is undertaken to design modular systems that reduce the mismatching impact and promote the plant to scale-up. VRFB modularity means independent battery element, but also a low power, bidirectional, DC/DC converter dedicated to each stack. From an architectural point of view, the DC/DC converter can be put in series or in parallel to form the desired topology, with distributed battery management systems that have been extensively studied with regard to the PV systems [167]. As for DC/DC converter topologies, in quite low-power application (kW class) as for the IS-VRFB, the current-fed dual active bridge is the most promising because it guarantees, with respect to the voltage fed dual active bridge, lower root mean square current and zero voltage switching through the whole operating range, thus reaching high efficiency values. Current-fed solutions are also preferred as active bridges on the VRFB part, where the input voltage is greatly sensitive to the charge/discharge operating mode. The experimental results given in [166], referring to a three-phase topology, that show high conversion efficiency in the range of 92%–96%, with the VRFB operating voltage range

between 24 and 48 V, the fixed output voltage at 288 V, and a transferred power between 1 and 5 kW.

2.4 Economic analyses

Some challenges still exist for successful commercialization through a widespread deployment of VRFB systems, in particular the capital cost targets. The U.S. Department of Energy (DOE) has fixed a long-range cost target of $\$100 \text{ kWh}^{-1}$ for grid-scale electrochemical energy storage devices. The achievement of this target should enable widespread commercialization, which is the final goal for VRFB research. Meanwhile, some potentially smaller electrochemical energy storage markets can tolerate higher costs. In fact, in many potential grid-scale energy storage applications, the relative value of electric energy and structures varies with the location [168]. Moreover, some electrochemical energy storage applications are power intensive, while others are energy-intensive with different amounts of both power and energy.

The difference between energy cost at peak demand needs to be extremely high for this use to become an attractive option. Nevertheless, many utility companies are also applying significant demand taxes, which are calculated based on the maximum absorbed power by the customer during the peak period that appear during the billing period. In these situations, energy storage (used to smooth out peak demands) is revealed to be a higher surplus value. Area regulation clearly assumes strong importance in this field. For example, California Proposition 755 (Prop 755) allows the payments for power capacity being bid into the market [169]. Prop 755 further rewards performance by providing additional entrance to fast responding units. Indeed, the response time for all electrochemical energy storage devices is extremely fast (Sec.9) in the order of a few milliseconds, whereas conventional plants, such as gas turbines, respond in a matter of a few seconds.

An energy storage system has practically twice the capacity of its rated power and can change its mode from charge to discharge (or vice versa), providing the frequency regulation in power. This can be achieved with conventional batteries, even if the capacity of battery power is greatly reduced over a lifetime and VRFB can successfully cover this deficiency. This is one of the main reasons, because this particular electrochemical energy storage application is gaining traction where the utilities are willing to accept the new regulations and mandates, because there are existing electrochemical energy storage devices that can satisfy the requirements. As discussed, there are many other applications that could potentially benefit from storage beyond area regulation. In fact, the potential economic benefit of electrochemical energy storage applications requires a discharge time higher than 1 h at nominal power; in one study it is estimated that these applications cover the 72% of the total estimated electrochemical energy storage market in the USA [170].

Energy-intensive applications are renewable leveling, power, quality, and voltage regulation. Avoiding wind reduction may require battery recharge for a period greater than 15 m before some generators start to reduce their production. Tackling the deviation between scheduled and actual generation could take up to an hour of stored energy (charge or discharge), which is an energy consumption application. If the deviation persists in the same way, this can be further addressed by using online battery monitoring or taking gas turbine generators off-line. Depending on the energy price and the regulation price, the benefits of regulation can be calculated. In the case of peak shaving, the benefits of avoiding peak power usage can be easily computed. For example, in the case where the peak load appears at the time of high-energy price, the double gains from arbitrage and peak shaving can be estimated by accounting for the costs addressed by paying for additional energy related to the efficiency of the battery.

2.4.1 Cost distribution for VRFB

The main barrier to commercialization is the economic issue; namely, the capital cost of VRFB systems that must be further reduced to enable attractive value in major electrochemical energy storage markets. Moreover, other technological improvements could also make VRFB systems more attractive, such as higher round-trip energy efficiencies, enhanced reliability, and additional long-lifetime demonstrations under real-world conditions. Although VRFBs present

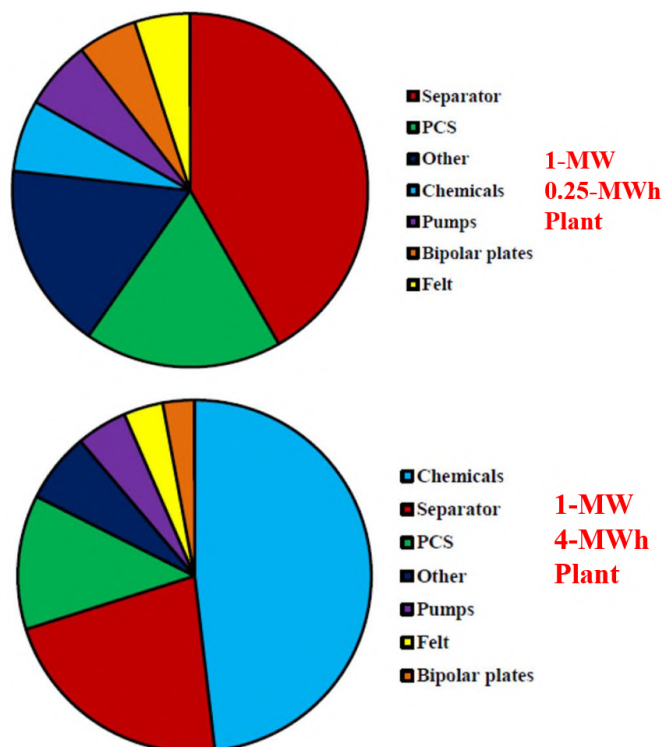


FIGURE 2.10: Component cost distribution for Gen-2 chemistry (PNNL's all-vanadium redox flow battery). Chemical costs are dominant for the 1-MW/4-MWh system at 48%, while membrane (separator) material costs are 22%. Conversely, for the 1-MW/0.25-MWh system, the stack costs are dominant, led by membrane costs at 42% [171].

lower energy efficiency than Li-ion batteries, they are more competitive in terms of life cycle assessment, i.e. environmental impact, because Vanadium is completely recyclable differently from Lithium [172], [173]. Various capital cost estimations are available for RFB systems (typically given in dollars per energy per cycle) at a fixed rated power output (\$/kWh per cycle) [174], [175]. However, these values are rarely accompanied by the energy-to-power ratio for the VRFB system. The actual performance of the VRFB cell stack is also not always considered, and the cost is provided simply in terms of the energy capacity available from the electrolyte volume. Pacific Northwest National Laboratory (PNNL) recently studied a cost model that considers the real performance of the VRFB system [176]. Indeed, the cost was computed based on the estimated delivered power and energy capacity of the whole system. The model also includes optimization of the key stack and system design parameters. For example, the optimization of reactant flow frames (and relative flow channels) within the stack and connections between stacks was performed to reduce overall losses. The model iterates across a range of channel dimensions to calculate the optimal values that minimize the overall system cost.

To guarantee reasonably inexpensive large scale industrial applications, the enlargement of the active single cell area assumes crucial importance [177]. The cell area is usually limited to 0.1 m^2 by the size of the BP due to the manufacturing processes [178]. The development of an innovative extrusion process that aims to obtain a novel large-area compound BP with 2.7 m^2 and a scale factor of ≈ 30 is the object of the research and development, to obtain a megawatt VRFB single stack [179]. In fact, for such power-intensive electrochemical energy storage applications, the stack needs to be used at the maximum allowed power density to minimize the stack size.

Similarly, for the fuel cells, the stack power density is related to the specific current density, which is a function of stack-design features (for example electrode-specific area, membrane thickness, electrode thickness, and contact resistance between each part of the stack). For energy storage intensive applications, it might be more useful to operate the stack at higher energy efficiencies to minimize the operating cost, even though it may result in a higher capital cost. This mode would require running the stack at lower power densities, and to operate at a different

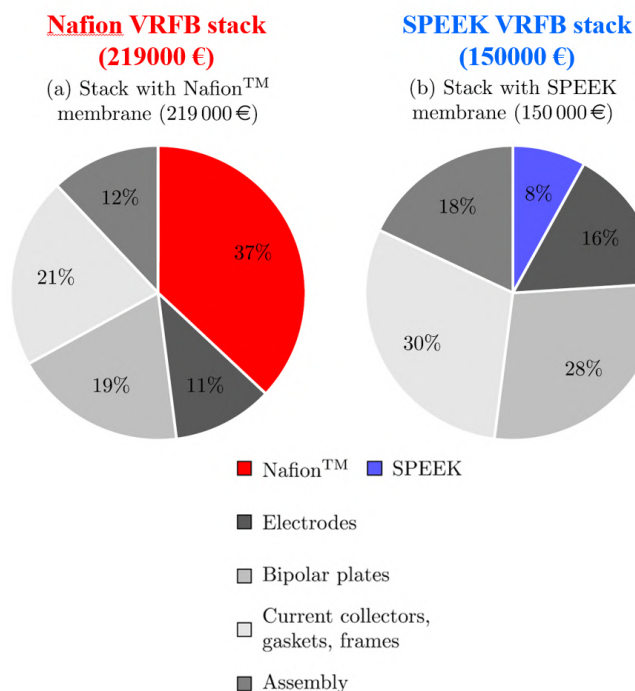


FIGURE 2.11: Cost sharing of 250 kW VRFB stack with Nafion and SPEEK membrane [177].

depth of discharge. Nevertheless, in both cases, the impact that the cell-stack efficiency has and the cost of the needed electrolytes must also be counted, which is especially important due to the higher cost of the vanadium electrolyte. In [171], the component-cost distribution for a VRFB is reported (Fig.2.10). As expected, electrolyte costs and membrane costs dominate for the larger 1 MW/4 MWh system and are overcome by the stack cost in the smaller 1 MW/0.25 MWh.

In both cases, membrane is a key component in terms of costs, as reported in [180]. The standard material Nafion is expensive and therefore several alternatives are the focus of research studies (Sec2.3.4). For the sake of comparison, the cost structure of a 250 kW VRFB stack with two different membranes: Nafion™ and SPEEK membrane is reported in [177], Fig.2.11.

More detailed information can be found in [181], with an executable file that can be downloaded, and the open source code that can be obtained from [182], with the suitability for users to interactively modify the source code with the Github, providing a flexible and automatic version control.

2.4.2 Reliability Metrics

Regarding the electrochemical energy storage system, the costs are typically given in terms of $\$/\text{kWh}$ without considering the actual performance of the storage system for a particular application. The alternative of the previous feature is the $\$/\text{kWh}^{-1}$ per discharge cycle value.

However, the cost also changes based on the energy/power ratio of the system, and should be preferable for reporting the costs in either $\$/\text{kW}^{-1}$ or $\$/\text{kWh}^{-1}$ by specifying the energy/power ratio, and ideally, also dividing the $\$/\text{kW}^{-1}$ and $\$/\text{kWh}^{-1}$ for the appropriate components separately, together with the total $\$/\text{kWh}^{-1}$, at specific energy/power ratio. For RFB systems, it should be evident that the $\$/\text{kW}^{-1}$ and $\$/\text{kWh}^{-1}$ components will change with the energy/power ratio, and the best overall system cost ($\$/\text{kWh}^{-1}$) will always be obtained for higher discharge times. In fact, in RFBs, more energy capacity only requires additional electrolytes, which cost less than the total system on a $\$/\text{kWh}^{-1}$ basis.

Accordingly, the cost of RFB systems scale very differently than conventional battery systems, such as lithium batteries, which require the addition of both reactants and inactive materials to add energy capacity. Ultimately, RFB systems will be most cost-competitive for energy-intensive

TABLE 2.1: Featured of electrochemical energy storage technologies for stationary services ([19])

ECES	Energy density [Wh kg ⁻¹]	Disch. time [h]	Resp. time	RTE [%]	Cycle life [10 ³]	CAPEX [k€ kW ⁻¹]	CAPEX [€ kWh ⁻¹]	CAPEX [k€ kWh ⁻¹ Cycle ⁻¹]
Adv. <i>Pb-acid</i>	25-50	1-2	ms	75	0.8	1.9	770	96.3
<i>Na-S</i>	150-120	2-6	ms	89	4.5	3.6	450	10.0
<i>Na-Ni-Cl</i>	95-120	0.5-2	ms	90	4.5	3.55	1638	36.4
<i>Li-ion</i>	100-200	1	ms	87	4.0	0.71	1246	31.1
<i>H₂/FCs</i>	800-1300	≥10	10 ² ms	24	0.3	7.1	≤1880	≤626.7
VRFB	24	≥10	ms	75	20	2.65	≤663	≤4.4

electrochemical energy storage applications, especially where long lifetimes with thousands of deep discharge cycles are required Tab.2.1.

2.4.3 Main VRFB plants installed

VRFB are already commercially available [183]. Installation trends show 50 installed systems in 2015, with a total installed power of 23 MW [177], Fig.2.12. The sum of installed power and energy is dominated by single megawatt demonstration projects in Japan and China [184].

Over the last few years, more companies have installed these plants. There are VRFBs for both industrial and domestic uses. Typical systems are in the order of kW to MW. Some major plants installed are described in chronological order, as follows:

- 1996: 200 kW/800 kWh installed by Mitsubischi Chemicals at Kashima-Kita Electric Power, Japan, for load-leveling [185].
- 1996: 450 kW/900 kWh installed by Sumitomo Electric Industries at Tasumi Sub-Station, Kansai Electric, Japan, for peak-shaving.
- 2000: 200 kW/1.6 MWh installed by Sumitomo Electric industries at Kansai Electric, Japan, for peak shaving.
- 2001: 170 kW/1 MWh installed by Sumitomo Electric industries at Hokkaido Electric Power Wind farm, Japan, for wind turbine output power stabilization.
- 2001: 1.5 MW/1.5 MWh installed by Sumitomo Electric Industries in a semiconductor fabrication plant at Tottori Sanyo Electric, Japan, for peak-shaving and emergency back-up power [186].
- 2001: 250 kW/500 kWh installed by VRFB Power at Stellen-bosch University for ESKOM Power Corporation, South Africa, for peak-shaving and UPS back-up power.
- 2001: 500 kW/5 MWh installed by Sumitomo Electric Industries at Gwansei Gakuin University, Japan, for peak shaving.
- 2001: 45 kW/90 kWh installed by Sumitomo Electric Industries at CESI, Milan, Italy, for R& D about distributed power systems.
- 2003: 500 kW/2 MWh installed by Sumitomo Electric Industries in a High-Tech factory in Japan for UPS/peak-shaving [186].
- 2003: 250 kW/1 MWh installed by Pinnacle VRFB for Hydro Tasmania at Huxley Hill Wind Farm on King Island for wind energy storage and diesel fuel replacement [187].
- 2004: 250 kW/2 MWh installed for Pacific Corp by VRFB Power at Castle Valley, Moab, US-UT, for voltage support and rural feeder augmentation.

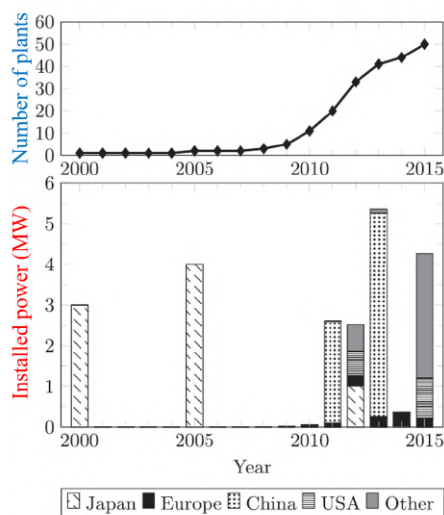


FIGURE 2.12: Cumulative VRFB systems installation for stationary applications (2000 to 2015) and installed power in selected country [177].

- 2005: 4 MW/6 MWh installed by Sumitomo Electric Industries for Electric Power Development Co, Ltd in Tomamae, Hokkaido, Japan, for wind energy storage and wind power stabilization [188].
- 2010: 100 kWh made of 18 kW stacks in Vierakker, The Netherlands, by Cellstrom GmbH, Austria.
- 2012: 1 MW/5 MWh installed by Sumitomo Electric Industries at Yokohama, Japan, for energy storage and support of a solar plant.
- 2015: 1 MW/4 MWh installed by Flow battery builder UniEnergy Technologies (UET) at the Turner Substation in Pullman, Washington, to support Washington State University’s smart campus operations [189].
- 2015: 15 MW/60 MWh installed by Hokkaido Electric Power Co at Also, Japan, for frequency regulation [190].
- 2017: 2 MW/ 8 MWh installed by UniEnergy Technologies (UET) and Snohomish County Public Utility District (SnoPUD) at SnoPUD substation in Everett, Washington, powerful enough to keep the lights on in as many as 1000 homes for eight hours [191][192].
- 2017: 2 MW/ 8 MWh installed by Utility San Diego Gas and Electric (SDG&E) and Sumitomo Electric (SEI) at San Diego, California, to study how the technology can reliably integrate renewable energy and improve flexibility in grid management [193].

2.5 Standards for flow batteries (Information updated July 2019)

The organizing committee for the first International Flow Battery Forum (IFBF) identified the need to develop standards to support the growing flow battery industry, and following successful discussions at the following year’s meeting it was agreed to develop a Workshop Agreement to cover the flow battery industry. The staff of “Comitato Europeo di Normazione ELEttroteC-nica” CENELEC guaranteed to form the CENELEC Workshop on Flow Batteries (CLC WS 5) in November 2011, with the intention of developing a CWA “Flow batteries – Guidance on the specification, installation, and operation.” A number of companies participated in the workshop, and were supported by several individuals with a keen interest in the topic. The Osterreichischer

Verband fur Elektrotechnik (OVE) provided the Secretariat, and the Chairman was provided by Swanbarton Limited acting on behalf of the IFBF. The Workshop ran from November 2011 and the CWA 50611: "Flow batteries – Guidance on the specification, installation, and operation" was published in April 2013. The document is available through CENELEC national members or from OVE. Note that the CWA is a CENELEC published document and must be purchased through the OVE. The IFBF is unable to supply copies but some standards can be found in Appendix B.

This document may be used by industry, pending the development of full standards published by national or international standardization bodies.

All those working in the flow battery industry should be aware of the relevant national and international standards that cover batteries and energy storage systems, as well as the specific work covering flow batteries. Some international standards include:

- CWA 50611: Flow batteries — Guidance on the specification, installation and operation
- IEC 61427-2: Secondary cells and batteries for renewable energy storage - General requirements and methods of test - Part 2: on-grid applications

Those interested in standards for large-scale energy storage should also be aware of the IEC TC 120 on Electrical Energy Storage Systems.

There is ongoing work between IEC TC/21 and IEC TC 105 in a joint working group (JWG 7). The JWG has developed a suite of standards, which are in the final stages of consultation and approval. These are

- IEC TC21/TC105 JWG 7 "Flow Batteries"
- IEC 62932-1 ED1 "Flow Battery Systems for Stationary applications - Part 1: Terminology"
- IEC 62932-2-1 ED1 "Flow Battery Energy System for Stationary Applications-Part 2-1: Performance general requirements and test methods"
- IEC 62932-2-2 ED1 "Flow Battery Systems for Stationary applications - Part 2-2 Safety requirements"

There is also a possibility of JWG 7 developing a standard for vanadium electrolyte in flow batteries, based on the example of: IEC 62877 "Electrolyte and water for vented lead acid accumulators."

The IEC TC/120 is developing standards for Electrical Energy Storage Systems. Many members of the CENELEC workshop are now also participants in the IEC TC 21 / TC 105 Joint Working Group on Flow Batteries, and there are several members of IEC TC 120 who have knowledge and experience of flow batteries.

Chapter 3

IS-VRFB stack

The power part of the IS-VRFB is constituted by the stack [194]. It is the most complex part of a VRFB system and its design requires expertise in mechanical engineering, materials science, electrochemistry, chemistry, and modeling by means computational simulations. Generally, the modular design provides ease of construction, assembly, and mass production. In this regard, conventional series stacks (CSSs) are clearly the most compact configuration, which is usually reported as being the best configuration. In fact, this stack has the advantages of being scalable by increasing the area of the electrode and the cells and stack number. At the beginning, the electrode area value and cell number must be selected depending on the desired output voltage, current, and flow rate consideration [74]. A first estimation can be obtained by using dimensional analysis and simulation that provides a dynamic optimization [40].

The IS-VRFB stack follows this conventional design, known as a bipolar plate (BP) configuration [74], which consists of 40 cells 600 cm² active area electrically connected in series and hydraulically in parallel. In this regard, the cells are interposed with frames encasing conducting graphite plates (BPs), which work as current collectors and interconnect the cells electrically while separating the solutions on different sides. This design uses thick electrodes that limit their pressure drop resulting in relatively large ohmic losses [76]. Each cell is composed of a Nafion[®] 212 membrane and two 5.7 mm thick (after compression) graphite felt electrodes (Beijing Great Wall, China). Before assembly, the felts are processed with a thermo-chemical treatment to enhance their electrochemical performance (Sec.3.1.3).

The solutions are distributed in each half cell through ramified channels grooved into the frames, which follow an equal path length (EPL) design. Fig.3.1 shows the main directions of the flow pattern in the two electrolytes, in both manifolds and electrode. This consists of a sort of cross-flow distribution that takes place through the channel that forms the "flow frame." In both porous electrodes, the solutions flow from the lower to upper manifold, to ease the removal of gas bubbles that may develop [40].

Generally, the electrolyte manifolds can be internal in the bulk or can be constituted by external rubber tubes. Recent trends in stack design include the grouping of cells into sub-stacks separated by an intermediate current collector within the same compression end plate [195]. Such a design is intended to reduce the number of cells that have a common manifold in order to minimize the parasitic shunt-currents (Sec.5.2). Moreover, a uniform and dispersed electrolyte flow should be guaranteed to maintain uniform current and cell voltage distribution by avoiding stagnant zones that can damage the cell. Flow dispersers can be placed next to the manifolds to spread the flow and reduce jets, for example by using engraved ribs or obstacles (Sec.2.3.4).

In [196], a dimensionless parameter that expresses the effect of manifold jets and flow development was treated, giving a measure of the predominance of manifold flow as the cell size decreases. The same group developed another model of fluid dispersion in carbon felt electrodes [197]. The IS-VRFB cell and frame design (conceived in view of future series production) follows this concept, involving different materials and aiming for easy manufacturing and assembly. The following sections aim to address some design and technological aspects of the main parts of the IS-VRFB stack.

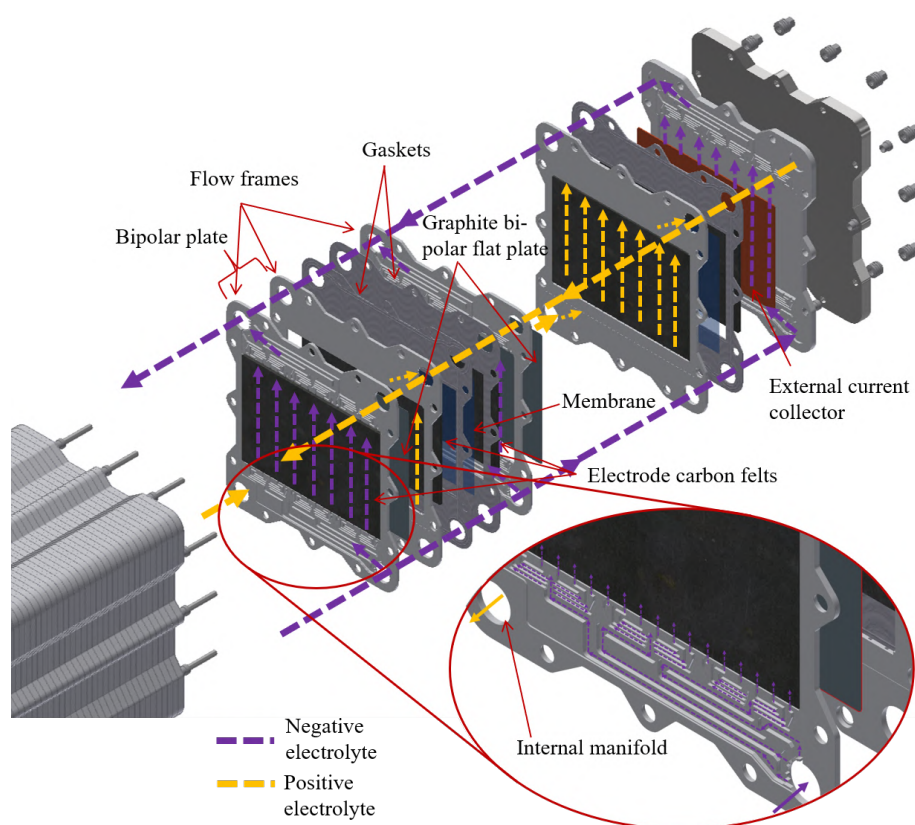


FIGURE 3.1: IS-VRFB stack flow distribution.

3.1 Bipolar plates

From a mechanical and technological point of view, the most critical component in the stack is the BP, which can potentially induce electrolyte leakages between frames. A traditional BP of a VRFB is formed from different components, which requires a time-consuming assembly process, an important feature of the final cost of the stack. Performance and technological issues are well-known problems of VRFBs that have not been fully solved, despite research that has been carried out on the matter [136]. To minimize losses due to the shunt currents and hydraulics, in a traditional design a flow field is realized on two electrically insulated flow frames with a graphite BP in between [198]. The IS-VRFB BP follows this concept, consisting of two identical 5 mm thick flow frames, made of polypropylene plate. Two flow frames are assembled with the graphite flat plate in between, forming the BP.

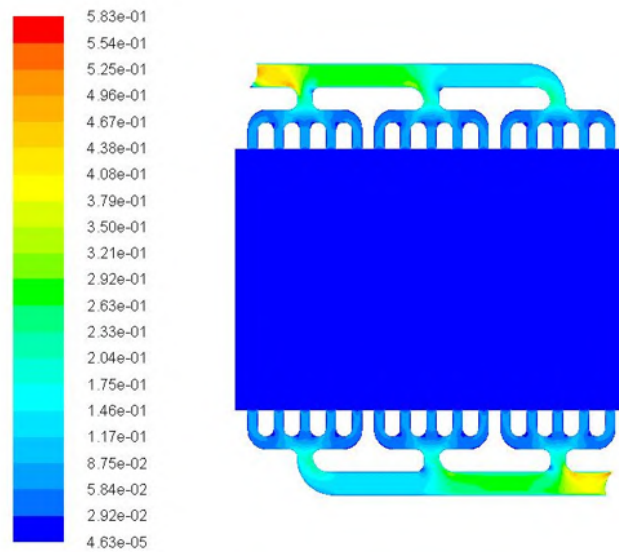
3.1.1 Flat graphite plates

The current collector for each cell is constituted by the TF6 graphite flat plate, supplied by SGL carbon (Germany). The physical properties are reported in Fig.3.2. Future tests can be conducted to self-produce this component by using a laminator and a large range of mixtures of different resins and graphite flakes to achieve the optimal composition, representing the trade-off between a good mechanical strength and electrical conductivity. Clearly, the higher the relative concentration of the resin, the better the mechanical properties and the worse the electrical conductivity, and vice versa [134]. In this regard, an experimental campaign that aims to test different types of graphite plates is planned at the Electrochemical Energy Storage and Conversion Laboratory with a range of samples produced by the main world manufactures. The aim of this work will be the characterization of the present materials in a large-scale cell to consider all scale-up problems and issues.

Physical data			
Properties	Unit	Typical value	
Grade		PP20	TF6
Polymer type		Polypropylene	Fluor polymer
Polymer content	%	20	6
Thickness	[mm]	0.6	0.6
Density	[g/cm ³]	1.4	1.7
Tensile strength	[MPa]	22	20
Electrical resistivity (through plane)	[Ω -mm]	<1.5	<10
Thermal conductivity (in plane)	[W/mK]	300	300
Thermal conductivity (through plane)	[W/mK]	5	6
Thermal expansion CTE	[μ m/mK]	-1.5	-1.5
Permeability (helium)	[mg/s-m]	<1·10 ⁻³	<1·10 ⁻³
Impurities (metals / transition metals)	[ppm]	<150	<150



FIGURE 3.2: Graphite flat plate: physical data (left), products (right).

FIGURE 3.3: Contours of velocity magnitude (m s^{-1}) of a poor flow frame geometry, $Q_c=0.8 \text{ L min}^{-1}$, $SOC=50\%$.

3.1.2 Flow frames

Flow frame design

The design of a VRFB stack flow frame represents a compromise between efficiency, size, and technological complexity. The parasitic losses resulting from both hydraulic power and shunt currents are strictly related to the size and geometry of the flow frames. This requires a trade-off between those kinds of losses needs to be considered in a large VRFB systems to maximize the efficiency that can be achieved with an optimal flow-frame design.

Generally, longer and thinner flow channels are beneficial to reduce shunt currents but produce higher hydraulic losses [199]. In this regard, the flow frame geometry was simulated using CAD, CFD, and Multiphysics software. CFD simulations proved the uniformity of the flow through the whole electrode, demonstrating that the uniform distribution is quite independent of the type of the geometry of the distribution channels. This is due to the preponderance of the pressure drop in the porous felt compared to the others, as can be seen in a velocity plot of a simplified poor geometry in Fig.3.3. From an electrical perspective, the flow frame geometry is related to the ionic resistance inside the cells, i.e., the solution flows in paths in the cell channels and porous electrodes; then on the consequent electric potential φ distribution due to

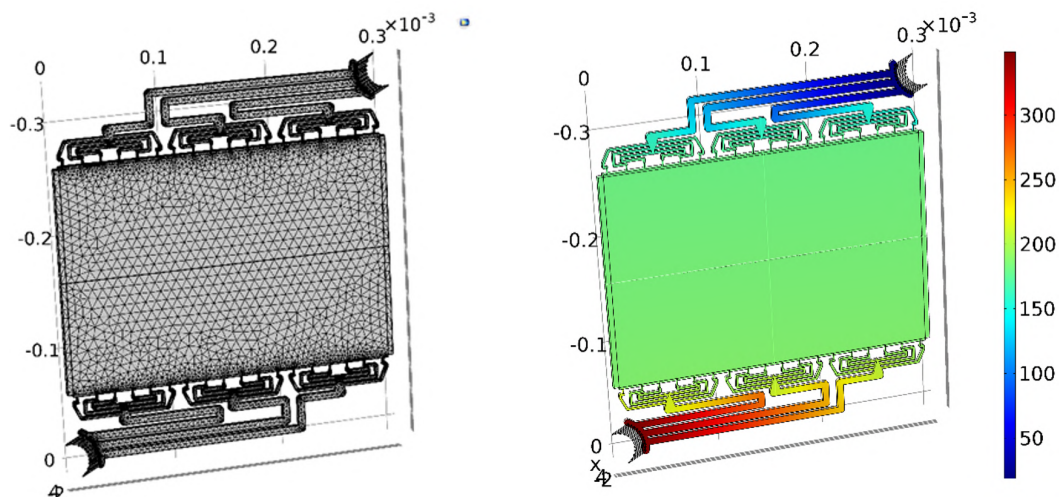


FIGURE 3.4: 3D model used to compute the cell flow resistance including distribution channels and porous electrodes. Left: 3D mesh color map of the electric potential; right: φ in V produced by a 1 A shunt current.

the shunt currents flow. This cell resistance $R_{c_{\pm,n}}$ was computed by means of a 3D FEM model implemented in COMSOL[®]. Fig.3.4 presents the geometry used for the present stack coupled with the electrical potential φ produced by 1 A shunt current, representing the modeled cell resistance $R_{c_{\pm,n}}$, from inlet to outlet at different *SOCs* values. Further explanations of this method can be found in Sec.5.2.

Flow frame manufacturing

Technological issues are also fundamental for good flow frames. Indeed, the optimal geometry design must be easy to produce, even to a small detriment of the performance just described section. The material for the polymeric frame should have a low cost and high chemical resistance, such as PP, PVC, HDPE, or PVDF. Classic fabrication techniques for the polymeric frames include CNC machining and injection molding. Both of these were tested, with cost analyses that revealed that CNC milling costs 80 times more than injection molding, by using polypropylene. This data justifies the engineering efforts in producing the flow frame by injection molding. Very few studies with a focus on this topic are present in the literature. In [198], an integrally molded BP was designed and fabricated to minimize the manufacturing cost by evaluating the effects of mold design and injection parameters. This study demonstrated that shrinkage could be reduced by using a large graphite plate within the flow frames.

In [200], a smart cure cycle was investigated to reduce the thermal residual stress of the E-glass/carbon/epoxy structure. In the IS-VRFB stack, the flow frames are machined separately and then joined with the BP. In this step, the efforts aimed to define a compound that could avoid sink marks and warping due to residual stresses that make the flow frame unsuitable for the sealing. In order to increase the knowledge on this issue, many prototypes with different types of compound have been developed. Among the various trials, a finished product with a mixture of polypropylene and glass fiber was tested, (Fig.3.5), with bad results. Some treatments were tested to reduce those defects, based on some cooling and reheating processes, with some mistakes in the procedure (Fig.3.5). In addition, PVC injection molding represents a challenge and requires an ad-hoc ventilation system, due to the chloride acid evolution during the molding. The best results have been obtained with a simple polypropylene mixture, although not yet satisfactory. For the sake of simplicity and expediency, in this prototyping phase CNC milling was employed to guarantee the required performance at the detriment of cost. In a future development, more tests can be conducted to achieve quality injection molded flow frames suitable for series production. Clearly, mass production greatly decreases cost but only if the design has been optimized and results are reliable. For example, in a recent study [201], the

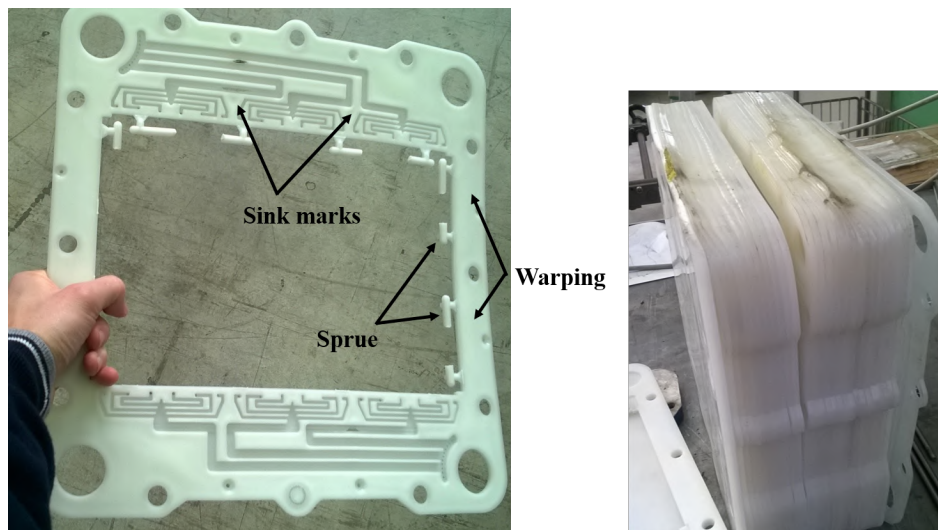


FIGURE 3.5: Left: Molded flow frame (polypropylene with glass fibers); right: effects of bad reheating (150 °C for 2 hours) in the tested cure.

BP was prepared by injecting molten polyethylene through micro pores of carbon fibers using a molding method. According to the authors' opinion, this method guarantees high conductivity and good mechanical strength, due to the special morphology of the conductive grid structure that result from the fibers connecting to each other.

Bipolar plates assembly

Two flow frames were assembled with the flat graphite plate in the middle, forming the BP. An alternative assembly technology can be constituted by the clip-in architecture [202]. For the IS-VRFB, the sealing was ensured by acetic silicon. This was deposited by using a CNC plot, with an air compressed piston that deposited it into the frames. The assembly process can be seen in Fig.3.6.

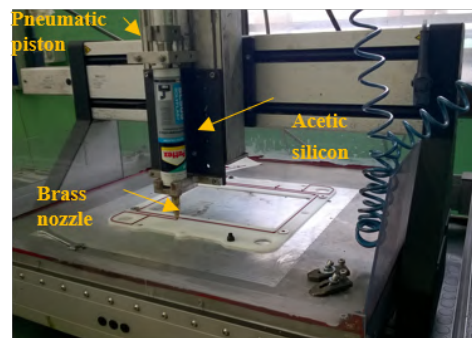
In the first phase, the correct coordinates of deposition were computed to put the silicon in the grooves engraved in the frames. This phase was performed at the beginning. Thereafter, during the deposition, the thickness of the silicon bead was decided by the speed of the plotter, while the pressure of the piston remained constant. After the deposition in the first frame, the graphite plate was positioned in a pocket of the frame together with a rheofore needed for the cell voltage measurements. At this point, the deposition of the second frame occurred and the resulting "sandwich" was pressed by a hydraulic press. This constitutes the last real assembly operation, after which a quality control assessment is required to detect any possible defects, such as some occlusion in the flow channels or macroscopic incorrect silicon expansion that could lead to leakage problems. If any problems appear, the BP must be reopened and the whole process undergone again. In the case of success, the BP is put to dry between two 1 cm thick steel plates, to avoid any possible warping or gaps between the two half-frames and the graphite plate due to the dry silicon. This process can appear quite row but has been demonstrated to be effective. Moreover, it can also be automated by using a workstation for each phase by using a CNC plotter and an assembly robot.

Nevertheless, alternative methods can be implemented. For example, use of epoxy composites to bind the electrode and frames have been investigated [200] in fluor elastomer/glass fiber composites. In addition, emerging additive manufacturing technologies such as 3D printing can support the design stage (rapid prototyping) [203], and in the future the whole production. 3D printers can build the cell bodies and electrodes constituting a specialized integrated and assembled RFB, due to the ability to print multiple materials (electrodes and membranes included) and produce flow cells, rather than only their components [203].

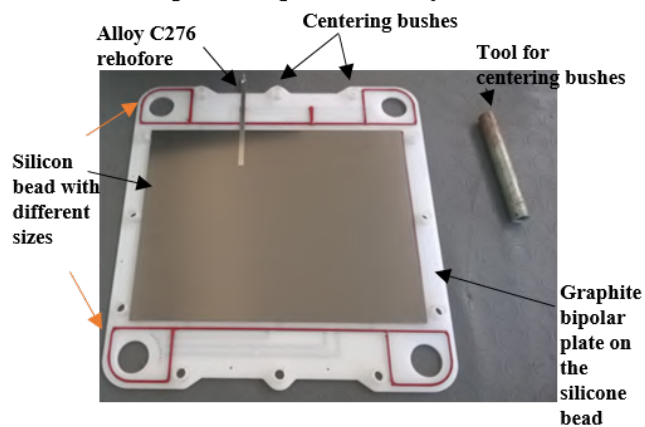
1° Determination of the coordinates of deposition



2° Acetic silicon deposition in the frame



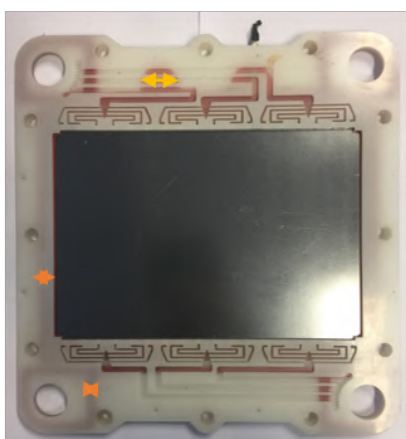
3° Graphite flat plate assembly



4° Compression on the press



5° Quality control



6° Drying



FIGURE 3.6: Bipolar plate assembly phases.

TABLE 3.1: Carbon felt Beijing Great Wall GFE-1 data sheet.

Typical value	GFE-1
Thickness [mm]	1 – 15
Thickness tolerance [mm]	± 0.29
Width [m]	1.3 \div 1.4
Length [m]	≥ 60
Density [g cm^{-3}]	0.09 – 0.1
Electrical resistance [$\Omega \text{ cm}$]	0.269
Carbon content [%]	99.9
Average liquid adsorption [g g^{-1}]	17.76
Average dropping crumbs [%]	0.168

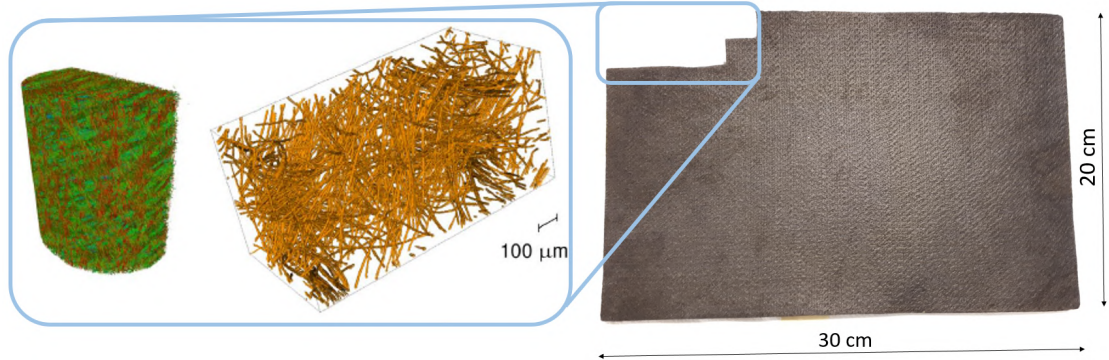


FIGURE 3.7: GFE-1 carbon felt X-ray computed tomography reconstruction.

3.1.3 Carbon felts

The IS-VRFB stack uses the GFE-1 graphite felt electrodes bought from Beijing Great Wall, (China). GFE-1 are graphite grade felts especially designed for VRFBs that adopt new carbon fiber raw material, and new fabricating and heat treating methods (according to the company data sheets). The declared physical properties are reported in Tab.3.1. As can be seen, the main missed parameters are represented by the porosity that assumes a crucial importance from the hydraulic point of view.

To gain a deep understanding of how such mechanisms can affect the performance of the real electrodes of VRFBs, analysis of the internal material microstructure has been conducted. Accordingly, X-ray computed tomography was performed (Fig.3.7) with the aim of studying the dispersion and reaction rates of electrolyte reactants in the flow battery, as reported by Maggiolo et. al [128]. In fact, analyzing non-accessible features is almost impossible with conventional methods. The porosity was evaluated using this technique, with results of 0.949. The porosity is defined as the measure of the void (i.e. "empty") spaces in a material, and is the fraction of the volume of voids over the total volume, between 0 and 1, or as a percentage between 0% and 100%, as follows:

$$\epsilon = \frac{V_{empty}}{V_e} \quad (3.1)$$

Moreover, the present porosity is referred to as normal condition, namely, when the felt is not compressed. Nevertheless, after the stack assembly the compression ratio ζ of the felts becomes 0.3 to achieve a no gap configuration between the flat plate and the membrane [40]. The real porosity is then recalculated as follows:

$$\epsilon_c = 1 - \frac{1}{1 - \zeta}(1 - \epsilon) \quad (3.2)$$

Before the assembly process, the carbon felts have undergone a series of thermochemical processes to enhance their electrochemical performance (Fig.3.8). Usually, graphite fiber properties can



FIGURE 3.8: Carbon felt thermo-chemical treatment.

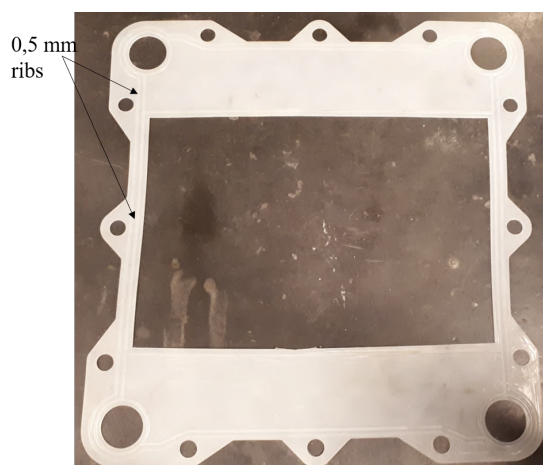


FIGURE 3.9: IS-VRFB EPDM gasket.

be improved by using sulfuric acid with a subsequent thermal treatment, which increases the chemical activity of the fibers surface, as reported in Sec.2.3.4. This process mainly consists of a series of boiling processes on the electrolyte, centrifugation, washing, drying, and calcination in an electric oven, resulting in electrochemical activated carbon felts. The detailed procedure is not reported due to confidentiality issues.

3.1.4 Gaskets

A typical VRFB stack can contain over fifty cells. Gaskets for each cell are required to keep the reactant electrolytes within their respective regions. If the gasket degrades or fails during operation or standby, the electrolyte can leak overboard or mix with each other directly, affecting the overall operation and performance of the VRFB. The gaskets in VRFBs typically consist of elastomeric materials such as ethylene-propylene-diene monomer (EPDM) and FKM viton, due to their resistance to the acidic liquid solutions and mechanical stress.

The long-term chemical and mechanical stability of the gaskets are clearly a critical issue that need to be considered in both the sealing and in the electrochemical performance. EPDM rubber is one of the fastest growing synthetic rubbers, which has an inherent resistance to heat and light [204]. For this reason, it is used for seals and gaskets in many industrial applications including fuel cells [205], [206], [207], which can be considered from the mechanical point of

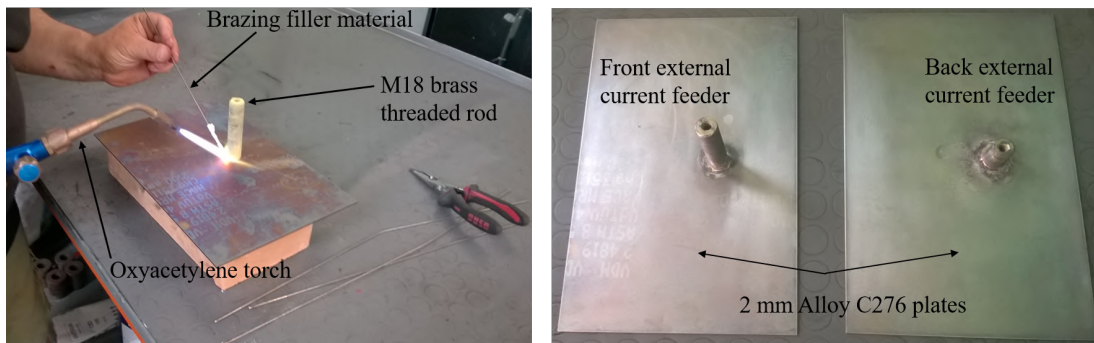


FIGURE 3.10: IS-VRFB current feeder realization.

view to be a similar application as for the VRFBs. In [208], the mechanical properties and chemical degradation are investigated showing that EPDM gaskets can be useful for PEM fuel cell applications. The IS-VRFB gaskets are made from EPDM (Fig.3.9). To improve the seal, these gaskets are not plain but are provided with shaped ribs all around the wetted zone from which the electrolyte can leak. The thickness of these gaskets is not random but designed to reduce to zero after stack compression, that is, after the compression load necessary to ensure the seals (approximately 50 kN). The main problem with this material is its viscoelastic property that can induce stress relaxation of the seal under constant strain [209].

This problem can be partially solved with the use of cup springs that expand over time to compensate for the relaxation of the gaskets. This solution is applied in the IS-VRFB stack with good results. Clearly, the shape of these gaskets requires a proper mold, which represents an additional cost in comparison to the plane gaskets that can be easily cut from the EPDM roll. In any case, this cost can be less incisive in a serial production and can be justified thanks to the significant reduction in losses compared to using flat gaskets, as shown by the author's experimental observations.

3.1.5 Current feeders

The stack also includes some ancillary elements such as external current feeders and electrical connections. The end-electrodes constitute the current feeders. These components can be subjected to failure due to the localized stress and cracking caused by non-uniform compression during the stack assembly.

The main challenges occur because of the sealing to avoid any contact between common metallic parts and the electrolyte. In this regard, some difficulties were reported by Gildemaster with a copper external current feeder that contaminated the electrolyte due to a leakage [210].

The IS-VRFB current feeder design follows an original architecture. The collector is made using Alloy C276 plates that substitute the graphite plate at the ends with a threaded brass brazed on them Fig.3.10. After a plate is preheated in an electric oven (600 °C) necessary to preserve the plates from warping during the next brazing, the threaded brass is attached. This phase is critical and clearly constitutes a weak point in the whole stack realization. The finished collector was assembled in the stack end plate and the seal was ensured by using an EPDM O-ring in a proper housing.

The connection between the current collector and the end plate was obtained by means of an M18 nut that presses the collector into the end-plate and O-ring. Until now, this current feeder has been considered functional and has not presented problems but still represents a weak part of the whole stack. This solution is quite unique in the actual VRFB stack and some improvements are needed in the future to remove this weak point.

3.1.6 End-plates

The IS-VRFB stack has a fairly complex geometry at the first part in the front Fig.3.11, [211]. Originally, this part (front end plate), allowed the electrolyte mixing operation in an

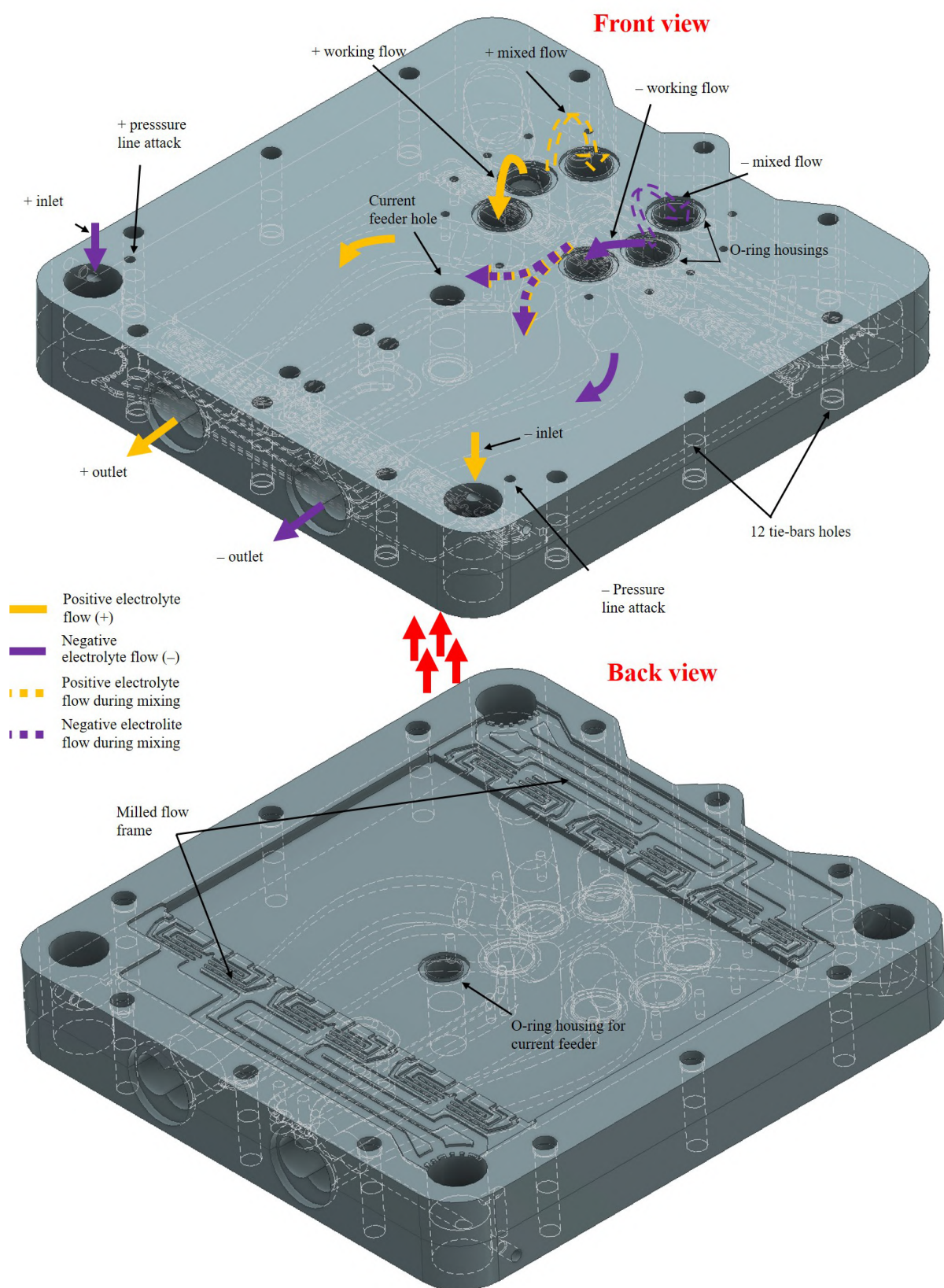


FIGURE 3.11: Front-end plate representation.

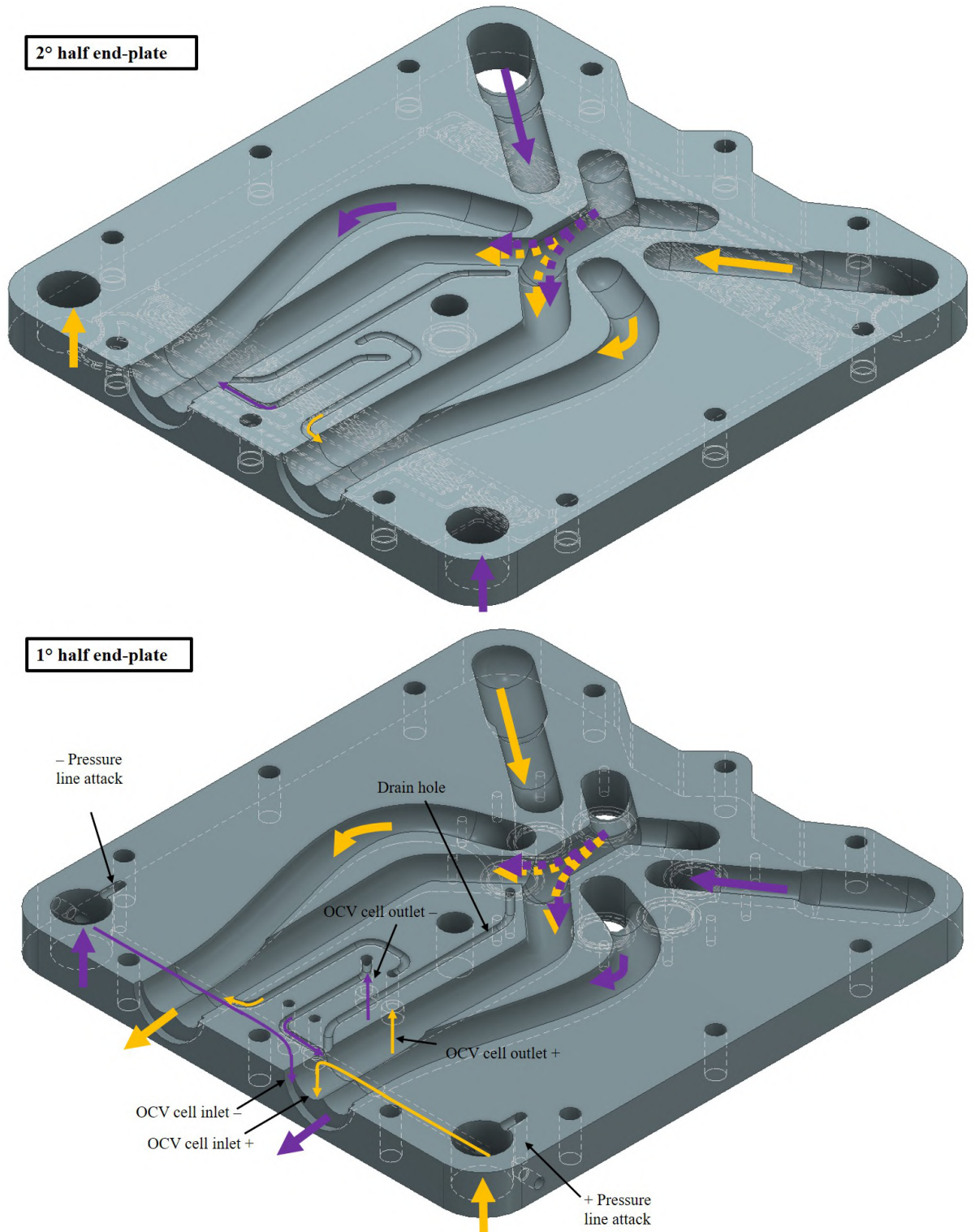


FIGURE 3.12: Front-end plate representation, internal flow path.

automatic and programmed way. In fact, a gradual electrolyte cross mixing occurs via the transport of reactive species, water and sulfuric acid through the membrane. This transport takes place through the ion exchange membranes caused by the electro-osmotic drag [212]. In fact, active species such as V^{2+} and V^{3+} can permeate through the membrane, coupled with the water between the two half-cells of RFBs, due to concentration gradients [213], [214]. An average amount of water between 3 and 4 mol per mole of ion can be expected [215]. Ions and water can move in opposite directions during charge and discharge [146], but these combined mechanisms produce dilution and concentration changes resulting in electrolyte imbalance and loss of energy. Rebalancing the electrolyte can be obtained by "watering," that is by adding chemical oxidants/reducers to the electrolytes or by real electrolyte mixing [216]. Moreover, the use of rebalancing electrochemical flow cells is also possible [217]. A different approach consists of passing the electrolyte through a packed column with a catalyst that changes the concentration of an electrolyte [218]. It has also been suggested that alternating cationic and anionic membranes in a stack could reduce this imbalance [83], although one of the membranes will underperform in the VRFB.

In the IS-VRFB, this operation is performed by adapting the hydraulic circuits that couple the inlets and the outlets of the tanks, allowing the correct mix of the electrolytes contained therein. This is the aim of this end plate, in which a RFB is proposed where the mixing and leveling operations were particularly simple, quick, and efficient.

This consists of a sort of division that comprises a small number of internal hydraulic circuits and external pipes that aim to have a less expensive stack compared to the batteries of the known types, and is barely subject to failures and malfunctions. Fig.3.11 and Fig.3.12 shows the hydraulic parts of this front end-plate; in particular, it is easy to see the positive and negative electrolyte inlet and outlet, respectively. From the inlet, both electrolytes enter the stack with a cross flow distribution (Fig.3.1). At the outlet of all cells, the electrolyte is collected to the output manifold for the positive and negative electrolytes. At this point, the electrolyte can be driven to the starting tank in a "continuous line" or alternatively, to the other tank in a "dotted line," to perform the mixing operation.

Originally, this possibility was guaranteed by a "six-ways mixing valve", mounted in front of the front end-plate that directed the flow to the front end-plate according to the desired mixing or working operations Fig.3.12. This system (old system in Fig.3.13) consisted of a small DC electric motor that could be driven by a 12 V signal coming from the battery management system (BMS). This signal could occur after *SOC* loss detection by the open circuit voltage *OCV* cell after many operation cycles. When the motor is activated, the valve body rotates to allow the electrolyte flow inversion, from working to mixing, or vice versa. This old system suffered leakage problems and a new system has been designed and realized in house, consisting of two three-way valves. It is cheap, efficient, and can be motorized by means of electro valves for future improvements (Fig.3.13). The front-end plate also provides two pressure line attacks that allow the measurement of the pressure drop in the stack, directly upstream and downstream. Moreover, this component is equipped with proper links to an *OCV* measuring cell that allow *SOC* detection. This cell is described in detail in the next Sec.3.1.7. As can be noted, this component has been demonstrated to be quite complex and expensive. It is made from PVC due to its relative hardness and rigidity compared to other polymers of reasonable cost. The most practical processing of this component is represented by a CNC milling using special tools as spherical milling cutters where a difficult face milling process is needed. Moreover, another critical issue arises with the two half-plates bonding, which is performed by a layer of TANGIT PVC-U (Henkel) in the middle, followed by compression in a hydraulic press. The whole procedure is quite complex and expensive resulting in a cost of €900 for just the front-end plate.

The back-end plate is easier, and consists of a support for the external current feeder and the rigid external steel plate. Both assembled end plates are represented in Fig.3.14. The milled flow channels need a shaped cover (which is bonded at the top), while twelve centering bushes ensure the alignment during the stack assembly through the tie bars. Regarding the front end plate, some difficulties have arisen during operation (after two years) due to some internal leakages in the middle of the two half-plates. It has been verified that this component does not have significant advantages with respect to the aforementioned issues, and alternative methods must

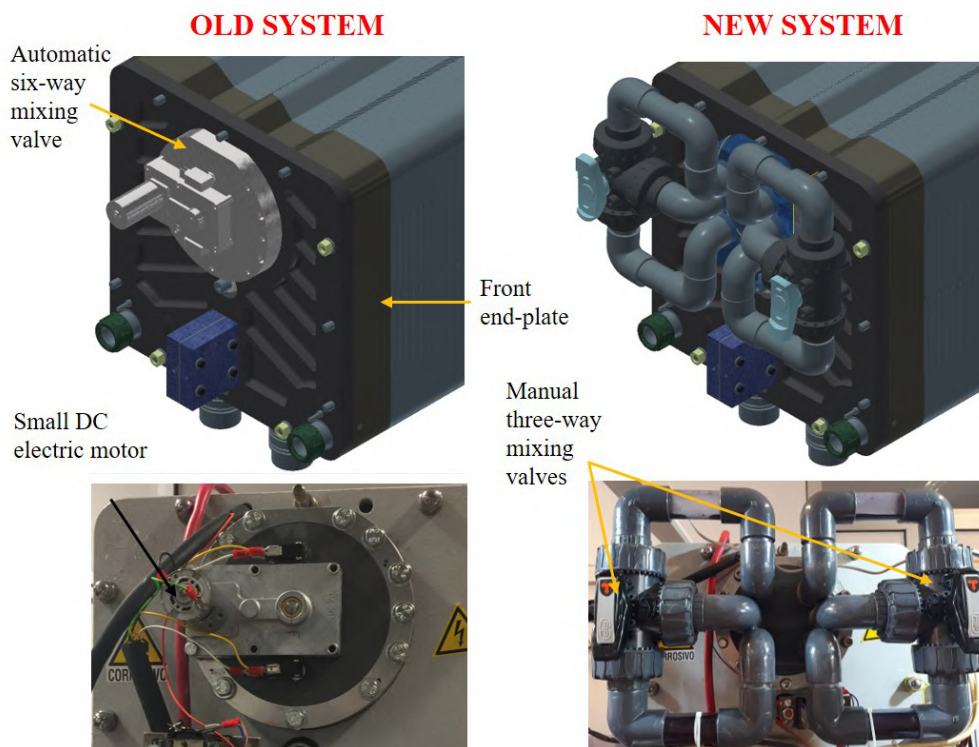


FIGURE 3.13: Left: six-way motorized mixing valve (old system); right: two three-way mixing valves (new system).

be designed in the future to perform an automatic programmed mixing without these problems.

3.1.7 SOC measuring

Since the first development of a VRFB in the 1980s, many different methods for *SOC* monitoring have been investigated. Measurement of the *OCV* is a widely used method using the Nernst law. The *OCV* changes from approximately 0.6 V to 1.6 V during charging (Fig.3.15), [219] and then can be used as an easy and cheap method for *SOC* measurements in commercial systems, as used in the IS-VRFB test facility and others [220]. The whole *OCV* measurement has the main limit of providing only global results, and more information about the state of the two electrolytes cannot be derived from this measure. For a more detailed investigation of both electrolytes, conductivity or half-cell measurements can be used. Skyllas-Kazacos [221] and Kazacos studied the correlation between the *SOC* and the electrolyte electrical conductivity. Nevertheless, these parameters are very sensitive to other variables as well, as they change with temperature, total vanadium, and sulfuric acid concentration. Alternative methods are based on optical measurements; for example UV-visible light spectroscopy, that can be used for the *SOC* determination in the negative electrolyte [221].

[222] examined the absorption on the positive electrolyte followed by the development of a real analytical model, and Petchsingh et al. [223] by using the same UV-vis spectroscopy. Moreover, Liu et al. used transmission spectra to measure the positive and negative electrolyte *SOC* [224], [225], [226], and a new type of sensor that uses infrared absorption has been proposed in [227].

Some problems are still present with this kind of measurement on the positive electrolyte, but these optical methods are reasonably able to provide reliable values to detect the state of charge of the battery. The main disadvantage of these principles is the complex calibration, due to the non-linear correlation between absorbed light and the real vanadium concentration that requires additional complex equipment. Other methods are based on other electrolyte properties, such as the change of density [228] or viscosity [229]. Recently, [230] proposed the use of the

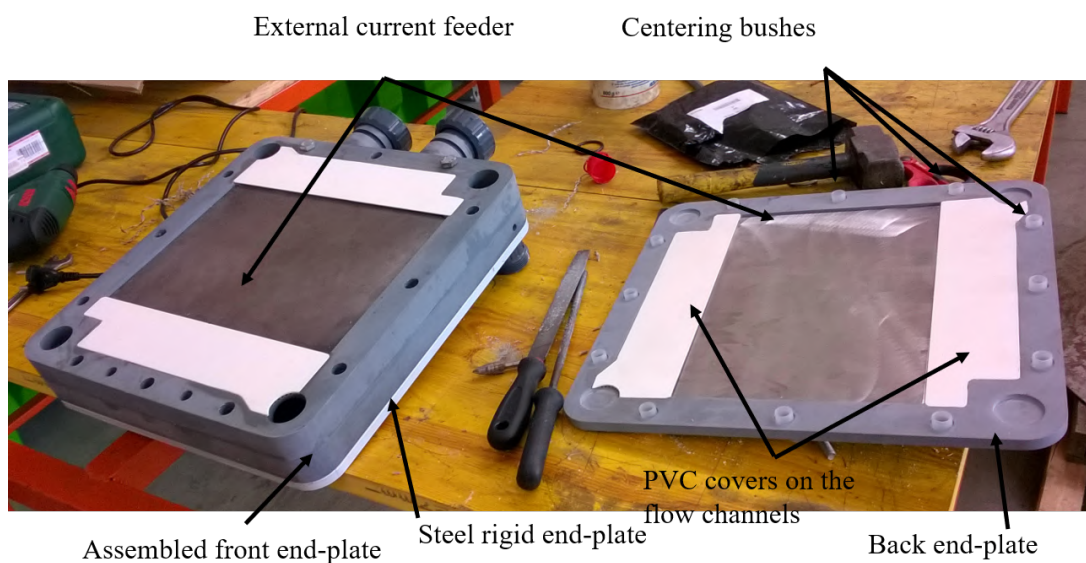


FIGURE 3.14: Left: front end-plate; right: back end-plate.

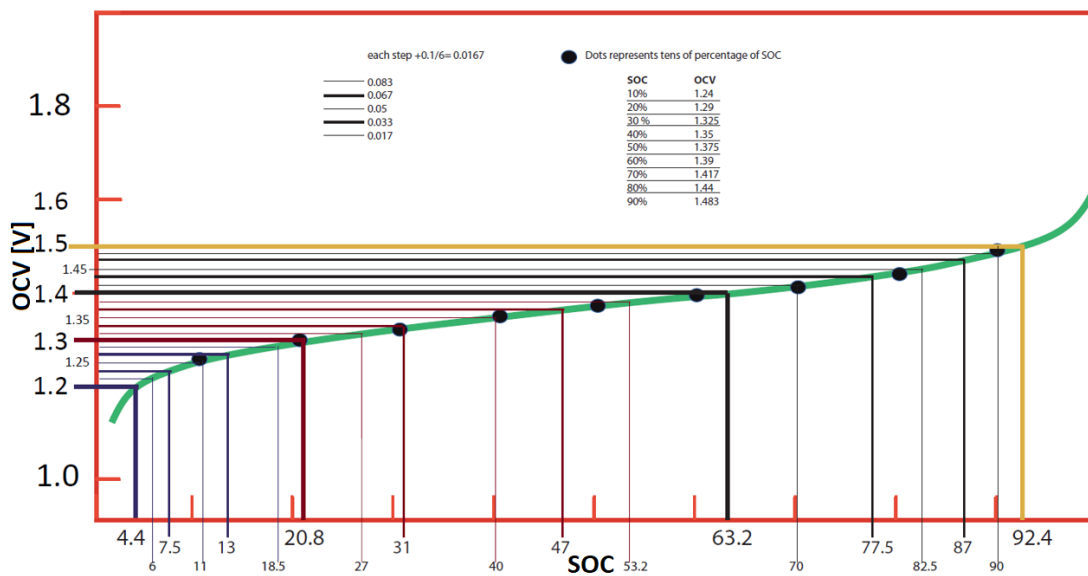
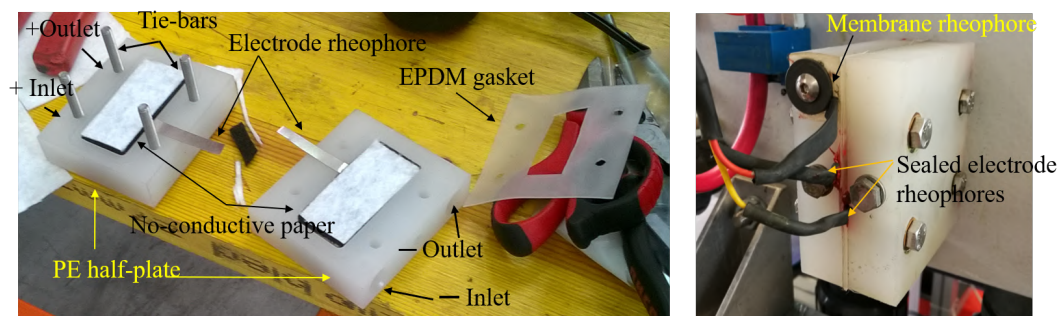


FIGURE 3.15: Nerst equation representation Eq.2.16 (Sec.2.2.1)

FIGURE 3.16: IS-VRFB *OCV* cell.

ultrasonic velocity as sensing method, which was previously applied for Li-ion batteries and in [231] a four-pole device was developed to measure the ionic resistance of the electrolyte.

Further recent methods take advantage of advanced mathematical models as reported in [232], [233], [234]. Very recently, [235] investigated a novel amperometric sensor that is able to detect the *SOC* and then provide precise information on the electrolyte imbalance. Among the aforementioned techniques, the *OCV* method was chosen for the IS-VRFB test facility. The *OCV* cell is shown in Fig.3.16. It is similar to a classic VRFB cell, with the only difference being the non-conductive paper placed between the felts and the membrane, which avoids the presence of an electric current that would alter the *OCV* measurement. This novel cell can monitor the two half-cells individually and determine the concentrations of each vanadium species. In fact, the two electrode potentials are measured from the membrane rheophore (neutral potentials) and the electrode rheophores (Fig.3.16). Both voltage signals are then acquired by the system supervisor and elaborated by the Nernst equation (Sec.2.2.1), which provide the local state of charge. Until now, this cell has been used only for the overall state of charge determination by means of the whole cell potential (between the two electrodes). Future developments can be conducted to detect the electrolyte imbalance through the single electrode potentials evaluation.

3.1.8 Stack assembly

The stack assembly procedure represents one of the most critical phases in the stack realization. A good assembly is vital to avoid electrolyte leakages, especially with a high number of cells. In fact, the assembly torque may have influence on the electrochemical behavior of the stack [236]. Some studies have been conducted on the stack compression. For example, in Proton Exchange Membrane (PEM) fuel cells, the sealing force prediction [237], temperature, and degradation [238] of the silicon gaskets are evaluated. After or before this phase, the carbon electrodes can receive a wetting treatment to remove air bubbles, as in the case of IS-VRFB where this treatment was completed before the assembly.

In general, in RFB technology, the end of separation between flat plate and the porous electrodes has a significant effect on overpotential losses during charge and discharge. As a result, this inter-electrode gap must always be minimized. In some cases, the contact between membranes and electrodes can be prevented by placing a polymer mesh between the electrodes, which can also work as turbulence promoter (Sec.2.3.4). In the IS-VRFB case, the electrodes are electrically connected to the graphite flat plates and the resistance of this connection changes depending on the compression force. This structure is called "zero gap" architecture [40] and greatly reduces the effect of electrode separation by pressing it against the membranes and the flat plates without turbulence promoters. In other RFB technologies, the contact resistance can depend on the formation of passivation films at the connection interface. The assembly was performed by a hydraulic press basement, starting from the back-end plate to the front end-plate. In each cell, the assembly order is as follows: BP, gasket, carbon felt, membrane, carbon felt, gasket, BP. Fig.3.17 represents this sequence for half-cell assembly and the finished assembled piling with all 40 cells during compression.



FIGURE 3.17: Left: IS-VRFB half-cell assembly; right: preliminary IS-VRFB stack compression by means the hydraulic press.

At this point, the cell piling can be compressed with the hydraulic press up to a preliminary position. In this phase, great care must be taken to avoid rupture of the membrane during the stack compression, and the compression ratio of the carbon felts must be considered.

The carbon felts are reduced by 30% of the initial length (from 8.1 to 5.7 mm). The alignment of the bushes is also important to ensure a uniform pressure on the cells. When all the cells are preliminarily assembled, the 12 tie-bars are inserted into the twelve holes and then screwed to achieve a preliminary alignment (Fig.3.18). In this phase, some measurements are needed to guarantee a uniform length for all the tie-bars and the four edges of the stack, to avoid failure of the end-plates due to the localized stress and cracking from non-uniform compression. After the preliminary alignment (directly on the press base), the stack is moved by using a crane to the horizontal position and the tie bars are led to the correct measurement.

During transport, the edges of the tie bars become the anchor points for eyebolts. The final length of the stack (59 cm) is decided to achieve a zero-gap configuration of the electrode and to bring the thickness of the gaskets rib to zero. This phase constitutes the definitive alignment that is carefully performed by using a ratchet wrench. In this phase, the cup springs are inserted according to the scheme in Fig.3.18. This scheme has ensured a good compensation of the relaxation of the gaskets after three years of operation. This is due to there being a good ratio between the gaskets and the spring stiffness. At this point, the other components, such as the OCV cell and the mixing valve, are then mounted on the front-end plate.

3.1.9 Quality control

A VRFB stack is clearly a complex device with many factors that can cause failure and difficulties. First, the hydraulic sealing is one of the major challenges to be solved. Some techniques can be applied that aim to achieve a preliminary quality control during the assembly. This is achieved using commercial pressure sensitive sheets to evaluate the uniformity of compression between the carbon felts and the membranes, between the gaskets and the BPs, to prevent the leakages [239], [236]. Moreover, after the stack assembly, a leakage detection can be performed as in the case of IS-VRFB stack. These tests were designed to become an automatic procedure, in view of a possible stack serial production, and basically consist of a pressurized nitrogen insufflation into the assembled stack (Fig.3.19). The stack is completely sealed using plugs. In this way, the leakage can be detected at the weak point, namely the space between the cell components and the front-end plate. This detection can be achieved with a simple soap or snoop liquid



FIGURE 3.18: IS-VRFB stack fastening procedure.

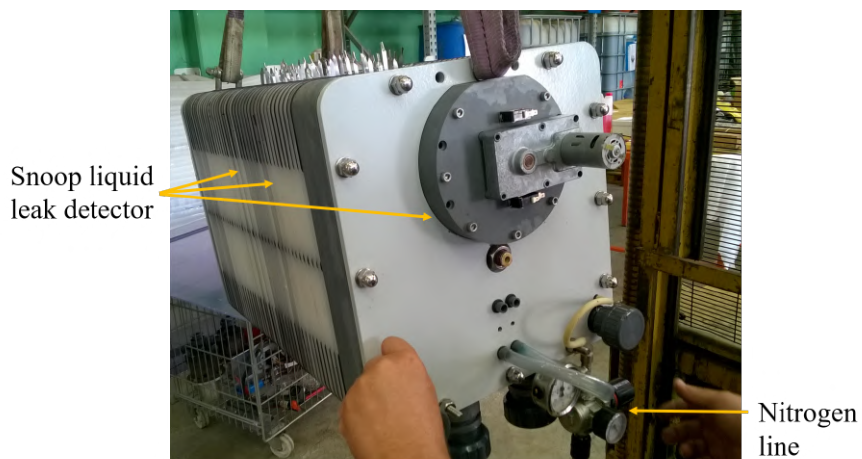


FIGURE 3.19: IS VRFB stack quality control by using nitrogen.

detector (Swagelok, USA) that is designed to detect the gas leakage on tube joints by means of bubble creation.

Moreover, if the internal pressure decreases over time, the leakage will be revealed and localized at the source of the bubbles. A similar test can also be conducted for each BP. Accordingly, a special die was built in order to test each BP with pressurized nitrogen, immediately after the BP assembly process (Sec.3.1.2).

Unfortunately, the operating time of this control was too high to justify its execution and it was decided to check the assembled stack by saving time. At the first trial, the test was successful and the stack was ready to be put into operation and installed on the IS-VRFB test facility.

Chapter 4

IS-VRFB test facility design

The original aim of this project was the design, construction, and testing of a kW/kWh class VRFB provided with a stack architecture directly transferable to an industrial production, with full instrumentation for a measurements campaign in laboratory-controlled conditions.

The original prefixed experimental tests are listed below:

- stack load voltage, current and power profiles as functions of time, *SOC*, both during charge and discharge and under controlled conditions;
- temperature analysis during charge/discharge cycles;
- distribution of voltage in the cells within the stack;
- open circuit voltage (*OCV*) vs *SOC*;
- polarization curves (voltage vs current density);
- efficiency evaluation;
- impedance spectroscopy for dynamic response analysis and equivalent electric circuit characterization;
- management units and supervisor systems;
- fast response analyses;

The layout was originally conceived for high accessibility, with the stack placed in an open space above two tanks, which are set side by side. According to the design, the pumps for circulating the solutions are positioned at the back, at a level that guarantees easy triggering, while the inverters driving the pump motors are placed in a front electric panel, for easy access to the local controls. Each hydraulic circuit is equipped with valves for fast maintenance operation. The tanks are hermetically sealed and their residual volumes are filled with nitrogen gas to prevent vanadium species from atmospheric oxygen contamination. Charge and discharge power control is provided by the power management system (PMS), consisting of a two-quadrant static converter that can be controlled both locally and remotely by a system supervisor. The plant is also fully instrumented with electrical, thermal, and fluid-dynamic probes.

A flexible battery management system (BMS), which represents the system supervisor, was built around a desktop computer with a data acquisition interface that allows fully customizable high-level SCADA (Supervisory Control And Data Acquisition)-like data management with experiment control. Instrumentation also includes multichannel electrochemical impedance spectroscopy (EIS) for each stack cell.

High operation safety was also ensured by the BMS in combination with the surveillance system that is built around a programmable logic controller (PLC) and provided with valve-status and flow rate sensors. The system was conceived for future expansions and upgrades. In particular, the hydraulic circuits were provided with ports for installing other small stacks where new materials and cell architectures could be easily tested before being used in a future upgraded larger stack. The major issue in designing the test facility was the compatibility of the materials for components with parts exposed to the electrolyte. In fact, the reactivity of the electrolytic solutions, which consist of 30% sulfuric acid (4.5 M) prevents the use of many usual materials (such as stainless steel, copper, or steel without paint protection). In the next

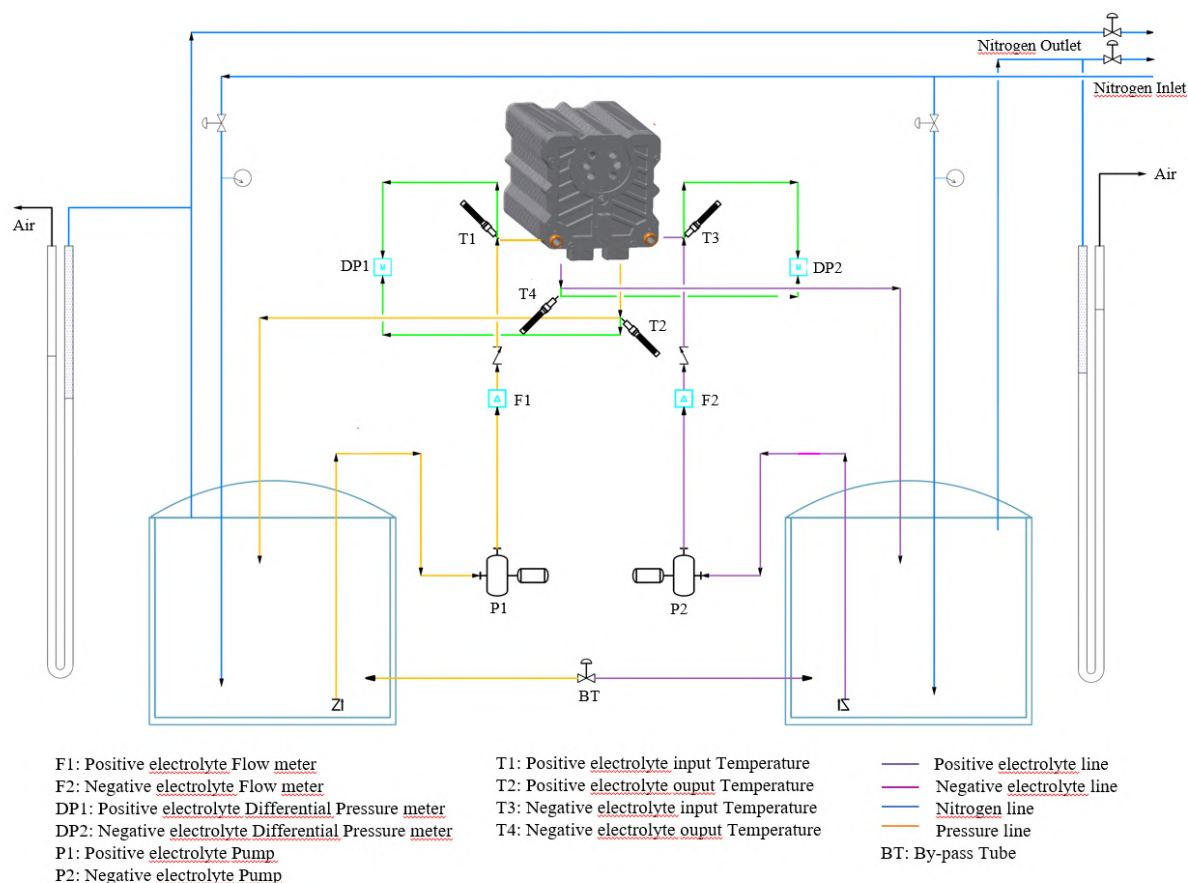


FIGURE 4.1: IS-VRFB simplified P&ID.

sections, the main design issue for each component are presented, beginning with the hydraulic balance of plant, the electric connections, the BMS, and the surveillance system.

4.1 Hydraulic design

In Fig.4.1 the simplified piping and instrumentation diagram (P&ID) of the two hydraulic circuits is shown, each including the tank, pump, piping, and valves for fast maintenance. All the hydraulic components are made of sulfuric acid-tolerant materials, in particular polyethylene (PE), polyvinyl chloride (PVC), and polypropylene (PP), to exclude corrosion issues.

4.1.1 Piping

The pipes were made with transparent PVC segments to allow direct visual inspection of the solution flow and color, which could provide an immediate indication of the solution state of charge. In addition, a by-pass pipeline, provided with manual valves, allows the balancing of the level in the two tanks by eliminating any pressure difference that could arise from variations in the electrolyte volumes caused by the ion and water crossover through the membranes [214]. The two circuits are also equipped with pick-up ports for collecting samples without opening the pipes, in order to perform physical-chemical measurements such as electric conductivity, dynamic viscosity, and potentiometric titration. The most important valves were equipped with sensorization made in-house using magnetic sensors. The position of the valves was determined using a BMS to detect the correct volumetric flow rate in the stack and to avoid incorrect

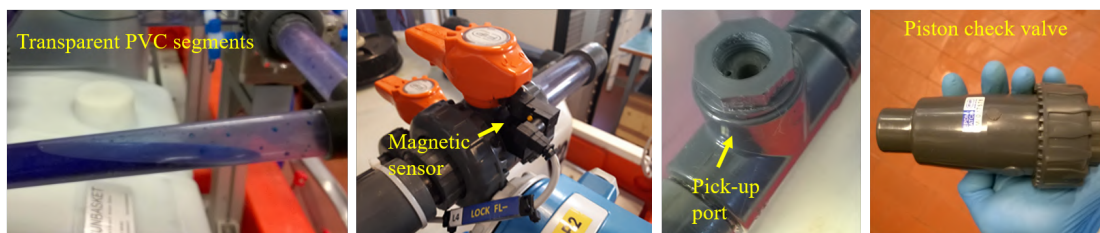


FIGURE 4.2: Main IS-VRFB hydraulic components.

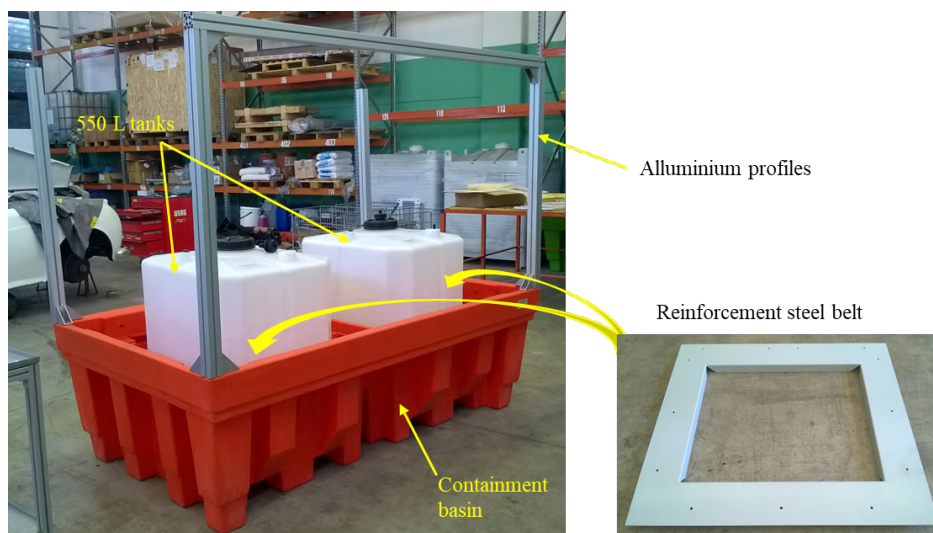


FIGURE 4.3: IS-VRFB tanks.

operations that could cause stack breakage, such as avoiding overpressure due to the downstream-looking valves. Easy triggering of the pumps was ensured by a non-return valve positioned on the suction side of the pump inside the tank.

The simple ball check valve was not demonstrated to be suitable for this task and was replaced with an heavier piston cheek valve, which is less influenced by overpressure at the bottom of the tank (caused by the relative high density of the electrolyte) (Fig.4.2).

4.1.2 Tanks

The tanks used in the VRFB were clearly fabricated with resistant polymers and their cost and complexity increased considerably with scale. The connections of multiple and medium-size tanks can reduce costs in larger systems and the addition of tanks can easily expand the capacity of the battery. The IS-VRFB tanks were chosen to guarantee the electrolyte mix through a spiral-shaped motion induced between the suction (at the bottom) and the drainpipe (at the top), which takes place because of an inclined orientation of the drain pipe. In larger plants, the electrolyte mix can also be obtained through a continuous recirculation of a portion of the pump flow; however, this was not convenient in our experimental test facility because of the additional complexity of the piping circuit and the relatively small tanks (550 L each).

After a trade-off process that involved assembly issues and the ability of the tank to guarantee the electrolyte mixing, two parallel-piped PE tanks were chosen. These were provided with two reinforcement steel belts designed in-house to prevent bulging, positioned inside a containment basin to avoid electrolyte dispersion in the unlikely event of a leak. This basin also constitutes the basement for the aluminum profiles rack that constitute the frame for the PVC barrier protection.

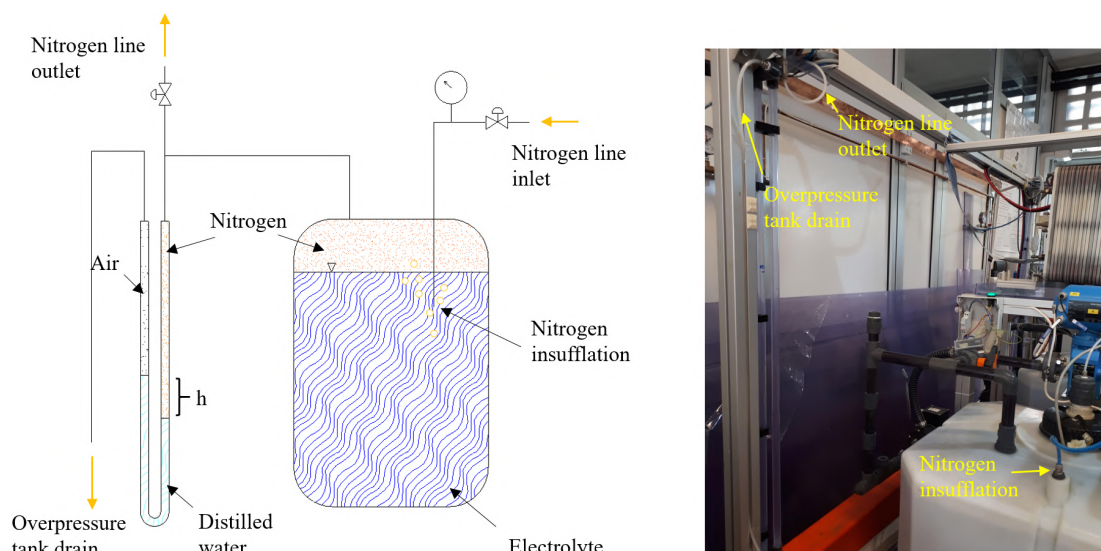


FIGURE 4.4: Millibaric pressure safe control system in inert atmosphere for highly reactive liquid solutions.

4.1.3 Inert atmosphere and differential pressure gauge

The electrochemical process in the VRFB is quite complex and involves some side reactions that include air oxidation of the $V(II)$ ions at the negative half-cell [87]. Accordingly, a nitrogen circuit that excludes the presence of atmospheric oxygen in the residual volumes of the tanks was designed and realized. This is an innovative multi-functional device that uses U-shaped PVC transparent pipes filled with water, capable of creating an overpressure with millibaric control in a sealed tank, using nitrogen gas (1st task). In this way, a difference of 1 cm reveals an overpressure of 1 mbar. Moreover, the entry of atmospheric oxygen that could pollute the solutions is also prevented (2nd task) and, simultaneously, the system allows the collection of any reaction gases that might develop inside the tanks for subsequent analysis (3rd task). The system also acts as an overpressure valve by ensuring an accurate control of the overpressure (4th task), (Fig.4.4).

4.1.4 Hydraulic pumps

Stacks and flow systems involve pressure drops and pumping needs that can only be computed with a preliminary estimation or by numerical simulations. Generally, the pressure drops in VRFB stacks can be determined by considering the Darcy's friction factor or permeability of the porous electrode felts, and the pressure drop that occurs at the internal manifolds and external piping circuits (Sec.5.1.2) [240], [241]. As a preliminary estimation, a maximum pressure drop of 0.5 bar has been estimated with a consequent dimensioning of the pumps.

It is important that this limit value is not exceeded, to remain outside the applicability of Pressure Equipment Directive (PED) 2014/68/EU that sets out the standards for the design and realization of pressure equipment (steam boilers, pressure vessels, safety valves, piping, and other components and assemblies subject to pressure loading) generally over 1 L in volume with a maximum pressure higher than 0.5 bar gauge. For this reason, a design simplification can be achieved by treating the test facility as a non-high pressure system with an operating pressure lower than 0.5 bar.

Regarding the flow rate, the pumps were sized to provide solution flow rates at the stack $Q=30$ L min^{-1} in excess of the minimum flow rates needed for the reaction stoichiometry, ensuring a flow factor $\alpha \geq 10$ at the expected maximum current of 75 A and $SOC=50\%$. To meet these requirements, several types of pump were evaluated, including peristaltic, flexible impeller, and gear pumps. Generally, volumetric pumps have a significant advantage in guaranteeing an easier flow rate control by controlling the motor speed, compared with centrifugal pumps where

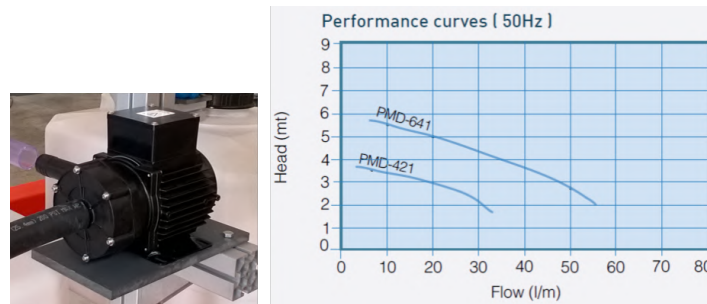


FIGURE 4.5: Left: IS-VRFB pump, PMD-641 by Sanso, Japan; right: PMD-641 characteristic curve.

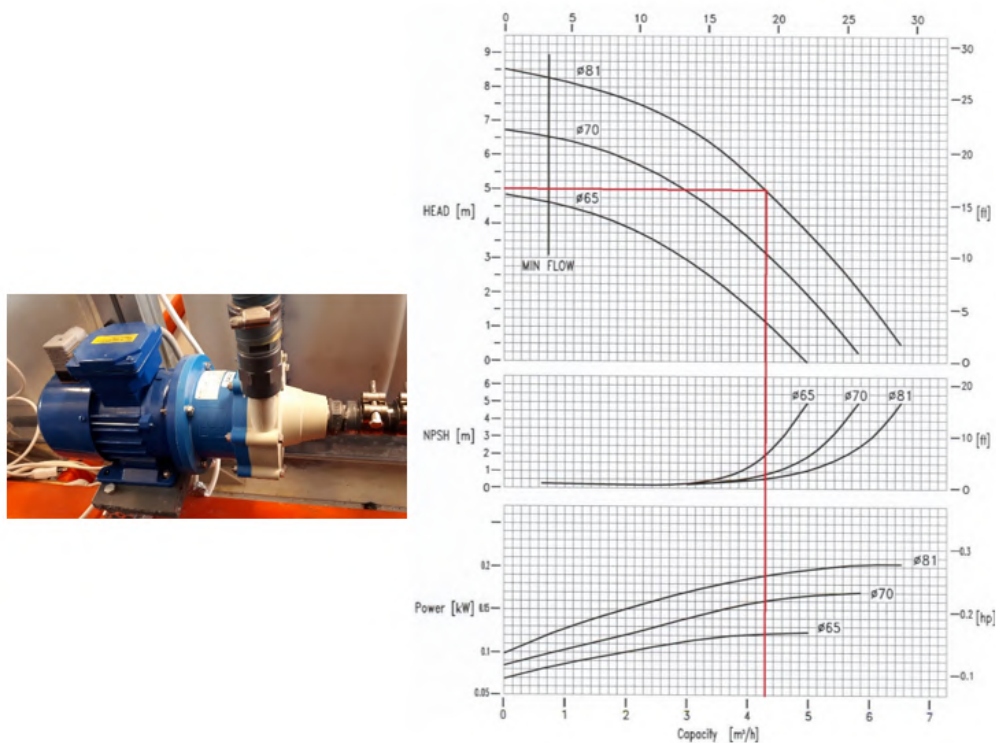


FIGURE 4.6: Left: IS-VRFB bigger pump, CM MAG – P06 by M Pumps Industry, Italy; right: CM MAG – P06 characteristic curve.

feedback loop and volumetric flow rate measurements are needed. Nevertheless, these pumps are more dangerous in the case of occlusion of the hydraulic circuits that can occur in a laboratory due to some incorrect action, and are usually more expensive in comparison to the centrifugal ones. A trade-off was made by choosing the PMD-641, produced by Sanso, Japan, with a PVC stator and rotor, the last being magnetically driven by a three-phase squirrel-cage induction electric motor. To ensure the flow rate control, two solid-state inverters (DC1 by Eaton, US) were installed to power the motors at variable frequencies through a feedback control signal, to operate the pumps at controlled flow rates. The characteristic curve of this pump is shown in Fig.4.5.

Very recently, larger pumps have been installed to aid with the investigation of VRFB behavior at higher flow (Fig.4.6). However, all the tests and results conducted in this thesis were obtained using PMD-641 pumps.

4.1.5 Thermo fluid-dynamic sensors

Several physical measurements are acquired from the system and by the BMS, to perform

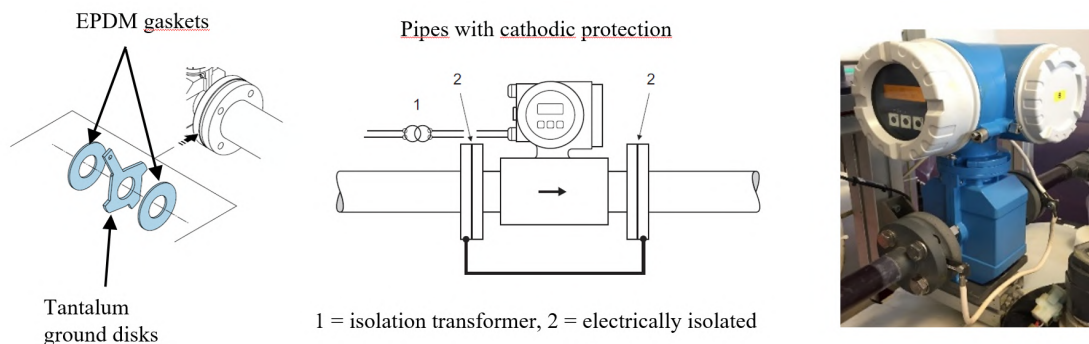


FIGURE 4.7: Volumetric flow-meters, Proline Promag by Endress+Hauser, Switzerland.

the research activity. In this regard, the flow rate determination in the RFB assumes crucial importance and accurate measurements are required. Different methods can be used for such measurements on sulfuric acid-based solutions, including ultrasonic, volumetric, Coriolis effect, and electromagnetic flow meters.

A good compromise between precision, cost, and reliability resulted in choosing the electromagnetic flow meters (Proline Promag by Endress+Hauser, Switzerland). Each flow meter is equipped with a polytetrafluoroethylene (PTFE) internal tube coating and a couple of tantalum grounding disks that eliminate the disturbance caused by the shunt currents through the conductive electrolytes. This is an important aspect for such measurements. Thus, while the reference potential is normally matched using the reference electrodes directly in the measuring tube, in the case of fiber-glass or PVC piping, it's necessary to install the measuring instrument without the potential in the piping to protect the tantalum electrode from corrosion (for example through electrochemical decomposition). The use of additional ground disks is recommended for potential matching and for the supply to the flow meter, by using an isolation transformer that decouples the flow meter from the grid Fig.4.7.

With regard to the pressure drop measurements, two customized differential pressure gauges (Deltabar PMD by Endress+Hauser) were chosen that measure the solution pressure drops between the stack inlets and outlets provided with a polyvinylidene fluoride (PVDF) internal inlay. The sensible sept was ordered in tantalum (that can normally work in a 4.5 M sulfuric acid solution); however, the effects of an applied electric field resulting from the contact with the conductive electrolyte at the inlet and at the outlet of the stack is still unknown. For this reason, an ad-hoc design was planned with Galden[®]-filled piping to prevent any contact between the gauge tantalum sensor and electrolytic solutions (Fig.4.8). The decoupling between the instrument and the grid was not important and no isolation transformer was required to prevent electrochemical decomposition of the sept.

From the thermal characterization, four resistance temperature detectors (RTDs) Pt-100 (TR11 by Endress+Hauser) were installed to measure the solution temperatures at the stack inlets and outlets (Fig.4.9). Their customized alloy C276 thermowells ensure a solid separation with the electrolyte and have been positioned for the accurate measurement of the electrolyte temperatures at the mean flow.

The level of the tanks also represents an important measure for evaluating the electrolyte imbalance [146] and preventing leakages due to the electrolyte overflowing above the upper level of the tank. For these reasons, two potentiometric-type level sensors (Val.Co S.r.l., Italy) have been installed, based on the gradual shutdown of resistor chains and reed contacts, placed inside the guiding rod, by the slide of a magnetic float. The only moving element is constituted by the float that moves along the measuring rod. In addition, a Pt-100 sensor is located at the bottom of the rod that monitors the tank temperature (Fig.4.10).

The measurement ranges for all the sensors were selected according to preliminary estimations in terms of maximum flow rate, pressure drop, temperature, and tank level, Tab.4.1.

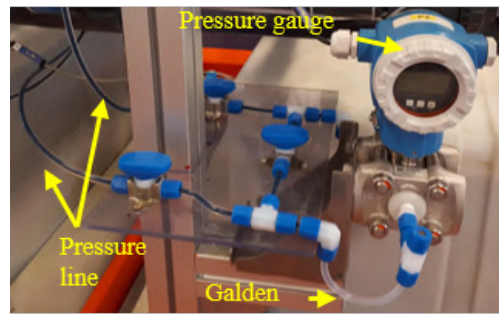


FIGURE 4.8: Differential pressure gauges (Deltabar PMD by Endress+Hauser).

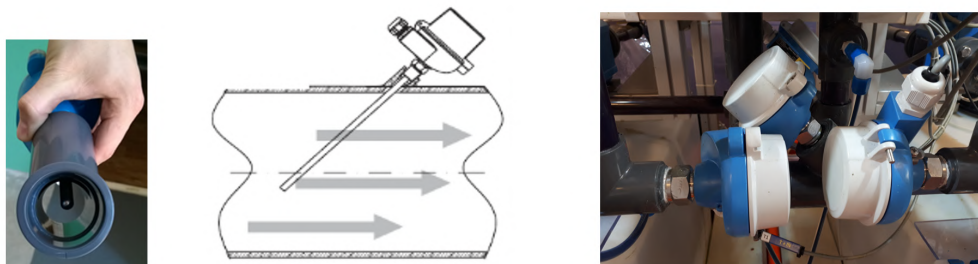


FIGURE 4.9: Resistance Temperature Detectors (RTDs) Pt-100 (TR11 by Endress+Hauser).

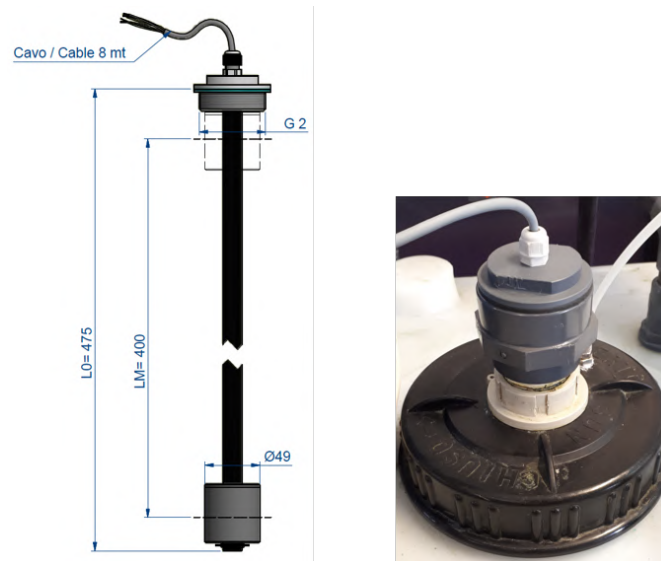


FIGURE 4.10: Potentiometric type level sensors, (Val.Co S.r.l., Italy).

TABLE 4.1: Measurement ranges and uncertainty of the thermo fluid-dynamic IS-VRFB sensors.

Measurement	Sensor	Range	Total uncertainty (95% confidence)
Stack pressure drop	Differential pressure transducer (Endress Hauser Deltabar PMD 75)	0-100 kPa	± 450 Pa
Electrolyte flow rate	Volumetric flow meter (Endress Hauser Promag 50 P)	0-60 L min ⁻¹	$\pm 5\%$
Electrolyte temperature	RTD temperature sensor (Omnigrad M TR11)	-50 to 250 °C	$\pm 0.15 + 0.002 T $ K
Electrolyte level	Potentiometric type level sensor (Val.Co S.r.l.)	0 too 400 mm	± 5 mm (4 L)

4.1.6 Test facility assembly

According to the designed P&ID scheme (resulting from the hydraulic circuit needs and based on the dimensions of selected components), an entire 3D model of the whole test facility was first realized. In this model, the actual 3D geometry of each component was used based on the manufacture drawings. This phase was rather onerous in terms of time, but proved to be smart during the next phase of assembly, where each component needed to be mounted in the right place, with no joint errors permitted. The 3D model of Fig.4.11 was drawn according to the layout that was conceived as an open frame design with the stack located in an open space over the two tanks, set side by side. As described in the first part of this chapter, the system was conceived for future expansions and upgrades with ports for installing other small stacks in which new materials and cell architectures could easily be tested before being used in a future upgraded larger stack.

After the 3D modeling operation, the assembly of the plant was performed according to the following main steps. First, the tanks and the aluminum rack were positioned inside the containment basin, Fig.4.12 (left). Next, the PVC tubes were joined using Tangit [242], Fig.4.12 (right), coupled with the installation of the flow meters, thermo resistances, and pressure transducers on the piping circuit.

When the piping assembly was completed, the pumps were installed and a sealing test was conducted using water circulation to test the piping circuit sealing. Only after these stages was the stack connected to the completed circuit and the tanks filled with fresh electrolyte (Fig.4.13).

The next phases were dedicated to the installation of the PMS and BMS and are described in Sec.4.2.1 and Sec.4.4.

Fig. 4.14 presents the results.

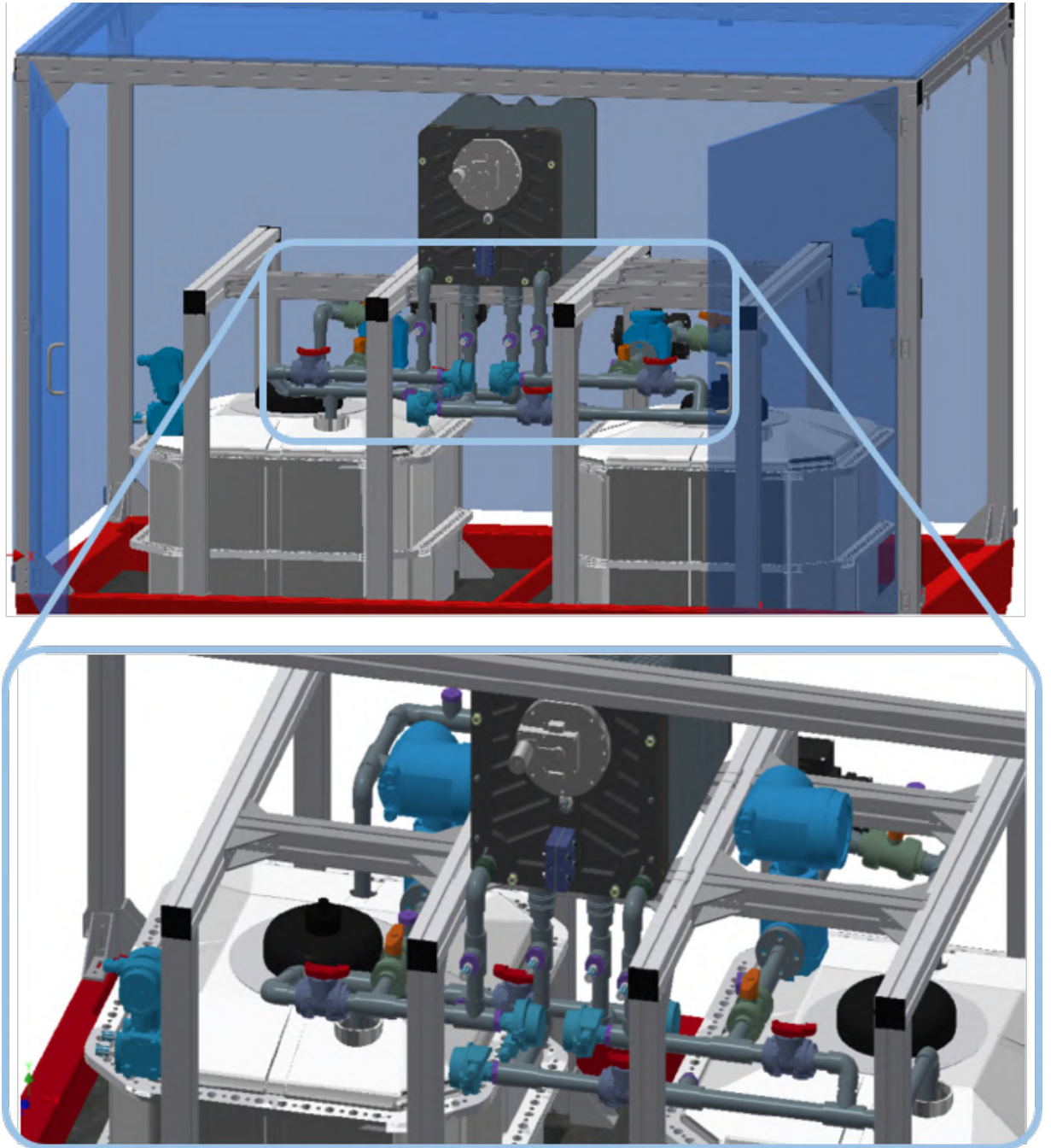


FIGURE 4.11: IS-VRFB 3D model.



FIGURE 4.12: IS-VRFB hydraulic plant assembly. Left: aluminum rack assembly; right: piping assembly.



FIGURE 4.13: Filling the tank with the electrolyte.

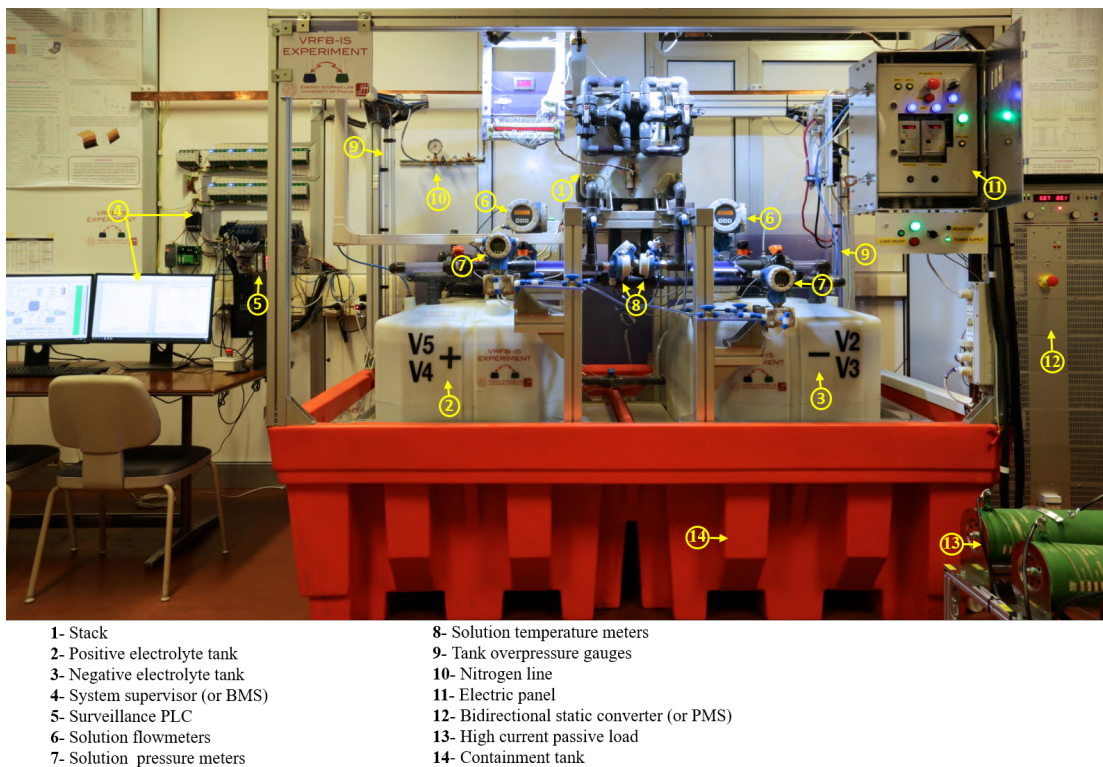


FIGURE 4.14: IS-VRFB test facility and the main components.

4.2 Electrical design

In a commercial VRFB system, the integrated power electronics are one of the main control components and are usually supplied by the electrical manufacturers [40], without a specific design for VRFB application. They determine the VRFB regime, namely, constant current, voltage, power, and the mode of operation. These also include: load following, frequency regulation, voltage control, and power system stabilization, [243]. The power conditioner usually consists of a transformer, a DC/AC bidirectional static converter, circuit breakers, and its own control units. This system also comprises sensors, data acquisition units, power conditioners, and computer control software.

These elements work together by constituting the BMS [244]. For example, operation algorithms are developed for specific applications, such as stabilization of the power grid connected to a wind farm or solar park. Automation also plays an important role, especially for mobile, remote, or backup power applications.

Furthermore, large utility-scale load levelling plants are monitored from central software control that includes safety protocols. In the case of an IS-VRFB test facility, the electrical design follows all the aforementioned requirements to achieve a fully flexible and safe system that allows a wide characterization of a kW-class VRFB stack. The electrical scheme (both power and control connections) was designed entirely in-house, and realized with the exception of some components such as the bidirectional static converter dubbed "power supply" and the six passive resistors that were bought, assembled, and connected.

4.2.1 Power management system (PMS)

The power management system (PMS) that provides electric power conditioning during charge and discharge consists of AC/DC bidirectional static converter (dubbed power supply, PS) remotely controlled by the BMS and of a passive load (PL) for high current discharges. The PS is rated 0–85 V DC and ± 75 A DC and its current/voltage profiles can be controlled by BMS algorithms, according to the experimental needs. It is equipped with a circuit breaker and

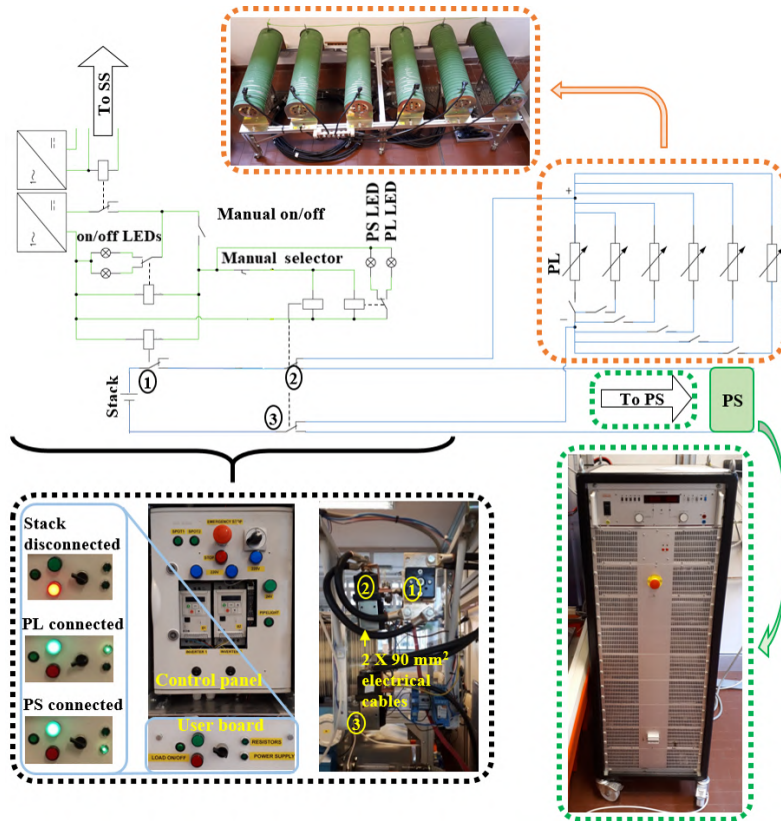


FIGURE 4.15: IS-VRFB power management system (PMS) with the power electrical scheme, including the PS, the PL, the user board and the power contactors (1, 2 and 3).

a step-down transformer that guarantees galvanic insulation from the grid. The PL consists of six variable resistors that allow discharges currents up to 600 A. Two three-way contactors, one for the positive (2) and one for the negative pole (3) allow selecting the PS or the PL to be connected to main bipolar contactor (1) of the power circuit. These contactors are controlled by the “manual selector” in the front “user board”, that is provided with LEDs indicating the connection state. Fig.4.15 shows the power electrical scheme with the PS, the PL, the user board, and the power contactors (1, 2 and 3). The connection of the PMS to the stack is performed by the main bipolar contactor (1) that is controlled by two switches in series. The first switch is controlled by a logic signal generated together by the surveillance system (SS) and by the BMS. The second switch is a “manual on/off” switch installed in the user board: if both switches are closed the main bipolar contactor is closed, a red LED turns off and a green LED turns on. The manual on-off can be used for fast disconnection in the case of a faulty condition. The power connections are made with a pair of 90 mm² cables, sized for a current of 600 A.

4.3 Electromagnetic interference

One of the main problems with measurement activities was the consistent presence of disturbance and interference. Particular voltages and currents, which are fundamental for the experimental control of the battery, were affected by these issues. The problem was pinpointed at the pulse-width modulation (PWM) inverters that command the pumps. These devices created both a conducted disturbance on the line and a radiated disturbance in the surrounding environment.

To eliminate this problem, many operations were conducted on the electrical plant. First, a filtered power entry module was installed upstream of the inverters power supply to limit the diffusion of conducted disturbance to the grid, and upstream of the CompactDAQ to limit the incoming interferences; however, but no significant results have been reported. Second, two

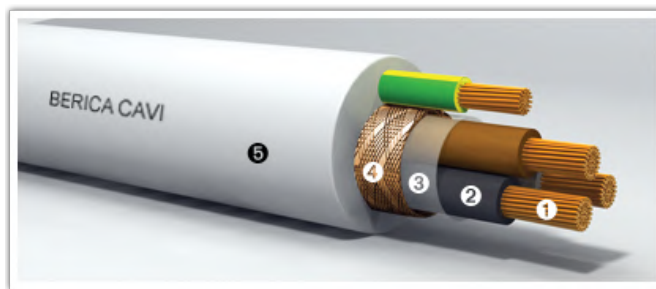


FIGURE 4.16: Inverter-motor cable section (courtesy of [246]).



FIGURE 4.17: Copper shielding pipes for motor-inverter cables.

parallel capacitors (1 η F and 100 nF respectively) were installed upstream of the LEM transducer to work as physical filters, but, again, no benefit has yet been noted.

Moreover, the signals and power cables that come from the LEM to the CompactDAQ were substitutes with shielded cables, and the results were not sufficiently good. Last, as suggested by the electro-magnetic compatibility regulation and reported in [245], the non-shielded cables that connect the pumps with the inverters were replaced with specific inverter-motor cables. Their peculiarity enables the separation of the grounding cables from the tripolar ones, which are shielded, as shown in Fig.4.16. In this way, even if some interference travels to the grounding cables it cannot propagate to the power cables.

The results agreed with what was expected by keeping the errors in an accepted range. To strengthen the effect of a copper shield, the power cables were inserted in additional external copper pipes (Fig.4.17). As the inverters are a source of radiated electromagnetism it was decided to construct a shield (Fig.4.18). A shield is typically a metallic barrier used for both reducing emissions from electrical equipment and increasing the immunity of a device [247].

The shielding effectiveness (defined as twenty times the logarithm of the ratio between the incident and the transmitted electric (or magnetic) field), is a positive number that represents a reduction of the magnitude of the phasor of the electric (or magnetic) field when subjected to a metallic shield. It is the sum of three terms: absorption loss A_{dB} , reflection loss R_{dB} , and multiple reflection loss M_{dB} . Absorption loss is a function of the thickness of the metal shield and the product of its conductivity and permeability. It increases with increasing frequency as \sqrt{f} , on a logarithmic scale. Reflection loss depends on the ratio between conductivity and permeability and varies with frequency at a rate of -10 dB/decade. It does not depend on the thickness of the shield. Multiple reflection loss can be neglected in the case of a thick shield [247].

Fig.4.19 shows the metal box made to enclose the two inverters and the electric panel with all its components. Before these operations the current value (measured by the LEM sensor) when only the inverters were activated but no current was given to the electric motors driving the pumps was approximately of 0.3 A instead of the expected null value. When the pumps

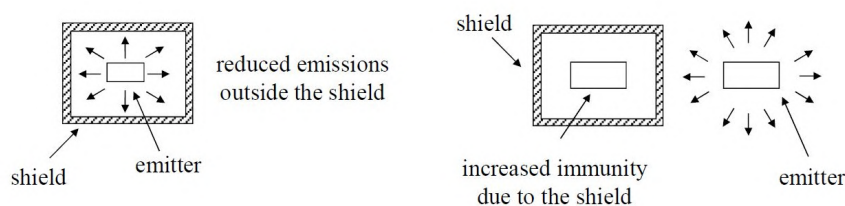


FIGURE 4.18: Electromagnetic shields examples [247].



FIGURE 4.19: Shielding metal box.

operated at 50 Hz power supply, the disturbance increased to 0.5 A for 0.8–1 A. After the installation of these protection devices, the interference was almost completely eliminated.

4.4 Battery management system (BMS)

VRFBs need to be configured for automatic unmanned operation, especially in remote installations where human intervention is limited. The development of an efficient BMS that provides such features represents a critical issue to guarantee successful operation [244]. In an industrial VRFB system, these functions should be provided by a low-cost PLC with well-tested software. Nevertheless, in an experimental system, the supervision functions can be more conveniently implemented by using a flexible and expandable system, with advanced programming features and with a human machine interface (HMI). The IS-VRFB BMS was built around a desktop computer equipped with LabVIEW software and NI (National Instruments, US) compact data acquisition (Compact DAQ NI 9179) device. These modules were chosen according to the type of measure.

The NI 9207 module can read both current and voltage signals through current acquisition channels and voltage acquisition channels, respectively. This module acquires current analog signals (such as flow rates and differential pressures) and voltage analog signals (such as stack voltage, stack current, *OCV*, and pump power losses) from the sensors. These signals are scanned, amplified, conditioned, and sampled by a 24-bit analog-digital converter. The accuracy for current channels is $\pm 0.87\%$ gain error and $\pm 0.05\%$ offset error, while the accuracy for the voltage channels is $\pm 0.52\%$ gain error and $\pm 0.04\%$ offset error [248].

The NI 9209 module can only read voltage signals, and is used to read the voltages for the 40 cells. These signals are scanned, saved in a buffer, conditioned, and then sampled by a 24-bit analog-digital converter. The accuracy of the voltage channels are $\pm 0.46\%$ gain error and $\pm 0.011\%$ offset error in the range of -40°C to 70°C . At 25°C , the gain error is $\pm 0.06\%$ and the offset error is $\pm 0.003\%$ [249].

The NI 9216 module is specific for temperature measures, and is used to read the electrolyte temperatures from the RTDs. In this case, the signals are filtered, and then additionally sampled by a 24-bit analog-digital converter. The accuracy is $\pm 0.15^\circ\text{C}$ at a temperature of 25°C [250].

The NI 9263 module is used to control actions using analog voltage outputs. These signals are sent to the inverters, which control the pumps engines simply changing the inverter frequency through a signal from 0 to 10 V. In this way, it is possible to vary the flow rate. Each channel is characterized by an analog-digital converter and a protection against short-circuits and overvoltage. The accuracy is $\pm 0.35\%$ gain error and $\pm 0.75\%$ offset error in the range from -40°C to 70°C . At 25°C the gain error is $\pm 0.03\%$ and the offset error is $\pm 0.1\%$ [251].

Noise suppression is guaranteed by a grounding system based on a large copper equipotential bar that provides a common reference for all voltage signals (Figs.4.21, 4.22). The BMS in-house software provides the test-facility with SCADA functions, (that is, it manages all acquired data by processing and logging, and performs the subsequent analyses). It also ensures experimental control of electrical, fluid-dynamic, and thermal management by using real-time procedures using real-time measurements for feedback control. For the sake of simplicity, two main control procedures are listed, as follows:

- thermal management system: to avoid $V(V)$ precipitation at high SOC , a LabVIEW algorithm that is enabled during standby condition continuously monitors the stack temperatures provided by the thermo-resistance and starts a stack washing cycle if temperatures exceed safe conditions (Sec.5.4);
- a precise flow rate control for each pump through a proportional-integrative-derivative (PID) controller is obtained, in which an analog voltage (0–10 V) signal drives the two inverter based on a negative feedback logic that uses the measured analog current signals (0–20 mA) provided by the flow meters.

4.4.1 Surveillance system (SS)

A surveillance system (SS) has been designed and installed to protect the facility against improper operations. It allows the stack current to be started only if a number of checks are enabled, and to be switched off immediately as any check toggles, namely if any dangerous or faulty condition arises during operation. To ensure these functions with a high degree of reliability, the SS is implemented in a dedicated PLC, different from the BMS. In particular, this PLC receives signals from the magnetic sensor installed on the hydraulic valves for detecting any wrong setting. In addition, safe VRFB operation in any condition is guaranteed by the coordinated actions of the SS and the BMS, based on a hierarchical protection logic. Some functions are described hereafter:

- the PMS can be activated only if the two electrolyte flows in the stack exceed the minimum values Q_{min} needed to sustain the electrochemical reactions, namely stoichiometric flow rate that avoids the occurrence of improper reaction inside the cells, that can damage its components. These minimal flows correspond to a minimal safe flow factor, (Eqs.8.12, 8.13) set at $\alpha_{min}=3.5$;
- in order to avoid any mechanical trouble in the hydraulic circuits, a PLC procedure block the pumps whenever the stack pressure drops exceed the maximum limit of 0.5 bar;
- the secondary reaction or gas formation during charging at high SOC ($\approx 90\%$), is avoided by a LabVIEW procedure that opens the main connector (1 in Fig.4.15) in one cell voltage exceeds a maximum limit (1.7 V);
- to prevent the occurrence of the absence of cell voltages that occurs when the cell flow is lower than the stoichiometric one, a LabVIEW procedure opens the main connector (1 in Fig.4.15) if any cell becomes lower than a the minimum limit of 0.1 V, which can occur during deep discharges by using the passive load. This lower limit is now to be revised in order to clarify if 0.4 V is suitable to avoid such problems.

TABLE 4.2: Measurement ranges and uncertainty of the electrical IS-VRFB sensors.

Measurement	Sensor	Range	Total uncertainty (95% confidence)
Stack current	Current transducer (LEM HASS 200-S)	-600 to 600 A	$\pm 1\%$
Cell voltage	Analog to digital converter (National Instruments NI 9209)	-10 to 10 V	$\pm 0.097\%$
Stack voltage	Stack voltage sensor (LEM CV 3-100/SP3)	-130 to 130 V	$\pm 0.2\%$
Inverter and pump power	Power analyzer (Seneca Z203-1)	0 to 2500 W	$\pm 5\%$

4.4.2 Electrical schemes

The schemes for the wiring connections were made using AutoCAD Electric software (Autodesk), a dedicated software package for drawing electrical circuits. Fig.4.20 represents the electrical connection among the devices dedicated to the measurements. On the left side, the potential grounding bar is represented, and the PLC is coupled with the National Instruments CompactDAQ with all modules shown in detail. Fig.4.21 is dedicated to the power connections including LEDs, lights, switches, relays, and electrical motors. In the two general schemes the cables are distinguished by different colors, as follows:

- blue: power connections for both alternate or continue currents;
- yellow: grounding connections for both protections and potential groundings;
- purple: measurement connections for both digital and analog signals coming from the sensors or the measurement devices;
- green: control connections for all the wirings where a current or voltage control is made.

4.4.3 Electrical sensors

Signal conditioning between the stack and Compact DAQ includes cell voltage galvanic insulation that consists of opto-isolators (Isoblock by Verivolt, US) and stack voltage galvanic insulation ensured by a DC/DC transformer (LEM CV 3-100/SP3). A total of 41 alloy C276 rheofores provide the individual cells and stack voltages in load conditions and a small cell, which is mounted and fed with the same electrolytes flowing in the stack, provides real-time open circuit voltage (*OCV*) measurement at any operating condition (Sec.3.1.7). Two current probes (HAS 50-S and HAS 200-S by LEM) are used to measure the stack current with high accuracy in both low and high current regimes. An independent voltmeter visualizes the stack and cell voltages. A wattmeter (Seneca Z203 single-phase analyzer) measures the power absorbed by the inverters feeding the two pumps and ensures the efficiency of the computation as presented in Sec.8.1.1. All the detected signals are conditioned and processed in the BMS as described in Sec.4.4. Tab.4.2 lists the electric measurement ranges and accuracies and Fig.4.22 shows the electrical sensors coupled with the Compact DAQ where all signals are acquired, and the copper grounding bar that provides the common reference to all voltage signals.

Multichannel EIS was performed by an ad-hoc developed analyzer (Material Mates, Italy) that allowed the cell impedances to be fully characterized in the frequency range of 0–20 kHz. This enabled the study of the discrepancies and aging effects on IS-VRFB as reported in Chap.11.

4.4.4 Software development

The battery management algorithms were developed in the LabVIEW (Laboratory Virtual Instrumentation Engineering Workbench, NI) environment [252]. This versatile graphic programming code makes use of visual instruments (VIs) which compose the block diagram and are visualized in the front panel of the human-machine-interface (HMI) [253]. VIs can contain subVIs. The front panel includes the input controls together with the indicators which display

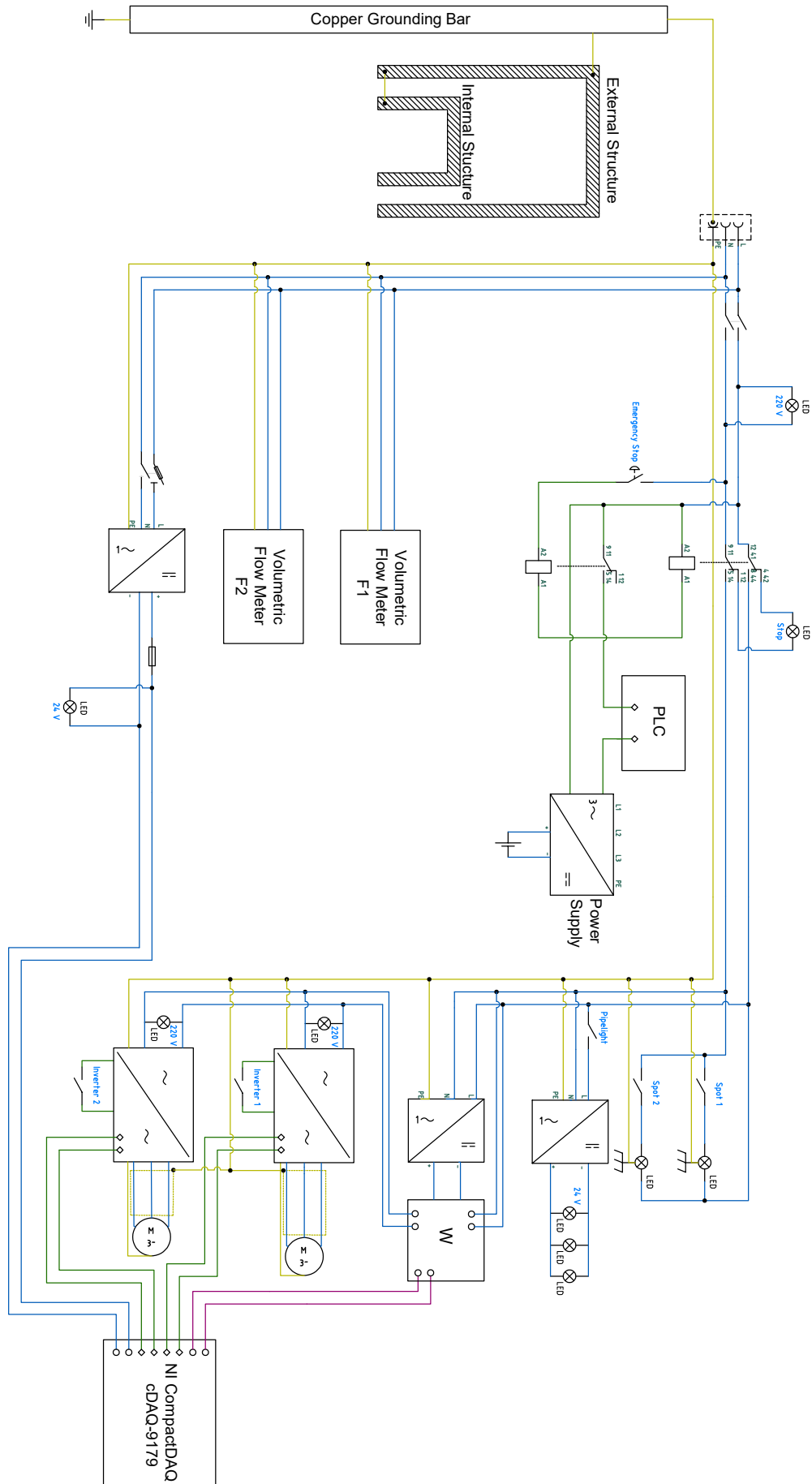


FIGURE 4.21: Simplified electrical power scheme.

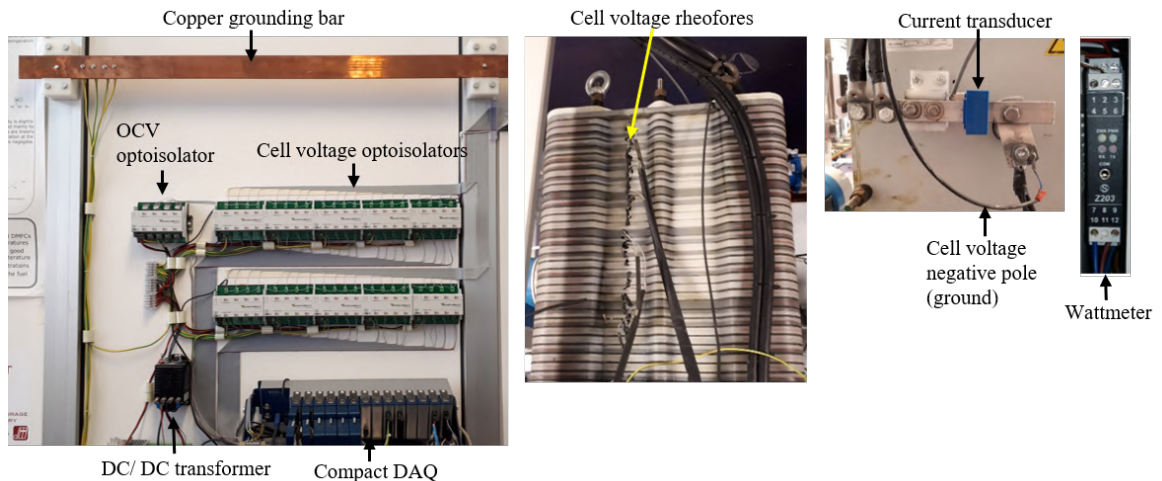


FIGURE 4.22: IS-VRFB electrical sensors.

results and interactive tools for the user. The block diagram is the environment where the code is written, by means of icons representing inputs, outputs, and functions, and their interaction wires. The LabVIEW project was focused on the development of routines based on some state machine for specific operations and on the creation of SubVIs to group some procedures and simplify the program structure. The three main sections which have been created to build the code of the IS-VRFB BMS are presented hereafter.

- *Initialization*: in this section, the program executes some preliminary operations needed to start-up the VI routines, detect the activation of the Compact DAQ and initialize all Compact DAQ modules. The code creates the FIFO queues that govern the state machines, resets some values from previous utilizations of the program, and generates a folder path inside the working folder named with the current date in the format “yyyymmdd”. Because this section is confined inside a time structure, before processing signals with the next operations, all ongoing processes must be concluded. All the error lines coming out from this section are merged in a single wire which governs the following error case structure.
- *Error Case Structure*: if one or more errors are generated in initialization, this structure toggles to “error case”, performs no further processing and brings all signals to the final sequence. If no errors appear, the sequence switches to “no error case” and the program is enabled to work. Inside this case structure four sub-structures are present: a while loop called “UI Handling Loop”, a control loop with state machine called “PFT Acquisition”, a while loop called “Voltage Acquisition Loop”, and a state machine called “Logging Loop”. This error case structure was split into these four sub-structures operating in parallel to allow performing different operations independently. Moreover, this arrangement allows selecting the velocity for each process by choosing high-speed mode or high-resolution mode [253].
 - *UI Handling Loop*: It consists of an event case inside a while loop. This user interface while loop is used to modify the execution sequence of the state machines after the activation of buttons in the front panel. The event case inside this while loop stays inactive and waits for the user to produce an event in order to avoid polling (namely, the code locks waiting for a missing event). Some special events occur in the loop, e.g. the arrest of the PFT Acquisition caused by the stop of the code commanded by user at the front panel. In this case, a warning message is produced asking the user to choose whether to confirm exit or the cancel the stop action.
 - *PFT Acquisition*; this routine manages signals acquisition of electrolyte flows, pressure drops, stack current, and stack and cells voltages during charge and discharge, temperatures, tank levels, and inverter power consumption. The acquisition of most

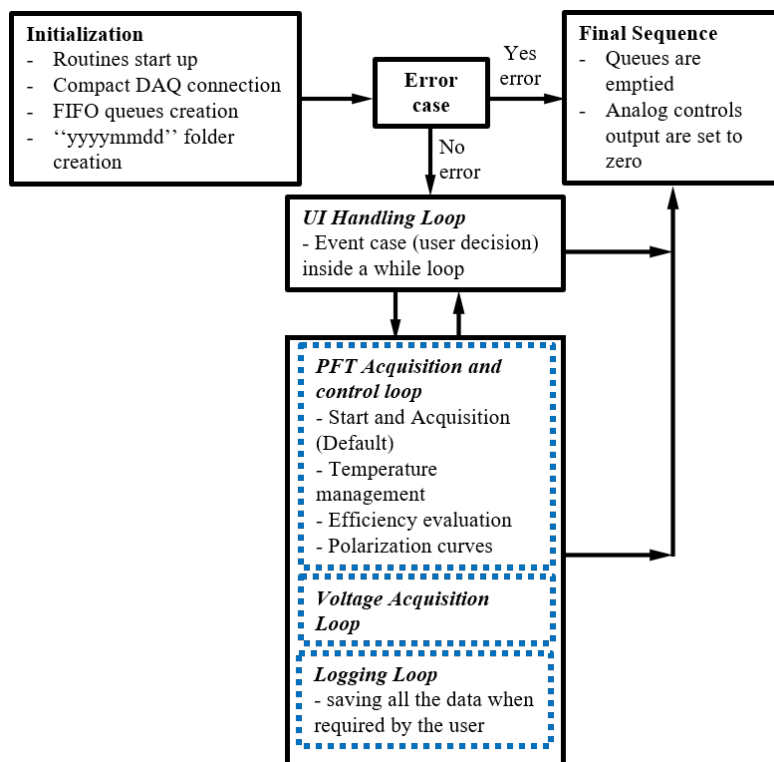


FIGURE 4.23: Software structure of IS-VRFB BMS.

of these signals is carried out continuously to guarantee that the user can control the state of the facility while performing other operations. The queue called “PFT” controls this routine in a while loop. This routine is split into four subroutines:

1. Start and Acquisition (Default): in this subroutine, the program resets and restarts some parameters and then passes to a default case. In this state, LabVIEW acquires all the data coming from the test facility and controls the pumps by sending a PID signal to the inverters and generates the graphs of the acquired signals. The program stops when the user pushes the STOP button on the front panel. In this subroutine some surveillance tasks are performed by LabVIEW and replicated by the PLC (see Sec.4.4.1). Moreover, this loop monitors the status of the valve microswitches. At any moment, the user can decide whether to save or start any of the following procedures 2 to 4 by clicking the corresponding save button.
 2. Temperature management: to avoid V(V) precipitation at high *SOC*, the stack temperature signals provided by the RTDs are continuously monitored and a stack washing cycle is started if they exceed safe conditions.
 3. Efficiency evaluation: this routine was developed to compute the energy exchanged by the facility during charge/discharge cycles while acquiring and controlling other signals, see Sec.8.1.1;
 4. Polarization curves: this procedure was developed to collect automatically the data needed to build the polarization curves, which are generated according to specific experimental protocols, see Sec.6.2;
- *Voltage Acquisition Loop*; this loop is dedicated to the acquisition of the cell voltages pre-processed in the NI 9209 modules. The values are shown in the indicators of the front panel (Fig.4.24) which inform about the state of every cells.
 - *Logging Loop*; this state machine is devoted to saving all the data into TDMS files when required by the user. A TDMS file is a binary file created to interface with

National Instruments products. It is a compact-size file totally compatible with Excel. This state machine contains four routines: one for manual saving, one for timed saving, one for data coming from the polarization subroutine, and the last for efficiency subroutine. The first two are activated by the user while the other two start automatically at the end of each process.

- *Final Sequence*; in this sequence all the queues are emptied and all the analog control outputs are set to zero. At the end, all the tasks are eliminated, and the error wires connected and sent to a VI that shows possible error message before the program stops (Fig.4.23).

4.4.5 Human Machine Interface (HMI)

The front panel constitutes the user interface with the program. It is divided into sections for a better understanding, as shown in Fig.4.24.

1. *Control Panel*: the status bar shows if the program is working. Each case is linked to an output message describing the occurring operation. The start and exit buttons allow the user to start and stop the program in each moment. If the stand-by button is activated, the program switches to the temperature management condition, in which the pumps are intermittently activated to provide a short electrolytes recirculation, any time the electrolyte temperature rises above a pre-set value or at prefixed time intervals. The “power switch” toggle, provided with a LED, allows activating the PS.
2. *Power Supply*: a LED (charge or discharge) turns on when the battery is charging or discharging: the condition is detected from the stack current sign. These LEDs switch on only if the current absolute value exceeds 1 A, to avoid flickering due to the signal noise. Time-variable current and voltage control signals can be sent to the PMS to perform potentiostatic (i.e. voltage source mode) or galvanostatic (i.e. current source mode) battery powering, as planned in the experimental sessions.
3. *Acquisition*: the left-hand side of the display visualizes the stack voltage and current, and hydraulic pumping power, based on the signals produced by on-board instrumentation. The control of the rms-sampling duration can be set to filter the measurements by computing the rms over the specified interval. At the right-hand side of the display, a *SOC* tank indicator is visualized, whose filling level and colour give an immediate perception of the battery state of charge. This *SOC* is computed from the *OCV* signal produced by the *OCV* cell.
4. *Flow Rate Control*: this section of the display has two identical parts at the top and at the bottom, which visualize the controls of the negative and positive electrolytes flow rates. The following parameter can be adjusted: PID gains stating the proportional, integral, and differential constants; maximum and minimum values of the voltage output range. The F1 and F2 flow-meter charts show the PID set points, together with the PID output signals and the flow-meter input signals. The effective flow factors α are also computed.
5. *Plant Scheme*: this is a schematic representation of the plant including valves, tanks, pipes, and the indicators of the measurement devices. It includes four colour-changing thermometers indicating the solution temperatures, two gauge-manometers showing the pressure drops, and two meters indicating the flow rates.
6. *Save Panel*: in the save panel section of the display all the options for saving are presented. The file path indicates the folder path with the file name in which data will be saved. When the save button is pressed the program starts saving the acquired data and stops only when the stop-saving button is pressed. Alternatively, data saving over a stated time duration can be specified by setting this interval in the “Time Target [s]” control and pressing the timed saving button. In any case, when the data registration is active, the “Saving?” LED turns on.

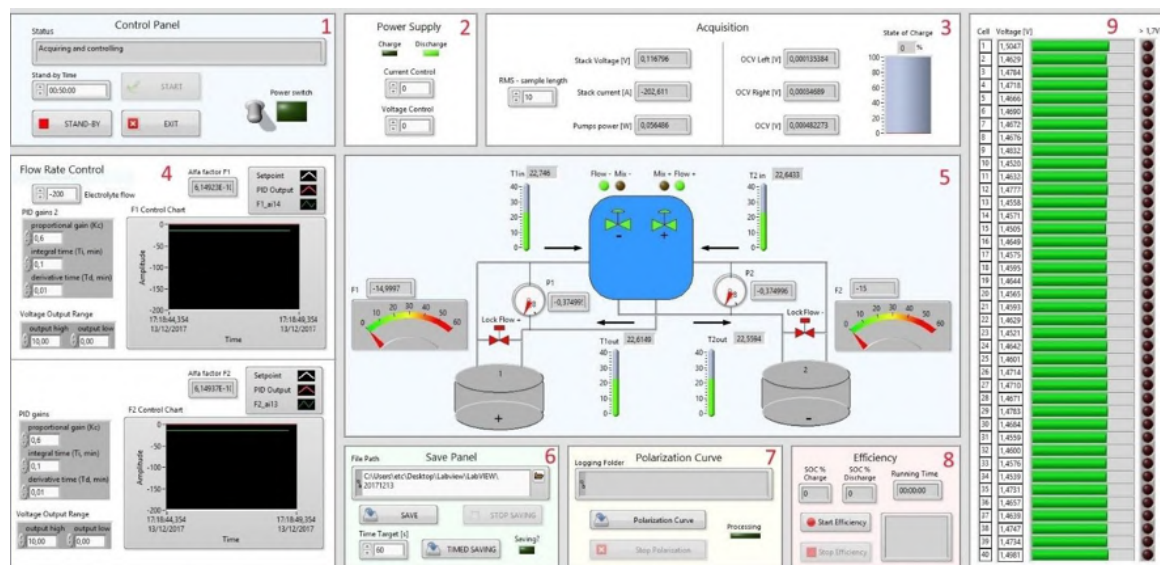


FIGURE 4.24: IS-VRFB human-machine interface.

7. *Polarization Curve*: this section is dedicated to the part of program developed to acquire data for computing and plotting polarization curves (Sec.6.2);
8. *Efficiency*: this section is dedicated to the part of program that is devoted to compute efficiency figures (Sec.8.1.1);
9. *Cell Voltage Indicators*: this section is dedicated to the state of all cells. The first column shows the cell labels (from 1 to 40), the second one the value of the voltages, the third is a bar indicator of such values, for easy comparison, and the last one consists of LEDs which turn on if the cell voltages exceed 1.7 V. In this case, the program stops immediately the PS in order to prevent dangerous cell conditions.

Furthermore, in the front panel two graphs are presented, not shown in Fig.4.24, that display explicitly some of the acquired data as a function of time. The first one is dedicated to flows and temperatures while in the second all the 40 stack voltage cells are plotted.

Chapter 5

IS-VRFB modeling

VRFB models should clearly be capable of predicting experimental features, for example: cell and stack voltage vs time, current density, efficiency under various operating conditions, the local distributions of electrolyte flow, and current density inside the cell. Typical models include several topics, such as multi-physics, techno-economics, electrical networks, and mechanical and chemical engineering. Some commercial software packages, (e.g. COMSOL, Simulink) can be utilized, which offer reliability and flexibility and reduce time with rapid redundancy. Accordingly, 0, 1, 2, and 3D static and dynamic models can be applied.

A description of the strategy, organization, and operation of the model can be found in [40]. Examples of such charts are provided by Bayanov [255], Viswanathan [176], et al. Zhao [256], but are not common used.

In general, very few models are validated by acquired data with complete experimental validation. The aim of this thesis is to partially fill this gap with a wide experimental validation of the developed numerical models. VRFBs are the most commonly utilized RFBs [85] and numerical modeling has been considered by several groups. Among them a general multi-physics dynamic approach that considers the electrolyte flow through homogeneous porous electrodes coupled to the electrochemical kinetics and mass transport is still being developed by Maggiolo et al. at the Division of Fluid Dynamics, Chalmers University of Technology (Sweden), with which the group at Padua is collaborating. For example, in [257] and [258] a model that well predicts the cell voltage vs. time with good distributions of vanadium concentrations, current, and voltage within a unit cell is proposed. The hydrogen and oxygen evolution are taken into account in [259], [260] and the non-isothermal distribution is considered in [261], during charge with a good agreement with the experimental results. The main studies based on the VRFB modeling include:

- thermal aspects i.e. temperature evolution during charge/discharge or stand-by conditions;
- hydraulic models;
- ion diffusion and crossover prediction;
- electrical aspects, i.e. the effect of the shunt currents on the performance;
- optimization of the stack geometry and modes of operation;
- capital cost sensitivity;
- aging model prediction.

All these fields are treated in the present work, with the exception of capital cost sensitivity, which will be the aim of future developments of the Padua research group and of the aging effect prediction that will be addressed only from an experimental point of view. The last involves practical problems such as irreversible electrode poisoning or electrical contact between feeders and porous electrodes, with the exception of membrane degradation, where much greater knowledge comes from the fuel cell field. It is important to note that models for the fuel cells [262], [263] are relevant to fluid flow, mass transport, fluid dispersion, and current distribution for the VRFBs. Nevertheless, the very different reaction environment based on sulfuric acid solution that compounds the liquid electrolyte in a VRFB, as well as the pressure drop and electrode connection requirements, must be considered with the development of dedicated models.

The main advantages of modeling in the VRFB field include minimization of the number of required experiments, extensions of performance expectation at different scales of operation, prediction of performance to aid battery and process design, and rationalization of the effects of variables in performances. Recently, Kodym et al. [264] demonstrated how the development of multi-dimensional models and the availability of computational power can make the macroscopic modeling of stacks of a parallel plate electrochemical reactor possible, which is applicable to RFB modules. Watt-Smith et al. [103] present the successful use of detailed, physics-based models for the rationalization and comprehension trends of data with an optimization of the performance. Such models would be particularly important during the process of scale-up (Sec.2.3.5), reducing the financial burden on physical experimentation with an acceleration of process development providing greater incentive for commercialization. In such a VRFB system, three scenarios might be possible: standby, charging, and discharging, and a proper model will be developed for each case. This chapter is organized as follows: in Sec.5.1 the hydraulic model concepts are described with some tables and graphs that can be used as a valuable tool for the design of other VRFB plants, providing the reader with the most important information for both the piping and the stack internal hydraulic circuits. In Sec.5.2, the equivalent electric scheme of the IS-VRFB stack is described to compute the shunt currents that result in the internal hydraulic path of the stack. In this section, only the stationary case will be addressed and the cell is modelled as an equivalent Thévenin with only an internal resistance, by neglecting the capacitive and inductive behavior, which is out of the scope of the present analyses. This aspect will be addressed in Chap.11. In Sec.5.3, the crossover model is explained to evaluate species migration from one half-cell to the other that results in heat and energy losses. Finally, in Sec.5.4 a cell resolved model that simulates the dynamic thermal behavior of an industrial VRFB stack is presented, during both operating and standby conditions. To the best of my knowledge, this is the first numerical model that also considers the effect of shunt currents, crossover, and entropic heat in computing the temperature distribution among the cells in the stack and its evolution. Moreover, the validation of all models will be reported in Chaps.7, 8.

5.1 Hydraulic modeling

In this section, the fundamental hydraulic principles that characterize a VRFB system will be presented. Pump losses are caused by the movement of electrolytes in a VRFB. The losses (due to electrode and flow frames) are dominant in terms of total pressure losses and can thus influence battery performance. In this section, the investigation of the influence of flow rate on pump losses is presented. The experimental results are presented in Chap.8.

5.1.1 Head loss in pipes

The pressure drop in pipes consists of head losses due to viscous effects in straight pipes, which are called distributed Δp_{di} (or major) losses, and pressure drop due to various pipe components such as elbows, bends, valves, and others are called concentrated Δp_{cn} (or minor) losses, shown as follows:

$$\Delta p_{pi} = \Delta p_{di} + \Delta p_{cn} \quad (5.1)$$

It is worth mentioning that "major" and "minor" do not necessarily reflect the relative importance of each type of loss. For example, for a very short pipe system with many components, minor losses may be of greater significance than major losses.

Major losses

Pressure drop and head losses depend on wall shear stress Γ_{wall} , between the fluid and pipe surfaces. There are two kinds of flow: laminar and turbulent flow. A fundamental difference between laminar and turbulent flow is that the shear stress for turbulent flow is a function of the density of the fluid, ρ , while for laminar flow the shear stress is independent of the density and is only a function of dynamic viscosity, μ . Pressure drop for laminar pipe flow is found to be independent from the roughness of the pipe because there is no thin viscous layer. Instead,

for turbulent pipe flow it is necessary to include this parameter because there is a thin viscous layer, so the pressure drop is expected to be a function of the wall roughness.

The dimensionless parameter that indicates the regime of the flow is the Reynolds number, defined as follows:

$$Re = \frac{\rho u D}{\mu} \quad (5.2)$$

where u is the average velocity, D is the characteristic length, ρ is the density, and μ is the dynamic viscosity. Typically, when the Re is lower than 2100 the flow is laminar, while when the Re is higher than 4000 the flow is turbulent. When Re occurs between 2100 and 4000 the flow is at the transition range. For both laminar and turbulent pipe flow, pressure drop should be proportional to the pipe length. The most widely used equation in fluid dynamics for expressing major losses is the Darcy-Weisbach equation, which can be applied for any fully developed, steady, incompressible pipe flow, as follows:

$$\Delta p_{di,m} = f \frac{l}{D} \frac{u^2}{2g} \quad (5.3)$$

The unit of measurement for this equation is the meter (m). It is possible to express the Darcy-Weisbach equation in Pascal as follows:

$$\Delta p_{di} = f \frac{l}{D} \frac{\rho u^2}{2} \quad (5.4)$$

where f is the Darcy friction factor. For laminar fully developed flow, the value of f is simply:

$$f = \frac{64}{Re} \quad (5.5)$$

For turbulent fully developed flow, the value of f is dependent on the Reynolds number Re and the relative roughness ξ/D :

$$f = \phi \left(Re, \frac{\xi}{D} \right) \quad (5.6)$$

It is not easy to relate the friction factor to the Reynolds number and roughness. The information available in the literature results from an experiment conducted by J. Nikuradse in 1933, and amplified by many others since then. Nikuradse used artificial roughened pipes made by himself by gluing sand grains on the pipe walls. The pressure drop needed to produce a certain flow rate was measured many times obtaining the friction factor for the corresponding Reynolds number and relative roughness. In this way, it has been possible to determine the function $f = \phi \left(Re, \frac{\xi}{D} \right)$. However, the roughness of commercial pipes is not uniform and well defined (as in the artificial pipes used by Nikuradse), but it is possible to obtain the relative roughness and thus the friction factor. For example, typical roughness values for various materials are defined in Tab.5.1 ([265]). In the case of the IS-VRFB, the PVC tube can be assumed to be smooth.

The Moody chart is shown in Fig.5.1 and correlates the data of Nikuradse in terms of the relative roughness of commercially available pipe materials. From $Re=2100$ to $Re=4000$ there are no friction factor values because in this transition range the flow may be laminar or turbulent or an unsteady mix of both, depending on the specific circumstances involved. It is worth noting that for any pipe, even smooth ones (relative roughness = 0), the head losses are not zero. This is a result of the no-slip boundary condition that requires any fluid to stick to any solid surface. The Colebrook formula (following) is valid for the entire non-laminar range within the Moody chart [265]:

$$\frac{1}{\sqrt{f}} = -2.0 \log \left(\frac{\xi/D}{3.7} + \frac{2.51}{Re\sqrt{f}} \right) \quad (5.7)$$

the difficulty of this relation is the non-linearity of the friction factor that requires an iterative scheme. Another equation, easier to use, is given by [265]:

$$\frac{1}{\sqrt{f}} = -1.8 \log \left[\left(\frac{\xi/D}{3.7} \right)^{1.11} + \frac{6.9}{Re} \right] \quad (5.8)$$

TABLE 5.1: Equivalent roughness for new pipes [265].

Pipe	Equivalent roughness [mm]
Riveted steel	0.9-9.0
Concrete	0.3-3.0
Wood stave	0.18-0.9
Cast iron	0.26
Galvanized iron	0.15
Commercial steel	0.045
Drawn tubing	0.0015
Plastic, glass	0.0 (smooth)

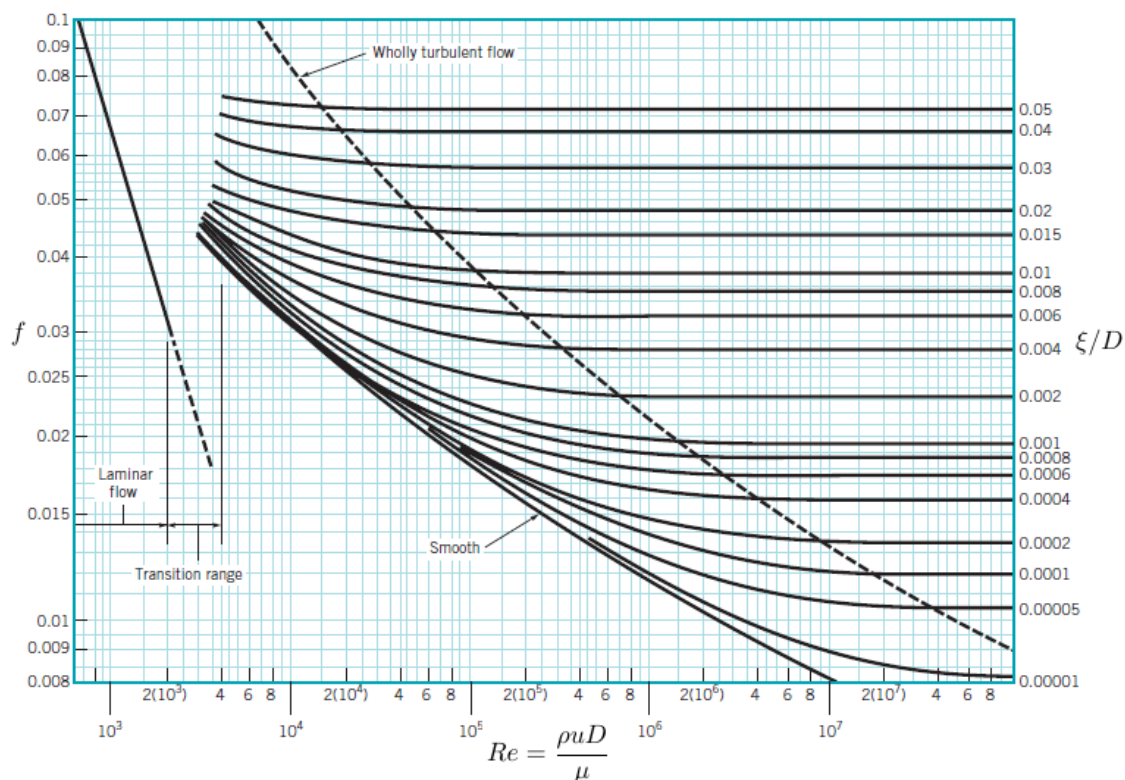


FIGURE 5.1: The Moody chart [265].

Minor losses

Most pipe systems as in the case of a VRFB plant are characterized by additional components such as elbows, bends, valves, and other features that increase the overall head losses of the system Fig.5.2, Fig.5.3, Fig.5.4. The most common method used to determine these head losses or pressure drops consists of specifying the loss coefficient ζ for any system component. This coefficient is strongly dependent on the geometry of the component considered, and it may depend on the fluid property, namely the Reynolds number. Therefore, the minor head losses

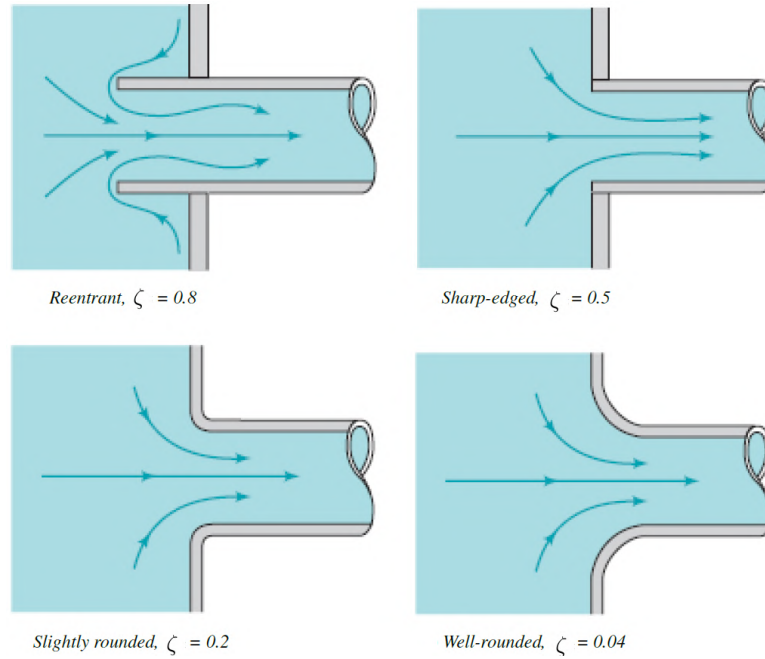


FIGURE 5.2: Entrance flow conditions and loss coefficient [265].

(due to the components along the pipe) are given by:

$$\Delta p_{cn,m} = \zeta \frac{u^2}{2g} \quad (5.9)$$

The unit of measurement of the last equation is the meter. It is possible to express this equation in Pascal as follows:

$$\Delta p_{cn} = \zeta \frac{\rho u^2}{2} \quad (5.10)$$

Minor losses are sometimes reported in terms of an equivalent length, l_{eq} . Namely, the head loss is given for a component in terms of the equivalent length of pipe that would produce the same head loss as the component. This method is shown as follows:

$$l_{eq} = \zeta \frac{D}{f} \quad (5.11)$$

$$\Delta p_{cn,m} = f \frac{l_{eq}}{D} \frac{u^2}{2g} \quad (5.12)$$

Many pipe systems can be characterized by various transition sections in which the pipe diameter changes from one size to another. These pipe diameter changes may be smooth or abrupt, and also produce head losses [265].

Moreover, pipes with bends produce greater head losses than straight pipes due to the separation region of flow near the inside of the bend and the swirling secondary flow that occurs, caused by the curvature of the pipe centerline that results in an imbalance of centripetal forces.

The associated values of ζ for a 90° bend are shown in Fig.5.5 [265]:

- The entrance of flow from a reservoir to a pipe (Fig.5.2) or the exit of flow from a pipe to a reservoir (Fig.5.3) are cases of pipe diameter changes that produce a head loss. It is worth noting that each geometry has an associated loss coefficient;
- A sudden contraction is another common head loss. The loss coefficient for a sudden contraction is a function of the area ratio A_2/A_1 as is shown in Fig.5.4 (left).

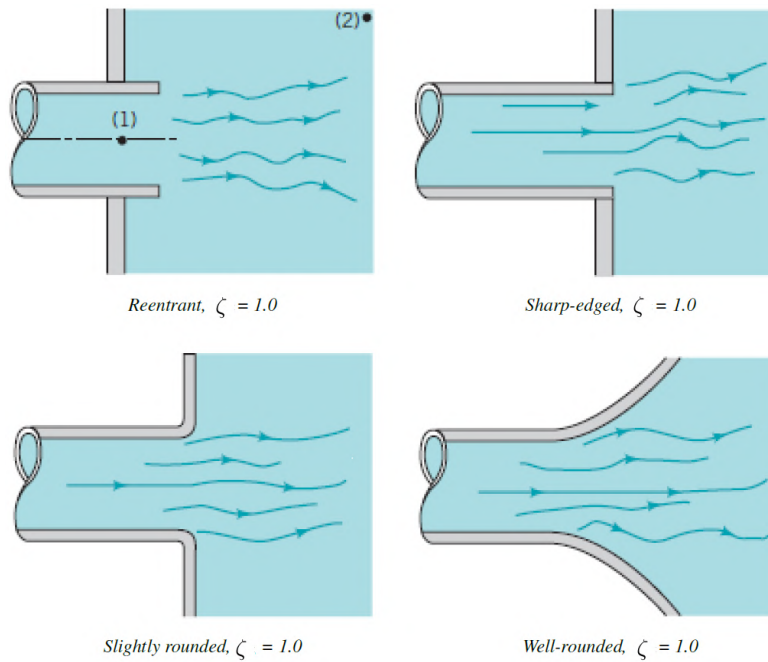


FIGURE 5.3: Exit flow conditions and loss coefficient [265].

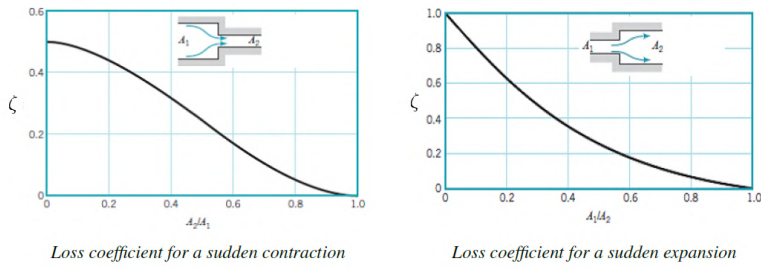


FIGURE 5.4: Loss coefficient for a sudden contraction and a sudden expansion [265].

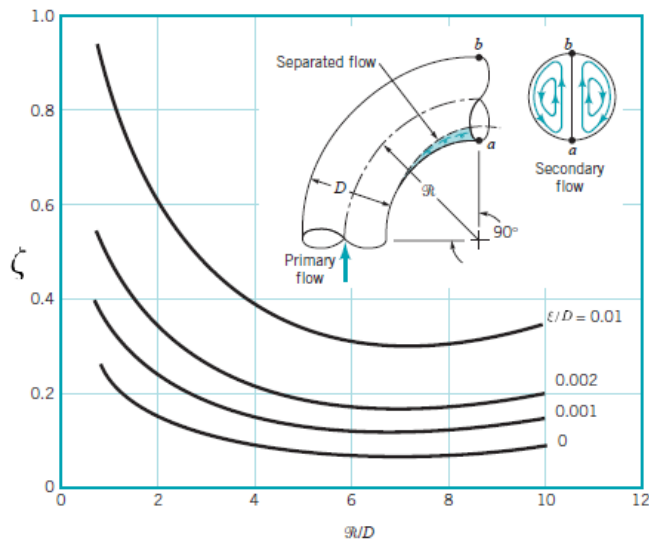


FIGURE 5.5: Loss coefficients of a 90° bend pipe [265].

TABLE 5.2: Loss coefficients for pipe components.

Component	ζ	
Elbows regular 90° flanged	0.3	
Elbows regular 90° threaded	1.5	
Elbows long radius 90° flanged	0.2	
Elbows long radius 90° threaded	0.7	
Elbows long radius 45° flanged	0.2	
Elbows regular 45° threaded	0.4	
180° return bends flanged	0.2	
180° return bends threaded	1.5	
Tees line flow flanged	0.2	
Tees line flow threaded	0.9	
Tees branch flow flanged	1.0	
Tees branch flow threaded	2.0	
Union thread	0.08	
Valves globe fully open	10.0	
Valves angle fully open	2.0	
Valves gate fully open	0.15	
Valves gate 1/4 closed	0.26	
Valves gate 1/2 closed	2.1	
Valves gate 3/4 closed	17.0	
Valves swing check forward flow	2.0	
Valves swing check backward flow	∞	
Valves ball fully open	0.05	
Valves ball 1/3 closed	5.5	
Valves ball 2/3 closed	210.0	

- A sudden expansion is also a head loss and it is possible to obtain the loss coefficient by means of simple analysis. Considering the continuity and the momentum equations, the loss coefficient may be found by:

$$\zeta = \left(1 - \frac{A_1}{A_2}\right)^2 \quad (5.13)$$

And plotted in Fig.5.4 (right).

Finally, components such as elbows, tees, reducers, valves, and filters can also produce head losses. The values of ζ for such components strongly depend on the shape of the component, and weakly on the Reynolds number. Loss coefficients for pipe components are shown in Tab.5.2 ([265]).

5.1.2 Stack pressure losses

The pressure losses inside the stack are mainly due to the pressure drop through the porous electrodes and flow frame.

As discussed in Sec.3.1.2, the flow frames are characterized by long channels and manifolds with a small cross-sectional area, which helps to reduce the shunt currents and other electrical issues. On the other hand, they produce a considerable pump loss associated with the higher-pressure drop that affects the system's efficiency. Therefore, an appropriate trade-off between pump loss and flow frame design can improve system efficiency. Pressure losses through manifolds and channels can be calculated by using the scheme represented in Fig.5.6 that shows a portion of the hydraulic circuits for conventional series stack topology (CSS). In this case, the hydraulic resistances represent the following hydraulic segments:

R_1 = internal manifold segments between adjacent cells;

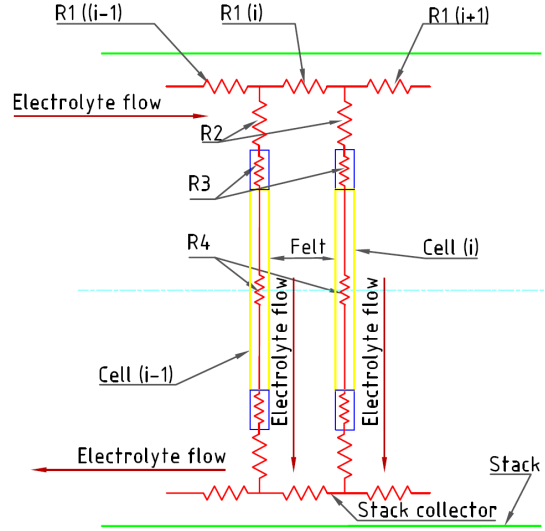


FIGURE 5.6: Segments of hydraulic circuits (lumped representation).

R_2 = internal feeding pipes connecting cells and manifolds;

R_3 = cell flow channels;

R_4 = cell porous electrode;

To calculate the pressure drop associated with each hydraulic resistance, the aforementioned Darcy-Weisbach analytical expressions can be used. A significant pressure drop in the reaction cell is caused by porous electrodes, and this can be considered a typical porous medium. The pressure drop (through a given porous electrode) can be determined by Darcy's law as follows:

$$\Delta p = \frac{\mu \varepsilon l'_x u}{\aleph} = \frac{\mu \varepsilon l'_x Q}{\aleph A_{cross}} \quad (5.14)$$

where:

$$u = \frac{Q}{A_{cross}} = \frac{1}{\varepsilon V_e} \int_{V_e} u dV_e \quad (5.15)$$

where l'_x is the length of the porous electrode, A_{cross} is the cross-sectional area through which the electrolyte flows, \aleph is the permeability of the porous electrode, u is the bulk intrinsic velocity of the generic cubic domain V_e along the stream wise direction, μ is the dynamic viscosity, and ε is the porosity of the porous electrode. The pressure gradient $\Delta p/l$ corresponds to the applied body force. The permeability can be calculated if the pressure drop is available, or can be imposed by applying the Kozeny-Carman equation for a medium composed of cylindrical fibers, as follows:

$$\aleph = \frac{d_f^2 \varepsilon^3}{K_{kc}(1 - \varepsilon)^2} \quad (5.16)$$

where ε is still the porosity of the porous electrode, K_{kc} is the Kozeny-Carman constant, and d_f is the fiber diameter. Some numerical analyses have been carried out with ANSYS[®] Fluent 15 (Sec.3.1.2).

The porous electrodes were modeled by adding two source terms to the standard momentum equations, i.e. a viscous loss term and an inertial loss term. These sources were introduced as pressure gradients proportional to the fluid velocity as follows:

$$\Delta p = - \left(\frac{\mu u(i)}{\aleph} + \frac{C_2 \rho |u| u(i)}{2} \right) \quad (5.17)$$

Both these terms depend on the transport properties of the fluid, which is the density ρ and dynamic viscosity μ (Tab.7.1), and on the geometrical characteristics of the porous media (Tab.3.1) by means of the permeability \aleph and inertial loss coefficient C_2 . These were evaluated with the

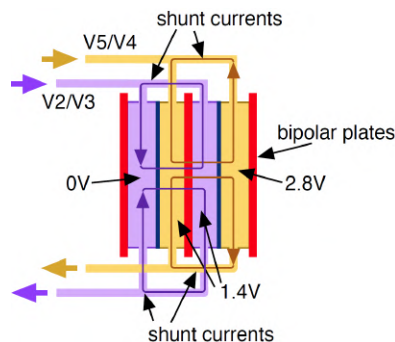


FIGURE 5.7: Four conductive loops with shunt currents formed in the hydraulic segments of a two-cell stack.

Ergun and Blake-Kozeny relations, from the electrode porosity ε and the hydraulic diameter d_f of cylindrical fibers constituting the carbon porous electrode (as follows):

$$\kappa = \left(\frac{d_f^2 \varepsilon^3}{150(1 - \varepsilon)^2} \right) \quad (5.18)$$

$$C_2 = \left(\frac{3.5(1 - \varepsilon)}{d_f^2 \varepsilon^3} \right) \quad (5.19)$$

For the boundary conditions, the velocity was imposed at the inlet of the cell frame and an atmospheric pressure was set at the outlet [74].

5.2 Electric modeling

Shunt current is a common phenomenon in all electrochemical bipolar cell stacks that provide parallel hydraulic flow and a common conductive electrolyte manifold. Strictly speaking, these are not "shunt" currents, e.g. those flowing in a shunt resistor used for precise current measurements. "Stray currents" might possibly be a more appropriate term, but as the term "shunt currents" has been used in the RFB community for many years, we maintain it to avoid confusion. Clearly, these currents have an undesirable effect as they reduce stack current, energy efficiency, and can also lead to other problems such as gas evolution, corrosion, and dendrite growth inside the cell channels that can restrict or block the electrolyte flow [266].

The magnitude of the shunt currents depends on the resulting system voltage, the electrolyte resistivity, and the geometry of the electrolyte feeding system. In fact, bipolar reactors must therefore be designed to achieve shunt current minimization, which is usually achieved by incorporating long, narrow channels to increase the electric resistance to the current flow through these pathways, as reported in Sec.3.1.2.

During the design of the cell components for a stack, an estimation of the expected shunt current losses is needed. In general, two main methods have been reported in the literature to compute the magnitude of the shunt currents in a common bipolar plate stack, namely a model-based approach and an experimental based approach. In the first case, the estimation of the shunt current loss is based on an equivalent circuit model. Originally, [267] suggested that a bipolar cell stack could be modeled like an electrical circuit where the current that flows through each path could be calculated based on Kirchoff's Laws. This approach required a model that could describe the electrochemical system. The model developed by Kaminski and Savinell [268] has been successfully applied to several industrial cells. Successively, other studies have also suggested more efficient numerical methods to solve the model [269], [270].

The second method is mainly based on experiments that measure shunt currents either directly or indirectly. In [271], an experimental technique is reported where a current probe directly measures the current that flows through the electrolyte flow path. The main disadvantage of this technique is the insignificant order of magnitude field generated, as shunt currents are generally

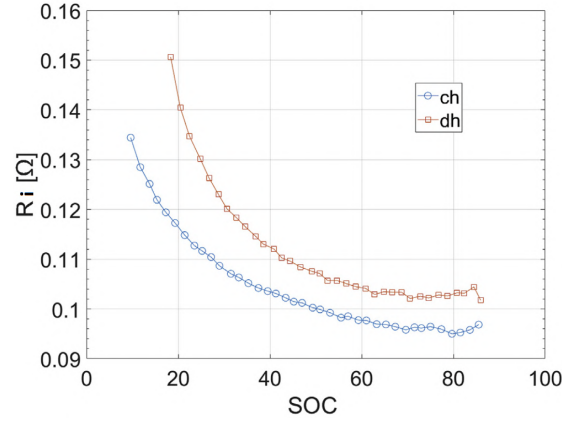


FIGURE 5.8: IS-VRFB stack internal resistance profile vs. *SOC* during charge (*ch*) and discharge (*dh*).

very small. In [272] an approach devoted to measuring the voltage drop directly through the electrolyte channels and manifolds is presented. This allows the calculation of the shunt currents to be obtained. Moreover, [273] proposed a method that simulates the shunt currents evolution experimentally, resulting in a correlation between load and shunt current.

Although there are many other examples of applications that use electrochemical reactors where this problem occurs, RFB technology is one of the most important due to recent global interest. The necessity of producing large voltages requires the use of multi-cell stacks where the two half-cell electrolytes are fed through each cell hydraulically in parallel by means of a common manifold Sec.2.3.3.

Being the homologous electrodes at different electrical potentials along the stack, electrical loops provided with voltage sources are created by those paths, where currents flow Fig.5.7. It is worth noticing that a VRFB stack always presents shunt currents when cells are filled with charged electrolytes, in both load and standby modes. Conversely, a single cell never experiences shunt currents.

The study of shunt currents in flow batteries began in the 1970s, by NASA. Prokopius, (NASA Technical Memorandum NASA TM X-3359, 1976) proposed a model for computing shunt currents in an RFB system by using the circuit analogue method to develop an equivalent electrical circuit model. Other models have also been proposed for fuel cells [274], [275], [276]. In addition, in some RFBs where technologies involve the deposition of a metal during charging, the shunt currents can be quite dangerous as their presence can lead to dendrite growth within the channels that block the flow of electrolyte, as stated at the beginning of this section.

Fortunately, because the VRFB reactions do not involve the deposition of a metal during charging/discharging, dendrite growth problems do not represent an issue. However, the shunt current minimization is still needed to maximize performance in terms of efficiencies, uniformity of current, and potential distribution along the cell that can result in under-performance in the central part of the stack, and interference with instrumentation such as flow meters (Sec.4.1.5). Accordingly, shunt currents should aim to be $\leq 1\%$ of the stack current. Unfortunately, only a few studies report on the shunt current of the VRFB [277].

Xing et al. [278] developed a shunt-current model for a VRFB stack based on the electrical equivalent circuit method. Yin et al. [279] developed a coupled three-dimensional electrochemical model to investigate shunt-current distribution and its effects on coulombic efficiency Sec.8.1.3. König et al. [280] and Ye et al. [281] developed some numerical models to investigate the effects of a piping *P&ID* and battery design on shunt currents and pumping power consumption.

5.2.1 IS-VRFB shunt current model

In our model, the shunt currents in the segments of the hydraulic circuits inside the stack were computed with an equivalent lumped circuit that accounts for the *SOC* in each *n-th* segment [74].

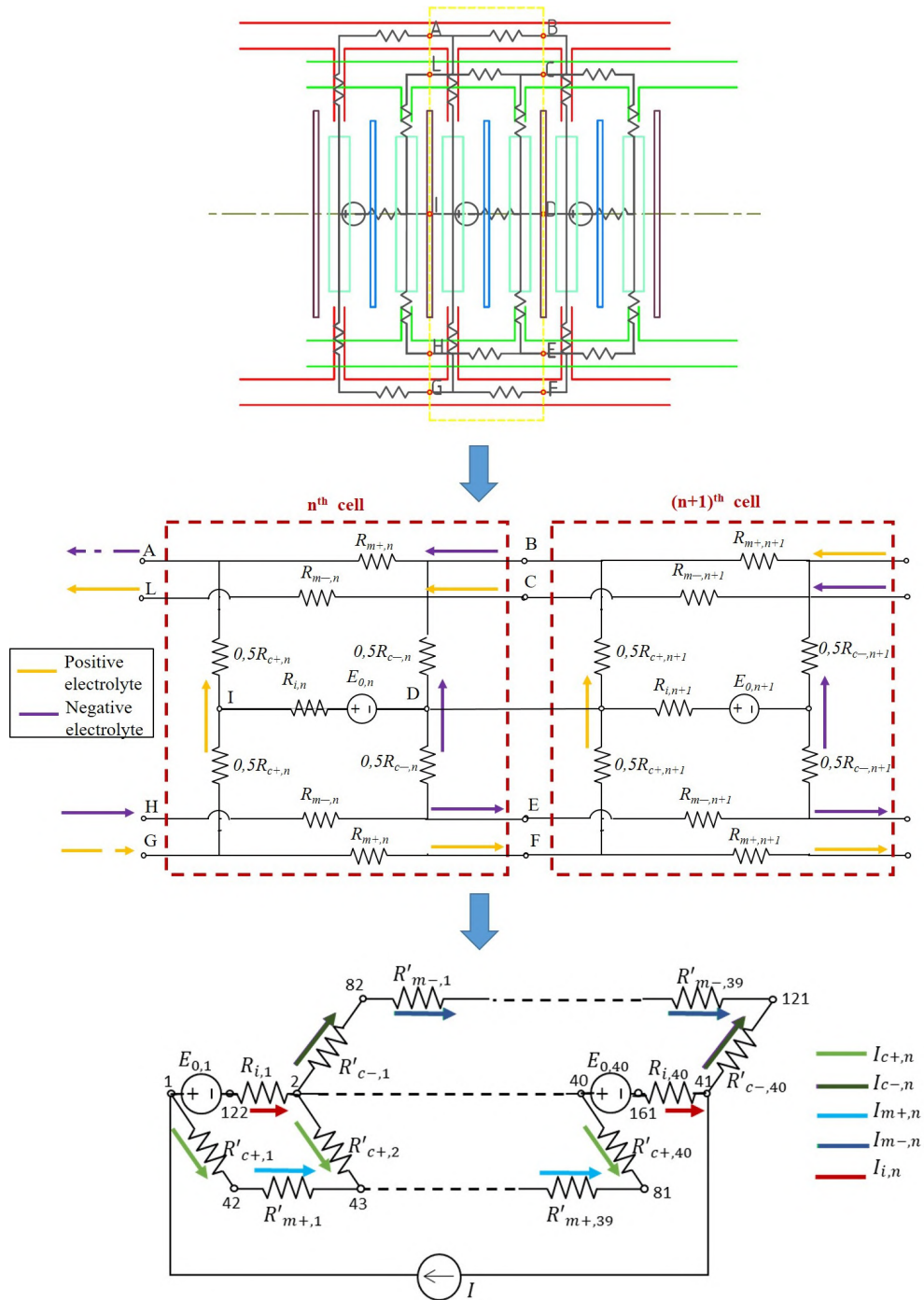


FIGURE 5.9: Equivalent electric circuit of a 40-cell stack used in computing the shunt currents.

The n -th cell was represented as a Thévenin equivalent, consisting of a voltage source $E_{o,n}$ in series with a resistor $R_{i,n}$. $E_{o,n}$ corresponds to the cell OCV and was computed by means of the Nernst equation, which, in terms of ion concentrations, reads as Eq.2.17. Based on the definition of state of charge:

$$\begin{cases} SOC_+ = \frac{C_{V+}}{C_{V+} + C_{IV+}} \\ SOC_- = \frac{C_{II-}}{C_{II-} + C_{III-}} \end{cases} \quad (5.20)$$

the vanadium species concentrations can be expressed in terms of SOC s as $C_V = C_+SOC_+$, $C_{II} = C_-SOC_-$, $C_{IV} = C_+(1 - SOC_+)$ and $C_{III} = C_-(1 - SOC_-)$, so that Eq. 2.17 becomes:

$$E_0 = E'_0 + \frac{KT}{F} \ln \frac{SOC_+SOC_-}{(1 - SOC_+)(1 - SOC_-)} \quad (5.21)$$

$R_{i,n}$ accounts for all cell over-voltages, such as polarization, concentration, and membrane voltage drops, and its value can be experimentally determined for the stack under investigation. Fig.5.8 shows the values of $R_{i,n}$ as a function of the average SOC in charge and discharge, experimentally obtained. These data show that $R_{i,n}$ is lower during charge, due to the different kinetics, where VO^{2+} oxidation is faster than VO_2^+ reduction.

Piping segments were modeled as resistors having resistance, as follows:

$$R_{k\pm,n} = \frac{l_{k,n}}{\sigma_{\pm,n}A_{k,n}} \quad (5.22)$$

with $k = c$ for cell or $k = m$ for manifold and $+$, $-$ for positive and negative compartments.

The electric conductivity $\sigma_{\pm,n}$ depends on the mix of vanadium ions, that is, on the SOC of the solutions in each cell, which vary during standby because of self-discharge:

$$\sigma_- = SOC_- \sigma_{II} + (1 - SOC_-) \sigma_{III} \quad (5.23)$$

$$\sigma_+ = SOC_+ \sigma_V + (1 - SOC_+) \sigma_{IV} \quad (5.24)$$

For the sake of simplicity and due to the limited thermal variations expected, the solution conductivities σ_j (with $j = II, III, IV, V$) were assumed to be independent of the temperatures. The manifold resistances $R'_{m+,n}$, $R'_{m-,n}$ account for each segment of the manifold feeding the cells in parallel, whereas the cell flow resistances $R_{c+,n}$, $R_{c-,n}$ account for the input and output distribution channels and porous electrodes of each cell. By assuming uniform electrolyte concentrations in the whole plant (consistently with the high flow factor α), the resistance network of Fig.5.9 could be considered symmetric regarding the cell and stack design, which allows the electric circuit to be simplified by introducing equivalent elements. Adopting this assumption, the n -th manifold resistances $R'_{m+,n}$, $R'_{m-,n}$ can be calculated as [74]:

$$\begin{cases} R'_{m-,n} = 0.5 \frac{1}{\sigma_{-,n}} \frac{l_{m,n}}{A_{m,n}} \\ R'_{m+,n} = 0.5 \frac{1}{\sigma_{+,n}} \frac{l_{m,n}}{A_{m,n}} \end{cases} \quad (5.25)$$

The cell flow resistances $R_{c\pm,n}$ depend on solution flow paths in the cell channels and porous electrodes, and on the consequent electric potential distribution due to the shunt currents flow (Fig.5.10).

Flow and potential distributions can be determined by means of 3D FEM analysis, to account for the real cell design accurately. In this simulations, the IS-VRFB design was considered as shown in Fig.5.10 and the analysis was performed with the COMSOL[®] code [282].

The computational domain consisted of graphite felt porous electrodes (with conductivity σ_e and porosity ε) and the flow field feeding the electrodes. The flow frame geometry that was considered in the computation is shown in Fig.5.10. Positive and negative compartments have the same geometry. Fig.5.10 shows the plot of the distribution of the electrical potential φ when

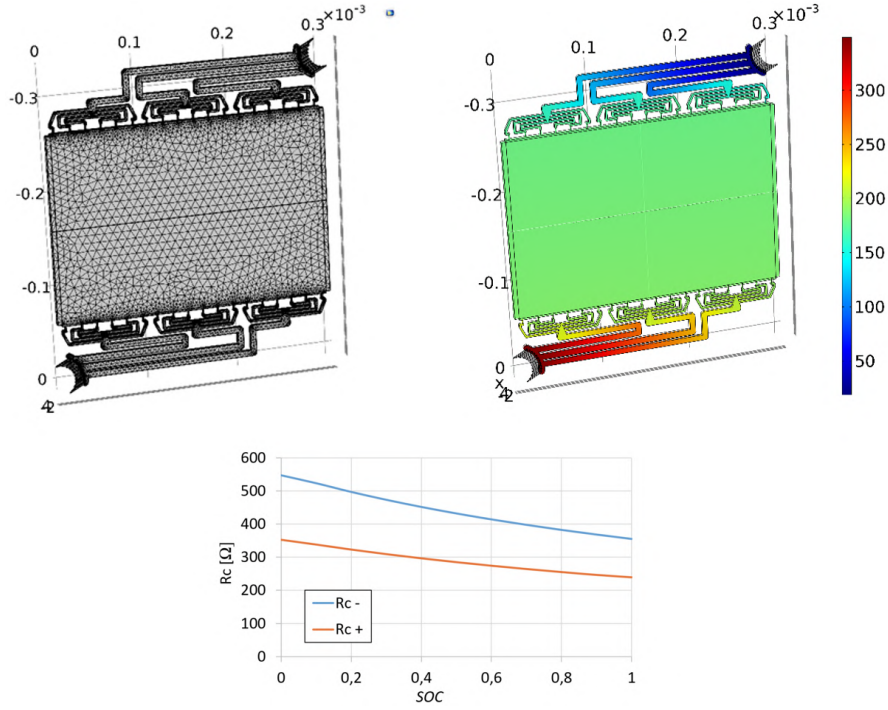


FIGURE 5.10: 3D model used to compute the cell flow resistances $R_{c+,n}$, $R_{c-,n}$ including distribution channels and porous electrode. In this case, the IS-VRFB flow frame design with flat bipolar plates was considered. Top left: electrode and flow frame tessellation, top right: color map of the electric potential φ in V produced by a 1 A shunt current, bottom: resulting $R_{c+,n}$, $R_{c-,n}$ as functions of SOC .

a given shunt current I_{\pm} flows for a fixed SOC . From the total voltage drop $\Delta\varphi_{\pm}(SOC_{\pm})$ in the positive and negative compartments at each SOC , the cell flow resistances were computed as $R_{c\pm} = \Delta\varphi_{\pm}(SOC_{\pm})/I_{\pm}$.

Fig.5.9 presents the resistance values obtained for both compartments as functions of SOC . Due to symmetry conditions as discussed, $R'_{c+,n}$, $R'_{c-,n}$ are simplified into the following:

$$R'_{c-,n} = 0.25R_{c-,n} \quad (5.26)$$

$$R'_{c+,n} = 0.25R_{c+,n} \quad (5.27)$$

$$P_{i,n} = I_{i,n}v_{i,n} \quad (5.28)$$

The resulting equivalent network of Fig.5.9 was solved with a Matlab[®] in-house code implementing sparse tableau analysis for computing shunt currents $i_{k\pm,n}$, and voltages $v_{k\pm,n} = R_{k\pm,n}i_{k\pm,n}$ in all branches. Shunt current losses are computed by multiplying shunt currents by shunt voltages in each element of the equivalent network, as follows:

$$\begin{cases} P_{c+,n} = I_{c+,n}v_{c+,n} \\ P_{c-,n} = I_{c-,n}v_{c+,n} \end{cases} \quad (5.29)$$

$$\begin{cases} P_{m+,n} = I_{m+,n}v_{m+,n} \\ P_{m-,n} = I_{m-,n}v_{c+,n} \end{cases} \quad (5.30)$$

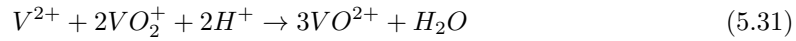
During standby, the battery is disconnected from the charger or the load, and the pumps are switched off and have stopped circulating solutions between tanks and stack. Unless the electrolyte in the internal channels is drained, the cells and channels are still filled with conductive

electrolyte, so internal pathways are still available for the flow of ions. In this scenario, the discharge process continues until there are still active species in the electrolyte volume inside the pile. Conversely, during discharging, the electrical switch that connects the load to the battery is closed, so the cell voltages will lead the spontaneous cell reactions with electrons that flow through the external circuit. Similarly, during charging, the battery stack is usually connected to an external AC/DC converter and a voltage is applied to drive the reactions in the opposite direction [266].

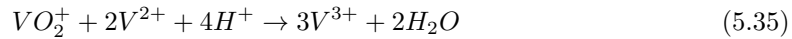
5.3 Crossover modeling

Crossover through the membrane consists of $V(II)$ and $V(III)$ ions crossing from the negative to the positive electrode and of $V(IV)$ and $V(V)$ ions crossing from the positive to the negative electrode, which are due to both electrical [283] and concentration causes [284]. Although crossover has been considered for some decades [285], its causes and effects are objects of growing interest in the literature [146], [286], [287]. In fact, although crossover does not cause cross-contamination and fast aging in VRFBs, in each compartment (half-cell) the crossing ions react with the ions already present in the half-cell, producing an exothermal reaction. The final effect, beside the release of heat, is a decrease of the charged species in both compartments and an imbalance between the two tanks, that is, a loss of capacity [288], [289], [290]. Ideally, membranes should be impermeable to vanadium ions but perfectly permeable to protons. Several studies have been published on the development of new membrane materials capable of dramatically reducing crossover without affecting ionic conductivity and durability [291], [292], [293], [154]. However, as long as crossover occurs, it causes exothermal side reactions, in which the released heat equates to the whole enthalpy of reaction [294] without electrical energy conversion but producing self-discharge instead.

As V^{3+} and V^{2+} diffuse from the negative to the positive compartment, they react with VO^{2+} and VO_2^+ [295]:



Similarly, as VO^{2+} and VO_2^+ diffuse from the positive to the negative compartment, they react with V^{3+} and V^{2+} :



Reactions 5.31 and 5.32 at the positive compartment and 5.34 and 5.35 at the negative compartment, which involve the charged species VO_2^+ and V^{2+} , respectively, are the prevailing effects as long as VO_2^+ is present at the positive compartment and V^{2+} at the negative one.

Reactions 5.33 and 5.36 only occurs when either VO_2^+ or V^{2+} are depleted in the positive and negative compartments, respectively.

5.4 Thermal modeling

The capability of VRFBs to operate at nearly room temperature is one of their advantages, which allows complex and costly thermal control systems to be avoided [19]. Nevertheless, thermal control is emerging as an important issue for VRFB stacks, as reported by Arenas

et al.[40] and Skyllas et al. [296]. High solution concentrations are desirable because they provide higher energy density, but unfortunately they also imply ion precipitation issues [86], [297]. Typically, 1.6 M vanadium solutions in 5 M sulfuric acid are known to operate safely at temperatures between 10 °C and 40 °C. More recently, the use of sulfate-chloride mixed electrolyte solutions that allows dissolving 2.5 M vanadium, which remains stable between -5 °C and 50 °C, was reported by Li et al. [94], whereas the use of additives has been tested by Skyllas-Kazacos et al. [90], which allowed vanadium concentrations of 2.7 M to be achieved. However, chemical stabilization of the vanadium species by means of organic or inorganic additives [298] can only constitute a partial solution to prevent precipitation.

Upper limits depend on the poor stability of VO_2^+ at the positive electrolyte, which can result in V_2O_5 precipitation. This salt precipitation occurs according to the following irreversible reaction [294]:



this effect varies with VO_{2+} and H_2SO_4 concentrations[88]: it can occur when temperatures over 40 °C are maintained for long periods [86], [299]. Moreover, V^{2+} at the negative electrolyte can precipitate at low temperatures depending on its concentration [300]. Salt precipitation must be avoided, because it causes energy loss and can result in the occlusion of the cell flow channels, triggering major problems during battery operations or during stand-by period with pumps turned-off, as reported by Kim et al. [297] and Yan et al. [296]. In addition, high temperatures can enhance major side effects, such as hydrogen and oxygen evolution [301]. Recently, Oboroceanu et al. [299] highlighted how the induction time, after which precipitation occurs, depends on vanadium concentration and temperature, even at low values of the latter. In addition, the electrolyte temperature affects ion diffusion through the membrane (crossover), resulting in increased self-discharge and a faster approach of the upper temperature limit. All these issues are of pivotal importance in the case of industrial-scale batteries, built around stacks of several cells with large active areas, which are expected to operate automatically.

Recently, a strategy for improving VRFB efficiency has been proposed [302], [303], that consists of reducing the reversible cell voltage during charge and increasing it during discharge by changing the electrolyte temperature. Thermal control has also been recommended in the integration of micro flow batteries with electronic devices, which could support coping of power supply demand and thermal management of printed boards for microelectronics used in high-performance servers [304], [305].

Thermal analyses are important, because a number of parameters crucial for VRFB performance (such as electrolyte viscosity, cell internal resistance, and electrode potentials) depend on the electrolyte temperature. Analysis of these issues can benefit remarkably from thermal numerical analyses. Thermal models can be important tools in the optimization of VRFB control procedures in standby and operating conditions. Thermal behavior in critical operating modes (e.g. short-circuits, pump stopping) has been investigated by Oboroceanu et al. [299], who found that extreme conditions do not arise, because of the structure of VRFBs. Control systems that use data from temperature probes and, possibly, real time model simulations have already been developed and implemented [306], [307].

5.4.1 Standby thermal modeling

In this condition, no electric current is generated and no solution flow is consequently needed. The circulation pumps are usually turned off and the solutions are at rest in the tanks and in the stack at a given *SOC*, thus avoiding hydraulic losses to optimize the round-trip efficiency. In these conditions, the cooling effect of the solution flowing through the stack is absent, but some losses still occur in the stack. Controlling the inherent thermal evolution in this case at reduced power and cost, without compromising the *RTE*, is a challenge that deserves accurate modelling and analysis. Thermal evolution in the stack in standby conditions depends on two major VRFB side effects, both involving losses and heat generation, that is, ion crossover in the polymeric membrane separating the two electrodes of each cell, and shunt currents in the internal piping and manifolds, which feed the cells forming the stack in parallel.

In spite of the significant number of previous investigations on crossover and shunt current losses in charge and discharge (i.e. load) conditions, to our knowledge only a few studies have tackled the computation of the thermal evolution of a VRFB stack in standby conditions. In [294], Tang et al. presented a study of the thermal evolution in no-load conditions due to the ion crossover only. Later, Tang et al. presented a dynamic model for computing the thermal effects of both crossover side reactions and shunt currents in standby conditions [308]. This study was developed on a 5 kW stack of 40 cells with 1500 cm² Selecion CMV membranes (capable of current densities not larger than 100 mA cm⁻²) and demonstrated that both coulombic efficiency and energy efficiency are strongly affected by high shunt currents caused by a poor flow-frame design. The paper indicated that the dominating cause of standby thermal evolution is crossover side reactions. However, the paper did not report the temperature distribution among the cells, although it is well known that shunt currents, and their thermal effects, are more intense in the cells at the end of the stack.

Furthermore, the model used in [308] to compute the energy balance gives rise to some doubts on its physical consistency. This section presents a numerical dynamic model that allows the computation of the cell-resolved temperature and concentration distributions inside a VRFB stack in standby condition with pumps turned off, due to the losses produced by ion crossover through the membrane, and shunt currents in the stack internal channels and manifolds. This type of analysis is of interest regarding industrialized VRFB stacks made with a large number of cells. The model takes into account the main parameters affecting the stack thermal behavior, based on the assumptions listed as follows:

- after ion crossover, self-discharge side reactions 5.31, 5.32, 5.33, 5.34, 5.35, 5.36 are instantaneous;
- inside each cell a perfect solution mixing occurs in each compartment, i.e. temperature and ions concentrations are uniform (such as in a double continuous stirred tank reactor, CSTR), as in [261];
- initially, all cells are at the same temperature;
- oxygen and hydrogen evolutions do not occur when *SOC* is in the range 0.1–0.9 [294];
- Because the model is intended to study the stack temperature distribution in standby mode with circulating pumps turned off, zero flow rate inside the cells was assumed and mass transport only depended on diffusion effects.

It was validated against the IS-VRFB stack. In a high power-density stack, shunt currents can have a major effect on standby thermal behavior. Validation has been carried out by means of a thermal imager that allowed the comparison of the numerical and experimental values of the temperature distribution on the stack lateral surface, as discussed in Sec.7.1. This section is structured as follows. The first part describes the physical aspects of the stand-by phase, with its simplifying assumptions. In the second part, the numerical model is described that consists of three sub-models in relation to mass balance, energy balance, and thermal balance. The shunt current model was presented in the previous section with $I = 0$.

Standby mode development

The standby mode occurs in the absence of external energy conversion, that is, in no-load with zero electric power exchange. Standby evolves through three phases, each dominated by specific side reactions:

- "phase 1" when the charged species V^{2+} and VO_2^+ are present in their respective half-cells: in this condition the reactions 2.38 sustain shunt currents and reactions 5.31, 5.32, 5.33, 5.34, 5.35, 5.36 occur due to crossover;
- "phase 2" when either V^{2+} in the negative compartment or VO_2^+ in the positive one is depleted: in this condition, reactions 5.33 and 5.36 also occur and shunt currents are negligible;

- "phase 3" when both V^{2+} in the negative compartment and VO_2^+ in the positive one are depleted. In this case the diffusion of V^{3+} and VO^{2+} through the membrane only occurs (i.e. mixing), with no reaction. In this phase both shunt currents and released heat are negligible.

Mass balance

Crossover of the four vanadium species through the membrane was modelled by means of Fick's law, considering an Arrhenius-like temperature dependence of the diffusivity coefficients [294]:

$$k_{j,n} = k_j e^{-\frac{E_a}{\kappa T_n}} \quad (5.38)$$

where $k_{j,n}$ is the diffusivity coefficient of the vanadium species j ($j = II, III, IV, V$) in the membrane of the n -th cell, k_j is a diffusivity reference coefficient, and E_a is the activation energy, which was assumed equal for all vanadium species. Mass balance in phase 1 of the standby mode is the same as in power mode, and differs from balances in phases 2 and 3.

- In phase 1 the cell mass balance is affected by self-discharge side reactions 5.31, 5.32 and 5.34, 5.35 with the shunt currents, resulting in the following equations:

$$\frac{V_c}{2} \frac{\partial C_{II-,n}}{\partial t} = \frac{A}{d} \left[-k_{II,n} C_{II-,n} - 2k_{V,n} C_{V+,n} - k_{IV,n} C_{IV+,n} \right] + \frac{I_{i,n}}{F} \quad (5.39)$$

$$\frac{V_c}{2} \frac{\partial C_{III+,n}}{\partial t} \quad (5.40)$$

$$\frac{V_c}{2} \frac{\partial C_{III-,n}}{\partial t} = \frac{A}{d} \left[-k_{III,n} C_{III-,n} + 3k_{V,n} C_{V+,n} + 2k_{IV,n} C_{IV+,n} \right] - \frac{I_{i,n}}{F} \quad (5.41)$$

$$\frac{V_c}{2} \frac{\partial C_{IV-,n}}{\partial t} = 0 \quad (5.42)$$

$$\frac{V_c}{2} \frac{\partial C_{IV+,n}}{\partial t} = \frac{A}{d} \left[-k_{IV,n} C_{IV+,n} + 3k_{II,n} C_{II-,n} + 2k_{III,n} C_{III-,n} \right] - \frac{I_{i,n}}{F} \quad (5.43)$$

$$\frac{V_c}{2} \frac{\partial C_{V+,n}}{\partial t} = \frac{A}{d} \left[-k_{V,n} C_{V+,n} - 2k_{II,n} C_{II-,n} - k_{III,n} C_{III-,n} \right] + \frac{I_{i,n}}{F} \quad (5.44)$$

- in phase 2 if V^{2+} is depleted before VO_2^+ :

$$\frac{V_c}{2} \frac{\partial C_{II-,n}}{\partial t} = 0 \quad (5.45)$$

$$\frac{V_c}{2} \frac{\partial C_{III+,n}}{\partial t} = 0 \quad (5.46)$$

$$\frac{V_c}{2} \frac{\partial C_{III-,n}}{\partial t} = \frac{A}{d} \left[-k_{III,n} C_{III-,n} - k_{V,n} C_{V+,n} \right] \quad (5.47)$$

$$\frac{V_c}{2} \frac{\partial C_{IV-,n}}{\partial t} = \frac{A}{d} \left[-k_{IV,n} (C_{IV-,n} - C_{IV+,n}) + 2k_{V,n} C_{V+,n} \right] \quad (5.48)$$

$$\frac{V_c}{2} \frac{\partial C_{IV+,n}}{\partial t} = \frac{A}{d} \left[k_{IV,n} (C_{IV-,n} - C_{IV+,n}) + 2k_{III,n} C_{III-,n} \right] \quad (5.49)$$

$$\frac{V_c}{2} \frac{\partial C_{V+,n}}{\partial t} = \frac{A}{d} \left[-k_{V,n} C_{V+,n} - k_{III,n} C_{III-,n} \right] \quad (5.50)$$

- conversely, in phase 2, if VO_2^+ is depleted before V^{2+} :

$$\frac{V_c}{2} \frac{\partial C_{II-,n}}{\partial t} = \frac{A}{d} \left[-k_{II,n} C_{II-,n} - k_{IV,n} C_{IV+,n} \right] \quad (5.51)$$

$$\frac{V_c}{2} \frac{\partial C_{III+,n}}{\partial t} = \frac{A}{d} \left[k_{III,n} (C_{III-,n} - C_{III+,n}) + 2k_{II,n} C_{II-,n} \right] \quad (5.52)$$

$$\frac{V_c}{2} \frac{\partial C_{III-,n}}{\partial t} = \frac{A}{d} \left[-k_{III,n} (C_{III-,n} - C_{III+,n}) + 2k_{IV,n} C_{IV+,n} \right] \quad (5.53)$$

$$\frac{V_c}{2} \frac{\partial C_{IV+,n}}{\partial t} = \frac{A}{d} \left[-k_{IV,n} C_{IV+,n} - k_{II,n} C_{II-,n} \right] \quad (5.54)$$

$$\frac{V_c}{2} \frac{\partial C_{IV-,n}}{\partial t} = 0 \quad (5.55)$$

$$\frac{V_c}{2} \frac{\partial C_{V+,n}}{\partial t} = 0 \quad (5.56)$$

- finally, in phase 3, both VO_2^+ and V^{2+} are depleted and no more self-discharge reactions occur inside the cell. Instead, diffusion of V^{3+} and VO^{2+} ions through the membrane will continue until the solutions of both compartments become a 50/50 mixture of V^{3+} and VO^{2+} (often referred to as $V^{3.5}$):

$$\frac{V_c}{2} \frac{\partial C_{II-,n}}{\partial t} = 0 \quad (5.57)$$

$$\frac{V_c}{2} \frac{\partial C_{III+,n}}{\partial t} = \frac{A}{d} \left[k_{III,n} (C_{III-,n} - C_{III+,n}) \right] \quad (5.58)$$

$$\frac{V_c}{2} \frac{\partial C_{III-,n}}{\partial t} = \frac{A}{d} \left[-k_{III,n} (C_{III-,n} - C_{III+,n}) \right] \quad (5.59)$$

$$\frac{V_c}{2} \frac{\partial C_{IV+,n}}{\partial t} = \frac{A}{d} \left[k_{IV,n} (C_{IV-,n} - C_{IV+,n}) \right] \quad (5.60)$$

$$\frac{V_c}{2} \frac{\partial C_{IV-,n}}{\partial t} = \frac{A}{d} \left[-k_{IV,n} (C_{IV-,n} - C_{IV+,n}) \right] \quad (5.61)$$

$$\frac{V_c}{2} \frac{\partial C_{V+,n}}{\partial t} = 0 \quad (5.62)$$

Energy balance

Heat release in the cells varies with the phase of the standby mode. During phase 1, three contributions are present, namely:

- the heat P_{co} released by the crossover side reactions Eqs.5.31, 5.32 and 5.34, 5.35:

$$P'_{co} = \frac{A}{d} \left[k_{II,n} C_{II-,n} (-\Delta H_2) + k_{III,n} C_{III-,n} (-\Delta H_3) + k_{IV,n} C_{IV+,n} (-\Delta H_4) + k_{V,n} C_{V+,n} (-\Delta H_5) \right] \quad (5.63)$$

- the heat Joule losses P_{sc} produced by the shunt currents (computed as in Sec.5.2.1);

$$P_{sc} = P_{m+,n-1} + P_{m-,n-1} + P_{c+,n} + P_{c-,n} + P_{i,n} \quad (5.64)$$

- the heat P_{re} inside the cells caused by the reactions (2.38) supplying the shunt currents [309]:

$$P_{re} = \frac{I_{i,n} (-T_{sta} \Delta S_- - T_{sta} \Delta S_+)}{zF} \quad (5.65)$$

$\Delta H_2, \Delta H_3, \Delta H_4, \Delta H_5$ are the enthalpies of reactions expressed in Eqs.5.31, 5.32 and 5.34, 5.35. $T_{sta}\Delta S_+ = T_{sta}(S_{VO_2^+} + S_{H_2O} - S_{VO_2^+})$ and $T_{sta}\Delta S_- = T_{sta}(S_{V^{3+}} - S_{V^{2+}})$ are the entropic reaction heats at the positive and the negative compartments of reactions 2.38 needed to energize shunt currents.

Because the entropy values could be deduced from [308], [49] only at standard temperature $T_{sta} = 298,15$ K (Tab.7.1), the values in Eq.5.65 were considered constant with T . The energy balance equation for the n -th cell is:

$$\rho C_p V_C \frac{\partial T_n}{\partial t} = P_{tr} + P'_{co} + P_{sc} + P_{re} \quad (5.66)$$

where P_{tr} is the transmitted heat, computed as shown in the thermal balance presented below. In phase 2, shunt-currents are negligible and only crossover self-discharge is taken into account. If V^{2+} is depleted first, heat is released by reactions 5.32 and 5.36 only:

$$P''_{co} = \frac{A}{d} \left[k_{III,n} C_{III-,n} (-\Delta H_3) + k_{V,n} C_{V+,n} (-\Delta H_3) \right] \quad (5.67)$$

likewise, if VO_2^+ is depleted first, heat is released by reactions 5.33 and 5.34 only:

$$P''_{co} = \frac{A}{d} \left[k_{II,n} C_{II-,n} (-\Delta H_4) + k_{IV,n} C_{IV+,n} (-\Delta H_4) \right] \quad (5.68)$$

in both cases, the energy balance in the n -th cell becomes:

$$\rho C_p V_C \frac{\partial T_n}{\partial t} = P_{tr} + P''_{co} \quad (5.69)$$

In phase 3, only the term P_{tr} is taken into account so that P_{co} vanishes, that is, an equation similar to Eq.5.69 holds, with $P''_{co} = 0$.

Thermal balance

Cell temperature distribution and evolution depend on the heat transfer between adjacent cells and toward the surrounding air. For the n -th cell ($n = 2$ to $N-1$), the heat transfer was modelled as follows:

$$P_{tr} = U_x A_x (T_{n+1} - T_n) + U_x A_x (T_{n-1} - T_n) + 2U_y A_y (T_{air} - T_n) + 2U_z A_z (T_{air} - T_n) \quad (5.70)$$

where U_x, U_y and U_z are the total heat transfer coefficients in the x, y, z directions (Fig.5.11), and A_x, A_y , and A_z are the corresponding cross-sections. For the 1-st and N -th cells, which have one face exchanging with the room, the term $U_x A_x (T_{n-1} - T_n)$ was replaced with $U_{end} A_{end} (T_{air} - T_1)$, and the term $U_x A_x (T_{n+1} - T_n)$ with $U_{end} A_{end} (T_{air} - T_N)$, respectively.

U_{end} is the total heat transfer coefficient toward the room in x direction, including the stack end plates, and A_{end} the corresponding cross-section. Assuming a thin gap between adjacent cell frames produced by the gaskets, the external stack surface consists of a closely spaced array of parallel plates (Fig.5.11). The resulting geometry corresponds to the array of fins of a vertical-gap natural convection heat sink. Its convection heat transfer coefficient h_{air} has been computed with the experimental correlation proposed in [310]:

$$Nu = \frac{h_{air} b}{\lambda_{air}} = \frac{Ra}{24} \left[1 - e^{\left(-\frac{35}{Ra} \right)^{0.75}} \right] \quad (5.71)$$

with

$$Ra = \frac{\rho_{air}^2 g \beta C_{p,air} b^4 \Delta T}{\mu_{air} \lambda_{air} L_{fin}} \quad (5.72)$$

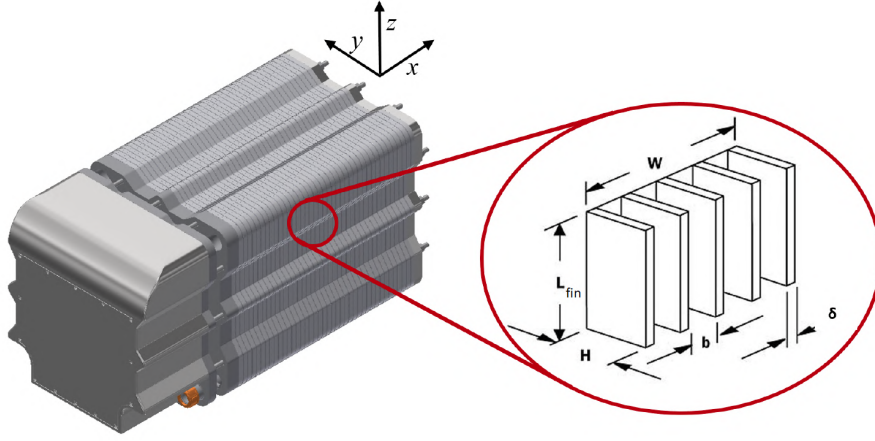


FIGURE 5.11: Due to the gaps caused by the gasket thickness, the stack lateral thermal exchange surface was modeled as a vertically oriented array of parallel flat fins.

Once Nu is known from the third term in Eq.5.72, h_{air} can be computed from the second term, and the total heat transfer rate in y -direction for the n -th cell was computed as:

$$P_{tr,n} = h_{air} A_{fin} \theta_{fin} (T_{sur,n} - T_{air}) = U_y A_y (T_n - T_{air}) \quad (5.73)$$

A_{fin} is the fin area [310] and θ_{fin} is the dimensionless fin heat exchange efficiency that was assumed to be equal to 1. The total heat transfer coefficient U_y in the finned side of the stack is as follows:

$$U_y = \left[\frac{\delta_y}{\lambda_{PP}} + \frac{1}{h_{air} \left(\frac{A_{fin}}{A_y} \right)} \right]^{-1} \quad (5.74)$$

δ_y is the propylene thickness of the cell frame in y -direction, and λ_{PP} is the propylene conductivity. In Eq.5.73, $T_{sur,n}$ is the average surface temperature on the n -th cell lateral face. Accordingly, the model provided dynamic temperature distributions on both the axis and the lateral surface of the cells along the stack.

5.4.2 Operation thermal modeling

In normal operation during both charge and discharge, the solutions are pumped through the stack constituting a means of removing the heat generated inside the stack by the internal losses, providing effective cooling. Several studies have been carried out and published on this issue, for example by Wei et al. [311], [312] and Skyllas-Kazacos et al. [296], [309], however these neglected the reaction of entropic heat and the effect in a large VRFB system. The model presented here takes into account, at a cell level, the reversible entropic heat of the electrochemical reactions, irreversible heat due to over potentials, self-discharge reactions due to ion crossover, and shunt current losses both in charge and discharge high current operation. The experimental validation is presented in Chap.7.

Mass balance

In load conditions, the species balance for the n -th cell depends on the cell current $I_{i,n}$ resulting from the stack current I and shunt currents $I_{c\pm,n}$, as well as on the species crossover and related side reactions 5.31, 5.32, 5.34, 5.35. By modelling the species crossover across the membrane with Fick's law, the mass balance equations for the negative compartment were

written as follows:

$$\frac{V_c}{2} \frac{\partial C_{II-,n}}{\partial t} = \frac{A}{d} (-k_{II,n} C_{II-,n} - 2k_{V,n} C_{V+,n} - k_{IV,n} C_{IV+,n}) + \frac{I_{i,n}}{F} + Q_{c,-} (C_{II-,ta} - C_{II-,n}) \quad (5.75)$$

$$\frac{V_c}{2} \frac{\partial C_{III-,n}}{\partial t} = \frac{A}{d} (-k_{III,n} C_{III-,n} + 3k_{V,n} C_{V+,n} + 2k_{IV,n} C_{IV+,n}) - \frac{I_{i,n}}{F} + Q_{c,-} (C_{III-,ta} - C_{III-,n}) \quad (5.76)$$

$$\frac{V_c}{2} \frac{\partial C_{IV-,n}}{\partial t} = 0 \quad (5.77)$$

Similar equations were used for the positive compartment, as follows:

$$\frac{V_c}{2} \frac{\partial C_{V+,n}}{\partial t} = \frac{A}{d} (-k_{V,n} C_{V+,n} - 2k_{II,n} C_{II-,n} - k_{III,n} C_{III-,n}) + \frac{I_{i,n}}{F} + Q_{c,+} (C_{V+,ta} - C_{V+,n}) \quad (5.78)$$

$$\frac{V_c}{2} \frac{\partial C_{IV+,n}}{\partial t} = \frac{A}{d} (-k_{IV,n} C_{IV+,n} + 3k_{II,n} C_{II-,n} + 2k_{III,n} C_{III-,n}) - \frac{I_{i,n}}{F} + Q_{c,+} (C_{IV+,ta} - C_{IV+,n}) \quad (5.79)$$

$$\frac{V_c}{2} \frac{\partial C_{III+,n}}{\partial t} = 0 \quad (5.80)$$

In the previous equations, the diffusion coefficient of the j -th vanadium species ($j = II, III, IV, V$) in the n -th membrane was modelled with an Arrhenius-like dependence on temperature (Eq.5.38).

Heat generation

In load operation, heat generation inside the stack is related to different factors, presented as follows:

- the irreversible main heat rate P_{il} produced by the electric currents $I_{i,n}$ as stated in Sec.5.2; it must be noted that this heat rate occurs by far inside the cells (where it consists of the over potential losses represented by the internal resistances $R_{i,n}$) while the other hydraulic segments (represented by $R_{c,n}$ and $R_{m,n}$) produce negligible contributions;
- the reversible entropic heat rate P_{re} released or absorbed inside the cells by the electrochemical reactions, which generate the electric currents $I_{i,n}$ during discharge and charge, respectively [309];
- the heat rate P_{co} due to exothermic self-discharge reactions 5.31, 5.32, 5.34, 5.35 occurring after species crossover.

The last two terms were computed as P_{re} by using Eq.5.65 and P_{co} by Eq.5.63.

Energy balance

The temperature of each cell was computed by taking into account its thermal balance equation, as follows:

$$\rho C_p V_C \frac{\partial T_n}{\partial t} = P_{il} + P_{re} + P_{co} + P_{tr} + P_{fl} \quad (5.81)$$

where the last two terms express the heat exchanges as described hereafter. The heat transfer (both conductive and convective) of the n -th cell (except the end ones) toward the other cells and the surrounding air, was computed as follows:

$$P_{tr} = U_x A_x (T_{n+1} - T_n) + U_x A_x (T_{n-1} - T_n) + 2U_y A_y (T_{air} - T_n) + 2U_z A_z (T_{air} - T_n) \quad (5.82)$$

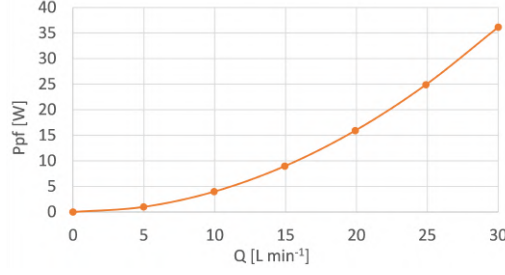


FIGURE 5.12: Energy losses of the pumps (SANSO PMD-641) as a function of flow rate.

The convective heat transfer coefficients in the x , y , and z directions U_x , U_y , and U_z (Eq.5.11) were computed as reported in [313]. As the same that the standby analysis the equations for the first and last cells had to take into account that one face in x direction exchanges with the surrounding air so that the pertinent term of Eq.5.82 was replaced with $U_{end}A_{end}(T_{air} - T_1)$ and $U_{end}A_{end}(T_{air} - T_1)$, respectively. The heat exchange due to the electrolyte flow in each cell was obtained as follows:

$$P_{fl} = \rho C_p Q_{c+}(T_{ip+} - T_n + \rho C_p Q_{c-}(T_{ip-} - T_n) \quad (5.83)$$

The heat dissipation of the piping and tanks were computed considering their outer surfaces subject to natural convection. Regarding the internal surfaces, forced convection was assumed in the pipes due to the high solution velocity and natural convection in the tanks. Heat exchanged by the positive electrolyte along the two pipe segments connecting the tank to the stack and the stack back to the tank, were written as:

$$\rho C_p V_{ip} \frac{\partial T_{ip+}}{\partial t} = \rho C_p Q_+(T_{ta+} - T_{ip+}) + U_{ip} A_{ip}(T_{air} - T_{ip+}) + P_{pf} \quad (5.84)$$

$$\rho C_p V_{op} \frac{\partial T_{op+}}{\partial t} = \rho C_p Q_+(T_{op+} - T_{ta+}) + U_{op} A_{op}(T_{air} - T_{op+}) + P_{pf} \quad (5.85)$$

where the subscripts have the following meanings: ip = inlet pipe segment from tank to stack, op = outlet pipe segment from stack to tank; ta = tank. P_{pf} is the pump heating from hydraulic friction, given in the pump data sheet (Fig.5.12). The other symbols in Eqs.5.84 and 5.85 are explained in Tab.7.1. The thermal equation of the electrolyte in the positive tank was written as follows:

$$\rho C_p V_{ta} \frac{\partial T_{ta+}}{\partial t} = \rho C_p Q_+(T_{op+} - T_{ta+}) + U_{ta} A_{ta}(T_{air} - T_{ta+}) \quad (5.86)$$

Equations similar to 5.84, 5.85, and 5.86 hold for the piping and tank at the negative side.

5.5 Thermal model implementation

Fig.5.13 shows the flow chart of the overall algorithm for the solution of mass and energy balance equations in the cases of charging/discharging operations. A similar algorithm was used to simulate the standby condition. At the beginning of the simulation, the parameters that define the conditions of the simulation in terms of thermal-fluid dynamic characteristics were set. In this phase, the time interval and the time step (Δt) were also defined. In an RFB device, thermal evolution can be accurately evaluated with $\Delta t = 5s$ due to the rather slow kinetics of the heat exchange from the stack and piping to the environment. Conversely, after ion crossover, the self-discharge side reactions 5.31, 5.32, 5.33 and 5.34, 5.35, 5.35 were considered instantaneous in each step (i -th) iteration on the flowchart Fig.5.13. After the initialization of the vectors and variables, a simple iterative cycle allowed the mass balance equations to be solved to calculate the concentration variations for each vanadium species in each cell and from them the heat flux P_{co} . In addition, for each iteration, the shunt currents were calculated based on the tableau analysis technique, which solves the electrical problem, that is, currents and voltages, associated with the lumped circuit representation of the stack. Accordingly, the overall irreversible main

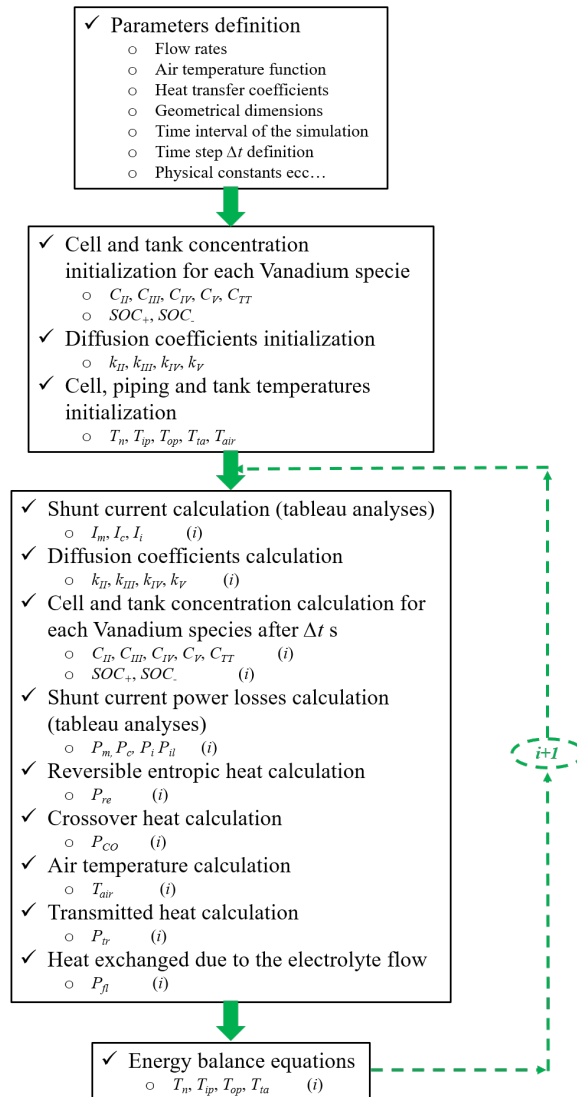


FIGURE 5.13: Thermal model algorithm for charge/discharge operation.

heat rate P_{il} and reversible entropic heat flux P_{re} were computed. Similarly, P_{tr} and P_{fl} were computed, starting from the computed temperature at the $(i-1)th$ iteration and the energy balance equations (final part of the flowchart in Fig.5.13 providing the dynamic temperature evolution for each cell at the $i-th$ iteration. The whole model was implemented in Matlab[®] and was run on a Dell Workstation provided with 2 Intel[®] Xeon[®] processors and 32 GB RAM 2.10 GHz clock.

Chapter 6

Polarization curves

According to the recent authoritative review [40], very few contributions have considered polarization tests on pilot-scale devices and the effect on performance of cell design, reaction environment, electrode structure, and operational conditions.

The scant performance data reported on such kW-class systems includes: 160 mA cm⁻² at 16.6 × 10⁻³ cm s⁻¹ achieved in a 15-cell 780 cm² stack [199]; 90 mA cm⁻² at 16.6 × 10⁻³ cm s⁻¹ in a 2714-cm² 31-cell stack [314]; 320 mA cm⁻² at $q=25.6 \times 10^{-3}$ cm s⁻¹ in a 20-cell 780-cm² [78]; and 240 mA cm⁻² at $q=25.6 \times 10^{-3}$ cm s⁻¹ in a 3-cell 780-cm² [315].

The objective of this chapter is to contribute to filling this gap by reporting the experimental results for an IS-VRFB stack obtained during charge and discharge in two working modes: fast and steady-state. These occur when the battery switches on and after concentration gradients stabilize inside the electrodes. These two operation modes are representative of the real working conditions of a battery, which occur for example in primary frequency regulation and peak shaving.

6.1 Theoretical background

In a single-cell experiment, a polarization curve plots the cell voltage versus current density. In this case, polarization curves present the voltage at the stack terminals as a function of the load current. In general, three zones can be identified in polarization curves, at low, mean, and high current density, where the prevailing loss effects are activation, ohmic, and concentration over potentials, respectively (Fig.2.3, Sec.2.2.2), ([316], [317]).

According to Sec.2.2.2 the stack voltage can be expressed as follows:

$$V = NE_0(s) - V_a - V_o - V_t \quad (6.1)$$

where V_a , V_o and V_t are the three over potentials of the whole stack. Activation over potentials V_a are caused by the electrochemical reactions that turn reactants into products during both charge and discharge. This zone is characterized by a rapid, non-linear change of stack voltage with increasing current, typically modelled by the Butler-Volmer equation ([317]). Ohmic over potentials are resistive effects, linearly varying with the current, mainly imputable to ionic and electronic conduction in membranes, electrodes, and current collectors. At high current densities, reactants are consumed and products are produced at a high rate causing strong mass transport effects and high concentration gradients. These gradients cause voltage variations that increase much more than linearly with current, producing a ‘knee’ in the polarization curve and an abrupt voltage decrease. In a real case, one of the over potentials can have a dominant effect on the polarization curve, causing the others to become negligible. Because the *OCV* and over potentials depend on the *SOC* and Q , the polarization curves vary with them resulting in a family of curves.

In these tests, the *SOC* was varied from 10% to 90% in steps of 10%, corresponding to an *OCV* ranging between 1.257 V and 1.483 V to prevent hydrogen evolution [259]. Two figures of merit were considered to qualify the solution flow rate. One was the specific flow rate q , namely the flow rate related to the total cell active area NA :

$$q = Q/NA \quad (6.2)$$

In the IS-VRFB experiments presented here, the flow rate Q was varied between 10 L min^{-1} and 29.5 L min^{-1} , corresponding to q ranging between $6.9 \times 10^{-3} \text{ cm s}^{-1}$ and $20.5 \times 10^{-3} \text{ cm s}^{-1}$ [318], [319], [320].

The upper limit was the maximum value achievable in the IS-VRFB with the PMD-641 SANSO pumps. The second parameter considered was the flow factor, that is the ratio between Q and the stoichiometric demand Q_{sto} required by the reactions in all cells at a current I as expressed by Eq.8.12, 8.13. In the IS-VRFB, α was usually controlled to remain above 7, but in certain operating conditions lower figures (due to pump power limitations) were tolerated, to allow for exploring extreme operating regimes.

6.2 Experimental method

Polarization curves were carried out using the PMS and variable passive resistors remotely controlled by the BMS. As discussed in Sec.4.4, the in-house software architecture of the BMS was based on a state machine working principle to allow automatic routines to be implemented to control the experiment. All LabVIEW procedures were parametrized for easy execution of similar tests at different settings. An automatic procedure was also developed to collect the necessary data for computing the polarization curves. The procedure was set inside the "PFT Loop" and was composed of several cases inside a case structure. In this way, if the user wants to acquire data for polarization, the program will keep control of the other inputs. In the polarization curve section of the LabVIEW front panel interface, there are four elements: the polarization logging folder path line, the start polarization and stop polarization buttons, and a square LED labelled processing. The folder indicator simply shows the path where the files are saved. The start button is programmed to start the polarization process, as shown in Fig.6.1. The stop button is programmed to stop the entire procedure at any point of the process. Whatever was done until this period remains saved.

The LED displays when the process is running. Fig.6.1 presents the flowchart of the procedure to collect data from LabVIEW. After the start polarization button is pressed, the program calls a SubVI named polarization settings (refers to Fig.6.2) that opens a support window where the user can set several parameters: choose between charge or discharge and insert flow rate, stack voltage, current step, SOC , and max current values. The cancel button makes the program return to the default acquisition case. The OK button confirms the introduced values and makes the procedure continue. For every step, a different message appears in the "status" to indicate the program status.

The flowchart in Fig.6.1 is explained as follows:

- Start Polarization: this starts with the control of the active buttons (enable or disable), sets the current control to zero, and writes the set stack voltage on the voltage control. Every time the current or the voltage control are modified, the user can check the actual value in the power supply section on the front panel;
- Wait 10 s: the procedure is controlled for 10 s. This allows the voltage in the cells to stabilize;
- Add Current Step: in a preliminary step, the actual current value, virtually added, is compared to the max current value. The result enters a case structure. If it is true (lower) the loop can continue, otherwise it moves outside the loop because the set max value for the current is reached;
 - "False": Limit Reached: this is the control of the active buttons (enable or disable), that sets the current control to zero and restarts the program to the acquisition case. A message will inform the user that the max current value is reached and the acquisition of polarization curves data ended;
 - "True": gives the new value to the current control;
- Impose I: the new value of current is imposed on the power supply;

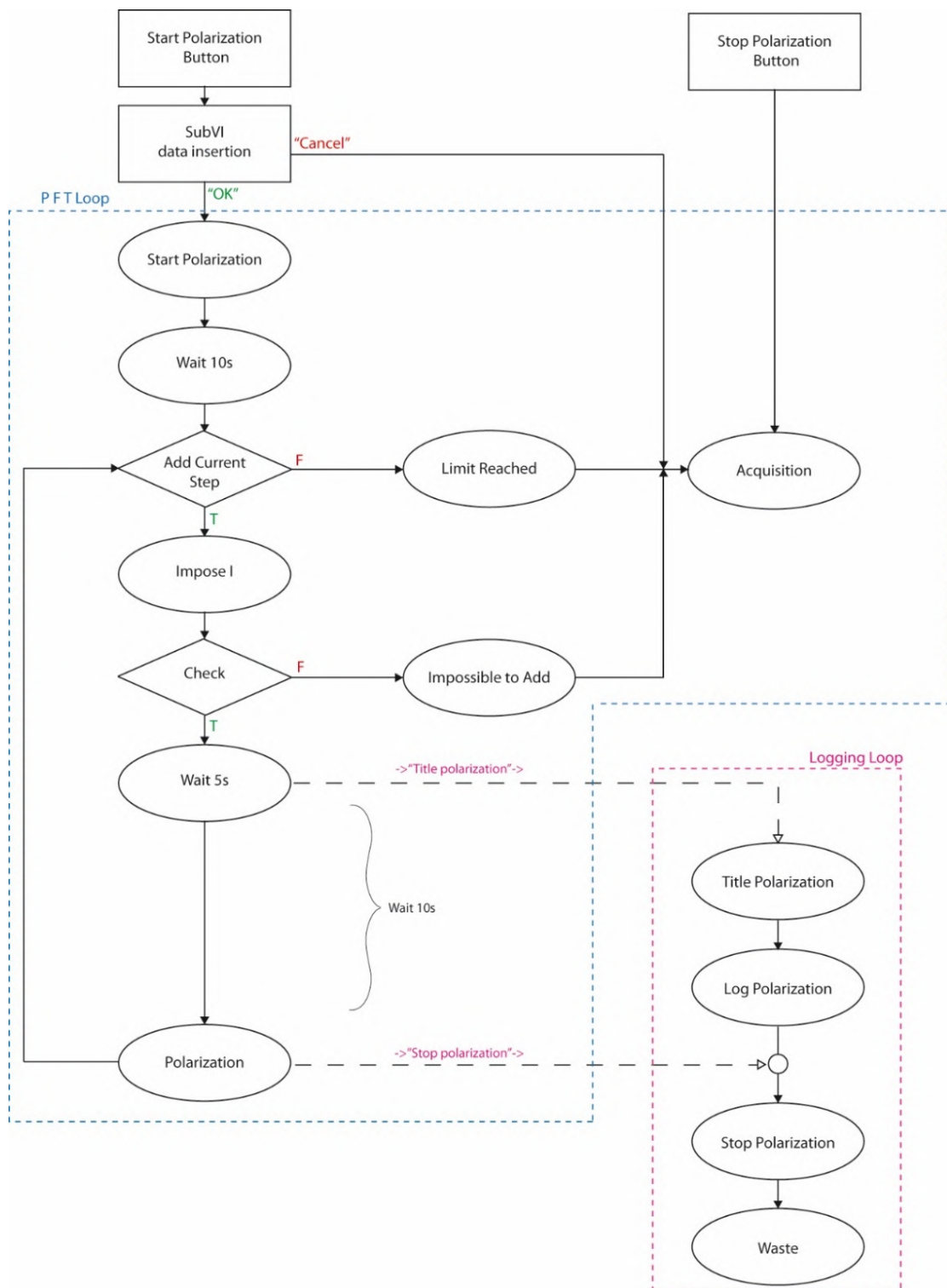


FIGURE 6.1: Flowchart of the automatic procedure to collect data for polarization curve computation.

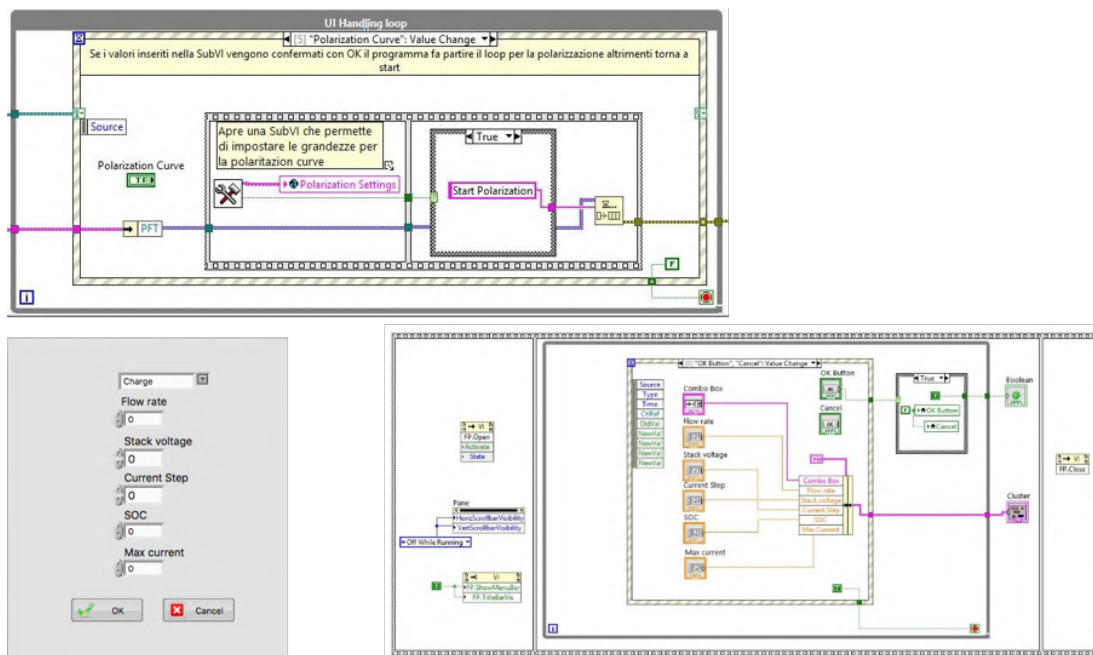


FIGURE 6.2: Top: the Polarization case in the UI Handling loop; bottom-left: the window that allows the user to set the parameter for the polarization routine; bottom-right: the SubVI internal structure.

- Check: if a voltage limit is set, the power supply is programmed to limit the output current. In this step, the output current value is checked in order to reach the set value or if it is limited by the power supply. The result enters to a case structure;
 - "False": Impossible to Add: this is the control of the active buttons (enable or disable), that sets the current control to zero and restarts the program to the acquisition case. A message will show that the current cannot be raised anymore and the acquisition ends;
 - "True": continues with the loop;
- Wait 5s: the procedure is controlled for 5 s. It gives the command to the logging loop and starts a parallel procedure in which a logging file is created and written;
 - Title Polarization: this creates the title of the file by using the input values that the user set at the beginning of the procedure;
 - Log Polarization: stack voltage and current are written in the new .xls file;
 - Stop Polarization: the procedure ends;
- Polarization: in this case, the program waits 10 s before giving the stop to the logging loop and make the procedure turn back to the add current step case.

Once the procedure ends, the program has created a set of files that are ordered in a folder. Their names indicate the date, flow, current, and the *SOC* (e.g. '20171023 30 L-min 8A SOC 40.xls'). For each current step, stack voltage and current are acquired several times during 10 s, to make the measure as precise as possible. After, a Matlab code computes the average of these data and writes them to a new single file.

6.3 Results

When a load is connected, a VRFB takes some time to reach steady state conditions. In particular, if no galvanostatic control is applied, an overcurrent establishes which reduces and stabilizes at a steady-state value I after a transient period. This behavior is due to the time

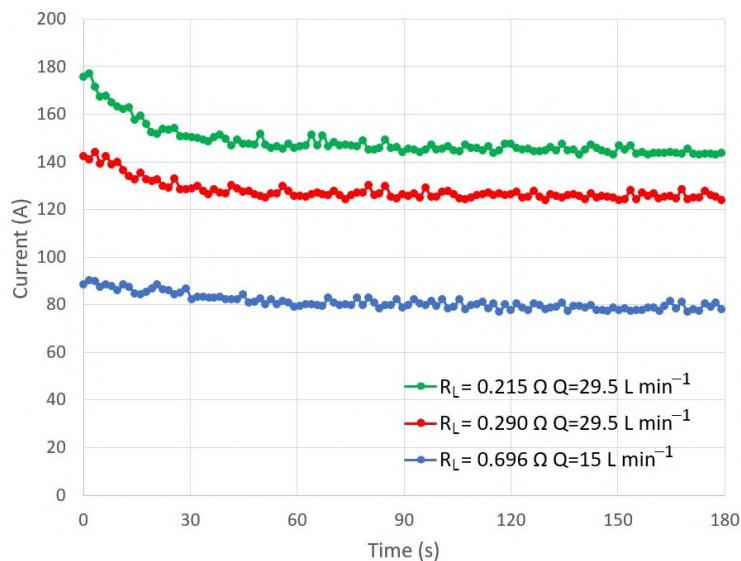


FIGURE 6.3: Time evolution of the stack current after connection at $SOC=40\%$ and at different values of flow rate Q and load resistance R_L .

needed for the creation of concentration gradients of both reactants and products in the electrodes starting from the rest uniform bulk distributions [321], [322], which affect both activation and concentrations overpotentials [323]. This dynamic behavior is usually modelled by means of a Warburg element (i.e. a constant-phase impedance) [324]. Fig.6.3 presents the current evolutions in the IS-VRFB when the stack is connected to the variable passive load, and shows that the ratio between peak and steady-state currents I_p/I_{ss} , is higher at higher currents (about 120% at $I_p=176$ A and 113% at $I_p=143$ A). According to the analyses carried out, the duration of these transients varies with SOC , flow rate, and I_{ss} , and can last as long as 180 s.

These analyses enabled two different modes of operation to be identified of the stack, which were applied during the experiments. The first, referred to as "fast" in the following, was considered in both charge and discharge: data acquisition ran between 5 and 20 s after current start-up, namely when the concentration gradients had not yet stabilized in the electrodes. In the second mode, referred to as "steady-state" in the following, data acquisition was started once concentration gradients had stabilized in the electrodes, typically 45–180 s after current start-up and was extended over 20 s. It is worth noticing that both conditions have practical importance, as they correspond to different services that a VRFB can be required to provide, for example primary frequency regulation in the first case and peak shaving in the second case [325], [118], [326].

6.3.1 Fast mode measurement procedure

In both fast and steady state modes, each point of a polarization curve below 75 A was provided by the PMS remotely controlled by the BMS, whereas points at higher discharge currents were obtained on the passive load. In the case of the fast tests, the LabVIEW procedure described was implemented in the BMS to control the PMS, and data acquisition occurred according to the following sequence: the load was connected and after an idle time $\tau_i = 5$ s, voltages and currents were acquired over an acquisition time $\tau_a = 15$ s at a sampling frequency of 1.25 Hz. The averages of the sampled data were used as points of the polarization curves. The LabVIEW procedure controlled the construction of the polarization curves at steps of 2 A from 0 A to 74 A [327]. To test higher discharge currents, the passive load was used and a manual resistor adjustment was needed, introducing some variability in the acquisition of data points at the same 2 A current steps. Moreover, the manual adjustments produced delays between successive measurements, not as constant as with the remotely controlled PMS, which caused irregular electrolyte refreshing and concentration recovery in the porous electrodes and, consequently, produced some variability in the stack voltage V .

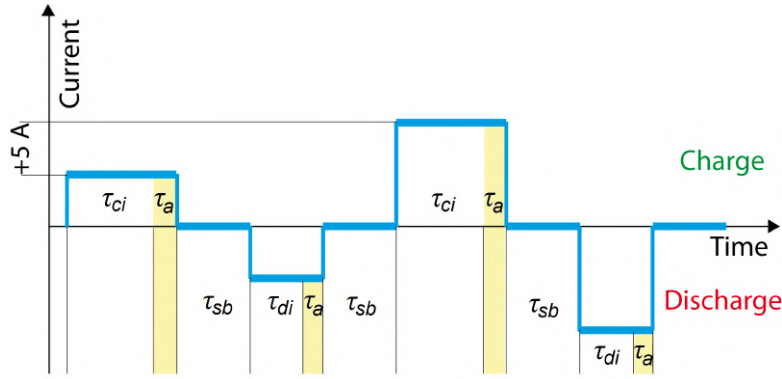


FIGURE 6.4: Reference current profile during data harvesting in steady-state condition controlled by the automatic LabVIEW routine to drive the PMS in both charge and discharge modes.

6.3.2 Steady-state mode measurement procedure

To acquire data of the polarization curves in the steady-state mode, longer load operations were needed, which affected the *SOC*. Accordingly, to obtain a whole polarization curve at a fixed *SOC*, this effect was re-biased after each measurement at a given load current by means of the specific LabVIEW procedure described above. This controlled the following actions for each *i*-th data point: turn on the PMS at a desired charge current $I_{ch}(i)$, wait for a charge idle time τ_{ci} needed to reach steady-state conditions, acquire data during an acquisition time $\tau_a = 20$ s at a sampling frequency of 1.25 Hz, turn off the current, wait for a standby time $\tau_{sb} = 90$ s, turn on the PMS at a discharge current $I_{dh}(i) = -I_{ch}(i)$, wait for a discharge idle time τ_{di} needed to reach steady-state conditions, acquire data during an acquisition time $\tau_a = 20$ s at a sampling frequency of 1.25 Hz, wait for a standby time $\tau_{sb} = 90$ s, set the next charge current $I_{ch}(i+1) = I_{ch}(i) + 5$ A. This sequence was started at $I_{ch}(0) = 5$ A and iterated up to $I_{ch}(i) = 75$ A, which is the maximum PMS current. The idle times τ_{ci} and τ_{di} varied between 45 and 180 s, depending on the *SOC* and the electrolyte flow rate Q . The higher the two, the shorter τ_{ci} and τ_{di} because the battery reached steady-state conditions more quickly. In the worst conditions (low *SOC* and low Q), 180 s were needed to assure steady-state conditions. Alternating charge and discharge allowed the initial conditions to be the initial conditions restored, that is, maintaining a constant *SOC* during the construction of each polarization curve [323]. Accordingly, τ_{ci} was kept longer than τ_{di} to restore the charged species, which were consumed by side effects during the previous operation (i.e. species crossover) Sec.5.3 and shunt currents Sec.5.2 ([281], [279]). After some trimming tests, a value $\tau_{ci} = \tau_{di} + 20$ s was found to be a proper choice to this end.

Fig.6.4 shows a graphical representation of the current control time profile produced by the LabVIEW procedure automatically driving the PMS. The procedure was trimmed after observing the effects of different idle times τ_{di} on the stack current and cell voltages, and could only run on the remotely controlled PMS. Conversely, manual regulation of the passive load at high discharge current was performed with a time procedure similar to the "fast" mode.

Measurements were acquired at each load configuration after τ_{di} elapsed, and again some time variability was unavoidable. However, steady-state conditions were relatively easy to achieve with the manual resistor adjustment (due to both longer times and stabilized gradients) and consequently steady-state polarization curves occurred more regular than fast ones.

In all conditions, a safety procedure controlled the measurements, automatically stopping the operation when one of the following limits was reached:

- any cell voltage fell below 0.1 V in discharge;
- any cell voltage exceeded 1.65 V in charge;
- the flow factor α in charge fell below 3.5.

6.3.3 Experimental tests

Fast and steady state data were acquired regarding both charge and discharge modes to obtain polarization and power curves at different *SOC* and *Q*.

6.3.4 Fast mode tests

Polarization and power curves were first traced with the IS-VRFB operated in fast mode [328]. The internal resistance R_i was computed as the ratio between the voltage variation and the current variation corresponding to two points in the linear zone of the polarization curves in charge and discharge. The resulting R_i values include not only the felts and membranes ohmic resistances but also other ohmic loss causes (e.g. contact resistances and current collectors) [130], [129]. Fig.6.5 presents the R_i values obtained at different *Q* and *SOC* in charge and discharge, respectively. In charge R_i ranged between 92 m Ω and 150 m Ω , corresponding to average cell area specific resistances (ASRs) between 55 Ω cm² and 90 Ω cm². In discharge, R_i ranged from 98 m Ω to 272 m Ω , corresponding to ASRs between 59 Ω cm² and 163 Ω cm². In both cases, the R_i values varied with *Q* and *SOC*, with a general trend of decreasing with increasing *SOC* and *Q*.

Charge and discharge polarization and power curves in fast mode at different *SOCs* with $Q = 29.5$ L min⁻¹ are shown in Fig.6.5. In charge, the behavior demonstrates extreme linearity in the explored current range (up to 75 A). Consistently, the *OCV* increases with the *SOC*. As regards discharge, a linear correlation exists between stack voltage and current at *SOC* \geq 50%, meaning that ohmic losses dominate the polarization curves at all current densities. Conversely, at *SOC*=10% concentration, over potentials produced by the feeble mass transport prevail, causing a sharp voltage drop already at low currents. The limiting current, that is the maximum current that can be obtained when voltage drops to zero, was found to increase with *SOC* and *Q*, as expected [329]. A lower limiting current of 35 A (corresponding to a limiting current density of 58 mA cm⁻²) was found at *SOC*=10% and $Q=29.5$ L min⁻¹ ($q = 20.5 \times 10^{-3}$ cm s⁻¹). Conversely, during discharge a maximum averaged current of 370 A (617 mA cm⁻²) was achieved on the passive load with a residual stack voltage of 22 V at *SOC*=90% and $Q=29.5$ L min⁻¹. Because $I_{dh}(i)$ values were averaged during τ_a , the initial currents were higher, and notably, they peaked to 400 A in the case of $I_{dh}(i)=370$ A at *SOC*=90%.

Even if this current value still appeared far from the limiting current at high *SOC*, tests were limited at 400 A because a very critical flow factor $\alpha=1.5$ was achieved with the present maximum $Q=29.5$ L min⁻¹. Moreover, 400 A was also the current rating of the electric circuit contactor and of the passive load. Assuming a linear extrapolation of the measured data, as in [329], the limiting current should be as high as 600 A (1000 mA cm⁻²). However, these high current values will only be explored after upgrading the hydraulic and electric circuits (by using the biggest pumps CM MAG-P06 Sec.4.1.4). The power curves of Fig.6.5 show that the power peak was reached at all *SOCs* and it increased with the *SOC*, as expected. The maximum power at *SOC*=90% and $Q=29.5$ L min⁻¹ was 8.9 kW (corresponding to a cell power density of 370 mW cm⁻²) and occurred at 300 A (500 mA cm⁻²).

6.3.5 Steady-state mode tests

Polarization and power curves were also traced in steady-state mode. The LabVIEW procedure described in Sec.6.2 was allowed to obtain a *SOC* deviation limited between 0.27% and 0.44% during each curve construction. In this case, the internal stack resistance R_i was also calculated from the charge and discharge polarization curves at different *Q* and *SOC* with the same method, as in Sec.5.2.1. In charge R_i ranged between 92 m Ω and 156 m Ω , corresponding to average *ASRs* of 55 Ω cm² and 94 Ω cm². In discharge R_i ranged from 106 m Ω and 187 m Ω , corresponding to average *ASRs* of 64 Ω cm² and 112 Ω cm². In both cases, data showed a dependence on *Q* and *SOC*. In charge, R_i exhibited a decrease with increasing *SOC* down to a minimum value, after which R_i started to increase. These minimal values occur between 50% and 80% of *SOC* with increasing *Q*. This behavior is related to the decrease of the flow factor α during charge in operations at high *SOC*. In discharge a more regular decrease of R_i with

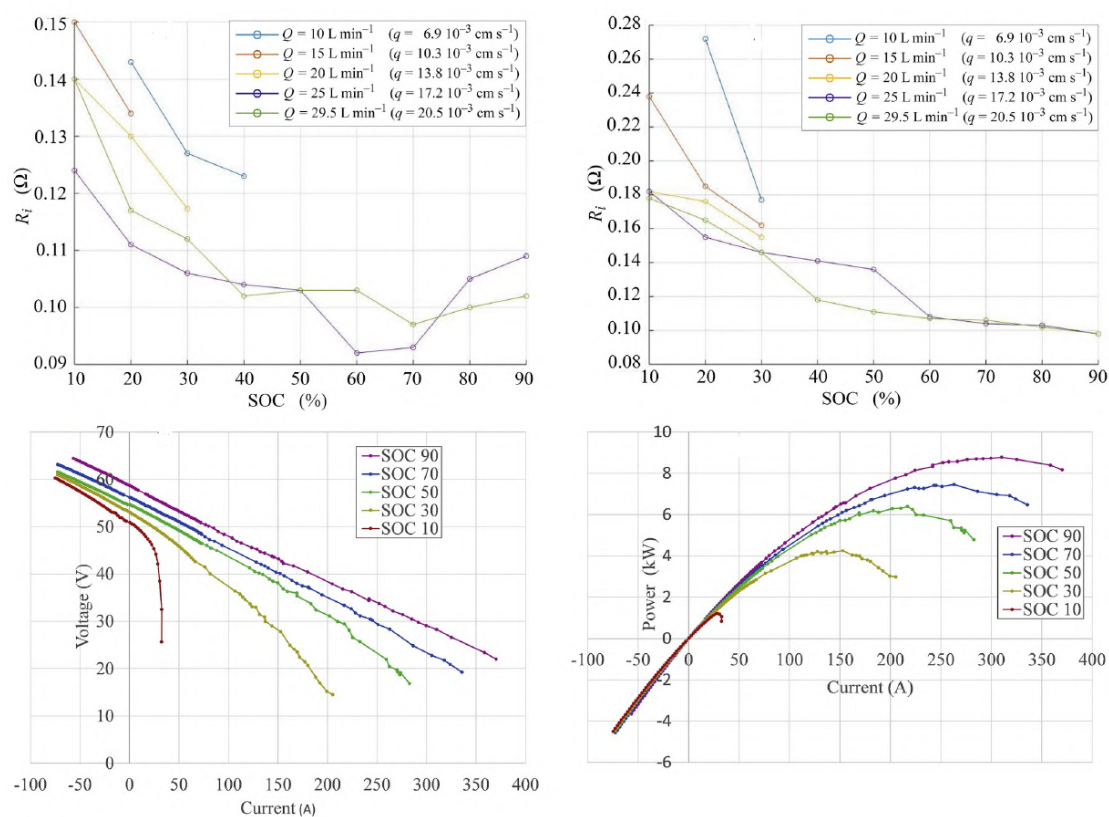


FIGURE 6.5: Fast mode tests. Top-left: Internal resistance during charge at different flow rates Q (i.e. specific flow rates q); top-right: internal resistance during discharge at different flow rates Q (and q); bottom-left: polarization curves at different SOC's with $Q=29.5$ L min⁻¹ ($q=20.5 \times 10^{-3}$ cm s⁻¹); bottom-right: power curves at different SOC's with $Q=29.5$ L min⁻¹ ($q=20.5 \times 10^{-3}$ cm s⁻¹).

increasing SOC and Q is observed, even if a small increase at high SOC and Q appears in this case.

Fig. 6.6 shows the charge and discharge polarization and power curves, respectively, at different SOC s with $Q = 29.5 \text{ L min}^{-1}$. In this case, the charge curves also demonstrate a linear behavior, whereas discharge curves show that concentration losses are important at $SOC \leq 30\%$. Exploring the performances at lower Q , it was found that these losses become relevant at higher SOC s as Q decreases. However, in the majority of cases, the polarization curve results were linear, which highlights that ohmic over potentials are the dominant loss effect in steady-state mode as well. The maximum averaged currents during τ_a ranged between the limiting current of 20 A (33 mA cm^{-2}) at $SOC=10\%$ and more than 350 A (with a current density of 583 mA cm^{-2}) achieved at $SOC=90\%$ with a residual stack voltage of 18.5 V. The maximum power reached almost 8 kW (with a power density of 370 mW cm^{-2}) at 255 A (427 mA cm^{-2}). Because these measurements were achieved in steady-state conditions, the maximum values can be maintained steadily in energy management grid services. Higher currents will be explored after the hydraulic and electric circuits are upgraded (Sec.4.1.4). However, an extrapolation of the polarization curve at $SOC=90\%$ suggests that a limiting current of 520 A (867 mA cm^{-2}) could be achieved in steady-state conditions.

Other interesting results can be deduced from Fig.6.7 that plots the power curves at $SOC=70\%$ and different flow rates. By varying Q , the maximum power changes, covering a wide range of values in this example from 4.38 kW to more than 6.9 kW at $Q=10 \text{ L min}^{-1}$ and 29.5 L min^{-1} , respectively. This leads to an overlap in the achieved powers at different SOC s, meaning that the delivered power can be maintained constant while the SOC reduces by modulating Q .

6.3.6 Effect of concentration dynamics at start-up

The combined effect of SOC and flow rate can also be seen on the appearance of concentration losses, in addition to peak power as illustrated in the discussion on Fig.6.5 and Fig.6.6. Fig.6.8 compares two fast polarization and power curves taken at a relatively low $SOC=30\%$ and at high and low flow rates $Q = 10$ and 29.5 L min^{-1} . In the case of $SOC=30\%$ and low $Q=10 \text{ L min}^{-1}$, it shows that the curves present two different trends, one at low currents (obtained by driving the battery with the BMS and PMS), and one at high currents (obtained with the manual passive load regulation). The first trend presents a voltage drop of approximately 50 A, and consequently a local power peak, evidencing the early growth of concentration losses due to the fast operating sequence imposed by the LabVIEW data acquisition routine driving the PMS, as described above. The selected standby time τ_{sb} was too short to allow a full recovery of uniform bulk concentrations in the electrodes during power off, while the selected idle times τ_{ci} and τ_{di} were also too short to allow steady-state gradients to be reached during power on, causing a progressive depletion of the reactants in the electrodes.

Conversely, when using the passive load at higher currents (that involved longer standby times for regulating the resistors) the curve retraced the linear behavior dominated by ohmic losses typical of operation at higher SOC and Q , allowing the peak power of ca. 4.5 kW to be reached, thus demonstrating that concentration gradients were compensated during standby. The first trend did not appear instead if the curves were traced at $SOC=30\%$ and high $Q=29.5 \text{ L min}^{-1}$, demonstrating that the latter can compensate concentration loss effect due to low SOC .

6.3.7 Comparison between fast and steady state curves

In general, the better linearity of the steady-state polarization curves depends on both the acquisition pattern designed to keep the OCV more stable, and on the stack operating conditions, as fast data are more susceptible to variations in experiment timing than those in steady-state conditions. The stack internal resistance R_i presents the same dependency on SOC and Q in both fast and steady-state cases and its limit values are comparable, meaning that it is weakly affected by the evolution of concentration gradients in the electrodes. Further investigations will enable deduction of the incidence on R_i of the main cell parameters such as membrane conductivity and thickness, electrode porosity, conductivity and thickness, and electrode-current collector clamping pressure. These data will be used to address the development of numerical models of the stack, and can be used to clarify the effect of other parameters such as temperature.

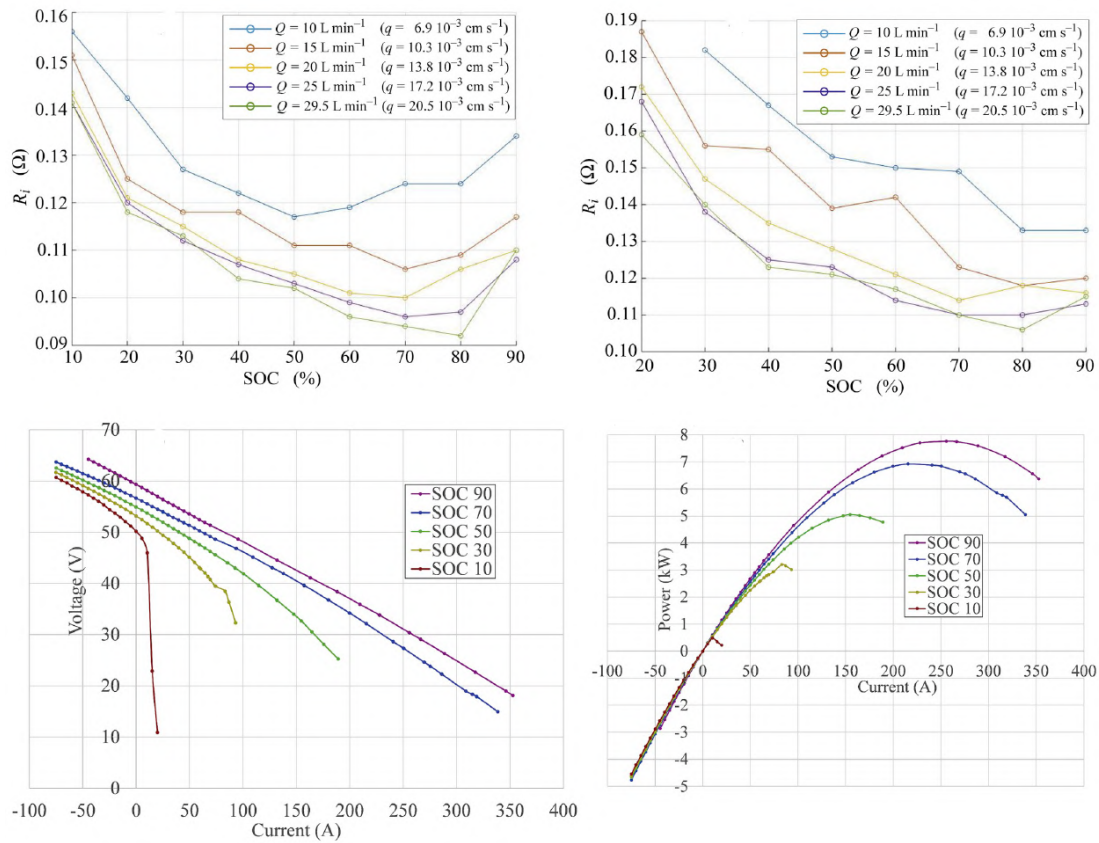


FIGURE 6.6: Steady-state mode tests. Top-left: internal resistance during charge at different flow rates Q (i.e. specific flow rates q); top-right: internal resistance during discharge at different flow rates Q (and q); bottom-left: polarization curves at different SOC's with $Q=29.5$ L min^{-1} ($q=20.5 \times 10^{-3}$ cm s^{-1}); bottom-right: power curves at different SOC's with $Q=29.5$ L min^{-1} ($q=20.5 \times 10^{-3}$ cm s^{-1}).

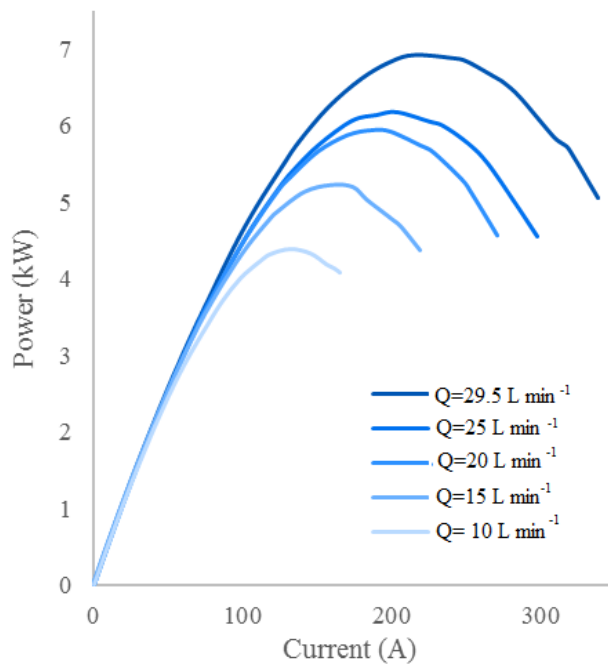


FIGURE 6.7: Discharge power curve (on PMS and passive load) at SOC=70% and different flow rates Q .

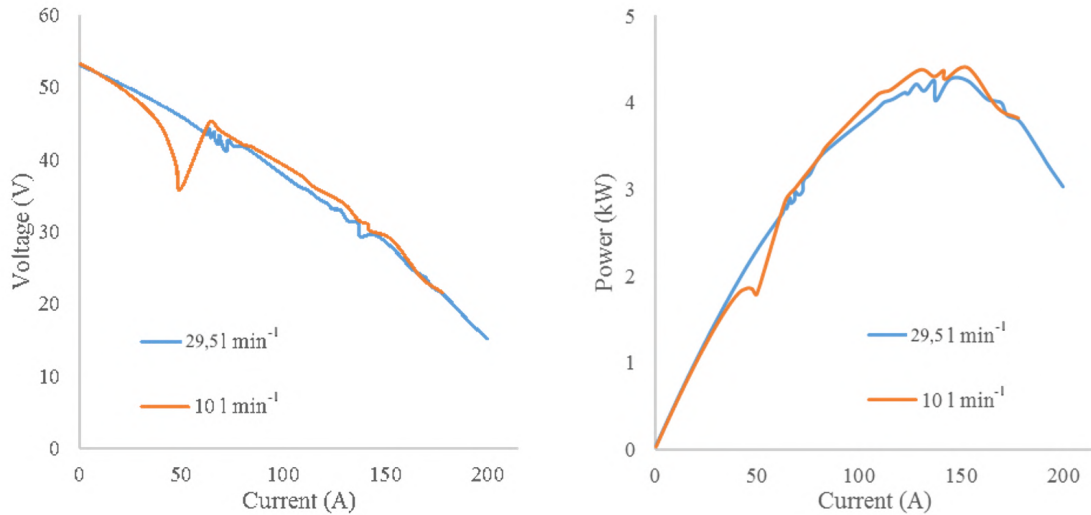


FIGURE 6.8: Comparison between discharge polarization (left) and power (right) curves at $SOC=30\%$ and $Q=10$ and 29.5 $L\ min^{-1}$.

The maximum averaged current densities of $617\ mA\ cm^{-2}$ and $583\ mA\ cm^{-2}$ obtained in fast and steady-state conditions, respectively, at a specific flow rate of $q=20.5 \times 10^{-3}\ cm\ s^{-1}$ constitute an interesting performance, considering they were obtained in a stack of 40 cells with a $600\ cm^2$ active area. The overcurrent in the fast mode with respect to the steady-state mode was 105.8%. In addition, at load connection, the current density peaked at $665\ mA\ cm^{-2}$, which constitutes an overcurrent of 107.7% with respect to fast mode value and of 114.0% with respect to the steady-state value, indicating that no major reduction occurs when concentration gradient develops and stabilizes in the electrodes. It should be noted that the previous maximum averaged currents were obtained at an average residual cell voltage of 0.45–0.55 V, namely below the limiting current density. The maximum power densities were $370\ mW\ cm^{-2}$ at $500\ mA\ cm^{-2}$, and $330\ mW\ cm^{-2}$ at $427\ mA\ cm^{-2}$ in the fast mode and steady-state mode, respectively, with an overvalue in the fast mode with respect to the steady-state mode of 112%. This confirmed that concentration gradients and the related over potential losses have a minor effect on the stack performance.

The achieved experimental values constitute a notable performance, particularly when compared with the performance values reported in other papers [314], [199], [78], particularly in view of developing competitive VRFBs suitable for providing energy storage services in future grids. In fact, they suggest that VRFBs can achieve high current and power densities in industrial systems making them profitable for many grid applications in both fast and slow operations. Analyzing the device stability over long operation times was out of the scope of the present study, which was devoted to investigating the polarization curves of the battery. However, it is worth noting that obtaining the data presented in this thesis required the execution of approximately one hundred charge/discharge cycles with a total working time of 1200 h. After all these operations, no significant aging effect was noted on the above polarization curves (Chap.10).

The performance of a VRFB also depends on temperature: the present tests were carried out at a room temperature of $21^\circ C$ and the loss heat was removed by natural convection in the piping and tanks. Additional measurements showed that the solution temperatures were maintained below $25^\circ C$. The correlation between battery performance and temperature evolution was out of the scope of this study and has been developed within a different investigation carried out after high-current endurance operations (Sec.7.2).

6.4 Key points

This chapter has reported the experimental results obtained on the IS-VRFB stack during both charge and discharge operations in two conditions representative of real operative scenarios,

namely primary frequency regulation requiring fast operation, and peak shaving requiring slow operation. Tests were performed at different flow rates and *SOC*s, from almost fully charged to almost fully discharged.

Results show that high current densities in excess of 600 mA cm^{-2} can be achieved in the large 600 cm^2 membranes used in this stack at high state of charge, provided that an adequate flow factor is guaranteed. After these tests, the system has been upgraded by substituting the pumps and the electric circuitry to allow higher currents without modifying the stack.

Data extrapolation suggests that current densities as high as 1 A cm^{-2} could be achieved. The developed procedure for VRFB testing in fast mode and steady-state mode allows investigation for the first time in a kW-class stack regarding the time needed for creating steady-state concentration gradients and for analysis of the differences among the performance in the two modes.

The testing procedures that have been finalized can be used as standards for performance assessment in kW-class VRFBs, which at present are missing. In addition, they can contribute to developing metrics for the comparison of the performance of different VRFB systems. Ultimately, this chapter provides guidance for VRFB experts on the behavior of a kW-class stack, and for non-experts it provides information on how a large cell operates, in a way that enables comparison with test data from smaller cells.

Chapter 7

Thermal analyses

As discussed in Sec.5.4, few thermal models of a large VRFB stack have been studied in both standby and operating conditions. In [330], a two-dimensional model calculated the temperature distribution in the porous electrodes of a single cell, whereas [294], [331] presented a dynamic thermal model of a 2.5 kW/15 kWh VRFB based on energy and mass conservation equations, although neglecting the reaction entropic heat [301]. In [332], the same research unit examined the effects of cell number, flow rate, tank dimension, and environmental temperature on the thermal behavior of a VRFB stack in load condition and modelled the shunt current effects on the battery temperature evolution in [308]. However, few experimental analyses on large stacks have been documented [333], and no experimental validation of thermal models of industrial-scale VRFBs has yet been reported, to our knowledge. In this chapter, I present the results of the cell-resolved dynamic model capable of simulating the temperature distribution in a VRFB stack in any operating conditions which takes into account the entropic heat, ions crossover and inherent side reactions, and shunt current losses, as discussed in Sec.5.4. The model has also been validated against the experimental data taken from the IS-VRFB test facility in both standby and operating conditions.

7.1 Standby thermal analyses

This section presents the results of the described model capable of simulating the thermal behavior of a VRFB stack in standby condition. The model is applied to the IS-VRFB stack and validated against measurements from a thermal imager. Numerical results show that shunt currents affect the temperature in the stack and can be responsible for local increases of cell temperatures up to 10 °C if the solutions are initially at a high state of charge.

This effect can be critical if standby occurs after a period of operation, with the electrolyte stack temperature markedly higher than the air temperature. In addition, results show that shunt currents can play a major role in the thermal behavior of compact stacks, based on new materials capable of high-power density and low ion crossover. The results presented here can constitute the basis for advanced cooling strategies in standby conditions.

7.1.1 Model validation

The values for the model parameters used when simulating the behavior of the IS-VRFB stack are reported in Tab.7.1. The time-step used in the simulation was set at 5 s in all different analyses, as this value was considered smaller than the expected characteristic times of the system. Tests were carried out to check the numerical stability of the chosen time-step, by running a simulation with a smaller time-step of 1 s and checking that no significant difference appeared with respect to the chosen 5 s time-step. The model was then validated against experimental data for the lateral surface temperature on the IS-VRFB stack resolved in space and time, taken using a thermal imager (Jade 3 MWIR by CEDIP, France) at a thermal resolution ± 2 °C and a space resolution of 320×240 pixels. The validation test was performed with an initial $SOC=80\%$ of the solutions in the stack, the battery in no-load condition, and the pumps turned off. During the test, a Pt-100 sensor was used to measure the room air temperature, and the BMS performed continuous monitoring of the temperatures detected by all Pt-100 sensors. The tanks' residual volumes were filled with nitrogen to avoid solution contamination from atmospheric oxygen (Sec.4.1.3). Thus, assumption of Sec.5.4.1 was ensured.

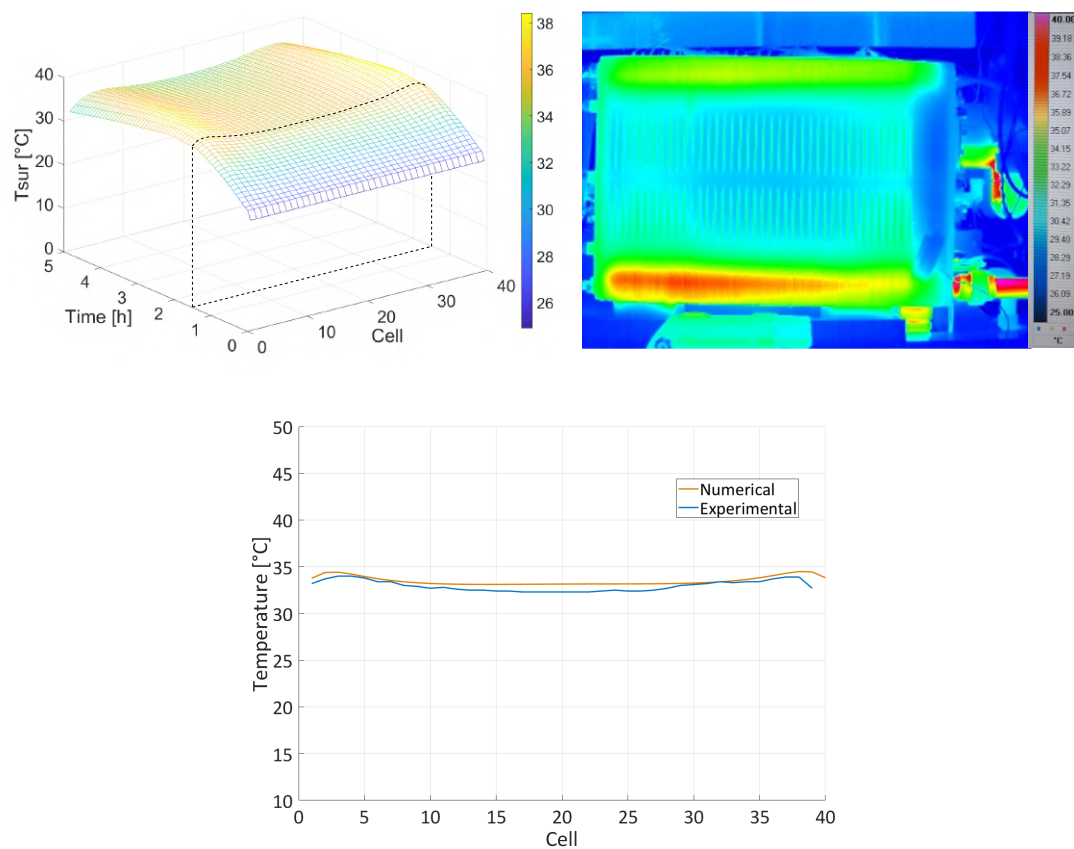


FIGURE 7.1: Validation of the stack thermal model on the IS-VRFB with initial $SOC=80\%$:. Top-left: computed evolutions of the average temperatures over the cell lateral surfaces; top-right: thermal imager measurements after 1.5 h; bottom: comparison of the average temperature distributions after 1.5 h.

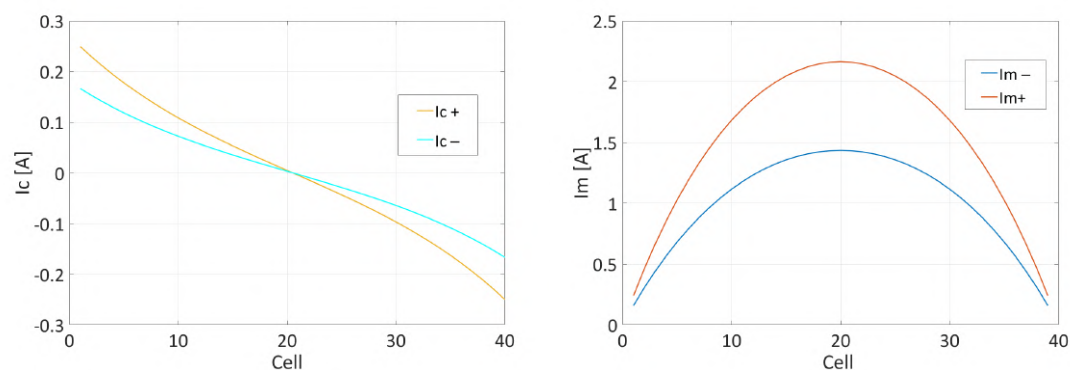


FIGURE 7.2: Distributions of the computed shunt currents in the IS-VRFB stack after 15 min. Left: Shunt current I_{c+} and I_{c-} in the positive and negative cell compartments (where the electric resistances are higher); right: shunt current I_{m+} and I_{m-} in the positive and negative manifolds (where electric resistances are much lower). These distributions are responsible for the different cell temperature shown in Fig.7.1.

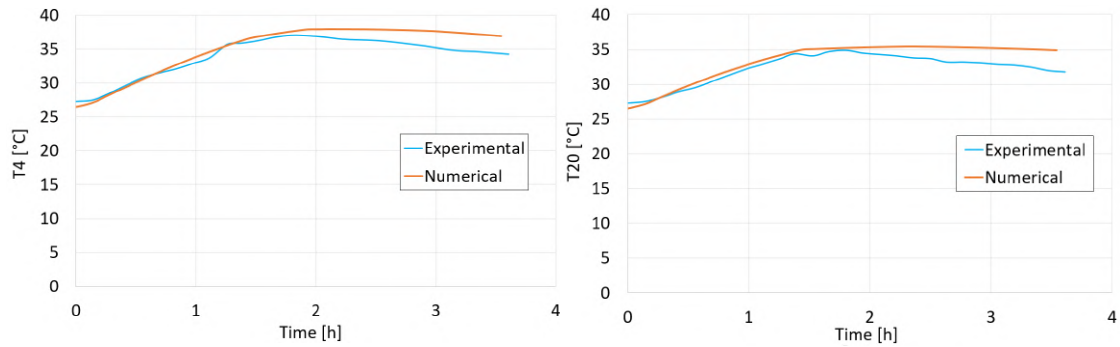


FIGURE 7.3: Comparison between the IS-VRFB experimental data and numerical results of two lateral cell temperatures over a period of 4 h (after which all loss events are exhausted). Left: T4 in the 4-*th* cell (hottest); right: and T20 in the 20-*th* cell (coldest). Discrepancies are below 3.1 °C.

The test was run over 4 h, and thermal images of the lateral face of the stack were acquired every 2 s. Fig.7.1 (top-left) shows the evolution of the temperatures on cell lateral surfaces computed with the model, whereas the thermal measurements provided by the thermal imager after 1.5 h are shown in Fig.7.1 (top-right). Fig.7.1 (bottom) presents the computed temperature distribution after 1.5 h of Fig.7.1 (top-left) together with the distribution of the average cell temperature from the thermal imager of Fig.7.1 (top-right): the comparison shows a discrepancy below 1 °C. In addition, the numerical results reproduce well the spatial distribution of the temperature measurements, which show the coldest cells in the stack central positions and the hottest close to the ends. This distribution is due to the cell-channel shunt currents, which are higher in the end cells (Fig.7.2). Instead, the manifold shunt currents are higher in the center, but these hydraulic segments have much lower electric resistances and thus lower Joule losses.

The temperatures captured by the thermal imager in the lower part of the stack were higher and more uniform than in the upper part. The first effect is due to the small polypropylene thickness in correspondence with the internal manifolds, whereas the second effect depends on the faster heat propagation by conduction in the electrolyte contained in the manifold (unlike in other positions), where heat transmission in x direction is hampered by the graphite BP and propylene, causing higher temperature differences between adjacent cells. Fig.7.3 (left) and (right) compare the experimental and numerical lateral temperature distributions of the 4-*th* cell and the 20-*th* (i.e. central) cell, which present the highest and lowest temperature values, respectively, over a time period of 4 h, after which no more heat was released. The maximum error between the computed and measured values is below 3.1 °C, which can be considered an acceptable result for this kind of heat transfer problem, due to the intrinsic uncertainty of some thermal parameters used in the simulation: for example the empirical formula for h_{air} can have uncertainties as large as $\pm 25\%$ [334]. It is worth noting that the model correctly reproduced the cell temperature distribution: the higher values near the end cells were only due to the shunt current losses. This effect has not been reported or attributed to shunt currents previously, to the best of our knowledge. Fig.7.4 shows the computed time evolution of the cell internal temperatures obtained in the validation test conditions. A maximum value of 54 °C was found in both the 3-*rd* and 37-*th* cells and occurred after 2 h 10 min, when the temperature of the central cells (coldest) was 8 °C lower.

7.1.2 Model simulations and results

The model was used to simulate the standby thermal behavior of a VRFB stack in challenging conditions. To investigate the effect of shunt currents in comparison with species crossover, simulations were carried out that both considered and neglected shunt current effects. Similarly

TABLE 7.1: IS-VRFB parameters used in validation and simulations of the thermal model.

Symbol	Description	Value
<i>Latin</i>		
A	membrane active area	600 cm ²
A_x	heat transfer cross-section along x	600 cm ²
A_y	heat transfer cross-section along y	16.48 cm ²
A_z	heat transfer cross-section along z	24.16 cm ²
b	gap between adjacent plates	0.4 cm
C_p	electrolyte specific heat capacity	3200 J kg ⁻¹ K ⁻¹
$C_{p,air}$	air specific heat capacity at constant pressure	1006 J kg ⁻¹ K ⁻¹
C_{sa}	total sulfuric acid concentration	4.5 mol L ⁻¹
C	total vanadium concentration	1.6 mol L ⁻¹
d	membrane thickness	50 μm
E_o'	corrected standard reversible potential	1.37 V
E_a	activation energy of the diffusion coefficients	17340 J mol ⁻¹
H	fin depth	3.5 cm
h_{air}	air heat transfer coefficient	0.71 W m ⁻² K ⁻¹
k_{II}	V ²⁺ diffusivity reference coefficient in Nafion 212 [294]	5.76×10 ⁻³ cm ² min ⁻¹
k_{III}	V ³⁺ diffusivity reference coefficient in Nafion 212 [294]	2.1×10 ⁻³ cm ² min ⁻¹
k_{IV}	VO ²⁺ diffusivity reference coefficient in Nafion 212 [294]	6.26×10 ⁻³ cm ² min ⁻¹
k_V	VO ₂ ⁺ diffusivity reference coefficient in Nafion 212 [294]	3.84×10 ⁻³ cm ² min ⁻¹
L_{fin}	vertical fin height	0.16 m
N	number of cells	40
$T_{sta}\Delta S^-$	negative half-reaction entropic heat at $T_{sta} = 298.5$ K [146], [49]	-11.291 kJ mol ⁻¹
$T_{sta}\Delta S^+$	positive half-reaction entropic heat at $T_{sta} = 298.5$ K [146], [49]	-26.351 kJ mol ⁻¹
U_{end}	end total heat transfer coefficient along x	2.877 W m ⁻² K ⁻¹
U_{ip}	overall heat transfer coefficient of inlet piping [296]	3.667 W m ⁻² K ⁻¹
U_{op}	overall heat transfer coefficient of outlet piping [296]	3.667 W m ⁻² K ⁻¹
U_{ta}	overall tank heat transfer coefficient [296]	5.734 W m ⁻² K ⁻¹
U_x	total heat transfer coefficient along x	21.67 W m ⁻² K ⁻¹
U_y	total heat transfer coefficient along y	2.413 W m ⁻² K ⁻¹
U_z	total heat transfer coefficient along z	1.376 W m ⁻² K ⁻¹
V_c	cell volume	496.8 cm ³
V_{ip}	volume of piping from tank to stack inlet	20.2×10 ⁻³ m ³
V_{ip}	volume of piping from stack outlet to tank	20.2×10 ⁻³ m ³
V_{ta}	tank volume	0.5 m ³
z	electron number per reaction	1
<i>Greek</i>		
ε	electrode porosity	0.94
β	thermal expansion coefficient of air	3.67×10 ⁻³ °C ⁻¹
ΔH_2	enthalpy of reaction Eq.5.31 [296]	-220 kJ mol ⁻¹
ΔH_3	enthalpy of reaction Eq.5.32 [296]	-64 kJ mol ⁻¹
ΔH_4	enthalpy of reaction Eq.5.34 [296]	-91.2 kJ mol ⁻¹
ΔH_5	enthalpy of reaction Eq.5.35 [296]	-246.8 kJ mol ⁻¹
ΔT	surface to air temperature drop	15 °C
δ	fin propylene thickness	0.036 m
θ_{fin}	fin heat exchange efficiency	1
λ_{air}	air thermal conductivity	0.0258 W m ⁻¹ K ⁻¹
λ_{PP}	propylene conductivity [294]	0.16 W m ⁻¹ K ⁻¹
μ_{air}	air dynamic viscosity	18.2 μPa s
ρ	electrolyte density	1354 kg m ⁻³
ρ_{air}	air density	1.2 kg m ⁻³
σ_e	electrode conductivity	1000 (1-ε) ^{1.5} S m ⁻¹
σ_{II}	V ²⁺ conductivity [74]	27.5 S m ⁻¹
σ_{III}	V ³⁺ conductivity [74]	17.5 S m ⁻¹
σ_{IV}	VO ²⁺ conductivity [74]	27.5 S m ⁻¹
σ_V	VO ₂ ⁺ conductivity [74]	41.3 S m ⁻¹

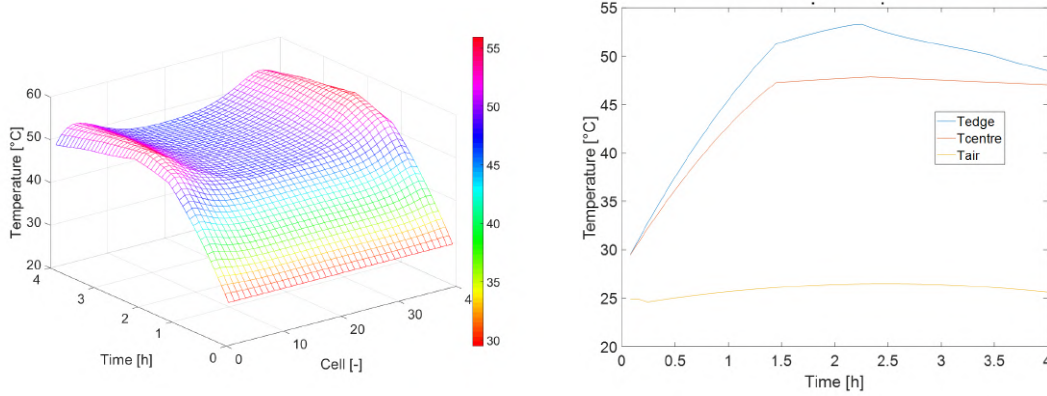


FIGURE 7.4: Numerical results of the internal temperature evolution in the IS-VRFB stack obtained in the validation test conditions. Left: plot of numerical temperature distribution; right: temperature evolution of the 3-*rd* and 37-*th* cell (i.e. end and hottest) and 20-*th* cell (i.e. central and coldest).

to [296], a daily swing of the air temperature T_{air} was considered to simulate the operation of the IS-VRFB in open air, as follows:

$$T_{air}(t) = 25 - 8\sin\left(\frac{\pi}{12}t + \frac{\pi}{6}\right)^{\circ}C \quad (7.1)$$

with time t measured in hours (h) and starting time ($t = 0$) at 22:00 on the first day. An initial state of charge $SOC=95\%$ was set, which constitutes the most critical condition, as in this case the largest losses occur.

Dynamic distributions of the cell species concentrations

Fig.7.5 presents the evolution of concentrations of the vanadium ions in the cell compartments considering and neglecting shunt currents. In both cases, the ion crossover effects were taken into account. Simulation results show that in both cases approximately 36 h were needed to complete all three phases of the standby mode (Sec.5.4.1) and to achieve a 50/50 mixture of V^{3+} and VO_2^{+} . Simulations also show that shunt currents reduced the duration of phase 1 to 1.8 h, namely by 2.2 h. V^{2+} in the negative compartment depleted faster, due to its higher diffusion, than VO_2^{+} in the positive compartment. Shunt currents were also responsible for a wider spread of the dynamic distributions of concentration in the 40 cells as clearly shown by the comparison in Fig.7.4. This also indicates that the central cells discharged faster, and this effect was enhanced by the shunt currents. These behaviors are confirmed by the measurements of the cell *OCVs*, which decreased with cell *SOCs*.

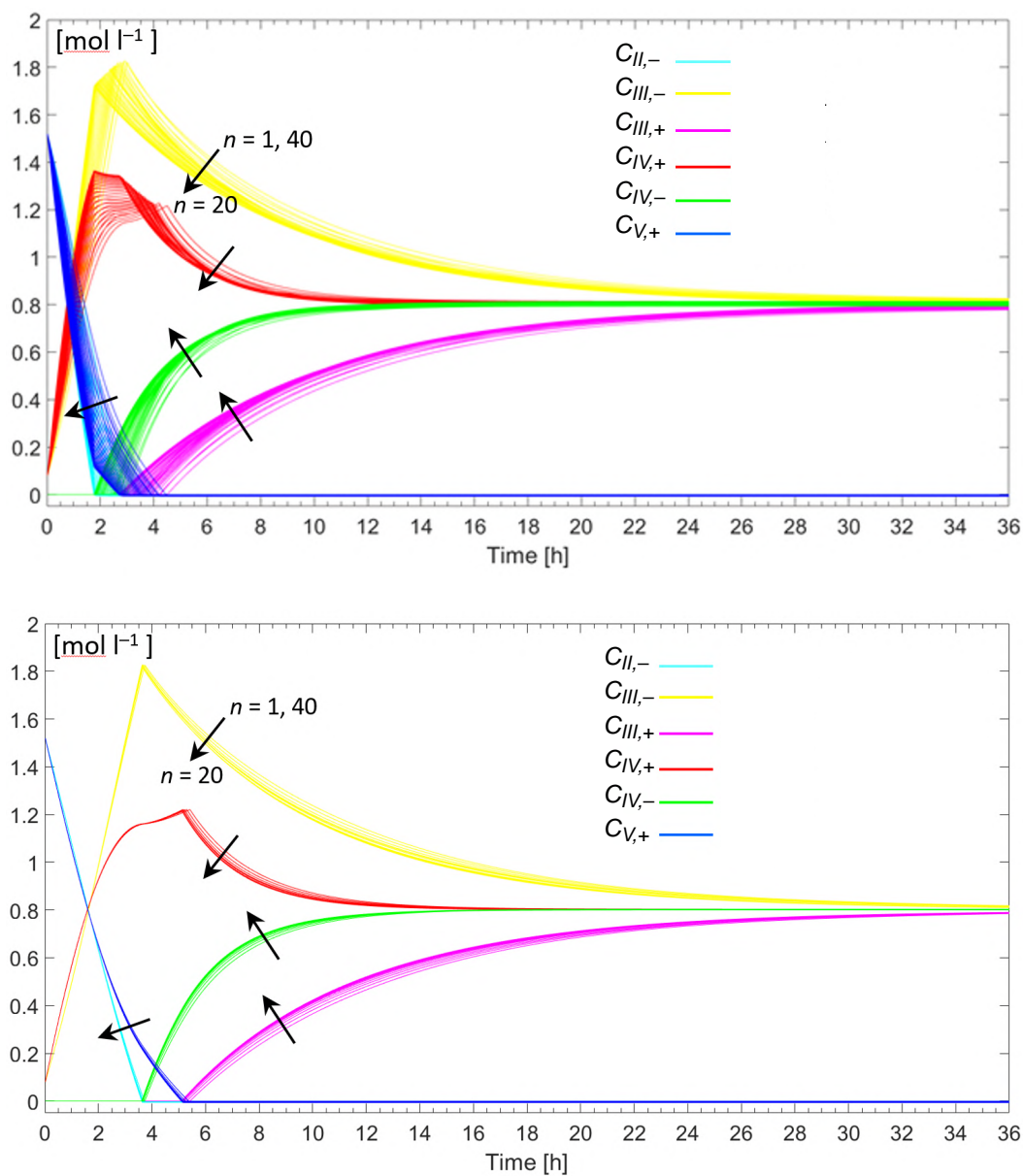


FIGURE 7.5: Computed evolutions of ion concentrations in the IS-VRFB 40 cells over a 36 h with initial $SOC=95\%$. The cross represents the gradient from the external (1-*st* and 40-*th* cells) to the central cell (20-*th* cell). Top: with shunt currents thermal effects; bottom: neglecting shunt currents effects.

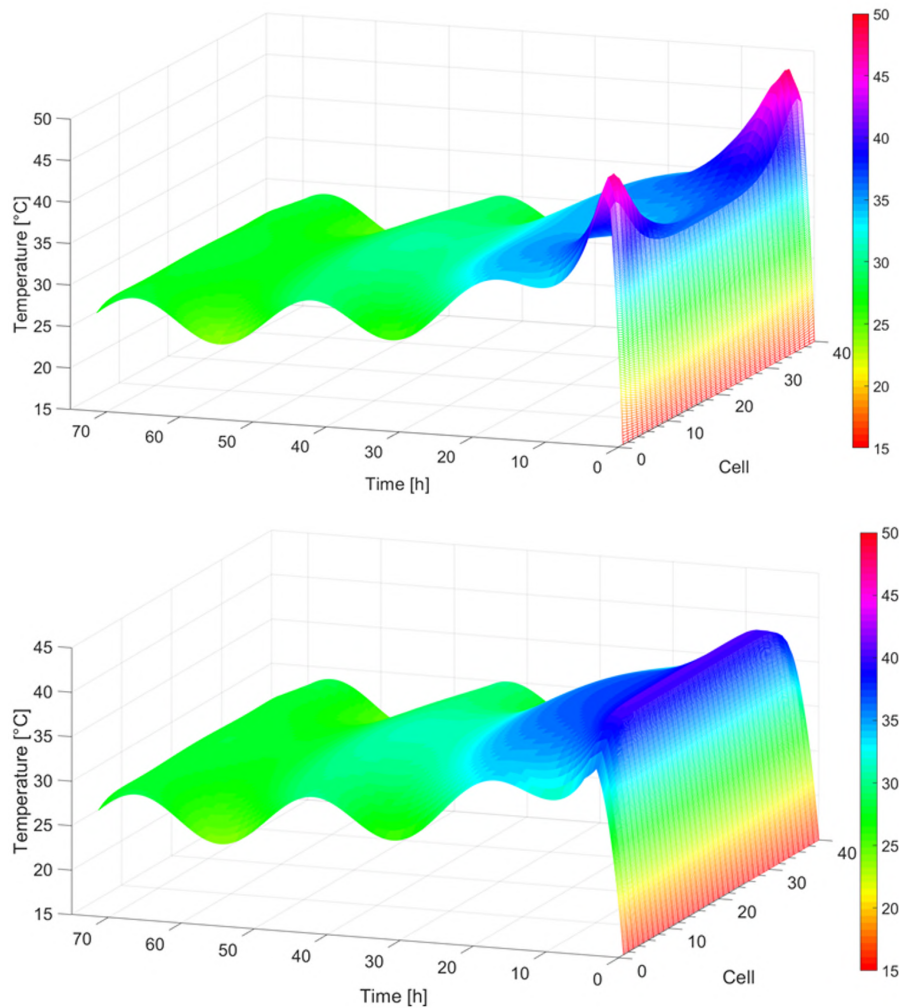


FIGURE 7.6: Evolutions of the temperatures in the IS-VRFB 40 cells during a 72 h simulation with initial $SOC=95\%$. Top: considering shunt currents; bottom: neglecting shunt currents.

Effects of shunt currents on the temperature distribution

Fig.7.6 shows cell temperature evolution over a 72 h simulation, considering and neglecting shunt currents. Here again, shunt currents caused larger temperature differences among the cells, with markedly higher values in the end cells. Shunt currents also caused an $8\text{ }^{\circ}\text{C}$ increase in the maximum stack temperature. This increase may lead to VO_2^+ precipitation, suggesting that suitable cooling should be provided in the case of high air temperature. Fig.7.7 presents the Joule losses produced by the shunt currents in the cells, manifolds, and internal equivalent resistances (i.e. over potential losses). After phase 1 (lasting 1.8 h), shunt currents became negligible. Shunt current losses were larger in the cells than in the manifolds and were larger than over potential losses (represented by the internal equivalent resistances of Fig.5.8).

This effect is due to the higher resistances of the hydraulic paths inside the cell, consisting of porous electrodes and thin flow frame channels, which ensure uniform electrolyte distribution over the electrodes [74]. Fig.7.7(a) and (d) show that cell losses are higher in the end cells of the stack with a gradual reduction towards the center, because of the similar distribution of shunt currents. Manifold losses, Fig.7.7(b) and Fig.7.7(e), and equivalent internal resistance losses (i.e. due to over voltages) Fig.7.7(c) and Fig.7.7(f), show an opposite but less important behavior.

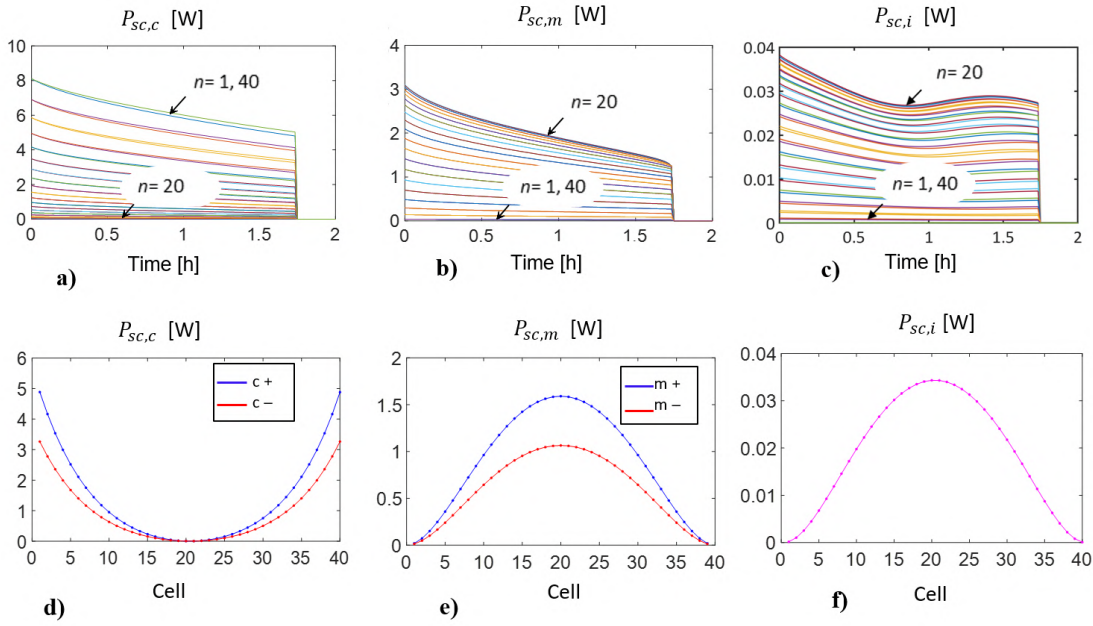


FIGURE 7.7: Evolution during phase 1 of the Joule losses produce by the shunt current in the IS-VRFB cells ($n=1$ to 40) with initial $SOC=95\%$: a) cells (– and + together); b) manifolds (– and + together); c) internal equivalent resistances (representing over potential losses). Initial ($t=0$) distribution of Joule losses among: d) cells; e) manifolds; f) internal equivalent resistances.

Thermal effects of each loss term

Based on the model assumptions, losses occur and heat is released only during phases 1 and 2, whereas in phase 3 only pure diffusion across the membrane takes place, without any reactions. Heat release in phases 1 and 2 is due to ion crossover for 47%, shunt current losses for 42%, and shunt currents feeding reactions for 11%. These results indicate that ion crossover causes the largest losses in the IS-VRFB, but shunt-current Joule losses are of comparable magnitude. The relative contributions of these factors change in the case of different flow frame designs and size, and a low flow-frame electric resistance can cause larger losses and temperature increase. Nevertheless, the membrane active area and the stack volume are of significance.

Today, new materials for membranes and electrodes are under development, exhibiting higher current density and lower ion crossover. These materials can substantially change the scenario in VRFB standby thermal evolution. For a given number of cells (i.e. a given stack voltage), compact cells with a small active area operating at high current density (for example, the IS-VRFB exceeds 650 mA cm^{-2}) and with low species crossover, can present a higher contribution from shunt currents, which is thus the dominant cause of standby thermal evolutions.

7.1.3 Key points

The model was successfully validated against experimental data acquired on the IS-VRFB test facility. To the best of our knowledge, this is the first numerical model that takes into account the effect of shunt currents in computing the temperature distribution among the cells in the stack and its evolution. Simulations demonstrated that shunt currents significantly affect the temperature distribution in the cells and can cause a local increase of cell temperature of up to $10 \text{ }^\circ\text{C}$. This effect is higher if the standby mode occurs at high SOC after a period of operation, with the starting electrolyte temperature markedly higher than ambient temperature.

This temperature increase can cause VO_2^+ precipitation, and therefore requires an appropriate cooling strategy. Such accurate thermal modelling of the stack can be a valuable tool in the design of advanced temperature control algorithms, for example to activate periodic electrolyte washing inside the stack, or in sizing the cooling of solutions in the tanks of an industrial storage

system. Using the model results in combination with an advanced battery management supervisor, a smart control algorithm capable of keeping the stack temperature below safe limits can be implemented.

In addition, results show that shunt currents can play a major role in the thermal behavior of compact stacks, made with new materials capable of high energy and power densities. In this regard, important information can be obtained by comparing the simulations of the heat released in compact stacks, such as those based on novel membranes capable of high current density and low ion crossover, with larger stacks operating at lower current densities where shunt current effects are of minor importance (e.g. the stack presented in [308]). Furthermore, these results can be used to address the design of optimized flow frames, aimed at maximizing battery efficiency.

7.2 Operation thermal analyses

The cell-resolved model that simulates the dynamic thermal behavior of a VRFB during charge and discharge is applied here. At the cell level, it takes into account the reversible entropic heat of the electrochemical reactions, irreversible heat due to over potentials, self-discharge reactions due to ion crossover, and shunt current losses. As described in Sec.5.4, the model accounts for heat transfer between cells and toward the environment, pump hydraulic losses, and heat transfer of piping and tanks. It provides the electrolyte temperature in each cell, at the stack inlet and outlet, along the piping and in the tanks. Validation has been carried out against the charge/discharge measurements from the IS-VRFB test facility. An application of the model simulating the high current (400 A) long duration (8 h) operations of a large VRFB system is also presented. Important information was obtained about the electrolyte temperature evolution in next-generation industrial scale VRFB systems to identify critical thermal conditions that might occur, making stacks capable of operating at high current density. The most critical condition was found at the end of a long discharge, when temperatures above 50 °C occurred, possibly resulting in VO_2^+ precipitation and battery faults. These results suggest the need for heat exchangers tailored to assist high-power VRFB systems.

7.2.1 Experimental validation

The dynamic thermal model was validated against experimental data taken from the IS-VRFB test facility, operated in discharge and charged at a stack current of $I=70$ A with solution flow rates of $Q_+=Q_-=30$ L min⁻¹ (i.e. a specific flow rate $q = Q/NA = 20.8 \times 10^{-3}$ cm s⁻¹) for 2.25 h. Correspondingly, the battery was discharged from $SOC=78\%$ to 35% and charged from $SOC=8\%$ to 50%. To ensure that the ambient condition was almost the same, tests were started at the same time (9:00 a.m.) on each of two consecutive days. The temperatures at the stack inlet and outlet, provided by the four sensors T1–T4 (Fig.4.1) were recorded every 0.8 s.

The additional Pt-100 sensor monitored the air temperature, which was approximately 24 °C at the start of the test, and gradually increased by 2 °C during both the tests. All simulations were carried out using the parameters listed in Tab.7.1, and based on actual experimental conditions, the initial temperature in the tanks and the stack was set at 32 °C in discharge and at 29.4 °C in charge. Validations for both charge and discharge were performed by comparing T1 with T_{ip+} and T2 with T_{op+} for the positive side and T3 with T_{ip-} and T4 with T_{op-} for the negative side.

Fig.7.8 shows the evolutions of the measured and computed electrolyte temperatures at these positions. During discharge (Fig.7.8 top-left and bottom-left), simulated and measured temperatures present a maximum discrepancy of 0.9 °C as a result of the assumed simplifications and the uncertainty of some thermal coefficients taken from the literature. Such a small discrepancy indicates that the model is able to simulate the temperature increase in the electrolytes properly. The comparison between simulated and measured temperatures during charge (Fig.7.8 top-right and bottom-right) shows a lower maximum discrepancy, below 0.2 °C, indicating that in this phase the model reproduces the temperature decrease in both electrolytes even better, at the limit of instrument accuracy. The temperature increases during discharge and decreases during charge because of the different effect of P_{il} and P_{re} : while the former is always positive, the latter is positive during discharge (being the reactions exothermic) and negative during charge

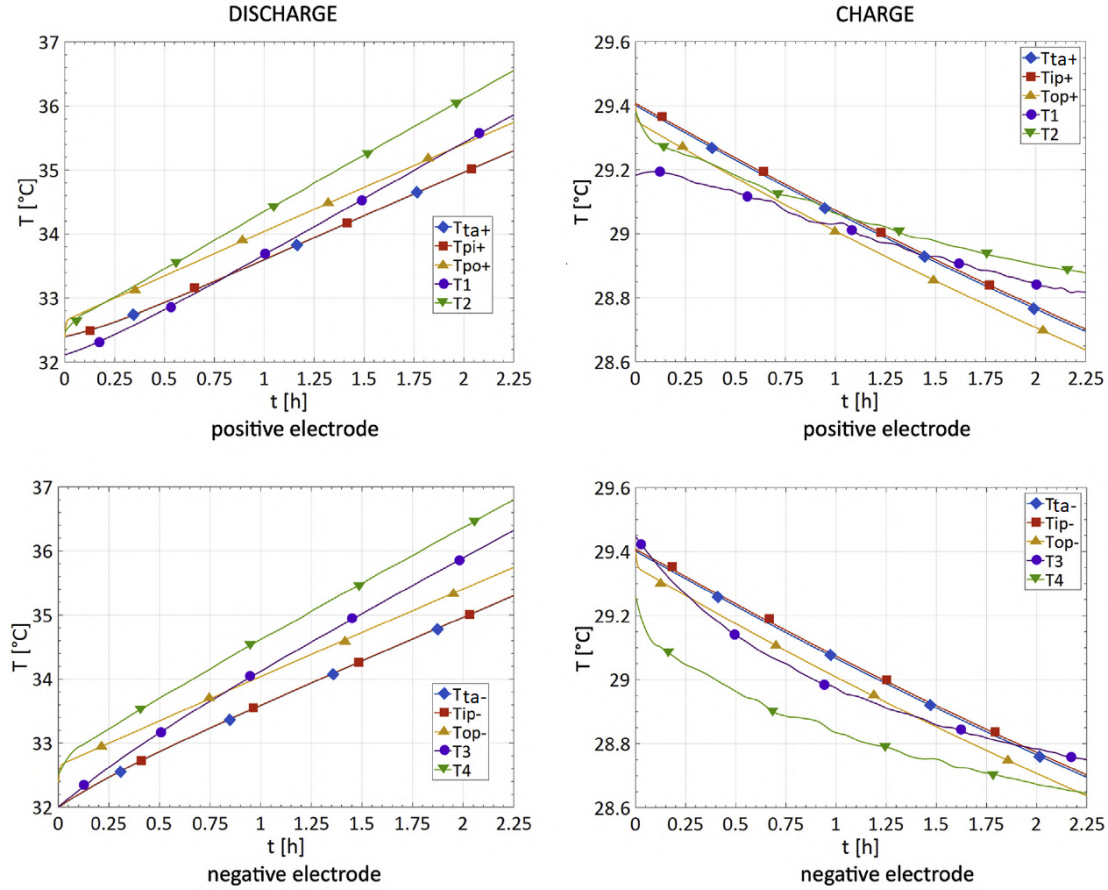


FIGURE 7.8: Computed and measured electrolyte temperature evolutions at the inlet and outlet pipes during charge and discharge. $T_{ta\pm}$ = computed electrolyte temperatures in the positive/negative tank; $T_{ip\pm}$ = computed electrolyte temperatures in the positive/negative input pipes; $T_{op\pm}$ = computed electrolyte temperatures in the positive/negative output pipes; $T1/3$ = measured electrolyte temperatures in the positive/negative input pipes; $T2/4$ = measured electrolyte temperatures in the positive/negative output pipes.

(being the reactions endothermic), with $P_{il} < P_{re}$. In both cases, P_{co} is much lower than the previous two heat rates. Under the assumptions of Sec.5.4.1 and with the parameters used in the model (Tab.7.1), the computed temperatures of the positive and negative solutions are the same. The small discrepancies between the numerical results and the measured values show that the model was appropriate for simulating the thermal behavior of the system during both charge and discharge processes.

7.2.2 High-current simulations of a large VRFB

The model was applied to investigate the thermal behavior of an industrialized VRFB unit under heavy operating conditions. The study assumed the same stack as in the IS-VRFB, but working at 400 A (i.e. at current density above 650 mA cm^{-2}) with a flow rate $Q=30 \text{ L min}^{-1}$ for the positive and negative electrolytes (this performance was actually achieved in IS-VRFB with a cell voltage of 0.45 V, Chap.6). The study was intended to investigate the battery thermal behavior over a working period as long as 8 h both in charge and discharge; a proper tank capacity was considered for this aim. In particular, the assumed flow rate (quite low for the given current), imposed a *SOC* within a narrow range to ensure adequate reactant flow, even considering a flow factor (i.e. ratio of flux of ions provided by the electrolyte flow with respect

to the generated electric current, Eqs.8.12, 8.13) as low as $\alpha_{min}=2$. The maximum SOC during charge and the minimum SOC in discharge, both reached after 8 h of operation, were as follows:

$$SOC_{ch,max} = 1 - \frac{NI\alpha_{min}}{Fc_vQ} \quad (7.2)$$

$$SOC_{dh,min} = \frac{NI\alpha_{min}}{Fc_vQ} \quad (7.3)$$

Consequently, the SOC could be varied in the range of 5% – 59% during charge and in the range of 95% – 41% during discharge. Accordingly, a capacity of 5000 L for each tank was assumed, with an energy capacity of 240 kWh. Consequently, the pipe lengths and tank surfaces were assumed to be tenfold larger than those of the IS-VRFB, while the thermal parameters of pipes and tanks were given the values of Tab.7.1.

During both charge and discharge, the air temperature was set at 20 °C, a value compatible with an installation in an air-conditioned room or container. The initial solution temperature in the tanks and stack was set at 32 °C, resulting from some previous operation.

Fig.7.9 a) and b) show the stack reversible entropic heat rate P_{re} in load operations: it is positive (because the reactions are exothermic) during discharge and negative (endothermic reactions) during charge [313]. In both operations, the P_{re} values are almost constant and the very small variations shown in the figures are due to secondary effects. Fig.7.9 c) and d) show the stack irreversible heat rate P_{il} together with the contribution in three cells $P_{il,n}$ with $n=1, 20$ and 40 (the last one) in both discharge and charge. In agreement with the internal resistance profiles of Fig.5.8, these heat rates increase with decreasing SOC during discharge and decrease with increasing SOC during charge. During discharge (Fig.7.9 c), the cell contributions $P_{il,n}$ are almost equal. In fact, different $P_{il,n}$ values could arise from different values of the shunt currents in the hydraulic segments [313], [74], but in the discharge conditions studied here, shunt currents are much lower than the stack current I , so that all cells present almost the same current $I_{i,n} \simeq I$. During charge (Fig.7.9 d), some small differences between $P_{il,n}$, lower than 1%, appear because shunt currents are larger than in discharge, due the higher stack voltage.

Fig.7.9 e and f show the crossover heat rate P_{co} in both discharge and charge: in both cases it increases as a consequence of the species diffusivity dependence on the increasing temperature. However, P_{co} is two orders of magnitude lower than P_{il} so that it is negligible in the overall thermal balances. Fig.7.9 g and h present the resulting temperature evolution in the three cells $n=1, 20$, and 40. During discharge (Fig.7.9 g), there is no evident difference between the cells, as a consequence of the heat generation discussed above. In addition, it can be noted that most of the heat is removed equally from all cells by the solution circulation, that is, by P_{fl} , conversely than in standby condition with pumps turned-off [313], thus enhancing the cell temperature equalization. During charge (Fig.7.9 h), this requires higher stack voltages, and a marginal difference in the cell temperatures appear as consequence of the slightly different released heat rates described above. During discharge, all the heat rates have positive values, concurring to produce a temperature rise of 16 °C in 8 h of operation, while the temperature increases more than linearly, due to the increasing values of P_{il} and $P_{il,n}$. During charge, P_{il} is positive whereas P_{re} is negative, producing counteracting thermal effects. Because $P_{il} > |P_{re}|$, a net heat generation occurs, resulting in a temperature increase of 6 °C in an 8 h charge, smaller than during discharge over the same period of time, when both P_{il} and P_{re} are positive.

It should be noted that when smaller load currents are applied, for example 70 A as in the validation simulations, $P_{il} < |P_{re}|$ can occur during charge, because the former term roughly scales with the square of the current while the latter is directly proportional to the current. Therefore, a temperature decrease occurs, as shown in Fig.7.8 b) and d). Operations at very high currents also present major thermal issues because of this effect.

Finally, Fig.7.10 a) shows the temperature evolution of the electrolytes during an 8 h discharge at some points of the hydraulic circuits. The same profiles apply for the positive and negative compartments because the model does not account for differences between the two solutions, as already stated. The temperatures at the tank and stack inlet increase by 13 °C in 8 h, while the temperatures at the stack outlet increase by 21 °C, due to the combined effects of the reaction reversible entropic heat and irreversible internal losses. The maximum electrolyte temperature after 8 h exceeds 50 °C, which can cause precipitation of VO_2^+ in the stack and tank. Therefore,

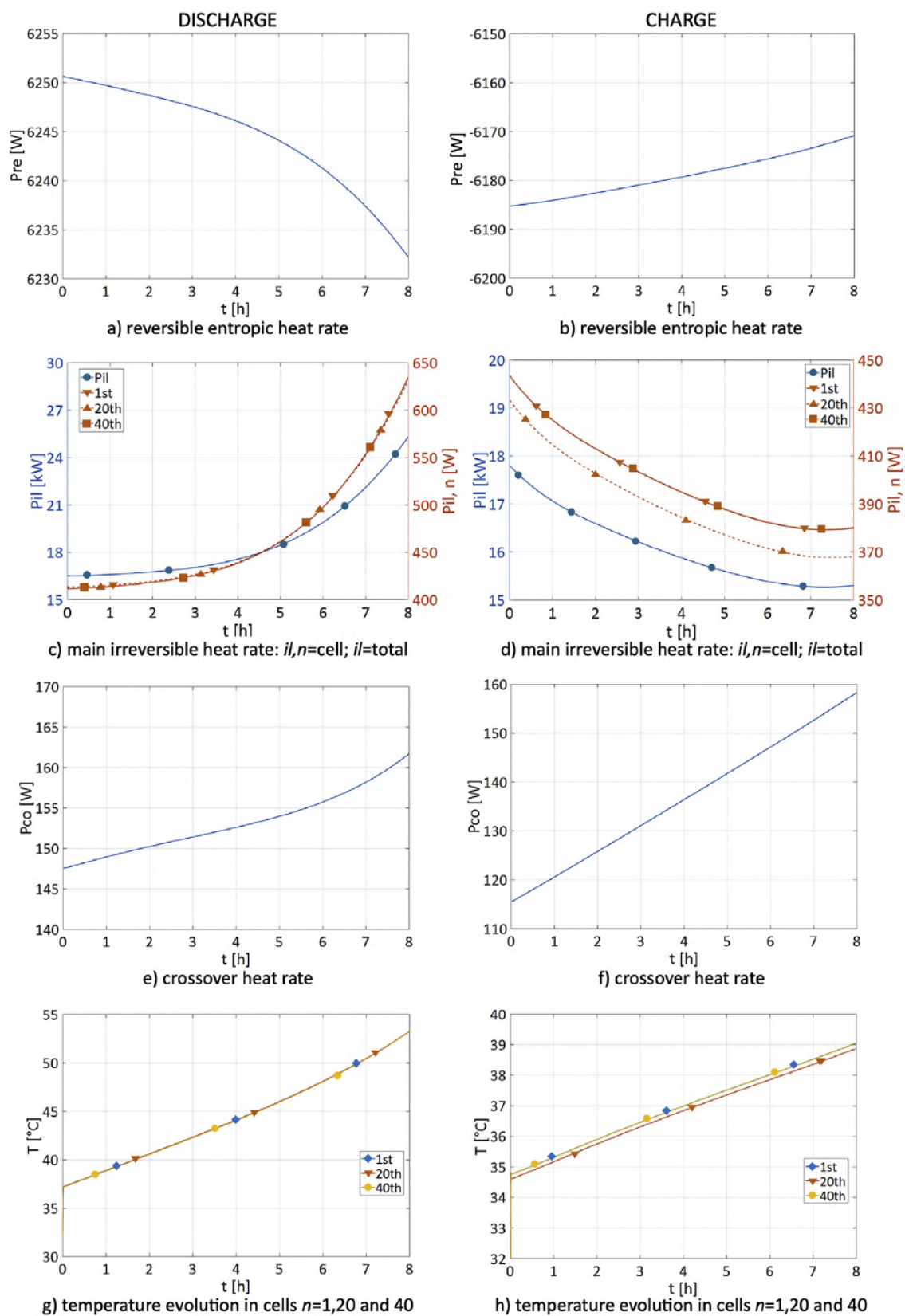


FIGURE 7.9: Simulation of high-current (400 A) long-duration (8 h) discharge and charge: heat rate contributions and electrolyte temperature in cells $n= 1, 20$ and 40 .

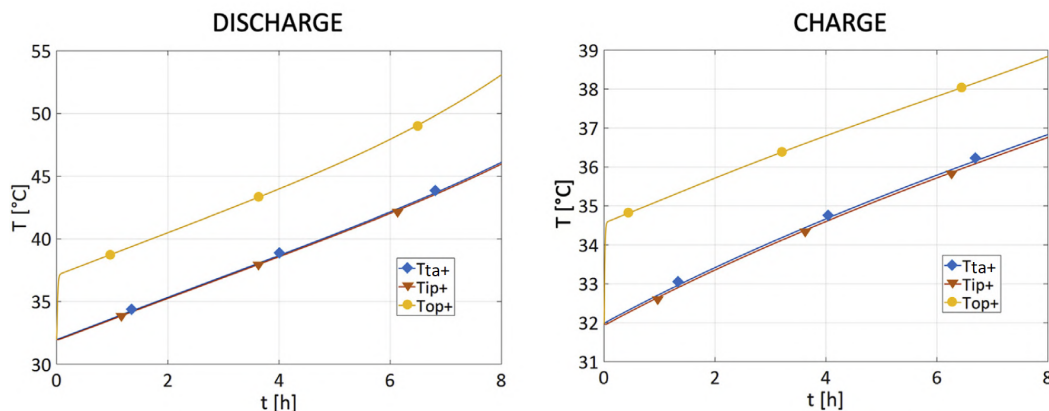


FIGURE 7.10: Simulation of high-current (400 A) long-duration (8 h) discharge (left) and charge (right): positive electrolyte temperature at stack inlet (*ip*) and outlet (*op*) piping, and in the tank (*ta*) (negative electrolyte has a similar evolution).

when a VRFB is operated at high current density as in these simulations, an electrolyte cooling system is needed to prevent such side effect. Fig.7.10 b shows the temperature evolution of the electrolytes during an 8 h charge. In this case, all temperatures increase, but to a smaller extent, consistently with the behaviors presented in Fig.7.9.

A maximum temperature below 40 °C is reached, which is not critical for VO_2^+ precipitation. Due to the reduction of the irreversible heat with increasing *SOC* (i.e. of the internal resistance of Fig.5.8) during charge, the temperature slope reduces during the process. It is worth noticing that this simulation did not account for a heat exchanger specifically designed for battery thermal management.

Such a component can enhance heat transfer and reduce temperature increases in the solutions to prevent species precipitation, in addition to optimizing the battery performance. Moreover, because irreversible heat P_{il} plays a major role in heat generation at high current density, a strategy aimed at reducing the internal losses (i.e. the internal resistances $R_{i,n}$ of Fig.5.8) is crucial not only to maximize VRFB efficiency as reported in [128], but also to control thermal behavior and minimize the risk of VO_2^+ precipitation.

7.2.3 Key points

The model here evaluated heat caused by reversible and irreversible effects, which occur inside the cells and the stack, including main electrochemical reactions, over potentials, shunt currents, and species crossover with consequent self-discharge reactions. The crossover diffusion coefficients were considered temperature dependent (Sec.5.3), while the solution conductivities took into account the state of charge. To compute shunt currents and related losses in the cells and hydraulic segments, an equivalent electric circuit was implemented Sec.5.2.1.

This includes cell equivalent internal resistances, which take into account over potential effects and were measured experimentally. Shunt current losses occurring in the flow channels and manifolds were evaluated, and results were negligible from the thermal point of view. The heat released by circulation pump losses was also taken into account (Fig.5.12). The model was validated against the measurements from an IS-VRFB test facility, showing that it is suitable to simulate the thermal behavior of an industrialized VRFB system during charge and discharge. More simulations were developed on a possible larger industrialized VRFB plant provided with the same stack and capable of discharging at 400 A (i.e. at current density above 650 mA cm^{-2}) through discharge/charge duration of 8 h, to reproduce real thermal stress conditions. This long duration was intended to consider a major advantage of the VRFB technology, namely independent sizing of power and energy that can be exploited to ensure long discharges.

The simulations aimed to investigate critical thermal conditions, which may occur in a big plant installed in an air-conditioned container for grid services such as peak shaving. The reversible heat associated with the main half-reactions has alternating thermal effects, being

exothermic during discharge and endothermic during charge, which constitutes an advantage over other kind of batteries. Therefore, the simulations showed the maximum temperatures at the end of a discharge phase. In the case of the high current long-duration operation, a critical temperature above 50 °C was reached, which constitutes an issue for positive electrolyte thermal stability. In fact, when working at high current densities (as expected from next-generation industrial VRFBs), generated irreversible heat can exceed the absolute value of reversible heat, because the former contribution roughly scales with the square of the stack current and the latter is directly proportional to the stack current. Consequently, when operating at high current, the temperatures increase during both charge and discharge, requiring an efficient cooling system to prevent species precipitation at high temperature. Even if the highest temperatures occur at the end of a discharge phase, when the concentration of VO_2^+ is low, VO_2^+ precipitation could represent an issue resulting in the occlusion of the small flow channels in the cell frames and battery faults. It can be concluded that the next generation VRFBs, capable of higher power densities and high current densities, require specific heat exchangers to thermally assist the VRFB operations.

Chapter 8

Maximizing VRFB efficiency

Energy loss evaluation assumes a very important role for VRFB characterization in order to increase the efficiency of the battery. Very few papers describe the relationship between hydraulic, electrical, and chemical contributions to system energy losses, especially in a large size VRFB system. First, an overall loss assessment based on both numerical and experimental results was carried out and described in Sec.8.1. Second, in Sec.8.2, some improvements in battery management strategy and stack engineering are proposed, which result from this work and can help future designers to develop more efficient VRFB stacks with a compact design. Finally, in Sec.8.2, a fluid dynamics characterization of the IS-VRFB test facility is described, considering internal resistance as the sum of activation, ohmic, and transport resistances.

8.1 Energy losses distribution

Conductive liquid electrolytes involve electrical and hydraulic losses. The former are caused by different cell electric potentials that drive the vanadium charged species to move along the flow paths inside the stack hydraulic paths, resulting in shunt currents and related Joule losses (Sec.5.2.1). The latter are caused by friction losses in the porous electrodes, the stack hydraulic paths (Sec.5.1.2), and in the external hydraulic piping (Sec.5.1.1). In addition, losses are also due to hydraulic ancillary devices, cell electrochemical over potentials, and to self-discharge effects resulting from vanadium species crossover through the membranes. Shunt currents and hydraulic losses can be kept low with a proper hydraulic circuit design, even if the problem suggests opposing choices. In fact, the trade-off between shunt currents and pumping losses is the crucial issue in designing VRFB hydraulic circuits [281], [76], [335], [336]. High electrolyte flow rates reduce concentration over potentials, resulting in improved electric performance, but degrade the overall system efficiency due to higher hydraulic losses.

Some studies have analyzed pressure drops and pumping power at varying electrolyte flow rates in the hydraulic circuit [309], [319], [311], but they do not analyze the origin of these losses and how each affects system efficiency. The combined effects of shunt currents and hydraulic losses were analyzed by Ye et al. [281], for stacks with different numbers of cells and for a battery made with several stacks. They concluded that long and narrow pipes are preferable for minimizing shunt current losses. Very few papers provide a comparative analysis that considers other types of losses in addition to hydraulic and shunt current terms in multicell stacks. Zang et al. [337] presented a hydraulic and electric equivalent circuit of a 1 kW/1 kWh VRFB focused on the computation of stack electrical performance and pump power consumption. Their model adopted some simplifying assumptions and was supported by a partial experimental validation based on data provided by Kim et al. [199]. To the best of our knowledge, studies that account for all major loss causes and are experimentally validated on a kW-class system are missing in the literature. This section presents such a study.

It considers major losses that occur during charge/discharge cycles in a real VRFB system, namely those occurring from the following: cell over potentials, shunt currents, vanadium species crossover in the membranes, hydraulic pressure drops in the stack, hydraulic pressure drops in the piping, and ancillary devices (pumps, motors, and their inverters). The system that was investigated is an IS-VRFB. Some loss contributions used in the analyses were obtained from experimental data taken on the test facility, while others were evaluated by means of numerical models. Synthetic efficiency values were used to account for ancillary losses. The analysis

combined experimental data (provided by sensors and meters) and numerical results provided by numerical models. Losses were evaluated as functions of solution flow rates at stack currents of 30, 50, and 70 A. Charge-discharge cycles performed at a constant flow factor equal to 8 and thus variable flow rates were analyzed. Model validations were made against some measurements obtained on the test facility: validation details are given in Sec.8.1.4. Sec.8.1.5 presents the efficiency analyses developed by considering the loss contributions and energy converted by the battery in a charge/discharge cycle.

8.1.1 Experimental method

LabVIEW routines

The LabVIEW automatic routine was developed to compute the energy absorbed (or provided) by the plant while continuing to acquire and control all the other signals. This procedure can be controlled either manually or automatically. The program is designed to stop automatically at the desired *SOC* and can be interrupted at any time by the user. The routine controls can be found in the efficiency window in the front panel.

It is composed of several elements, as follows: the start efficiency and stop efficiency buttons, which start or stop the routine, respectively, the *SOC* charge and *SOC* discharge numeric indicators, a timing indicator labelled efficiency running time, and a status window. Two numeric indicators show the limits set by the user that must be reached by the battery after the charge or discharge process. Two buttons make the routine start or stop by sending a command to the "Handling Loop" section. When the start command is activated, LabVIEW launches a dedicated SubVI and an additional window opens. At this time, the user can set several parameters: first, the user chooses between charge or discharge mode, imposes the desired current, the limit of the *SOC*, and the stack voltage. The bidirectional converter is designed to work as follows: once voltage and current are set and imposed, it provides a constant current to the battery, but if the voltage limit is reached it automatically reduce the current. Therefore, the charge (or the discharge processes) are performed at constant current and then at constant voltage. The OK button confirms the introduced values and enters them as a global variable; then the cancel button will make the program return to the default acquisition case.

This routine is explained more in detail in the following:

- *Start Efficiency*: Time is recorded and memorized through a shift register. Some buttons and windows are enabled or disabled. Stack voltage and current are taken out of the global variable and are written on the respective controls. A preliminary check on the introduced data is made by confirming that *SOCs* are coherent with the actual status of the battery (e.g. OK if the battery is at 20% and the command is to charge it up to 90%, error if the battery is at 20% and the command is to charge up to 10%. The dual thing in the case of discharge). If any error is detected, the routine shifts to error efficiency, otherwise the efficiency acquisition process can continue;
- *Impose Settings Efficiency*: If no errors are detected, the procedure imposes the set values (current and voltage) to the power supply;
- *Efficiency*: This case is subdivided into two subcases: one for the charge and one for the discharge. After, the charge case is explained in detail and the discharge dual values are written in brackets. Inside the case, some operations are performed continuously while others follow a sequential structure. In particular, the pump control, which is ensured with proportional integral derivative (PID), the computation of the integrals, and the running time, are independent so that they are carried out every time the routine calls this case.
 - $SOC < SOC_{Max}$?: This first case checks whether the set maximum (or minimum) limit of charge is still above (or under) the current state of charge. If this is true, this means the battery needs to be charged (or discharged) more and so the procedure can follow. Conversely, the program will go to the finish efficiency case meaning that the whole process of charge (or discharge) has ended and the collected data can be stored. (In the discharge case the condition is $SOC > SOC_{min}$);

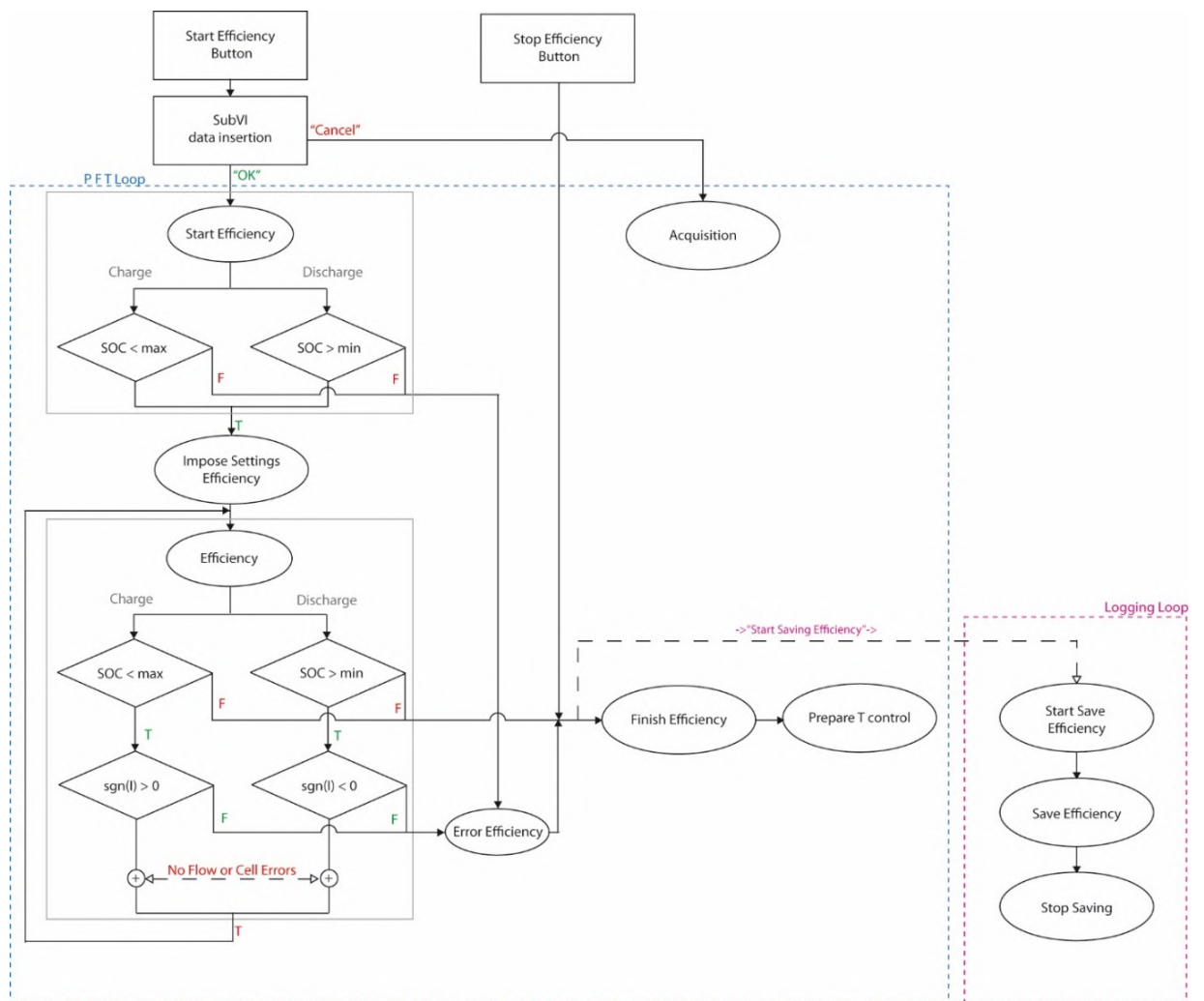


FIGURE 8.1: Flowchart of the routine for the efficiency evaluations. The whole process is complicated by the presence of several security layers. In fact, the high energy the device can store makes the charge and discharge process very long and delicate so there must be a way to keep it under control. Problems connected to the over-charging or over-discharging of the device can be the corruption of the electrodes or the formation of hydrogen that must be totally avoided [259].

- $Sign(I) > 0$?: This intermediate case is necessary because if the user chose for example the "Charge" setting but the power supply (bidirectional converter) is in "Sink" or "Discharge" mode, even if the current SOC is lower than the maximum expected, the battery will never reach it. In fact, it will decrease instead of increasing. According to the operational mode of the power supply ("Source" or "Sink") the current is registered as positive or negative. In the case of charge the current is expected to be positive, so if the sign is positive no error is present. In this case, even if the condition to $sign(I) > 0$ is "true" a "false" output is generated. This was established because the following step accepts as an input to continue the procedure a "false" value, meaning that no error is present. In addition to the current signal input, the next case structure receives the flow meter and the cells voltages values as an input. For the flow meter, the "false" output is generated when the flow is higher than a pre-set value, while for the cells voltage it is "false" if none achieve over 1.7 V. If this condition is ensured, the procedure continues by simply returning to the efficiency case and repeating the double check procedure again, otherwise if just one of these conditions is "true," stack current and voltage are set to zero and the routine will proceed to the error efficiency case. (In the discharge case the condition is $Sign(I) < 0$?).

When the finish efficiency string (sequence of ASCII characters) is enqueued inside the PFT loop queue, the start log efficiency string is sent to the Logging Loop queue, by giving it the command of starting the procedure to store the collected data in a *.tdms* file.

- *Error Efficiency*: This case shows two error messages to the user. One is in the status string indicator in the control panel section, which will disappear after several seconds and inform the user by displaying "INCORRECT SET VALUES – SOC is higher or lower than the current or the power supply is working as incorrect mode". The second appears in a string indicator in the efficiency section of the front panel warning the user that "Error Occurred, Check Settings or Power Supply mode." This message does not disappear until the start efficiency button is pressed again, or the program is restarted, to allow for a longer check of the status of the efficiency routine. Even if some error occurs the program automatically starts the procedure to save the data;
- *Finish Efficiency*: After enabling or disabling some buttons and indicators, the case stores the collected data inside the data saving queue, as follows: time efficiency, by subtracting the current time to the registered time at the beginning of the procedure in the start efficiency case; stack energy; pump energy and hydraulic stack positive electrolyte and negative electrolyte energy losses, which are converted into Wh by dividing them by 7200; current; initial and final SOC ; stack coulomb charge; and voltage efficiency, which is the mean value of the voltage during the charge or discharge process. As a matter of fact, every iteration of the while loop is completed by imposing a wait time of 500 ms. If no wait time is given to the program, the iteration time is not constant and the LabVIEW integration tool works with samples and not with time steps. Ultimately, the obtained result is based on a samples scale and not on a time domain. Once completed, the program switches to the prepare T control case and the whole system is put in standby mode controlling the temperature. In combination, the logging loop cycle goes to the start save efficiency case;
- *Start Save Efficiency*: In this case, the *.tdms* saving file is created and opened in the file path where the LabVIEW VI is saved;
- *Save Efficiency*: Time efficiency and all the energies data coupled with the set current, the initial SOC , and the final SOC are written in the file;
- *Stop Saving*: The data queue is emptied to avoid future overwriting and it closes the *.tdms* file.

Simultaneously, during the procedure, the user can stop the acquisition and save the computed data by simply clicking the stop efficiency button as shown in the flowchart (Fig.8.1) and the loop will move to the finish efficiency case.

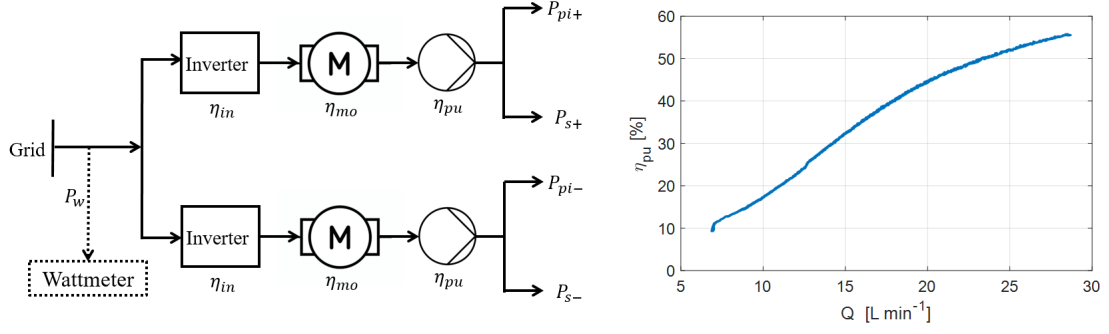


FIGURE 8.2: Left: ancillary power losses composition; right: pump efficiency η_{pu} vs. vanadium solution flow rate Q as resulting from Eq.8.4. In order to obtain this diagram, the same flow rates were imposed in the positive and negative hydraulic circuits.

Energy computation

The study was based on evaluating and comparing the work (energy) converted and/or lost during battery charge and discharge, which were computed by integrating the pertinent power over time, given by either measurements or numerical models:

$$\int_{\tau_{rt}} P dt \quad (8.1)$$

Numerical integration was performed using the Newton-Cotes formula midpoint rule of $W = \Delta t \Sigma_x P_x$, at time steps of $\Delta t = 0.8$ s equal to the sampling time of the BMS, which is four orders of magnitude smaller than the integration interval, i.e. the charge/discharge durations τ_{rt} , which ranged from 4 to 12 h, thus making negligible the numerical integration error.

The electrical power converted in the stack to develop the energies W_{ch} charged into and W_{dh} discharged from the electrolyte solutions was obtained by multiplying measurements of the stack voltage V and current I : $P = VI$. Similarly, the hydraulic power loss P_s driving from the circulation of the electrolytes inside the stack were obtained by multiplying the measurements of the flow rates Q_{\pm} and of the stack pressure drops $\Delta p_{s\pm}$ in each hydraulic circuit, as follows:

$$P_s = Q_+ \Delta p_{s+} + Q_- \Delta p_{s-} \quad (8.2)$$

Instead, the electrolytes circulation in the piping is forced by pressure drops $\Delta p_{pi\pm}$ that induce a hydraulic power loss P_{pi} in the piping corresponding to the hydraulic circuits, which connect the stack to the tanks and include the pumps. The net hydraulic circuit pressure drops were thus $\Delta p_{h\pm} = \Delta p_{s\pm} + \Delta p_{pi\pm}$, which equated with the pump heads. Correspondingly, the total power losses in the hydraulic circuits were as follows:

$$P_h = P_s + P_{pi} \quad (8.3)$$

Because no measurement was available for determining $\Delta p_{pi\pm}$ and P_{pi} , these terms were computed by means of the numerical model described in Sec.5.1.1. The total hydraulic losses P_w supplied by the AC grid and measured by the wattmeter were affected by the additional power losses P_{an} in ancillary devices, namely pumps, motors, and inverters (Fig.8.2). The contribution of these losses was accounted for by means of the device efficiencies, namely of the pump impeller η_{pu} , of the electric motors η_{mo} , and of the inverters η_{in} :

$$P_w = P_h + P_{an} = \frac{P_h}{\eta_{in} \eta_{mo} \eta_{pu}} \quad (8.4)$$

The inverter data sheet provided an efficiency of $\eta_{in}=95\%$ that was assumed constant in every working condition, whereas a bench test on a very similar small three-phase motor gave an efficiency of $\eta_{mo}=50\%$ that was considered constant in the analyses due to the frequency-controlled

TABLE 8.1: Values of the empirical minor loss coefficients (concentrated) ζ used in calculating the concentrated pressure losses.

Component	Number in each circuit	ζ	Reference
Elbow 90°	3	1.5	[340]
T-joints, 180° flow	5	0.9	[340]
T-joints, 90° flow	5	2	[340]
Joints	2	0.08	[340]
Pipe inlet (tank outlet)	1	0.8	[340]
Pipe outlet (tank inlet)	1	1	[340]
Flow meter	inlet (contraction)	1	0.38
	outlet (expansion)	1	0.48
Valves	2	0.42	[341]

operation performed by the inverters. Because no data was available for the pump friction losses (namely for the impeller), the efficiency η_{pu} was evaluated as $\eta_{pu} = P_h / (P_w \eta_{in} \eta_{mo})$. This relation provided the efficiency variable with the flow rate Q shown in Fig.8.2 (right), as expected for centrifugal pumps [338]. By using the above efficiency values, the power losses in the inverter, pump motors, and pump impellers in any operating condition were computed as $P_{in} = (1 - \eta_{in})P_w$, $P_{mo} = (1 - \eta_{mo})\eta_{in}P_w$, and $P_{pu} = (1 - \eta_{pu})\eta_{mo}\eta_{in}P_w$, respectively.

8.1.2 Numerical model

Numerical models provided energy losses not available from measurements, namely, the losses related to hydraulic pressure drops in the piping, shunt currents, cell over potentials, and vanadium species crossover in the membranes. A cell-resolved dynamic model of the IS-VRFB system were used for this aim (Chap.5).

Hydraulic losses

A standard hydraulic analytical model was used to compute each electrolyte pressure drop Δp_{pi} in the piping as function of the flow rate Q for both the positive and negative electrolyte hydraulic circuits [339], [337], [340]. The piping layout for the positive and negative electrolytes is shown in Fig.8.3, together with the 3D model of the whole balance of the plant. Each $\Delta p_{pi\pm}$ was computed as the sum of distributed term $\Delta p_{di\pm}$ due to friction in the straight pipes [340], and a concentrated term $\Delta p_{cn\pm}$ occurring in elbows, junctions, T-joints, flow meters, and valves: $\Delta p_{pi\pm} = \Delta p_{di\pm} + \Delta p_{cn\pm}$ as described in detail in Sec.5.1.1. $\Delta p_{di\pm}$ was computed by Eq.5.4 and $\Delta p_{cn\pm}$ by Eq.5.10. The fluid density ρ and dynamic viscosity μ needed to compute Re were determined experimentally for both electrolytes at $SOC=50\%$. The measurements were performed with a 1637/02 U-tube reverse flow BS/IP viscometer (Cannon-Fenske) and a pycnometer (Thomas Scientific), and yielded the results reported in AppendixA. These values were assumed constant in the model, as an average during the charge/discharge cycles.

The empirical minor loss coefficients ζ , whose values are reported in Tab.8.1 were obtained from the literature [340] or from the manufacturer's data sheet [341]. The piping pressure drop $\Delta p_{pi\pm}$ caused the hydraulic piping losses P_{pi} :

$$P_{pi} = Q_+ \Delta p_{pi+} + Q_- \Delta p_{pi-} \quad (8.5)$$

Electrical losses

The numerical solution of the equivalent electric circuit (Sec.5.2) yielded the shunt current $I_{k\pm,n}$ in each segment, from which the pertinent power losses were computed as $P_{k\pm,n} = R_{k\pm,n} I_{k\pm,n}^2$. Summing up all the contributions of the manifold m , cell flow channels, and felts c , the overall shunt current power losses were obtained. The cell internal power losses associated with the over potentials were computed similarly, considering the internal resistances, which represent over potential voltage drop: $P_{i,n} = R_{i,n} I_{i,n}^2$.

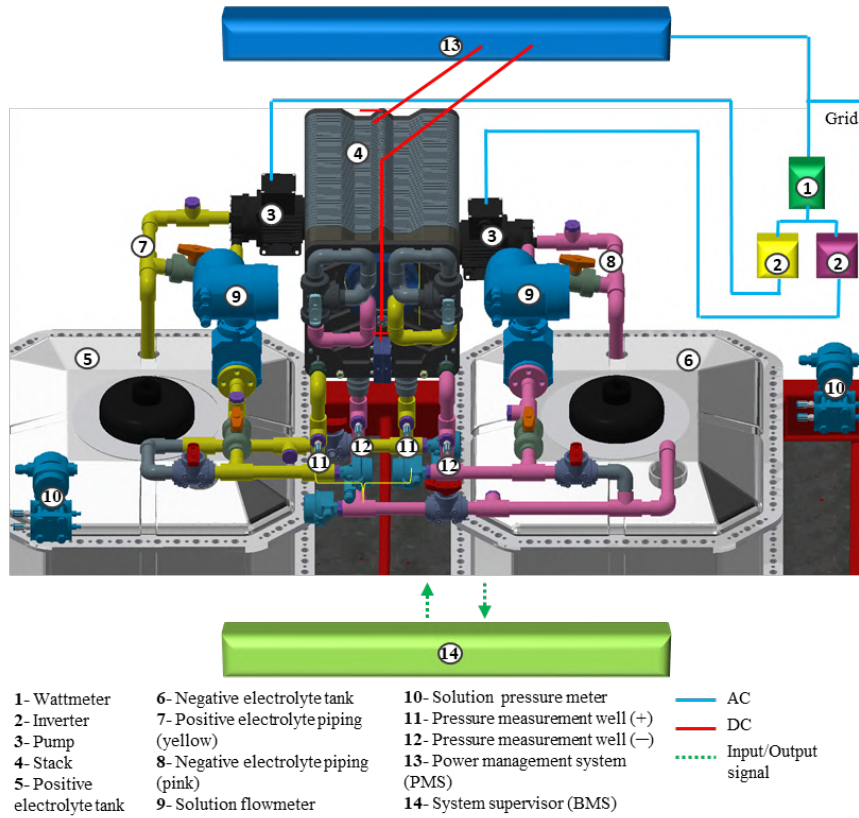


FIGURE 8.3: 3D representation of IS-VRFB balance of plant.

Crossover losses

The complete description of the model for crossover analysis is reported in Sec.5.3. In the computation of energy losses assessment, the vanadium species crossover through the membrane reduces the reacting moles available in the proper compartments. This loss occurs, resulting in a rate $dM(j)/dt$ and reduces the reacting V^{2+} moles available in the proper compartments due to the highest crossover rate of this species, so that it drives the battery energy reduction rate, expressed as follows:

$$P_{co} = -\Delta G \frac{dM_{II}}{dt} = zFE_0 \frac{A}{d} \sum_{n=1}^N (K_{II,n} C_{II,n-} - 2K_{V,n+} C_{V,n+} - 2K_{IV,n} C_{IV,n+}) \quad (8.6)$$

where $\Delta G = -zFE_0$ is the total Gibbs reaction energy, with E_0 the cell Nernst potential, and $z = 1$ stated as the number of charges involved in the electrochemical reactions [342]. It should be noted that this expression is different from Eq.5.63. In Eq.5.63, the losses represent a net internal heat generated due to the exothermal side reactions 5.31, 5.32, 5.34, 5.35. Indeed, Eq.8.6 represents a loss of exergy (such as electrical work).

8.1.3 Energy efficiencies

A number of efficiency figures are proposed in the literature for assessing the performance of VRFBs, such as voltage efficiency (VE) [240] and coulombic efficiency (CE) [343]:

$$VE = \frac{EE}{CE} \quad (8.7)$$

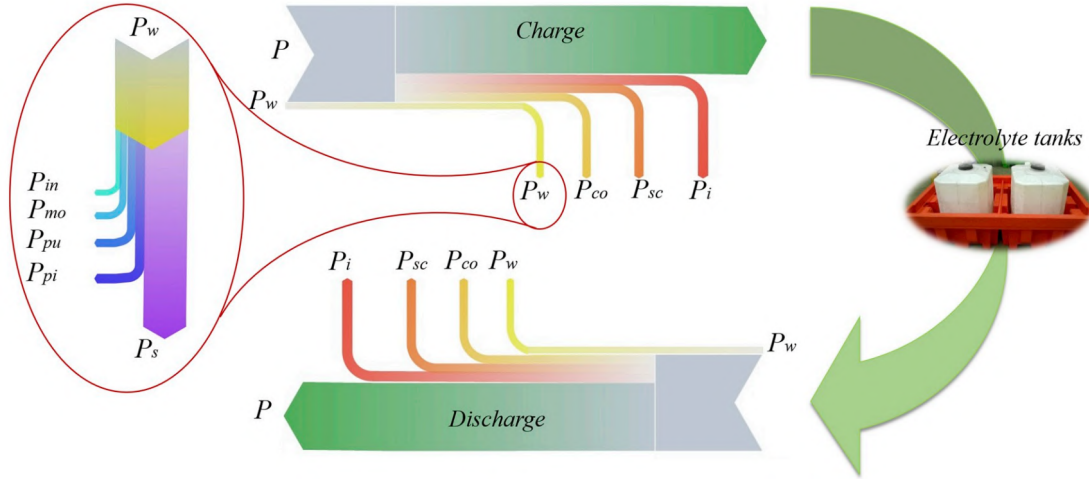


FIGURE 8.4: Sankey diagram of the power flows and loss terms which affect the energy flows and on the energy efficiency.

$$CE = \frac{\int_{\tau_{dh}} Idt}{\int_{\tau_{ch}} Idt} \quad (8.8)$$

A common definition, also dubbed energy efficiency (EE), consists of the ratio between the energy released from the stack during discharge and the energy released to the stack during charge:

$$EE = \frac{\int_{\tau_{dh}} P dt}{\int_{\tau_{ch}} P dt} = \frac{W_{dh}}{W_{ch}} \quad (8.9)$$

In this expression, the energies converted by the stack account for the loss terms due to over potentials, shunt currents, and species crossover. This figure can be convenient for qualifying a single cell, but can be less significant if related to a stack, because it neglects the pumping power when independently supplied. This occurrence is schematic in the Sankey diagram of Fig.8.4, which provides a brief overview of how the different loss terms impact on energy efficiency. Round-trip efficiency (RTE) is a figure of merit that summarizes the others and is presented in the literature in different forms. A more comprehensive definition of the round-trip efficiency suitable for stacks (dubbed system efficiency (SE)) was used in our analyses [343], as follows:

$$SE = \frac{\int_{\tau_{dh}} P - P_w dt}{\int_{\tau_{ch}} P + P_w dt} = \frac{W_{dh} - W_w}{W_{ch} + W_w} \quad (8.10)$$

8.1.4 Analysis of results

Hydraulic model validation

The hydraulic circuit model was validated by means of the pump head value $\Delta p_{h-} = 0.45$ bar stated in the data sheet at a flow rate $Q=29.5 \text{ L min}^{-1}$, which was obtained when supplying the motors at a frequency of 50 Hz (violet point Fig.8.5 (left) and Fig.8.5 (right)). At this same flow rate, the measured stack pressure drop in the negative electrolyte was $\Delta p_{s-}=0.28$ bar. From the previous data, the piping pressure drop was estimated as $\Delta p_{pi-} = \Delta p_{h-} - \Delta p_{s-}=0.17$ bar to be compared with the model results. At the same $Q = 29.5 \text{ L min}^{-1}$, the hydraulic model gave a pressure drop in the negative electrolyte piping $\Delta p_{pi-}=0.19$ bar, with an error of 0.02 bar, which was sufficiently small for the aim of the analysis [344]. A validation in the positive electrolyte piping provided very similar results.

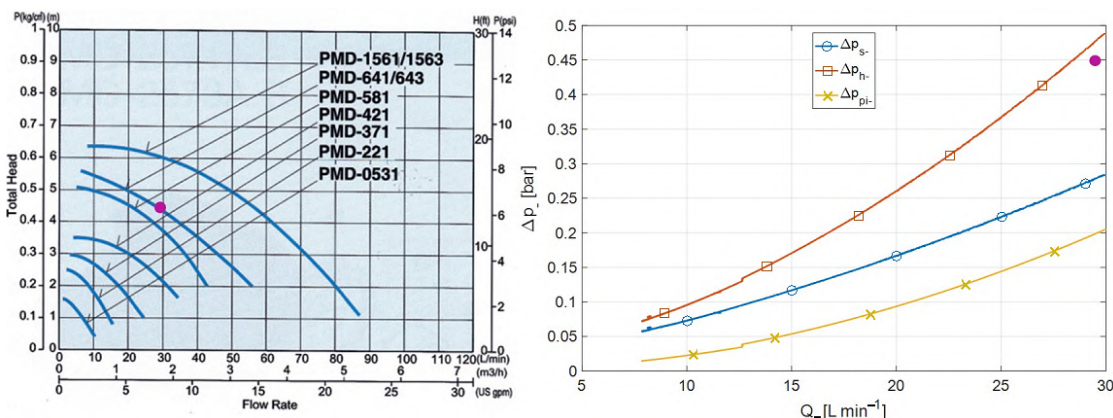


FIGURE 8.5: Left: characteristic curve of the pump (PMD 641); right: pressure drop profiles in the negative electrolyte circuit vs. flow rate Q at $SOC=50\%$ (the positive electrolyte piping pressure has a similar profile).

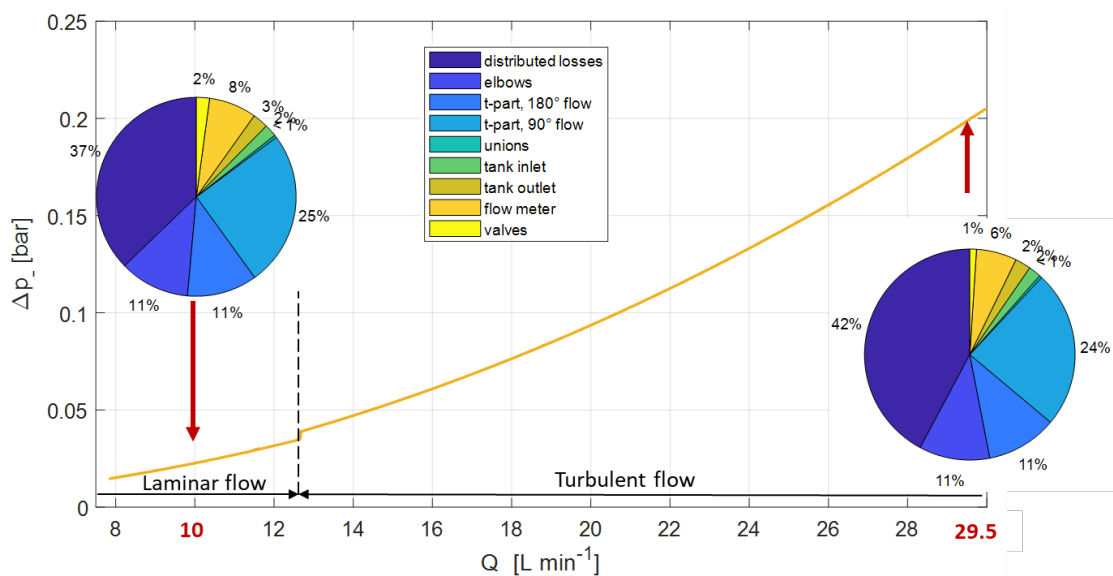


FIGURE 8.6: Negative electrolyte piping pressure drop profile vs. flow rate with pie chart of its contribution in laminar and turbulent flow at $SOC=50\%$ (the positive electrolyte piping pressure has a similar profile).

Fig.8.5 (right) shows that the negative circuit total pressure drop Δp_{h-} and its contributions in the stack Δp_{s-} and in the piping Δp_{pi-} . The former provides the major contribution even in the case of the complex IS-VRFB piping geometry.

However, the relative contribution of Δp_{pi-} with respect to Δp_{s-} increased at higher flow rates, because a turbulent regime occurs in the piping earlier than in the stack where it remains laminar. Δp_{s-} never reduced below 58% of the total. This result is consistent with data reported in the literature, which indicates that porous electrodes and cell flow channels inside the stack are responsible for pressure drops larger than those in external piping. In the case of industrial designs with minimized piping lengths, the Δp_s relative contribution is expected to be higher.

For the sake of comparison, 70% of the whole hydraulic losses occurring in the porous electrode were reported in [199].

Hydraulic losses impact on the efficiency

Fig.8.6 shows the pressure drop in the negative piping Δp_{pi-} as a function of Q . The pie diagrams present the relative contributions to Δp_{pi-} of the different effects at 10 L min⁻¹ (i.e.

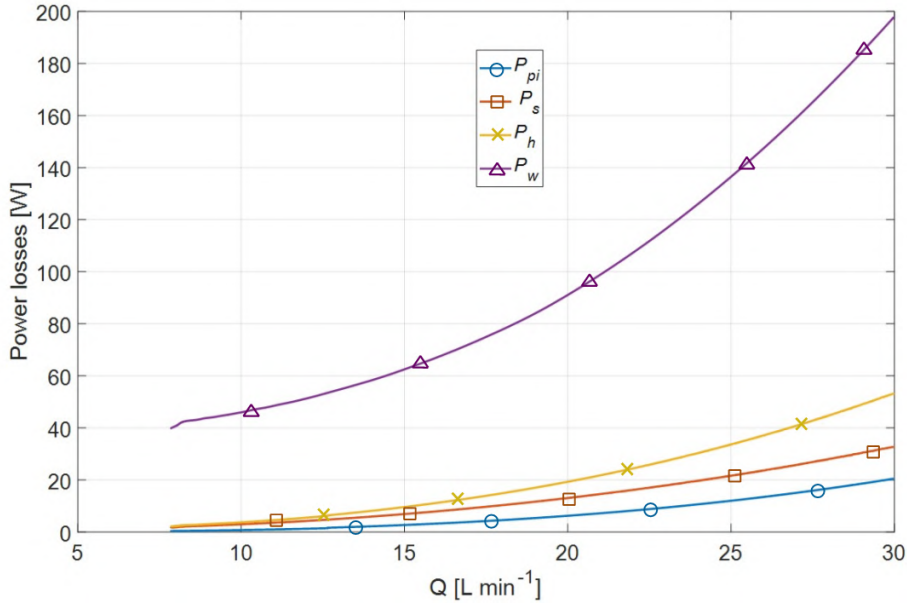


FIGURE 8.7: Profiles of power losses for electrolyte circulation vs. flow rate at $SOC=50\%$ in both positive and negative compartments. The difference between the total value P_w measured by the wattmeter and the hydraulic circuit losses $P_h = P_s + P_{pi}$ is due to P_w in the pump impellers, electric motors and electronic inverters.

at a specific flow rate of $6.9 \cdot 10^{-3} \text{ cm s}^{-1}$) and 29.5 L min^{-1} ($20.5 \cdot 10^{-3} \text{ cm s}^{-1}$). Similar values were obtained for the positive electrolyte. Transition from the laminar to the turbulent flow in the piping occurs at $Q=12.8 \text{ L min}^{-1}$ as shown in Fig.8.6. In all cases, the concentrated pressure drop $\Delta p_{cn\pm}$ has a major effect on the total piping pressure drop $\Delta p_{pi\pm}$: it amounts to 63% at 10 L min^{-1} and to 58% at 29.5 L min^{-1} , the remaining being ascribed to the distributed term $\Delta p_{di\pm}$. The 90° T-joints give a higher contribution (25% and 24%) than 180° T-joints and elbows, because the latter present a smoother curvature. Approximately 7% of the pressure drops occur in the flow meters, due to their reduced internal cross-section. As already noted, the piping pressure drops Δp_{pi} and their contributions are expected to be lower in an industrial design, because the piping of the IS-VRFB facility is fully instrumented and designed for high accessibility and flexible operation, resulting in increased pressure drops.

Fig.8.7 shows the hydraulic power losses P_h and their contributions P_{pi} and P_s together with the power losses P_w measured by the wattmeter (Fig.8.2 (left)), summed for the positive and negative circuits as functions of the flow rate Q at $SOC = 50\%$. These profiles, which are similar to those published in [199], highlight the low impact of the net hydraulic power losses compared to the ancillary devices, namely inverters, electric motors, and impellers, which, due to their relatively small sizes, are together responsible for 72% of the total losses at $Q = 29.5 \text{ L min}^{-1}$, and for an even larger portion at lower flow rates. Further analyses are reported hereafter in Sec.8.3.4, where a detailed characterization in the stack fluid-dynamic is presented.

8.1.5 Comparison of loss contributions

Evaluations of the losses in charge/discharge cycles, either measured or computed, were performed at three stack current values of 30, 50, and 70 A and results are reported in Tab.8.2. Measurements (*exp*) provided the electric energy released to the stack in charge W_{ch} , the electric energy released from the stack in discharge W_{dh} , and the overall hydraulic energy $W_{w,rt}$ measured by the wattmeter in the whole cycle. Models (*num*) provided the energy losses due to cell over potentials $W_{i,rt}$, shunt currents $W_{sc,rt}$, and species crossover $W_{co,rt}$ in the whole cycle. Two sets of system efficiency SE values are also reported in the Tab.8.2: the SE values based on measurements (*exp*), obtained by using W_{ch} , W_{dh} and W_w in Eq.8.10, and the SE values based on computations (*num*), obtained as follows:

TABLE 8.2: Numerical and experimental energy terms and system efficiencies during charge/discharge cycles. W_{ch} = converted electric energy in charge, W_{dh} = converted electric energy in discharge, $W_{w,rt}$ = round-trip total hydraulic losses (i.e. for electrolyte circulation), $W_{i,rt}$ = round-trip losses due to cell over potentials, $W_{sc,rt}$ = round-trip losses due to shunt currents, $W_{co,rt}$ = round-trip losses due to species crossover, SE = system efficiency; *exp* = experimental, *num* = numerical.

I [A]	SOC range [%]	W_{ch} (<i>exp</i>) [Wh]	W_{dh} (<i>exp</i>) [Wh]	$W_{w,rt}$ (<i>exp</i>) [Wh]	$W_{i,rt}$ (<i>num</i>) [Wh]	$W_{sc,rt}$ (<i>num</i>) [Wh]	$W_{co,rt}$ (<i>num</i>) [Wh]	SE (<i>exp</i>) [%]	SE (<i>num</i>) [%]	Rel. error [%]
30	13.1–87	17941	13610	1205	1991	2049	2771	70.35	70.72	+0.53
50	19.9–78.5	14273	10165	717	2473	985	1340	67.10	66.67	-0.64
70	28.0–72.7	10809	7133	492	2406	515	699	62.42	62.81	+0.62

$$SE_{num} = \frac{W_{ch} - W_{i,rt} - W_{sc,rt} - W_{co,rt} - W_{w,dh}}{W_{ch} + W_{w,ch}} \quad (8.11)$$

The relative errors between the two sets of SE values was always lower than 1%, confirming the model reliability. In addition, the SE values presented in the table are in agreement with the efficiencies reported in the literature for large VRFB systems [19], [345].

Charge/discharge analyses

The flow factor Eqs.8.12, 8.13 is a performance figure expressing the ratio between the flow rate of the electric charges moving in the stack due to the electrolyte flow and the electric current generated in the stack from the electrochemical reactions. In the charge/discharge phases it is given by the following:

$$\alpha = \frac{Q F c_v (1 - SOC)}{NI} \quad (8.12)$$

$$\alpha = \frac{Q F c_v SOC}{NI} \quad (8.13)$$

where F is the Faraday constant and c_v the electrolyte total concentration.

In all experiments performed at 30, 50, and 70 A, the flow factor was kept constant at $\alpha=8$. This figure is close to the value of 7.5 reported as an optimal value in a study carried out by Tang et al. on a 40-cell stack [240]. Fig.8.8 shows the bar and pie diagrams of the energy loss contributions during the performed charge/discharge cycles in the SOC ranges shown in Tab.8.2. Contributions to the overall hydraulic losses shown in the pie diagrams did not present significant differences in the three cases. The two small electric motors were responsible for almost half of the losses (48%), followed by the impellers ($\approx 37\%$). In fact, a large proportion of the losses were due to inverters, electric motors, and impellers, which did not depend on the design of the stack and hydraulic circuits. Instead, the hydraulic losses in the stack and piping together constituted approximately 10% of the overall hydraulic losses. This evidence highlights that high-efficiency devices (pumps, electric motors, and inverters) contribute significantly to overall system efficiency. The total hydraulic losses W_w were more important when charge/discharge cycles were executed at low-current, due to the longer duration of the operation and to low pump efficiency η_{pu} at low flow rate (Fig.8.1(left)). W_w was 1205 Wh in the operation at 30 A, namely more than twice the value at 70 A. The losses due to shunt currents and crossover were also observed to increase with decreasing stack current, due to the longer duration of the operation (Fig.8.1). It must be noted that shunt current losses should also be taken into account.

Several studies report that shunt currents do not markedly affect the electrical performance of a VRFB, being two order of magnitudes lower than the nominal stack current, as reported by Zang et al. [337] and Bhattacharjee et al. [316]. Conversely, our results show that in a compact VRFB stack they have an influence comparable to other losses, especially at low load, thus significantly affecting VRFB efficiency. In fact, we found shunt-current losses greater than the total hydraulic losses in the 30 and 50 A operations. In addition, the comparison between stack hydraulic losses and shunt current losses from Tab.8.2 reveals that the former with respect

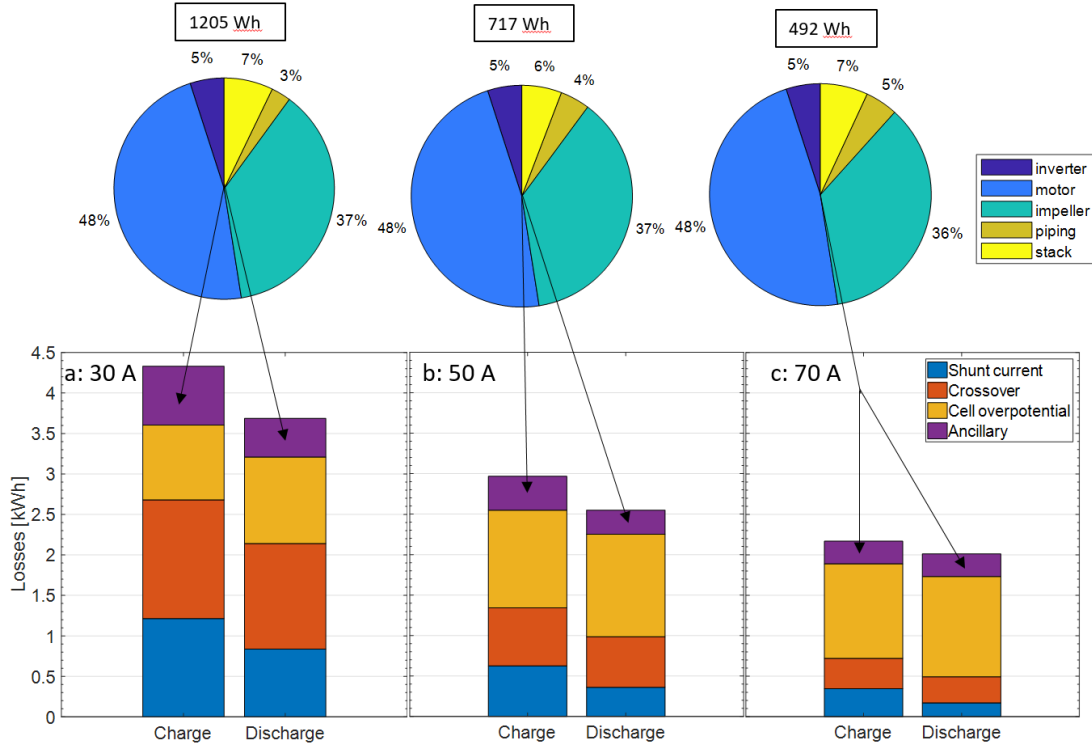


FIGURE 8.8: Battery energy losses contributions in charge/discharge cycles performed at stack currents of: a) 30 A, b) 50 A, c) 70 A in the *SOC* ranges shown in Tab.8.2.

to the latter are 4.1% (84 Wh out of 2049 Wh), 4.3% (43 Wh out of 985 Wh) and 6.7% (34.4 Wh out of 985 Wh) in charge-discharge cycles at 30, 50, and 70 A, respectively.

8.1.6 Key points

From the present analyses, some conclusions can be drawn. First, the design of a compact VRFB stack with a quite large number of cells should be addressed to reduce shunt currents by maximizing the electrolyte electric resistances in the internal manifolds and flow channels, with marginal consequences on the hydraulic performance. In other words, longer and thinner flow paths should be preferred in the trade-off between shunt currents and hydraulic losses, with the limit that flow channels do not risk being clogged by electrolyte impurities. For example, the flow channels of the flow frame could be lengthened without significant effects on hydraulic losses.

Second, at high-current operations the cell over potential losses are larger than crossover losses. Consequently, the cell internal equivalent resistances (which are mainly due to the membrane and carbon felts ohmic over potentials), impact on the efficiency more than the membrane species permeability from which the crossover losses originate, particularly in a compact VRFB stack capable of operating at higher current density than those usually reported in the literature (e.g. the 19-cell stack with 1500 cm² area of the 2.5 kW/15 kWh reported by Tang et al. [308]) and thus provided with a smaller cell active area. In fact, in our study crossover losses were a little higher than the over potential losses only in the 30 A operation (Tab.8.2). Consequently, increasing the membrane ion conductivity is a more important issue than reducing its vanadium species permeability, especially in a high current operation.

Third, hydraulic losses were found to depend largely on the low-efficiency of electric motors and of the pumps, as typically occur in small devices (e.g. 50% and 20% – 55%, respectively, in our study). Conversely, we found that only less than a quarter of overall hydraulic losses were due to the hydraulic circuit, that is, to the stack and piping. It must be noted, however, that ancillary device efficiencies can be much higher in larger units fitted to larger systems. For

instance, a 5 kW motor suitable for a 150 kW VRFB can have an efficiency above 75% and larger motors can easily exceed 90%. To the best of our knowledge, similar analyses of the effect of ancillary losses were largely overlooked in the existing literature.

8.2 Optimization of flow rate management system

Electrolyte transport issues are also receiving increasing attention to obtain better cell performance. Several studies have been published that investigate the effect of different cell structure designs [76], [335] and it has been shown that the management of process variables strongly affects the overall battery performance, especially in the case of large-scale VRFB systems [343], [103], [346]. The charging procedure is normally borrowed from other batteries, such as a lead acid battery. A standard operation consists of charging the battery under constant current until the voltage reaches a given value, and then the charge is switched to constant voltage mode [338].

In VRFBs, such a charging profile is convenient for preventing hydrogen and oxygen evolution. Nevertheless, it must also be noted that such a profile can be profitable in a laboratory VRFB for maximizing the charge capacity or the round-trip efficiency. Further, it can be adopted in charging batteries for portable electronics and electric cars; however, it is not really indicative of the ability of an industrial size battery to interact with renewable sources on a real grid, where it must compensate the mismatch between power generation from these intermittent sources and load demand [19], [345]. Because of these operating features, the electrolyte flow rate control assumes pivotal importance in the management strategy with the aim of optimizing battery performance. Few studies have been published on this problem so far.

Indeed, some techniques based on numerical algorithms have been investigated at an analytical level, such as the fuzzy logic controller [347], and the gain scheduling control [318].

Methods like these follow synthetic schemes, which fail to take into account all real physical variables of the battery. High electrolyte flow rates improve energy efficiency by reducing cell over potentials, but increase hydraulic losses and pumping power demand. Some analyses have examined the pressure drop and pumping power demand under varying electrolyte flow rates [319], [309], [348] in the cell distribution architectures (i.e. flow frame or flow channels geometry) designed to provide optimal electrolyte flow beds in the electrodes [349].

Xu et al. developed an analysis of the effect of *SOC*-dependent electrolyte viscosity on battery performance [350], but they did not propose a consequent control strategy. Yang et al. have analyzed cell performance while keeping the flow rate constant during operation, only varying the current density according to the state of charge (*SOC*) to optimize battery efficiency [351]. Ling et al. studied the effect of a pulsating electrolyte flow rate in a single cell VRFB, showing that a short flow period followed by a long flow termination period can reduce pumping power demand by more than 50% [352]. Ma et al. proposed an electrolyte flow rate control strategy that optimizes battery efficiency simply by stepping up the flow rate at the end of charge and discharge to compensate for low reactant concentration in a 1 kW-scale VRFB system [353]. They demonstrated that this strategy can improve the system's efficiency by 8% compared to a constant flow rate, indicating that a variable flow rate is a profitable choice.

Further numerical analysis has been proposed by Fu et al. [321], consisting of a model of a VRFB that investigates the effect of the flow rate on battery efficiency by taking into account the concentration over potentials and related pumping power. They propose a framework for determining the optimal flow rate under varying operating conditions, which can increase the stack efficiency by 3%. Very recently, Xiao and Tan have proposed a numerical model for a complete VRFB system to predict its efficiency [354], in which the flow rate is varied within a given range to obtain high system and coulomb efficiencies. Their simulations indicate an increase of 3.34% and 3.84%, respectively, for the two efficiencies, confirming that superior performance can be achieved with respect to an operation at a constant flow rate.

Tang et al. have analyzed the effect in terms of flow factor [240]. The use of a flow rate higher than the minimum value imposed by the stoichiometry of Faraday's law (namely a flow factor greater than 1) was investigated, and found that as long as this flow factor is kept constant, a value of 7.5 provides the highest system efficiency. König et al. developed a numerical investigation of the behavior of a 6 kW VRFB, indicating that the efficiency can be improved

by varying the flow factor depending on the *SOC* and battery current [355]. Nevertheless, very few experimental studies of flow rate control performed on kW-class VRFB systems have been reported, especially regarding the correlation of the flow rate with battery performance and cell losses related to cell over potentials.

The profile of the battery voltage as a function of the cell current density depends on three over potentials that are responsible for energy losses. Cell over potentials impact differently on the polarization curves and losses as stated in Sec.2.2.2. Activation over potentials, which appear at low current density, typically have a minor role in VRFBs, in which the dominating effect consists of the linear ohmic over potentials, whereas concentration over potential contributions may prevail at high current density, causing a dramatic voltage drop and voltage vanishing at the limiting current density. Indeed, the relative effects of the three over potentials in each VRFB depend on several parameters: battery chemistry, electrodes design, membrane features, and electrolyte flow rates.

The aim of this section is to investigate the possibility of modulating electrolyte flow rate to minimize the battery voltage drop, and hence maximize the efficiency by means of an experimental investigation carried out on a kW-class VRFB test system. Based on such analyses, optimal flow rate management was developed and implemented in a LabVIEW environment in the VRFB BMS. In addition, the method proposed can represent a useful experimental protocol for testing internal losses and their dependence on cell current, state of charge, and electrolyte flow rate, which can be easily applied to other RFBs to find the optimal flow rate for each operating condition in terms of and *SOC*, *I*.

8.2.1 Experimental method

The experimental campaign was conducted as follows. First, different values of flow factors, applied currents, and *SOC*s were chosen. For every value of *SOC* and for every value of applied current these tests were replicated, changing the value of flow factor every time. Thus, it was possible to investigate the behavior of the battery at various *SOC*s, applied currents, and flow rates.

In every test, the acquired data were saved for 60 s by LabVIEW only when the cell voltages were stable (namely when the stationary condition was reached). In particular, LabVIEW automatically saved a sample of data every 0.8 s in an Excel file. The measures acquired by LabVIEW were the cell voltages, the stack voltage, the applied current, the open circuit voltage, the inlet and outlet temperatures, and the pump power.

It is worth nothing that some experimental points are missing. In some cases it was not possible to carry out some tests with small flow factor values because the flow rate was too low (i.e. lower than 2.0 L min^{-1}) and in other cases it was not possible to conduct some tests with large flow factor values because the flow rate was too high (i.e. higher than 29.5 L min^{-1} , the limit of actual pumps). Moreover, it is worth mentioning that at *SOC*=20% (and in some cases at very low values of flow factor, i.e. lower than 6) the cell voltages did not reach stationary conditions, meaning it has not been possible to report the results.

8.3 Analysis of mass transport losses

The analyses presented here after made use of the measurement taken on IS-VRFB during charge and discharge operations, which were carried out at different stack currents *I*, state of charges *SOC*s, and electrolyte flow rates *Q*. In VRFBs, due to species crossover occurring through cell membranes, the volume of the positive electrolyte decreases and the volume of the negative electrolyte increases during the charge phase, and viceversa during the discharge phase. The net effect in a round-trip cycle is that the volume of the positive electrolyte increases and the volume of the negative electrolyte decreases, as reported in [146]. During the experiments on IS-VRFB, a volume changes of $\simeq 4 \text{ L}$ (i.e. 0.7%) in each charge/discharge cycle was observed. A balancing operation through a bypass pipe interconnecting the two tanks was operated every ten cycles to compensate this effect [194].

At the cell level, the polarization curve of an electrochemical device, namely the voltage as a function of the current density, depends on three overpotentials which are responsible for energy

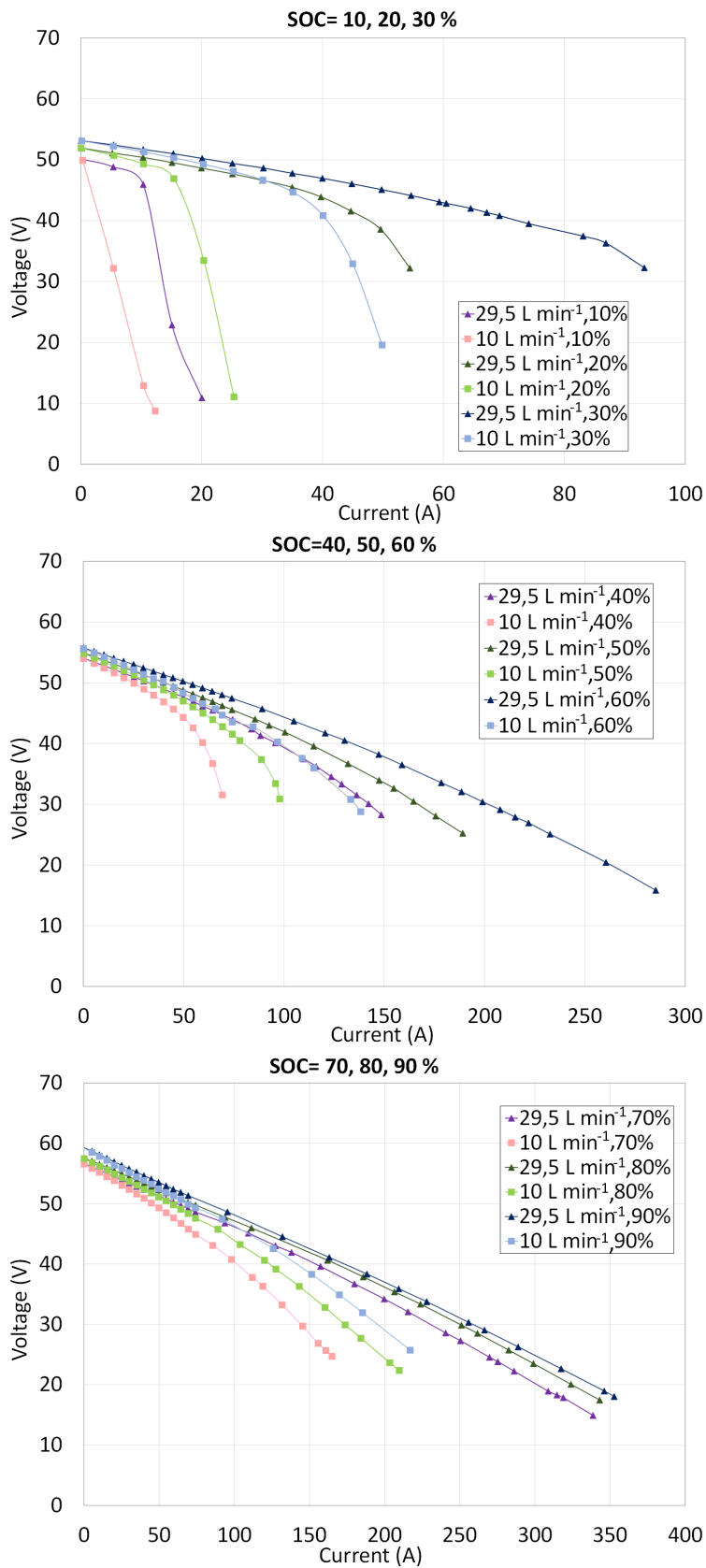


FIGURE 8.9: Experimental polarization curves (V vs. I) during discharge obtained on the IS-VRFB test facility at different flow rates: $Q=10 \text{ L min}^{-1}$, 20 L min^{-1} and 29.5 L min^{-1} and $SOCs$ (10%, 20%, 30%, 40%, 50%, 60%, 70%, 80%, 90%).

losses [356]. Activation overpotentials appear at low current density and have typically a minor role in VRFBs, in which the dominating effect in a large range of current density consists of the linear ohmic overpotentials. Concentration overpotentials may prevail at high current density, causing a dramatic voltage drop and the rapid vanishing of voltage at the limiting current densities. At a battery level, similar polarization curves correlate the stack voltage and current. The relative effects of the three overpotentials in a VRFB depend on several parameters, such as current collector and electrodes design, membrane composition and thickness, electrolyte flow rates, and state of charge.

Fig. 8.10 shows such discharge polarization curves taken on the IS-VRFB, in steady-state operating conditions. They have been obtained at *SOC* ranging between 10% and 90% and at electrolyte flow rates of $Q=10 \text{ L min}^{-1}$ and 29.5 L min^{-1} (i.e. at a specific flow rate q of $6.9 \times 10^{-3} \text{ cm s}^{-1}$ and $20.8 \times 10^{-3} \text{ cm s}^{-1}$, respectively).

Since the scope of the analysis was investigating the steady state performance of the battery expressed by these curves, the dynamic capacitive effects of the electrodes were neglected and only the resistive effects were taken into account. All these polarization curves are non-linear over the whole electric current range so that, to the aim of the following analysis, they were modeled by means of non-linear electrical resistances [357] and the stack voltage drop ΔV was expressed as:

$$\Delta V = V_0 - V = (R_a + R_o + R_t)I = R_i I \quad (8.14)$$

where R_a , R_o and R_t are the activation, ohmic and transport equivalent resistances, respectively and their sum R_i is the internal stack resistance [358, 343, 359]. These resistances are functions of I , due to the non-linearity of the $V(I)$ curves, and also of *SOC* and Q . R_a mainly affects the polarization curve at small I values, R_o in the medium range and R_t at high values, consistently with the aforementioned overpotential features.

Fig. 8.10 shows that, at $I = 0$ the curves with the same *SOC* present the same open circuit voltage (*OCV*), $V_0(\text{SOC})$, independently of Q . Fig. 8.10 also shows that most polarization curves $V(I)$ of IS-VRFB exhibit a linear behavior at low I values, indicating that the activation losses are small compared to the other two terms, as reported in the literature for other VRFB systems [329, 360, 361], so that we can assume:

$$R_i \approx R_o + R_t \quad (8.15)$$

On the other hand, most curves present a sudden voltage drop as I increases and this drop occurs as sooner as *SOC* is smaller, in both cases at $Q = 10 \text{ L min}^{-1}$ and 29.5 L min^{-1} . In polarization curves at low *SOC* and low Q these dramatic voltage decreases present an early occurrence. This behavior, that is due to transport losses, is modeled with a strong increase of the electrical resistance R_t . It indicates how crucial flow rate control is, in order to pump the optimal amount of electrolyte that avoids wasting pumping power while keeping at the highest levels the battery electrical performance, i.e. while maintaining the internal resistance as low as possible. The flow factor α is a useful parameter to correlate electrolyte flow rates and electric performance. As already stated, it is given by the ratio between the flux of charges provided by the electrolyte flow for the reactions and the electric current generate in all the cells. In the charge/discharge phases it is respectively expressed by Eq.8.12, Eq.8.13.

with F the Faraday constant, c_V the Vanadium total concentration and N the number of cells in the stack. The flow factor can not be smaller than $\alpha = 1$, since in such condition the electrolyte flow rates provide exactly the ions needed to produce the electric current I . Such $\alpha = 1$ would be the ideal condition as regards minimizing the pumping power, but it would be very dangerous operating the battery at such α value, because it is almost impossible that all reagent ions can reach the active sites: $\alpha = 1$ would involve reactions in cell materials other than the electrolytes, resulting in cell malfunction and even battery failures [362, 363]. Consequently, α is usually kept at higher values, typically around 7 – 8, in order to ensure efficient reactions [364]. Eq. 8.12 and 8.13, show that, once Q is fixed, α changes during a VRFB operation because of *SOC* and I variations. In particular, Fig. 8.10 shows that, in discharge polarization curves, α reduces with I at fixed Q and at any given I increases with Q .

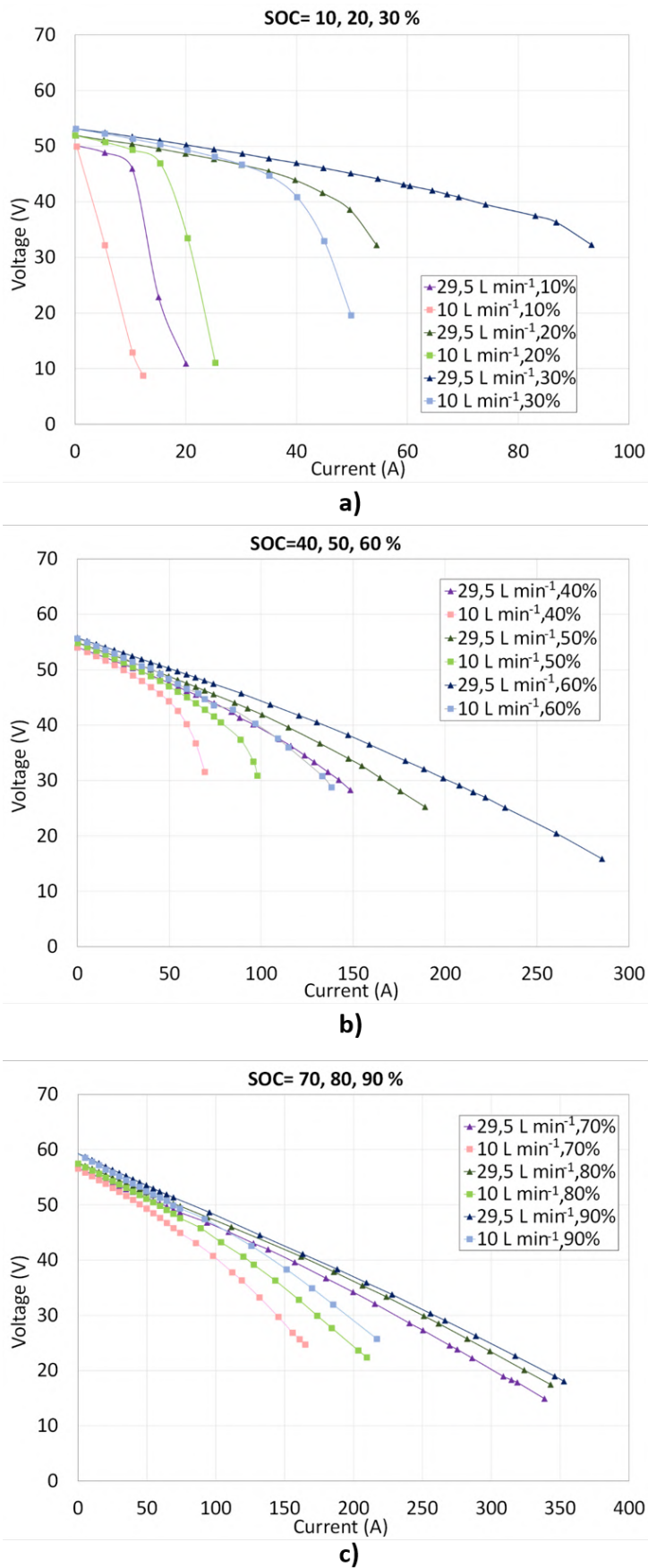


FIGURE 8.10: Experimental polarization curves (V vs. I) during discharge obtained on the IS-VRFB test facility at different flow rates: $Q=10 \text{ L min}^{-1}$ ($q= 6.9 \cdot 10^{-3} \text{ cm s}^{-1}$) and 29.5 L min^{-1} ($q= 20.5 \cdot 10^{-3} \text{ cm s}^{-1}$): a) $SOC = 10\%, 20\%, 30\%$; b) $SOC = 40\%, 50\%, 60\%$; c) $SOC = 70\%, 80\%, 90\%$.

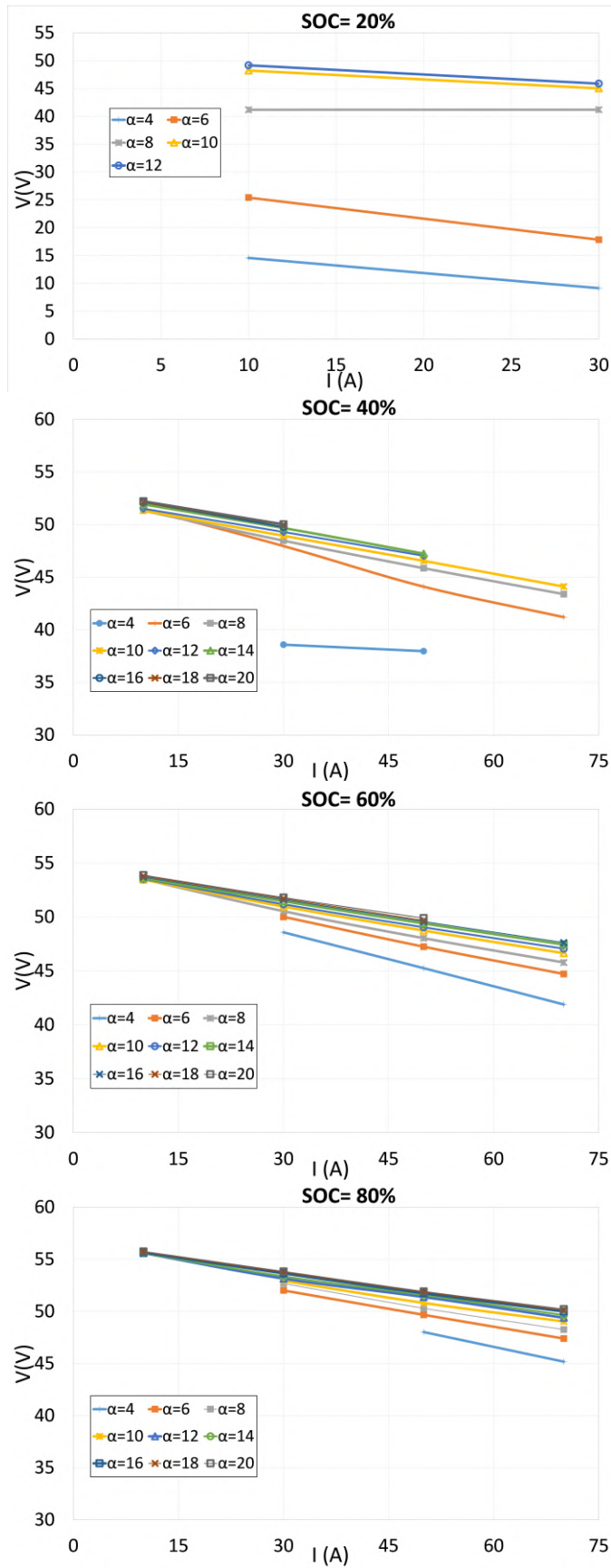


FIGURE 8.11: Experimental polarization curves (V vs. I) during discharge obtained on the IS-VRFB test facility at fixed flow factors α ($\alpha=4, 6, 8, 10, 12, 14, 16, 18, 20$).

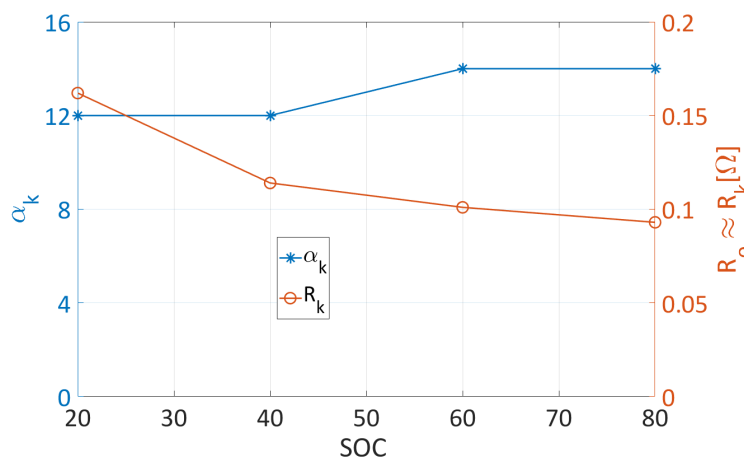


FIGURE 8.12: Key flow factor α_k and corresponding key electrical resistance $R_o \simeq R_k$ vs. SOC

8.3.1 Optimal flow rate identification

In order to investigate this behavior, a new set of polarization curves $V(I)$ was built by using the measurements of a new experimental campaign carried out at different $SOCs$, in which Q was continuously varied so as to keep α constant while increasing I , exploiting the operational flexibility allowed of the pumps feedback control. Several α values could be explored (up to 9 for each SOC) with the lower and upper limits imposed by the minimum and maximum pump flow rates, i.e. $Q = 3 \text{ L min}^{-1}$ and $Q = 29.5 \text{ L min}^{-1}$.

Fig. 8.11 shows these polarization curves drawn at constant α for four $SOCs$. Each curve appears linear, resulting in a constant internal resistance R_i , with no dramatic increases at high currents. In addition, the reduction of the slope with increasing α results in a lower and lower R_i . As α is increased and approaches a key value α_k , these polarization curves converge to a limit linear profile with a minimal slope, namely with minimal internal resistance $R_k = -\Delta V_k / \Delta I$ and the cell electrical performance cannot be enhanced any more by increasing α .

These results indicate that, when a VRFB is operated at fixed Q , transport losses are important as long as $\alpha < \alpha_k$. Conversely, when α is higher than α_k the ohmic losses are the dominant effect that produces the linear behavior of $V(I)$. Once the concentrations of the reactant ions supplied at the active sites in the porous electrodes exceeds the values needed to efficiently sustain the reactions, a further increase of the flow rate cannot improve the reaction rate anymore. In these conditions, the transport equivalent resistance R_t becomes much smaller than the ohmic equivalent resistance R_o . This latter resistance depends on the cell and electrolyte electric properties but not on the electrolyte flow rate, in such a way that at constant SOC the relationship between voltage and current results linear. Fig. 8.12 shows that α_k is a weakly increasing function of SOC .

We infer that controlling Q according to each different operating condition, namely according to SOC and I , so as to maintain $\alpha \simeq \alpha_k$, constitutes an optimal strategy for maximizing the electrical performance of a VRFB, i.e. for minimizing the hydraulic losses without affecting the power conversion performance.

8.3.2 Characterization at $\alpha \geq \alpha_k$

Since the convergence profile of all polarization curves at $Q = const$ and $\alpha \geq \alpha_k$ is linear, it is characterized only by its slope, i.e. by its key internal resistance, $R_k = \Delta V_k / \Delta I$ that is a function of the SOC only: $R_k(SOC)$. Similarly to the ohmic losses that it represents, the resistance R_o included in Eq.8.15 depends on the resistive behavior of the bipolar plates, of the ions-saturated porous electrodes, of the ion exchange membrane and of the contacts between these components. Instead, R_o does not depend on α and, consequently, any increase of R_i

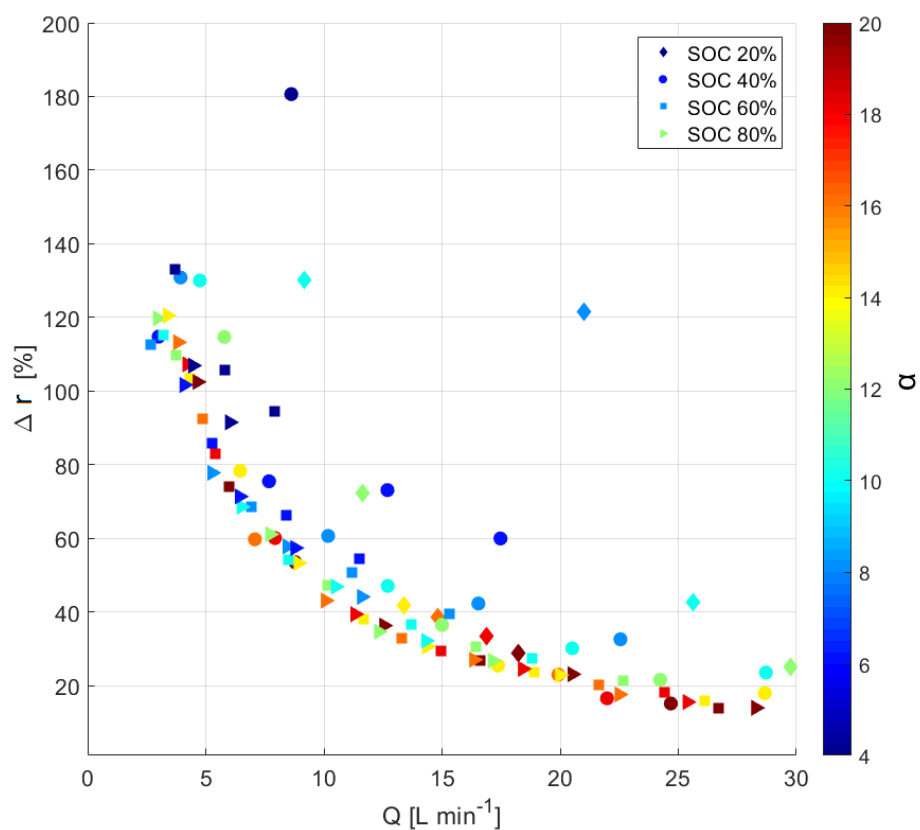


FIGURE 8.13: Relative difference between resistance R_i and R_k at different flow rate Q , different flow factor α and different SOC . Data point are code-colored as function of α , showing that as α increases this fraction Δr tends to a minimum value dependent on Q and independent of SOC

occurring when α is smaller than α_k can be attributed to the transport losses represented by R_t . Hence, we can assume that:

$$R_o \simeq R_k \quad (8.16)$$

On the other hand, at different SOC , the electrolyte ion concentrations in the porous electrodes changes, causing a variation of the ohmic resistance $R_o = R_o(SOC)$. Fig. 8.12 shows that R_o is a decreasing function of SOC , due to the higher concentration of reagent ions in the electrolytes at larger SOC when the battery is discharging. In order to check the consistency of the previous assumptions, R_o was evaluated as the series of the cell membranes, with total resistance R_m , of the cell porous felt electrodes, with total resistance R_e , and of the the graphite bipolar plates, with total resistance R_b . The contact resistances were neglected:

$$R_o = R_m + R_e + R_b \quad (8.17)$$

R_m was determined from the area specific resistance (ASR) data of Nafion[®] 212 [365] and R_b from the conductivity provided in graphite plate data sheet (TF6 fluor polymer bipolar plate by SGL Carbon, Germany) [366]. The calculation of the carbon felt resistance R_e took into account the electronic conduction in the solid phase (i.e. the porous felts) and the ionic conduction in the liquid phase (i.e. the electrolytes). For the sake of simplicity, the Bruggeman correlation was used to evaluate the effective conductivity σ_f^{eff} of the porous felts [330]:

$$\sigma_f^{eff} = \sigma_s(1 - \varepsilon_c)^{1.5} \quad (8.18)$$

where σ_s is the conductivity of the solid material constituting the felts and ε_c is their porosity after compression [367]:

$$\varepsilon = \frac{\varepsilon - \varsigma}{1 - \varsigma} \quad (8.19)$$

In Eq. 8.19, ε is the porosity before compression and ς is the felt compression ratio defined as:

$$\varsigma = 1 - \frac{h_{cr}}{h_0} \quad (8.20)$$

where h_0 and h_{cr} are the average electrode thickness before and after compression, respectively. Taking again into account the Bruggeman correlation, the effective electrolyte conductivity σ_{el}^{eff} at the positive and negative compartments was evaluated as:

$$\sigma_{el}^{eff} = \frac{F^2}{KT} \sum_j c_j z_j^2 \sigma_j \varepsilon_c^{1.5} \quad (8.21)$$

where K is the gas constant, T is the temperature, z is the number of electrons transferred in the reaction, c is the concentration of the reacting species and the subscript j stands for the species $V(IV)$, $V(V)$ in the positive electrode and for $V(II)$, $V(III)$ in the negative one. Given the state of charge of the positive and negative electrolytes SOC_+ and SOC_- and their total concentrations $c_+ = c_- = c_V$, each species concentration is given by:

$$c_{II} = c_- SOC_- \quad c_{III} = c_- (1 - SOC_-) \quad (8.22)$$

$$c_{IV} = c_+ (1 - SOC_+) \quad c_V = c_+ SOC_+ \quad (8.23)$$

The resistances R_e of the porous electrodes soaked with liquid electrolytes were obtained as the parallel resistances of the two phases, for each cell compartment:

$$R_e = \left(\frac{1}{\sigma_f^{eff} + \sigma_{el+}^{eff}} + \frac{1}{\sigma_f^{eff} + \sigma_{el-}^{eff}} \right) \frac{Nh_{cr}}{A} \quad (8.24)$$

The parameters used in these calculations are listed in Tab.8.3. Measured and computed values of R_o present an acceptable agreement for the aim of this analysis. Results show that

TABLE 8.3: Stack components physical properties

Component	Property	Value	Reference
Nafion® 212 membrane	Membrane area resistance (ASR) [$\Omega \text{ cm}^2$]	0.41	[365]
Beijing Great Wall, carbon felt electrode	Solid electrode conductivity σ_s [S m^{-1}]	1000	[330]
/	Felt porosity before compression ε	0.94	[128]
/	Felt thickness before compression h_0 [mm]	8.1	/
/	Felt thickness after compression h_{cr} [mm]	5.7	/
/	Felt compression ratio	0.3	/
TF6 fluor polymer bipolar plate by SGL Carbon	Bipolar plate resistivity σ_b [$\Omega \text{ cm}$]	7.6×10^{-4}	[366]
Liquid electrolyte	$V(II)$ conductivity σ_{II} [S m^{-1}]	27.5	[74]
/	$V(III)$ conductivity σ_{III} [S m^{-1}]	17.5	[74]
/	$V(IV)$ conductivity σ_{IV} [S m^{-1}]	27.7	[74]
/	$V(V)$ conductivity σ_V [S m^{-1}]	41.3	[74]

the electrodes provide the major contribution to the ohmic resistance, being R_e at least 70 % of R_o ; the membrane resistance R_m contributes for about 20% and the graphite bipolar plate resistance R_b only for 10%. This evidence is in agreement with the results reported by Ke et al. [72], indicating that in the flow-through distribution the contribution of the electrodes to the ohmic resistance is much higher than in other distributions, such as flow-by. In addition, the dependence of R_e on the SOC , expressed in Eqs.8.21, 8.23 and 8.24 explains the behavior of R_o shown in Fig. 8.12.

8.3.3 Comparison of the loss equivalent resistances

The minimum internal electrical resistance $R_k(SOC) = -\Delta V_k/\Delta I$ involves that at a given SOC R_k presents the same linear behavior of $V(I)$ for any Q with $\alpha \geq \alpha_k$. In this condition, the electric power delivered by the battery at a given SOC can be expressed as $P = V_0 I - R_k I^2$ with a constant $R_k \approx R_o$. In order to characterize the activation and transport losses in any conditions with $\alpha \leq \alpha_k$, Eqs.8.14, 8.15 and 8.16 can be combined to obtain:

$$\Delta V = R_i I = (R_k + R_t + R_a) I \quad (8.25)$$

As far as $R_k(SOC)$ is known, by measuring $R_i = \Delta V/I$ at different SOC and Q , and thus at different α , from Eq. 8.25 we obtain:

$$R_a + R_t = R_i - R_k \quad (8.26)$$

Since $R_k = -\Delta V_k/\Delta I$ expresses the local slope of the polarization curve at $\alpha \geq \alpha_k$ starting from a current value $I > 0$, i.e. in the full linearity ohmic region, and R_i expresses the mean slope of the polarization curve starting from $I = 0$, Eq. 8.26 and also the relative difference $\Delta r = (R_i - R_k)/R_k$ constitutes an index of the incidence of $R_a + R_t$ and also of the non-linearity of the polarization curves. The plot also confirms that transport losses are the leading effect at small α : in these conditions R_t increases as α reduces and it can become even one order of magnitude larger than R_k . On the other hand, when both I and Q are small and $\alpha \rightarrow \alpha_k$ transport losses are small (i.e. R_t vanishes) and activation losses (i.e. R_a) become not negligible: they allow all polarization curves with the same SOC to start from the same OCV : $V_0(SOC)$, as can be inferred from Fig.8.11. It must be remarked that, once α reaches α_k ensuring that the

dominating resistance is R_o , increasing the flow rate only results in an increase of the hydraulic losses with no beneficial effect on the power conversion.

It is worth noticing instead that, once the optimal flow regime is achieved, i.e. the battery operation is optimized, a further reduction of the internal losses, i.e. of R_k , can be obtained from an improved cell design. At this regards, tortuous porous microstructure of the electrodes, if properly designed, can promote a more efficient macroscopic diffusion of the species flowing through the electrodes: the faster the electrolyte mixes in the electrode pores, the higher the reaction rate. Recent studies [368, 369] indicate that this process involves an anomalous diffusivity, namely that the diffusion process presents a non-linear dependence on time. This means that the mean squared displacement (MSD) of the fluid particles varies more than linearly with time, whereas in a classical diffusion process this increase is linear [370]. However, at the aim of an easy calculation, an effective diffusivity coefficient in the porous electrode can be used which, for liquids, is proportional to the average flow velocity, i.e. to Q , as usually done when resorting to the Bruggeman correlation.

The performance of a VRFB also depends on temperature: our tests were performed at a room temperature of 20 °C and the losses heat was removed by natural convection at piping and tanks. Temperature measurements picked up by the stack inlet and outlet sensors showed that the solution over temperatures during charge and discharge operations remained in the order of few degrees. More extended investigations on the correlation between battery performance and temperature were out of the scope of this paper and were reported elsewhere in the case of high-current operations [371] and stand-by conditions [313].

8.3.4 Stack hydraulic losses computation

In this section, analyses of the pump losses based on the experimental data are reported. From the experimental tests, the pump power needed to circulate the electrolytes and differential pressure between the inlet and outlet of the stack are analyzed to study the relation between these data and the flow rate, to observe a correlation with the theoretical results.

The pressure drop between the inlet and outlet of the stack can be obtained by Darcy's law:

$$\Delta P_s = \frac{\mu l'_x \varepsilon_c Q}{\aleph l'_y l'_z N} \quad (8.27)$$

where Q is the flow rate, l'_x , l'_y , and l'_z are the length, width, and thickness of the porous electrode, ε_c is the porosity of the porous electrode, μ is the dynamic viscosity, N is the number of cells, and \aleph is the permeability. These specifications are summarized in Tab.8.4.

TABLE 8.4: Specifications of IS-VRFB stack for pressure drop computation.

<i>Parameters</i>	<i>Description</i>	<i>Value</i>
l'_x	felt length (flow direction)	0.2 [m]
l'_y	felt length (width direction)	0.3 [m]
l'_z	felt length (thickness direction)	0.0057 [m]
l_{pi}	total length of the straight pipes (positive side \approx negative side)	3.96 [m]
D	pipe diameter	0.027 [m]
ε_c	porosity	0.69

The total stack power lost P_s inside the stack can be found by the product between the pressure drop and the total flow rate as follows:

$$P_s = \Delta p_s Q \quad (8.28)$$

And considering the ΔP_s defined in Eq.8.27:

$$P_s = \frac{\mu l'_x \varepsilon_c}{k l'_y l'_z N} Q^2 \quad (8.29)$$

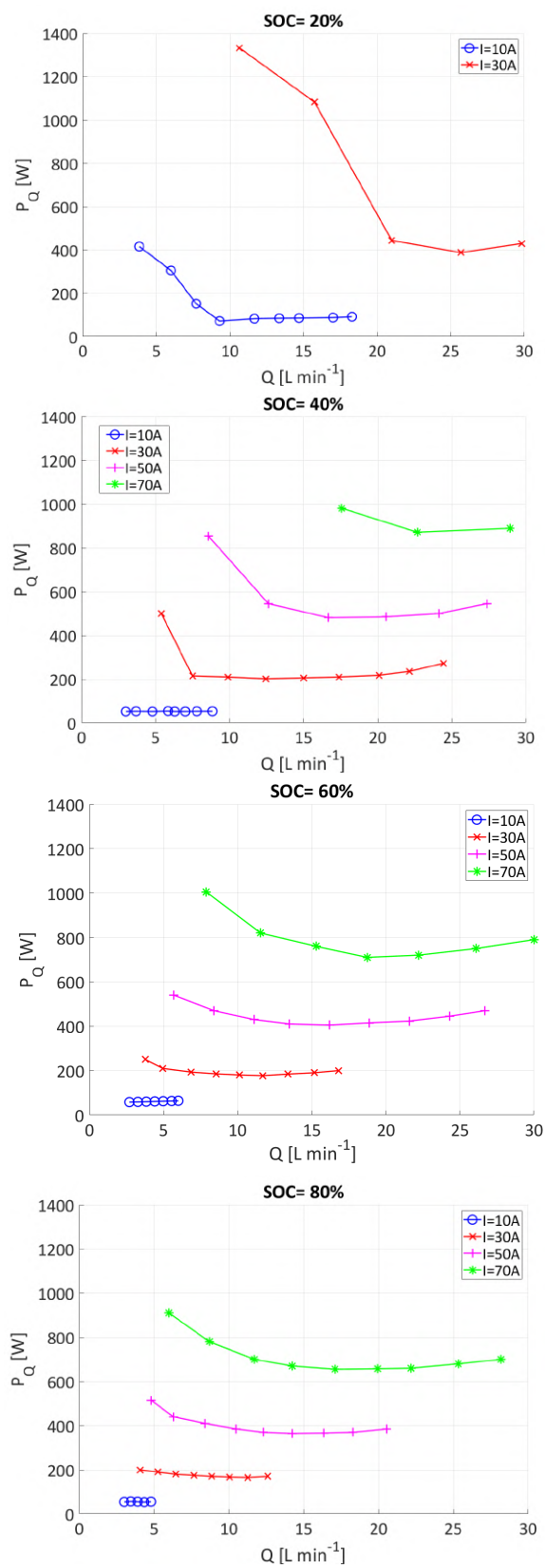


FIGURE 8.14: Flow-rate dependent losses P_Q by contours plotted for different current I and flow rate Q .

From the experimental results, it is expected that a relation with the flow rate will be found that is at least quadratic, according to the theory. The Fig.8.15, shows that this relation is a little more than quadratic. This is probably due to inertial effects at high values of flow rate when the Reynolds number is higher. The data fit of P_s at various SOC s as a function of flow rate is summarized in Tab.8.5.

TABLE 8.5: Data fit of $P_s(Q)$.

SOC [%]	P_s vs Q	R -square
20	$P_s = 2.44E + 8Q^{2.26}$	0.9999
40	$P_s = 1.98E + 8Q^{2.24}$	0.9998
60	$P_s = 1.68E + 8Q^{2.22}$	0.9999
80	$P_s = 1.42E + 8Q^{2.21}$	0.9998

The previous figures also show the pump power P_w measured, which is needed for the functioning of the plant. As is evident, this pump power is much greater than the total stack power lost inside the stack (as already noticed in Sec.8.1.4).

This ratio enhanced rapidly to a certain value of flow rate, and then it stabilized to a value approximately equal to 16%. This behavior is caused by the low flow rates and their low values of pump efficiency that affect system efficiency. This ratio seems very low and fits with the considerations reported in Sec.8.1.4.

8.4 Identifying optimal flow rate modulation

The identification of the optimal flow rate modulation made use data of the Q -dependent losses, i.e. the internal losses due to cell overpotentials $P_i = R_i I^2$ and the total losses P_w in the hydraulic circuits and their ancillaries, which occur in the stack, in the piping connecting stack and tanks, in the pumps, in the driving motors and in the controlling inverters. In IS-VRFB, P_w is provided by the specific wattmeter interposed between grid and inverters [344]:

$$P_Q = P_i + P_w \quad (8.30)$$

It must be noted that on the one hand P_Q also depend on the stack current I and on the SOC and, on the other hand, that the battery electric performance is also affected by the losses due to species crossover through the membranes, shunt currents and the losses in the power management system PMS. However these last losses do not vary with Q , so that they were not taken into account in the optimization of the flow rate.

Fig.8.14 shows the profiles of P_Q as functions of the flow rate Q at different I and SOC values and Tab.8.6 presents the combination of Q , SOC and I values used to build such profiles. The profiles highlight that every curve presents a minimum: the electrolyte flow rate Q that minimizes P_Q at every SOC and I defines the flow factor α that ensures optimal operation, i.e. minimal losses and maximum efficiency. The results in Fig.8.14 regard discharge operations, but similar considerations hold in the case of charge.

8.5 Implementation and validation

8.5.1 Implementing the control algorithm

The implement the optimal control was made at a software level, by developing an apposite LabVIEW algorithm in the BMS of IS-VRFB. Such algorithm uses the experimental data illustrated in Fig.8.14 and 8.6. At this aim, these data were arranged in a 3-D matrix, as functions of Q , SOC and I values. The algorithm uses the matrix as a look-up table in order to identify the optimal Q_{opt} which minimizes P_Q for each couple of SOC and I operating values. Q_{opt} is then compared with the actual Q measured by the flowmeters and error signals are created which feed back the pump inverters with PID control routines. In this way, the actual Q , and hence

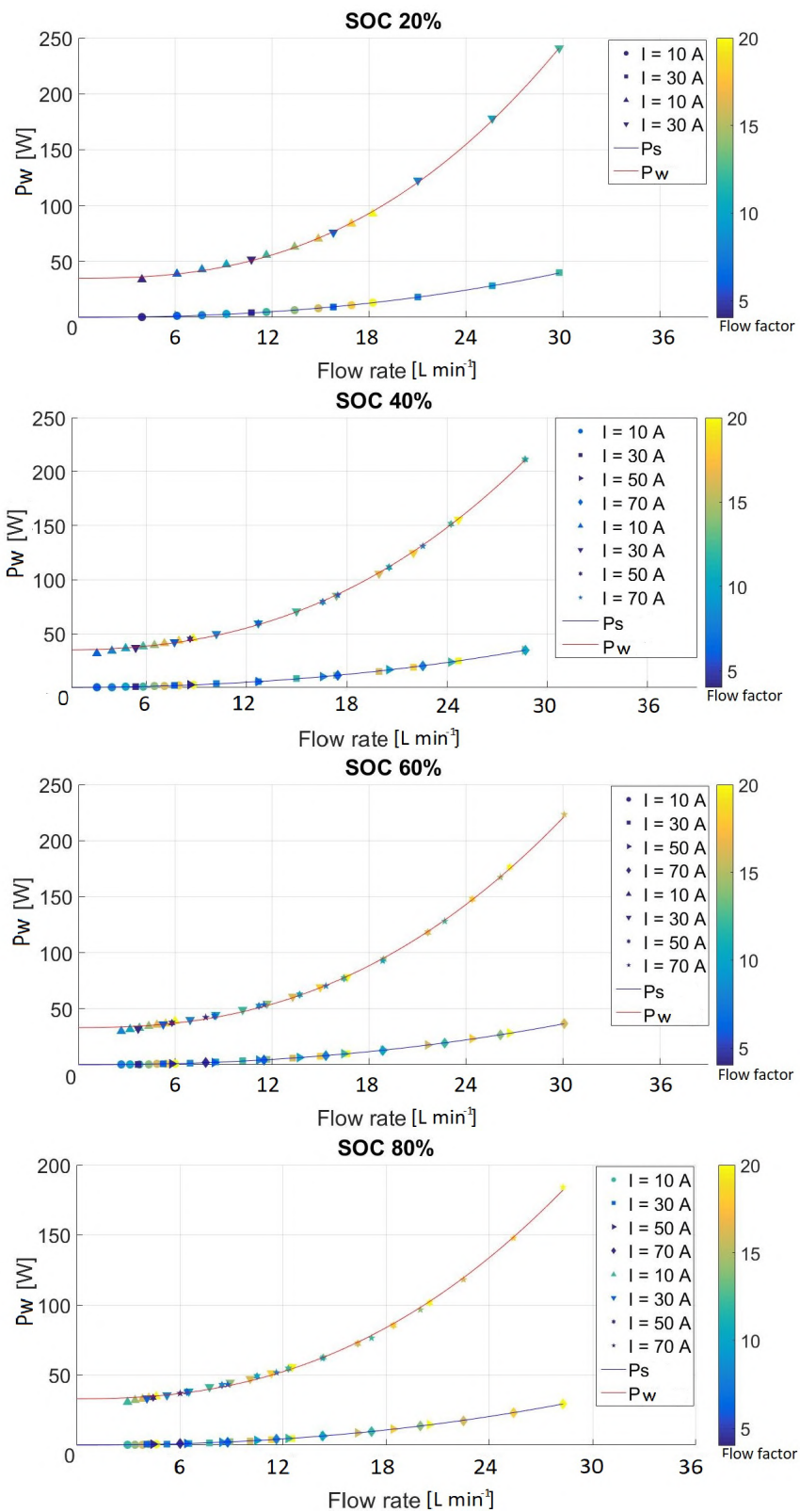


FIGURE 8.15: P_w and P_s vs flow rate with different SOC's.

TABLE 8.6: Experimental campaign for optimal flow rate identification

<i>SOC</i> [%]	Applied current <i>I</i> [A]	Flow factor α [-]
20	10	4, 6, 8, 10, 12, 14, 16, 18, 20
20	30	4, 6, 8, 10, 12
40	10	6, 8, 10, 12, 14, 16, 18, 20
40	30	4, 6, 8, 10, 12, 14, 16, 18, 20
40	50	4, 6, 8, 10, 12, 14
40	70	6, 8, 10
60	10	8, 10, 12, 14, 16, 18, 20
60	30	4, 6, 8, 10, 12, 14, 16, 18, 20
60	50	4, 6, 8, 10, 12, 14, 16, 18, 20
60	70	4, 6, 8, 10, 12, 14, 16
80	10	12, 14, 16, 18, 20
80	30	6, 8, 10, 12, 14, 16, 18, 20
80	50	4, 6, 8, 10, 12, 14, 16, 18, 20
80	70	4, 6, 8, 10, 12, 14, 16, 18, 20

TABLE 8.7: Round trip efficiency (*RTE*) at different *SOC* range and current *I* at fixed α and modulated α .

<i>I</i> [A]	<i>SOC</i> range [%]	<i>RTE</i> [%]	
		fixed α	modulated α
30	13.1 – 87.0	70.35	72.41
50	19.9 – 78.5	67.10	69.05
70	28.0 – 72.7	62.42	63.95

the actual α , is continuously modulated to match the minimum P_Q during the whole battery operation.

8.5.2 Validation tests

An experimental analysis of the effectiveness of the proposed optimal control of the electrolyte flow rate was performed [344]. These validation tests were carried out on IS-VRFB in charge/discharge cycles and the round-trip efficiency (*RTE*) was considered as the performance figure (the cost function of the optimization procedure). Consistently with the scope of the investigation, a definition of *RTE* was assumed that includes all Q -related losses P_Q [372]:

$$RTE = \frac{\int_0^{t^{dh}} [P(t) - P_w(t)] dt}{\int_0^{t^{ch}} [P(t) + P_w(t)] dt} \quad (8.31)$$

where $P(t) = V(t)I(t)$ is the electric power converted (consumed/delivered) by the stack. Results of the charge and discharge tests were compared with similar tests performed at constant α . In particular, a benchmark α was adopted, in accordance with the optimal $\alpha = 7.5$ reported in the literature [364]. Comparative tests showed that an increase of around 2% of the *RTE* when operating the VRFB at modulated flow factor with the respect to the operation at constant α , as shown in Tab.8.7.

8.5.3 Key points

The experimental study performed on the 9 kW / 27 kWh IS-VRFB test facility has shown the effectiveness of modulating the electrolyte flow rate and flow factor in order to minimize the stack transport losses without affecting the electrical performance of a redox flow battery during charge and discharge cycles. This maximization of the efficiency requires to control the electrolyte flow rates so as to minimize the flow-rate depended losses under the constraint of providing a key flow factor to properly sustain the stack current at every electrolyte *SOC*, i.e.

with minimized transport losses. We have found that operating the battery at $\alpha \approx \alpha_k(SOC)$ allows to minimize the cell internal losses leading to an increase of the *RTE* of around 2% with respect to an operation at optimal constant flow factor (i.e. at $\alpha = 7.5$ as proposed in previous reports [364]).

Notably, the proposed flow factor modulation can be implemented at a software level in the control routines of the system supervisor (i.e. the BMS), without modifying the system hardware. The procedure required a preliminary experimental campaign that consists in mapping the flow factor values at different Q .

It is worth noting that the procedure here presented has a wide applicability and can be adopted in other RFBs, made with different materials for membranes and porous electrodes and even based on other chemistries.

In addition, from the present study two directions for future development emerge. On the one hand, the ohmic resistance results the leading parameter at optimized flow rate: reducing it will allow to achieve larger limiting currents and higher deliverable powers. This target can be achieved by focusing on the electrode resistance that can constitute the major contribution to the total ohmic resistance, particularly in the case of flow-through architecture as in IS-VRFB. On the other hand, a reduction of the value of α_k and of the consequent pumping power can be achieved using specifically designed porous electrodes with microstructure capable of enhancing electrolyte dispersion, to minimizing the transport losses [128].

Chapter 9

Fast response analyses

According to the scale-up challenge, transient characteristics of large VRFB systems assume crucial importance in guaranteeing VRFBs employment, especially in frequency regulation [373]. In general, the transient characteristics are well known as the important feature of the battery [374] and the VRFB presents a "high" response time according to Skyllas-Kazacos et al. [42]. To take advantage of the fast response of a VRFB, power conversion circuits [375], [359], [316] and flow management [358], [240], [318] need to be designed with a better understanding of this phenomenon. In [376] the energy and power response capability of 5 kW/10 kWh and 0.5 MW/1 MWh VRFB systems are experimentally investigated in terms of charge/discharge power rating and time, resulting in threshold values of 1.4 and 1.35, respectively. In [377], a physics-based model was developed for predicting the power range of large-scale VRFB systems, and in [322] an analytical method successfully predicted the discharge voltage when a VRFB operates under different temperatures, to aid the design optimization process. In addition, [329] established a relationship between the limiting current density and operating conditions with some experimental results in a $3.2 \times 3.2 \text{ cm}^2$ single cell.

In [378], a real-time peak power estimator was built based on an on line adaptive battery model with an experimental validation on a 100 cm^2 single cell. However, an extensive experimental campaign, which enabled the investigation of the fast response of a large-scale VRFB system in a wide range of operating conditions was largely overlooked, especially in terms of the first milliseconds time scale, the stack current, voltage, and power timing evolution. According to the authors, such a campaign can constitute a valuable tool for providing important information that can increase the potential applications of this technology. In addition, further analyses of the voltage evolution of each cell in different operating conditions can become important for evaluating the IS-VRFB stack design, especially in terms of electrolyte flow distribution.

9.1 Theoretical Background

The output of electrical power depends on the internal state of the cell that changes during operation by varying current and flow rate. To consider the transient mass transport phenomena in the cell, the main and side electrochemical reactions during the charge–discharge process were coupled with the mass balance equations for the negative and positive half-cell, as described in Sec.5.4, ([371]). In general, the cell internal state depends on the vanadium species concentrations, which represent the main state variable, the gradient of which can be written as follows:

$$\frac{V_c}{2} \frac{\partial C_j}{\partial t} = f(Q, CO, I) = Sh_Q + Sh_{CO} + Sh_I \quad (9.1)$$

where C_j is the cell specific molar concentration (mol m^{-3}) for the j -th vanadium ions with $j=II, III, IV, V$ and Sh_Q, Sh_{CO} , and Sh_I are the flow rate, crossover, and current dependent shares that affect the concentration gradient in each cell. Regarding the fast response analyses that evaluates a limited time in the range of few minutes, the absence of ion crossover through the membrane (and consequently of the side reactions) appear a reasonable assumption [377],

[319], which results in neglecting *SOC*. In this case, the concentration gradient of each cell can be formulated as follows:

$$\frac{V_c}{2} \frac{\partial C_j}{\partial t} = Sh_Q + Sh_I = Q_c(C_{j,T} - C_j) + \frac{I}{F} \quad j=II \text{ and } V \quad (9.2)$$

$$\frac{V_c}{2} \frac{\partial C_j}{\partial t} = Sh_Q + Sh_I = Q_c(C_{j,T} - C_j) - \frac{I}{F} \quad j=III \text{ and } IV \quad (9.3)$$

Clearly, the internal state of the cell can be described by means of the *SOC*, which is given by the ratio between the concentrations of the charged species and all species in each half-cell Eq.5.20. The output effect is the *OCV* computed by means of the Nernst equation Eq.5.21, and the stack voltage output, which is affected by three different losses that can be modelled as equivalent electrical resistances Eq.8.14.

9.2 Experimental method

To describe the fast-dynamic response of an IS-VRFB quantitatively, stack voltage and current were acquired immediately after the connection of a resistive load to the stack. Two different time intervals involving different phenomena occurring in the cell were analyzed. In the first case, the first 20 mS were acquired using an oscilloscope (RIGOL DS1204B) with a sample rate of 2 GSa s⁻¹. The voltage and current measurements of the stack were performed using two different channels of the oscilloscope connected directly to the output voltage of LEM CV 3-100/SP3 and LEM HASS 200-S, respectively, for the voltage and current.

Both provided a transduced voltage output signal with a different scale that could be acquired directly by the oscilloscope providing instantaneous values of the real stack voltage and current. In the second case, the first 120 s were considered and LabVIEW system acquisition was used with a sample rate of 0.8 Sa s⁻¹. In this interval, high discharge current could alter the passive load resistance due to a temperature increase. In this regard, some tests were conducted to verify the constant value of the resistance along this time interval and to guarantee the test conditions. These tests proved that the resistance remain constant in the range of ±1%.

9.3 Results and discussion

Different conditions were examined, to explore the VRFB fast response more widely, by varying *SOCs*, flow rates, and passive load. Three *SOCs* were considered: 20%, 50%, and 90%, with three different stack flow rates (*Q*), i.e. 10 L min⁻¹, 20 L min⁻¹, and 30 L min⁻¹, which correspond to (*q*): 6.9×10⁻³ cm s⁻¹, 13.8×10⁻³ cm s⁻¹, and 20.7×10⁻³ cm s⁻¹, respectively, in terms of specific flow rates. In addition, three different loads were used, which correspond to three different discharge currents for each condition. In the following analyses, these are referred to as small load (*sl*), medium load (*ml*), and high load (*hl*), corresponding to 0.17 Ω, 0.34 Ω, and 1 Ω, respectively.

Overall, 27 tests were carried out in both time intervals. For the sake of simplicity, nine tests are represented in a graph in Fig.9.1. Three flow rates for each *SOC* are shown by using a common load: *sl* in 90%, *ml* in 50%, and *hl* in 20%. Similar behavior and information can be found in the other cases. The first 20 mS presented a common "peak transient" region in all cases, in which both current and voltage changed more, even up to 50%. This time region never exceeded 7 ms and the stack could not provide useful power suitable for real application.

Then, a "peak steady" region occurred, where the peak values appear (referred to as *I_p* and *V_p*), which represent the maximum values reached for the entire duration of the tests. As can be seen for each state of charge, both *I_p* and *V_p* did not depend on the flow rate during the first 20 mS using the same load. Clearly in this time scale, only the reactant species already present in the cell participated in the reaction without any contribution of the flow rate dependent share *Sh_Q* in the cell concentration gradient, (Eqs.9.2, 9.3). For the large time scale, different behaviors occurred depending on the flow rate, *SOC*, and passive load. Clearly, the higher the flow rate and *SOC* the shorter the transient regime ("complete transient") and a "complete steady" regime is achieved (Fig.9.1) with constant current and voltage values over time. This is due to the higher

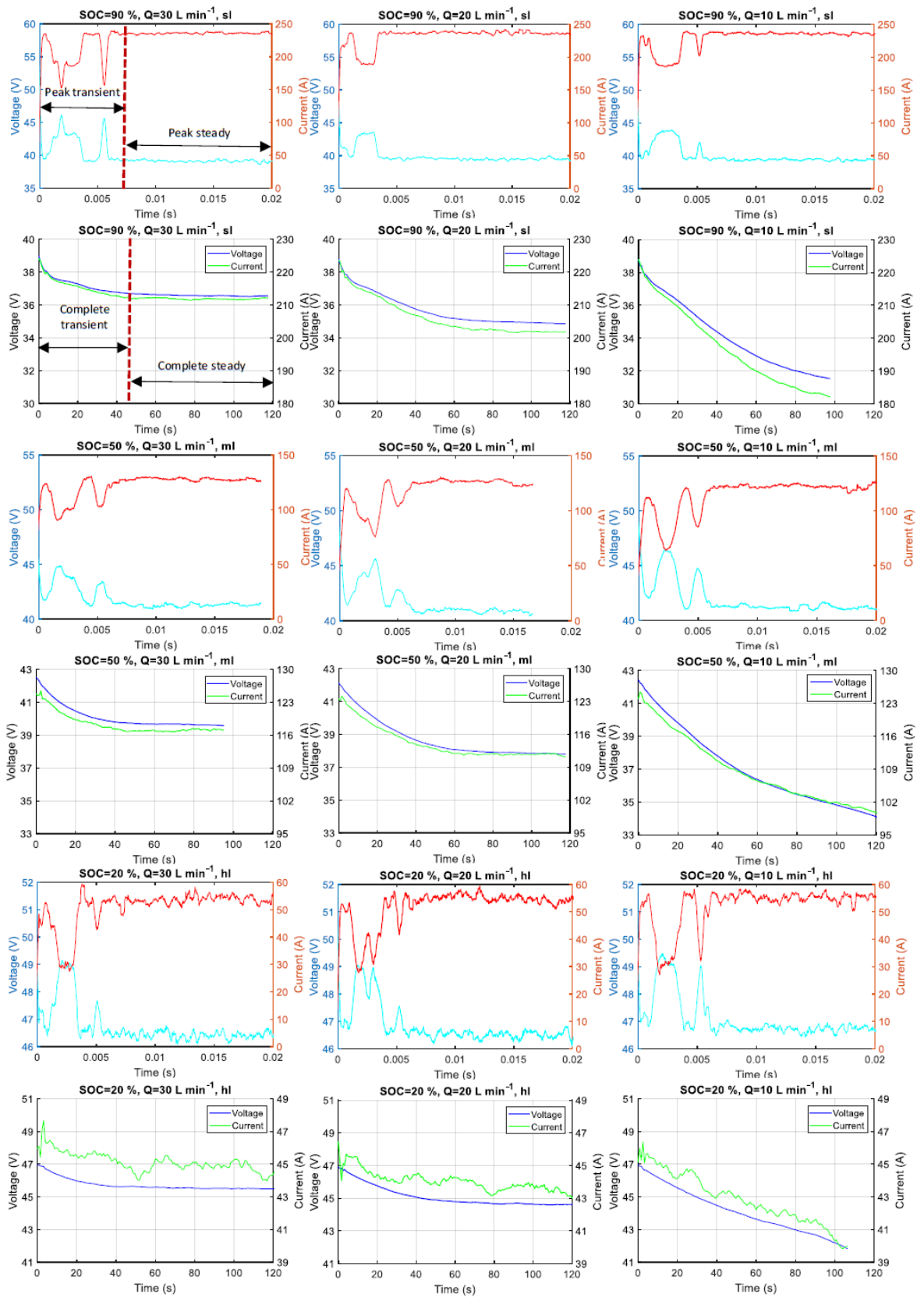


FIGURE 9.1: Current and voltage trend over time in 0–20 ms and 0–120 s time range.

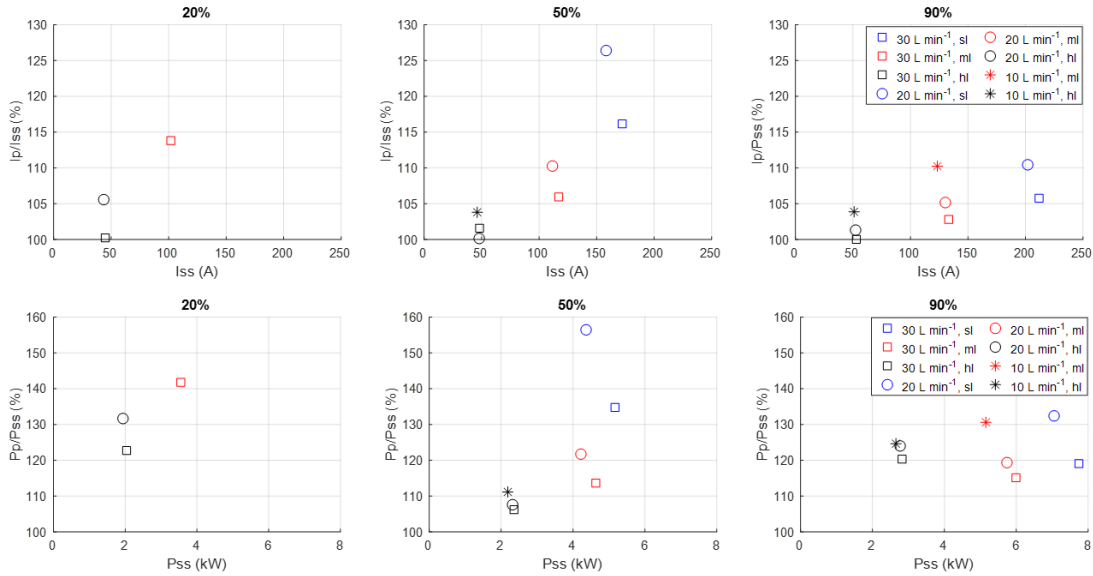


FIGURE 9.2: Current I_p/I_{ss} and power P_p/P_{ss} ratios evolution v.s. Q , SOC and load.

value of the flow factor α that represent the ratio between the flow of electrolyte charges and the current intensity Eqs.8.12, 8.13. The larger α the smaller the concentration gradient in the cell, which means a fairly constant electrical response over time. This time with transitory behavior is included between 40 s and 80 s, and depends on transport resistance (which is higher as the flow rate reduces). In some tests with small flow, small SOC, and small load, the complete steady regime was not reached (Fig.9.1), and the test was stopped before 120 s after a continuously decreasing trend. Fig.9.2 shows the ratio between the peak current I_p and the steady state current value I_{ss} , in all the tests in which it appears. For each flow, this ratio increases with the steady state current I_{ss} , but it increases much more with lower SOC, clearly due to the lower α values. This ratio is between 100% and 130%.

In both time scales, voltage and current presents the same behavior. In the "transient peak" region (i.e. the first 7 mS), a current increase corresponds to a decrease in voltage unlike the other regions, where the opposite occurs. These trends can be shown more clearly in the power graph, in which power follows the tendency of voltage and current and represents a useful engineering feature in real applications (Fig.9.3). In the power case, the ratio P_p/P_{ss} behaves similarly to the current case but some important differences appear. The range is between 100% and 160% and for each flow, this ratio increases with the steady state power P_{ss} much more that with the lower SOC. Moreover, at SOC=90% this ratio remains fairly constant between 115% and 135%. Indeed, at higher power operation with a higher current ≈ 250 A, the stack overpotential does not present a significant difference between P_p and P_{ss} .

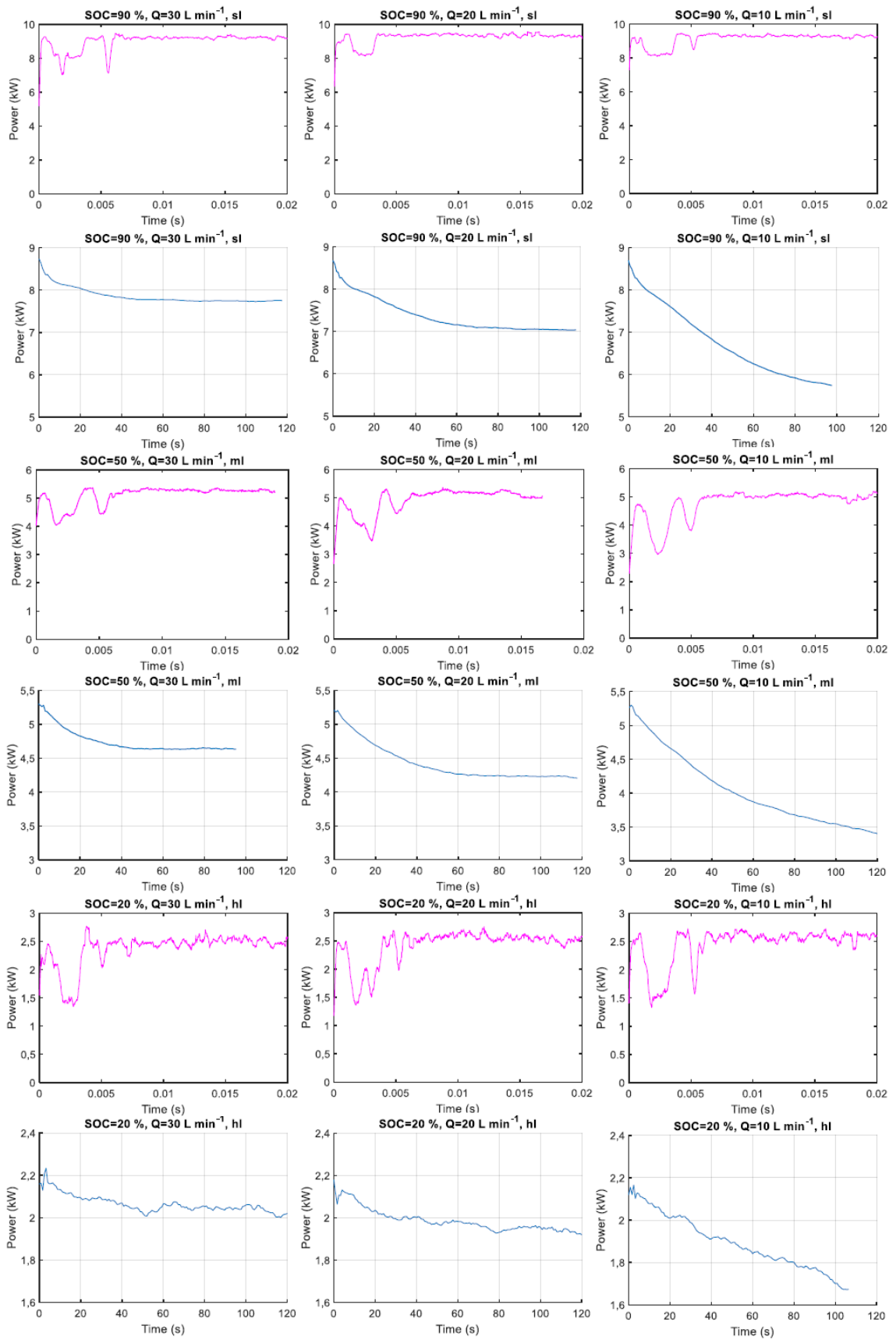
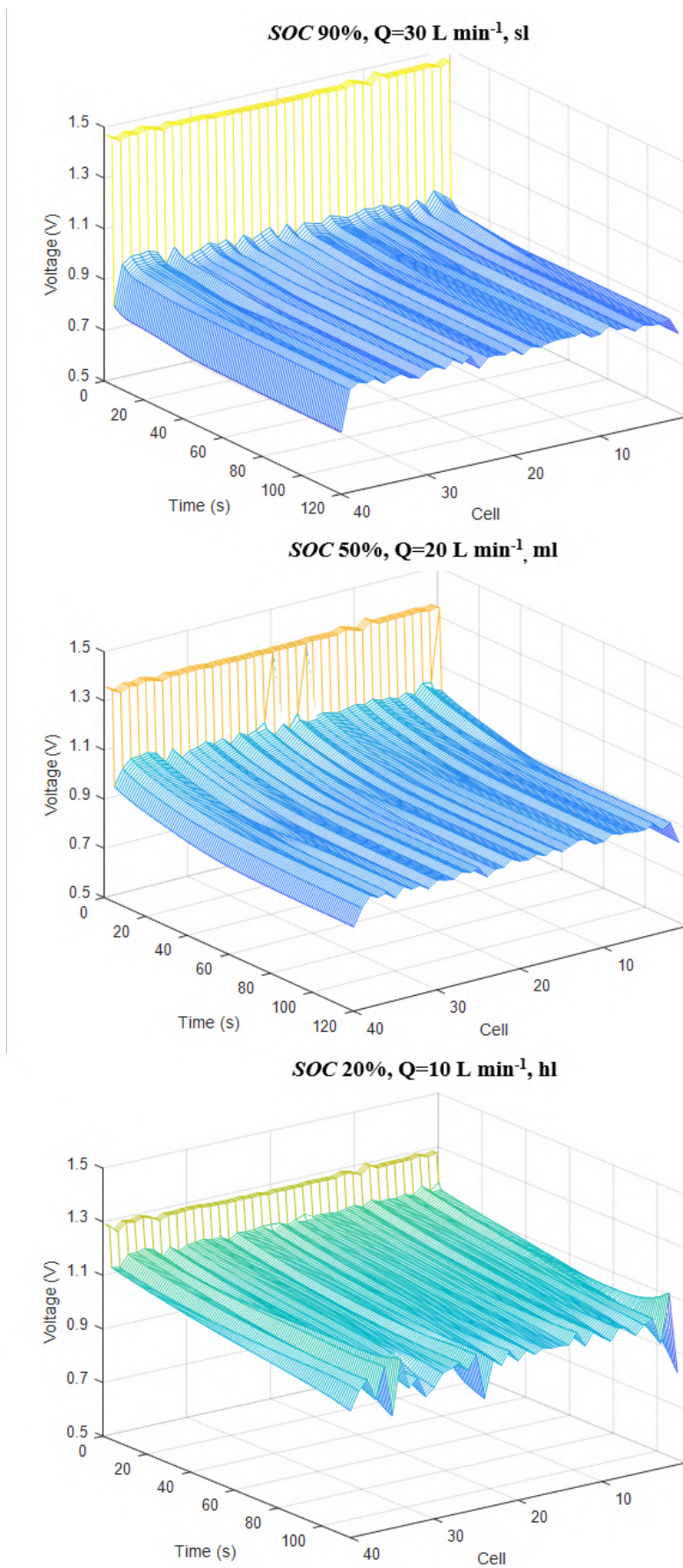


FIGURE 9.3: Power trend over time in 0–20 ms and 0–120 s time range.

FIGURE 9.4: Cell voltage evolution at different *SOC* and *Q*.

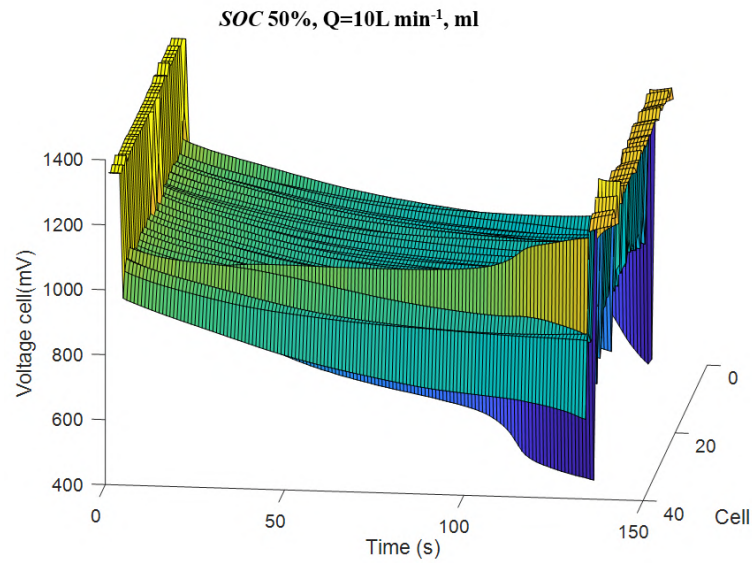


FIGURE 9.5: Cell voltage evolution with voltage unbalance.

9.3.1 Cells voltage evolution

Fig.9.4 shows the evolution of cell voltage under different conditions, for example different *SOC*, *Q*, and current *I*. The voltage profiles appear fairly smooth in the central cells and only the case *SOC*=20% (Fig.9.4 bottom) shows some irregularities. This is due to the low α compared to the other cases (Fig.9.4 top and middle). However, in all cases the edge voltage cells are lower than those in the center. This reflects a discrepancy in feed homogeneity (lower local α) due to hydraulic feeding. Further investigation is required in future studies.

In addition, strange behavior can be noted between two consecutive cells (especially in the Fig.9.4 bottom). This unbalance can be better shown in Fig.9.5 and can result in some troubles on the surveillance system (Sec.4.4.1), especially if the system stops when a cell voltage decreases to below a low limit value. Further investigations must be carried out to understand the physical meaning of this phenomenon more deeply.

Chapter 10

Aging Effects investigations

10.1 Disassembly and check operations

After one year of operation and approximately one hundred charge/discharge cycles with a total working time of 1200 h and 2500 kWh of stored energy, the stack was submitted to a maintenance, repair, and operation procedure to check whether any detriment of material or problems had arisen from the inspection. The whole operation was planned in detail in advance. First, the laboratory was prepared to ensure that every operation could be performed safely. The red hydraulic press was equipped with an in-house designed aluminum rack to host the stack during dismantling operations (Fig.10.1).

During the first phase, the appendix devices, such as the electrical connections, were removed from the stack, namely the LEM current transducer and external current collector. The cables connecting each cell to the corresponding measure line were disconnected and marked for future reconnection. All BPs were marked with the same number as the cables. The horizontal profile and some cabling were moved and stored separately (Fig.10.2).

In the second phase, the mixing valve at the front side of the stack was removed, emptied from the remaining electrolyte, and stored separately. No leakage was detected between the valve and the PVC front panel Fig.10.3.

When the stack was unlocked from any cabling, connections, and devices, (phase three) the yellow lifting crane (Fig.10.4) was used to move the stack to the aluminum rack in a horizontal position and then turned vertically with its front face down (phase four). After the moving operations were completed, some electrolyte leakages were detected near the solutions inlets. As can be noticed from Fig.10.5, blue crystals that formed due to the leakage of $V(IV)$ solution from the badly sealed plates were found. These residuals were adequately cleaned, and a first visual inspection on the external health state of the plates was performed to detect any issues. After this, wooden clips were applied as shown in Fig.10.5 to keep the plates together after the stack was disassembled.

During the fifth phase, the membranes were separated and each component stored in different boxes after a visual control. The first detected issue was the presence of small PVC shavings that blocked some of the flow channels. Their presence was caused by previous maintenance operations on the PVC head, which were performed without removing the drilling chips. This does not represent a significant issue for VRFB performance because the shavings only partially covered the plate inlets. As a first control, none of the components presented irreparable damage due to operational conditions (Fig.10.6).

In the sixth phase, the metal plate was removed from the front PVC plate. Some leakage was detected from secondary preciseness bonding made during the panel construction (Fig.10.7). The acid solution did not cause any harm to the metal plate due to the protection paint.

The seventh phase was devoted to performing a more accurate check of the condition of components. The BPs were washed with bi-distilled water, and the acetic silicon seal and the state of the graphite plates were checked. The inspection is described and commented on below (Fig.10.8).

Fig.10.9 reports the flaws identified on the membrane with two gasket components. First, in a) a hole can be seen in one of the carbon felts. There are few this kind of damage reported, which was, most probably, already present during the assembly of the stack. In b), the behavior of the acetic silicon is shown when immersed in a corrosive environment and subjected to an electric field.



FIGURE 10.1: Aluminum rack and hydraulic pressure jack.

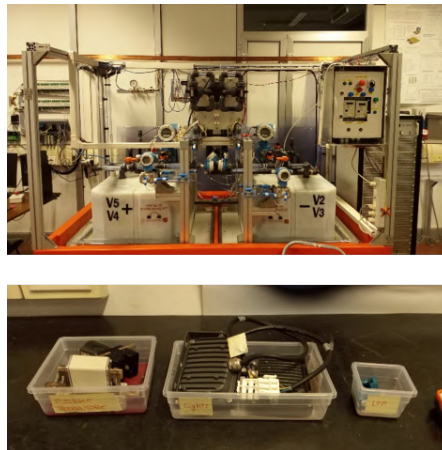


FIGURE 10.2: Top: plant after the first phase (*OCV* cell, LEM and horizontal upper profile removed); bottom: the removed objects accurately separated.

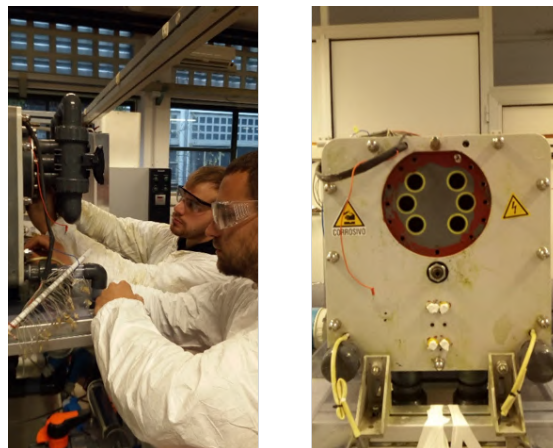


FIGURE 10.3: Second phase: the mixing valve is dismantled from the frontal panel.

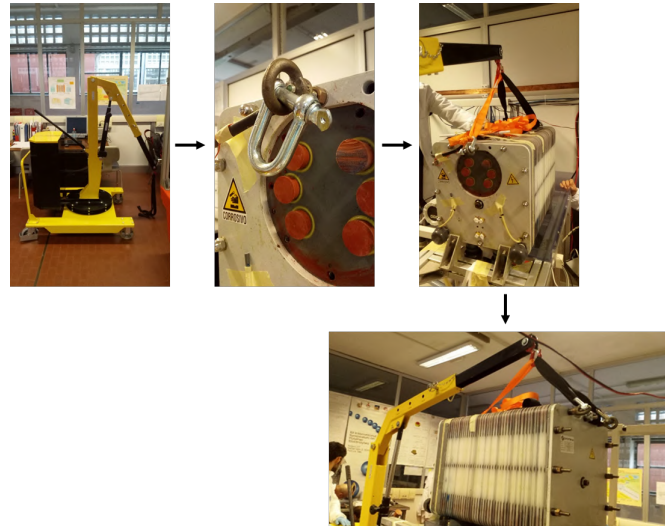


FIGURE 10.4: Third phase: the stack's hung and moved with a crane and placed horizontally.



FIGURE 10.5: Fourth phase: the stack's turned vertically. Left: some electrolyte leakage is detected from the bottom part, center: clips are applied to avoid polypropylene plates to open completely as it can be noticed in right.

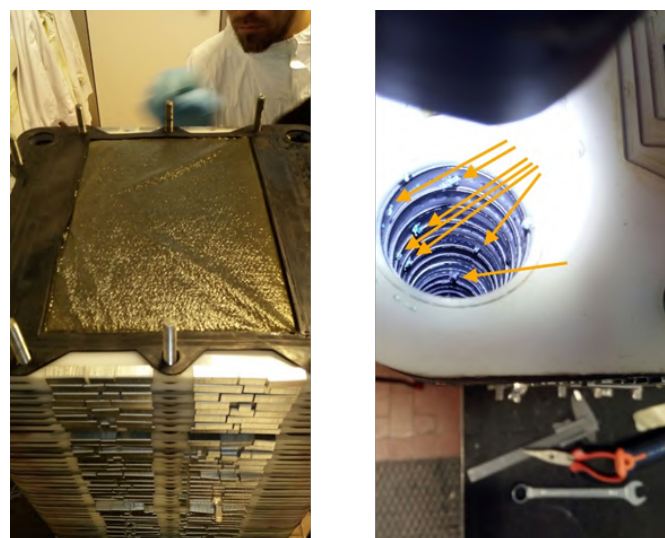


FIGURE 10.6: Fifth phase: membrane disassembled and preliminary visual check. In right: some manifold channels are blocked up by PVC shavings due to previous drilling maintenance operations on the head plate.

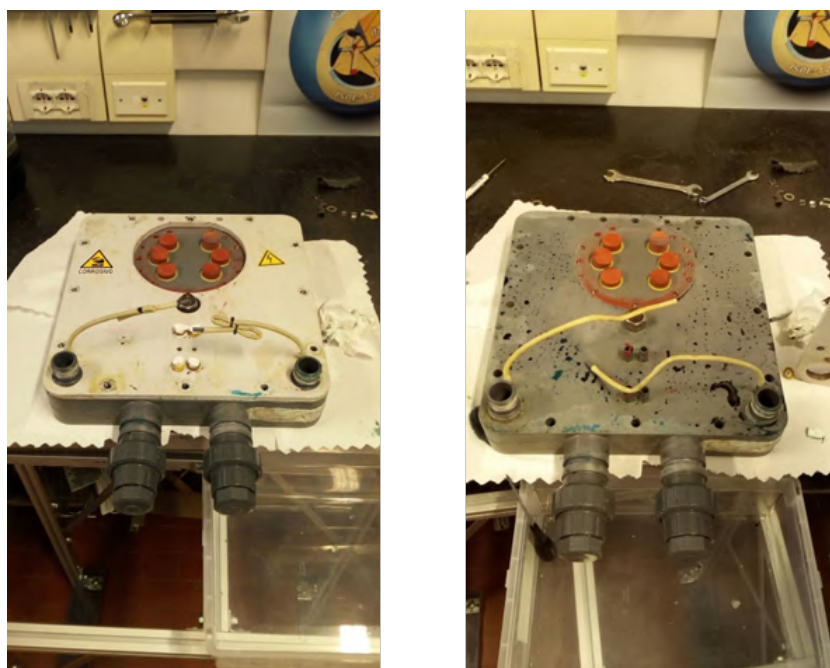


FIGURE 10.7: Sixth phase: PVC frontal plate is divided from its metal where more electrolyte leakage are detected.



FIGURE 10.8: Seventh phase: each membrane with two gaskets is divided and each bipolar plate is washed with bi-distilled water and accurately examined.

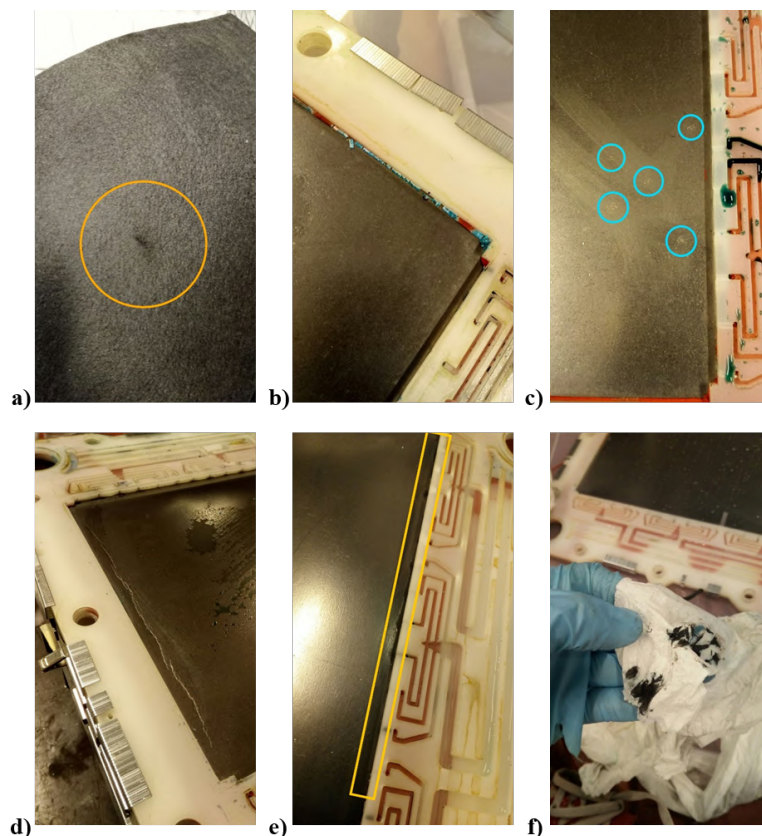


FIGURE 10.9: Some of the flaws found on the plates: a) a carbon felts hole, b) acetic silicon behavior in presence of corrosive environment and electric field, c) and d) imperfections on bi-polar plates surface, e) and f) carbon felts deposit close to the plate inlets.

The elastic red paste was transformed into a white powder compound wetted with blue electrolyte. Its consistency was impalpable and it disrupted easily simply by touching it; however, it did not seem to compromise the sealing or to create problems by blocking the electrolytes inlets. c) shows some point defects on a BP, while d) shows a linear bending scratch. Several plates presented one or both of these defects (in the form of single or multiple points or as a linear scratch). These flaws were not due to any incorrect treatment of the battery but seem to be local imperfections of the material already present in the assembly process. Last, e) and f) show the deposition of carbon material on the bottom side of a BP. This phenomenon was observed in a few plates and resulted in a slight detriment of the carbon plate covered with the deposit. The precipitated did not occluded the holes of the inlet manifold and seemed not to affect the performances.

A further aging effect was observed in 10 plates, and this was indicated as the cause of the leakage shown in Fig.10.5 (left). This was due to the bad seal of the acetic silicon caused by several factors. First, acetic silicon was not the most adequate choice to bond the two plates together. Second, even if the silicon was deposited by an industrial plotter, the lines in the polypropylene structure were not suitable for ensuring a perfect deposition of silicon and the consequent bonding between plates. In fact, as shown by Fig.10.5 (right), plate 34 was open around the main electrolyte inlet; however, because of the clips the two halves did not separate completely. Correct silicon sealing is clearly necessary due to electrolyte pressure. Carbon felts were not subject to a deeper analysis than a visual one, but their status was reported to be satisfactory. With regard to the membranes, none presented visual defects or irreversible damage due to working conditions or consistent aging effects.

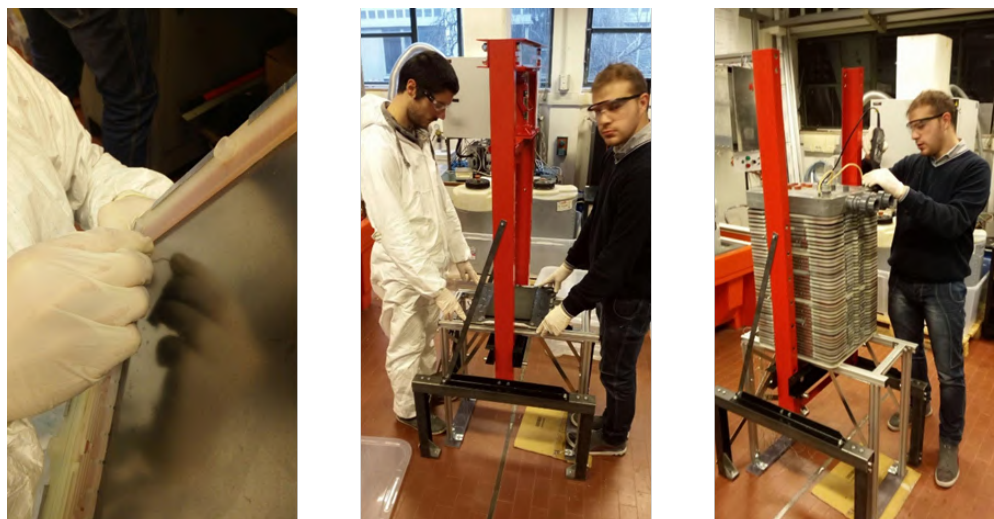


FIGURE 10.10: Reassembly procedure's operations. Left: a final and accurate check on the manifolds holes status. Center: first cells assembled on the designated aluminum rack. Right: all the cells reassembled and final operations on the head of the battery.

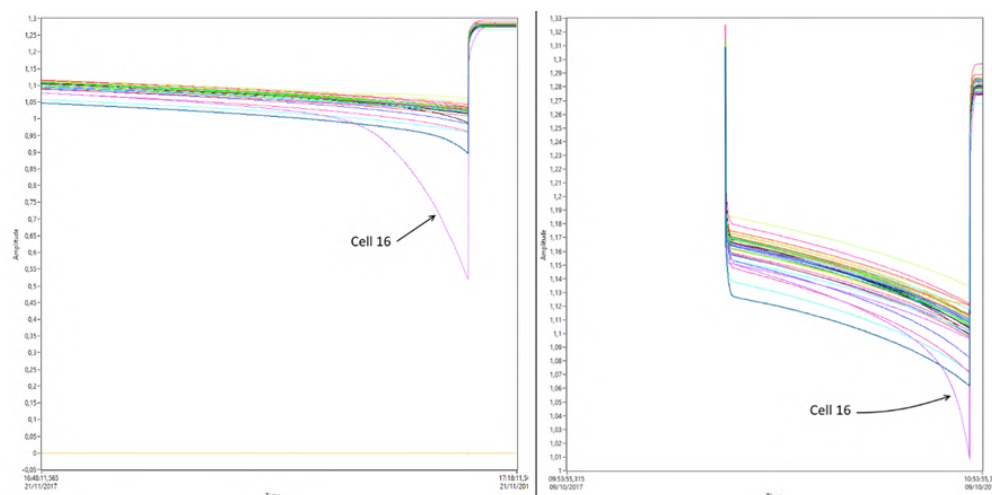


FIGURE 10.11: Voltage vs time graph of the stack's cells. Cell 16's behavior is pointed.

10.2 Stack reassembly

The procedure to reassemble the stack and to settle it back to the original position is described in Fig.10.10. This procedure is similar to the initial assembly procedure (Sec.3.1.8).

To preserve the membranes from drying out, they were stored in a sealed and humidified box and the piling procedure was performed during a single day of work. At first, every hole of the manifold on each plate was accurately checked and inspected to eliminate any possible residue that could cause an occlusion and invalidate further tests. During this check, plate 16 was found to have a consistent part of its holes occluded due to a construction defect. This plate's status could be responsible for the drastic voltage drop registered in some cases while discharging.

Fig.10.11 shows the plot of voltage versus time of the cells and the fall of cell 16 is pointed. As a matter of fact, if not enough reagents are fed to the cell, the resistance rises, and the voltage drops if the current is constant.

All the occlusions were removed successfully and the plate restored to its standard conditions. After, the stack was reassembled in the same order. Fig.10.12 shows the described phases. Plates 17 and 34 were replaced due to a consistent separation between the two halves, which could compromise future battery performance.



FIGURE 10.12: Stack measuring and pressing.

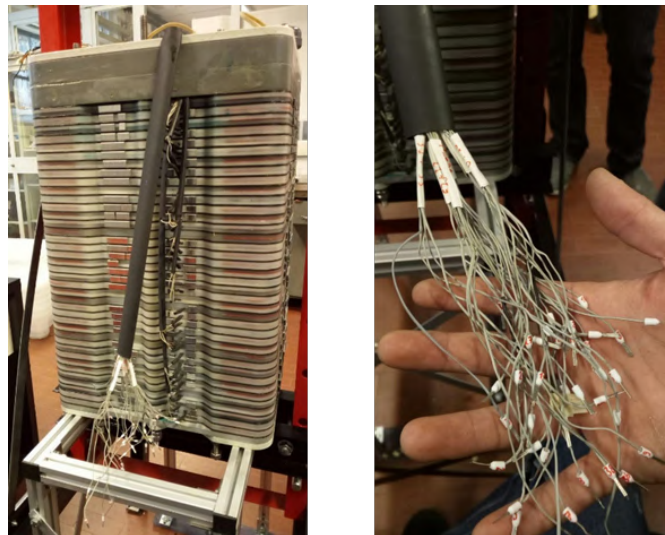


FIGURE 10.13: Single cells cabling.

After, the components were set in position, the red press and the aluminum rack were used together to press the stack to its original size. Periodic measurements were performed to verify the total length. Finally, a manual and more precise compression was completed with the threaded bars on the perimeter of the stack. When the stack reached its original dimensions all the cabling of the single cells were restored and marked as shown in Fig.10.13. Then, with the yellow crane, the stack was moved, set horizontally and mounted in the original position Fig.10.14.

As a final operation, a nitrogen tightness test was completed by using soapy water to detect eventual leakage by the formation of soap bubbles. No outflows were observed, even up to 0.5 bar Fig.10.15. After that, the piping was restored, the maintenance procedure was concluded, and the test facility was ready to proceed with the experimental activity.

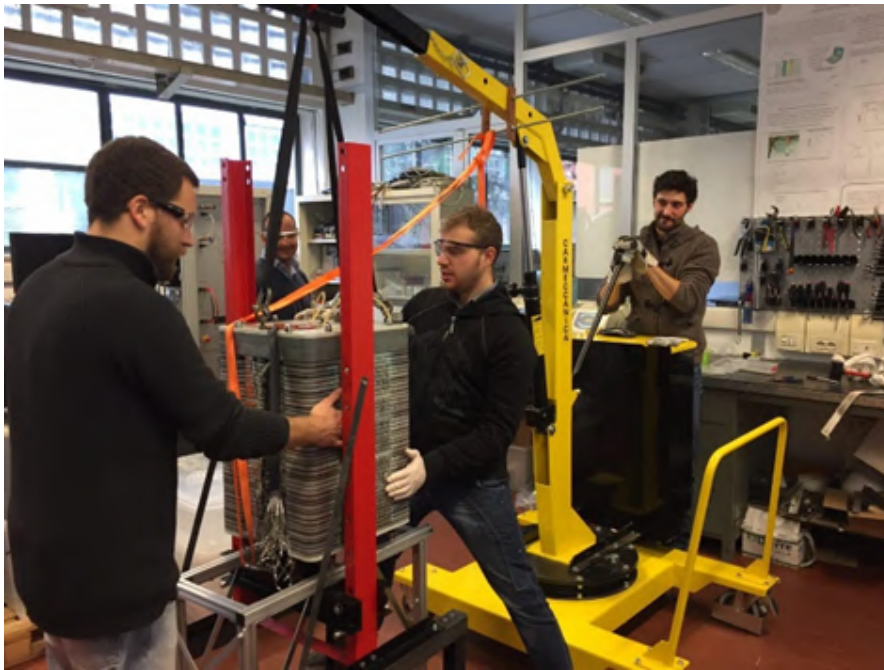


FIGURE 10.14: The stack is repositioned horizontal.



FIGURE 10.15: The gas sealing test.

Chapter 11

EIS tests

11.1 Theoretical background

Electrochemical impedance spectroscopy (EIS) is a powerful and complex technique used to investigate the mechanisms and electrochemical reactions that occur during the operation of an electrochemical cell. The same technique can be applied directly to obtain the equivalent electric scheme of a battery, which can be treated as a simple circuit element. This technique has experienced a growing interest in the scientific community due to its particular characteristics [379]:

- it is a linear technique that can be interpreted in terms of linear systems;
- it can be used to measure a high frequency range, which allows the characterization of all the physical and chemical mechanisms involved in the system;
- it has proven experimental efficiency;
- the validation of the data can be carried out using techniques of transformed integrals (Kramers-Kronig), which are independent of the physical processes.

Among its most important applications, it can be applied to the study of corrosion in metals, adsorption and desorption on the surface of electrodes, the electrochemical synthesis of different materials, catalytic kinetic reactions, and the mobility of electrons inside batteries and supercapacitors. It is presented therefore as a complex and powerful technique, which is used within a wide range of technologies, being object of analysis in this chapter the measurement of the impedance inside the IS-VRFB stack. During an EIS test, there are sinusoidal signals from $V(t)$ and $I(t)$, and the impedance term Z represents this impedance to the current flow through the circuit. There are two main ways to conduct these tests. When a voltage signal is applied by measuring a current signal, it refers to the potentiostatic mode.

Conversely, when a current signal is applied by measuring a voltage signal, this refers to the galvanostatic mode. For the potentiostatic case, a voltage is applied with the following form:

$$V(t) = V_{max} \cos(\omega t) \quad (11.1)$$

where V_{max} represents the amplitude of the sinusoidal signal, ω is the angular frequency in units of rad s^{-1} , and t is the time, so the term (ωt) represents the phase of the signal. Conversion between the angular frequency and the frequency (expressed in Hz) is given by the following equation:

$$\omega = 2\pi f \quad (11.2)$$

The system is non-linear, but it can be linearized around a working point, in the case of small excitation amplitude, as can be seen in Fig.11.1. The result of the intensity signal is also a sinusoidal wave with the same frequency as the original signal, but shifts of a certain angle with respect to the original:

$$I(t) = I_{max} \cos(\omega t - \phi) \quad (11.3)$$

where I_{max} is the amplitude of the signal and ϕ is the angular offset, represented in Fig.11.2.

A more convenient way to describe sinusoidal waves is by using Euler's formula, which is defined as follows:

$$e^{jx} = \cos(x) + j\sin(x) \quad (11.4)$$

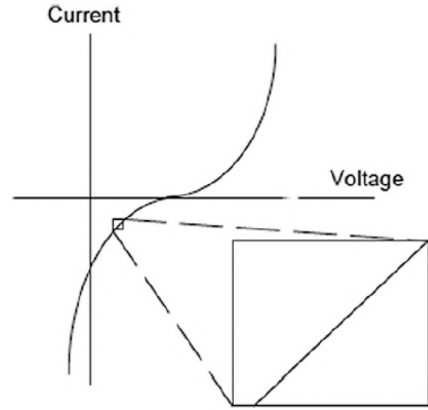


FIGURE 11.1: Application of small excitation amplitudes allows the signal to be linearized [380].

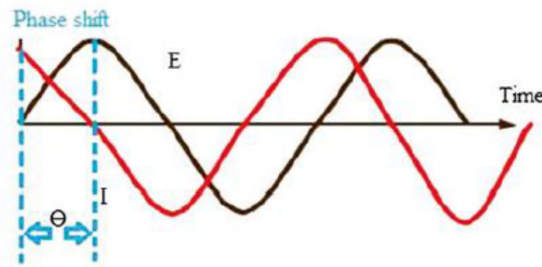


FIGURE 11.2: Angular offset between the voltage and current waves [380].

where the term j refers to the imaginary unit, and x is any real number. Using complex number theory, Eqs.11.1, 11.3 provides the following:

$$V(t) = V_{max}e^{j\omega t} \quad (11.5)$$

$$I(t) = I_{max}e^{j\omega t - \phi} \quad (11.6)$$

and by applying Ohm's law:

$$Z = \frac{V_{max}e^{j\omega t}}{I_{max}e^{j\omega t - \phi}} = Z_{max}e^{j\phi} \quad (11.7)$$

where Z_{max} represents the amplitude of the impedance. Finally using Euler's form, the equation can be rewritten as follows:

$$Z = Z_{max}(\cos(\phi) + j\sin(\phi)) = Z_{rea} + jZ_{im} \quad (11.8)$$

in which the terms Z_{rea} and Z_{im} refer to the real part and imaginary part, respectively, of the total impedance.

A typical EIS test consists of applying a sine wave of voltage (or current) that varies along different frequencies, and measuring the resulting current wave (or voltage) to obtain the value of the internal impedance by applying the Eq.11.7. The test allows values of both the real and the imaginary part of the impedance to be obtained at different frequencies. These impedance values depend on the different mechanisms and electrochemical reactions that are carried out inside the battery, which allows a characterization of the internal phenomena of the energy storage system. Apart from achieving this linearity, stability is the required condition at the time of the test. This ensures the repeatability of the electrochemical properties of the battery once the test has been completed. Once the impedance values have been obtained after the test (real part and

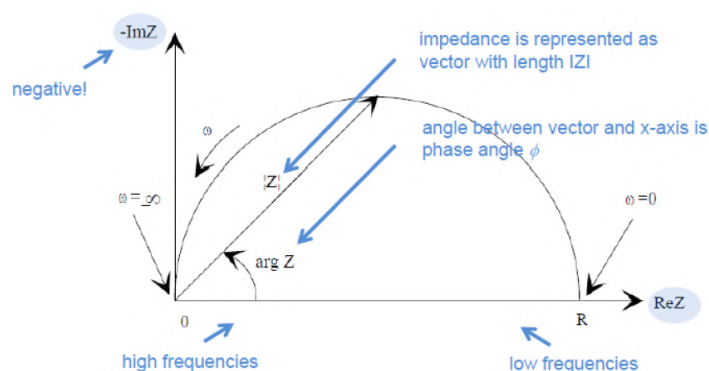


FIGURE 11.3: Nyquist diagram of a specific system [381].

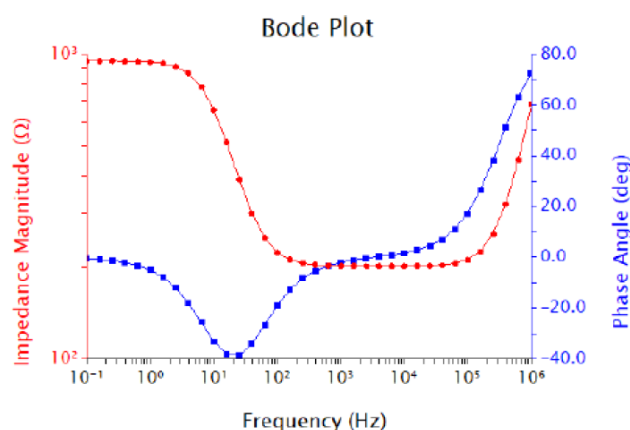


FIGURE 11.4: Bode diagram of a specific system.

imaginary part), the Nyquist diagrams that characterize the system are obtained, as shown in Fig.11.3.

In this graph, the imaginary part values are represented on the ordinate axis (in the opposite direction), while the values of the real part are represented on the abscissa axis. Each point represents the internal impedance of the battery at a certain frequency. However, there is no information on the frequency from which each point corresponds. If these points are converted to module and argument, another representation is obtained (the Bode diagram), as shown in Fig.11.4, which presents these values vs. their frequency. These graphs can be represented by equivalent electrical circuits, where each element reproduces a physical phenomenon. These equivalent circuits can be a valuable tool for analyzing the internal processes and mechanisms during the operation of the battery. They are usually composed of the three main electric elements, such as resistors, capacitors, and inductors, whose properties depend on the frequency. For example, the larger the Nyquist circles, the higher the ohmic losses due to the internal resistances, i.e. the cell overpotentials.

Among these representations, the most common used in the electrochemical storage systems sector is the Randles circuit, which is observed in Fig.11.5.

In a Randles circuit, the following elements can be observed:

- R_{el} represents the internal resistance of the electrolyte, which depends on the concentration of the ions, the type of ions, their temperature, and the active area of the cell;
- C_{dl} represents the double layer that exists at the interface between the electrode and the nearby electrolyte. This form creates ions "attached" to the surface of the electrode, where the charge electrodes are separated from the charged ions, forming a kind of capacitance.

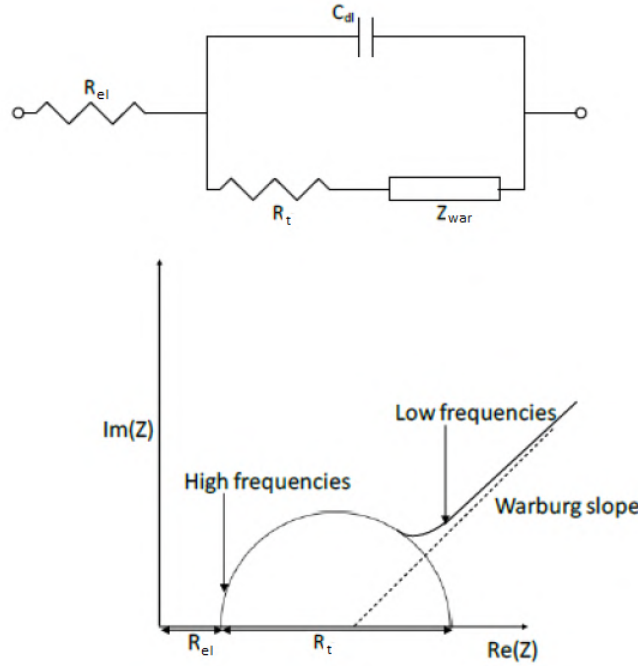


FIGURE 11.5: Randle's circuit (top) and the analogous Nyquist diagram (bottom) [382]

The value of this capacity depends on the potential of the electrode, the temperature, the concentration of the ions, the type of ions, the presence of oxide layers, and the robustness of the electrode;

- R_t represents the electrochemical polarization reactions, so it is the transport resistance of the charge carriers (Chap.6);
- at low frequencies, a higher impedance appears called Warburg impedance (Z_{war}), which represents the phenomena of diffusion.

Analogously, these elements are represented by the Nyquist diagram, whereby at high frequency domain the dominant element is the internal resistance of the electrolyte. The frequency decreases as the total impedance increases, due to the contribution of the polarization resistance and the capacitance of the electrochemical double layer. At low frequencies, the electrochemical double layer is fully charged so that the limitation of mass transfer rises, due to the increase in the internal impedance of the battery, which is represented by the slope of the Warburg impedance.

Fig.11.6 shows a diagram of the physical processes involved in this analog circuit. In this circuit, in the ranges of high and medium frequencies where the Warburg impedance does not become relevant, the expression of the total impedance as a function of the frequency is given by the following:

$$Z(\omega) = R_{el} + \frac{R_t}{1 + \omega^2 R_t^2 C_{dl}^2} - \frac{j\omega R_t^2 C_{dl}}{1 + \omega^2 R_t^2 C_{dl}^2} \quad (11.9)$$

where the real part is given by:

$$Z_{rea}(\omega) = R_{el} + \frac{R_t}{1 + \omega^2 R_t^2 C_{dl}^2} \quad (11.10)$$

and the imaginary part:

$$Z_{im}(\omega) = -\frac{j\omega R_t^2 C_{dl}}{1 + \omega^2 R_t^2 C_{dl}^2} \quad (11.11)$$

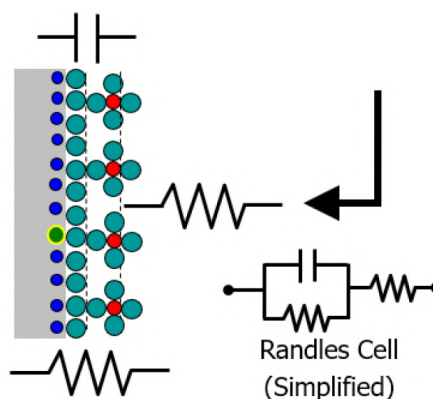


FIGURE 11.6: Physical meaning associated with a Randles circuit [383].

Both R_{el} , R_t and C_{dl} can be calculated experimentally in the Nyquist diagram, while the Warburg impedance can be obtained mathematically according to the following expression:

$$Z_{war} = \frac{\sigma_{war}}{\sqrt{j\omega}} \quad (11.12)$$

where σ_{war} is the Warburg diffusion coefficient. The slope of this impedance in the Nyquist diagram approaches 45° . Due to the difficulty of determining linearity, causality, and stability during an EIS test, it is necessary to carry out a validation study of results after the data collection at the end of the test.

The study of linearity, causality, and stability can be carried out by applying Kramers-Kronig transforms, which are mathematical relations for the real and imaginary parts of a complex system that define the degree of linearity [384].

11.2 EIS measurement tests

11.2.1 Experimental method

Experimental measurements were provided by using MMulty SP program developed by Materials Mates Instruments (Italy) dedicated to monitoring, controlling, and managing the measurement test of EIS.

It has several measurement modes executable and configurable from its graphical interface, where real-time monitoring of the main parameters is carried out during the execution of the test.

At the beginning, the user must create a save path and choose the desired parameters to save inside, such as the real part of the impedance, the imaginary part, the phase, the argument, the current, or the applied voltage with the main current and resulting harmonic voltages. The signal applied for the measurement of the impedance can be a current (galvanostatic option) or a voltage (potentiostatic option). The bias value refers to the volts or amperes applied during the execution of the test, a parameter that can be modified. The soft change option allows the user to achieve the bias value slowly and progressively. This voltage or current signal is not applied until the user decides to connect the equipment to the cell through the ON/OFF button, at which point the signal is forced to circulate constantly. The program allows three different measurement modes related to this signal, represented by a virtual filter that measures the influence of the stability and the bandwidth of the measurement:

- high stability: more stable values but with lower bandwidth, recommended for measurement applying direct current and to systems with an impedance with a strong capacitive behavior;
- high speed: less stability but a large bandwidth, recommended in systems where measurement requires a rapid response capacity;

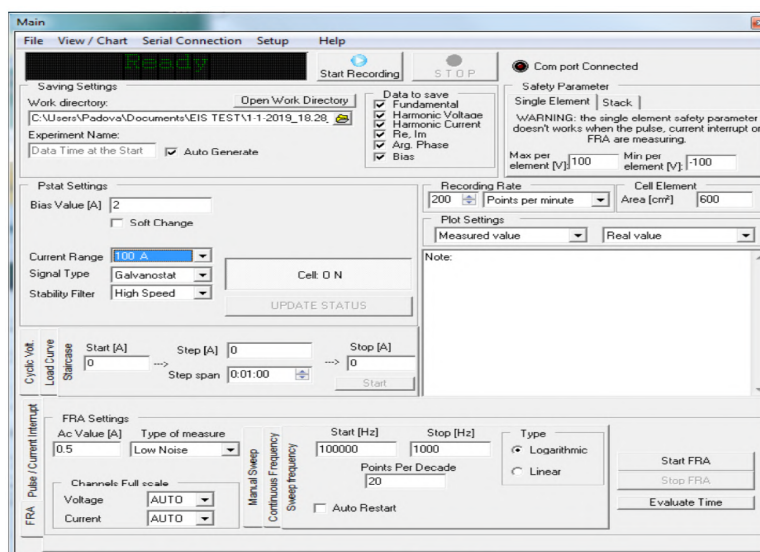


FIGURE 11.7: MMulty SP graphic interface.

- low noise: intermediate point between stability and bandwidth, recommended in systems subjected to different sources of electrical noise, such as inverters and power regulators:

The sampling rate of the frequency can also be changed, and 200 points per minute (default) was used in the test.

Fig.11.7 shows the graphical interface of the measurement program MMulty SP together with the parameters discussed above.

Fig.11.7 shows the safety parameters (maximum current, and maximum and minimum voltages) accepted for each cell during the performance of the tests. Once a cell was outside this range, all cells were automatically disconnected and the test measurement stopped. The area of each cell is a parameter that can be used to measure the value of impedance in both absolute (Ω) and specific values ($\Omega \text{ cm}^2$).

There are different techniques for measuring the impedance. The following is a brief summary:

- ladder signal: the applied signal varies from an initial to a final value following a certain step. Each step has a certain duration. The step can be positive (from a small to a larger signal) or negative (from a large to a smaller one). The slope of this variation can be modified;
- pulse generator: a certain excitation wave is applied to the system and the response of the system is monitored. A sinusoidal standard signal can be used, as well as another arbitrary waveform;
- interrupted current: this consists of the application of a current signal (only in galvanostatic mode) so that this signal is stopped and the behavior and response of the system is measured in the instants after the signal disappears. In this mode, you can modify both the delay time by applying the signal and the current interruption time before applying the signal again;
- FRA: this is the measurement of the impedance using a frequency response analyzer. It consists of the application of a signal of alternating current or voltage at certain frequency to obtain the response of the system at that frequency. The input parameters in this mode are the bias voltage or current value and its amplitude, as well as the frequency values to be analyzed. This frequency can be set with a logarithmic or linear change slope, and it is also possible to program the desired measurement frequencies.

Fig.11.8 shows the graphical interface of the parameter monitoring program during the execution of the tests. Finally, a list of the main technical characteristics of the measurement equipment is shown in Tab.11.1.

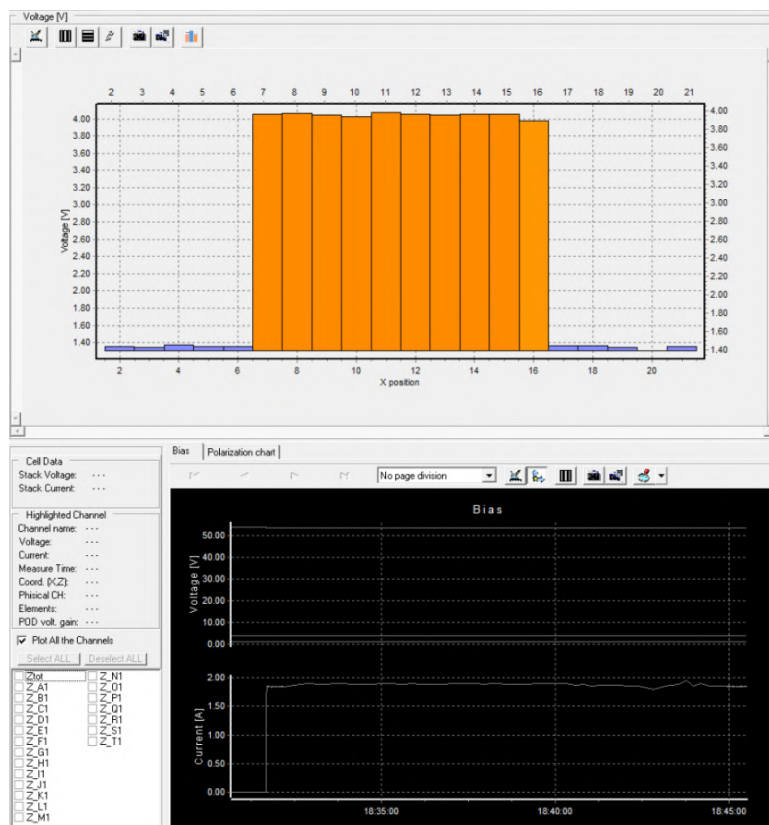


FIGURE 11.8: Graphical interface for parameter monitoring of the MMulty SP program.

TABLE 11.1: Technical data sheet MMulty SP

Description	Value
Max load voltage	100 V
Maximum bias current	100A
Maximal dissipating power	1500 W (water), 800 W (air)
Maximum frequency	100 kHz
Accuracy	$\pm 0.2 \% \text{ F.S} \pm 0.1 \text{ reading}$

11.3 Calibration tests

Preliminary tests were performed to understand the operation and influence of all parameters related to the EIS measurement tests to improve the accuracy of the measurements. In these tests, the impedance of well-known electric circuits were compared with the measured values. The key points associated with the results of the calibration tests are reported below:

- in low impedance devices (such as the RFB), the application of a 10 mV voltage wave can cause an associated current flow, changing the battery conditions. For this reason, it is suggested that the galvanostatic mode is used, where the voltage wave is replaced with a current wave more appropriate to control and measure the change of the internal impedance in an RFB;
- when the measurements show a circuit with high R , of the order of 1 Ω , and a low capacity, the EIS measuring device is able to obtain the internal impedance of the circuit with high precision, without the influence of noise;
- as the resistance of the circuit is lower (in the order of 0.01 – 0.1 Ω) and the capacitance of the circuit is greater, the test loses precision in the measurement. This is caused by the inductance of the wiring that becomes an electrical noise with a high value among the total impedance of the circuit;
- in the analysis of the three types of filters (low noise, high speed, and high stability), the measurements and the results are very similar; however, the presence of power inverters and pumps in the electrochemical battery affect the tests;
- in the low noise filter mode, the EIS measurement results are not conditioned by the presence of electrical noise associated with the power inverters and the pumps;
- the higher the bias current, the better the accuracy of the measurements with lower dispersion between each point;
- the configuration and layout of the circuit affects the results: more precise values are given if the electrical wiring is twisted to remove the possible inductance due to the circulation of current;
- there are no differences associated with the channel number and identical behavior of all channels can be ensured.

In conclusion, the main problem that must be avoided in the measurement of the internal impedance of the battery is high inductance of the electrical wiring, an error that reaches its highest value the higher the frequency of the test. To improve the accuracy and precision of the measurements, it was decided to reduce as much as possible the length of all wiring (electrical and instrumentation) to minimize the relative inductance.

11.4 Cabling optimization

According to the calibration results, it was observed that the measurements of low resistive-capacitive impedance were affected by the inductance of the electrical wiring, so it was decided to reduce the maximum length of the cables, placing the data acquisition cards as close as possible to the stack. First, support consisting of five data acquisition cards was designed and realized. This support was placed at the upper part of the stack, close to the cells signals cables.

Next, an in-house constructed electronic board was built to be responsible for transmitting data received from the different stack cells to both the EIS measurement program and the BMS, as well as to a series of LEDs indicators installed to check, by means of a quick visual inspection, cell voltage homogeneity.

This electronic board was placed at the top of the previous plastic support. In this electronic board, the good connection of the various components assumed crucial importance in avoiding

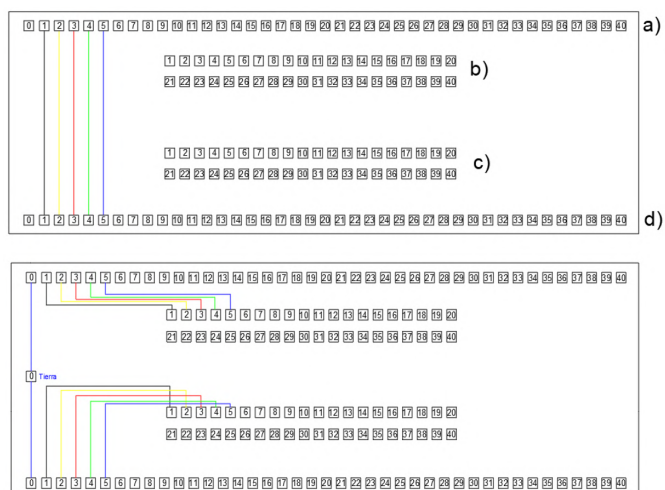


FIGURE 11.9: Schematic of electrical connections of the electronic plate (it has welded on both sides).

errors in the measurement and possible malfunction of the measurement system. The electrical connection scheme of the electronic board is shown in Fig.11.9.

For better schematic clarity, only the ground connection (port 0) and the first five connections (ports 1, 2, 3, 4, and 5) are shown in Fig.11.9. The plate was composed of four parts, named in Fig.11.9 as *a)*, *b)*, *c)*, and *d)* welded together, with connections as follows:

- *a)* connection with the 40 cells of the stack;
- *b)* connection to the BMS;
- *c)* connection to the indicator LEDs;
- *d)* connection to the data acquisition cards, which redirect data to the EIS device.

The final result of the electronic board is shown in Fig.11.10.

All have the common objective of reducing the inductance caused by the cables, i.e. minimization of the distance between the object to be measured and the electronic board (reduction of the cable length), and by twisting the wire.

First, connections were made from the 40 cells to part *a)* of the electronic board, (Fig.11.11).

Second, connections were made between the electronic board and the BMS. Fig.11.12 shows the terminal *c)* that is connected to the electronic board with the indicator LEDs, placed on a glass front panel, (Fig.11.13).

Last, the connections of terminal *d)* were made, which connect the electronic board with the data acquisition cards of the EIS measurement device. There were five measuring modules, each composed of four connection terminals; therefore, 20 cells could be measured. This connection is shown in Fig.11.14.

Finally, the connection diagram of all parts involved in the electronic board is presented in Fig.11.15 below.

Once the connections on the electronic board were completed, the power cable could be simply connected corresponding to the galvanostatic signal (current source) provided by the EIS measuring device to the stack. This was placed following the same principles of minimum induction to minimize the length of the wiring and to twist the cables around each other. Ultimately, short circuit problems in the welding were avoided by testing the connections between the different channels. The internal impedance of the EIS system was measured by an LRC meter. As a result, a maximum current of a few milliamps was calculated with a negligible effect on the entire measurement chain. For the sake of simplicity, no more details regarding this issue are reported.

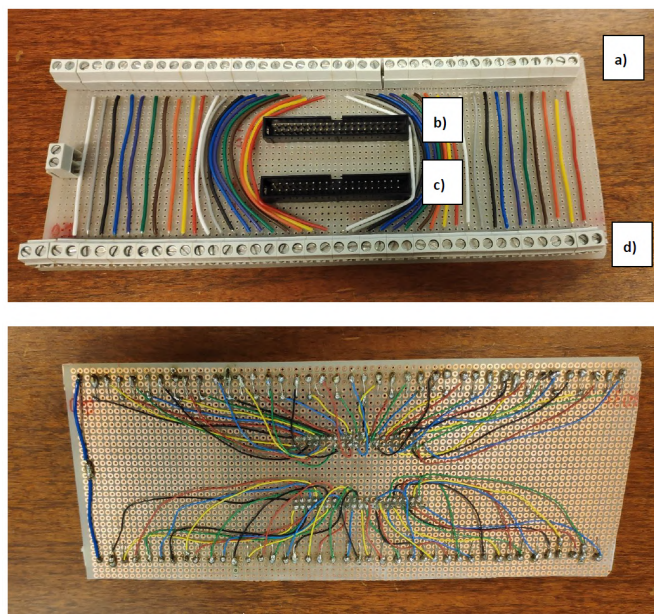


FIGURE 11.10: Final result of electrical connections of the electronic board.

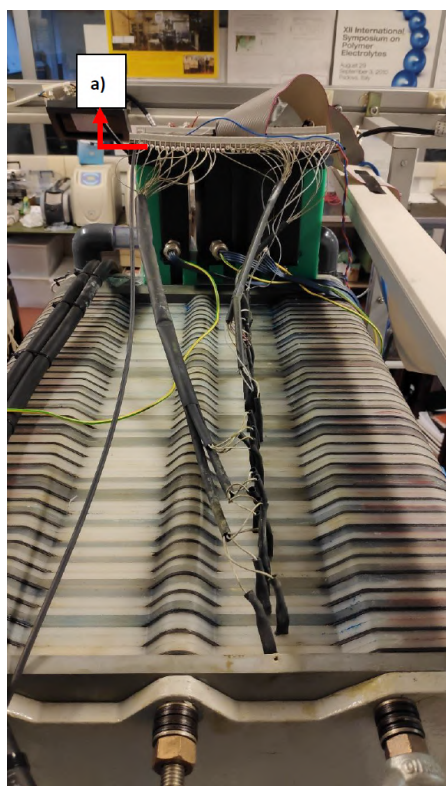


FIGURE 11.11: Connection between each terminal of the electrochemical cells and the electronic board.

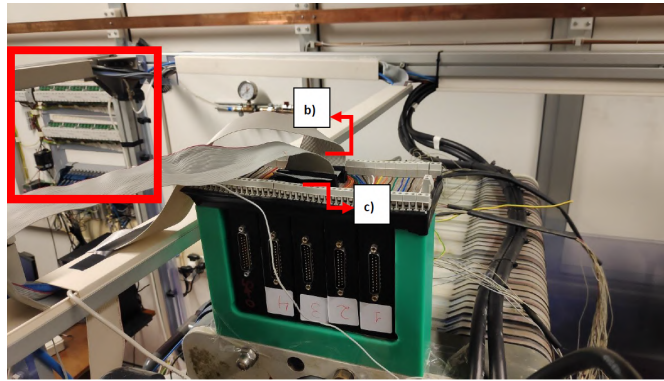


FIGURE 11.12: Connection between the data acquisition cards (terminal in red box) managed by LabVIEW software and its terminal on the electronic board *b*).

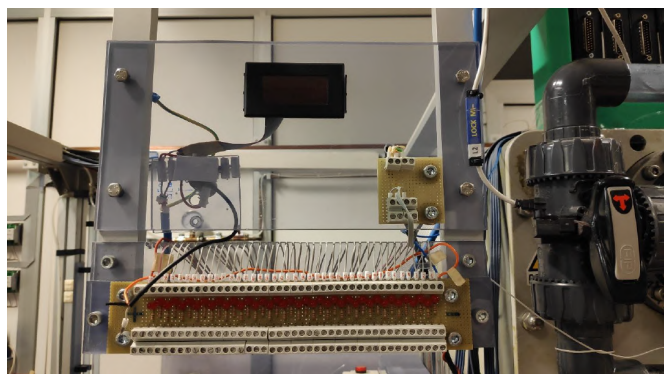


FIGURE 11.13: Front panel of indicator LEDs.



FIGURE 11.14: Connection between the data acquisition cards of the EIS measurement program and its corresponding terminal *d*) of the electronic board.

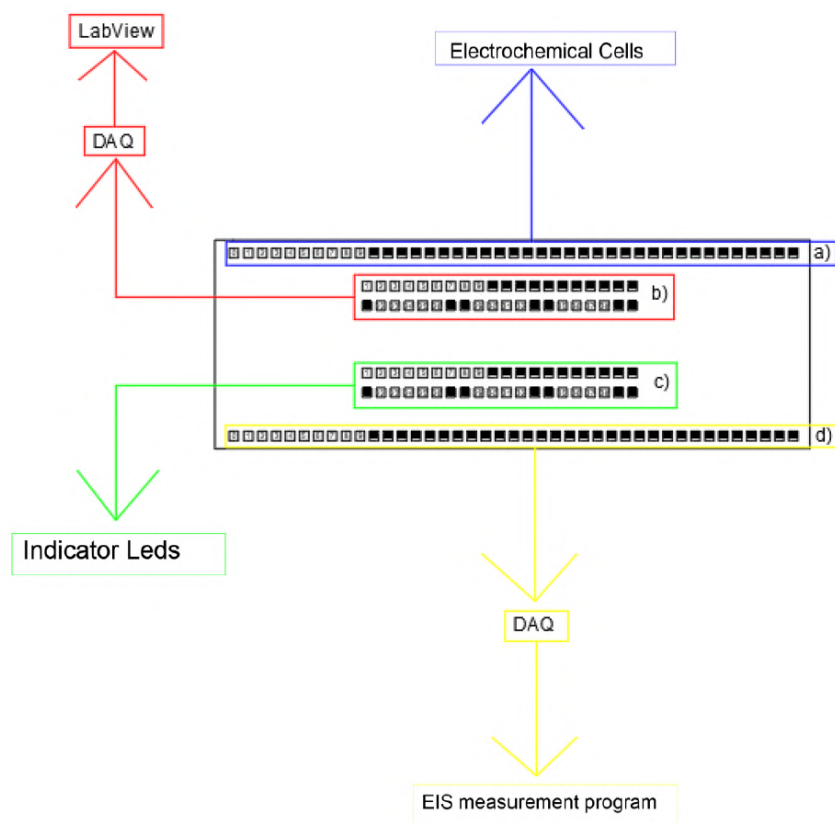


FIGURE 11.15: Final connection diagram of the electronic board.

11.5 Influence parameters

The main factors that affect the internal impedance of the RFB can be assumed as follows:

- the State of charge, which generally results in a decrease of the internal impedance of the battery as the *SOC* increase in a large part of battery [385];
- High electrolyte flow rate, which results in a decrease of the electrolyte resistance. As the flow increases, the transport losses decrease by improving the mass transport between the electrode and the electrolyte [386];
- The operating temperature also plays an important role in the value of the internal impedance of the battery. The temperature decreases as the resistance increases [324];
- The number of cycles (time in continuous operation) of the battery causes an increment of the internal impedance, which is caused by aging effects [324];
- Finally, there are other factors that alter the internal impedance in the RFB, such as the application of different treatments in the porous electrode, the use of different ion exchange membrane, and electrolytes [387].

11.6 Preliminary results on IS-VRFB

Some preliminary results are presented here. Much more must be done and a future extensive experimental campaign needs to be carried out on the IS-VRFB stack. Until now, preliminary analysis has demonstrated the suitability of the model in Fig.11.16 to predict the electrical behavior the stack cells.

The equivalent circuit consists of an equivalent Thèvenin potential (which is a function of the *SOC*), temperature of the cell, an internal ohmic resistance, R_{el} , which corresponds to the effect

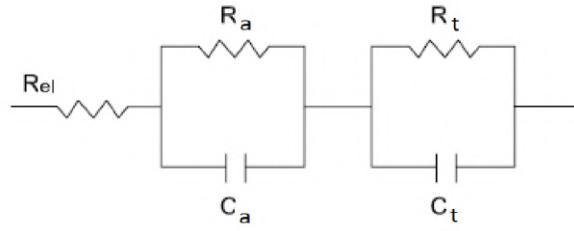


FIGURE 11.16: Theoretical equivalent circuit of the battery

TABLE 11.2: Equivalent electric scheme model parameters on 6-*th*, 12-*th*, 16-*th*, 20-*th* cells.

6 th cell	Value	12 th cell	Value	Units
R_a	8.87×10^{-4}	R_a	9.43×10^{-4}	Ω
R_t	0.0019	R_t	0.0018	Ω
C_a	0.106	C_a	0.116	F
C_t	0.0012	C_t	0.0016	F
R_{el}	7.3×10^{-6}	R_{el}	9.26×10^{-5}	Ω
16 th cell	Value	20 th cell	Value	Units
R_a	8.63×10^{-4}	R_a	8.40×10^{-4}	Ω
R_t	0.00172	R_t	0.002	Ω
C_a	0.114	C_a	0.122	F
C_t	0.0018	C_t	0.0012	F
R_{el}	1.37×10^{-4}	R_{el}	5.10×10^{-6}	Ω

of current excitation in the cell stack, a pair of in-series resistor/capacitor (RC) networks, which represent the time-dependent VRFB dynamics of activation (R_a , C_a), and transport losses (R_t , C_t) [388].

For the sake of simplicity, the parameters of the 6-*th*, 12-*th*, 16-*th*, and 20-*th* cells at $SOC=60\%$ with 20 L min^{-1} and $I=80 \text{ A}$ are reported (Tab.11.2 and Fig.11.17), showing good agreement between the experimental and numerical data. Similar results have been verified for other conditions. The upper limit of the frequency range (1–20000Hz) is related to the limitations of the measurement system, in particular the power cables which connect the battery to the EIS analyzer, produce a non-negligible inductive effect that alters the results with higher frequencies. In this preliminary experimental campaign the lower limit of the frequency was 1 Hz because of the absence of clear information at lower frequencies e.g Warburg impedance effect etc. Those results show a quite good uniformity among the cells (Fig.11.17). At present, differences between the cells enlarge with increasing battery load conditions, but further investigations are needed to investigate this issue more thoroughly.

Moreover, a state of health (SOH) analysis is planned in cooperation with the University of Salerno that aims to investigate the parameter identification of the lumped circuit and the implementation of a diagnostics technique for such industrialized VRFBs.

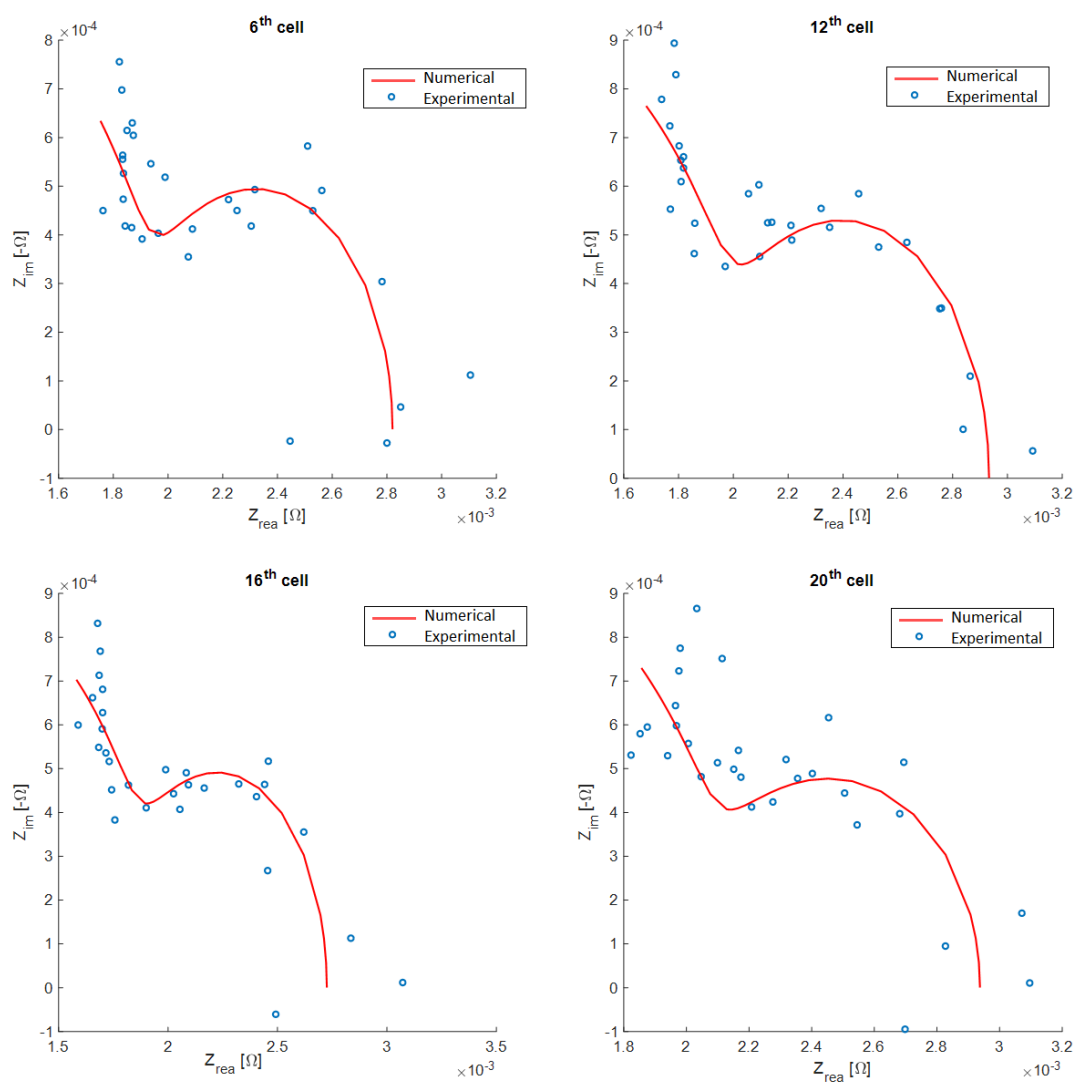


FIGURE 11.17: EIS diagrams: EIS measurements from cell $n=6, 12, 16$ and 20 (out of 40 cells) in the range 1–20.000 Hz, at $SOC=60\%$, with a flow rate $Q=20 \text{ L min}^{-1}$, $I=80 \text{ A}$ and modulated current = 0.8 A.

Chapter 12

Main results summary

The IS-VRFB test facility was completed and put into operation at the Energy Storage and Conversion Lab at the University of Padua. The main aim of this work was to present the design, construction, and testing of a 9 kW/27 kWh VRFB provided with a stack architecture directly transferable to industrial production, fully instrumented for measurement campaigns in laboratory-controlled conditions. It consists of a 40-cell stack with a 600-cm² active area.

Accordingly, polarization curves are reported during both charge and discharge operation in two conditions representative of real operative scenarios, for example, primary frequency regulation requiring fast operation, and peak shaving, which requires slow operation. Tests were performed at different flow rates and *SOCs*, from almost fully charged to almost fully discharged. Results show that high current densities in excess of 600 mA cm⁻² can be achieved at a high state of charge, provided that an adequate flow factor is guaranteed. The developed procedure for VRFB testing in fast and steady state modes enables the investigation of the time needed for creating steady-state concentration gradients in a kW-class stack for the first time. Further, it enables the analysis of the differences among the performance in the two modes. The testing procedures (which have been finalized) can be used as standards for performance assessment in kW-class VRFBs, which at present are missing. In addition, they can contribute to developing metrics for the comparison of the performance of different VRFB systems. This thesis therefore provides guidance for VRFB experts on the behavior of kW-class stacks, and for non-experts it provides information on how a large cell operates, in a way that enables comparison with test data from smaller cells.

Extensive numerical modelling was performed to predict the performance behavior of such a system. In this regard, a numerical model is presented that has been developed for simulating the thermal behavior of a VRFB stack both in standby and operating conditions, taking into account ion crossover through the membrane, shunt currents losses, and the inherent self-discharge effects. This 0D model involves all the main aspects that appear in such system. The model was successfully validated against experimental data acquired on the IS-VRFB test facility. To the best of our knowledge, this is the first numerical model that considers the effect of shunt currents in computing the temperature distribution among the cells in the stack and its evolution. Simulations demonstrated that shunt currents significantly affect the temperature distribution in the cells, and can cause a local increase of cell temperature of up to 10 °C in standby conditions. This effect is higher if the standby mode occurs at high *SOC* after a period of operation, with the starting electrolyte temperature markedly higher than ambient temperature. This temperature increase can cause VO_2^+ precipitation, and requires an appropriate cooling strategy. Such accurate thermal modelling of the stack can be a valuable tool in the design of advanced temperature control algorithms, for example to activate periodic electrolyte washing inside the stack, or in sizing the cooling of solutions in the tanks of an industrial storage system. Using the model results in combination with an advanced battery management supervisor, a smart control algorithm capable of keeping the stack temperature below safe limits can be implemented. In addition, results show that shunt currents can play a major role in the thermal behavior of compact stacks, made with new materials capable of high energy and power densities. Accordingly, important information can be obtained by comparing the simulations of the heat released in compact stacks, such as those based on novel membranes capable of high current density and low ion crossover, with larger stacks operating at lower current densities where shunt current effects have minor importance (e.g. the stack presented in [308]).

More simulations were developed on a possibly larger industrialized VRFB provided with the same stack and capable of discharging at 400 A (i.e. at current density above 650 mA cm^{-2}) through discharge/charge duration of 8 h to reproduce real thermal stress conditions. This long duration was intended to consider a major advantage of the VRFB technology, namely the independent sizing of power and energy that can be exploited to ensure long discharges. The simulations aimed to investigate critical thermal conditions, which may occur in a big plant installed in an air-conditioned container for grid services such as peak shaving. The reversible heat associated with the main half reactions has alternating thermal effects, being exothermic during discharge and endothermic during charge, which constitutes an advantage over other kinds of batteries. Consequently, the simulations showed the maximum temperatures at the end of a discharge phase. In the case of the high current long-duration operation, an optimum temperature above $50 \text{ }^\circ\text{C}$ was reached, which constitutes an issue for positive electrolyte thermal stability. In fact, when working at high current densities, as expected from next-generation industrial VRFBs, the generated irreversible heat can exceed the absolute value of reversible heat, because the former contribution roughly scales with the square of the stack current, and the latter is directly proportional to the stack current. Consequently, when operating at high current, the temperatures increase during both charge and discharge, calling for an efficient cooling system to prevent species precipitation at high temperatures. Even if the highest temperatures occur at the end of a discharge phase, when the concentration of VO_2^+ is low, VO_2^+ precipitation could represent an issue resulting in occlusion of the small flow channels in the cell frames and battery faults. It can be concluded that the next generation VRFBs, capable of higher power densities and high current densities, require specific heat exchangers to thermally assist the VRFB operation.

The losses and efficiency analysis investigated both experimentally and numerically provided results for the IS-VRFB system on which they were measured and computed. However, some general considerations can be drawn, which apply to any other large industrial-scale VRFB system. First, the design of a compact VRFB stack provided with a quite large number of cells should be addressed to reduce shunt currents, by increasing the electrolyte electric resistances in the internal manifolds and flow channels, with marginal consequences on the hydraulic performance. In other words, longer and thinner flow paths should be preferred in the trade-off between shunt current and hydraulic losses, with the limit that flow channels do not risk being clogged by electrolyte impurities. For example, the flow channels of the flow frame (e.g. those of IS-VRFB test facility) could be lengthened without significant effects on hydraulic losses. Second, for high-current operations the cell over potential losses are larger than crossover losses. Consequently, the cell internal equivalent resistances (which are mainly due to the membrane ohmic over potentials), impact on efficiency more than the membrane species permeability from which the crossover losses originate, particularly in a compact VRFB stack, namely capable of operating at higher current density than those usually reported in the literature (e.g. the 19-cell stack with 1500 cm^2 area of the 2.5 kW/15 kWh reported by Tang et al. [308]) and thus provided with a smaller cell active area. In fact, in our study crossover losses were a little higher than the over potential losses only in the 30 A operation (Tab.8.2). Consequently, increasing the membrane ion conductivity is a more important issue than reducing its vanadium species permeability, especially in a high current operation. Third, hydraulic losses were found to depend largely on the low efficiency of electric motors and pumps as typically occur in small size devices (e.g. 50% and 20%–55%, respectively, in our study). Conversely, we found that only less than a quarter of overall hydraulic losses were due to the hydraulic circuit (i.e. to stack and piping). It must be noted, however, that ancillary device efficiencies can be much higher in larger units fitted to larger systems. For instance, a 5 kW motor suitable for a 150 kW VRFB can have an efficiency above 75% and larger motors can easily exceed 90%. To the best of our knowledge, similar analyses of the effect of ancillary losses were largely overlooked in the existing literature.

The experimental study performed on this system has shown the effectiveness of modulating the electrolyte flow rate and flow factor in minimizing the stack transport losses, without affecting the electrical performance of an RFB during charge and discharge cycles. In particular, to achieve the best efficiency performance it is crucial to control the electrolyte flow rates, minimizing the flow-rate depended losses under the constraint of providing a proper flow factor to sustain the current I at a given SOC . As an additional statement, we have found that operating the battery

at $\alpha = \alpha_k$ enables the minimization of cell internal losses. Accordingly, the equivalent internal resistance is minimized and reduced to the ohmic value only, $R \simeq R_k(SOC)$. In these conditions, a linear behavior of the polarization curves $V(I)$ occurs, that is, a constant value of the total battery resistance R , over the whole I range and at any fixed SOC . This strategy yields more efficient results in terms of maximizing the RTE than operating the stack at constant flow factor. In particular, the proposed strategy was found to produce an increase of the RTE of approximately 2% with respect to operation at a constant flow factor of $\alpha = 8$, which is very close to the optimal constant $\alpha = 7.5$ reported in the literature [240]. It is important to note that the proposed flow factor modulation does not require any change of the system hardware. Instead, it can be easily implemented at a software level in the control routines of the system supervisor (i.e. the BMS). In addition, we can note that further improvement of the battery performance, namely further reductions of internal losses can be obtained by reducing the ohmic resistance, which allows for larger limiting currents and maximum delivered power. This result can be obtained mainly by reducing the carbon felts and membrane resistances [389]. In addition, the use of advanced electrode materials capable of better mass transport can reduce the value of α_k and thus reduce the requested Q and the consequent pumping power. This aspect requires efficient porous electrodes to enhance electrolyte dispersion on the active sites, which can be obtained through innovative design of the electrode micro- and macro-structures [128]. Finally, the method that we have developed for investigating the optimal flow factor in IS-VRFB can constitute a simple method for controlling the electrolyte flow rates in every operating condition, with the aim of maximizing the efficiency of large VRFBs.

Transient characteristics have also been analyzed. Different conditions were examined to explore the VRFB fast response, by varying $SOCs$, flow rates, and passive load. The first 20 mS presented a common "peak transient" region in all cases, in which both current and voltage changed more, even up to 50%. This time region never exceeded 7 ms, and the stack could not provide useful power that can be used successfully in a real application. Further investigations are necessary in this regard.

An aging effect evaluation was performed after one year of operation with a full inspection of each component, and no major defect was found.

Finally, preliminary results are presented on EIS analyses. Much more must be done and a future extensive experimental campaign needs to be carried out on the IS-VRFB stack. Until now, preliminary analysis has demonstrated the suitability of the model in Fig.11.16 to predict the electrical behavior of the stack cells.

The equivalent circuit consists of an equivalent Thévenin potential, which is a function of the SOC , temperature of the cell, an internal ohmic resistance, R_{el} , which corresponds to the effect of current excitation into the cell stack, a pair of in-series resistor/capacitor (RC) networks, which represent the time-dependent VRFB dynamics of activation (R_a, C_a), and transport losses (R_t, C_t).

For the sake of simplicity, the parameters of the 6-th, 12-th, 16-th, and 20-th cells at $SOC=60\%$ with 20 L min^{-1} and $I=80 \text{ A}$ are reported (Tab.11.2 and Fig.11.17) that show good agreement between the experimental and numerical data. Similar results have been verified for other conditions. Results from this preliminary experimental campaign show quite good uniformity among the cells (Fig.11.17). At present, differences between the cells enlarge with increasing battery load conditions, but further investigations are needed to investigate this issue more thoroughly. Moreover, a state of health (SOH) analysis is planned, in cooperation with the University of Salerno, which aims to investigate the parameter identification of the lumped circuit and the implementation of a diagnostics technique for such industrialized VRFBs.

Chapter 13

Conclusion and future work

The work reported in this thesis constitutes a contribution to the technological development and scaling-up of redox flow battery systems. The work was carried out wholly or mainly by the candidature during the PhD program (09/01/2016–09/30/2019). This thesis has been entirely written by the candidate, who developed by himself or together with other in a leading role all the reported work. The main activities which have been carried out by the author are reported hereafter:

- design of the IS-VRFB test facility with particular regard to the balance of plant;
- manufacturing of the test facility, including stack and balance of plant, with a continuative presence in the producer premises (Proxima s.r.l., Medicina BO) along a period of eight months;
- assembly of the IS-VRFB in the Energy Storage and Conversion Lab at UNIPD-DII;
- selection and installation of the whole instrumentation;
- commissioning of IS-VRFB, including all corrective action that were needed in this phase;
- development and implementation of the measurement system and BMS;
- development and implementation of the BMS software for data processing and experiment control;
- numerical modelling of IS-VRFB for investigating the electrical, energetic and thermal performances;
- responsibility of coordination and supervision of n. 3 ERASMUS master students, n. 3 master students and n. 8 undergraduate student in their thesis works. In addition, two master graduated scholarship holders have been led in their research programs. All these activities were both numerical and experimental.

This topic has a strong multidisciplinary focus and requires expertise in mechanical engineering, electrical engineering, materials science, electrochemistry, chemistry, and modelling by means of computational simulations. Accordingly, future activities are planned in terms of collaboration with universities, research institutes (both national and international) to conduct this new research field. This topic was first proposed by my supervisor Prof. Massimo Guarnieri and its importance is also recognized by many groups, for example, first by the groups of the University of Southampton (UK), University of New South Wales (Australia) and Fraunhofer (Germany).

Some of the main guidelines for driving future research on IS-VRFBs are identified as follows:

- Further investigation on fast response to reproduce real frequency regulation and peak shaving scenarios from real cases in photovoltaic systems PV and wind parks;
- an extensive EIS experimental campaign to complete electric modelling in transient regimes (actually realized for stationary regime);
- extraordinary maintenance to solve some leakage problem by testing innovative and advanced techniques such as plasma welding and bonding with new glues;

- the IS-VRFB is designed for future expansions and upgrades. In particular, the hydraulic circuits will be provided with ports for installing small stacks, in which new materials and cell architectures can be tested before being adopted in a future larger stack. This activity will be developed first by using quite a small single cell suitable to test samples provided by several international producers;
- plasma treatment of graphite BPs and felts in large scale cells to improve the electrical performance of the cell;
- implementation of an advanced thermal management system based on the developed thermal models;
- potentiometric titration by using a glove box to develop accurate measurements of the *SOC* as a function of *OCV*;
- advanced methods for *SOC* prediction using numerical techniques;
- the system was recently upgraded by substituting the pumps and the discharge electric circuitry to allow operating the stack at higher currents. Data extrapolation suggests that current densities as high as 1 A cm^{-2} could be achieved;
- an extension of the investigations performed with CT and the Lattice Boltzmann method to other felt samples provided by several international producers;
- development of a general multiphysics dynamic numerical model that considers the electrolyte flow through homogeneous porous electrodes coupled to the electrochemical kinetics and mass transport, in collaboration with the Division of Fluid Dynamics at Chalmers University of Technology (Sweden);
- investigation on the electrolyte volume change during charge/discharge operations;
- simulation of polarization curves as a function of several control parameters by means of an advanced numerical model, in cooperation with Prof. Federico Moro (UNIPD).

Achievements

The results from this work have been partially reported in publications in high impact international journals.

Journal papers published

- Federico Moro, **Andrea Trovò**, Stefano Bortolin, Davide Del Col, Massimo Guarnieri. An alternative low-loss stack topology for vanadium redox flow battery: Comparative assessment. In: Journal of Power Sources 340 (2017), pp. 229-241. issn: 0378-7753. doi: <https://doi.org/10.1016/j.jpowsour.2016.11.042>. url: <http://www.sciencedirect.com/science/article/pii/S0378775316315683>. Impact factor: 7.467. Citations (29/11/2019): 12.
- Massimo Guarnieri, **Andrea Trovò**, Angelo D'Anzi, Piergiorgio Alotto. Developing vanadium redox flow technology on a 9-kW 26-kWh industrial scale test facility: Design review and early experiments. In: Applied Energy 230 (2018), pp. 1425-1434. issn: 0306-2619. doi: <https://doi.org/10.1016/j.apenergy.2018.09.021>. url: <http://www.sciencedirect.com/science/article/pii/S0306261918313291>. Impact factor: 8.426. Citations (29/11/2019): 15.
- Dario Maggiolo, Filippo Zanini, Francesco Picano, **Andrea Trovò**, Simone Carmignato, Massimo Guarnieri. Particle based method and X-ray computed tomography for pore scale flow characterization in VRFB electrodes. In: Energy Storage Materials 16 (2019), pp. 91-96. issn: 2405-8297. doi: <https://doi.org/10.1016/j.ensm.2018.04.021>. url: <http://www.sciencedirect.com/science/article/pii/S2405829718300072>. Cite score: 15.09. Citations (29/11/2019): 9.
- **Andrea Trovò**, Giacomo Marini, Alessandro Sutto, Piergiorgio Alotto, Federico Moro, Massimo Guarnieri. Standby thermal model of a vanadium redox flow battery stack with crossover and shunt-current effects. In: Applied Energy 240 (2019), pp. 893-906. issn: 0306-2619. doi: <https://doi.org/10.1016/j.apenergy.2019.02.067>. url: <http://www.sciencedirect.com/science/article/pii/S0306261919303642>. Impact factor: 8.426. Citations (29/11/2019): 7.
- **Andrea Trovò**, Alberto Saccardo, Monica Giomo, Massimo Guarnieri. Thermal modeling of industrial-scale vanadium redox flow batteries in high-current operations. In: Journal of Power Sources 424 (2019), pp. 204-214. issn:0378-7753. doi: <https://doi.org/10.1016/j.jpowsour.2019.03.080>. url: <http://www.sciencedirect.com/science/article/pii/S0378775319303271>. Impact factor: 7.467. Citations (29/11/2019): 3.
- Massimo Guarnieri, **Andrea Trovò**, Giacomo Marini, Alessandro Sutto, Piergiorgio Alotto. High current polarization tests on a 9kW vanadium redox flow battery. In: Journal of Power Sources 431 (2019), pp. 239-249. issn: 0378-7753. doi: <https://doi.org/10.1016/j.jpowsour.2019.05.035>. url: <http://www.sciencedirect.com/science/article/pii/S0378775319305907>. Impact factor: 7.467. Citations (29/11/2019): 3.
- **Andrea Trovò**, Francesco Picano, and Massimo Guarnieri. Comparison of energy losses in a 9kW vanadium redox flow battery. In: Journal of Power Sources 440 (2019), p. 227144. issn: 0378-7753. doi: <https://doi.org/10.1016/j.jpowsour.2019.227144>. url: <http://www.sciencedirect.com/science/article/pii/S0378775319311371>. Impact factor: 7.467. Citations (29/11/2019): 0.

Published Papers in Conference Proceedings

- **Andrea Trovò**, Francesco Picano, Massimo Guarnieri. Maximizing Vanadium Redox Flow Battery Efficiency: Strategies of Flow Rate Control. IEEE 28th International Symposium on Industrial Electronics (ISIE), IEEE; 2019. 1977-1982; <https://doi.org/10.1109/ISIE.2019.8781152>. Citations (29/11/2019): 1.

Cumulative impact factor: 61.81.

Journal papers submitted

- Massimo Guarnieri, **Andrea Trovò**, Francesco Picano. Enhancing the efficiency of kW-class Vanadium Redox Flow Batteries by flow factor modulation: an experimental method (Submitted Appl Energy). Impact factor: 8.426.
- **Andrea Trovò**, Piergiorgio Alotto, Monica Giomo, Federico Moro, Massimo Guarnieri. A validated dynamical model of a kW-class Vanadium Redox Flow Battery (Submitted MATCOM, Impact factor: 1.88, first quartile).

Patent applications deposited

- Millibaric pressure safe control system in inert atmosphere for highly reactive liquid solutions; **Andrea Trovò**, Massimo Guarnieri.
- State of charge management tank for redox flow battery; **Andrea Trovò**, Francesco Picano, Massimo Guarnieri.
- Anisotropic carbon felt electrodes for improving performance on vanadium redox flow battery; Dario Maggiolo, **Andrea Trovò**, Francesco Picano, Massimo Guarnieri.

Collaborations

- ENI S.p.a. (Italy): technical support on vanadium redox flow battery plant of ENI;
- Chalmers University (Sweden): development of a general multiphysics dynamic approach by using Lattice-Boltzmann method to investigate carbon felts hydraulic properties;
- Skolkovo University (Russia): performance improvements on Vanadium Redox Flow Battery;
- Fraunhofer institute (Germany): graduated students internship to Fraunhofer laboratories on Vanadium Redox Flow Battery as common exchange program.

Presentations given at conferences

By the autor

Oral presentation

- **Andrea Trovò**, Piergiorgio Alotto, Monica Giomo, Federico Moro, Massimo Guarnieri; Recent results on industrial-scale energy storage with Vanadium Redox Flow Battery. The 13th international conference of the IMACS TC1 Committee, Electrimacs 2019, Salerno (Italy), 21–23 May 2019;
- **Andrea Trovò**, Francesco Picano, Massimo Guarnieri; Energy Losses Analyses in a 9 kW Vanadium Redox Flow Battery Test Facility. VIII International Conference on Coupled Problems in Science and Engineering, Coupled 2019, Barcelona, (Spain), 03–05 June 2019.

Poster

- **Andrea Trovò**, Stefano Bortolin, Davide Del Col, Federico Moro, Piergiorgio Alotto, Massimo Guarnieri; An alternative stack topology for vanadium redox flow battery. 2nd International Conference on Battery and Fuel Cell Technology, Rome (Italy), 27–28 July 2017;
- **Andrea Trovò**, Stefano Bortolin, Davide Del Col, Federico Moro Piergiorgio Alotto, Massimo Guarnieri; An alternative stack topology for vanadium redox flow battery. 33th International CAE conference, Vicenza (Italy), 06–07 November 2017;
- **Andrea Trovò**, Giacomo Marini, Alessandro Sutto, Piergiorgio Alotto, Massimo Guarnieri; The UNIPD 9-kW/26-kWh IS-VRFB experiment. ET 2018 XXXIV Riunione Annuale dei Ricercatori di Elettrotecnica, Rome (Italy), 14–15 June 2018;
- **Andrea Trovò**, Giacomo Marini, Alessandro Sutto, Piergiorgio Alotto, Massimo Guarnieri; The UNIPD 9-kW/26-kWh IS-VRFB experiment. The International Flow Battery Forum Lausanne, (Switzerland), 10–12 July 2018;
- **Andrea Trovò**, Giacomo Marini, Alessandro Sutto, Piergiorgio Alotto, Massimo Guarnieri; The UNIPD 9-kW/26-kWh IS-VRFB experiment. 69th Annual meeting of the International Society of Electrochemistry, Bologna (Italy), 02–07 September 2018;
- **Andrea Trovò**, Federico Moro, Piergiorgio Alotto, Massimo Guarnieri; Experimental and numerical research on industrial scale vanadium flow batteries. ET 2019 XXXV Riunione Annuale dei Ricercatori di Elettrotecnica, Viterbo (Italy), 20–21 June 2019;
- **Andrea Trovò**, Monica Giomo, Federico Moro, Piergiorgio Alotto, Massimo Guarnieri; Thermal modelling of industrialized VRFB. The International Flow Battery Forum 2019, Lyon (France), 09–11 July 2019.

Main oral presentations with Andrea Trovò as coauthor

- Dario Maggiolo, **Andrea Trovò**, Francesco Picano, Simone Carmignato, Massimo Guarnieri; Characterization of fluid flow dispersion in electrodes by means of computed tomography and Lattice-Boltzmann simulations. PRIME 2016, Honolulu (US-Hi), 02-07 October 2016;
- Dario Maggiolo, **Andrea Trovò**, Francesco Picano, Filippo Zanini, Simone Carmignato, Massimo Guarnieri; Lattice-Boltzmann and Lagrange Particle Tracking methods based on porous medium X-ray Computed Tomography for analysing fluid dispersion in Flow Battery electrodes. Coupled Problems 2017, Rhodes Island (Greece), 12-14 June 2017;
- Dario Maggiolo, **Andrea Trovò**, Francesco Picano, Filippo Zanini, Simone Carmignato, Massimo Guarnieri; Lattice-Boltzmann and Lagrange Particle Tracking methods based on porous medium X-ray Computed Tomography for analyzing fluid dispersion in Flow Battery electrodes. 21st SSI, Padua (Italy), 18-23 June, 2017;
- **Andrea Trovò**, Francesco Picano, Massimo Guarnieri; Maximizing Vanadium Redox Flow Battery Efficiency: Recent Results on a 9kw-27kWh test facility. The International Flow Battery Forum 2019, Lyon (France), invited, 09-11 July 2019;
- **Andrea Trovò**, Francesco Picano, Massimo Guarnieri; Maximizing Vanadium Redox Flow Battery Efficiency: Strategies of Flow Rate Control. IEEE 28th International Symposium on Industrial Electronics (ISIE), Vancouver (Canada), 12-14 June 2019;
- Francesco Picano, **Andrea Trovò**, Massimo Guarnieri; Impact of Flow Dynamics on the Performance of a Vanadium Redox Flow Battery. Coupled 2019, Barcelona, (Spain), 03–05 June 2019.

Awards

- Best Poster Award. 2nd International Conferences on Battery and Fuel Cell Technology, Rome (Italy), 27-28 July 2017;
- Certificate of Achievement for his outstanding contribution to the poster session. The International Flow Battery Forum Lausanne, (Switzerland), 10–12 July 2018;
- Best paper award. The 13th international conference of the IMACS TC1 Committee, Electrimacs 2019, Salerno (Italy), 21–23 May 2019.

Funding

This work was funded by the University of Padua under the strategic project MAESTRA 2011 "From Materials for Membrane-Electrode Assemblies to Electric Energy Conversion and Storage Device" (cod. STPD11XNRY 002), and the Project 2016 of the Interdepartmental Centre Giorgio Levi Cases for Energy Economics and Technology (GUAR RICERCALASCITOLEVI1702).

Appendix A

Electrolyte properties investigations

A.1 Viscosity measurements

Data regarding the mechanical properties of electrolytes in VRFB systems is largely missing from existing literature. Different concentrations of vanadium and sulfuric acid are selected to adjust properties such as the energy density [390]. Mixing different additives is also common as a means to improve the stability of the solution at extreme temperatures Sec.5.4. In addition, the properties of the electrolyte change with the *SOC* as a chemical reaction takes place. The viscosity and density of the present electrolytes, consisting of an aqueous solution of 4.5 mol L⁻¹ sulfuric acid and 1.6 mol L⁻¹ of vanadium (without further additives) were measured and the results presented here. First, the battery was charged up to *SOC*=90% and then discharged by 10% for each step. After each interval, small probes of 25 ml were withdrawn from both the positive and negative sides making use of "pick-up" ports in the pipes (Sec.4.1.1). The use of syringes enables the withdrawal of the correct amount of liquid, and precision of dosage for measurements. This operation is presented in the following Fig.A.1 (left).

First, the density was measured by using a pycnometer, which is a vessel that takes up the exact volume of liquid (25 ml), as shown in Fig.A.1 (center). The density can be calculated directly by dividing the measured weight by the liquid volume. In the next step, the kinematic viscosity of the electrolyte was determined by using a U-tube reverse flow viscometer from PSL-rheotek (type BS/IP/RF; size 2). This measurement device consists of a U-shaped glass pipe with sections of different diameters. The principle is based on the time measurement, whereby a certain amount of liquid needs to flow through the pipe, driven by its own gravity.

The kinematic viscosity is proportional to this time measurement and can simply be obtained with a given calibration constant. The viscometer used here is shown in Fig.A.1 (right), where the filling tube is at the left side and the measuring tube at the right side. The measurement was completed in the following way: first, the tube was filled with liquid up to the mark; second, the measuring tube was sealed so that the levels in both tubes could not balance. This is shown in Fig.A.2. Then, the sealing plug was lifted slightly to arrest the liquid levels exactly at both start marks. At the beginning of the measurement, the seal was removed completely and the liquid was released to flow from the filling tube to the measuring tube, driven only by the gravitational force. The time required to move through the upper extended section of the measuring tube was measured and the kinematic viscosity ν was computed:

$$\nu = ck \times t \tag{A.1}$$

The measured time t and the constant ck is a calibration constant, which was determined for the individual U-tube and provided by the manufacturer. In this case, it amounts to 0.009888 mm² s⁻² and is valid for standard conditions of 25 °C. Therefore, it should be corrected when the temperature differs significantly from these conditions. In this case, the battery was discharged step by step, so that the heat release during discharge could not raise the internal temperature over ± 2 ° from the standard conditions, and the average temperature amounted to 25.7 °C. Consequently, the temperature was considered to be close enough to the standard temperature. The results of the density measurements at different *SOC* between 10% and 90% are shown in

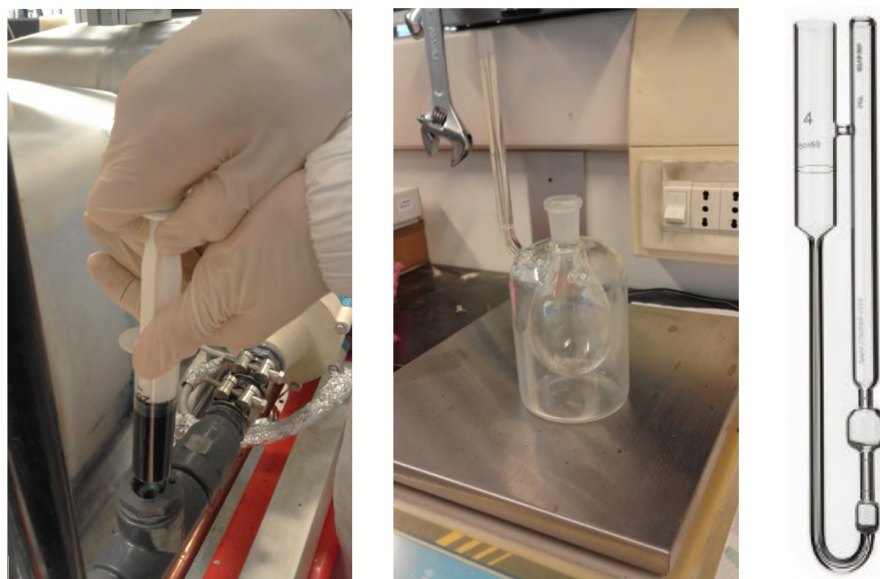


FIGURE A.1: Left: withdrawal of electrolyte with a syringe; center: pycnometer on the scale; right: reverse flow U-tube viscometer.

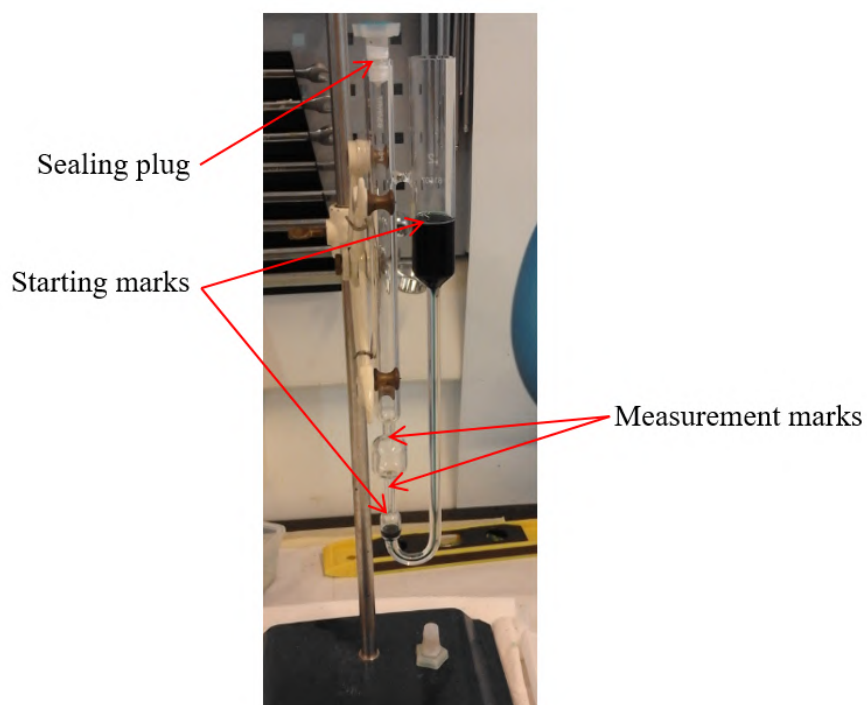


FIGURE A.2: Viscosimeter with sealed measuring tube to arrest the levels precisely at the starting marks.

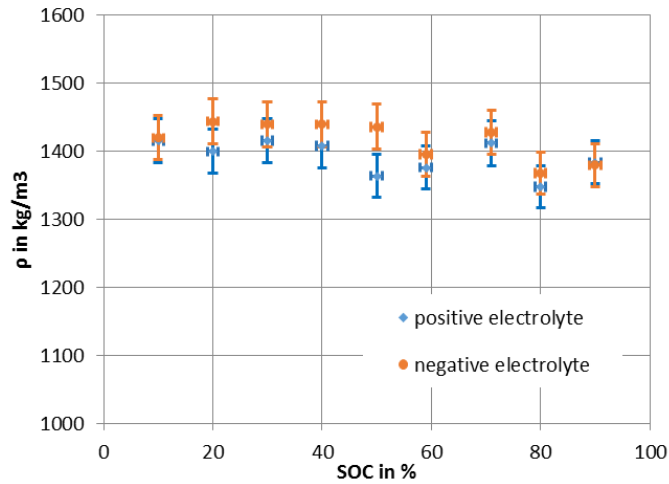
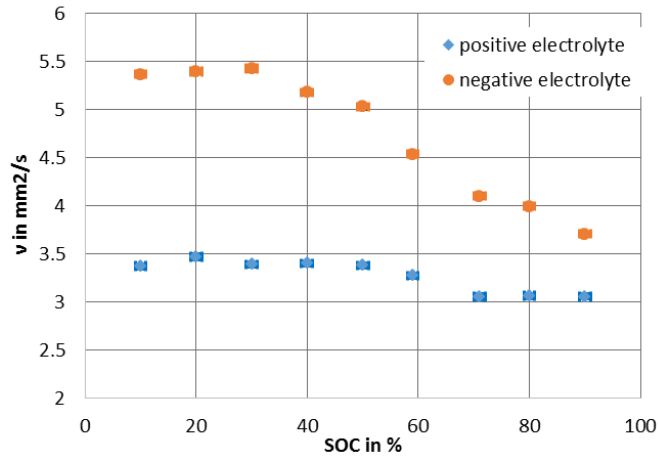
FIGURE A.3: Measured density ρ values of the positive and negative electrolyte.FIGURE A.4: Measured kinematic viscosity ν of the positive and negative electrolyte.

Fig.A.3. The estimated uncertainty of the density value and the uncertainty of the determination of SOC , which is estimated with $\pm 1\%$, is also shown. The densities of both electrolytes were generally nearly constant along the whole range of SOC .

An average value of 1392 kg m^{-3} for the positive electrolyte and 1417 kg m^{-3} for the negative electrolyte were measured. The measurement results for the kinematic viscosity are displayed in Fig.A.4.

While the positive electrolyte with $V(V)$ and $V(IV)$ only showed a very slight increase of viscosity as SOC decreased, the values of the negative electrolyte with $V(III)$ and $V(II)$ rose significantly. The former had a viscosity of approximately $3.45 \text{ mm}^2 \text{ s}^{-1}$ at low SOC (between 10% and 40%) and it dropped to $3.06 \text{ mm}^2 \text{ s}^{-1}$ above $SOC=60\%$. The latter showed a nearly constant viscosity of approximately $5.45 \text{ mm}^2 \text{ s}^{-1}$ below $SOC=30\%$ and then started decreasing to $3.71 \text{ mm}^2 \text{ s}^{-1}$ at $SOC=90\%$. Similar behavior was found by Li et al. [229], who reported a strong increase of viscosity with decreasing SOC , especially for the negative electrolyte.

The viscosity values have a low uncertainty because the U-tube can be filled with liquid very accurately, and it is designed to obtain long measurement durations of approximately 5–9 m to reduce the uncertainty of time. As a result, the vertical uncertainty is not even visible in the figure A.3. Concluding the effect of the kinematic viscosity variation with the SOC needs to be taken into account. Accordingly, they are fitted numerically by using a second order polynomial function, for which the parameters are shown in Tab.A.1:

TABLE A.1: Empirical parameters in Eq.A.1 for the SOC -dependence of the kinematic viscosity of both electrolytes.

	A	B	C
Positive electrolyte	-8×10^{-5} $mm^2 s^{-1} SOC(\%)^{-2}$	0.0022 $mm^2 s^{-1} SOC(\%)^{-1}$	3.4078 $mm^2 s^{-1}$
Negative electrolyte	-0.0002 $mm^2 s^{-1} SOC(\%)^{-2}$	0.0005 $mm^2 s^{-1} SOC(\%)^{-1}$	5.4872 $mm^2 s^{-1}$

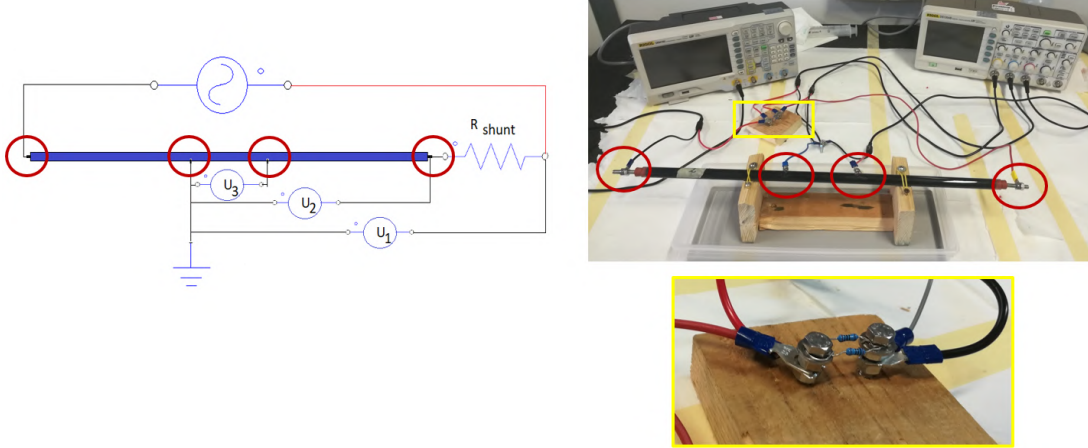


FIGURE A.5: Four pole electrode for electric conductivity measurements.

$$\nu = A \times SOC^2 + B \times SOC + C \quad (\text{A.2})$$

The considerably higher viscosity of the negative electrolyte (compared to the positive one) always causes a bigger pressure drop in the negative hydraulic circuit. This effect has already been noticed during operation.

A.2 Electrical conductivity measurements

A low-cost conductivity meter was built and used based on the four-pole structure. Fig.A.5. It was used to assess conductivity, upon variation of the state of charge of a standard vanadium solution ($SOC=50\%$). First, the physical limits of such a four-pole device were revealed, as follows: susceptibility to the polarization effect in DC and at low frequencies (lower than 20 kHz), and the ability to perform measurements only in AC. Indeed, as a direct component (a bias), it caused the electro deposition of ions on the electrodes, not allowing the stability over time of the system to the input voltage. This was caused by using the wrong material (stainless steel).

Further investigations demonstrate that graphite is a proper electrode material. In the future, further activities should be carried out to build a four-pole device based on graphite electrodes that eliminates the polarization effects, by ensuring the measurements of the electrical conductivity in comparison to the declared value from the literature (from which the electric model was built).

Appendix B

Standards Publication



BSI Standards Publication

Secondary cells and batteries for renewable energy storage — General requirements and methods of test

Part 2: On-grid applications

National foreword

This British Standard is the UK implementation of EN 61427-2:2015. It is identical to IEC 61427-2:2015. Together with BS EN 61427-1:2013, it supersedes BS EN 61427:2005 which is withdrawn.

The UK participation in its preparation was entrusted to Technical Committee PEL/21, Secondary cells and batteries.

A list of organizations represented on this committee can be obtained on request to its secretary.

This publication does not purport to include all the necessary provisions of a contract. Users are responsible for its correct application.

© The British Standards Institution 2016.
Published by BSI Standards Limited 2016

ISBN 978 0 580 74814 1

ICS 27.160; 29.220.20

Compliance with a British Standard cannot confer immunity from legal obligations.

This British Standard was published under the authority of the Standards Policy and Strategy Committee on 30 April 2016.

Amendments/corrigenda issued since publication

Date	Text affected
------	---------------

EUROPEAN STANDARD

EN 61427-2

NORME EUROPÉENNE

EUROPÄISCHE NORM

November 2015

ICS 29.220.20

English Version

**Secondary cells and batteries for renewable energy storage -
General requirements and methods of test - Part 2: On-grid
applications
(IEC 61427-2:2015)**

Accumulateurs pour le stockage de l'énergie renouvelable -
Exigences générales et méthodes d'essais - Partie 2:
Applications en réseaux
(IEC 61427-2:2015)

Wiederaufladbare Zellen und Batterien für die Speicherung
erneuerbarer Energien - Allgemeine Anforderungen und
Prüfverfahren - Teil 2: Netzgekoppelte Anwendungen
(IEC 61427-2:2015)

This European Standard was approved by CENELEC on 2015-10-02. CENELEC members are bound to comply with the CEN/CENELEC Internal Regulations which stipulate the conditions for giving this European Standard the status of a national standard without any alteration.

Up-to-date lists and bibliographical references concerning such national standards may be obtained on application to the CEN-CENELEC Management Centre or to any CENELEC member.

This European Standard exists in three official versions (English, French, German). A version in any other language made by translation under the responsibility of a CENELEC member into its own language and notified to the CEN-CENELEC Management Centre has the same status as the official versions.

CENELEC members are the national electrotechnical committees of Austria, Belgium, Bulgaria, Croatia, Cyprus, the Czech Republic, Denmark, Estonia, Finland, Former Yugoslav Republic of Macedonia, France, Germany, Greece, Hungary, Iceland, Ireland, Italy, Latvia, Lithuania, Luxembourg, Malta, the Netherlands, Norway, Poland, Portugal, Romania, Slovakia, Slovenia, Spain, Sweden, Switzerland, Turkey and the United Kingdom.



European Committee for Electrotechnical Standardization
Comité Européen de Normalisation Electrotechnique
Europäisches Komitee für Elektrotechnische Normung

CEN-CENELEC Management Centre: Avenue Marnix 17, B-1000 Brussels

European foreword

The text of document 21/862/FDIS, future edition 1 of IEC 61427-2, prepared by IEC/TC 21 "Secondary cells and batteries" was submitted to the IEC-CENELEC parallel vote and approved by CENELEC as EN 61427-2:2015.

The following dates are fixed:

- latest date by which the document has to be implemented at national level by publication of an identical national standard or by endorsement (dop) 2016-07-02
- latest date by which the national standards conflicting with the document have to be withdrawn (dow) 2018-10-02

Attention is drawn to the possibility that some of the elements of this document may be the subject of patent rights. CENELEC [and/or CEN] shall not be held responsible for identifying any or all such patent rights.

Endorsement notice

The text of the International Standard IEC 61427-2:2015 was approved by CENELEC as a European Standard without any modification.

In the official version, for Bibliography, the following notes have to be added for the standards indicated:

IEC 60623	NOTE	Harmonized as EN 60623.
IEC 60730-1	NOTE	Harmonized as EN 60730-1.
IEC 60812	NOTE	Harmonized as EN 60812.
IEC 60896-11	NOTE	Harmonized as EN 60896-11.
IEC 60896-21	NOTE	Harmonized as EN 60896-21.
IEC 60896-22	NOTE	Harmonized as EN 60896-22.
IEC 61025	NOTE	Harmonized as EN 61025.
IEC 61427-1	NOTE	Harmonized as EN 61427-1.
IEC 61508	NOTE	Harmonized in EN 61508 series.
IEC 61508-7	NOTE	Harmonized as EN 61508-7.
IEC 62133	NOTE	Harmonized as EN 62133.
IEC 62259	NOTE	Harmonized as EN 62259.

IEC 62485-3	NOTE	Harmonized as EN 62485-3.
IEC 62619 ¹⁾	NOTE	Harmonized as EN 62619 ¹⁾ .
IEC 62620	NOTE	Harmonized as EN 62620.
IEC 62675	NOTE	Harmonized as EN 62675.

1) At draft stage..

CONTENTS

FOREWORD.....	4
1 Scope.....	6
2 Normative references	6
3 Terms and definitions	6
4 General considerations.....	13
5 General test conditions.....	14
5.1 Accuracy of measuring equipment	14
5.1.1 Voltage measurements	14
5.1.2 Current measurements	14
5.1.3 Temperature measurements	14
5.1.4 Time measurements	14
5.2 Test object considerations	14
5.3 Test object battery selection and size considerations	15
5.4 Test plan.....	16
6 Battery endurance	20
6.1 General.....	20
6.2 Test for endurance in frequency-regulation service	20
6.3 Test for endurance in load-following service	25
6.4 Test for endurance in peak-power shaving service	28
6.5 Test for endurance in photovoltaic energy storage, time-shift service.....	30
7 Battery properties and electrical performance.....	33
7.1 Declaration of the system properties	33
7.2 Determination of energy content at +25 °C ambient temperature.....	36
7.3 Determination of the energy efficiency during endurance tests at +25 °C ambient temperature	36
7.4 Determination of the energy efficiency during endurance tests at the minimum and maximum ambient temperature	38
7.5 Determination of waste heat generated during endurance tests at the maximum ambient temperature	42
7.6 Determination of energy requirements during periods of idle state at +25 °C ambient temperature	44
Annex A (informative) Battery-related hazards	47
A.1 General.....	47
A.2 Examples	47
Bibliography.....	49
Figure 1 – Boundary of the full-sized battery (FSB).....	15
Figure 2 – Two-step selection process of the test object battery (TOB)	16
Figure 3 – Workflow for the determination of endurance properties and electrical performance of the TOB as governed by the sequence of test data generation within 6.2 to 6.5	17
Figure 4 – Sequence of performance tests carried out with TOB 1 within an endurance test 6.x	17
Figure 5 – Workflow and decision tree for endurance tests 6.2 through 6.5	19
Figure 6 – Frequency regulation service test routine profile (6.2) – Profile a	22
Figure 7 – Frequency regulation service test routine profile (6.2) – Profile b	22

Figure 8 – Frequency regulation service test routine profile (6.2) – Profile c	23
Figure 9 – Schematic view of the evolution of battery voltage over time during cycling with constant power discharge and charge pulses.....	24
Figure 10 – Load-following service test routine profile (6.3) – Profile a	26
Figure 11 – Load-following service test routine profile (6.3) – Profile b	27
Figure 12 – Load-following service test routine profile (6.3) – Profile c.....	27
Figure 13 – Daily peak-power shaving service test routine profile (6.4)	29
Figure 14 – Daily photovoltaic energy storage time-shift service test routine (6.5) – 3 kW	32
Figure 15 – Daily photovoltaic energy storage time-shift service test routine (6.5) – 30 kW	32
Figure 16 – Schematic view of the location of the two sets of energy values (energy to auxiliaries and energy to and from TOB) to be used for the determination of the energy storage efficiency factor η	37
Figure 17 – Schematic view of the location of the two sets of energy values (energy to auxiliaries and energy to and from battery) to be used for the determination of the amount of waste heat generated	43
Figure 18 – Schematic view of the location of the two sets of energy values (energy to auxiliaries and energy to battery) to be used for the determination of the energy requirements during periods of idle state of the battery	45
Table 1 – Summary of endurance test related electrical property data of the full-sized (FSB) and the test object (TOB) battery	34
Table 2 – Summary of physical dimension data of the full-sized battery (FSB)	35
Table 3 – Summary description of the full-sized battery (FSB)	35
Table 4 – Summary description of the test-object battery (TOB).....	35
Table 5 – Summary of the constant power discharge performance of the TOB at an ambient temperature of $+25\text{ °C} \pm 3\text{ K}$	36
Table 6 – Summary of energy efficiencies determined in endurance tests at an ambient temperature of $+25\text{ °C} \pm 3\text{ K}$	38
Table 7 – Summary of energy efficiencies determined in endurance cycle tests at the minimum and maximum ambient temperature	40
Table 8 – Parameters to achieve and maintain the target operational state of charge, SoC_{OT} , during tests at the minimum ambient temperature.....	41
Table 9 – Parameters to achieve and maintain the target operational state of charge, SoC_{OT} , during tests at the maximum ambient temperature.....	42
Table 10 – Summary of energy released as heat during endurance tests at the maximum ambient temperature	44
Table 11 – Summary of energy required during idle state periods at $+25\text{ °C} \pm 3\text{ K}$ ambient temperature	46
Table A.1 – Non-exhaustive listing of potential battery-related hazards to be taken in consideration in risk assessment activities.....	47
Table A.2 – Non-exhaustive listing of potential installation-related hazards to be taken in consideration in risk assessment activities	48

INTERNATIONAL ELECTROTECHNICAL COMMISSION

**SECONDARY CELLS AND BATTERIES
FOR RENEWABLE ENERGY STORAGE –
GENERAL REQUIREMENTS AND METHODS OF TEST –****Part 2: On-grid applications**

FOREWORD

- 1) The International Electrotechnical Commission (IEC) is a worldwide organization for standardization comprising all national electrotechnical committees (IEC National Committees). The object of IEC is to promote international co-operation on all questions concerning standardization in the electrical and electronic fields. To this end and in addition to other activities, IEC publishes International Standards, Technical Specifications, Technical Reports, Publicly Available Specifications (PAS) and Guides (hereafter referred to as "IEC Publication(s)"). Their preparation is entrusted to technical committees; any IEC National Committee interested in the subject dealt with may participate in this preparatory work. International, governmental and non-governmental organizations liaising with the IEC also participate in this preparation. IEC collaborates closely with the International Organization for Standardization (ISO) in accordance with conditions determined by agreement between the two organizations.
- 2) The formal decisions or agreements of IEC on technical matters express, as nearly as possible, an international consensus of opinion on the relevant subjects since each technical committee has representation from all interested IEC National Committees.
- 3) IEC Publications have the form of recommendations for international use and are accepted by IEC National Committees in that sense. While all reasonable efforts are made to ensure that the technical content of IEC Publications is accurate, IEC cannot be held responsible for the way in which they are used or for any misinterpretation by any end user.
- 4) In order to promote international uniformity, IEC National Committees undertake to apply IEC Publications transparently to the maximum extent possible in their national and regional publications. Any divergence between any IEC Publication and the corresponding national or regional publication shall be clearly indicated in the latter.
- 5) IEC itself does not provide any attestation of conformity. Independent certification bodies provide conformity assessment services and, in some areas, access to IEC marks of conformity. IEC is not responsible for any services carried out by independent certification bodies.
- 6) All users should ensure that they have the latest edition of this publication.
- 7) No liability shall attach to IEC or its directors, employees, servants or agents including individual experts and members of its technical committees and IEC National Committees for any personal injury, property damage or other damage of any nature whatsoever, whether direct or indirect, or for costs (including legal fees) and expenses arising out of the publication, use of, or reliance upon, this IEC Publication or any other IEC Publications.
- 8) Attention is drawn to the Normative references cited in this publication. Use of the referenced publications is indispensable for the correct application of this publication.
- 9) Attention is drawn to the possibility that some of the elements of this IEC Publication may be the subject of patent rights. IEC shall not be held responsible for identifying any or all such patent rights.

International Standard IEC 61427-2 has been prepared by IEC technical committee 21: Secondary cells and batteries.

A list of all parts in the IEC 61427 series, published under the general title *Secondary cells and batteries for renewable energy storage – General requirements and methods of test*, can be found on the IEC website.

The text of this standard is based on the following documents:

FDIS	Report on voting
21/862/FDIS	21/863/RVD

Full information on the voting for the approval of this standard can be found in the report on voting indicated in the above table.

This publication has been drafted in accordance with the ISO/IEC Directives, Part 2.

The committee has decided that the contents of this publication will remain unchanged until the stability date indicated on the IEC website under "<http://webstore.iec.ch>" in the data related to the specific publication. At this date, the publication will be

- reconfirmed,
- withdrawn,
- replaced by a revised edition, or
- amended.

SECONDARY CELLS AND BATTERIES FOR RENEWABLE ENERGY STORAGE – GENERAL REQUIREMENTS AND METHODS OF TEST

Part 2: On-grid applications

1 Scope

This part of IEC 61427 relates to secondary batteries used in on-grid Electrical Energy Storage (EES) applications and provides the associated methods of test for the verification of their endurance, properties and electrical performance in such applications. The test methods are essentially battery chemistry neutral, i.e. applicable to all secondary battery types.

On-grid applications are characterized by the fact that batteries are connected, via power conversion devices, to a regional or nation- or continent-wide electricity grid and act as instantaneous energy sources and sinks to stabilize the grid's performance when randomly major amounts of electrical energy from renewable energy sources are fed into it.

Related power conversion and interface equipment is not covered by this part of IEC 61427.

2 Normative references

The following documents, in whole or in part, are normatively referenced in this document and are indispensable for its application. For dated references, only the edition cited applies. For undated references, the latest edition of the referenced document (including any amendments) applies.

None.

3 Terms and definitions

For the purposes of this document, the following terms and definitions apply.

3.1

accuracy

<of a measuring instrument>

quality which characterizes the ability of a measuring instrument to provide an indicated value close to a true value of the quantity to be measured

Note 1 to entry: This term is used in the "true" value approach.

Note 2 to entry: Accuracy is better when the indicated value is closer to the corresponding true value.

[SOURCE: IEC 60050-311:2001, 311-06-08]

3.2

accuracy class

category of measuring instruments, all of which are intended to comply with a set of specifications regarding uncertainty

[SOURCE: IEC 60050-311:2001, 311-06-09]

3.3

ambient temperature

average temperature of the air or another medium in the vicinity of the equipment

Note 1 to entry - During the measurement of the ambient temperature the measuring instrument/probe should be shielded from draughts and radiant heating.

[SOURCE: IEC 60050-826:2004, 826-10-03]

3.4

maximum ambient temperature

<for battery operation> highest ambient temperature at which the battery is operable and should perform according to specified requirements

[SOURCE: IEC 60050-426:2008, 426-20-17, modified — In the definition, “trace heating” has been replaced with “battery”.]

3.5

minimum ambient temperature

<for battery operation> lowest ambient temperature at which the battery is operable and should perform according to specified requirements

[SOURCE: IEC 60050-426:2008, 426-20-20, modified — In the definition, “trace heating” has been replaced with “battery”.]

3.6

ampere hour

quantity of electrical charge obtained by integrating the current in amperes with respect to time in hours

Note 1 to entry: The SI unit for electric charge is the coulomb (1 C = 1 As) but in practice it is usually expressed in ampere hours (Ah).

3.7

battery

two or more cells fitted with devices necessary for use, for example case, terminals, marking and protective devices

[SOURCE: IEC 60050-482:2004, 482-01-04, modified — In the definition, “one” has been replaced with “two”.]

3.8

battery management system

BMS

battery management unit

BMU

electronic system associated with a battery which monitors and/or manages its state, calculates secondary data, reports that data and/or controls its environment to influence the battery's performance and/or service life

Note 1 to entry: The function of the battery management system can be fully or partially assigned to the battery pack and/or to equipment that uses this battery.

Note 2 to entry: A battery management system is also called a "battery management unit" (BMU).

Note 3 to entry: This note applies to the French language only.

Note 4 to entry: This note applies to the French language only.

3.9**idle state**

<of a battery system> state of a battery which is fully functional but not actively delivering or absorbing energy

Note 1 to entry: Such a system can deliver and absorb energy on demand with a reaction time as required by the application.

Note 2 to entry: The reaction time can vary from a few milliseconds to a few seconds.

3.10**battery support system****BSS**

group of interconnected and interactive parts that perform an essential task as a component of a battery system

Note 1 to entry: Such systems are for example electrolyte storage tanks and circulation pumps, cooling and heating devices, exhaust gas abatement systems, fire extinguishers, spill catchment systems, safety barriers, racks and similar facilities.

Note 2 to entry: This note applies to the French language only.

3.11**capacity**

<of cells and batteries> quantity of electric charge which a cell or battery can deliver under specified discharge conditions

Note 1 to entry: The SI unit for electric charge, or quantity of electricity, is the coulomb (1 C = 1 As) but in practice, capacity is usually expressed in ampere hours (Ah).

[SOURCE: IEC 60050-482:2004, 482-03-14, modified — In the definition, “quantity of” has been added.]

3.12**charging**

<of a battery> operation during which a secondary battery is supplied with electric energy from an external circuit which results in chemical changes within the cell and thus the storage of energy as chemical energy

Note 1 to entry: A charge operation is defined by its maximum voltage, current, duration and other conditions as specified by the manufacturer.

[SOURCE: IEC 60050-482:2004, 482-05-27, modified — Note 1 to entry has been added.]

3.13**constant power charge**

<of a battery> operation in which the charge power input, i.e. the product of charge current and charge voltage, is held constant and where the current and voltage freely adjust according to polarization effects of the battery

3.14**discharge**

operation by which a battery delivers, to an external electric circuit and under specified conditions, electric energy produced in the cells

[SOURCE: IEC 60050-482:2004, 482-03-23]

3.15**constant power discharge**

<of a battery> operation in which the discharge power output, i.e. the product of discharge current and discharge voltage, is held constant and where the current and voltage freely adjust according to polarization effects of the battery

3.16**electrolyte**

substance containing mobile ions that render it ionically conductive

Note 1 to entry: The electrolyte may be a liquid, solid or a gel.

[SOURCE: IEC 60050-482:2004, 482-02-29]

3.17**endurance**

<of a battery> numerically defined performance during a given test simulating specified conditions of service

[SOURCE: IEC 60050-482:2004, 482-03-44]

3.18**endurance test**

<of a battery> test carried out over a time interval to investigate how the properties are affected by the application of stated stresses and by their time duration or repeated application

[SOURCE: IEC 60050-151:2001, 151-16-22, modified — “<of a battery>” has been added before the definition and “of an item” has been deleted from the definition.]

3.19**energy**

<of a battery> energy which a battery delivers under specified conditions

Note 1 to entry: The SI unit for energy is the joule (1 J = 1 Ws) but in practice, energy of a battery is usually expressed in watt hours (Wh) (1 Wh = 3 600 J).

Note 2 to entry: Such energy content is generally determined with a constant power (W) discharge.

Note 3 to entry: k or M are unit prefixes in the metric system denoting multiplication of the unit by one thousand (k) or one million (M).

[SOURCE: IEC 60050-482:2004, 482-03-21, modified — Notes 2 and 3 to entry have been added.]

3.20**actual energy**

<of a battery> energy content value, determined experimentally at a defined instant of time with a constant power discharge at a specified rate to a specified final voltage and at a specified temperature

Note 1 to entry: This value is expressed in watt hours (Wh) and varies over the operational cycle or life of the battery.

3.21**final voltage**

end-of-discharge voltage

cut-off voltage

end-point-voltage

U_{final}

<of a battery> specified voltage of a battery at which the battery discharge is terminated

[SOURCE: IEC 60050-482:2004, 482-03-30]

3.22**flow cell**

secondary cell characterized by the spatial separation of the electrode from the fluid volumes which contain active materials

Note 1 to entry: The fluids, consisting of liquids, solutions, suspensions or gases, flow separately through the electrode spaces.

Note 2 to entry: A flow cell in which one of the active materials is, depending on the state of charge, a solid deposited on one of the electrodes, is called a hybrid flow cell.

3.23**flow battery**

two or more flow cells electrically connected in series and including all components for their use as an electrochemical energy storage system

Note 1 to entry: The components can be tanks, pumps, thermal and battery management systems, piping and similar.

3.24**frequency regulation service**

<with batteries> regulation mode of the electrical power grid with energy drawn from or supplied to batteries to maintain the system frequency within defined limits

Note 1 to entry: This balancing of the temporal variations of grid frequency occurs typically over time periods of the order of seconds to minutes.

3.25**full charge**

<of a battery> state of charge wherein the battery has been completely charged in accordance with the manufacturer's recommended charging conditions.

3.26**full-sized battery****FSB**

complete battery that meets the absolute requirements of power capability and energy content, as defined in the respective endurance test clauses

Note 1 to entry: This battery is an assembly of n cells, modules or stacks and is equipped with the relative BMS and BSS as needed.

Note 2 to entry: This note applies to the French language only.

3.27**laboratory test**

<of a battery> test made under prescribed and controlled conditions that may or may not simulate field conditions

[SOURCE: IEC 60050-192:2015, 192-09-05]

3.28**load following service**

<with batteries> regulation mode of the electrical power grid with energy drawn from or supplied to batteries to compensate for temporary variations in load demand

Note 1 to entry: This balancing of the temporary variations of grid load demand occurs typically over time periods of the order of a few minutes to one hour.

3.29**module**

standardized and interchangeable assembly of cells connected in series and/or parallel and associated hardware designed for easy assembly into a commercial battery

3.30**operating voltage range
operating voltage limits**

<of a battery> voltage range, as declared by the manufacturer, in which the battery is to be operated and performs according to specifications

3.31**maximum operating voltage
upper voltage limit** U_{\max}

<of a battery> upper limit of the voltage range in which the battery is operable and performs according to specifications

3.32**minimum operating voltage
lower voltage limit** U_{\min}

<of a battery> lower limit of the voltage range in which the battery is operable and performs according to specification

3.33**peak-power shaving service
load levelling service**

<with batteries> process of energy demand management consisting of supplementing the energy in a localized power grid, during periods of excessive demand or instantaneous high electricity costs, with energy drawn from a battery

Note 1 to entry: The energy utilized to “shave off” the demand peak is recharged into the battery in periods of low energy demand or cheap energy supply.

Note 2 to entry: This demand peak-shaving activity lasts typically over time periods of one to several hours.

3.34**PV energy storage time-shift service**

<with batteries> process of energy demand management consisting of storing photovoltaic energy in a battery for a time deferred release into a localized power grid

Note 1 to entry: This energy demand management occurs typically with a 24 h day/night rhythm.

3.35**performance**

<of a battery> characteristics defining the ability of the battery to achieve the intended function

[SOURCE: IEC 60050-311:2001, 311-06-11, modified — In the definition, “measuring instrument” has been replaced with “battery”.]

3.36**performance test**

test carried out to determine the electrical characteristics of a battery

3.37**secondary cell**

<electrochemical> basic manufactured unit of an electrochemical system capable of storing electric energy in chemical form and delivering that electrical energy back by reconversion of its stored chemical energy.

[SOURCE: IEC 60050-811:1991, 811-20-01, modified]

3.38**service life**

<of a battery> total period of useful life of a cell or battery in operation

Note 1 to entry: For secondary cells and batteries, the service life may be expressed in time, number of charge/discharge cycles, or total throughput in ampere hours (Ah).

[SOURCE: IEC 60050-482:2004, 482-03-46, modified — Note 1 to entry has been deleted.]

3.39**maximum service temperature****maximum operating temperature****maximum permissible temperature**

<of a battery> highest temperature which the battery is allowed to attain in normal use as a result of ambient temperatures, induced heat and heat caused by the battery itself

[SOURCE: IEC 60050-442:1998, 442-06-41, modified — In the definition, “connecting device” has been replaced with “battery”.]

3.40**minimum service temperature****minimum operating temperature****minimum permissible temperature**

<of a battery> lowest temperature which the battery is allowed to attain in normal use as a result of ambient temperatures and forced cooling

3.41**stack**

<of a flow battery> two or more flow cells connected in series or in parallel with associated electrical connections and fluid piping

3.42**state of charge****SoC**

<of a battery> amount of stored charge in ampere hours (Ah) or energy in watt hours (Wh) related to the actual capacity or energy content

Note 1 to entry: This definition is applicable throughout and only to this part of IEC 61427.

Note 2 to entry: State of charge is expressed as a percentage.

Note 3 to entry: This note applies to the French language only.

3.43**target operational state of charge****SoC_{OT}**

<of a battery> pre-defined state of charge to which the energy storage system is driven by a controller or BMS under pre-defined conditions

Note 1 to entry: This SoC_{OT} is to be attained or/and maintained when bidirectional energy transfers to and from the battery are to be achieved within set voltage and SoC limits.

Note 2 to entry: State of charge is expressed as a percentage.

Note 3 to entry: SoC_{OT} is typically the desired or recommended average operating SoC during the specified application scenario. It is selected to improve electrical energy storage (EES) system performance and/or improve the EES system service life in the specified application.

3.44**test**

<of a battery> technical operation that consists of the determination of one or more characteristics of a given battery according to a specified procedure

Note 1 to entry: A test is carried out to measure or classify a characteristic of a property of a battery by applying to the battery a set of environmental and operating conditions and/or requirements.

[SOURCE: IEC 60050-151:2001, 151-16-13, modified — In the definition, “product, process or service” has been replaced with “battery”.]

3.45**test object**

item submitted to a test, including any accessories, unless otherwise specified

[SOURCE: IEC 60050-151:2001, 151-16-28]

3.46**test object battery****TOB**

assembly of $x \times 1/n$ units consisting of cells, modules or stacks of the full-sized battery (FSB), which when assembled in n units, form the FSB which meets the absolute requirements of power capability and energy content as defined in the respective endurance test clauses

Note 1 to entry: The test object battery (TOB) is fully representative of the full-sized battery (FSB) in terms of scalability so that obtained test results can be generalized accurately to the FSB.

Note 2 to entry: The TOB is equipped with the relative BMS and BSS as needed.

Note 3 to entry: This note applies to the French language only.

3.47**time-shift service**

<with batteries> process of energy demand management consisting in providing to the grid, at suitable moments, energy stored in batteries at times of ample production or weak demand

Note 1 to entry: This supplying of energy to the grid occurs over time periods typically of the order of a few hours, days or even seasons.

4 General considerations

The supply of energy from renewable energy sources such as wind, solar radiation or tidal forces is characterized by a high degree of intermittency and a low degree of predictability. When their output is fed into the power transmission and distribution grid, overload and instability conditions may develop which make it highly desirable to use rechargeable batteries to temporarily store this energy and then release it in a controlled fashion to smooth and stabilize the flow of power in the grid.

Such instabilities and imbalances in power grids may also result when insufficient power generation capability is present.

The aim of this part of IEC 61427 is to advise and guide future system operators to identify and select suitable rechargeable batteries for grid-connected electrical energy storage (EES). This process will be aided by a set of common test methods that quantify the capability of battery systems of different chemistries and designs in a particular application scenario.

The requirements for battery endurance and electrical performance are linked to the specific EES scenarios to be implemented for the management of excess energy in the grid and the associated capital and operating expenditures for such an installation.

These requirements, expressed as energy efficiency, service life, cumulated energy throughput, installation space and similar, are highly variable since they are eminently application-scenario related and furthermore strongly tied to local costs/benefits and payback time considerations.

Therefore, this part of IEC 61427 does not define these requirements but offers instead test methods to determine and compare the endurance and electrical performance of the candidate storage systems.

All EES batteries have to exhibit safe behaviour. Proper design and associated qualification testing by the battery manufacturers shall ensure this at all levels from the cell to the overall system level.

An informal listing of hazards associated with batteries and battery installations is included in this part of IEC 61427. This list should help in the assessment of the possible reactions of the batteries when they are exposed to abnormal and abusive service conditions.

5 General test conditions

5.1 Accuracy of measuring equipment

5.1.1 Voltage measurements

The instruments used shall be of an accuracy class of at least 0,5 (%) or better.

5.1.2 Current measurements

The instruments used shall be of an accuracy class of at least 0,5 (%) or better.

NOTE Particular attention has to be given to the accuracy of current measurement and current-over-time integration devices as any degraded accuracy or instability can negatively impact the effectiveness of SoC stabilization routines.

5.1.3 Temperature measurements

The instrument used shall have a resolution of 0,5 K. The accuracy of the instrument shall be ± 2 K or better.

5.1.4 Time measurements

The instrument used shall have a resolution of 1 s and an accuracy of 0,1 % of the measured time interval.

5.2 Test object considerations

This part of IEC 61427 and the resulting test results are intended to assist the future operator of an electrical energy storage system in the selection of the most suitable battery for the target application by providing comparable data of candidate systems.

The battery system to be tested shall include the cells or modules or stacks and, when they are essential for the operation of the battery, the battery management system (BMS) and battery support systems (BSS).

The boundary of this battery system is outlined by the dotted line in Figure 1.

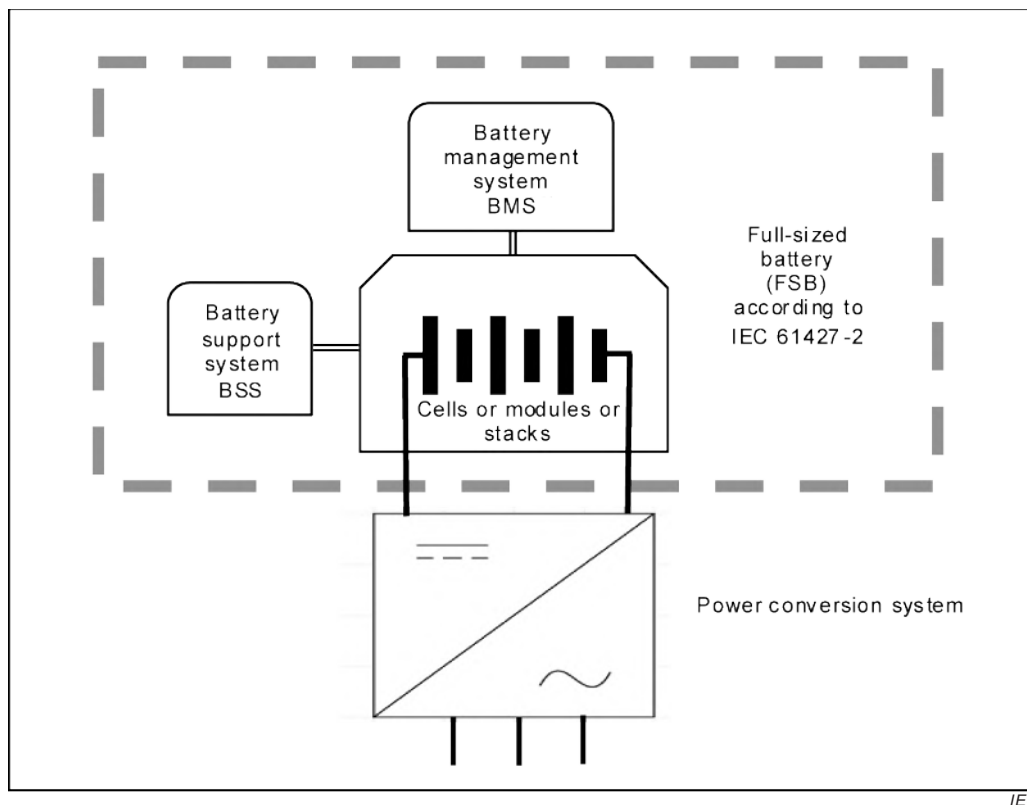


Figure 1 – Boundary of the full-sized battery (FSB)

Power conversion systems and components and associated interfaces are not within the scope of this part of IEC 61427 and are not necessarily present when the tests, according to Clauses 6 and 7, are carried out.

5.3 Test object battery selection and size considerations

The battery systems offered by the manufacturers for on-grid electric energy storage reflect the intrinsic constraints of each cell chemistry and design as well as the specific needs of the target application or service. Such batteries range typically from a few kilowatts to up to 50 MW in power capability and up to 100 MWh in energy content. No common size exemplifying each prospective cell chemistry is yet available.

When the manufacturer or end-user carries out the testing of a battery system to generate data in compliance with this part of IEC 61427, freedom shall be granted to choose that design, model and size which is most suitable for yielding the endurance and electrical performance needed for the selected application or service. These applications or services are exemplified by the endurance tests specified in 6.2 through 6.5. These battery sizes and layouts may vary from one cell chemistry or application to another.

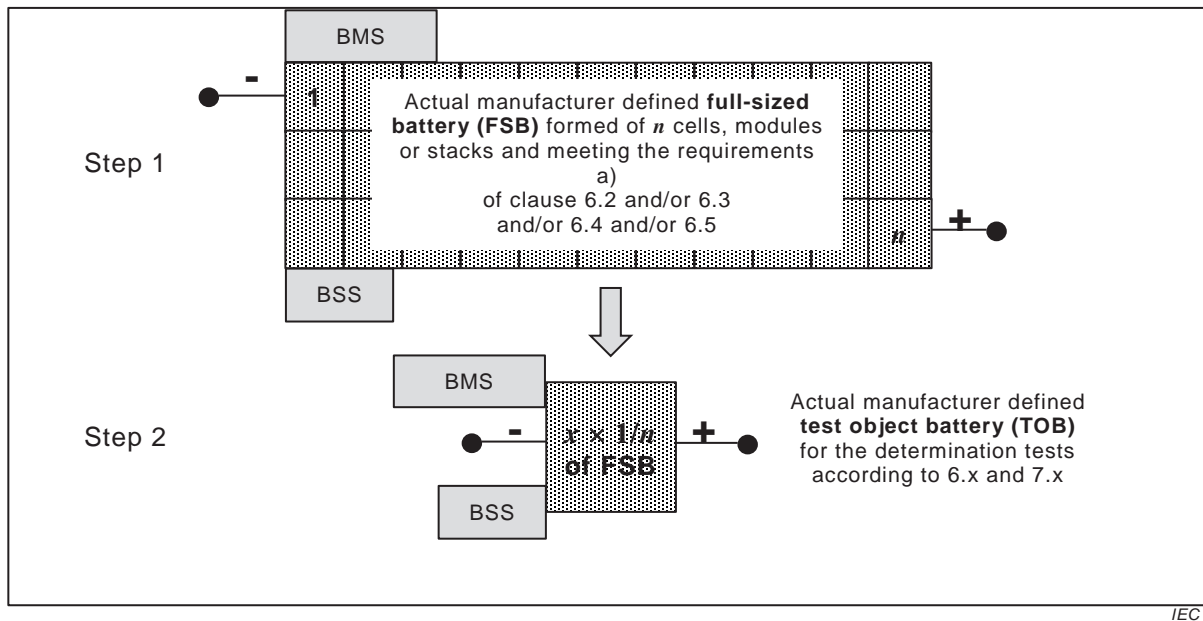


Figure 2 – Two-step selection process of the test object battery (TOB)

In order to assure the generation of comparable test data, the following constraints shall be respected.

- Throughout this part of IEC 61427 the relevant batteries are defined as below.
 - Full-sized battery (FSB)** – The FSB shall consist of the complete battery that meets the absolute requirements of power capability and energy content as defined in 6.2 or 6.3 or 6.4 or 6.5, as applicable. This battery may be an assembly of n cells, modules or stacks and shall be equipped with the relevant BMS and BSS as needed. Thus up to five different FSBs may be defined.
 - Test object battery (TOB)** – The TOB and its associated BMS and BSS shall be representative of each of the FSBs above in terms of scalability of endurance and performances so that test results can be extrapolated accurately and hence demonstrate the performance of the FSB. The TOB shall be an assembly of $x \times 1/n$ cells, modules or stacks as present in the above FSB. The minimum number x is defined in the relevant test clause. Unless otherwise specified, all the tests shall be carried out on this TOB.

The steps to define this TOB are outlined in Figure 2.

- All the TOB's utilized for the verification of the behaviour in the selected application service, as exemplified by test 6.2 or 6.3 or 6.4 or 6.5, shall be of the same size, design and features. No ad-hoc adaptation of the design, just to meet a particular test environment, is permitted.
- Any BMS and BSS essential for the operation of the TOB shall be included.
- Only those endurance tests for which the battery is designed/specified shall be carried out.
- When an available battery-based EES system with different power capability and/or energy content requires testing for compliance with the clauses of this part of IEC 61427, then such a choice is permitted provided that all other provisions are fulfilled and this deviation is stated in the test documentation.

5.4 Test plan

The following provisions apply.

- The tests for the verification of the suitability of a battery, for a particular application scenario, shall be accomplished with not more than two individual and identical TOBs.

- TOB 1 shall be used to carry out the relevant endurance test 6.2 or 6.3 or 6.4 or 6.5 and the associated nested performance tests 7.2 through 7.5. See also Figure 3, Figure 4 and Figure 5.

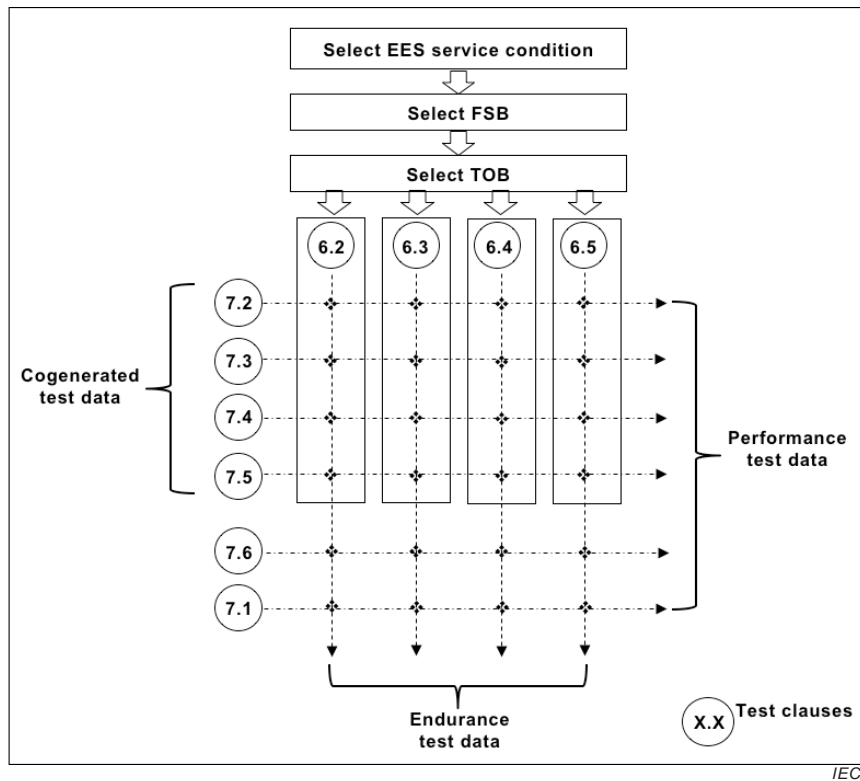
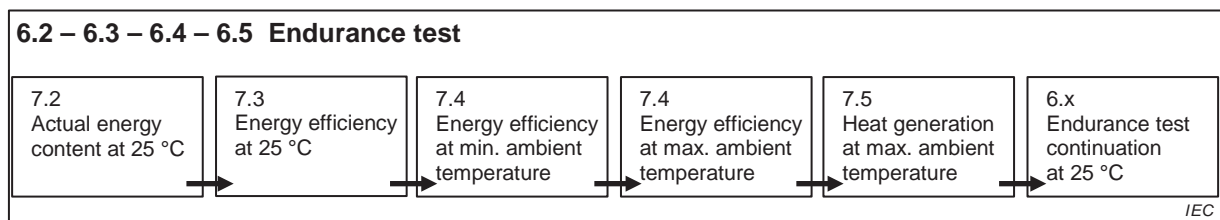


Figure 3 – Workflow for the determination of endurance properties and electrical performance of the TOB as governed by the sequence of test data generation within 6.2 to 6.5



NOTE 1 The details of the performance test are specified in 7.2 through 7.5.

NOTE 2 The performance tests 7.2 to 7.5 are sequential and combined with the relevant endurance test.

NOTE 3 The test profile used in the performance tests 7.3 to 7.5 is that of the relative endurance test.

Figure 4 – Sequence of performance tests carried out with TOB 1 within an endurance test 6.x

- TOB 2 shall be used to carry out the low-stress-level performance test 7.6 (Energy requirement in idle state), which could precede any endurance test allowing ultimately to reduce the number of TOBs, per application scenario verification, to a single TOB. The number of TOBs eventually used shall be reported in Table 1.
- Subclause 7.1 requires the summarizing of data and does not require an additional TOB.
- The test conditions of 7.4, and associated subclause 7.5, keep the TOB within acceptable thermal stress levels at the manufacturer’s specified lowest and highest ambient temperatures. At these temperatures the battery is declared operable by the manufacturer

and performs according to specified requirements; thus, no additional TOB is needed for these tests.

- The manufacturer shall carry out only those endurance tests for which the FSB, and by derivation the TOB, has been designed/specified.
- An endurance test can be terminated at any moment when the battery manufacturer has demonstrated the declared service life of the FSB design with a robust extrapolation of the energy acceptance and delivery capability, over time, of the TOB.
- Relevant changes in materials and design of an FSB which impact endurance or performance shall be evaluated for their bearing on the test results in Clauses 6 and 7 by repeating the tests most likely to be impacted by the change.

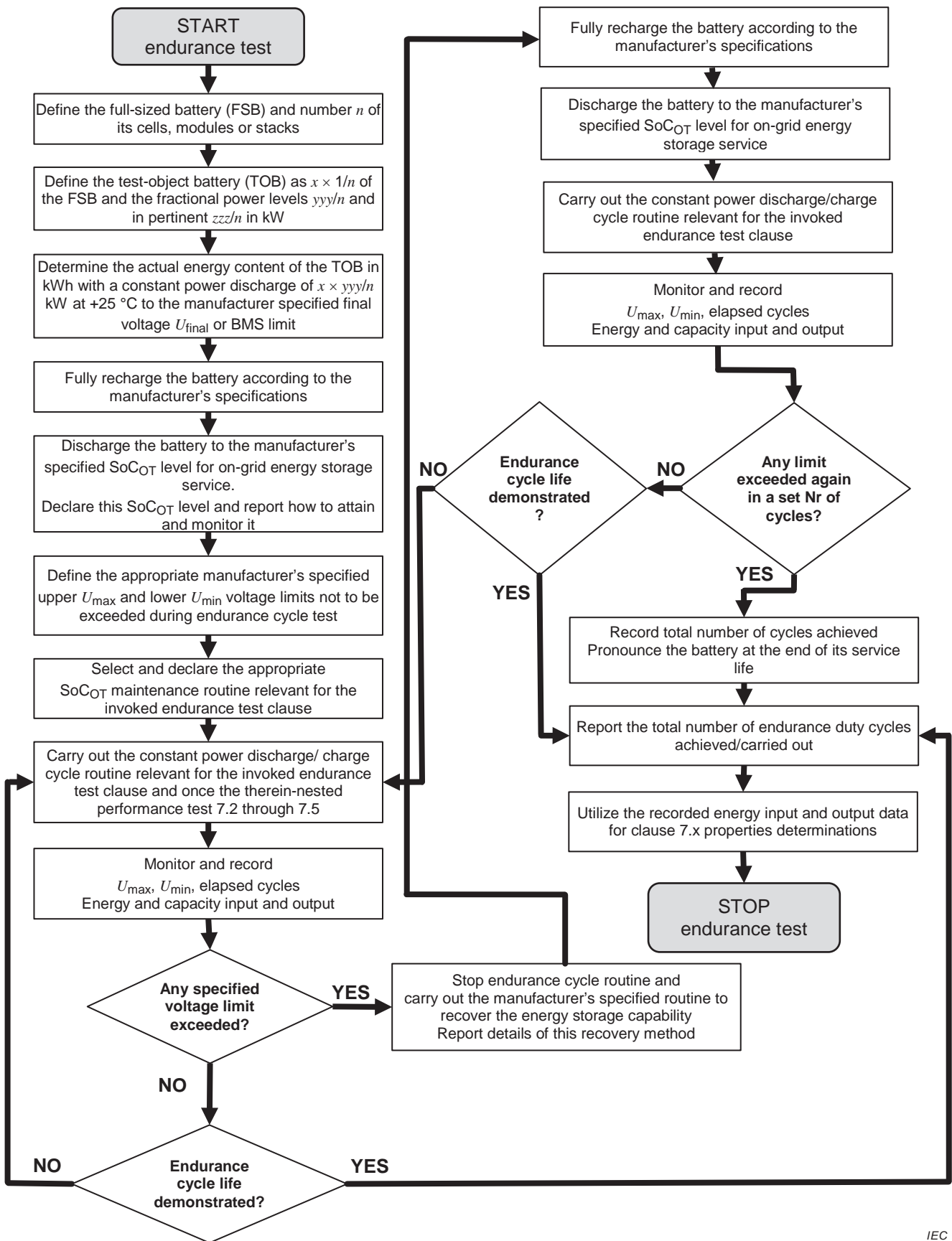


Figure 5 – Workflow and decision tree for endurance tests 6.2 through 6.5

6 Battery endurance

6.1 General

The endurance tests in this part of IEC 61427 are intended to determine the suitability of the battery design to accept and deliver energy under experimental conditions that reproduce in a simplified way the duty the battery will be expected to perform in on-grid energy storage applications.

The key stress factors in such a service are

- a) the charge and discharge power levels per available energy content,
- b) the operation in a state of charge (SoC) of less than 100 %, and
- c) the large number of duty cycles to be accomplished over the service life.

The test conditions are formulated to quantify the battery endurance in the following four application scenarios: frequency-regulation, load-following, peak-power shaving and photovoltaic energy storage time-shift duty.

The highly random energy transfer to and from the battery in on-grid energy storage is simulated with more simplified energy exchange routines.

It is recognized that the individual energy exchange routines chosen may not replicate exactly all the service conditions in the field, which is typical of laboratory tests.

The regular use of these tests, for product development and for qualification purposes, will nevertheless guide the manufacturer and EES system operator in developing and selecting the proper battery.

6.2 Test for endurance in frequency-regulation service

The test conditions are as follows.

- a) The manufacturer shall select and define a full-sized battery (FSB) which is able to
 - 1) supply and accept continued 500 kW and 1 000 kW constant power pulses as per j) within the battery operating voltage limits specified by the manufacturer and when the battery is thermally equilibrated at an ambient temperature of +25 °C, and
 - 2) tolerate such energy transfers multiple times per hour and 24 h per day without exceeding the manufacturer's specified operating voltage limits.
- b) The manufacturer shall report how many cells, modules or stacks make up such a FSB. This value is termed n .
- c) The manufacturer shall define the fraction of power (500/ n) kW and (1 000/ n) kW such a cell, module or stack will deliver or accept when it is part of the FSB and this battery meets the conditions of 1) to 2) in 6.2 a).
- d) The manufacturer shall assemble with x of such cells, modules or stacks the appropriate TOB having at least
 - 1) four (4) cells in series (only if these cells are commercialized individually),
or
 - 2) one or more modules that result in at least four (4) cells in series,
or
 - 3) one stack with at least four (4) flow cells in series,
and incorporate the relevant BMS and BSS peripherals.
- e) When a battery based EES system with different power capability and/or energy content requires testing for compliance with this part of IEC 61427, then such choice is acceptable

provided that all other provisions are fulfilled and this deviation is stated in the test documentation.

- f) The actual energy content E (in kWh) of this TOB, after the manufacturer specified full charge and thermal equilibration in air at $+25\text{ °C} \pm 3\text{ K}$ ambient temperature, shall be determined with a constant power discharge at the $(x \times 500/n)$ kW power level to the final voltage U_{final} or to the BMS mandated discharge limit as specified by the manufacturer so as to generate the data as required in 7.2.
- g) The TOB shall then be fully recharged according to the manufacturer's specifications.
- h) The TOB shall then be discharged to such a target operational state of charge (SoC_{OT}) that it can repetitively deliver and accept the fractional power and energy levels without exceeding the manufacturer's specified operating voltage limits.
- i) The manufacturer shall report this target operational state of charge (SoC_{OT}) level, expressed as a percentage of the actual energy content as determined in f), and ways to achieve it in Table 1.
- j) The TOB shall then be submitted, at an ambient temperature of $+25\text{ °C} \pm 3\text{ K}$, to a continuous sequence of discharge/charge pulses defined in 1) through 8) and associated SoC_{OT} adjustment profiles a or b or c. The minimum and maximum battery voltage and the cumulative discharged and charged capacity (in Ah) and energy (in kWh) of the TOB shall be monitored and recorded.
- 1) Discharge for 2 min with constant power at the fractional power level of $(x \times 500/n)$ in kW.
 - 2) Discharge for 1 min with constant power at the fractional power level of $(x \times 1\ 000/n)$ in kW.
 - 3) Charge for 2 min with constant power at the fractional power level of $(x \times 500/n)$ in kW.
 - 4) Charge for 1 min with constant power at the fractional power level of $(x \times 1\ 000/n)$ in kW.
 - 5) Discharge for 1 min with constant power at the fractional power level of $(x \times 1\ 000/n)$ in kW.
 - 6) Discharge for 2 min with constant power at the fractional power level of $(x \times 500/n)$ in kW.
 - 7) Charge for 1 min with constant power at the fractional power level of $(x \times 1\ 000/n)$ in kW.
 - 8) Charge for

2 min with constant power at the fractional power level of $(x \times 500/n + a)$ in kW where a is the additional power i.e. energy needed to maintain the target operational state of charge SOC_{OT} . The manufacturer shall specify and report the value a in Table 1. The value of $(x \times 500/n + a)$ in kW shall be equal to or less than $(x \times 1\ 000/n)$ in kW (see, for example, Figure 6 – Profile a).

or

$(2 + t)$ min with constant power at the fractional power level of $(x \times 500/n)$ in kW where t is the additional time of charge needed to maintain the target operational state of charge SOC_{OT} . The manufacturer shall specify and report the value t (see, for example, Figure 7 – Profile b) in Table 1.

or

2 min with constant power at the fractional power level of $(x \times 500/n)$ in kW and every K cycles, i.e. number of completed pulse discharge and charge cycles, 1 through 8, carry out a SoC_{OT} maintenance charge with a power not larger than $(x \times 1\ 000/n)$ in kW and a duration as specified by the manufacturer. The manufacturer shall specify and report the value K and the power level and duration of this SoC_{OT} maintenance charge (see, for example, Figure 8 – Profile c) in Table 1.

- 9) Return to 1) and perform 1) to 8) 840 times to sequentially generate the test data according to 7.3 followed by those according to 7.4 and 7.5. See also Figure 4.

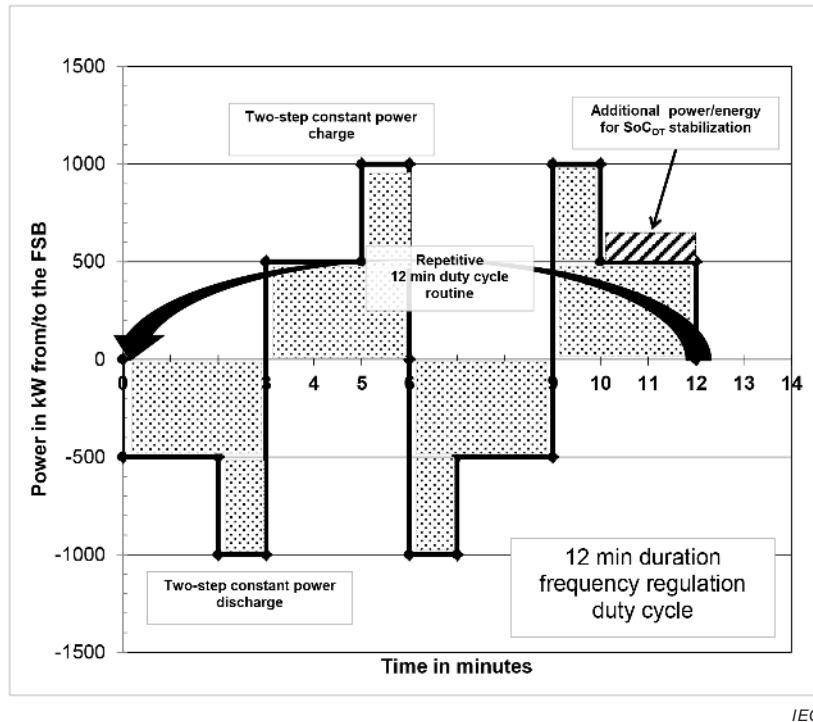


Figure 6 – Frequency regulation service test routine profile (6.2) – Profile a

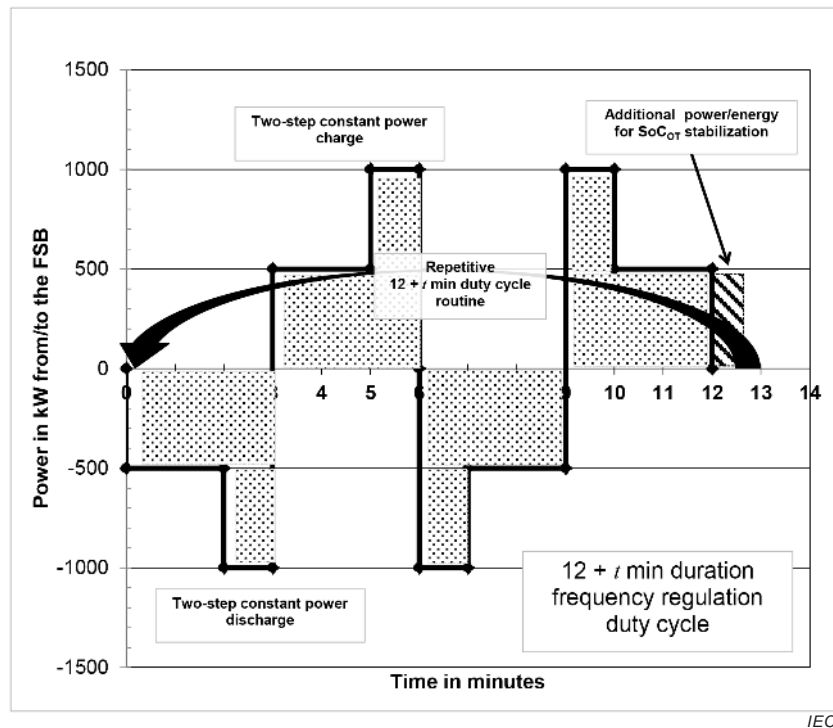


Figure 7 – Frequency regulation service test routine profile (6.2) – Profile b

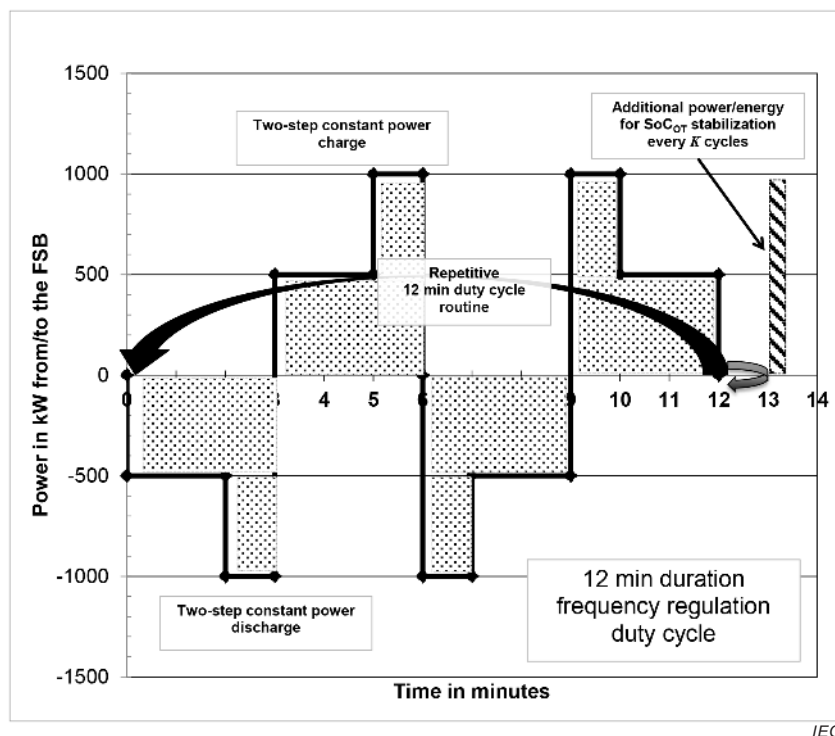


Figure 8 – Frequency regulation service test routine profile (6.2) – Profile c

- k) If the TOB voltage in j) exceeds the manufacturer's defined limits of operating voltages then the energy delivery or acceptance capability of the TOB, and by derivation that of the FSB, shall be considered degraded. Figure 9 gives a schematic view of the evolution of battery voltage.

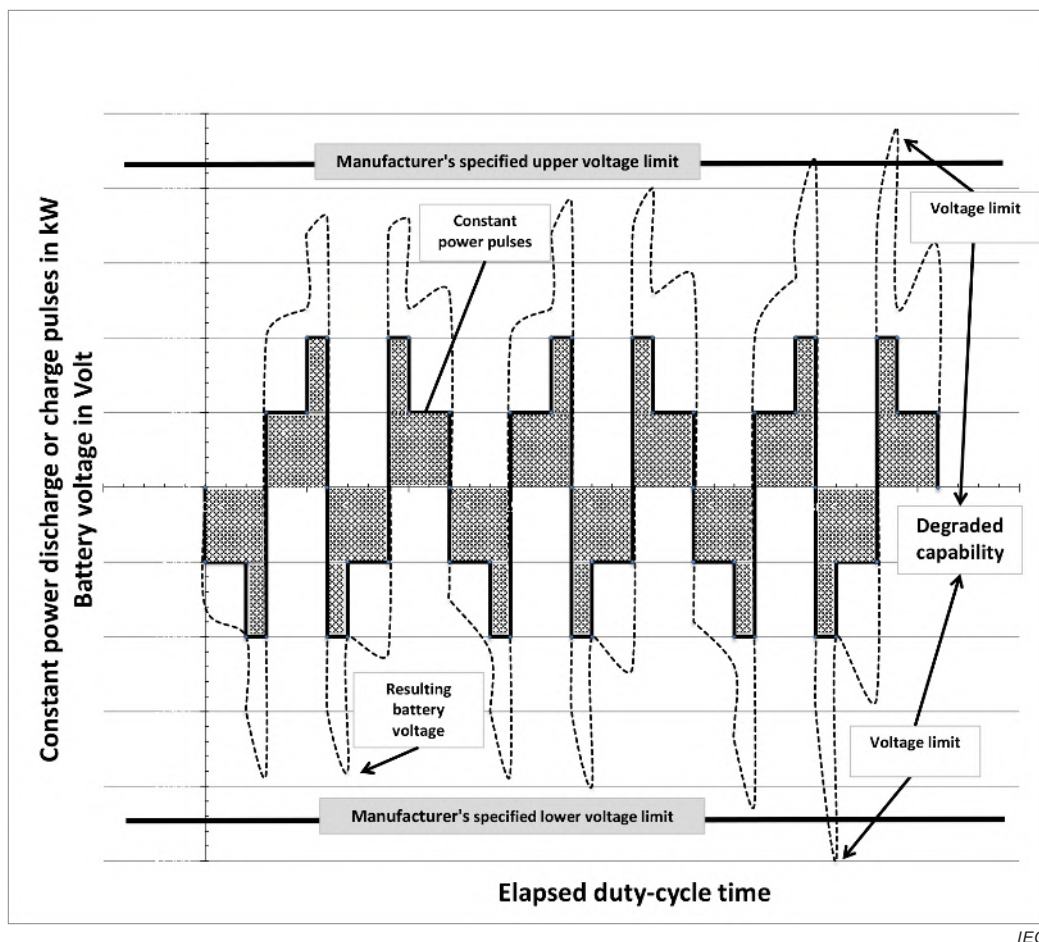


Figure 9 – Schematic view of the evolution of battery voltage over time during cycling with constant power discharge and charge pulses

- l) The cycling shall then be stopped and an attempt made to restore the capability of the TOB according to the manufacturer's specification. The details of this operation to recover the energy storage capability shall be reported in Table 1.
- m) A new set of operations h) through j) shall then be initiated. If the TOB voltage in j) exceeds the manufacturer's defined operating voltage limits again within 120 sequences j) items 1) to 8) (≈ 24 h), then the energy delivery or acceptance capability of the TOB, and by derivation that of the FSB, shall be considered irreversibly degraded and the TOB as having reached the end of its service life. Otherwise the cycle sequence specified in sequence j) shall be continued as specified or until the next occurrence of exceeding a limiting value as described in k).
- n) The endurance of the TOB, in a particular application scenario, is defined by the total number of completed sequences of j) items 1) to 8) before end-of-service life according to m) is reached.
- o) The energy efficiency during these endurance test segments shall be determined according to 7.3 or 7.4 and reported in Table 6 and Table 7, respectively.
- p) The heat generation at the maximum ambient temperature during the endurance test segment shall be determined according to 7.5 and reported in Table 10.
- q) If in j) the SoC_{OT} maintenance is achieved with the profile c), then the integration duration shall be adapted in such a manner that at least one such SoC_{OT} maintenance charge event c) is included.
- r) At the completion of the determination of energy efficiencies and heat generation according to 7.3, 7.4 and 7.5 within the endurance test 6.2, this endurance test shall be resumed at g) and carried out by ignoring section 9) and o), p) and q) until the TOB is

declared irreversibly degraded or the battery manufacturer has demonstrated the declared service life of the FSB design with a robust extrapolation of the energy acceptance and delivery capability, over time, of the TOB.

6.3 Test for endurance in load-following service

The test conditions are as follows.

- a) The manufacturer shall select and define a full-sized battery (FSB) which is able to
 - 1) supply and accept continued 180 kW and 360 kW constant power pulses as per j) within the battery operating voltage limits specified by the manufacturer and when the battery is thermally equilibrated at an ambient air temperature of +25 °C, and
 - 2) tolerate such energy transfers multiple times per hour and 24 h per day without exceeding the manufacturer's specified operating voltage limits.
- b) The manufacturer shall report how many cells, modules or stacks make up such a FSB. This value is termed n .
- c) The manufacturer shall define the fraction of power $(180/n)$ kW and $(360/n)$ kW such a cell, module or stack will deliver or accept when it is part of the FSB and this battery meets the conditions of 1) to 2) in 6.3 a).
- d) The manufacturer shall assemble with x of such cells, modules or stacks the appropriate TOB having at least
 - 1) four (4) cells in series (only if these cells are commercialized individually),
 - or
 - 2) one or more modules with at least four (4) cells in series,
 - or
 - 3) one stack with at least four (4) flow cells in series,
 and incorporate the relevant BMS and BSS peripherals.
- e) When a battery based EES system with different power capability and/or energy content requires testing for compliance with this part of IEC 61427, then such choice is acceptable provided that all other provisions are fulfilled and this deviation is stated in the test documentation.
- f) The actual energy content E (in kWh) of this TOB, after the manufacturer specified full charge and thermal equilibration in air at +25 °C \pm 3 K ambient temperature, shall be determined with a constant power discharge at the $(x \times 180/n)$ kW power level to the final voltage U_{final} or to the BMS mandated discharge limit as specified by the manufacturer so as to generate the data as required in 7.2.
- g) The TOB shall then be fully recharged according to the manufacturer's specifications.
- h) The TOB shall then be discharged to such a target operational state of charge (SoC_{OT}) that it can repetitively deliver and accept the fractional power and energy levels without exceeding the manufacturer's specified operating voltage limits.
- i) The manufacturer shall report this target operational state of charge (SoC_{OT}) level, expressed as percentage of the actual energy content as determined in f), and ways to achieve it in Table 1.
- j) The TOB battery shall then be submitted, at an ambient temperature of +25°C \pm 3K, to a continuous sequence of discharge/charge pulses defined in 1) through 8) and associated SoC_{OT} adjustment profiles a or b or c. The minimum and maximum battery voltage and the cumulative discharged and charged capacity (in Ah) and energy (in kWh) of the TOB shall be monitored and recorded.
 - 1) Discharge for 8 min with constant power at the fractional power level of $(x \times 180/n)$ in kW.
 - 2) Discharge for 4 min with constant power at the fractional power level of $(x \times 360/n)$ in kW.

- 3) Charge for 8 min with constant power at the fractional power level of $(x \times 180/n)$ in kW.
- 4) Charge for 4 min with constant power at the fractional power level of $(x \times 360/n)$ in kW.
- 5) Discharge for 4 min with constant power at the fractional power level of $(x \times 360/n)$ in kW.
- 6) Discharge for 8 min with constant power at the fractional power level of $(x \times 180/n)$ in kW.
- 7) Charge for 4 min with constant power at the fractional power level of $(x \times 360/n)$ in kW.
- 8) Charge for

8 min with constant power at the fractional power level of $(x \times 180/n + a)$ in kW where a is the additional power, i.e. energy needed to maintain the target operational state of charge (SoC_{OT}). The manufacturer shall specify and report the value a in Table 1. The value of $(x \times 180/n + a)$ in kW shall be equal to or less than $(x \times 360/n)$ in kW (see, for example, Figure 10 – Profile a).

or

$(8 + t)$ min with constant power at the fractional power level of $(x \times 180/n)$ in kW where t is the additional time of charge needed to maintain the target operational state of charge (SoC_{OT}). The manufacturer shall specify and report the value t (see, for example, Figure 11 – Profile b) in Table 1.

or

8 min with constant power at the fractional power level of $(x \times 180/n)$ in kW and every K cycles, i.e. number of completed pulse discharge and charge cycles 1) through 8), carry out a SoC_{OT} maintenance charge with a power not larger than $(360/n)$ in kW and a duration as specified by the manufacturer. The manufacturer shall specify and report the value K and the power level and duration of this SoC_{OT} maintenance charge (see, for example, Figure 12 – Profile c) in Table 1.

- 9) Return to 1) and perform 1) to 8) 210 times to sequentially generate the test data according to 7.3 followed by those according to 7.4 and 7.5. See also Figure 4.

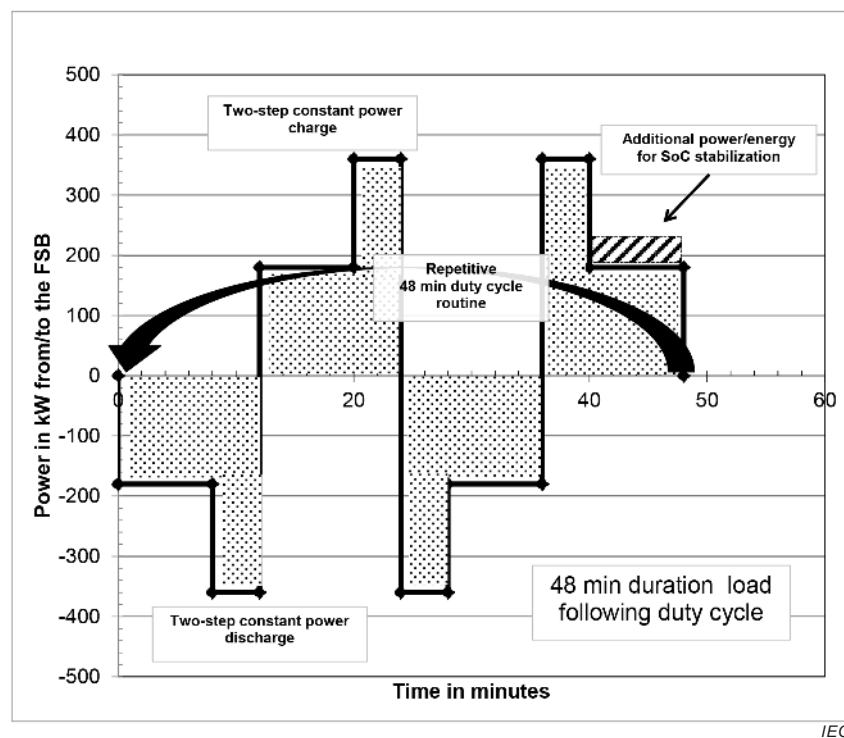


Figure 10 – Load-following service test routine profile (6.3) – Profile a

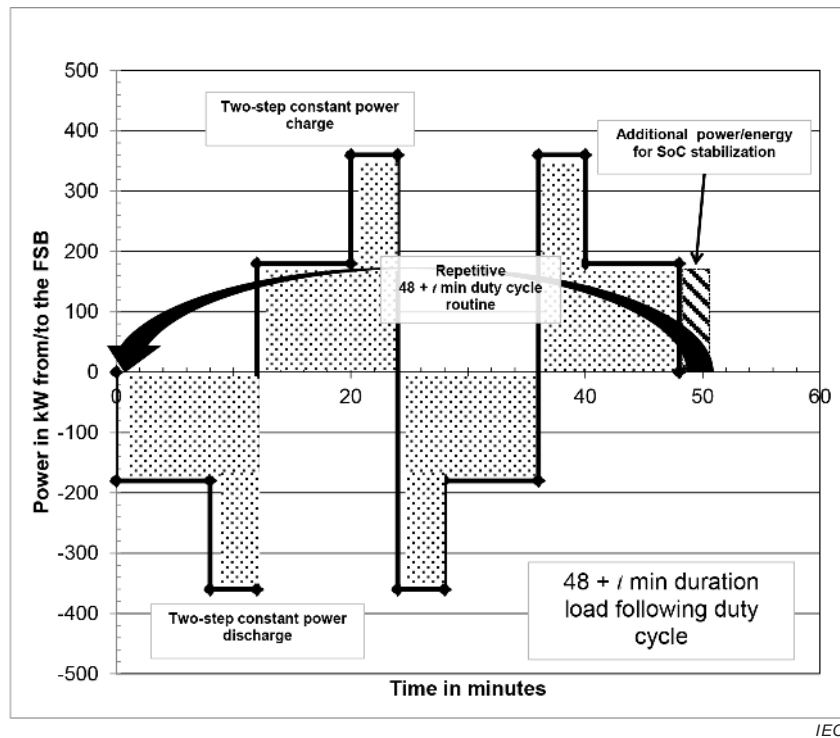


Figure 11 – Load-following service test routine profile (6.3) – Profile b

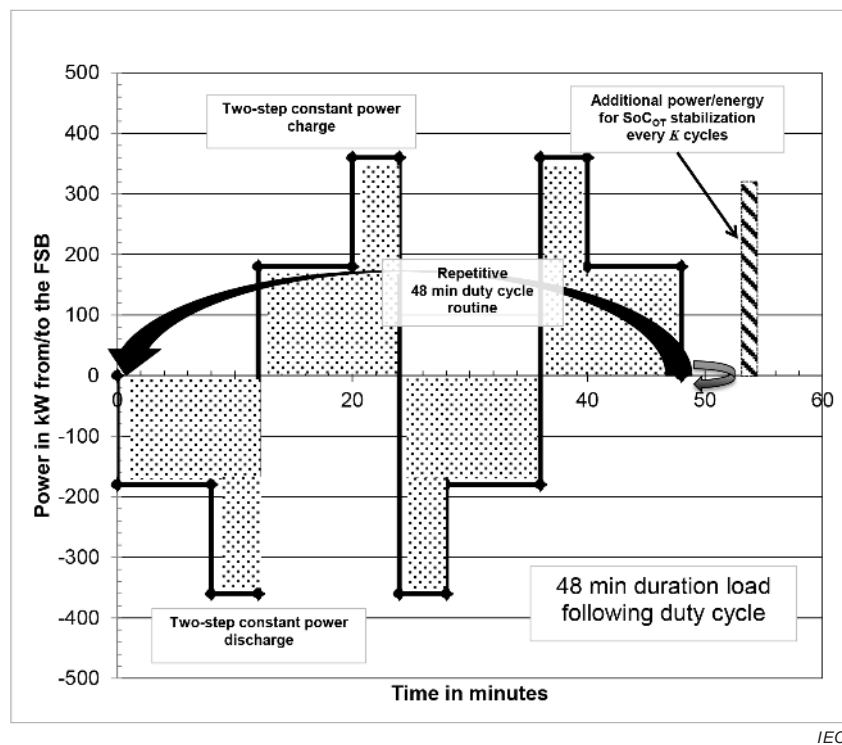


Figure 12 – Load-following service test routine profile (6.3) – Profile c

- k) If the TOB voltage in j) exceeds the manufacturer's defined limits of operating voltages, then the energy delivery or acceptance capability of the TOB, and by derivation that of the FSB, shall be considered degraded.
- l) The cycling shall then be stopped and an attempt made to restore the capability of the TOB according to the manufacturer's specification. The details of this operation to recover the energy storage capability shall be reported in Table 1.

- m) A new set of operations h) through j) shall then be initiated. If the test TOB voltage in j) exceeds the manufacturer's defined operating voltage limits again within 60 sequences j) items 1) to 8) (≈ 48 h), then the energy delivery or acceptance capability of the TOB, and by derivation that of the FSB, shall be considered irreversibly degraded and the TOB as having reached the end of its service life. Otherwise the cycle sequence specified in sequence j) shall be continued until the next occurrence of exceeding a limiting value as described in k).
- n) The endurance of the TOB, in a particular application scenario, is defined by the total number of completed sequences of j) items 1) to 8) before end-of-service life according to m) is reached.
- o) The energy efficiency during these endurance test segments shall be determined according to the provisions of 7.3 or 7.4 and reported in Table 6 and Table 7, respectively.
- p) The heat generation at the maximum ambient temperature during the endurance test segment shall be determined according to 7.5 and reported in Table 10.
- q) If in j) the SoC_{OT} maintenance is achieved with the profile c), then the integration duration shall be adapted in such a manner that at least one such SoC_{OT} maintenance charge event c) is included.
- r) At the completion of the determination of energy efficiencies and heat generation according to 7.3, 7.4 and 7.5 within the endurance test 6.3, this endurance test shall be resumed at g) and carried out by ignoring section 9) and o), p) and q) until the TOB is declared irreversibly degraded or the battery manufacturer has demonstrated the declared service life of the FSB design with a robust extrapolation of the energy acceptance and delivery capability, over time, of the TOB.

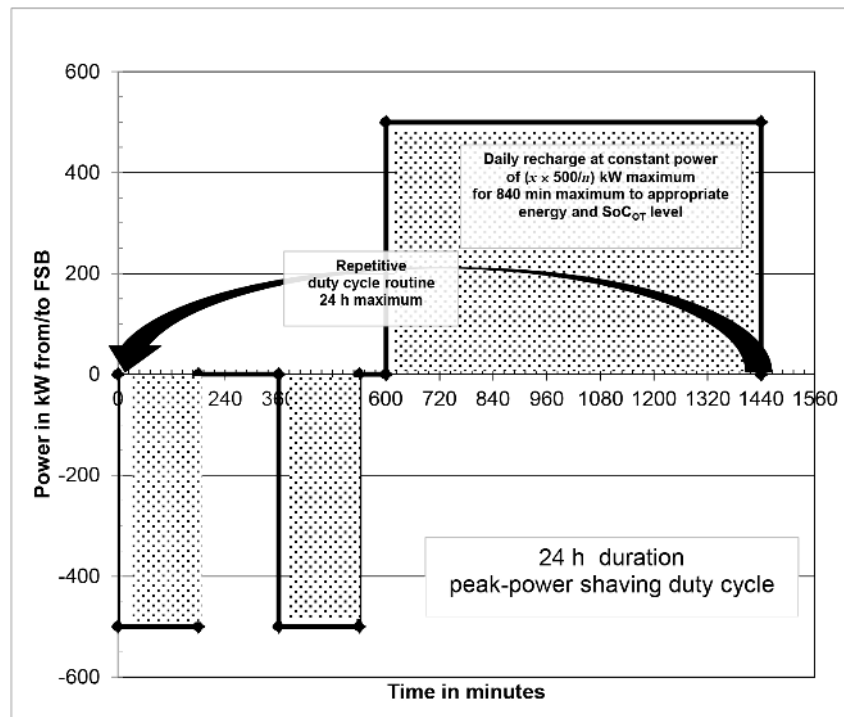
6.4 Test for endurance in peak-power shaving service

The test conditions are as follows.

- a) The manufacturer shall select and define a full-sized battery (FSB) which is able to
 - 1) supply multiple 500 kW constant power discharge pulses as per 6.4 i) within the battery operating voltage limits specified by the manufacturer and when the battery is thermally equilibrated at an ambient air temperature of $+25$ °C, and
 - 2) tolerate such energy transfers every day without exceeding the manufacturer's specified operating voltage limits.
- b) The manufacturer shall report how many cells, modules or stacks make up such a FSB. This value is termed n .
- c) The manufacturer shall define the fraction of power ($500/n$) kW such a cell, module or stack will deliver or accept when it is part of the FSB and this battery meets the conditions of 1) to 2) in 6.4 a).
- d) The manufacturer shall assemble with x of such cells, modules or stacks the appropriate TOB having at least
 - 1) four (4) cells in series (only if these cells are commercialized individually),
 - or
 - 2) one or more modules with at least four (4) single cells in series,
 - or
 - 3) one stack with at least four (4) flow cells in series,
 and incorporate the relevant BMS and BSS peripherals.
- e) When a battery based EES system with different power capability and/or energy content requires testing for compliance with this part of IEC 61427, then such a choice is acceptable provided that all other provisions are fulfilled and this deviation is stated in the test documentation.
- f) The actual energy content E (in kWh) of this TOB, after the manufacturer specified full charge and thermal equilibration in air at $+25$ °C ± 3 K ambient temperature, shall be determined with a constant power discharge at the $(x \times 500/n)$ kW power level to the final

voltage U_{final} or to the BMS mandated discharge limit as specified by the manufacturer so as to generate the data as required in 7.2.

- g) The TOB shall then be fully recharged according to the manufacturer's specifications.
- h) The manufacturer shall report the target operational state of charge (SoC_{OT}) level and ways to achieve it in Table 1.
- i) The TOB battery shall then be submitted, at an ambient temperature of $+25\text{ °C} \pm 3\text{ K}$, to a sequence of discharge/open-circuit/charge events defined in 1) through 5) without exceeding the manufacturer's specified operating voltage limits. The minimum and maximum battery voltage and the cumulative discharged and charged capacity (in Ah) and energy (in kWh) of the TOB shall be monitored and recorded.
 - 1) Discharge for 180 min with constant power at the fractional power level of $(x \times 500/n)$ in kW (example of morning peak-power shaving activity). The test profile is as shown, for example, in Figure 13.
 - 2) Do not deliver energy for 180 min.
If the BMS or BSS is powered directly by the battery then the battery can supply this energy also during the "off-power" period of step 2 and step 4. This amount of energy shall be taken into account in the efficiency calculation as below (7.3 and 7.4).
 - 3) Discharge for 180 min with constant power at the fractional power level of $(x \times 500/n)$ in kW (example of afternoon peak power shaving activity).
 - 4) Do not deliver energy for 60 min.
 - 5) Charge for not more than 840 min with a fractional power level not greater than $(x \times 500/n)$ in kW, maximum voltage and total energy input as specified by the manufacturer. After not more than 840 min the battery shall have reached again a SoC_{OT} as specified by the manufacturer. The recharge parameters shall be reported in Table 1.
- 6) Return to 1) and perform 1) to 5) seven times to sequentially generate the test data according to 7.3 followed by those according to 7.4 and 7.5. See also Figure 4.



IEC

Figure 13 – Daily peak-power shaving service test routine profile (6.4)

- j) If the TOB voltage in i) exceeds the manufacturer's defined limits of operating voltages then the energy delivery or acceptance capability of TOB, and by derivation that of the FSB, shall be considered degraded.
- k) The cycling shall then be stopped and an attempt made to restore the capability of the TOB according to the manufacturer's specification. The details of this operation to recover the energy storage capability shall be reported in Table 1.
- l) A new set of operations g) through i) shall then be initiated. If the test object battery TOB voltage in i) exceeds the manufacturer's defined operating voltage limits again within seven sequences i) items 1) to 5) (≈ 1 week), then the energy delivery capability of the TOB, and by derivation that of the FSB, shall be considered irreversibly degraded and the TOB as having reached the end of its service life. Otherwise the cycle sequence described in sequence i) shall be continued until the next occurrence of exceeding a limiting value as described in i).
- m) The endurance of the TOB, in a particular application scenario, is defined by the total number of completed sequences of i) items 1) to 5) before end-of-service life according to l) is reached.
- n) The energy efficiency during these endurance test segments shall be determined according to 7.3 and 7.4 and reported in Table 6 and Table 7 respectively.
- o) The heat generation at the maximum ambient temperature during the endurance test segment shall be determined according to 7.5 and reported in Table 10.
- p) At the completion of the determination of energy efficiencies and heat generation according to 7.3, 7.4 and 7.5 within the endurance test 6.4, this endurance test shall be resumed at g) and carried out by ignoring section 6) and n) and o) until the TOB is declared irreversibly degraded or the battery manufacturer has demonstrated the declared service life of the FSB design with a robust extrapolation of the energy acceptance and delivery capability, over time, of the TOB.

6.5 Test for endurance in photovoltaic energy storage, time-shift service

The test conditions are as follows:

- a) The manufacturer shall select and define a full-sized battery (FSB) which is able to
 - 1) accept daily photovoltaic energy at a constant power level of either 3 kW and 1,5 kW or 30 kW and 15 kW as per j) within the battery operating voltage limits specified by the manufacturer and when the battery is thermally equilibrated at an ambient air temperature of +25 °C,
 - 2) deliver the stored photovoltaic energy at power levels of 3 kW or 30 kW, and
 - 3) tolerate such energy transfers every day without exceeding the manufacturer's specified operating voltage limits.
- b) The manufacturer shall report how many cells, modules or stacks make up such a FSB. This value is termed n .
- c) The manufacturer shall define the fraction of power ($3/n$) kW or ($30/n$) kW such a cell, module or stack will accept and deliver when it is part of the FSB and this battery meets the conditions of 1) to 3) in 6.5 a).
- d) The manufacturer shall assemble with x of such cells, modules or stacks the appropriate TOB having at least
 - 1) four (4) cells in series (only if these cells are commercialized individually),
 - or
 - 2) one or more modules with at least four (4) cells in series,
 - or
 - 3) one stack with at least four (4) flow cells in series,
 and incorporate the relevant BMS and BSS peripherals.
- e) When a battery based EES system with different power capabilities and/or energy content requires testing for compliance with this part of IEC 61427, then such a choice is

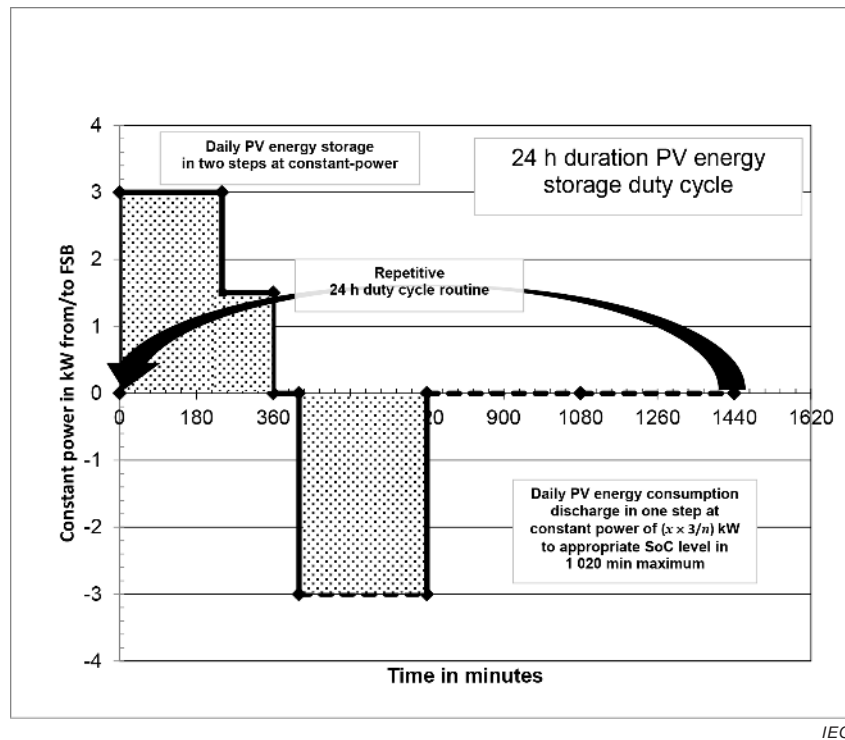
acceptable provided that all other provisions are fulfilled and this deviation is stated in the test documentation.

- f) The actual energy content E (in kWh) of this TOB, after the manufacturer specified full charge and thermal equilibration in air at $+25\text{ °C} \pm 3\text{ K}$ ambient temperature, shall be determined with a constant power discharge at the $(x \times 3/n)$ or $(x \times 30/n)$ kW power level to the final voltage U_{final} or to the BMS mandated discharge limit as specified by the manufacturer so as to generate the data as required in 7.2.
- g) The TOB shall then be fully recharged according to the manufacturer's specifications.
- h) The TOB shall then be discharged to such a target operational state of charge (SoC_{OT}) so that it can accept the fractional power and energy levels without exceeding the manufacturer's specified operating voltage limits.
- i) The manufacturer shall report this target operational state of charge (SoC_{OT}) level and ways to achieve it in Table 1.
- j) The TOB battery shall then be submitted, at an ambient temperature of $+25\text{ °C} \pm 3\text{ K}$, to a sequence of discharge/open-circuit/charge events defined in 1) through 5). The minimum and maximum battery voltage and the cumulative discharged and charged capacity (in Ah) and energy (in kWh) of the TOB shall be monitored and recorded.
 - 1) Charge for 240 min with constant power at the fractional power level of $(x \times 3/n)$ or $(x \times 30/n)$ kW (photovoltaic energy storage activity). The test profile is as shown, for example, in Figure 14 and Figure 15.
 - 2) Charge for 120 min with constant power at the fractional power level of $0,5(x \times 3/n)$ or $0,5(x \times 30/n)$ kW (photovoltaic energy storage activity).
 - 3) Do not receive or deliver power for 60 min.

NOTE The two-step constant power PV energy storage profile reflects in part the somewhat bell-shaped profile of the energy output of solar cells during the day.

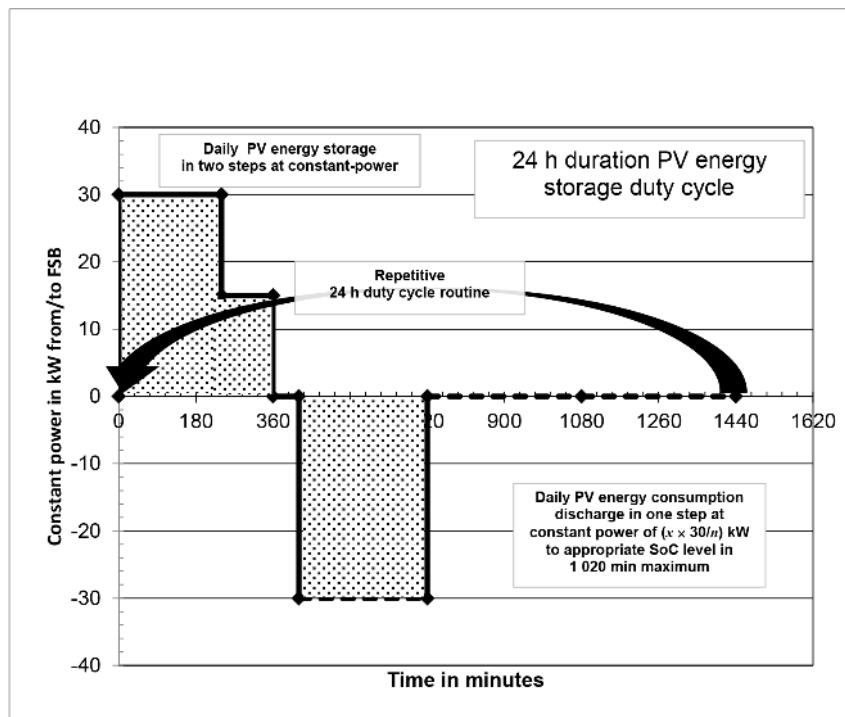
If the BMS or BSS is powered directly by the battery then this energy can be supplied by the battery also during the "off-power" period of step 3. This amount of energy shall be taken in account in the efficiency calculation as below (7.3 and 7.4).

- 4) Discharge with constant power at the fractional power level of $(x \times 3/n)$ or $(x \times 30/n)$ kW (stored photovoltaic energy use activity) until the manufacturer specified final voltage (U_{final}), SoC_{OT} (%) or discharged energy (kWh) or capacity (Ah) level is reached and the battery can again accept, during the next daylight period, PV energy for the duration and power levels defined in 1) and 2) above. The discharge parameters shall be reported in Table 1.
- 5) At the termination of the discharge as per 4), do not receive or deliver power for the remaining time to 1 440 min (24 h) elapsed cycle time.
- 6) Return to 1) and perform 1) to 5) seven times to sequentially generate the test data according to 7.3 followed by those according to 7.4 and 7.5. See also Figure 4.



IEC

Figure 14 – Daily photovoltaic energy storage time-shift service test routine (6.5) – 3 kW



IEC

Figure 15 – Daily photovoltaic energy storage time-shift service test routine (6.5) – 30 kW

- k) If the TOB cannot accept the specified energy at the power level defined in j) without exceeding the manufacturer's defined operating voltage limits, then the energy storage capability of the TOB, and by derivation that of the FSB, shall be considered degraded.

- l) The cycling shall then be stopped and an attempt made to restore the capability of the TOB according to the manufacturer's specification. The details of this operation to recover the energy storage capability shall be reported in Table 1.
- m) A new set of operations j) shall then be initiated. If the test TOB voltage in j) exceeds the manufacturer's defined operating voltage limits again within seven sequences j) items 1) to 5) (1 week), then the energy acceptance capability of the TOB, and by derivation that of the FSB, shall be considered irreversibly degraded and the battery as having reached the end of its service life. Otherwise the cycle sequence described in sequence j) shall be continued until the next occurrence of exceeding a limiting value as described in k).
- n) The endurance of the TOB, in a particular application scenario, is defined by the total number of completed sequences of j) items 1) to 5) before end-of-service life according to m) is reached.
- o) The energy efficiency during these endurance test segments shall be determined according to 7.3 or 7.4 and reported in Table 6 and Table 7, respectively.
- p) The heat generation at the maximum ambient temperature during the endurance test segment shall be determined according to 7.5 and reported in Table 10.
- q) At the completion of the determination of energy efficiencies and heat generation according to 7.3, 7.4 and 7.5 within the endurance test 6.5, this endurance test shall be resumed at g) and carried out ignoring section 6) and o) and p) until the TOB is declared irreversibly degraded or the battery manufacturer has demonstrated the declared service life of the FSG designs with a robust extrapolation of the energy acceptance and delivery capability, over time, of the TOB.

7 Battery properties and electrical performance

7.1 Declaration of the system properties

The key features of the full-sized battery (FSB) and test object battery (TOB) of 6.2 through 6.5, as available from the manufacturer or determined experimentally, shall be reported in Tables 1, 2, 3 and 4 with appropriate accuracy.

Table 1 – Summary of endurance test related electrical property data of the full-sized (FSB) and the test object (TOB) battery

Properties	Unit	Battery of subclause				
		6.2	6.3	6.4	6.5	6.5
Declared FSB capability	kW	500 to 1 000	180 to 360	500	3	30
Declared energy content E in kWh of the FSB at the indicated power level	kW	500	180	500	3	30
	kWh					
FSB formed of n cells, modules or stacks	n					
TOB formed of ($x \times 1/n$) cells, modules or stacks	x					
Manufacturer's specified method to achieve full charge of the TOB	n/a	Describe	Describe	Describe	Describe	Describe
Minimum (U_{\min}) and maximum (U_{\max}) operating voltage of TOB	V_{\min}					
	V_{\max}					
Fractional discharge power level in $x \times \text{kW}/n$ and actual energy content E in kWh of the TOB when discharged according to subclauses 6.x item f) and 7.2 at $+25 \text{ °C} \pm 3 \text{ K}$ ambient temperature to U_{final} or to the BMS mandated discharge limit	kW					
	kWh					
	V					
	BMS Yes No					
Total number of endurance sequences i) or j) achieved with the TOB until the end-of-life limit of item l) or m) in subclauses 6.x was reached	No.					
Target operational state of charge level (SoC_{OT}) of TOB as a percentage of the actual energy content E and ways to achieve it in the endurance test of 6.2, 6.3 and 6.5	%			n/a		
	kW					
	V					
	min					
Manufacturer recommended SoC_{OT} maintenance procedure for the TOB used in 6.2 j) 8) and 6.3 j) 8) (Values a or t or K , kW, kWh and time) Profile a, b or c	kW			n/a	n/a	n/a
	kWh					
	min					
	No.					
Profile	Profile					
Peak-power shaving duty 6.4 i) recharge parameters of the TOB as specified by the manufacturer (Values of SoC_{OT} , kW, time, V)	%	n/a	n/a		n/a	n/a
	kW					
	min					
	V					
PV energy storage time-shift duty 6.5 j) 4) discharge parameters of the TOB as specified by the manufacturer (Values of SoC_{OT} , kW, time, V)	%	n/a	n/a	n/a		
	kW					
	min					
	V					
Method to recover the energy storage capability of the TOB as used in 6.x l) or k) and as specified by the manufacturer	kW					
	V					
	min					

Properties	Unit	Battery of subclause				
		6.2	6.3	6.4	6.5	6.5
Endurance and performance tests carried out on <i>n</i> number of TOB's	No.					
TOB operated with a dedicated BMS and/or BSS	Yes					
	No					

Table 2 – Summary of physical dimension data of the full-sized battery (FSB)

Properties	Unit	Battery of subclause				
		6.2	6.3	6.4	6.5	6.5
Declared FSB capability	kW	500 to 1 000	180 to 360	500	3	30
Battery (FSB) – operated with a dedicated BMS and/or BSS	Yes					
	No					
Battery (FSB) – projected footprint with BMS and BSS installed	m ²					
Battery (FSB) – weight with BMS and BSS installed	kg					
Battery (FSB) – height with BMS and BSS installed	m					

Table 3 – Summary description of the full-sized battery (FSB)

Properties	Unit	Battery of subclause				
		6.2	6.3	6.4	6.5	6.5
Declared FSB capability	kW	500 to 1 000	180 to 360	500	3	30
Battery chemistry	n/a					
Brand or model name	n/a					
Type designation	n/a					
Manufacturer	n/a					
Hardware and software version	n/a					
Any other useful information	n/a					

Table 4 – Summary description of the test-object battery (TOB)

The required description shall allow understanding of the test object battery (TOB) by listing and illustrating its design features and characteristics so as to be able to extrapolate its performance to that of the full-sized battery (FSB).	
TOB of 6.2	<i>(Description) (Add pages)</i>
TOB of 6.3	<i>(Description) (Add pages)</i>
TOB of 6.4	<i>(Description) (Add pages)</i>
TOB of 6.5 3 kW	<i>(Description) (Add pages)</i>
TOB of 6.5 30 kW	<i>(Description) (Add pages)</i>

7.2 Determination of energy content at +25 °C ambient temperature

The discharge performance data of the TOB thermally equilibrated at +25 °C ± 3 K ambient temperature shall be determined and reported. These data shall be cogenerated during the execution of the endurance tests of 6.2 through 6.5 and item f).

The test shall be carried out with a TOB and its subsystems of the size identified in 5.3 and the data reported in Table 5.

Table 5 – Summary of the constant power discharge performance of the TOB at an ambient temperature of +25 °C ± 3 K

Properties	Unit	Battery of subclause				
		6.2	6.3	6.4	6.5	6.5
Declared discharge power capability of the full-sized battery (FSB)	kW	500	180	500	3	30
Fractional discharge power level $x \times \text{kW}/n$ and actual energy content E in kWh of the TOB when discharged at +25 °C ± 3 K ambient temperature to U_{final} or BMS mandated (Yes/No) discharge termination	kW					
	kWh					
	V					
	Yes No					
TOB open-circuit voltage at +25 °C ± 3 K ambient temperature and fully-charged prior to the discharge with constant power	V					
TOB final discharge voltage (U_{final})	V					
TOB voltage after 10 % of the duration of the constant power discharge	V					
TOB voltage after 50 % of the duration of the constant power discharge	V					
Current after 10 % of the duration of the constant power discharge	A					
Current at U_{final} or at the BMS mandated discharge termination	A					
Total duration of the constant power discharge to U_{final} or to the BMS mandated discharge termination	min					
Actual energy E discharged from the TOB	kWh					
Actual capacity discharged from the TOB during the determination of energy content E	Ah					

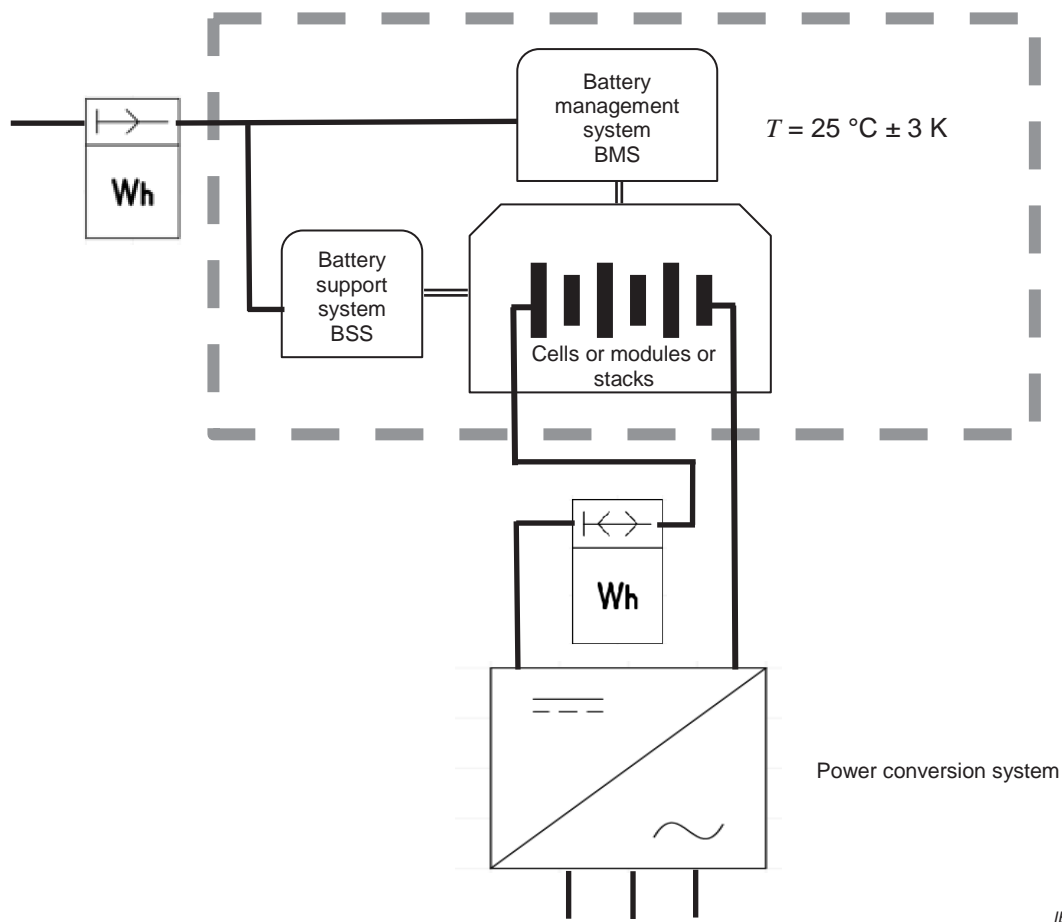
7.3 Determination of the energy efficiency during endurance tests at +25 °C ambient temperature

The energy storage efficiency of the TOB shall be determined at +25 °C ± 3 K ambient temperature and reported. These data shall be cogenerated during the execution of the endurance tests of 6.2 through 6.5 starting with item g) and over 840, 210, 7 and 7 repetitions of sequence i) (6.4) or j) (6.2, 6.3 and 6.5), respectively.

The test shall be carried out with a TOB and its subsystems of the size identified in 5.3 and as shown schematically in Figure 16.

The energy storage efficiency factor η is defined as the ratio between net energy discharged (i.e. the difference of discharged energy and the auxiliary (BMS/BSS) energy consumption during the discharge phase) and the total charged energy (i.e. the sum of the charged energy and the auxiliary (BMS/BSS) energy consumption during the charge phase) according to the formula

$$\eta = \frac{E_{\text{out}}}{E_{\text{in}}} = \frac{E_{\text{discharge}} - E_{\text{aux,discharge}}}{E_{\text{charge}} + E_{\text{aux,charge}}}$$



IEC

Figure 16 – Schematic view of the location of the two sets of energy values (energy to auxiliaries and energy to and from TOB) to be used for the determination of the energy storage efficiency factor η

This value shall be calculated, from the gathered data, at the beginning and advantageously also toward the end of the endurance test, to track efficiencies during the course of the endurance test and reported in Table 6.

**Table 6 – Summary of energy efficiencies determined
in endurance tests at an ambient temperature of +25 °C ± 3 K**

Properties	Unit	Battery of subclause				
		6.2	6.3	6.4	6.5	6.5
Declared FSB capability	kW	500 to 1 000	180 to 360	500	3	30
Number of endurance test sequences i) or j) over which the energy efficiency factor η is to be determined according to 6.2, 6.3, 6.4, 6.5	No.	840	210	7	7	7
Actual number of endurance test sequences i) or j) over which the energy efficiency factor η has been determined	No.					
Energy consumed by the BMS and BSS of the TOB during the reported number of endurance test sequences i) or j) at +25 °C ± 3 K ambient temperature	kWh					
Energy charged into the TOB during the reported number of endurance test sequences i) or j) at +25 °C ± 3 K ambient temperature	kWh					
Energy discharged from the TOB during the reported number of endurance test sequences i) or j) at +25 °C ± 3 K ambient temperature	kWh					
Energy efficiency factor η at the beginning of the endurance test $\eta = \frac{E_{out}}{E_{in}} = \frac{E_{discharge} - E_{aux,discharge}}{E_{charge} + E_{aux,charge}}$	n/a					
Energy efficiency factor η at the end of the endurance test $\eta = \frac{E_{out}}{E_{in}} = \frac{E_{discharge} - E_{aux,discharge}}{E_{charge} + E_{aux,charge}}$	n/a					

NOTE The energy efficiencies are tied to the intrinsic electrochemical reaction efficiencies during discharge and charge, the energy consumed by the auxiliaries and the charging strategy used to maintain the required SoC_{OT} of the battery.

7.4 Determination of the energy efficiency during endurance tests at the minimum and maximum ambient temperature

The energy storage efficiency of the TOB shall be determined at the manufacturer specified minimum and maximum ambient temperature at which the battery is operable and performs according to specified requirements. These data shall be cogenerated during the execution of the endurance tests of 6.2 through 6.5 starting with item g) and over 840, 210, 7 and 7 repetitions of sequence i) (6.4) or j) (6.2, 6.3 and 6.5), respectively.

The test shall be carried out with a TOB and its subsystems of the size identified in 5.3 and the data reported in Table 7.

- a) Prior to the test, the TOB, including any external electrolyte volumes, shall be kept for 24 ± 1 h at the manufacturer's specified minimum ambient temperature within a range of ± 3 K. This may be achieved by placing the TOB into a temperature-controlled cabinet with forced airflow or other equivalent means.

If the temperature limits differ between that admissible during charge or discharge, then a unique value suitable for both conditions may be chosen.

- b) While still in the cabinet, the TOB shall, starting with item g) of the endurance test subclause, be submitted to a number of endurance test sequences i) or j) as specified below:

Subclause 6.2 = 840, Subclause 6.3 = 210, Subclause 6.4 = 7, Subclause 6.5 = 7

- c) During the execution of test sequences i) or j), the SoC_{OT} stabilization conditions of profile a, b or c shall be adapted, according to the manufacturer's specifications, in such a way that the required SoC_{OT} level is also reached/maintained at this low ambient temperature. These conditions shall be reported in Table 8.
- d) At the conclusion of the low-temperature cycle test, the TOB shall be fully charged according to the manufacturer's specifications.
- e) Prior to the test, the TOB, including any external electrolyte volumes, shall then be kept for 24 ± 1 h at the manufacturer's specified maximum ambient temperature within a range of ± 3 K. This may be achieved by placing the TOB into a temperature-controlled cabinet with forced airflow or other equivalent means.
- f) While still in the cabinet, the TOB, starting with item g) of the endurance test clause, shall be submitted to a number of endurance test sequences i) or j) as specified below:
Subclause 6.2 = 840, Subclause 6.3 = 210, Subclause 6.4 = 7, Subclause 6.5 = 7
- g) During the execution of test sequences i) or j), the SoC_{OT} stabilization conditions of profile a, b or c shall be adapted, according to the manufacturer's specifications, in such a way that the required SoC_{OT} level is also reached/maintained at this high ambient temperature. These conditions shall be reported in Table 9.
- h) The energy storage efficiency factor η shall be determined with the formula

$$\eta = \frac{E_{out}}{E_{in}} = \frac{E_{discharge} - E_{aux,discharge}}{E_{charge} + E_{aux,charge}}$$

for each of the two temperatures during the relevant and applicable endurance tests and reported in Table 7.

Table 7 – Summary of energy efficiencies determined in endurance cycle tests at the minimum and maximum ambient temperature

Properties	Unit	Battery of subclause				
		6.2	6.3	6.4	6.5	6.5
Declared FSB capability	kW	500 to 1 000	180 to 360	500	3	30
Number of endurance test sequences i) or j) over which the energy efficiency factor η is to be determined according to 6.2, 6.3, 6.4, 6.5	No.	840	210	7	7	7
Actual number of endurance test sequences i) or j) over which the energy efficiency factor η has been determined	No.					
Energy consumed by the BMS and BSS of the TOB during the reported number of endurance sequences i) or j) at minimum and maximum ambient temperature	kWh					
	°C _{min}					
	kWh					
	°C _{max}					
Energy charged into the TOB during the reported number of endurance sequences i) or j) at minimum and maximum ambient temperature	kWh					
	°C _{min}					
	kWh					
	°C _{max}					
Energy discharged from the TOB during the reported number of endurance sequences i) or j) at minimum and maximum ambient temperature	kWh					
	°C _{min}					
	kWh					
	°C _{max}					
Energy efficiency factor η at minimum ambient temperature $\eta = \frac{E_{out}}{E_{in}} = \frac{E_{discharge} - E_{aux,discharge}}{E_{charge} + E_{aux,charge}}$	n/a					
Energy efficiency factor η at maximum ambient temperature $\eta = \frac{E_{out}}{E_{in}} = \frac{E_{discharge} - E_{aux,discharge}}{E_{charge} + E_{aux,charge}}$	n/a					

Table 8 – Parameters to achieve and maintain the target operational state of charge, SoC_{OT}, during tests at the minimum ambient temperature

Properties	Unit	Battery of subclause				
		6.2	6.3	6.4	6.5	6.5
Declared FSB capability	kW	500 to 1 000	180 to 360	500	3	30
Minimum (U_{\min}) and maximum (U_{\max}) operating voltage of TOB at minimum ambient temperature	x					
SoC _{OT} of TOB as a percentage of the actual energy content E and ways to achieve it in the endurance test of 6.2, 6.3 and 6.5 at minimum ambient temperature	%			n/a		
	kW					
	V					
	min					
Manufacturer recommended SoC _{OT} maintenance procedure for the TOB used in 6.2 j) 8) and 6.3 j) 8) Values a or t or K , kW and time) Profile a, b or c	kW			n/a	n/a	n/a
	kWh					
	min					
	No.					
	Profile					
Peak-power shaving duty 6.4 item i) 5) recharge parameters of the TOB as specified by the manufacturer (Values of SoC _{OT} , kW, time, V) at minimum ambient temperature	%	n/a	n/a		n/a	n/a
	kW					
	min					
	V					
PV energy storage time-shift duty 6.5 j) 4) discharge parameters of the TOB as specified by the manufacturer (Values of SoC _{OT} , kW, time, V) at minimum ambient temperature	%	n/a	n/a	n/a		
	kW					
	min					
	V					
Method to recover the energy storage capability of the TOB used in 6.x l) or k) and as specified by the manufacturer at minimum ambient temperature	kW					
	V					
	min					
TOB operated with a dedicated BMS and/or BSS	Yes No					

Table 9 – Parameters to achieve and maintain the target operational state of charge, SoC_{OT}, during tests at the maximum ambient temperature

Properties	Unit	Battery of subclause				
		6.2	6.3	6.4	6.5	6.5
Declared FSB capability	kW	500 to 1 000	180 to 360	500	3	30
Minimum (U_{min}) and maximum (U_{max}) operating voltage of TOB at maximum ambient temperature	x					
SoC _{OT} of TOB as a percentage of the actual energy content E and ways to achieve it in the endurance test of 6.2, 6.3 and 6.5 at maximum ambient temperature	%			n/a		
	kW					
	V					
	min					
Manufacturer recommended SoC _{OT} maintenance procedure for the TOB used in 6.2 j) 8) and 6.3 j) 8) Values a or t or K , kW and time) Profile a, b or c	kW			n/a	n/a	n/a
	kWh					
	min					
	No.					
	Profile					
Peak-power shaving duty 6.4 i) 5) recharge parameters of the TOB as specified by the manufacturer (Values of SoC _{OT} , kW, time, V) at maximum ambient temperature	%	n/a	n/a		n/a	n/a
	kW					
	min					
	V					
PV energy storage time-shift duty 6.5 j) 4) discharge parameters of the TOB as specified by the manufacturer (Values of SoC _{OT} , kW, time, V) at maximum ambient temperature	%	n/a	n/a	n/a		
	kW					
	min					
	V					
Method to recover the energy storage capability of the TOB used in 6.x l) or k) and as specified by the manufacturer at maximum ambient temperature	kW					
	V					
	min					
TOB operated with a dedicated BMS and/or BSS	Yes No					

7.5 Determination of waste heat generated during endurance tests at the maximum ambient temperature

Batteries generate heat when they are in idle state or are being charged and discharged. This heat results from electrochemical reaction enthalpy changes, resistive losses, and from the energy conversion inefficiencies of secondary systems such as the BMS and BSS.

The amount of energy wasted, and released as heat, by the TOB shall be determined at the maximum ambient temperature and reported. These data shall be cogenerated during the execution of the tests in 6.x and 7.4 at the maximum ambient temperature.

The test shall be carried out with a TOB and its subsystems of the size identified in 5.3. Particular attention shall be placed on the correct scalability of the TOB waste heat value to that of a FSB.

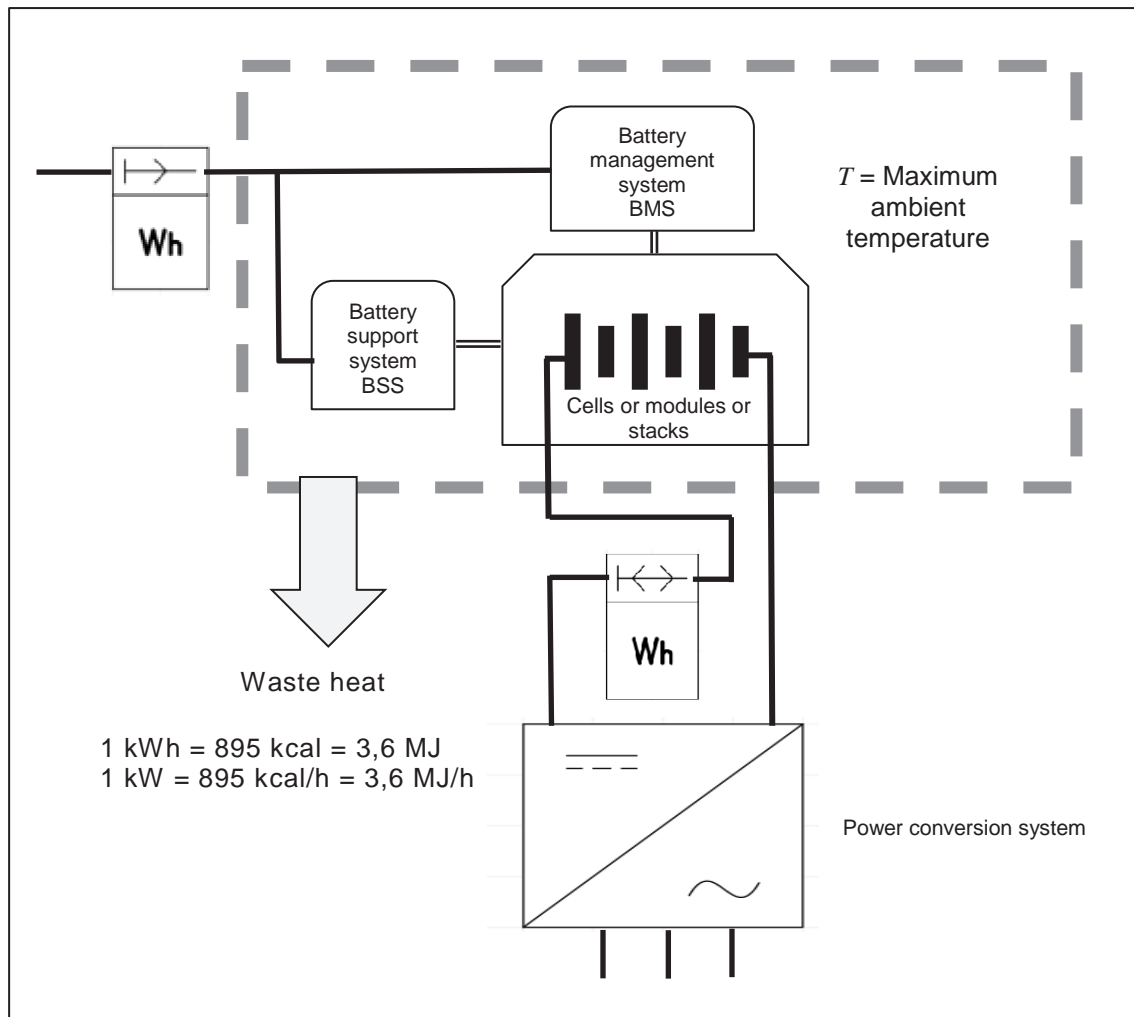


Figure 17 – Schematic view of the location of the two sets of energy values (energy to auxiliaries and energy to and from battery) to be used for the determination of the amount of waste heat generated

The amount of heat generated shall be obtained from the integration of the absolute energy values as shown in Figure 17. The integration shall be carried out over defined endurance test sequences i) and j) as specified in 7.4 and the waste energy value, E_w (in kWh), calculated with the formula below and reported in Table 10.

$$E_w = \sum E_{\text{supp}} + \sum E_{\text{charge}} - \sum E_{\text{discharge}}$$

where

- E_{supp} is the energy supplied to the BMS/BSS,
- E_{charge} is the energy charged into the battery,
- $E_{\text{discharge}}$ is the energy discharged from the battery.

NOTE 1 1 000 Wh of energy correspond to 895 kcal or 3,6 MJ; 1 000 W of power correspond to 895 kcal/h or 3,6 MJ/h.

Table 10 – Summary of energy released as heat during endurance tests at the maximum ambient temperature

Properties	Unit	Battery of subclause				
		6.2	6.3	6.4	6.5	6.5
Declared FSB capability	kW	500 to 1 000	180 to 360	500	3	30
Number of endurance test sequences j) over which the waste energy value, E_w , is to be determined according to 6.2, 6.3, 6.4, 6.5	No.	840	210	7	7	7
Actual number of endurance test sequences i) or j) over which the waste energy value, E_w , factor has been determined	No.					
Energy consumed (A) by the BMS and BSS of the TOB during the reported number of endurance sequences i) or j) at maximum ambient temperature	kWh					
	°C _{max}					
Energy charged (B) into the TOB during the reported number of endurance sequences i) or j) at maximum ambient temperature	kWh					
	°C _{max}					
Energy discharged (C) from the TOB during the reported number of endurance sequences i) or j) at maximum ambient temperature	kWh					
	°C _{max}					
Net energy released as heat by the TOB over the reported test sequences i) or j) $E_w = A + B - C$	kWh					
	MJ					
	kcal					
Comments and remarks concerning potential heat release scalability issues	n/a					

NOTE 2 The energy input into BMS and BSS is assumed to result in a 100 % conversion into heat.

The energy loss/heat release values are intended as guidance only and are not constant over an energy transfer cycle. The time dependency of heat generation intensity should be taken in consideration when cooling or heating infrastructure is dimensioned.

7.6 Determination of energy requirements during periods of idle state at +25 °C ambient temperature

Batteries require energy during periods of idle state to compensate for the self-discharge losses and cater for the energy needs of the BMS and BSS.

A battery in “idle state” is ready to deliver and absorb energy on demand with a reaction time as required by the application.

NOTE 1 Such reaction time may vary from few milliseconds (i.e. within the duration of a half sine wave of a.c. current) to several seconds.

The energy needed by the TOBs, when kept in idle state, shall be determined and reported.

The test shall be carried out with a TOB and its subsystems of the size identified in 5.3.

The energy required (in kWh) to keep the TOB in the idle state as defined above, shall be determined over 30 days and at $+25\text{ °C} \pm 3\text{ K}$ ambient temperature for each TOB of 6.2 through 6.5. This shall be done by physically monitoring

- a) the amount of charge energy needed to keep the TOB at the SoC_{OT} level appropriate for the test sequence i) or j) of the application scenario (6.2 through 6.5),
and
- b) the electrical energy consumed by the auxiliaries such as BMS and BSS so to keep the TOB at the SoC_{OT} level appropriate for duty cycle i) or j) of the application scenario (6.2 through 6.5),

and the data reported in Table 11. See also Figure 18.

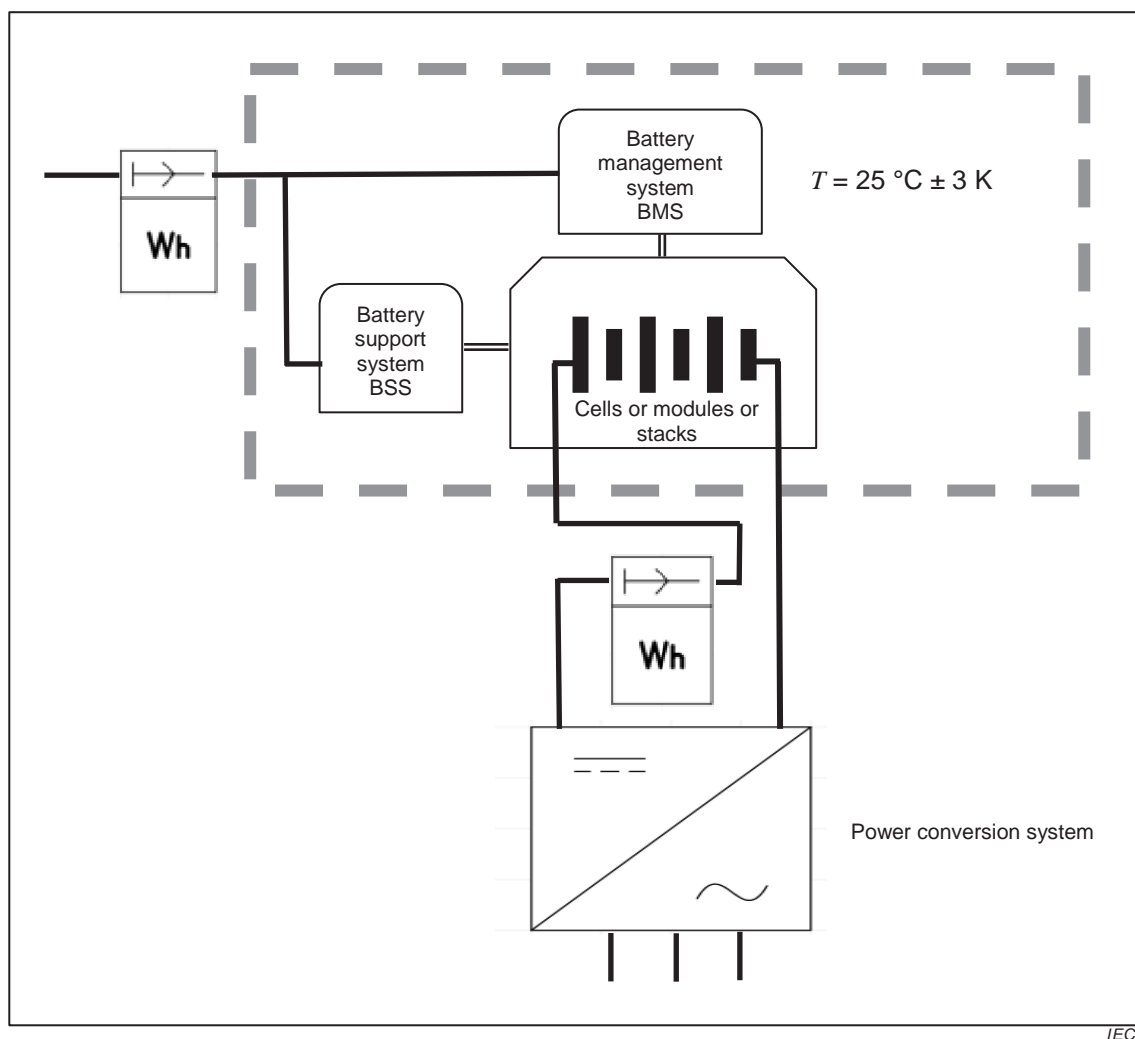


Figure 18 – Schematic view of the location of the two sets of energy values (energy to auxiliaries and energy to battery) to be used for the determination of the energy requirements during periods of idle state of the battery

**Table 11 – Summary of energy required during idle state periods
at +25 °C ± 3 K ambient temperature**

Properties	Unit	Battery of subclause				
		6.2	6.3	6.4	6.5	6.5
Declared FSB capability	kWh	500 to 1 000	180 to 360	500	3	30
Duration of time over which maintenance energy value E_M is to be determined	days	30				
Actual duration of time over which maintenance energy value E_M has been determined	days					
Energy consumed (A) by the BMS and BSS of the TOB during reported number of days in idle state at +25 °C ± 3 K ambient temperature so to maintain the mandated SoC _{OT} for endurance test purposes	kWh					
Energy charged (B) into the TOB during reported number of days in idle state at +25 °C ± 3 K ambient temperature so to maintain the mandated SoC _{OT} for endurance test purposes	kWh					
Net maintenance energy required by the TOB in idle state over the reported period.	kWh					
$E_M = A + B$ and per day	kWh per day					

NOTE The energy requirement values obtained at +25 °C may differ at the higher or lower ambient temperatures.

Annex A (informative)

Battery-related hazards

A.1 General

Batteries intended for electrical energy storage can be a source of dangerous voltages, elevated uncontrollable electrical currents and hazardous and toxic chemicals.

The hazards presented by such batteries have been given the necessary attention at the cell and module levels during their development and the product qualification tests. The individual battery product standards bear witness to these efforts and their consultation is highly recommended.

However, the sheer size and complexity of the planned battery systems and their associated controls make it necessary to conduct a hazard analysis very early in the planning stage to assess such hazards and risks.

Several IEC standards such as IEC 60812, IEC 61025, the IEC 61508 series, IEC 60730-1 (Annex H) and other relevant functional safety standards and methods (FTA, FMEA) can be used for such assessments.

This assessment should be carried out, prior to product procurement, in close collaboration with the battery manufacturer, the battery system builder and integrator and the future EES system operator.

A.2 Examples

A non-exhaustive list of hazard sources and events is listed in Tables A.1 and A. 2. Their occurrence is tied to the chemistry, the design of the cells and of the full-sized battery and battery plant.

**Table A.1 – Non-exhaustive listing of potential battery-related hazards
to be taken in consideration in risk assessment activities**

Examples of hazards caused by the battery itself
Emission of combustible, toxic or explosive gases
Emission of combustible, toxic or corrosive liquids
Ejection of combustible or toxic solids
Ground short currents
Fire or explosions
Heat damage and associated personal injuries
Loss of system functionality
Electrical arcs and shocks

Table A.2 – Non-exhaustive listing of potential installation-related hazards to be taken in consideration in risk assessment activities

Examples of external hazards impacting on the battery
Loss of air-conditioning and battery cooling
Loss of battery room ventilation
Loss of battery heating controls
Loss of battery voltage control functions
Over-discharge of cells due to a ground fault
Overcharge due to control function loss, data drift or software error
Overcurrent due to control function loss, shunt calibration error or drift
Short-circuit in control and diagnostic cabling on the battery
Massive shorts in the power cabling from the battery to the PCS or to the d.c. load
Loss of BMS/BSS functions
Seismic events
Fire in immediate vicinity of the battery
Sprinkler action, drip-water exposure and flooding
Crushing of cells due to rack or building collapse
Vandalism and theft
Operator errors
Improper disposal and recycling of cells and modules

Bibliography

The following International Standards and Technical Reports give valuable background information on the cells and batteries involved in the tests according to this part of IEC 61427. The status of the most recent version can be found at www.iec.ch.

IEC 60050 (all parts), *International Electrotechnical Vocabulary* (available from: <http://www.electropedia.org>)

IEC 60623, *Secondary cells and batteries containing alkaline or other non-acid electrolytes – Vented nickel-cadmium prismatic rechargeable single cells*

IEC 60730-1, *Automatic electrical controls – Part 1: General requirements*

IEC 60812, *Analysis techniques for system reliability – Procedure for failure mode and effects analysis (FMEA)*

IEC 60896-11, *Stationary lead-acid batteries – Part 11: Vented types – General requirements and methods of tests*

IEC 60896-21, *Stationary lead-acid batteries – Part 21: Valve regulated types – Methods of test*

IEC 60896-22, *Stationary lead-acid batteries – Part 22: Valve regulated types – Requirements*

IEC 61025, *Fault tree analysis (FTA)*

IEC 61427-1, *Secondary cells and batteries for renewable energy storage – General requirements and methods of test – Part 1: Photovoltaic off-grid application*

IEC 61508 (all parts), *Functional safety of electrical/electronic/programmable electronic safety-related systems*

IEC 61508-7, *Functional safety of electrical/electronic/programmable electronic safety-related systems – Part 7: Overview of techniques and measures*

IEC TR 62060, *Secondary cells and batteries – Monitoring of lead acid stationary batteries – User guide*

IEC 62133, *Secondary cells and batteries containing alkaline or other non-acid electrolytes – Safety requirements for portable sealed secondary cells, and for batteries made from them, for use in portable applications*

IEC 62259, *Secondary cells and batteries containing alkaline or other non-acid electrolytes – Nickel-cadmium prismatic secondary single cells with partial gas recombination*

IEC 62485-1, *Safety requirements for secondary batteries and battery installations – Part 1: General safety information*

IEC 62485-2, *Safety requirements for secondary batteries and battery installations – Part 2: Stationary batteries*

IEC 62485-3, *Safety requirements for secondary batteries and battery installations – Part 3: Traction batteries*

IEC 62619, *Secondary cells and batteries containing alkaline or other non-acid electrolytes – Safety requirements for large format secondary lithium cells and batteries for use in industrial applications*¹

IEC 62620, *Secondary cells and batteries containing alkaline or other non-acid electrolytes – Secondary lithium cells and batteries for use in industrial applications*

IEC 62675, *Secondary cells and batteries containing alkaline or other non-acid electrolytes – Sealed nickel-metal hydride prismatic rechargeable single cells*

IEC 62897, *Stationary Energy Storage Systems with Lithium Batteries – Safety Requirements*²

¹ Under consideration.

² Under consideration.

British Standards Institution (BSI)

BSI is the national body responsible for preparing British Standards and other standards-related publications, information and services.

BSI is incorporated by Royal Charter. British Standards and other standardization products are published by BSI Standards Limited.

About us

We bring together business, industry, government, consumers, innovators and others to shape their combined experience and expertise into standards-based solutions.

The knowledge embodied in our standards has been carefully assembled in a dependable format and refined through our open consultation process. Organizations of all sizes and across all sectors choose standards to help them achieve their goals.

Information on standards

We can provide you with the knowledge that your organization needs to succeed. Find out more about British Standards by visiting our website at bsigroup.com/standards or contacting our Customer Services team or Knowledge Centre.

Buying standards

You can buy and download PDF versions of BSI publications, including British and adopted European and international standards, through our website at bsigroup.com/shop, where hard copies can also be purchased.

If you need international and foreign standards from other Standards Development Organizations, hard copies can be ordered from our Customer Services team.

Subscriptions

Our range of subscription services are designed to make using standards easier for you. For further information on our subscription products go to bsigroup.com/subscriptions.

With **British Standards Online (BSOL)** you'll have instant access to over 55,000 British and adopted European and international standards from your desktop. It's available 24/7 and is refreshed daily so you'll always be up to date.

You can keep in touch with standards developments and receive substantial discounts on the purchase price of standards, both in single copy and subscription format, by becoming a **BSI Subscribing Member**.

PLUS is an updating service exclusive to BSI Subscribing Members. You will automatically receive the latest hard copy of your standards when they're revised or replaced.

To find out more about becoming a BSI Subscribing Member and the benefits of membership, please visit bsigroup.com/shop.

With a **Multi-User Network Licence (MUNL)** you are able to host standards publications on your intranet. Licences can cover as few or as many users as you wish. With updates supplied as soon as they're available, you can be sure your documentation is current. For further information, email bsmusales@bsigroup.com.

BSI Group Headquarters

389 Chiswick High Road London W4 4AL UK

Revisions

Our British Standards and other publications are updated by amendment or revision.

We continually improve the quality of our products and services to benefit your business. If you find an inaccuracy or ambiguity within a British Standard or other BSI publication please inform the Knowledge Centre.

Copyright

All the data, software and documentation set out in all British Standards and other BSI publications are the property of and copyrighted by BSI, or some person or entity that owns copyright in the information used (such as the international standardization bodies) and has formally licensed such information to BSI for commercial publication and use. Except as permitted under the Copyright, Designs and Patents Act 1988 no extract may be reproduced, stored in a retrieval system or transmitted in any form or by any means – electronic, photocopying, recording or otherwise – without prior written permission from BSI. Details and advice can be obtained from the Copyright & Licensing Department.

Useful Contacts:

Customer Services

Tel: +44 845 086 9001

Email (orders): orders@bsigroup.com

Email (enquiries): cservices@bsigroup.com

Subscriptions

Tel: +44 845 086 9001

Email: subscriptions@bsigroup.com

Knowledge Centre

Tel: +44 20 8996 7004

Email: knowledgecentre@bsigroup.com

Copyright & Licensing

Tel: +44 20 8996 7070

Email: copyright@bsigroup.com



DPC: 16 / 30332632 DC

BSI Group Headquarters

389 Chiswick High Road London W4 4AL

Tel: +44 (0)20 8996 9000

Fax: +44 (0)20 8996 7400

www.bsigroup.com

Date: 07 October 2016

Origin: International

Latest date for receipt of comments: 30 November 2016

Project No. 2015/02893

Responsible committee: PEL/21 Secondary cells and batteries

Interested committees:

Title: Draft BS EN 62932-1 Ed 1.0 Flow battery systems for stationary applications

Part 1: General aspects, terminology and definitions

Please notify the secretary if you are aware of any keywords that might assist in classifying or identifying the standard or if the content of this standard

- i) has any issues related to 3rd party IPR, patent or copyright
- ii) affects other national standard(s)
- iii) requires additional national guidance or information

**WARNING: THIS IS A DRAFT AND MUST NOT BE REGARDED OR USED AS A BRITISH STANDARD.
THIS DRAFT IS NOT CURRENT BEYOND 30 November 2016**

This draft is issued to allow comments from interested parties; all comments will be given consideration prior to publication. No acknowledgement will normally be sent. **See overleaf for information on the submission of comments.**

No copying is allowed, in any form, without prior written permission from BSI except as permitted under the Copyright, Designs and Patent Act 1988 or for circulation within a nominating organization for briefing purposes. Electronic circulation is limited to dissemination by e-mail within such an organization by committee members.

Further copies of this draft may be purchased from BSI Shop <http://shop.bsigroup.com> or from BSI Customer Services, Tel: +44(0) 20 8996 9001 or email cservices@bsigroup.com. British, International and foreign standards are also available from BSI Customer Services.

Information on the co-operating organizations represented on the committees referenced above may be obtained from <http://standardsdevelopment.bsigroup.com>

Responsible Committee Secretary: **Mr Roger G Tanfield (BSI)**Direct tel: **020 8996 7218**E-mail: roger.tanfield@bsigroup.com

Introduction

This draft standard is based on international discussions in which the UK has taken an active part. Your comments on this draft are welcome and will assist in the preparation of the consequent standard. There is a high probability that this text could be adopted by CENELEC as a reference document for harmonization or as a European Standard. Recipients of this draft are requested to comment on the text bearing in mind this possibility.

UK Vote

Please indicate whether you consider the UK should submit a negative (with reasons) or positive vote on this draft.

Submission of Comments

- The guidance given below is intended to ensure that all comments receive efficient and appropriate attention by the responsible BSI committee. **Annotated drafts are not acceptable and will be rejected.**
- All comments must be submitted, preferably electronically, to the Responsible Committee Secretary at the address given on the front cover. Comments should be compatible with version 6.0 or version 97 of Microsoft Word for Windows, if possible; otherwise comments in ASCII text format are acceptable. **Any comments not submitted electronically should still adhere to these format requirements.**
- All comments submitted should be presented as given in the example below. Further information on submitting comments and how to obtain a blank electronic version of a comment form are available from the BSI website at: <http://drafts.bsigroup.com/>

Template for comments and secretariat observations

Date: xx/xx/20xx	Document: ISO/DIS xxxx
------------------	------------------------

1	2	(3)	4	5	(6)	(7)
MB	Clause No./ Subclause No./Annex (e.g. 3.1)	Paragraph/ Figure/ Table/Note	Type of comment	Comment (justification for change) by the MB	Proposed change by the MB	Secretariat observations on each comment submitted
	3.1	Definition 1	ed	Definition is ambiguous and needs clarifying.	Amend to read '...so that the mains connector to which no connection...'	
	6.4	Paragraph 2	te	The use of the UV photometer as an alternative cannot be supported as serious problems have been encountered in its use in the UK.	Delete reference to UV photometer.	



21/900/CD

COMMITTEE DRAFT (CD)

IEC/TC or SC: 21	Project number IEC 62932-1 Ed.1	
Title of TC/SC: Secondary cells and batteries	Date of circulation 2016-09-23	Closing date for comments 2016-12-16
Also of interest to the following committees 21A	Supersedes document 21/868/CD + 21/886/CC	
Proposed horizontal standard <input type="checkbox"/> Other TC/SCs are requested to indicate their interest, if any, in this CD to the TC/SC secretary		
Functions concerned: <input type="checkbox"/> Safety <input type="checkbox"/> EMC <input type="checkbox"/> Environment <input checked="" type="checkbox"/> Quality assurance		
Secretary: Y. Boudou	THIS DOCUMENT IS STILL UNDER STUDY AND SUBJECT TO CHANGE. IT SHOULD NOT BE USED FOR REFERENCE PURPOSES. RECIPIENTS OF THIS DOCUMENT ARE INVITED TO SUBMIT, WITH THEIR COMMENTS, NOTIFICATION OF ANY RELEVANT PATENT RIGHTS OF WHICH THEY ARE AWARE AND TO PROVIDE SUPPORTING DOCUMENTATION.	

Title:

IEC 62932-1: Flow battery systems for stationary applications – Part 1 : General Aspects, Terminology and Definitions

(Titre) :

IEC 62932-1: Systèmes de batterie d'accumulateurs à circulation d'électrolyte pour applications stationnaires - Partie 1: Généralités, Terminologie et Définitions

Introductory note

Copyright © 2016 International Electrotechnical Commission, IEC. All rights reserved. It is permitted to download this electronic file, to make a copy and to print out the content for the sole purpose of preparing National Committee positions. You may not copy or "mirror" the file or printed version of the document, or any part of it, for any other purpose without permission in writing from IEC.

CONTENTS

1
2
3
4
5
6
7
8

FOREWORD	3
1 Scope	Error! Bookmark not defined.
2 Normative references	Error! Bookmark not defined.
3 Terms and definitions.....	Error! Bookmark not defined.

Licensed copy: Care Segreteria – PADOVA , CRUI Conferenza dei Rettori delle, Version correct as of 10/10/2018

INTERNATIONAL ELECTROTECHNICAL COMMISSION

—————

FLOW BATTERY SYSTEMS FOR STATIONARY APPLICATIONS– PART 1 : TERMINOLOGY

FOREWORD

- 1) The International Electrotechnical Commission (IEC) is a worldwide organization for standardization comprising all national electrotechnical committees (IEC National Committees). The object of IEC is to promote international co-operation on all questions concerning standardization in the electrical and electronic fields. To this end and in addition to other activities, IEC publishes International Standards, Technical Specifications, Technical Reports, Publicly Available Specifications (PAS) and Guides (hereafter referred to as "IEC Publication(s)"). Their preparation is entrusted to technical committees; any IEC National Committee interested in the subject dealt with may participate in this preparatory work. International, governmental and non-governmental organizations liaising with the IEC also participate in this preparation. IEC collaborates closely with the International Organization for Standardization (ISO) in accordance with conditions determined by agreement between the two organizations.
- 2) The formal decisions or agreements of IEC on technical matters express, as nearly as possible, an international consensus of opinion on the relevant subjects since each technical committee has representation from all interested IEC National Committees.
- 3) IEC Publications have the form of recommendations for international use and are accepted by IEC National Committees in that sense. While all reasonable efforts are made to ensure that the technical content of IEC Publications is accurate, IEC cannot be held responsible for the way in which they are used or for any misinterpretation by any end user.
- 4) In order to promote international uniformity, IEC National Committees undertake to apply IEC Publications transparently to the maximum extent possible in their national and regional publications. Any divergence between any IEC Publication and the corresponding national or regional publication shall be clearly indicated in the latter.
- 5) IEC itself does not provide any attestation of conformity. Independent certification bodies provide conformity assessment services and, in some areas, access to IEC marks of conformity. IEC is not responsible for any services carried out by independent certification bodies.
- 6) All users should ensure that they have the latest edition of this publication.
- 7) No liability shall attach to IEC or its directors, employees, servants or agents including individual experts and members of its technical committees and IEC National Committees for any personal injury, property damage or other damage of any nature whatsoever, whether direct or indirect, or for costs (including legal fees) and expenses arising out of the publication, use of, or reliance upon, this IEC Publication or any other IEC Publications.
- 8) Attention is drawn to the Normative references cited in this publication. Use of the referenced publications is indispensable for the correct application of this publication.
- 9) Attention is drawn to the possibility that some of the elements of this IEC Publication may be the subject of patent rights. IEC shall not be held responsible for identifying any or all such patent rights.

International Standard IEC 62932-1 has been prepared by Joint Working Group JWG7: Flow Batteries, of IEC technical committee TC:21.

The text of this standard is based on the following documents:

FDIS	Report on voting
XX/XX/FDIS	XX/XX/RVD

Full information on the voting for the approval of this standard can be found in the report on voting indicated in the above table.

This publication has been drafted in accordance with the ISO/IEC Directives, Part 2.

The committee has decided that the contents of this publication will remain unchanged until the stability date indicated on the IEC web site under "<http://webstore.iec.ch>" in the data related to the specific publication. At this date, the publication will be

- reconfirmed,
- withdrawn,
- replaced by a revised edition, or

62 • amended.

63

64 The National Committees are requested to note that for this publication the stability date is 20XX.

65 THIS TEXT IS INCLUDED FOR THE INFORMATION OF THE NATIONAL COMMITTEES AND WILL BE DELETED AT THE
66 PUBLICATION STAGE.

67

68

69
70
71
72
73
74
75
76
77
78
79
80
81
82
83
84
85
86
87
88
89
90
91
92
93
94
95
96
97
98
99
100
101
102
103
104
105
106
107
108

Flow Battery SYSTEMS for Stationary applications – Part 1 : Terminology

1 Scope

This International Standard relates to flow batteries energy storage systems used in Electrical Energy Storage (EES) applications and provides the main terminology of this technology including terms necessary for the definition of unit parameters, test methods, planning, installation, safety and environmental issues.

2 Normative references

The following documents, in whole or in part, are normatively referenced in this document and are indispensable for its application. For dated references, only the edition cited applies. For undated references, the latest edition of the referenced document (including any amendments) applies.

All normative documents are subject to revision. Parties of agreements based on this terminology standard are encouraged to investigate the possibility of applying the most recent editions of the normative documents indicated below. Members of IEC and ISO maintain registers of currently valid International Standards.

For the purposes of this document, the terms and definitions given in IEC 60050 and the following apply:

IEC 60050-192: 2015, International Electrotechnical Vocabulary - Part 192: Dependability;

IEC 60050-151: 2001, International Electrotechnical Vocabulary - Part 151: Electrical and magnetic devices;

IEC 60050-351: 2006, International Electrotechnical Vocabulary - Part 351: Control technology;

IEC 60050-411: 1996, International Electrotechnical Vocabulary – Part 411: Rotating machinery;

IEC 60050-415: 1999, International Electrotechnical Vocabulary - Part 415: Wind turbine generator systems;

IEC 60050-426: 2008, International Electrotechnical Vocabulary - Part 426: Equipment for explosive atmospheres;

IEC 60050-482: 2004, International Electrotechnical Vocabulary - Part 482: Primary and secondary cells and batteries;

IEC 60060-212:2010, High-voltage test techniques - Part 1: General definitions and test requirements;

IEC 60950-1:2005, Information technology equipment – Safety - Part 1: General requirements;

IEC 61427-2, Secondary cells and batteries for renewable energy storage – General requirements and methods of test – Part 2: On-grid applications;

IEC 62282-3-100: 2012, Fuel cell technologies - Part 3-100: Stationary fuel cell power systems – Safety;

IEC 62477-1: 2012, Safety requirements for power electronic converter systems and equipment - Part 1: General;

ISO 13850:2006, Safety of machinery - Emergency stop - Principles for design;

109 3 Terms and definitions for FBESS

110 3.1

111 **auxiliary energy**

112 energy consumed by all the equipment and components of the flow battery energy storage system

113 Note 1 to entry: The equipment and components include, but are not limited to, pumps, valves, BMS, heat exchanger and
114 heating system.

115 3.2

116 **battery management system**

117 BMS

118 electronic system associated with a flow battery energy storage system which monitors and manages its
119 state, calculates secondary data, reports that data and controls its environment to influence the flow
120 battery energy storage system's performance and service life

121 Note 1 to entry: The function of the battery management system can be fully or partially assigned to the battery and to
122 equipment that uses flow battery energy store system.

123 [SOURCE: IEC 61427-2: 2013, 3.12,modified]

124 3.3

125 **battery support systems**

126 BSS

127 auxiliary units used in the flow battery energy storage system which are not part of the fluid circulation
128 system, stacks, PCS, and BMS, like heat exchanger, ventilation system, safety system, inertisation
129 system. The battery support system is controlled by the battery management system

130 3.4

131 **bus**

132 functional unit for the transfer of data between several participants, these being functional units for data
133 processing, via a common transmission path, wherein participants are not involved in the transfer of
134 data between other participants

135 Note 1 to entry: The logic and functional definition of a bus applies independently of the topological configuration and physical
136 implementation of the bus. A bus may have a line or a ring configuration.

137 Note 2 to entry: In some cases, transmission rights are distributed by another participant, for example by a bus arbitrator.

138 Note 3 to entry: This entry was numbered 351-32-10 in IEC 60050-351:2006.

139 [SOURCE: IEC 351-56-10]

140 3.5

141 **cold stand-by**

142 standby state requiring warm up before a demand to operate can be met

143 Note 1 to entry: A cold standby state may apply to redundant or stand-alone items.

144 Note 2 to entry: In this context "warm up" includes meeting any conditions required to operate as required (e.g. achieving the
145 required temperature, speed, pressure).

146 [SOURCE: IEC 192-02-11]

147 3.6

148 **emergency shutdown**

149 rapid shutdown of the flow battery energy storage system triggered by a protection system or by manual
150 intervention

151 [SOURCE: IEC 60050-415: 1999, 415-01-11]

152 3.7

153 **emergency stop**

154 function that is intended to avert arising, or reduce existing hazards to persons, damage to machinery or
155 to work in progress and it is initiated by a single human action

156 [SOURCE: ISO 13850:2006, 3.1]

157 3.8

158 **energy efficiency**

159 ratio of the electrical energy provided from the flow battery energy storage system during discharge to
160 the electrical energy supplied during the preceding charge

- 161 Note 1 to entry: It shall include necessary energy required for fluid circulation system, thermal management system and battery
162 management system.
- 163 [SOURCE: IEV 482-05-53, modified - “flow battery energy storage system” instead of “secondary battery”
164 and Note 1 to entry added]
- 165 **3.9**
166 **energy storage fluid**
167 contains active materials and flows through the flow battery cell, consisting of liquid, solution,
168 suspension or gasses
- 169 **3.10**
170 **end of charge**
171 condition that indicates that the charging stage of flow battery energy storage system is ended based on
172 the manufacture specifications
- 173 **3.11**
174 **end of discharge**
175 condition that indicates that the discharging stage of flow battery energy storage system is ended based
176 on the manufacture specifications
- 177 **3.12**
178 **forced ventilation**
179 movement of air and its replacement with fresh air by mechanical means
- 180 [SOURCE: IEC 62282-3-300: 2012, 3.9]
- 181 **3.13**
182 **flow battery cell**
183 secondary cell characterized by the spatial separation of the electrodes and the movement of the
184 energy storage fluids
- 185 **3.14**
186 **flow battery energy storage system**
187 FBESS
188 energy storage system which consists of flow battery system and power conversion system
- 189 **3.15**
190 **flow battery system**
191 FBS
192 two or more flow battery cells electrically connected including all components for its use in an
193 electrochemical energy storage system such as BMS, BSS and energy storage fluid
- 194 **3.16**
195 **fluid circulation system**
196 system which consists of components and equipment to store and circulate energy storage fluids, such
197 as tanks, pipes, manual valves, electrical valves, pumps and sensors
- 198 **3.17**
199 **fully charge**
200 when the flow battery energy storage system reaches the end of charge point
- 201 **3.18**
202 **fully discharge**
203 when the flow battery energy storage system reaches the end of discharge point
204
- 205 **gas release**
206 liberation of gases flows the flow battery system which is intended as a normal function
- 207 [SOURCE: IEC 60060-212:2010, 212-18-25, modified]
- 208 **3.19**
209 **hot stand-by**
210 standby state providing for immediate operation upon demand
- 211 Note 1 to entry: A hot standby state may apply to redundant or stand-alone items.
- 212 Note 2 to entry: In some applications, an item in a hot standby state is considered to be operating.
- 213 [SOURCE: IEV 192-02-12]

- 214 **3.20**
215 **hybrid flow battery cell**
216 flow battery cell in which one of the active materials is, depending on the state of charge, a solid
217 deposited on one of the electrode surfaces
- 218 **3.21**
219 **indoor use**
220 use of the flow battery energy storage system sheltered from external weather conditions by being
221 installed within a building
- 222 **3.22**
223 **input power**
224 electrical power applied to the flow battery energy storage system during a charging event
- 225 **3.23**
226 **insulation resistance**
227 resistance under specified conditions between two conductive elements separated by insulating
228 materials
229 [SOURCE: IEC 60050-151: 2001, 151-15-43]
- 230 **3.24**
231 **interlock**
232 control to prove the physical state of a required condition and to furnish that proof to the safety related
233 control device which performs the safety shutdown
234 [SOURCE: IEC 62282-3-100: 2012, 3.20]
- 235 **3.25**
236 **material leakage**
237 unplanned escape of energy storage fluids, gasses or other material from a flow battery cell or a flow
238 battery system
239 [SOURCE: IEC 60050-482: 2004, 482-02-32]
- 240 **3.26**
241 **natural ventilation**
242 movement of air and its replacement with fresh air due to the effects of wind and/or temperature
243 gradients
244 [SOURCE: IEC 60050-426: 2008, 426-03-07]
- 245 **3.27**
246 **negative terminal**
247 accessible conductive part provided for the connection of an external electric circuit to the negative
248 electrode of the flow battery or the hybrid flow battery
249 [SOURCE: IEC 60050-482: 2004, 482-02-24, modified]
- 250 **3.28**
251 **non operating state**
252 state of not performing any required function
253 Note 1 to entry: The adjective “non-operating” designates an item in a non-operating state.
254 [SOURCE: IEC 192-02-06]
- 255 **3.29**
256 **operating state**
257 state of performing as required
258 Note 1 to entry: The adjective “operating” designates an item in an operating state.
259 Note 2 to entry: In some applications, an item in an idle state is considered to be operating.
260 [SOURCE: IEC 192-02-04]

- 261 **3.30**
262 **operational coordination**
263 mutual correlated operation for the flow battery system among equipment and systems such as power
264 conversion system, BMS, BSS and external ventilation system
- 265 **3.31**
266 **outdoor use**
267 use of the flow battery energy storage system exposed to external weather conditions
- 268 **3.32**
269 **output power**
270 electrical power supplied by the flow battery energy storage system during the preceding discharge
- 271 **3.33**
272 **overcharge**
273 continued charging of a fully charged secondary cell or battery
274 [SOURCE: IEC 60050-482: 2004, 482-05-44]
- 275 **3.34**
276 **pipe**
277 passage provided to guide the energy storage fluids including hose
278 Note 1 to entry: The pipe includes its fittings such as, but not limited to, flange, reducer and elbow.
279 [SOURCE: IEC 60050-411: 1996, 411-44-11, modified]
- 280 **3.35**
281 **positive terminal**
282 accessible conductive part provided for the connection of an external electric circuit to the positive
283 electrode of the flow battery or the hybrid flow battery
284 [SOURCE: IEC 60050-482: 2004, 482-02-25, modified]
- 285 **3.36**
286 **power conversion system**
287 PCS
288 one or more power electronic converters intended to work together with other equipment
289 [SOURCE: IEC 62477-1: 2012, 3.46, modified]
- 290 **3.37**
291 **rated energy**
292 quantity of energy, declared by the manufacturer, which under the specified conditions can be
293 discharged from fully charged flow battery energy storage system, to fully discharge
294 Note1 to entry: The rated energy is expressed in watt hour (Wh).
- 295 **3.38**
296 **rated energy efficiency**
297 energy efficiency of a flow battery energy storage system under the condition of charging and
298 discharging at rated power
- 299 **3.39**
300 **rated input power**
301 electrical power, declared by the manufacturer, which under the specified operating conditions is the
302 maximum input power designed to work
303 Note 1 to entry: The rated input power is normally express in watt (W).
- 304 **3.40**
305 **rated output power**
306 electrical power, declared by the manufacturer, which under the specified operating conditions is the
307 maximum output power designed to achieve
308 Note 1 to entry: The rated output power is normally express in watt (W).
- 309 **3.41**
310 **routine test**
311 test to which each individual sample is subjected during or after manufacture to check if the sample
312 complies with certain criteria

313 [SOURCE: IEC 60950-1:2005, 1.2.13.3]

314 **3.42**

315 **sampling test**

316 test on a number of samples taken at random from a batch

317 [SOURCE: IEC 60950-1:2005, 1.2.13.2]

318 **3.43**

319 **service life**

320 total period of useful life of a cell or a battery in operation

321 [SOURCE: IEC 482-03-46]

322 **3.44**

323 **short-circuit current**

324 maximum current which can be delivered by a cell or battery into an external circuit with zero electric
325 resistance, or an external circuit which depresses the cell or battery voltage to approximately zero volts

326 [SOURCE: IEC 60050-482: 2004, 482-03-26]

327 **3.45**

328 **site requirements**

329 requirements for an installation site in order to operate the flow battery energy storage system safely or
330 in the intended ambient conditions

331 **3.46**

332 **stack**

333 group of connected flow battery cells, assembled in a contiguous form and usually connected in series
334 electrically

335 Note 1 to entry: In theory, stacks can also be formed by connecting cells in parallel. But due to minimum voltage requirements,
336 the cells are usually connected in series.

337 **3.47**

338 **standby state**

339 non-operating up state during required time

340 [SOURCE: IEC 192-02-10]

341 **3.48**

342 **type test**

343 test on representative sample with the objective of determine if, as designed and manufactured, it can
344 meet the requirements of this standard

345 [SOURCE: IEC 60950-1:2005, 1.2.13.1]

346

347



DPC: 16 / 30332627 DC

BSI Group Headquarters

389 Chiswick High Road London W4 4AL

Tel: +44 (0)20 8996 9000

Fax: +44 (0)20 8996 7400

www.bsigroup.com

Date: 07 October 2016

Origin: International

Latest date for receipt of comments: 30 November 2016

Project No. 2015/02892

Responsible committee: PEL/21 Secondary cells and batteries

Interested committees:

Title: Draft BS EN 62932-2-2 Ed 1.0 Flow battery systems for stationary applications

Part 2-2: Safety requirements

Please notify the secretary if you are aware of any keywords that might assist in classifying or identifying the standard or if the content of this standard

- i) has any issues related to 3rd party IPR, patent or copyright
- ii) affects other national standard(s)
- iii) requires additional national guidance or information

**WARNING: THIS IS A DRAFT AND MUST NOT BE REGARDED OR USED AS A BRITISH STANDARD.
THIS DRAFT IS NOT CURRENT BEYOND 30 November 2016**

This draft is issued to allow comments from interested parties; all comments will be given consideration prior to publication. No acknowledgement will normally be sent. **See overleaf for information on the submission of comments.**

No copying is allowed, in any form, without prior written permission from BSI except as permitted under the Copyright, Designs and Patent Act 1988 or for circulation within a nominating organization for briefing purposes. Electronic circulation is limited to dissemination by e-mail within such an organization by committee members.

Further copies of this draft may be purchased from BSI Shop <http://shop.bsigroup.com> or from BSI Customer Services, Tel: +44(0) 20 8996 9001 or email cservices@bsigroup.com. British, International and foreign standards are also available from BSI Customer Services.

Information on the co-operating organizations represented on the committees referenced above may be obtained from <http://standardsdevelopment.bsigroup.com>

Responsible Committee Secretary: **Mr Roger G Tanfield (BSI)**Direct tel: **020 8996 7218**E-mail: roger.tanfield@bsigroup.com

Introduction

This draft standard is based on international discussions in which the UK has taken an active part. Your comments on this draft are welcome and will assist in the preparation of the consequent standard. There is a high probability that this text could be adopted by CENELEC as a reference document for harmonization or as a European Standard. Recipients of this draft are requested to comment on the text bearing in mind this possibility.

UK Vote

Please indicate whether you consider the UK should submit a negative (with reasons) or positive vote on this draft.

Submission of Comments

- The guidance given below is intended to ensure that all comments receive efficient and appropriate attention by the responsible BSI committee. **Annotated drafts are not acceptable and will be rejected.**
- All comments must be submitted, preferably electronically, to the Responsible Committee Secretary at the address given on the front cover. Comments should be compatible with version 6.0 or version 97 of Microsoft Word for Windows, if possible; otherwise comments in ASCII text format are acceptable. **Any comments not submitted electronically should still adhere to these format requirements.**
- All comments submitted should be presented as given in the example below. Further information on submitting comments and how to obtain a blank electronic version of a comment form are available from the BSI website at: <http://drafts.bsigroup.com/>

Template for comments and secretariat observations

Date: xx/xx/20xx	Document: ISO/DIS xxxx
------------------	------------------------

1	2	(3)	4	5	(6)	(7)
MB	Clause No./ Subclause No./Annex (e.g. 3.1)	Paragraph/ Figure/ Table/Note	Type of comment	Comment (justification for change) by the MB	Proposed change by the MB	Secretariat observations on each comment submitted
	3.1	Definition 1	ed	Definition is ambiguous and needs clarifying.	Amend to read '...so that the mains connector to which no connection...'	
	6.4	Paragraph 2	te	The use of the UV photometer as an alternative cannot be supported as serious problems have been encountered in its use in the UK.	Delete reference to UV photometer.	



21/901/CD

COMMITTEE DRAFT (CD)

IEC/TC or SC: 21	Project number IEC 62932-2-2 Ed.1	
Title of TC/SC: Secondary cells and batteries	Date of circulation 2016-09-23	Closing date for comments 2016-12-16
Also of interest to the following committees 21A	Supersedes document 21/870/CD + 21/888/CC	
Proposed horizontal standard <input type="checkbox"/> Other TC/SCs are requested to indicate their interest, if any, in this CD to the TC/SC secretary		
Functions concerned: <input checked="" type="checkbox"/> Safety <input type="checkbox"/> EMC <input type="checkbox"/> Environment <input type="checkbox"/> Quality assurance		
Secretary: Y. Boudou	THIS DOCUMENT IS STILL UNDER STUDY AND SUBJECT TO CHANGE. IT SHOULD NOT BE USED FOR REFERENCE PURPOSES. RECIPIENTS OF THIS DOCUMENT ARE INVITED TO SUBMIT, WITH THEIR COMMENTS, NOTIFICATION OF ANY RELEVANT PATENT RIGHTS OF WHICH THEY ARE AWARE AND TO PROVIDE SUPPORTING DOCUMENTATION.	

Title:

IEC 62932-2-2: Flow battery systems for stationary applications – Part 2-2: Safety requirements

(Titre) :

IEC 62932-2-2: Systèmes de batterie d'accumulateurs à circulation d'électrolyte pour applications stationnaires
Partie 2-2: Prescriptions de sécurité

Introductory note

Copyright © 2016 International Electrotechnical Commission, IEC. All rights reserved. It is permitted to download this electronic file, to make a copy and to print out the content for the sole purpose of preparing National Committee positions. You may not copy or "mirror" the file or printed version of the document, or any part of it, for any other purpose without permission in writing from IEC.

CONTENTS

1			
2			
3	FOREWORD		5
4	INTRODUCTION		7
5	1 Scope		8
6	2 Normative references		8
7	3 Terms and definitions		8
8	3.1 Equipment, components and parts	Error! Bookmark not defined.	
9	3.2 Battery characteristics	Error! Bookmark not defined.	
10	3.3 Safety related terms	Error! Bookmark not defined.	
11	3.4 Installation	Error! Bookmark not defined.	
12	3.5 Test.....	Error! Bookmark not defined.	
13	4 Procedure of the risk analysis		9
14	5 Safety requirements and protective measures		9
15	5.1 General		9
16	5.2 Risk information		9
17	5.3 Electrical hazards.....		9
18	5.3.1 Electrical shock.....		9
19	5.3.2 Short circuits.....		10
20	5.3.3 Leakage currents	Error! Bookmark not defined.	
21	5.4 Gas hazards.....		10
22	5.4.1 General.....		10
23	5.4.2 Combustible gas		11
24	5.4.3 Harmful gas		11
25	5.4.4 Ventilation.....		11
26	5.4.5 Warning sign.....		11
27	5.4.6 Method of ventilation (informative)		11
28	5.4.7 Close vicinity to emission		12
29	5.5 Fluid hazards		12
30	5.5.1 General.....		12
31	5.5.2 Sealing performance of the fluid.....	Error! Bookmark not defined.	
32	5.5.3 Detection of the leakage		12
33	5.5.4 Protective measures against leakage		12
34	5.5.5 Specific information		12
35	5.6 Hazards of mechanical origin		13
36	5.7 Operational hazards		13
37	5.7.1 General.....		13
38	5.7.2 Start.....		13
39	5.7.3 Emergency shutdown		13
40	5.7.4 Manual emergency stop		13
41	5.7.5 Remote monitoring and control systems		14
42	5.7.6 Protection		14
43	6 Installation		14
44	7 Identification labels or marking.....		14
45	7.1 Name plate information		14
46	7.2 Safety information		14
47	8 Transport, storage, disposal and environmental aspects		15
48	8.1 Packing and transport		15

49	8.2	Dismantling, disposal, and recycling	15
50	9	Inspection	15
51	10	Tests of verification for protective measurements	15
52	10.1	General	15
53	10.1.1	Scope	15
54	10.1.2	Test object	15
55	10.1.3	Test category	16
56	10.2	External short circuit of the stack	16
57	10.2.1	Requirements	16
58	10.2.2	Category	16
59	10.2.3	Number of sample	16
60	10.2.4	Test	16
61	10.2.5	Acceptance criteria	Error! Bookmark not defined.
62	10.3	Electrical strength of fluid systems	16
63	10.3.1	Requirements	16
64	10.3.2	Category	16
65	10.3.3	Number of samples	16
66	10.3.4	Test	16
67	10.3.5	Acceptance criteria	17
68	10.4	Heat shock strength	Error! Bookmark not defined.
69	10.4.1	Requirements	Error! Bookmark not defined.
70	10.4.2	Category	Error! Bookmark not defined.
71	10.4.3	Number of sample	Error! Bookmark not defined.
72	10.4.4	Test	Error! Bookmark not defined.
73	10.4.5	Acceptance criteria	Error! Bookmark not defined.
74	10.5	Leakage of the stack	Error! Bookmark not defined.
75	10.5.1	Requirements	Error! Bookmark not defined.
76	10.5.2	Category	Error! Bookmark not defined.
77	10.5.3	Number of samples	Error! Bookmark not defined.
78	10.5.4	Test	Error! Bookmark not defined.
79	10.5.5	Acceptance criteria	Error! Bookmark not defined.
80	10.6	Operational sequence	17
81	10.6.1	Requirements	17
82	10.6.2	Category	17
83	10.6.3	Number of sample	17
84	10.6.4	Test	17
85	10.6.5	Acceptance criteria	18
86	10.7	Manual emergency stop	18
87	10.7.1	Requirement	18
88	10.7.2	Category	18
89	10.7.3	Number of samples	18
90	10.7.4	Test	18
91	10.7.5	Acceptance criteria	18
92	10.8	Protection	18
93	10.8.1	Requirements	18
94	10.8.2	Category	18
95	10.8.3	Number of sample	18
96	10.8.4	Test	18
97	10.8.5	Acceptance criteria	18
98	Annex A (informative)	Recommended structure of user manual	19

99	A.1	General	19
100	A.2	Contents	19
101	A.3	Safety warning	19
102	A.4	Introduction	19
103	A.5	Product description	19
104	A.5.1	Overview	19
105	A.5.2	Technical specifications	19
106	A.5.3	System structure	19
107	A.5.4	Applications	19
108	A.5.5	Operational sequence	20
109	A.6	Site requirements	20
110	A.6.1	Location and load	20
111	A.6.2	Access and clearance	20
112	A.6.3	Precautionary measures for fluid containment	20
113	A.6.4	Ventilation.....	20
114	A.6.5	Temperature	20
115	A.7	Operation	20
116	A.7.1	Checks before operation	20
117	A.7.2	Energizing and de-energizing the system	20
118	A.7.3	Valve status	21
119	A.7.4	Specific operations	21
120	A.7.5	Notices for operation.....	21
121	A.8	Alarms and fault finding.....	21
122	A.9	Maintenance	21
123	A.10	Disposal.....	Error! Bookmark not defined.
124	A.11	Contact information	22
125	Bibliography		23
126			
127	Figure 1 – Flow Battery System.....		7
128	Figure 2 – Concept of the application points of the test voltage		17
129			

INTERNATIONAL ELECTROTECHNICAL COMMISSION

FLOW BATTERY SYSTEMS FOR STATIONARY APPLICATIONS –**Part 2-2: Safety requirements**

FOREWORD

- 1) The International Electrotechnical Commission (IEC) is a worldwide organization for standardization comprising all national electrotechnical committees (IEC National Committees). The object of IEC is to promote international co-operation on all questions concerning standardization in the electrical and electronic fields. To this end and in addition to other activities, IEC publishes International Standards, Technical Specifications, Technical Reports, Publicly Available Specifications (PAS) and Guides (hereafter referred to as "IEC Publication(s)"). Their preparation is entrusted to technical committees; any IEC National Committee interested in the subject dealt with may participate in this preparatory work. International, governmental and non-governmental organizations liaising with the IEC also participate in this preparation. IEC collaborates closely with the International Organization for Standardization (ISO) in accordance with conditions determined by agreement between the two organizations.
- 2) The formal decisions or agreements of IEC on technical matters express, as nearly as possible, an international consensus of opinion on the relevant subjects since each technical committee has representation from all interested IEC National Committees.
- 3) IEC Publications have the form of recommendations for international use and are accepted by IEC National Committees in that sense. While all reasonable efforts are made to ensure that the technical content of IEC Publications is accurate, IEC cannot be held responsible for the way in which they are used or for any misinterpretation by any end user.
- 4) In order to promote international uniformity, IEC National Committees undertake to apply IEC Publications transparently to the maximum extent possible in their national and regional publications. Any divergence between any IEC Publication and the corresponding national or regional publication shall be clearly indicated in the latter.
- 5) IEC itself does not provide any attestation of conformity. Independent certification bodies provide conformity assessment services and, in some areas, access to IEC marks of conformity. IEC is not responsible for any services carried out by independent certification bodies.
- 6) All users should ensure that they have the latest edition of this publication.
- 7) No liability shall attach to IEC or its directors, employees, servants or agents including individual experts and members of its technical committees and IEC National Committees for any personal injury, property damage or other damage of any nature whatsoever, whether direct or indirect, or for costs (including legal fees) and expenses arising out of the publication, use of, or reliance upon, this IEC Publication or any other IEC Publications.
- 8) Attention is drawn to the Normative references cited in this publication. Use of the referenced publications is indispensable for the correct application of this publication.
- 9) Attention is drawn to the possibility that some of the elements of this IEC Publication may be the subject of patent rights. IEC shall not be held responsible for identifying any or all such patent rights.

International Standard IEC 62932-2-2 Ed.1.0 has been prepared by the joint working group JWG 7: Flow Battery Systems for Stationary applications linked to TC 105, of IEC technical committee 21: Secondary cells and batteries

The text of this standard is based on the following documents:

FDIS	Report on voting
XX/XX/FDIS	XX/XX/RVD

Full information on the voting for the approval of this standard can be found in the report on voting indicated in the above table.

This publication has been drafted in accordance with the ISO/IEC Directives, Part 2.

The committee has decided that the contents of this publication will remain unchanged until the stability date indicated on the IEC web site under "<http://webstore.iec.ch>" in the data related to the specific publication. At this date, the publication will be

- reconfirmed,
- withdrawn,
- replaced by a revised edition, or

184 • amended.

185

186 The National Committees are requested to note that for this publication the stability date is 20XX.

187 THIS TEXT IS INCLUDED FOR THE INFORMATION OF THE NATIONAL COMMITTEES AND WILL BE DELETED AT THE
188 PUBLICATION STAGE.

189

INTRODUCTION

Flow battery can be utilized as a main part of energy storage systems (ESS). Such ESS can be consists of not only the flow battery but also other equipment and surroundings. This standard does not intend to include domain other than the flow battery, and then the scope of this standard is provided as shown in the Figure 1 below.

Auxiliary power to the BMS or the BSS may be supplied in both ways that they are directly connected to external power source or connected through the power conversion system.

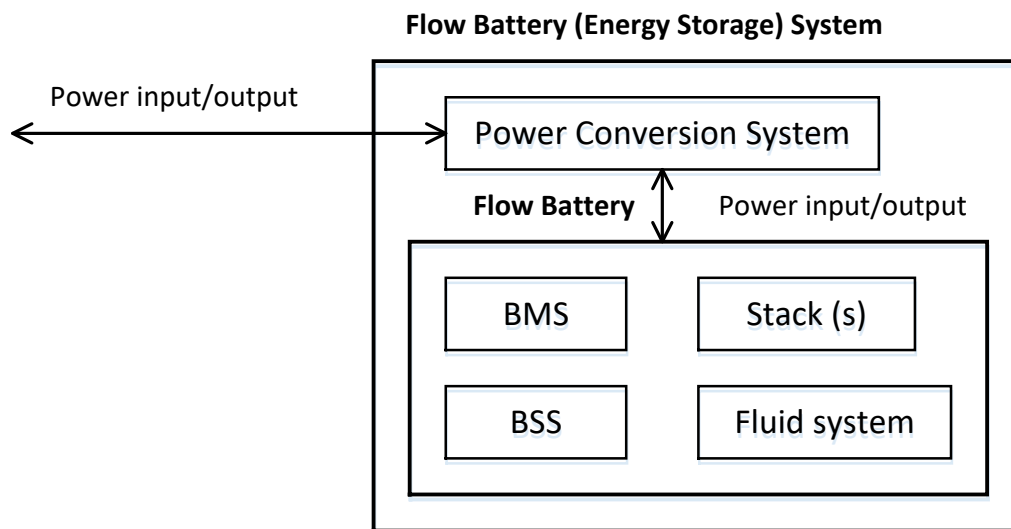


Figure 1 – Flow Battery System

FLOW BATTERY SYSTEMS FOR STATIONARY APPLICATIONS –

Part 2-2: Safety requirements

1 Scope

This part of IEC 62932-2-2 applies to flow battery systems for stationary use and its installations with a maximum voltage not exceeding DC 1 500 V in compliance with IEC 62932-1.

This International Standard defines the requirements and test methods for risk reduction and protection measures against significant hazards, relevant to the flow battery systems, to person, property and the environment, or to a combination of them.

This International Standard is applicable to stationary flow battery systems intended for indoor and outdoor commercial and industrial use in non-hazardous (unclassified) areas.

This standard contemplates significant hazards, hazardous situations and events, with the exception of those associated with natural disaster, relevant to the flow battery systems, when they are used as intended and under the conditions foreseen by the manufacturer including reasonably foreseeable misuse thereof.

The requirements of this International Standard are not intended to constrain innovations. When considering fluid, materials, designs or constructions not specifically dealt with in this International Standard, these alternatives shall be evaluated as to their ability to yield levels of safety equivalent to those prescribed by this International Standard.

2 Normative references

The following documents, in whole or in part, are normatively referenced in this document and are indispensable for its application. For dated references, only the edition cited applies. For undated references, the latest edition of the referenced document (including any amendments) applies.

IEC 60079-10-1:2015, Explosive atmospheres – Part 10-1: Classification of areas – Explosive gas atmospheres

IEC 60364-4-41, Low-voltage electrical installations – Part 4-41: Protection for safety – Protection against electric shock

IEC 60364-4-43, Low-voltage electrical installations – Part 4-43: Protection for safety – Protection against overcurrent

IEC 60812, Analysis techniques for system reliability – Procedure for failure mode and effects analysis (FMEA)

IEC 61025, Fault tree analysis (FTA)

IEC 62485-2:2010, Safety requirements for secondary batteries and battery installations – Part 2: Stationary batteries

IEC 62932-1, Flow battery systems for stationary applications – Part 1: General aspects, terminology and definitions

IEC 62932-2-1, Flow battery systems for stationary applications – Part 2-1: Performance general requirement and method of test

ISO 13850, Safety of machinery – Emergency stop – Principles for design

3 Terms and definitions

For the purposes of this document, the terms and definitions given in IEC 62932-1.

246 **4 Procedure of the risk analysis**

247 A written risk analysis shall be performed to ensure that:

- 248 a) all reasonably foreseeable hazards, hazardous situations and events including reasonably
249 foreseeable misuse throughout the anticipated flow batteries' lifetime have been identified;
- 250 b) the risk for each of these hazards has been estimated from the combination of probability of the
251 occurrence of the hazard and of its foreseeable severity;
- 252 c) the two factors which determine each one of the estimated risks (probability and severity) have been
253 eliminated or reduced to a level not exceeding the acceptable risk level as far as reasonably
254 possible the following principles in the order given:
- 255 – eliminate hazards or reduce risks by inherent design measures;
 - 256 – take the necessary protective measures in relation to risks that cannot be reduced by inherent
257 design and measures;
 - 258 – inform intended users and where appropriate other persons of the residual risks, indicate whether
259 any particular training is required and specify any need to use personal protective equipment.

260 For example failure mode and effects analysis (FMEA), fault tree analysis methods (FTA), hazard and
261 operability study (HAZOP) and the following standards could be used as guidance:

- 262 • IEC 60812;
- 263 • IEC 61025.

264 **5 Safety requirements and protective measures**

265 **5.1 General**

266 Each secondary battery has a “different” structure and therefore only the features specific to a flow
267 battery shall evoked. As the flow battery includes equipment or systems for fluid flow, appropriate
268 protective measures on those portions are necessary. For example, the functional safety requirements
269 of the pumps which are normally used to circulate fluids need to be considered as an integral part of the
270 whole system, along with operational coordination with other functions such as power electronic
271 converter systems.

272 From a chemical safety point of view, since all the volume of fluid is stored in tanks, pipes and stacks,
273 the sealing of the system storing and transporting fluid is an important factor. There is the possibility of
274 generation of hazardous gases and appropriate counter measures are required.

275 This clause specifies the safety requirements and protective measures in consideration with the aspects
276 above.

277 **5.2 Risk information**

278 It is recommended taking appropriate measurements to minimize the potential risk of danger, when
279 designing the flow battery system. The manufacturer shall provide the user with risk information based
280 on the risk analysis to describe hazards and the appropriate measures taken or to be taken to mitigate
281 them.

282 The information shall include a safety data sheet (SDS).

283 The information can be provided in a form of a user manual. The recommended structure of the user
284 manual is contained in Annex A.

285 **5.3 Electrical hazards**

286 **5.3.1 Electrical shock**

287 The flow battery system is an electrical energy storage device, and contains hazardous live parts of DC
288 and/or AC voltage which can cause the risk of electrical shock.

289 In general, secondary batteries retain their electrical charge, even when the power to the batteries is
290 disconnected. In case of the flow battery system, the voltage of the stacks can retained after
291 disconnection of the electrical power. Flow batteries are electrical energy source as long as fluid on the
292 electrode is present in the stacks. If the fluids are retained energy inside the stacks is discharged, the
293 retained electrical charge inside the stacks can be reduced. If such measures are not applied,

294 appropriate protection shall be taken instead. The potential live components shall be with properly
295 insulating measurements. In order to enhance the safety of flow battery, it is recommended to install
296 the grounding components according to the relevant standards require. For protection against electrical
297 shock, the protection schemes outlined in IEC 60364-4-41 shall be applied to the flow battery system.

298 **5.3.2 Short circuits**

299 The electrical energy stored in the flow battery system can be released in an inadvertent and
300 uncontrolled manner due to short circuiting the terminals. Because the considerable energy and hence
301 high current, heat generated can melt metal, produce sparks, cause explosion or vaporize fluid.

302 In order to avoid short circuits, all battery connections up to the battery fuse shall be installed in such a
303 way that a short circuit does not occur under any foreseeable conditions. For the type of conductor
304 arrangement of unprotected conductor sections, IEC 60364-4-43 shall be taken in consideration.

- 305 – As for protection measures, the flow battery system shall mitigate a short circuit fault which occurs
306 outside stacks.stopping the supply of fluids to the flow battery cells, and/or
- 307 – interrupting the short circuit current path.

308 The intrinsic safety of the stack to short-circuit conditions should be verified tested according to 10.2.

309 **5.3.3 Ground Faults**

310 Ground faults in flow batteries are, due the large amount of fluid and fluid handling parts (pumps, pipes,
311 stacks, tanks) a particular problem and the public shall be particularly well informed in this
312 matter.Ground faults can cause the following significant risks.

- 313 – electrocution when a person makes contact with fluid leaking from piping, cells and/or other
314 components of the fluid system

315 Note 1 to entry: In this case person's body becomes a part of circuit of the leakage current.

- 316 – arcs and fire when circuit of the leakage current is established by the fluid leaking from piping, cells
317 and/or other components of the fluid system

318 Note 1 to entry: The criticality of this risk depends on electrical conductivity of the fluid. If the fluid has low electrical
319 conductivity, leakage current becomes small and severity of the risk also becomes low.

320 The circuit of the flow battery system including fluids shall be properly insulated from other local
321 conductive parts and the ground. A high impedance grounding can be permitted, when the maximum
322 current that could flow through a human is limited to a safe level (below 10 mA). Therefore, the
323 resistance to ground should numerically be greater than the magnitude of the maximum dc voltage that
324 could exist between ground and the energised part divided by 10 mA.

325 The insulation shall be verified in accordance with the test method in 10.3.

326 Protective devices for detecting grounding faults shall be provided in the flow battery system or in the
327 external system such as a power electronic converter system to take account of a malfunction in the
328 insulation.

329 **5.4 Gas hazards**

330 **5.4.1 General**

331 Some flow batteries uses aqueous solution as fluids. Such system can generate combustible gas such
332 as hydrogen gas which is secondarily generated during operation in the process of electrolysis of water.
333 The flow batteries can also generate harmful gases depending on components of the fluids.

334 In general, the gases are produced in the stack and accumulated in the system. For example, in case of
335 the flow battery system which uses the electrolyte as the fluid, the gas is accumulated in the top portion
336 of the tanks.

337 Since the principles of the gas generation and stored portion of the gases depend on the characteristics
338 and system construction of the individual flow battery system, the gas hazards caused in the individual
339 system can cause different level of the risks.

340 Taking the hydrogen gas as an example, as the flow battery is charged above the rated voltage range
341 the generation rate of hydrogen becomes higher. The correlation between the charging voltage and the
342 gas generation cannot be expressed by a common equation, because the gas generation rate depends
343 highly on the characteristics of cell components and fluids which can vary between manufacturers.

344 The flow battery shall consider the gas emission/elimination measurements/equipments in designing
345 process. It is recommended to install the dangerous gas alarm equipments in need. Suitable interlocks
346 are provided if the dangerous gas alarm happens. This standard defines the general measurements to
347 reduce the risk of the gas hazards.

348 **5.4.2 Combustible gas**

349 The risk level of the combustible gas becomes higher, if the following hazards coincide.

- 350 – generation and accumulation of the combustible gas,
- 351 – mixture with oxygen,
- 352 – existence of ignition sources.

353 The flow battery system shall have protective measures against the hazards above such as, but not
354 limited to

- 355 – eliminate generation of the combustible gas,
- 356 – dilution of the combustible gas,
- 357 – impermeability of oxygen,
- 358 – elimination of ignition sources.

359 **5.4.3 Harmful gas**

360 The risk level of the combustible gas becomes higher, if the following hazards coincide.

- 361 – generation and accumulation of the harmful gas,
- 362 – human access to the vicinity of the harmful gas.

363 The flow battery system shall have protective measures against the hazards above such as, but not
364 limited to

- 365 – eliminate generation of the harmful gas,
- 366 – dilution of the harmful gas,
- 367 – collection of the harmful gas by a scrubber,
- 368 – limitation of human access.

369 **5.4.4 Ventilation**

370 The manufacturer shall inform users of the ventilation requirements, if necessary, for an indoor
371 installation of the flow battery system.

372 Reference should be made to the theoretical minimum ventilation flow rate to dilute the gases which is
373 given in IEC 60079-10-1:2015 Clause B.5

374 **5.4.5 Warning sign**

375 Appropriate warning signs which prohibit sparks, smoking, open flame and electrostatic discharges shall
376 be placed at the entrance of hazardous area considering classification of area defined in IEC 60079-10-
377 1:2015 Clause B.7.

378 **5.4.6 Method of ventilation (informative)**

379 **5.4.6.1 Classification of ventilation methods**

380 To meet the ventilation requirement, ventilation should be provided by either or a combination of the
381 following methods:

- 382 – natural ventilation;
- 383 – forced ventilation through room or enclosure.

384 **5.4.6.2 Natural ventilation**

385 When natural ventilation is used, battery rooms or enclosures should be equipped with an inlet and an
386 air outlet with a minimum free opening area which meets the ventilation requirements.

387 5.4.6.3 Forced ventilation

388 When forced ventilation is used, gases which are emitted from the flow battery system to the room or
389 enclosure, are extracted to the exterior atmosphere using a ventilation system, which may combine an
390 opening and fan, and will exhaust a mixture of air and the emitted gases.

391 5.4.7 Close vicinity to emission

392 The dilution of gases is not always assured in the close vicinity of the exhaust of released gases or at
393 the outlet of direct forced ventilation; therefore a safety distance from the outlet shall be observed. The
394 dispersion of gases depends on the gas emission rate and the type of ventilation close to the source of
395 emission.

396 5.5 Fluid hazards**397 5.5.1 General**

398 A typical aqueous liquid fluid used in the flow battery system can contain acid or alkali in water, and
399 these agents can cause hazard to people and the environment.

400 Non aqueous fluids used in some types of the flow battery system can have similar caustic or corrosive
401 properties.

402 Since the fluids are flowing through the fluid system, there is a possibility that the leakage of the fluid
403 could expand if the detection of the leakage and/or protection against the leakage are inappropriate.
404 And fluids supplied to the stacks are stored in the common tank in large volume. This clause defines the
405 basic measurements against such hazards.

406 Measures are made in such manners.

- 407 – ensuring the sealing performance of the fluid system,
- 408 – designing and manufacturing materials used in parts containing the fluid taking account on
409 deterioration from contact with the fluid,
- 410 – detecting leakage and appropriate measures,
- 411 – protecting leakage to the surroundings,
- 412 – providing information and marking about the fluid.

413 5.5.2 Detection of the electrolyte leakage

414 Leakage shall be detected by an appropriate protection device such as a leakage sensor. The detection
415 and protective functions shall be verified appropriately. The verification method shall be in accordance
416 with 10.8.

417 The detection of the fluid shall initiate the necessary operation to avoid the increase of leakage, such as
418 stopping the pumps.

419 5.5.3 Protective measures against leakage

420 The Flow battery system shall be equipped with a protective structure against fluid leakage such as, but
421 not limited to

- 422 – A moulded plastic tray,
- 423 – welded and coated metal containers,
- 424 – formed and sealed barriers.
- 425 – Containers with acid resistant layer

426 Otherwise, the flow battery system shall be installed in such place as where alternative protection
427 against leakage is provided.

428 5.5.4 Specific information

429 The manufacturer shall provide the information of the fluids which details

- 430 – the primary emergency measures that shall be taken if there is exposure to fluids,
- 431 – personal protective equipment.

432 The use of synthetic clothing which can cause electrostatic discharge is not recommended in a
433 hazardous area where explosive gas is present. Personal protective equipment should include flame
434 retardant and anti-static clothing. Flow path identification.

435 Most flow batteries operate with two distinct fluids in which the electrochemically active species are
436 either dissolved, suspended or present as gas.

437 Each of the fluids may require particular attention and methods of containment in case of spillage or
438 maintenance.

439 To reduce the risk of hazards during intervention on the fluid system, all the fluid pipes shall be clearly
440 identified with the name of positive fluid or negative fluid written in two distinct colours on the tanks and
441 pipes together with an arrow indicating the flow direction in the concerned pipes. The symbols “+” as
442 positive, “-“ as negative are also available for identification marking.

443 **5.6 Hazards of mechanical origin**

444 The flow battery is a complex assembly of electricity and fluid-carrying components housing large
445 volumes of chemicals.

446 All these structural components shall be properly dimensioned and tested taking in consideration
447 thermal and mechanical stresses, material aging processes and extreme conditions of temperature and
448 pressure.

449 Particular attention shall be placed also on the fact that the fluid are chemically aggressive and can
450 cause an accelerated loss of mechanical stability and cross-section loss.

451 **5.7 Operational hazards**

452 **5.7.1 General**

453 When the flow battery is designed to work with other equipment upstream and/or downstream a signal
454 interface or other means shall be provided to enable coordinated operation such as start, stop,
455 emergency shutdown, charge and discharge. Improper integration can cause unintentional operation
456 which can lead to risks.

457 Proper coordinated operation shall be confirmed by appropriate methods. The verification method may
458 be in accordance with 10.6 and 10.7.

459 **5.7.2 Start**

460 A starting operation is achieved through ensuring that:

- 461 – It is possible only when all the safeguards are in place and are functional;
- 462 – it is possible for automated flow battery system to be restarted after a stoppage only after the safety
463 conditions have been fulfilled;
- 464 – it is possible to restart the flow battery system by intentional actuation of a control provided for the
465 purpose, provided such restarting is verifiable as being non-hazardous.
- 466 – It is confirmed that suitable interlocks are provided for correct sequential starting;

467

468 **5.7.3 Emergency shutdown**

469 rapid shutdown of the flow battery system triggered by a protection system or by manual intervention

470 [SOURCE: IEC 60050-415: 1999, 415-01-11]

471 **5.7.4 Emergency stop**

472 function that is intended to

473

- 474 - avert arising, or reduce existing hazards to persons, damage to machinery or to work in progress,
- 475 - be initiated by a single human action

476 [SOURCE: ISO 13850:2006, 3.1]

Licensed copy: Care Segreteria - PADOVA, CRUI Conferenza dei Rettori delle, Version correct as of 10/10/2018

477 **5.7.5 Remote monitoring and control systems**

478 A system that can be operated remotely shall have a local, labelled switch or other means to disconnect
479 the system from remote signals that may be used while a local operator performs inspection or
480 maintenance. Remote monitoring system implementation should be considered in order to check if the
481 system is operating safely. The data provided automatically by the EES or through an EES system
482 inquiry can help to evaluate its state of health and the remaining life of its 1361 components. Diagnosis
483 is performed by monitoring change of capacity or changes in 1362 evolution of measured parameters.
484 These data can be transmitted through an information 1363 network in timely manner. Cyber security is
485 important not only for remote monitoring but also for the system connected to the internet. Refer to IEC
486 62351 for additional guidance.

487 **5.7.6 Protection**

488 The flow battery system shall be equipped with suitable protective devices to detect abnormal situations
489 and initiate emergency stop. The protective devices should detect, at least, over-current, over-voltage,
490 under-voltage, over-charge, ground fault, fluid leakage, over-temperature, under-temperature, over-
491 pressure of the fluids, under-pressure of the fluids and loss of control power.

492 The optional test to verify such protective functions may be in accordance with 10.8.

493 **5.7.7 Protection**

494 The flow battery system shall be equipped with suitable protective devices to detect abnormal situations
495 and initiate emergency stop. The protective devices should detect, at least, over-

496 **6 Installation**

497 The battery and its subsystems shall be installed according to the manufacturer's instructions.

498 The instructions provided by the manufacturers shall cover the layout schematics; the required building
499 materials and the installation and start-up instructions.

500 **7 Identification labels or marking**

501 **7.1 Name plate information**

502 The name plate/label(s) shall include the following information:

- 503 a) manufacturer's name;
- 504 b) manufacturer's or supplier's type reference;
- 505 c) serial number;
- 506 d) date and place of manufacture;
- 507 e) maximum AC or/and DC voltage in operation (V);
- 508 f) maximum AC or/and DC power in operation (kW);
- 509 g) maximum AC or/and DC current in operation (A);
- 510 h) rated energy (kWh);
- 511 i) transport weight (kg);
- 512 j) chemical type of battery (e.g. VRB, FeCr, ZnBr, HBr and so on)
- 513 k) Volume amount of hazardous material

514 **7.2 Safety information**

515 Warnings for alerting personnel to the potential for personal injury or equipment damage shall be
516 adequately marked on the constituents.

517 Follow national regulations for marking and labelling dangerous materials. In case there is none: All of
518 the relevant warning labels or markings shall be made in durable material and be affixed on multiple
519 locations on the battery so that a person approaching the battery from any directions could clearly
520 notice them. Pictograms are preferred over text.

521 **8 Transport, storage, disposal and environmental aspects**

522 **8.1 Packing and transport**

523 Various national and international regulations cover the packing and transport of the flow battery system
524 and these take into account the dangers of accidental short circuits, heavy mass and spillages of fluid.

525 For short-circuit protection, the fluids shall be emptied out of the stacks.

526 **8.2 Dismantling, disposal, and recycling**

527 Dismantling and disposal of the flow battery system shall be undertaken by competent and trained
528 personnel. The relevant national and international regulations shall be followed.

529

530 **9 Inspection**

531 A regular inspection of the flow battery system and its operation environment is required for functional
532 and safety reasons.

533 The inspection shall be conducted in accordance with the manufacturer's requirements, which should
534 include a check of

- 535 – The appearance of the equipment, for example any signs of physical damage such as dents or
536 physical damage or corrosion;
- 537 – leaks from stacks, pipes, valves, pumps and tanks;
- 538 – abnormal noise, vibration and odour from the equipment, especially from power electronic
539 equipment and machines such as pumps and fans.

540 **10 Tests of verification for protective measurements**

541 **10.1 General**

542 **10.1.1 Scope**

543 This clause specifies methods and criteria of the tests which may be applied to verify some of the
544 requirements in 5. The list of tests are summerized in Table 1.

545 Table 1 – List of tests of verification for protective measurements

Test	Test Category	Test Object	Sample Number
external short circuit	type test	stacks	1
electrical strength of fluid systems	routine test	system	whole system
operational sequence	routine test	system	whole system
emergency stop	routine test	system	whole system
protetion	routine test	system	shole system

546

547 **10.1.2 Test object**

548 Possible test objects can be

- 549 – component of the flow battery system,
- 550 – sub-system,
- 551 – whole system.

552 **10.1.3 Test category**

553 The following categories are applied:

- 554 – type test as defined in 3.5.3;
- 555 – sampling test as defined in 3.5.2;
- 556 – routine test as defined in 3.5.1.

557 **10.2 External short circuit of the stack**

558 **10.2.1 Requirements**

559 An external short circuit of the stack shall not cause fire, explosion or electrolyte leakage.

560 **10.2.2 Category**

561 This test is classified to type test.

562 **10.2.3 Number of sample**

563 One (1) sample shall be subject to this test.

564 **10.2.4 Test**

565 This test shall be conducted under the following conditions.

566 Note 1 to entry: This test can be destructive and that it has to be carried out in a suitable test facility under the supervision of
567 qualified persons.

- 568 a) ambient temperature in the range 20 °C to 25 °C;
- 569 b) the sample of the stack is placed in the system designated to this test;
- 570 c) fluids are fully charged;
- 571 d) the sample is short-circuited by connecting the positive and negative terminals of the sample with a
572 resistive circuit load having a total external resistance of less than or equal to 20 mΩ until 1)
573 completely discharged, 2) operation of an integral protective devices, 3) other results, in order to
574 check the operation of an integral protective devices or other results. In more practical case, stacks
575 will not fully discharged, but other protective device such as fuse cuts the short-circuit current path.

576 **10.2.5 Acceptance criteria**

577 The test is passed if there is no fire or explosion.

578

579 **10.3 Electrical strength of fluid systems**

580 **10.3.1 Requirements**

581 Fluid circulation systems including tanks and stacks have sufficient electrical resistance to avoid an
582 earth grounding fault in the EES system that d.c. circuit is not earthed..

583 **10.3.2 Category**

584 This test is classified as a routine test.

585 **10.3.3 Number of samples**

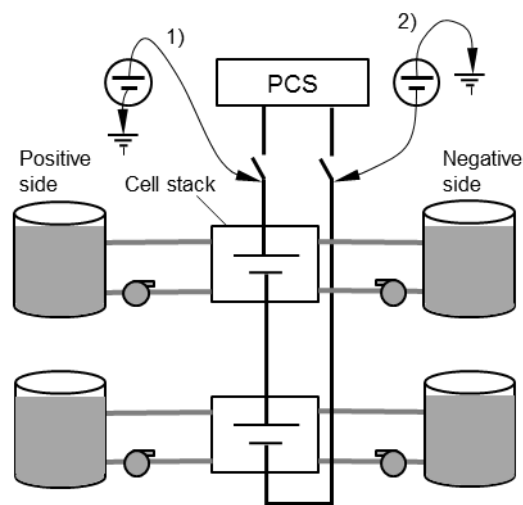
586 Each whole system shall be subjected to this test.

587 **10.3.4 Test**

588 This test shall be conducted under the following conditions.

- 589 a) the ambient temperature shall be maintained in manufacturer's specified rated temperature range;
- 590 b) The fluids' temperatures shall be maintained in the manufacturer's specified rated temperature
591 range;
- 592 c) The insulation resistance between the d.c. circuit, including fluid system and the ground, shall be
593 measured with a mega Ohmmeter of not less than 500V. The measured value after 1 minute is
594 recorded;
- 595 d) the test voltage shall be 1,5 times the manufacturer's specified maximum d.c. voltage.;

- 596 e) the voltage shall be raised gradually from zero to the prescribed voltage and held at that value for
597 10 minutes;
- 598 f) the application points for the test voltage shall be shown schematically in Figure 2. The actual
599 application points shall be determined as based on the actual construction of the sample system;
600 Note 1 to entry: The test voltage is applied to the fluid system through the stacks.
- 601 g) the test shall be conducted two times with a positive voltage applied to the positive terminal and
602 negative voltage applied to the negative terminal as shown in Figure 2;
603 Note 1 to entry: Applied voltage at the other side is reduced by the total voltage of the stacks. For example, given that the
604 total voltage of the stacks is 700V and the test voltage of 1 050 V is applied at the positive terminal, the applied
605 voltage at the negative terminal becomes 350 V. In this case, it is specified that the test is to be conducted two
606 times as specified above.
- 607 h) In the interests of safety, special care shall be taken so that positive voltage should not be applied
608 at the negative terminal or negative voltage should not be applied at the positive terminal. Whatever
609 voltage, either positive or negative, is applied at the terminal of the other polarity, the voltage at the
610 other pole exceeds the test voltage. An a.c. voltage also should not be applied since peak voltage at
611 both terminals exceeds the test voltage.
- 612 i) insulation resistance with ground shall be measured again;



613 **Figure 2 – Concept of the application points of the test voltage**

614 10.3.5 Acceptance criteria

615 As a result of this test, there shall be no significant drop in the insulation resistance.

617 10.4 Operational sequence

618 10.4.1 Requirements

619 The flow battery system shall be coordinated with the power electronic converter system to change its
620 operation mode between charging or discharging safely.

621 10.4.2 Category

622 This test is classified as a routine test.

623 10.4.3 Number of sample

624 All the whole systems shall be subjected to this test.

625 10.4.4 Test

626 This test shall be conducted under the following conditions whereby operating modes are changed as
627 follows.

- 628 a) Stop to charge and vice versa;
629 b) Stop to discharge and vice versa;
630 c) Charge to discharge and vice versa;

631 d) Charge to the end of charge;

632 e) Discharge to the end of discharge.

633 Note 1 to entry: Charge and discharge in the procedure of d) and e) shall be terminated by the charge termination condition or
634 discharge termination condition respectively.

635 **10.4.5 Acceptance criteria**

636 The sample system shall transfer operation modes safely. Main components such as circuit-breaker,
637 pumps, valves, indicating lamp and metering shall work according to the design.

638 **10.5 Emergency stop**

639 **10.5.1 Requirement**

640 The emergency stop shall work safely according to the system design.

641 **10.5.2 Category**

642 This test is classified as a routine test.

643 **10.5.3 Number of samples**

644 All whole systems shall be subjected to this test.

645 **10.5.4 Test**

646 This test shall be conducted under the following conditions:

- 647 a) the sample system is either charging or discharging;
- 648 b) emergency stop is initiated;

649 **10.5.5 Acceptance criteria**

650 The sample system shall completely stop safely when the manual emergency stop is used.

651 **10.6 Protection**

652 **10.6.1 Requirements**

653 Protection devices shall initiate the emergency shutdown procedure when fault conditions occur.

654 The flow battery system shall completely stop safely when fault conditions occur which initiate the
655 emergency shutdown procedure.

656 **10.6.2 Category**

657 This test is classified as a routine test.

658 **10.6.3 Number of sample**

659 All whole systems shall be subjected to this test.

660 **10.6.4 Test**

661 This test shall be conducted under the following conditions:

- 662 a) Actual faults or mimic faults shall initiate protection devices.
- 663 b) Emergency shutdown by following faults shall be confirmed.
 - 664 – grid faults such as over voltage, under voltage, over frequency, under frequency;
 - 665 – EES system faults such as over voltage, under voltage, over current, over temperature, under
666 temperature, over pressure, grand faults, fluid leak, control power down, and so on

667 **10.6.5 Acceptance criteria**

668 The flow battery system shall completely stop in a safe mode when the emergency shutdown procedure
669 is initiated by an actual or mimicked faults. .

670

Annex A (informative)

Recommended structure of user manual

A.1 General

The user manual is an important document that is designed to provide the user with all relevant information about the system.

This annex recommends the structure of the user manual which can contain chapters (sections) that address specifications, installation, site preparation, operating instructions, safety guidelines, fault finding and emergency procedure. The manual should be in a comprehensive format that includes illustrations, pictures and references to engineering drawings where appropriate.

This annex is not intended to constrain alternative structures for user manuals. This annex can be used to check whether the user manual includes contents which can be generally regarded to be necessary..

The clauses from A.2 to A.13 are the recommended structure and contents.

A.2 Contents

Contents and page numbers are shown in this chapter.

A.3 Safety warning

The manufacturer provides a summary of potential safety risks for the flow battery so that users/operators are aware of the importance of this section of the manual, and have a good understanding of all safety instructions prior to operating the system.

This chapter includes precautionary statements about restriction of access to the system, such that only trained and qualified personnel may access to the system.

Although a safety warning is comprehensively provided in this subsection, independent precautions are also provided to remind users of specific safety matters in the corresponding parts of the manual.

A.4 Introduction

This chapter provides a general introduction and an overview of the manual. It includes the purpose and structure of the manual.

A.5 Product description

A.5.1 Overview

This sub-chapter provides a general and brief description of the flow battery system to help in understanding the user manual.

A.5.2 Technical specifications

This sub-chapter includes details of parameters and additionally the physical dimensions, and weight, environmental transport and operating conditions and control & monitoring features.

A.5.3 System structure

This sub-chapter shows configuration of the flow battery system with illustration or drawings including electrical diagrams, piping diagrams, physical dimensions and the like.

Relevant documents and drawings of each component can be also provided as attachments.

A.5.4 Applications

This sub-chapter describes applications of the flow battery system. It can include a summary of the control principles of those applications.

712 **A.5.5 Operational sequence**

713 The operational sequence of both normal and abnormal operation (e.g. emergency shutdown) is shown
714 here. For example, it includes start, stop, charging or discharging operational sequences.

715 The information provided clarifies conditions at each step of the operational sequence such as, but not
716 limited to, breaker ON/OFF, pump ON/OFF, erroneous conditions or other mandatory conditions to
717 proceed with the sequence further.

718 **A.6 Site requirements**

719 **A.6.1 Location and load**

720 The floor loading requirements for the battery installation are stated in this sub-chapter including any
721 additional loads that occur during installation, for example cranes or fork lift trucks.

722 Any requirements for the provision of slope conditions of floors, or secondary containment walls are
723 also included.

724 If necessary, adequate descriptions and layout diagrams for positioning tanks and other equipment and
725 requirements for mounting and fixing are stated.

726 The conditions for fixing and installing cubicles for stacks, pumps, pipework and tanks, if applicable, are
727 also included.

728 **A.6.2 Access and clearance**

729 Specific space requirements are suggested in this sub-chapter to take into account safety and
730 installation, maintenance and cleaning,.

731 **A.6.3 Precautionary measures for fluid containment**

732 The manual provides instructions for protective measures against any potential leaks, spillage caused
733 by system failure or external events taking into account the corrosive, toxic or caustic nature of the
734 fluids.

735 **A.6.4 Ventilation**

736 Flow batteries can generate gases (such as hydrogen, chloride) or vapours (such as bromine) or
737 aerosols (fluid) during operation. Requirements for ventilation as a result of normal or abnormal
738 operation are provided in this sub-chapter.

739 **A.6.5 Temperature**

740 The safety, performance and life of flow batteries are temperature dependent. The suitable temperature
741 range for operation, transport and storage are stated here.

742 **A.7 Operation**

743 This chapter provides in full detail instructions for system start up, shut down, normal operations, as
744 well as how to deal with system alarms if applicable. It includes the following sub-chapter to make it
745 comprehensive.

746 **A.7.1 Checks before operation**

747 This sub-chapter describes check items to be confirmed before operation, such as receiving electrical
748 power.

749 **A.7.2 Energizing and de-energizing the system**

750 This sub-chapter describes procedures of energizing and de-energizing the flow battery system with
751 relevant pictures or diagrams for visual explanation.

752 The procedures include, but are not limited to, identification of circuit breakers to be switched on or off,
753 the order of switching on or off of the circuit breakers and indicator status such as lamps on / off.

754 The flow battery system can consist of several sets of equipment, and the procedures should provide a
755 clear and comprehensive order of energizing or de-energizing the equipment, such as identification of
756 the equipment to be energized first.

757 A.7.3 Valve status

758 The normal status of all the valves, such as open or closed, is shown in this sub-chapter.

759 A.7.4 Specific operations

760 This sub-chapter gives guidance to the user to start or stop specific operations such as scheduled peak-cutting, stabilizing renewable energy etc.

762 The procedures include, but are not limited to, control of human machine interfaces, such as BMS or
763 other equipment, setting parameter and indicator status, in such a way that a clear comprehensive order
764 is provided.

765 The operating procedure for remotely operating the system or data acquisition system, if any, is also
766 provided here.

767 A.7.5 Notices for operation

768 Specific recommendations from the manufacturer such as the effect of depth of discharge versus life
769 time, operations at low temperature or high temperature, if necessary, are provided in this subsection.

770 A.8 Alarms and fault finding

771 This chapter provides explanations and the actions/measures to be taken for all alarms of the system.

772 It can include corrective actions for each abnormal situation with protective measures to be taken prior
773 to any fault-finding activities.

774 A.9 Maintenance

775 This chapter describes the maintenance plan and procedures. Since the flow battery system consists of
776 various equipment and components, a comprehensive maintenance plan is described here.

777 The maintenance plan clarifies items, procedures and intervals and can be resulted in such categories
778 as:

- 779 – periodical maintenance such as daily, weekly and monthly inspections;
- 780 – replacement of parts;
- 781 – overhaul of equipment.

782 During maintenance operation people may work close to the battery system. Personnel involved in work
783 on or close to a battery shall be competent to carry out such work, and shall be trained in any special
784 procedures necessary. To minimise the risk of injury, the battery system shall be designed with battery
785 terminal covers which allow routine maintenance whilst minimising exposure of live parts;

- 786 - a minimum distance of 1,50 m between simultaneously touchable conductive live parts of the battery
787 having a potential exceeding DC 120 V (nominal voltage);
- 788 - devices to disconnect the battery into groups of less than DC 1500 V when operating batteries with
789 nominal voltages above DC 1500 V;
- 790 - fuse carriers which prevent contact with live parts.

791 All metallic personal objects shall be removed from the hands, wrists and neck before starting

792 work. For battery systems where the nominal voltage is more than DC 120 V, insulated protective
793 clothing and local insulated coverings will be required to prevent personnel making contact with the floor
794 or parts bonded to earth.

795 Batteries shall be neither connected nor disconnected when current is flowing. Isolate the circuit
796 elsewhere first.

797 Note 1 to entry: Back feeds from chargers or parallel batteries may cause the accessible contacts to be live when the
798 fuse is removed. Where screw type fuses are used, the battery output terminals shall be connected to the bottom
799 contact. Screw type fuses are not recommended where both terminals remain live after the fuse is removed, e.g.
800 within parallel battery systems. Batteries can be equipped with flame arrestor vent plugs (see IEC 60050-486-02-
801 28) to avoid internal explosions caused by external naked flame or spark.

802 Note 2 to entry: EN 60900 is a recommended standard

803 Note 3 to entry: For maintenance purposes, batteries having a nominal voltage above DC 120 V should be divided into
804 sections consisting of DC 120 V (nominal) or less.

805 **A.10 Contact information**

806 This chapter provides manufacturer's contact details including the company's name, website, hotline,
807 service telephone number, fax and email to allow customers to receive information or request help when
808 needed. Supplementary information, such as declarations or explanations of licenses, patents and
809 similar information is also included in this chapter.

810

811 Bibliography

812

813 IEC 60364-5-53, Electrical installations of buildings – Part 5-54: Selection and erection of electrical
814 equipment – Isolation, switching and control

815 IEC 60529, Degrees of protection provided by enclosures (IP Code)

816 IEC 60664-1, Insulation coordination for equipment within low-voltage systems – Part 1: Principles,
817 requirements and tests

818 IEC 60721-3-2, Classification of environmental conditions – Part 3: Classification of groups of
819 environmental parameters and their severities – Section 2: Transportation

820 IEC 61000 series, Electromagnetic compatibility (EMC)

821 IEC 61660-1, Short-circuit currents in d.c. auxiliary installations in power plants and substations – Part
822 1: Calculation of short-circuit currents

823 IEC 61660-2, Short-circuit currents in d.c. auxiliary installations in power plants and substations – Part
824 2: Calculation of effects

825 IEC 62477-1, Safety requirements for power electronic converter systems and equipment – Part 1:
826 General

827 IEC 62282-3-100, Fuel cell technologies – Part 3-100: Stationary fuel cell power systems –Safety

828 IEC 62282-3-300, Fuel cell technologies – Part 3-300: Stationary fuel cell power systems –Installation

829 ISO 3864 (all parts), Graphical symbols – Safety colours and safety signs

830 ISO 7000, Graphic symbols for use on equipment – Index and synopsis. Available from:
831 <<http://www.graphical-symbols.info/equipment>>

832 CENELEC WORKSHOP AGREEMENT, CWA 50611, Flow batteries – Guidance on the specification,
833 installation and operation

834 Globally Harmonized System of Classification and Labelling of Chemicals (GHS)

835

836

Bibliography

- [1] A.R. Dehghani-sanij, M. Soltani, and K. Raahemifar. “A new design of wind tower for passive ventilation in buildings to reduce energy consumption in windy regions”. In: *Renewable and Sustainable Energy Reviews* 42 (2015), pp. 182–195. ISSN: 1364-0321. DOI: <https://doi.org/10.1016/j.rser.2014.10.018>. URL: <http://www.sciencedirect.com/science/article/pii/S1364032114008351>.
- [2] A.R. Dehghani-Sanij et al. “Marine icing phenomena on vessels and offshore structures: Prediction and analysis”. In: *Ocean Engineering* 143 (2017), pp. 1–23. ISSN: 0029-8018. DOI: <https://doi.org/10.1016/j.oceaneng.2017.07.049>. URL: <http://www.sciencedirect.com/science/article/pii/S0029801817304353>.
- [3] Tam C Taylor P. Girouard N Konialis E. “Organization for Economic Cooperation and Development (OECD) and International Energy Agency (IEA) publications.” In: *OECD Green Growth Studies: Energy*. (2011). URL: <https://www.oecd.org/greengrowth/greening-energy/49157219.pdf>. [accessed 1 January 2019].
- [4] International Energy Agency. *World Energy Outlook 2015*. 2015, p. 600. DOI: <https://doi.org/10.1787/weo-2015-en>. URL: <https://www.oecd-ilibrary.org/content/publication/weo-2015-en>.
- [5] Herib Blanco and André Faaij. “A review at the role of storage in energy systems with a focus on Power to Gas and long-term storage”. In: *Renewable and Sustainable Energy Reviews* 81 (2018), pp. 1049–1086. ISSN: 1364-0321. DOI: <https://doi.org/10.1016/j.rser.2017.07.062>. URL: <http://www.sciencedirect.com/science/article/pii/S1364032117311310>.
- [6] Mukrimin Sevket Guney and Yalcin Tepe. “Classification and assessment of energy storage systems”. In: *Renewable and Sustainable Energy Reviews* 75 (2017), pp. 1187–1197. ISSN: 1364-0321. DOI: <https://doi.org/10.1016/j.rser.2016.11.102>. URL: <http://www.sciencedirect.com/science/article/pii/S1364032116308218>.
- [7] Arsalan Sepehri and Mohammad-Hossein Sarrafzadeh. “Effect of nitrifiers community on fouling mitigation and nitrification efficiency in a membrane bioreactor”. In: *Chemical Engineering and Processing - Process Intensification* 128 (2018), pp. 10–18. ISSN: 0255-2701. DOI: <https://doi.org/10.1016/j.cep.2018.04.006>. URL: <http://www.sciencedirect.com/science/article/pii/S0255270117312916>.
- [8] T Boden, G Marland, and B Andres. *Global CO₂ emissions from fossil-fuel burning, cement manufacture, and gas flaring: 1751-2008*. Oak Ridge, TN: Oak Ridge National Laboratory, Carbon Dioxide Information Analysis Center. 2011.
- [9] B.P. Heard et al. “Burden of proof: A comprehensive review of the feasibility of 100% renewable-electricity systems”. In: *Renewable and Sustainable Energy Reviews* 76 (2017), pp. 1122–1133. ISSN: 1364-0321. DOI: <https://doi.org/10.1016/j.rser.2017.03.114>. URL: <http://www.sciencedirect.com/science/article/pii/S1364032117304495>.
- [10] A.R. Dehghani-Sanij et al. “Study of energy storage systems and environmental challenges of batteries”. In: *Renewable and Sustainable Energy Reviews* 104 (2019), pp. 192–208. ISSN: 1364-0321. DOI: <https://doi.org/10.1016/j.rser.2019.01.023>. URL: <http://www.sciencedirect.com/science/article/pii/S1364032119300334>.
- [11] Holli Riebeek and Global Warming. *NASA Earth Obs*. 2010. URL: <https://earthobservatory.nasa.gov/Features/GlobalWarming/>.
- [12] TF Stocker et al. “Fifth Assessment Report of the IPCC-Working Group 1”. In: *New York, US: Intergovernmental Panel on Climate Change (IPCC)*. doi: <http://dx.doi.org/10.1017> (2013).

- [13] Yuqing Yang et al. “Battery energy storage system size determination in renewable energy systems: A review”. In: *Renewable and Sustainable Energy Reviews* 91 (2018), pp. 109–125. ISSN: 1364-0321. DOI: <https://doi.org/10.1016/j.rser.2018.03.047>. URL: <http://www.sciencedirect.com/science/article/pii/S1364032118301436>.
- [14] AECOM. *Energy storage study - funding and knowledge sharing priorities*. 2015. URL: <https://arena.gov.au/assets/2015/07/AECOM-Energy-Storage-Study.pdf> Accessed 29 October 2017.
- [15] IRENA. *The power to change: solar and wind cost reduction potential to 2025*. 2016. URL: http://www.irena.org/DocumentDownloads/Publications/IRENA_Power_to_Change_2016.pdf [Accessed 29 October 2017].
- [16] Xing Luo et al. “Overview of current development in electrical energy storage technologies and the application potential in power system operation”. In: *Applied Energy* 137 (2015), pp. 511–536. ISSN: 0306-2619. DOI: <https://doi.org/10.1016/j.apenergy.2014.09.081>. URL: <http://www.sciencedirect.com/science/article/pii/S0306261914010290>.
- [17] C. Pieper and H. Rubel. “Revisiting energy storage. There is a business case,” in: *Boston Consulting Group Report*. 2011.
- [18] Dhruv Bhatnagar and Verne Loose. “Evaluating Utility Procured Electric Energy Storage Resources: A Perspective for State Electric Utility Regulators”. In: *SAND 2012*. 2012.
- [19] M. Guarneri et al. “Vanadium Redox Flow Batteries: Potentials and Challenges of an Emerging Storage Technology”. In: *IEEE Industrial Electronics Magazine* 10.4 (2016), pp. 20–31. ISSN: 1932-4529. DOI: [10.1109/MIE.2016.2611760](https://doi.org/10.1109/MIE.2016.2611760).
- [20] R. Hebner, J. Beno, and A. Walls. “Flywheel batteries come around again”. In: *IEEE Spectrum* 39.4 (2002), pp. 46–51. ISSN: 0018-9235. DOI: [10.1109/6.993788](https://doi.org/10.1109/6.993788).
- [21] Siraj Sabihuddin, Aristides E. Kiprakis, and Markus Mueller. “A Numerical and Graphical Review of Energy Storage Technologies”. In: *Energies* 8.1 (2015), pp. 172–216. ISSN: 1996-1073. DOI: [10.3390/en8010172](https://doi.org/10.3390/en8010172). URL: <https://www.mdpi.com/1996-1073/8/1/172>.
- [22] Geoffrey J. May, Alistair Davidson, and Boris Monahov. “Lead batteries for utility energy storage: A review”. In: *Journal of Energy Storage* 15 (2018), pp. 145–157. ISSN: 2352-152X. DOI: <https://doi.org/10.1016/j.est.2017.11.008>. URL: <http://www.sciencedirect.com/science/article/pii/S2352152X17304437>.
- [23] Reddy TB. “Linden’s handbook of batteries 4th ed USA”. In: *McGraw Hill Professional* (2010).
- [24] Zhenguo Yang et al. “Electrochemical Energy Storage for Green Grid”. In: *Chemical Reviews* 111.5 (2011). PMID: 21375330, pp. 3577–3613. DOI: [10.1021/cr100290v](https://doi.org/10.1021/cr100290v). eprint: <https://doi.org/10.1021/cr100290v>. URL: <https://doi.org/10.1021/cr100290v>.
- [25] Md. Arafat Rahman, Xiaojian Wang, and Cuie Wen. “High Energy Density Metal-Air Batteries: A Review”. In: *Journal of The Electrochemical Society* 160.10 (2013), A1759–A1771. DOI: [10.1149/2.062310jes](https://doi.org/10.1149/2.062310jes). eprint: <http://jes.ecsdl.org/content/160/10/A1759.full.pdf+html>. URL: <http://jes.ecsdl.org/content/160/10/A1759.abstract>.
- [26] Bruce Dunn, Haresh Kamath, and Jean-Marie Tarascon. “Electrical Energy Storage for the Grid: A Battery of Choices”. In: *Science* 334.6058 (2011), pp. 928–935. ISSN: 0036-8075. DOI: [10.1126/science.1212741](https://doi.org/10.1126/science.1212741). eprint: <https://science.sciencemag.org/content/334/6058/928.full.pdf>. URL: <https://science.sciencemag.org/content/334/6058/928>.
- [27] Hussein Ibrahim and Adrian Ilinca. “Techno-Economic Analysis of Different Energy Storage Technologies”. In: *Energy Storage*. Ed. by Ahmed Faheem Zobaa. Rijeka: IntechOpen, 2013. Chap. 1. DOI: [10.5772/52220](https://doi.org/10.5772/52220). URL: <https://doi.org/10.5772/52220>.
- [28] T Shigematsu. “Redox flow battery for energy storage”. In: *SEI Technical Review* 73 (Oct. 2011), pp. 4–13.

- [29] *Big battery boom hits another roadblock: fire-fearing cities.* Bloomberg. 2018. URL: <https://www.bloomberg.com/news/articles/2018-05-18/the-big-battery-boom-hits-another-roadblock-firefearing-cities>[Accessed19November2018].
- [30] *International Electrotechnical Commission: IEC - TC 21 Work programme, secondary cells and batteries.* Iec.Ch. 2018. URL: [FSP_ORG_ID:1290,https://www.iec.ch/dyn/www/f?p=103:23:0](https://www.iec.ch/dyn/www/f?p=103:23:0). Accessed21November2018..
- [31] Z. G. Yang. “Is this the ultimate grid battery?” In: *IEEE Spectrum* 54.11 (2017), pp. 36–41. ISSN: 0018-9235. DOI: [10.1109/MSPEC.2017.8093799](https://doi.org/10.1109/MSPEC.2017.8093799).
- [32] *Vanadium is the latest beneficiary of the battery craze.* *The Economist*; 2018. URL: <http://www.economist.com/business/2018/07/21/vanadium-is-the-latest-beneficiary-of-the-battery-craze>. Accessed19November2018..
- [33] *Historical cobalt prices and price chart.* *Investment Mine*. 2018. URL: <http://www.informine.com/investment/metal-prices/cobalt/all/>. Accessed19November2018..
- [34] Elsa A. Olivetti et al. “Lithium-Ion Battery Supply Chain Considerations: Analysis of Potential Bottlenecks in Critical Metals”. In: *Joule* 1.2 (2017), pp. 229–243. ISSN: 2542-4351. DOI: <https://doi.org/10.1016/j.joule.2017.08.019>. URL: <http://www.sciencedirect.com/science/article/pii/S2542435117300442>.
- [35] Luis F. Arenas et al. “The characteristics and performance of hybrid redox flow batteries with zinc negative electrodes for energy storage”. In: *Renewable and Sustainable Energy Reviews* 90 (2018), pp. 992–1016. ISSN: 1364-0321. DOI: <https://doi.org/10.1016/j.rser.2018.03.016>. URL: <http://www.sciencedirect.com/science/article/pii/S1364032118301242>.
- [36] David G. Kwabi et al. “Alkaline Quinone Flow Battery with Long Lifetime at pH 12”. In: *Joule* 2.9 (2018), pp. 1894–1906. ISSN: 2542-4351. DOI: <https://doi.org/10.1016/j.joule.2018.07.005>. URL: <http://www.sciencedirect.com/science/article/pii/S2542435118302915>.
- [37] Wenjie Li et al. “A Long Lifetime Aqueous Organic Solar Flow Battery”. In: *Advanced Energy Materials* 9.31 (2019), p. 1900918. DOI: [10.1002/aenm.201900918](https://doi.org/10.1002/aenm.201900918). eprint: <https://onlinelibrary.wiley.com/doi/pdf/10.1002/aenm.201900918>. URL: <https://onlinelibrary.wiley.com/doi/abs/10.1002/aenm.201900918>.
- [38] Xiaoliang Wei et al. “Materials and Systems for Organic Redox Flow Batteries: Status and Challenges”. In: *ACS Energy Letters* 2.9 (2017), pp. 2187–2204. DOI: [10.1021/acsenenergylett.7b00650](https://doi.org/10.1021/acsenenergylett.7b00650). eprint: <https://doi.org/10.1021/acsenenergylett.7b00650>. URL: <https://doi.org/10.1021/acsenenergylett.7b00650>.
- [39] Luis F. Arenas, Carlos Ponce de León, and Frank C. Walsh. “Redox flow batteries for energy storage: their promise, achievements and challenges”. In: *Current Opinion in Electrochemistry* 16 (2019), pp. 117–126. ISSN: 2451-9103. DOI: <https://doi.org/10.1016/j.coelec.2019.05.007>. URL: <http://www.sciencedirect.com/science/article/pii/S2451910319300183>.
- [40] L.F. Arenas, C. Ponce de León, and F.C. Walsh. “Engineering aspects of the design, construction and performance of modular redox flow batteries for energy storage”. In: *Journal of Energy Storage* 11 (2017), pp. 119–153. ISSN: 2352-152X. DOI: <https://doi.org/10.1016/j.est.2017.02.007>. URL: <http://www.sciencedirect.com/science/article/pii/S2352152X16301736>.
- [41] Nobuyuki Tokuda et al. “Development of a redox flow battery system”. In: *SUMITOMO ELECTRIC TECHNICAL REVIEW-ENGLISH EDITION-* (1998), pp. 88–94.
- [42] M. Skyllas-Kazacos et al. “Progress in Flow Battery Research and Development”. In: *Journal of The Electrochemical Society* 158.8 (2011), R55–R79. DOI: [10.1149/1.3599565](https://doi.org/10.1149/1.3599565). eprint: <http://jes.ecsdl.org/content/158/8/R55.full.pdf+html>. URL: <http://jes.ecsdl.org/content/158/8/R55.abstract>.

- [43] Piergiorgio Alotto, Massimo Guarnieri, and Federico Moro. “Redox flow batteries for the storage of renewable energy: A review”. In: *Renewable and Sustainable Energy Reviews* 29 (2014), pp. 325–335. ISSN: 1364-0321. DOI: <https://doi.org/10.1016/j.rser.2013.08.001>. URL: <http://www.sciencedirect.com/science/article/pii/S1364032113005418>.
- [44] C. Ponce de León et al. “Redox flow cells for energy conversion”. In: *Journal of Power Sources* 160.1 (2006), pp. 716–732. ISSN: 0378-7753. DOI: <https://doi.org/10.1016/j.jpowsour.2006.02.095>. URL: <http://www.sciencedirect.com/science/article/pii/S037877530600437X>.
- [45] Toshikazu Shibata et al. “Redox flow batteries for the stable supply of renewable energy”. In: *SEI Tech. Rev* 76 (2013), pp. 14–22.
- [46] Mike L. Perry and Adam Z. Weber. “Advanced Redox-Flow Batteries: A Perspective”. In: *Journal of The Electrochemical Society* 163.1 (2016), A5064–A5067. DOI: [10.1149/2.0101601jes](https://doi.org/10.1149/2.0101601jes). eprint: <http://jes.ecsdl.org/content/163/1/A5064.full.pdf+html>. URL: <http://jes.ecsdl.org/content/163/1/A5064.abstract>.
- [47] Ryan O’hayre et al. *Fuel cell fundamentals*. John Wiley & Sons, 2016.
- [48] Alberto Cavallini and Lino Mattarolo. *Termodinamica applicata*. Cleup, 1992.
- [49] Allen J Bard, Larry R Faulkner, et al. “Fundamentals and applications”. In: *Electrochemical Methods 2* (2001), p. 482.
- [50] Wei Wang et al. “Electrochemical cells for medium- and large-scale energy storage”. In: ().
- [51] M. Zago and A. Casalegno. “Physically-based impedance modeling of the negative electrode in All-Vanadium Redox Flow Batteries: insight into mass transport issues”. In: *Electrochimica Acta* 248 (2017), pp. 505–517. ISSN: 0013-4686. DOI: <https://doi.org/10.1016/j.electacta.2017.07.166>. URL: <http://www.sciencedirect.com/science/article/pii/S0013468617316079>.
- [52] Christian Blanc. “Modeling of a vanadium redox flow battery electricity storage system”. PhD thesis. Verlag nicht ermittelbar, 2009.
- [53] Michael Sterner and Ingo Stadler. “Elektrochemische Energiespeicher”. In: *Energiespeicher - Bedarf, Technologien, Integration*. Berlin, Heidelberg: Springer Berlin Heidelberg, 2014, pp. 197–294. ISBN: 978-3-642-37380-0. DOI: [10.1007/978-3-642-37380-0_7](https://doi.org/10.1007/978-3-642-37380-0_7). URL: https://doi.org/10.1007/978-3-642-37380-0_7.
- [54] PA Pissoort. In: *FR Patent 754065* (1933).
- [55] Miyake Y. Ashimura S and DK. In: *Journal of power sources* 39 (1971).
- [56] Margaret A Reid and Randall F Gahn. “Factors affecting the open-circuit voltage and electrode kinetics of some iron/titanium redox flow cells”. In: (1977).
- [57] URL: <http://www.nedo.go.jp/english/index.html>, lastaccessed:Dec.2010.
- [58] URL: http://energy.electrochem.jp/NEDO_WS100702.pdf, lastaccessed:Dec.2010..
- [59] Spaziante M. In: *GBPatent2030349* (1978).
- [60] In: *AUPatent575247* (1986).
- [61] Brian Huskinson et al. “A metal-free organic–inorganic aqueous flow battery”. In: *Nature* 505.7482 (2014), p. 195.
- [62] Wei Wang et al. “Recent Progress in Redox Flow Battery Research and Development”. In: *Advanced Functional Materials* 23.8 (2013), pp. 970–986. DOI: [10.1002/adfm.201200694](https://doi.org/10.1002/adfm.201200694). eprint: <https://onlinelibrary.wiley.com/doi/pdf/10.1002/adfm.201200694>. URL: <https://onlinelibrary.wiley.com/doi/abs/10.1002/adfm.201200694>.
- [63] Feng Pan and Qing Wang. “Redox species of redox flow batteries: A review”. In: *Molecules* 20.11 (2015), pp. 20499–20517.

- [64] Bo Yang et al. “An Inexpensive Aqueous Flow Battery for Large-Scale Electrical Energy Storage Based on Water-Soluble Organic Redox Couples”. In: *Journal of The Electrochemical Society* 161.9 (2014), A1371–A1380. DOI: [10.1149/2.1001409jes](https://doi.org/10.1149/2.1001409jes). eprint: <http://jes.ecsdl.org/content/161/9/A1371.full.pdf+html>. URL: <http://jes.ecsdl.org/content/161/9/A1371.abstract>.
- [65] Yu Zhao and Hye Ryung Byon. “High-Performance Lithium-Iodine Flow Battery”. In: *Advanced Energy Materials* 3.12 (2013), pp. 1630–1635. DOI: [10.1002/aenm.201300627](https://doi.org/10.1002/aenm.201300627). eprint: <https://onlinelibrary.wiley.com/doi/pdf/10.1002/aenm.201300627>. URL: <https://onlinelibrary.wiley.com/doi/abs/10.1002/aenm.201300627>.
- [66] Yu Zhao, Lina Wang, and Hye Ryung Byon. “High-performance rechargeable lithium-iodine batteries using triiodide/iodide redox couples in an aqueous cathode”. In: *Nature communications* 4 (2013), p. 1896.
- [67] C.-H Bae, E.P.L Roberts, and R.A.W Dryfe. “Chromium redox couples for application to redox flow batteries”. In: *Electrochimica Acta* 48.3 (2002), pp. 279–287. ISSN: 0013-4686. DOI: [https://doi.org/10.1016/S0013-4686\(02\)00649-7](https://doi.org/10.1016/S0013-4686(02)00649-7). URL: <http://www.sciencedirect.com/science/article/pii/S0013468602006497>.
- [68] FC Walsh. “Electrochemical technology for environmental treatment and clean energy conversion”. In: *Pure and applied chemistry* 73.12 (2001), pp. 1819–1837.
- [69] H. S. Lim, A. M. Lackner, and R. C. Knechtli. “Zinc-Bromine Secondary Battery”. In: *Journal of The Electrochemical Society* 124.8 (1977), pp. 1154–1157. DOI: [10.1149/1.2133517](https://doi.org/10.1149/1.2133517). eprint: <http://jes.ecsdl.org/content/124/8/1154.full.pdf+html>. URL: <http://jes.ecsdl.org/content/124/8/1154.abstract>.
- [70] Maria Skyllas-Kazacos et al. “Recent advances with UNSW vanadium-based redox flow batteries”. In: *International Journal of Energy Research* 34.2 (), pp. 182–189. DOI: [10.1002/er.1658](https://doi.org/10.1002/er.1658). eprint: <https://onlinelibrary.wiley.com/doi/pdf/10.1002/er.1658>. URL: <https://onlinelibrary.wiley.com/doi/abs/10.1002/er.1658>.
- [71] Chris Menictas and Maria Skyllas-Kazacos. “Performance of vanadium-oxygen redox fuel cell”. In: *Journal of Applied Electrochemistry* 41.10 (2011), p. 1223. ISSN: 1572-8838. DOI: [10.1007/s10800-011-0342-8](https://doi.org/10.1007/s10800-011-0342-8). URL: <https://doi.org/10.1007/s10800-011-0342-8>.
- [72] Xinyou Ke et al. “Rechargeable redox flow batteries: flow fields, stacks and design considerations”. In: *Chem. Soc. Rev.* 47 (23 2018), pp. 8721–8743. DOI: [10.1039/C8CS00072G](https://doi.org/10.1039/C8CS00072G). URL: <http://dx.doi.org/10.1039/C8CS00072G>.
- [73] James A. Trainham and John Newman. “A comparison between flow-through and flow-by porous electrodes for redox energy storage”. In: *Electrochimica Acta* 26.4 (1981), pp. 455–469. ISSN: 0013-4686. DOI: [https://doi.org/10.1016/0013-4686\(81\)87024-7](https://doi.org/10.1016/0013-4686(81)87024-7). URL: <http://www.sciencedirect.com/science/article/pii/0013468681870247>.
- [74] Federico Moro et al. “An alternative low-loss stack topology for vanadium redox flow battery: Comparative assessment”. In: *Journal of Power Sources* 340 (2017), pp. 229–241. ISSN: 0378-7753. DOI: <https://doi.org/10.1016/j.jpowsour.2016.11.042>. URL: <http://www.sciencedirect.com/science/article/pii/S0378775316315683>.
- [75] R. M. Dell. “Industrial electrochemistry (second edition) by Derek Pletcher and Frank C. Walsh, Chapman and Hall, London, 1990, pp. xvi + 653, price £65.00. ISBN 0 412 30410 4”. In: *Journal of Chemical Technology & Biotechnology* 52.3 (1991), pp. 427–428. DOI: [10.1002/jctb.280520317](https://doi.org/10.1002/jctb.280520317). eprint: <https://onlinelibrary.wiley.com/doi/pdf/10.1002/jctb.280520317>. URL: <https://onlinelibrary.wiley.com/doi/abs/10.1002/jctb.280520317>.
- [76] Robert M. Darling and Mike L. Perry. “The Influence of Electrode and Channel Configurations on Flow Battery Performance”. In: *Journal of The Electrochemical Society* 161.9 (2014), A1381–A1387. DOI: [10.1149/2.0941409jes](https://doi.org/10.1149/2.0941409jes). eprint: <http://jes.ecsdl.org/content/161/9/A1381.full.pdf+html>. URL: <http://jes.ecsdl.org/content/161/9/A1381.abstract>.

- [77] D.S. Aaron et al. “Dramatic performance gains in vanadium redox flow batteries through modified cell architecture”. In: *Journal of Power Sources* 206 (2012), pp. 450–453. ISSN: 0378-7753. DOI: <https://doi.org/10.1016/j.jpowsour.2011.12.026>. URL: <http://www.sciencedirect.com/science/article/pii/S0378775311024451>.
- [78] David Reed et al. “Stack Developments in a kW Class All Vanadium Mixed Acid Redox Flow Battery at the Pacific Northwest National Laboratory”. In: *Journal of The Electrochemical Society* 163.1 (2016), A5211–A5219. DOI: [10.1149/2.0281601jes](https://doi.org/10.1149/2.0281601jes). eprint: <http://jes.ecsdl.org/content/163/1/A5211.full.pdf+html>. URL: <http://jes.ecsdl.org/content/163/1/A5211.abstract>.
- [79] C. R. Dennison et al. “Enhancing Mass Transport in Redox Flow Batteries by Tailoring Flow Field and Electrode Design”. In: *Journal of The Electrochemical Society* 163.1 (2016), A5163–A5169. DOI: [10.1149/2.0231601jes](https://doi.org/10.1149/2.0231601jes). eprint: <http://jes.ecsdl.org/content/163/1/A5163.full.pdf+html>. URL: <http://jes.ecsdl.org/content/163/1/A5163.abstract>.
- [80] In: *REDOX FLOW BATTERY SYSTEM AND CELL STACK, WO9939397 (A1)*, author=Pellegrini Alberto; Broman Barry Michael, year=1999, ()
- [81] David J Pickett. “Electrochemical reactor design / David J. Pickett”. In: *SERBIULA (sistema Librum 2.0)* (May 2019).
- [82] Álvaro Cunha et al. “Vanadium redox flow batteries: a technology review”. In: *International Journal of Energy Research* 39.7 (), pp. 889–918. DOI: [10.1002/er.3260](https://doi.org/10.1002/er.3260). eprint: <https://onlinelibrary.wiley.com/doi/pdf/10.1002/er.3260>. URL: <https://onlinelibrary.wiley.com/doi/abs/10.1002/er.3260>.
- [83] Alberto Pellegrini and Barry Michael Broman. *Redox flow battery system and cell stack*. US Patent 6,475,661. 2002.
- [84] In: *REDOX FLOW BATTERY SYSTEM WITH DIVIDED TANK SYSTEM, WO2012/094672A2*, author=Horne Craig, Hickey Darren, year=2012, ()
- [85] Gareth Kear, Akeel A. Shah, and Frank C. Walsh. “Development of the all-vanadium redox flow battery for energy storage: a review of technological, financial and policy aspects”. In: *International Journal of Energy Research* 36.11 (), pp. 1105–1120. DOI: [10.1002/er.1863](https://doi.org/10.1002/er.1863). eprint: <https://onlinelibrary.wiley.com/doi/pdf/10.1002/er.1863>. URL: <https://onlinelibrary.wiley.com/doi/abs/10.1002/er.1863>.
- [86] M. Skyllas-Kazacos, C. Menictas, and M. Kazacos. “Thermal Stability of Concentrated V(V) Electrolytes in the Vanadium Redox Cell”. In: *Journal of The Electrochemical Society* 143.4 (1996), pp. L86–L88. DOI: [10.1149/1.1836609](https://doi.org/10.1149/1.1836609). eprint: <http://jes.ecsdl.org/content/143/4/L86.full.pdf+html>. URL: <http://jes.ecsdl.org/content/143/4/L86.abstract>.
- [87] Chanyong Choi et al. “A review of vanadium electrolytes for vanadium redox flow batteries”. In: *Renewable and Sustainable Energy Reviews* 69 (2017), pp. 263–274. ISSN: 1364-0321. DOI: <https://doi.org/10.1016/j.rser.2016.11.188>. URL: <http://www.sciencedirect.com/science/article/pii/S1364032116309340>.
- [88] Maria Skyllas-Kazacos et al. “Vanadium Electrolyte Studies for the Vanadium Redox Battery—A Review”. In: *ChemSusChem* 9.13 (), pp. 1521–1543. DOI: [10.1002/cssc.201600102](https://doi.org/10.1002/cssc.201600102). eprint: <https://onlinelibrary.wiley.com/doi/pdf/10.1002/cssc.201600102>. URL: <https://onlinelibrary.wiley.com/doi/abs/10.1002/cssc.201600102>.
- [89] Asem Mousa and Maria Skyllas-Kazacos. “Effect of Additives on the Low-Temperature Stability of Vanadium Redox Flow Battery Negative Half-Cell Electrolyte”. In: *ChemElectroChem* 2.11 (), pp. 1742–1751. DOI: [10.1002/celec.201500233](https://doi.org/10.1002/celec.201500233). eprint: <https://onlinelibrary.wiley.com/doi/pdf/10.1002/celec.201500233>. URL: <https://onlinelibrary.wiley.com/doi/abs/10.1002/celec.201500233>.

- [90] Sarah Roe, Chris Menictas, and Maria Skyllas-Kazacos. “A High Energy Density Vanadium Redox Flow Battery with 3 M Vanadium Electrolyte”. In: *Journal of The Electrochemical Society* 163.1 (2016), A5023–A5028. DOI: [10.1149/2.0041601jes](https://doi.org/10.1149/2.0041601jes). eprint: <http://jes.ecsdl.org/content/163/1/A5023.full.pdf+html>. URL: <http://jes.ecsdl.org/content/163/1/A5023.abstract>.
- [91] Nadeem Kausar, Asem Mousa, and Maria Skyllas-Kazacos. “The Effect of Additives on the High-Temperature Stability of the Vanadium Redox Flow Battery Positive Electrolytes”. In: *ChemElectroChem* 3.2 (), pp. 276–282. DOI: [10.1002/ce1c.201500453](https://doi.org/10.1002/ce1c.201500453). eprint: <https://onlinelibrary.wiley.com/doi/pdf/10.1002/ce1c.201500453>. URL: <https://onlinelibrary.wiley.com/doi/abs/10.1002/ce1c.201500453>.
- [92] Jianlu Zhang et al. “Effects of additives on the stability of electrolytes for all-vanadium redox flow batteries”. In: *Journal of Applied Electrochemistry* 41.10 (2011), pp. 1215–1221.
- [93] S. Peng et al. “Vanadium species in CH₃SO₃H and H₂SO₄ mixed acid as the supporting electrolyte for vanadium redox flow battery”. In: *International Journal of Electrochemical Science* 7.1 (2012). cited By 39, pp. 643–649. URL: <https://www.scopus.com/inward/record.uri?eid=2-s2.0-84855468002&partnerID=40&md5=9a821af045b8299aff0448399891095f>.
- [94] Liyu Li et al. “A Stable Vanadium Redox-Flow Battery with High Energy Density for Large-Scale Energy Storage”. In: *Advanced Energy Materials* 1.3 (), pp. 394–400. DOI: [10.1002/aenm.201100008](https://doi.org/10.1002/aenm.201100008). eprint: <https://onlinelibrary.wiley.com/doi/pdf/10.1002/aenm.201100008>. URL: <https://onlinelibrary.wiley.com/doi/abs/10.1002/aenm.201100008>.
- [95] K. B. Hatzell et al. “Flowable Conducting Particle Networks in Redox-Active Electrolytes for Grid Energy Storage”. In: *Journal of The Electrochemical Society* 162.5 (2015), A5007–A5012. DOI: [10.1149/2.0011505jes](https://doi.org/10.1149/2.0011505jes). eprint: <http://jes.ecsdl.org/content/162/5/A5007.full.pdf+html>. URL: <http://jes.ecsdl.org/content/162/5/A5007.abstract>.
- [96] Chao Zhang et al. “Three-dimensional electrochemical process for wastewater treatment: A general review”. In: *Chemical Engineering Journal* 228 (2013), pp. 455–467. ISSN: 1385-8947. DOI: <https://doi.org/10.1016/j.cej.2013.05.033>. URL: <http://www.sciencedirect.com/science/article/pii/S1385894713006529>.
- [97] M. Inoue et al. “Carbon Fiber Electrode for Redox Flow Battery”. In: *Journal of The Electrochemical Society* 134.3 (1987), pp. 756–757. DOI: [10.1149/1.2100549](https://doi.org/10.1149/1.2100549). eprint: <http://jes.ecsdl.org/content/134/3/756.full.pdf+html>. URL: <http://jes.ecsdl.org/content/134/3/756.abstract>.
- [98] A. Tentorio and U. Casolo-Ginelli. “Characterization of reticulate, three — dimensional electrodes”. In: *Journal of Applied Electrochemistry* 8.3 (1978), pp. 195–205. ISSN: 1572-8838. DOI: [10.1007/BF00616422](https://doi.org/10.1007/BF00616422). URL: <https://doi.org/10.1007/BF00616422>.
- [99] Fernando F. Rivera et al. “The reaction environment in a filter-press laboratory reactor: the FM01-LC flow cell”. In: *Electrochimica Acta* 161 (2015), pp. 436–452. ISSN: 0013-4686. DOI: <https://doi.org/10.1016/j.electacta.2015.02.161>. URL: <http://www.sciencedirect.com/science/article/pii/S0013468615004697>.
- [100] Locksley F. Castañeda et al. “Graphite felt as a versatile electrode material: Properties, reaction environment, performance and applications”. In: *Electrochimica Acta* 258 (2017), pp. 1115–1139. ISSN: 0013-4686. DOI: <https://doi.org/10.1016/j.electacta.2017.11.165>. URL: <http://www.sciencedirect.com/science/article/pii/S0013468617325276>.
- [101] Chi Xu et al. “Ultrathin free-standing electrospun carbon nanofibers web as the electrode of the vanadium flow batteries”. In: *Journal of Energy Chemistry* 26.4 (2017), pp. 730–737. ISSN: 2095-4956. DOI: <https://doi.org/10.1016/j.jechem.2017.03.005>. URL: <http://www.sciencedirect.com/science/article/pii/S2095495617302036>.

- [102] G. Kear, A.A. Shah, and F.C. Walsh. “The all-vanadium redox flow battery: Commercialisation, cost analysis and policy led incentives”. In: *International Journal of Energy* 36 (2011). cited By 1, p. 1105.
- [103] M.J. Watt-Smith et al. “The importance of key operational variables and electrolyte monitoring to the performance of an all vanadium redox flow battery”. In: *Journal of Chemical Technology & Biotechnology* 88.1 (), pp. 126–138. DOI: [10.1002/jctb.3870](https://doi.org/10.1002/jctb.3870). eprint: <https://onlinelibrary.wiley.com/doi/pdf/10.1002/jctb.3870>. URL: <https://onlinelibrary.wiley.com/doi/abs/10.1002/jctb.3870>.
- [104] Aishwarya Parasuraman et al. “Review of material research and development for vanadium redox flow battery applications”. In: *Electrochimica Acta* 101 (2013), pp. 27–40. ISSN: 0013-4686. DOI: <https://doi.org/10.1016/j.electacta.2012.09.067>. URL: <http://www.sciencedirect.com/science/article/pii/S0013468612015459>.
- [105] M. Rychcik and M. Skyllas-Kazacos. “Evaluation of electrode materials for vanadium redox cell”. In: *Journal of Power Sources* 19.1 (1987), pp. 45–54. ISSN: 0378-7753. DOI: [https://doi.org/10.1016/0378-7753\(87\)80006-X](https://doi.org/10.1016/0378-7753(87)80006-X). URL: <http://www.sciencedirect.com/science/article/pii/037877538780006X>.
- [106] Jian-Zhang Chen et al. “All-vanadium redox flow batteries with graphite felt electrodes treated by atmospheric pressure plasma jets”. In: *Journal of Power Sources* 274 (2015), pp. 894–898. ISSN: 0378-7753. DOI: <https://doi.org/10.1016/j.jpowsour.2014.10.097>. URL: <http://www.sciencedirect.com/science/article/pii/S0378775314017066>.
- [107] Nathan S. Jacobson and Donald M. Curry. “Oxidation microstructure studies of reinforced carbon/carbon”. In: *Carbon* 44.7 (2006), pp. 1142–1150. ISSN: 0008-6223. DOI: <https://doi.org/10.1016/j.carbon.2005.11.013>. URL: <http://www.sciencedirect.com/science/article/pii/S000862230500686X>.
- [108] K. Jurewicz et al. “Ammoxidation of active carbons for improvement of supercapacitor characteristics”. In: *Electrochimica Acta* 48.11 (2003), pp. 1491–1498. ISSN: 0013-4686. DOI: [https://doi.org/10.1016/S0013-4686\(03\)00035-5](https://doi.org/10.1016/S0013-4686(03)00035-5). URL: <http://www.sciencedirect.com/science/article/pii/S0013468603000355>.
- [109] Marta Santiago et al. “Modified activated carbons for catalytic wet air oxidation of phenol”. In: *Carbon* 43.10 (2005), pp. 2134–2145. ISSN: 0008-6223. DOI: <https://doi.org/10.1016/j.carbon.2005.03.026>. URL: <http://www.sciencedirect.com/science/article/pii/S0008622305001946>.
- [110] Xu Li and Kiyoshi Horita. “Electrochemical characterization of carbon black subjected to RF oxygen plasma”. In: *Carbon* 38.1 (2000), pp. 133–138. ISSN: 0008-6223. DOI: [https://doi.org/10.1016/S0008-6223\(99\)00108-6](https://doi.org/10.1016/S0008-6223(99)00108-6). URL: <http://www.sciencedirect.com/science/article/pii/S0008622399001086>.
- [111] Xiao-gang Li et al. “Electrochemical behavior of diverse vanadium ions at modified graphite felt electrode in sulphuric solution”. In: *Journal of Central South University of Technology* 14.1 (2007), pp. 51–56. ISSN: 1993-0666. DOI: [10.1007/s11771-007-0011-6](https://doi.org/10.1007/s11771-007-0011-6). URL: <https://doi.org/10.1007/s11771-007-0011-6>.
- [112] C. Ponce de León et al. “Characterization of the reaction environment in a filter-press redox flow reactor”. In: *Electrochimica Acta* 52.19 (2007), pp. 5815–5823. ISSN: 0013-4686. DOI: <https://doi.org/10.1016/j.electacta.2007.02.080>. URL: <http://www.sciencedirect.com/science/article/pii/S0013468607003532>.
- [113] Lawrence H Thaller. *Electrically rechargeable redox flow cell*. US Patent 3,996,064. 1976.
- [114] Y. V. Makarov et al. “Operational Impacts of Wind Generation on California Power Systems”. In: *IEEE Transactions on Power Systems* 24.2 (2009), pp. 1039–1050. ISSN: 0885-8950. DOI: [10.1109/TPWRS.2009.2016364](https://doi.org/10.1109/TPWRS.2009.2016364).
- [115] Yuyan Shao et al. “Nitrogen-doped mesoporous carbon for energy storage in vanadium redox flow batteries”. In: *Journal of Power Sources* 195.13 (2010), pp. 4375–4379. ISSN: 0378-7753. DOI: <https://doi.org/10.1016/j.jpowsour.2010.01.015>. URL: <http://www.sciencedirect.com/science/article/pii/S0378775310000674>.

- [116] B. Sun and M. Skyllas-Kazacos. “Modification of graphite electrode materials for vanadium redox flow battery application—I. Thermal treatment”. In: *Electrochimica Acta* 37.7 (1992), pp. 1253–1260. ISSN: 0013-4686. DOI: [https://doi.org/10.1016/0013-4686\(92\)85064-R](https://doi.org/10.1016/0013-4686(92)85064-R). URL: <http://www.sciencedirect.com/science/article/pii/S001346869285064R>.
- [117] Bianting Sun and Maria Skyllas-Kazacos. “Chemical modification of graphite electrode materials for vanadium redox flow battery application—part II. Acid treatments”. In: *Electrochimica Acta* 37.13 (1992), pp. 2459–2465. ISSN: 0013-4686. DOI: [https://doi.org/10.1016/0013-4686\(92\)87084-D](https://doi.org/10.1016/0013-4686(92)87084-D). URL: <http://www.sciencedirect.com/science/article/pii/S001346869287084D>.
- [118] Puiki Leung et al. “Progress in redox flow batteries, remaining challenges and their applications in energy storage”. In: *RSC Adv.* 2 (27 2012), pp. 10125–10156. DOI: [10.1039/C2RA21342G](https://doi.org/10.1039/C2RA21342G). URL: <http://dx.doi.org/10.1039/C2RA21342G>.
- [119] Bianting Sun and M. Skyllas-Kazacos. “Chemical modification and electrochemical behaviour of graphite fibre in acidic vanadium solution”. In: *Electrochimica Acta* 36.3 (1991), pp. 513–517. ISSN: 0013-4686. DOI: [https://doi.org/10.1016/0013-4686\(91\)85135-T](https://doi.org/10.1016/0013-4686(91)85135-T). URL: <http://www.sciencedirect.com/science/article/pii/S001346869185135T>.
- [120] Z. González et al. “Enhanced performance of a Bi-modified graphite felt as the positive electrode of a vanadium redox flow battery”. In: *Electrochemistry Communications* 13.12 (2011), pp. 1379–1382. ISSN: 1388-2481. DOI: <https://doi.org/10.1016/j.electcom.2011.08.017>. URL: <http://www.sciencedirect.com/science/article/pii/S138824811100333X>.
- [121] Xiaoxin Wu et al. “Treatment of graphite felt by modified Hummers method for the positive electrode of vanadium redox flow battery”. In: *Electrochimica Acta* 138 (2014), pp. 264–269. ISSN: 0013-4686. DOI: <https://doi.org/10.1016/j.electacta.2014.06.124>. URL: <http://www.sciencedirect.com/science/article/pii/S0013468614013243>.
- [122] Mohammad Hadi Moghim et al. “Role of reduced graphene oxide as nano-electrocatalyst in carbon felt electrode of vanadium redox flow battery”. In: *Journal of Electroanalytical Chemistry* 789 (2017), pp. 67–75. ISSN: 1572-6657. DOI: <https://doi.org/10.1016/j.jelechem.2017.02.031>. URL: <http://www.sciencedirect.com/science/article/pii/S1572665717301248>.
- [123] W. Li, J. Liu, and C. Yan. “Multi-walled carbon nanotubes used as an electrode reaction catalyst for VO₂⁺/VO₂⁺ for a vanadium redox flow battery”. In: *Carbon* 49.11 (2011), pp. 3463–3470. DOI: [10.1016/j.carbon.2011.04.045](https://doi.org/10.1016/j.carbon.2011.04.045). URL: <https://www.scopus.com/inward/record.uri?eid=2-s2.0-79958247371&doi=10.1016%2fj.carbon.2011.04.045&partnerID=40&md5=554fe8eb1cb1237a788d22a9705f1d34>.
- [124] Xiaoxin Wu et al. “Microwave-treated graphite felt as the positive electrode for all-vanadium redox flow battery”. In: *Journal of Power Sources* 263 (2014), pp. 104–109. ISSN: 0378-7753. DOI: <https://doi.org/10.1016/j.jpowsour.2014.04.035>. URL: <http://www.sciencedirect.com/science/article/pii/S0378775314005230>.
- [125] L. Wei et al. “Copper nanoparticle-deposited graphite felt electrodes for all vanadium redox flow batteries”. In: *Applied Energy* 180 (2016), pp. 386–391. ISSN: 0306-2619. DOI: <https://doi.org/10.1016/j.apenergy.2016.07.134>. URL: <http://www.sciencedirect.com/science/article/pii/S0306261916310844>.
- [126] Hiroko Kaneko et al. “Vanadium redox reactions and carbon electrodes for vanadium redox flow battery”. In: *Electrochimica Acta* 36.7 (1991), pp. 1191–1196. ISSN: 0013-4686. DOI: [https://doi.org/10.1016/0013-4686\(91\)85108-J](https://doi.org/10.1016/0013-4686(91)85108-J). URL: <http://www.sciencedirect.com/science/article/pii/S001346869185108J>.
- [127] Alan M. Pezeshki et al. “The Cell-in-Series Method: A Technique for Accelerated Electrode Degradation in Redox Flow Batteries”. In: *Journal of The Electrochemical Society* 163.1 (2016), A5202–A5210. DOI: [10.1149/2.0251601jes](https://doi.org/10.1149/2.0251601jes). eprint: <http://jes.ecsdl.org/content/163/1/A5202.full.pdf+html>. URL: <http://jes.ecsdl.org/content/163/1/A5202.abstract>.

- [128] Dario Maggiolo et al. “Particle based method and X-ray computed tomography for pore-scale flow characterization in VRFB electrodes”. In: *Energy Storage Materials* 16 (2019), pp. 91–96. ISSN: 2405-8297. DOI: <https://doi.org/10.1016/j.ensm.2018.04.021>. URL: <http://www.sciencedirect.com/science/article/pii/S2405829718300072>.
- [129] Ki Hyun Kim, Bu Gi Kim, and Dai Gil Lee. “Development of carbon composite bipolar plate (BP) for vanadium redox flow battery (VRFB)”. In: *Composite Structures* 109 (2014), pp. 253–259. ISSN: 0263-8223. DOI: <https://doi.org/10.1016/j.compstruct.2013.11.002>. URL: <http://www.sciencedirect.com/science/article/pii/S0263822313005825>.
- [130] Peng Qian et al. “A novel electrode-bipolar plate assembly for vanadium redox flow battery applications”. In: *Journal of Power Sources* 175.1 (2008), pp. 613–620. ISSN: 0378-7753. DOI: <https://doi.org/10.1016/j.jpowsour.2007.09.006>. URL: <http://www.sciencedirect.com/science/article/pii/S0378775307017806>.
- [131] Jaeheon Choe et al. “Durability of graphite coated carbon composite bipolar plates for vanadium redox flow batteries”. In: *Composite Structures* 134 (2015), pp. 106–113. ISSN: 0263-8223. DOI: <https://doi.org/10.1016/j.compstruct.2015.08.030>. URL: <http://www.sciencedirect.com/science/article/pii/S0263822315007072>.
- [132] Ha Na Yu et al. “Plasma treatment of the carbon fiber bipolar plate for PEM fuel cell”. In: *Composite Structures* 94.5 (2012), pp. 1911–1918. ISSN: 0263-8223. DOI: <https://doi.org/10.1016/j.compstruct.2011.12.024>. URL: <http://www.sciencedirect.com/science/article/pii/S0263822311004922>.
- [133] Ha Na Yu et al. “A graphite-coated carbon fiber epoxy composite bipolar plate for polymer electrolyte membrane fuel cell”. In: *Journal of Power Sources* 196.23 (2011), pp. 9868–9875. ISSN: 0378-7753. DOI: <https://doi.org/10.1016/j.jpowsour.2011.06.102>. URL: <http://www.sciencedirect.com/science/article/pii/S0378775311015230>.
- [134] Ki Hyun Kim, Bu Gi Kim, and Dai Gil Lee. “Development of carbon composite bipolar plate (BP) for vanadium redox flow battery (VRFB)”. In: *Composite Structures* 109 (2014), pp. 253–259. ISSN: 0263-8223. DOI: <https://doi.org/10.1016/j.compstruct.2013.11.002>. URL: <http://www.sciencedirect.com/science/article/pii/S0263822313005825>.
- [135] Jaeheon Choe, Ki Hyun Kim, and Dai Gil Lee. “Corrugated carbon/epoxy composite bipolar plate for vanadium redox flow batteries”. In: *Composite Structures* 119 (2015), pp. 534–542. ISSN: 0263-8223. DOI: <https://doi.org/10.1016/j.compstruct.2014.09.022>. URL: <http://www.sciencedirect.com/science/article/pii/S0263822314004656>.
- [136] Minjoon Park et al. “Material selection and optimization for highly stable composite bipolar plates in vanadium redox flow batteries”. In: *J. Mater. Chem. A* 2 (38 2014), pp. 15808–15815. DOI: [10.1039/C4TA03542A](https://doi.org/10.1039/C4TA03542A). URL: <http://dx.doi.org/10.1039/C4TA03542A>.
- [137] Burak Caglar et al. “Development of carbon nanotube and graphite filled polyphenylene sulfide based bipolar plates for all-vanadium redox flow batteries”. In: *Journal of Power Sources* 256 (2014), pp. 88–95. ISSN: 0378-7753. DOI: <https://doi.org/10.1016/j.jpowsour.2014.01.060>. URL: <http://www.sciencedirect.com/science/article/pii/S0378775314000846>.
- [138] C. J. Brown et al. “Local mass transport effects in the FM01 laboratory electrolyser”. In: *Journal of Applied Electrochemistry* 22.7 (1992), pp. 613–619. ISSN: 1572-8838. DOI: [10.1007/BF01092609](https://doi.org/10.1007/BF01092609). URL: <https://doi.org/10.1007/BF01092609>.
- [139] Helen Prifti et al. “Membranes for Redox Flow Battery Applications”. In: *Membranes* 2.2 (2012), pp. 275–306. ISSN: 2077-0375. DOI: [10.3390/membranes2020275](https://doi.org/10.3390/membranes2020275). URL: <https://www.mdpi.com/2077-0375/2/2/275>.

- [140] Theresa Sukkar and Maria Skyllas-Kazacos. “Modification of membranes using polyelectrolytes to improve water transfer properties in the vanadium redox battery”. In: *Journal of Membrane Science* 222.1 (2003), pp. 249–264. ISSN: 0376-7388. DOI: [https://doi.org/10.1016/S0376-7388\(03\)00316-8](https://doi.org/10.1016/S0376-7388(03)00316-8). URL: <http://www.sciencedirect.com/science/article/pii/S0376738803003168>.
- [141] R.K. Nagarale, G.S. Gohil, and Vinod K. Shahi. “Recent developments on ion-exchange membranes and electro-membrane processes”. In: *Advances in Colloid and Interface Science* 119.2 (2006), pp. 97–130. ISSN: 0001-8686. DOI: <https://doi.org/10.1016/j.cis.2005.09.005>. URL: <http://www.sciencedirect.com/science/article/pii/S0001868605001107>.
- [142] Xianfeng Li et al. “Ion exchange membranes for vanadium redox flow battery (VRB) applications”. In: *Energy Environ. Sci.* 4 (4 2011), pp. 1147–1160. DOI: [10.1039/C0EE00770F](https://doi.org/10.1039/C0EE00770F). URL: <http://dx.doi.org/10.1039/C0EE00770F>.
- [143] Thomas A Davis, J David Genders, and Derek Pletcher. *A first course in ion permeable membranes*. Electrochemical Consultancy Romsey, 1997.
- [144] Dongyang Chen et al. “Selective anion exchange membranes for high coulombic efficiency vanadium redox flow batteries”. In: *Electrochemistry Communications* 26 (2013), pp. 37–40. ISSN: 1388-2481. DOI: <https://doi.org/10.1016/j.elecom.2012.10.007>. URL: <http://www.sciencedirect.com/science/article/pii/S1388248112004304>.
- [145] S.J. Peighambaroust, S. Rowshanzamir, and M. Amjadi. “Review of the proton exchange membranes for fuel cell applications”. In: *International Journal of Hydrogen Energy* 35.17 (2010), pp. 9349–9384. ISSN: 0360-3199. DOI: <https://doi.org/10.1016/j.ijhydne.2010.05.017>. URL: <http://www.sciencedirect.com/science/article/pii/S0360319910009523>.
- [146] Chenxi Sun et al. “Investigations on transfer of water and vanadium ions across Nafion membrane in an operating vanadium redox flow battery”. In: *Journal of Power Sources* 195.3 (2010), pp. 890–897. ISSN: 0378-7753. DOI: <https://doi.org/10.1016/j.jpowsour.2009.08.041>. URL: <http://www.sciencedirect.com/science/article/pii/S0378775309014153>.
- [147] Dongyang Chen et al. “Synthesis and characterization of novel sulfonated poly(arylene thioether) ionomers for vanadium redox flow battery applications”. In: *Energy Environ. Sci.* 3 (5 2010), pp. 622–628. DOI: [10.1039/B917117G](https://doi.org/10.1039/B917117G). URL: <http://dx.doi.org/10.1039/B917117G>.
- [148] Soowhan Kim et al. “Cycling performance and efficiency of sulfonated poly(sulfone) membranes in vanadium redox flow batteries”. In: *Electrochemistry Communications* 12.11 (2010), pp. 1650–1653. ISSN: 1388-2481. DOI: <https://doi.org/10.1016/j.elecom.2010.09.018>. URL: <http://www.sciencedirect.com/science/article/pii/S1388248110004121>.
- [149] Jingyu Xi et al. “Nafion/SiO₂ hybrid membrane for vanadium redox flow battery”. In: *Journal of Power Sources* 166.2 (2007), pp. 531–536. ISSN: 0378-7753. DOI: <https://doi.org/10.1016/j.jpowsour.2007.01.069>. URL: <http://www.sciencedirect.com/science/article/pii/S037877530700239X>.
- [150] Xiangguo Teng et al. “Nafion/organic silica modified TiO₂ composite membrane for vanadium redox flow battery via in situ sol-gel reactions”. In: *Journal of Membrane Science* 341.1 (2009), pp. 149–154. ISSN: 0376-7388. DOI: <https://doi.org/10.1016/j.memsci.2009.05.051>. URL: <http://www.sciencedirect.com/science/article/pii/S0376738809004232>.
- [151] Chuan Yao et al. “Cell architecture upswing based on catalyst coated membrane (CCM) for vanadium flow battery”. In: *Journal of Power Sources* 237 (2013), pp. 19–25. ISSN: 0378-7753. DOI: <https://doi.org/10.1016/j.jpowsour.2013.03.014>. URL: <http://www.sciencedirect.com/science/article/pii/S0378775313003947>.

- [152] Qingtao Luo et al. “Modification of Nafion membrane using interfacial polymerization for vanadium redox flow battery applications”. In: *Journal of Membrane Science* 311.1 (2008), pp. 98–103. ISSN: 0376-7388. DOI: <https://doi.org/10.1016/j.memsci.2007.11.055>. URL: <http://www.sciencedirect.com/science/article/pii/S0376738807008484>.
- [153] D. Schulte et al. “Nafion Hybrid Membranes for Use in Redox Flow Batteries”. In: *Journal of The Electrochemical Society* 157.9 (2010), A989–A992. DOI: [10.1149/1.3456625](https://doi.org/10.1149/1.3456625). eprint: <http://jes.ecsdl.org/content/157/9/A989.full.pdf+html>. URL: <http://jes.ecsdl.org/content/157/9/A989.abstract>.
- [154] Chuanyu Sun et al. “[Nafion/(WO₃)x] hybrid membranes for vanadium redox flow batteries”. In: *Solid State Ionics* 319 (2018), pp. 110–116. ISSN: 0167-2738. DOI: <https://doi.org/10.1016/j.ssi.2018.01.038>. URL: <http://www.sciencedirect.com/science/article/pii/S0167273817308949>.
- [155] Jan grosse Austing et al. “Layer-by-layer modification of Nafion membranes for increased life-time and efficiency of vanadium/air redox flow batteries”. In: *Journal of Membrane Science* 510 (2016), pp. 259–269. ISSN: 0376-7388. DOI: <https://doi.org/10.1016/j.memsci.2016.03.005>. URL: <http://www.sciencedirect.com/science/article/pii/S0376738816301338>.
- [156] X.L. Zhou et al. “Performance of a vanadium redox flow battery with a VANADion membrane”. In: *Applied Energy* 180 (2016), pp. 353–359. ISSN: 0306-2619. DOI: <https://doi.org/10.1016/j.apenergy.2016.08.001>. URL: <http://www.sciencedirect.com/science/article/pii/S0306261916310881>.
- [157] Xiaoliang Wei, Bin Li, and Wei Wang. “Porous Polymeric Composite Separators for Redox Flow Batteries”. In: *Polymer Reviews* 55.2 (2015), pp. 247–272. DOI: [10.1080/15583724.2015.1011276](https://doi.org/10.1080/15583724.2015.1011276). eprint: <https://doi.org/10.1080/15583724.2015.1011276>. URL: <https://doi.org/10.1080/15583724.2015.1011276>.
- [158] Bin Li et al. “Capacity Decay Mechanism of Microporous Separator-Based All-Vanadium Redox Flow Batteries and its Recovery”. In: *ChemSusChem* 7.2 (), pp. 577–584. DOI: [10.1002/cssc.201300706](https://doi.org/10.1002/cssc.201300706). eprint: <https://onlinelibrary.wiley.com/doi/pdf/10.1002/cssc.201300706>. URL: <https://onlinelibrary.wiley.com/doi/abs/10.1002/cssc.201300706>.
- [159] In: ().
- [160] Peng Gao, Cuifen Zhang, and Guangwu Wen. “Equivalent circuit model analysis on electrochemical impedance spectroscopy of lithium metal batteries”. In: *Journal of Power Sources* 294 (2015), pp. 67–74. ISSN: 0378-7753. DOI: <https://doi.org/10.1016/j.jpowsour.2015.06.032>. URL: <http://www.sciencedirect.com/science/article/pii/S0378775315010666>.
- [161] C. de Beer, P. S. Barendse, and P. Pillay. “Fuel Cell Condition Monitoring Using Optimized Broadband Impedance Spectroscopy”. In: *IEEE Transactions on Industrial Electronics* 62.8 (2015), pp. 5306–5316. ISSN: 0278-0046. DOI: [10.1109/TIE.2015.2418313](https://doi.org/10.1109/TIE.2015.2418313).
- [162] *Project HEALTH-CODE. Real operation pem fuel cells HEALTH-state monitoring and diagnosis based on dc-dc Converter embedded EIS. H2020-JTI-FCH-2014-1*. [Online]. Available: <http://www.pemfc.health-code.eu>.
- [163] S. Kouro et al. “Grid-Connected Photovoltaic Systems: An Overview of Recent Research and Emerging PV Converter Technology”. In: *IEEE Industrial Electronics Magazine* 9.1 (2015), pp. 47–61. ISSN: 1932-4529. DOI: [10.1109/MIE.2014.2376976](https://doi.org/10.1109/MIE.2014.2376976).
- [164] B. Zhao et al. “Overview of Dual-Active-Bridge Isolated Bidirectional DC–DC Converter for High-Frequency-Link Power-Conversion System”. In: *IEEE Transactions on Power Electronics* 29.8 (2014), pp. 4091–4106. ISSN: 0885-8993. DOI: [10.1109/TPEL.2013.2289913](https://doi.org/10.1109/TPEL.2013.2289913).
- [165] R. W. de Doncker, D. M. Divan, and M. H. Kheraluwala. “A three-phase soft-switched high power density DC/DC converter for high power applications”. In: *Conference Record of the 1988 IEEE Industry Applications Society Annual Meeting* (1988), 796–805 vol.1.

- [166] Z. Wang and H. Li. “A Soft Switching Three-phase Current-fed Bidirectional DC-DC Converter With High Efficiency Over a Wide Input Voltage Range”. In: *IEEE Transactions on Power Electronics* 27.2 (2012), pp. 669–684. ISSN: 0885-8993. DOI: [10.1109/TPEL.2011.2160284](https://doi.org/10.1109/TPEL.2011.2160284).
- [167] Nicola Femia et al. *Power electronics and control techniques for maximum energy harvesting in photovoltaic systems*. CRC press, 2012.
- [168] James M. Eyer and Garth P. Corey. “Energy storage for the electricity grid : benefits and market potential assessment guide : a study for the DOE Energy Storage Systems Program.” In: (). DOI: [10.2172/1031895](https://doi.org/10.2172/1031895).
- [169] FERC Order 755. *Implementation of Order 755 market design*. URL: <https://www.caiso.com/Documents/FERCOrderNo755TechnicalPaper.pdf>.
- [170] “”Vanadium Redox Flow Batteries An In-Depth Analysis ””. In: *Electric Power Research Institute (EPRI), Palo Alto, CA, USA, TN 1014836* ().
- [171] B. R. Chalamala et al. “Redox Flow Batteries: An Engineering Perspective”. In: *Proceedings of the IEEE* 102.6 (2014), pp. 976–999. ISSN: 0018-9219. DOI: [10.1109/JPROC.2014.2320317](https://doi.org/10.1109/JPROC.2014.2320317).
- [172] Carl Johan Rydh. “Environmental assessment of vanadium redox and lead-acid batteries for stationary energy storage”. In: *Journal of Power Sources* 80.1 (1999), pp. 21–29. ISSN: 0378-7753. DOI: [https://doi.org/10.1016/S0378-7753\(98\)00249-3](https://doi.org/10.1016/S0378-7753(98)00249-3). URL: <http://www.sciencedirect.com/science/article/pii/S0378775398002493>.
- [173] Selina Weber et al. “Life Cycle Assessment of a Vanadium Redox Flow Battery”. In: *Environmental Science & Technology* 52.18 (2018). PMID: 30132664, pp. 10864–10873. DOI: [10.1021/acs.est.8b02073](https://doi.org/10.1021/acs.est.8b02073). eprint: <https://doi.org/10.1021/acs.est.8b02073>. URL: <https://doi.org/10.1021/acs.est.8b02073>.
- [174] David R. Conover et al. “Protocol for Uniformly Measuring and Expressing the Performance of Energy Storage Systems”. In: (). DOI: [10.2172/1136613](https://doi.org/10.2172/1136613).
- [175] Kenneth Michaels and Gene Hall. “Cost projections for redox energy storage systems”. In: (1980).
- [176] Vilayanur Viswanathan et al. “Cost and performance model for redox flow batteries”. In: *Journal of Power Sources* 247 (2014), pp. 1040–1051. ISSN: 0378-7753. DOI: <https://doi.org/10.1016/j.jpowsour.2012.12.023>. URL: <http://www.sciencedirect.com/science/article/pii/S0378775312018691>.
- [177] Christine Minke, Ulrich Kunz, and Thomas Turek. “Techno-economic assessment of novel vanadium redox flow batteries with large-area cells”. In: *Journal of Power Sources* 361 (2017), pp. 105–114. ISSN: 0378-7753. DOI: <https://doi.org/10.1016/j.jpowsour.2017.06.066>. URL: <http://www.sciencedirect.com/science/article/pii/S0378775317308492>.
- [178] Christine Minke et al. “Cost and performance prospects for composite bipolar plates in fuel cells and redox flow batteries”. In: *Journal of Power Sources* 305 (2016), pp. 182–190. ISSN: 0378-7753. DOI: <https://doi.org/10.1016/j.jpowsour.2015.11.052>. URL: <http://www.sciencedirect.com/science/article/pii/S0378775315305504>.
- [179] *Thyssenkrupp Industrial Solutions AG, Megawatt Electricity Storage System for the Transition to Renewables 2016, (Accessed 13 March 2017)*. URL: <https://www.thyssenkrupp.com/en/newsroom/press-releases/press-release-47650.html>.
- [180] Christine Minke and Thomas Turek. “Economics of vanadium redox flow battery membranes”. In: *Journal of Power Sources* 286 (2015), pp. 247–257. ISSN: 0378-7753. DOI: <https://doi.org/10.1016/j.jpowsour.2015.03.144>. URL: <http://www.sciencedirect.com/science/article/pii/S0378775315005686>.
- [181] USA. Richland WA. *Interactive tool estimates capital costs for redox flow batteries*. URL: http://energyenvironment.pnnl.gov/highlights/9_13_redox.asp.
- [182] *PNNL-OE-Redox-Flow-Battery-Cost-Tool*. URL: [Available:https://github.com/](https://github.com/).

- [183] C. Minke and T. Turek. “Technology cycle analysis for emerging technologies on the example of the vanadium redox flow battery”. In: *2014 World Automation Congress (WAC)*. 2014, pp. 382–387. DOI: [10.1109/WAC.2014.6935957](https://doi.org/10.1109/WAC.2014.6935957).
- [184] Sandia Corporation, *DOE Global Energy Storage Database*, (Accessed 8 February 2016). URL: <http://www.energystorageexchange.org>.
- [185] A. Shibata. “Development of vanadium redox flow battery for electricity storage”. English. In: *Power Engineering Journal* 13 (3 1999), 130–135(5). ISSN: 0950-3366. URL: https://digital-library.theiet.org/content/journals/10.1049/pe_19990305.
- [186] T. Shigematsu et al. “Applications of a vanadium redox-flow battery to maintain power quality”. In: *IEEE/PES Transmission and Distribution Conference and Exhibition*. Vol. 2. 2002, 1065–1070 vol.2. DOI: [10.1109/TDC.2002.1177625](https://doi.org/10.1109/TDC.2002.1177625).
- [187] T. Hennessy and M. Kuntz. *Flow Battery Storage Application with Wind Power*. Undetermined. DOI: [10.1109/TDC.2006.1668626](https://doi.org/10.1109/TDC.2006.1668626).
- [188] McDowell. *International renewable energy storage conference*.
- [189] St. John Jeff Wesoff Eric. *Largest Capacity Flow Battery in North America and EU Is On-Line and Commissioned*. URL: <https://www.greentechmedia.com/articles/read/largest-capacity-flow-battery-in-north-america-and-eu-is-online-and-commiss#gs.ldd8xz>.
- [190] Mike Stone. *A Look at the Biggest Energy Storage Projects Built Around the World in the Last Year*. URL: <https://www.greentechmedia.com/articles/read/a-look-at-the-biggest-energy-storage-projects-built-around-the-world-in-the#gs.ldhh2e>.
- [191] *UET and Snohomish County PUD Dedicate the World’s Largest Capacity Containerized Flow Battery*, *Energy Storage News* (2017). URL: <http://energystorage.org/news/esa-news/uet-and-snohomish-county-pud-dedicate-worlds-largest-capacity-containerized-flow>.
- [192] Herald. *PUD invests \$11.2 million in energy-storing units (2017)*. URL: <https://www.waseniiorlobby.org/pud-invests-11-2-million-in-energy-storing-units/>.
- [193] *SDG and Sumitomo unveil largest vanadium redox flow battery in the US*, *Energy Storage News* (2017). URL: <https://www.energy-storage.news/news/sdge-and-sumitomo-unveil-largest-vanadium-redox-flow-battery-in-the-us>.
- [194] Massimo Guarnieri et al. “Developing vanadium redox flow technology on a 9-kW 26-kWh industrial scale test facility: Design review and early experiments”. In: *Applied Energy* 230 (2018), pp. 1425–1434. ISSN: 0306-2619. DOI: <https://doi.org/10.1016/j.apenergy.2018.09.021>. URL: <http://www.sciencedirect.com/science/article/pii/S0306261918313291>.
- [195] Shuhei Maeda, Jun Sugawara, and Hiroshi Hayami. *Bipolar plate for redox flow battery*. US Patent App. 13/641,651. 2013.
- [196] Á. Frías-Ferrer et al. “The effects of manifold flow on mass transport in electrochemical filter-press reactors”. In: *AIChE Journal* 54.3 (2008), pp. 811–823. DOI: [10.1002/aic.11426](https://doi.org/10.1002/aic.11426). eprint: <https://aiche.onlinelibrary.wiley.com/doi/pdf/10.1002/aic.11426>. URL: <https://aiche.onlinelibrary.wiley.com/doi/abs/10.1002/aic.11426>.
- [197] Jose González-García et al. “Development of a model for the characterization of fluid dispersion in electrochemical reactors”. In: *Journal of Hydroinformatics* 4.4 (2002), pp. 281–295.
- [198] Chih-Hsun Chang et al. “Development of Integrally Molded Bipolar Plates for All-Vanadium Redox Flow Batteries”. In: *Energies* 9.5 (2016). ISSN: 1996-1073. DOI: [10.3390/en9050350](https://doi.org/10.3390/en9050350). URL: <https://www.mdpi.com/1996-1073/9/5/350>.
- [199] Soowhan Kim et al. “1 kW/1 kWh advanced vanadium redox flow battery utilizing mixed acid electrolytes”. In: *Journal of Power Sources* 237 (2013), pp. 300–309. ISSN: 0378-7753. DOI: <https://doi.org/10.1016/j.jpowsour.2013.02.045>. URL: <http://www.sciencedirect.com/science/article/pii/S0378775313003182>.

- [200] Nam Soohyun et al. “Smart cure cycle for reducing the thermal residual stress of a co-cured E-glass/carbon/epoxy composite structure for a vanadium redox flow battery”. In: *Composite Structures* 120 (2015), pp. 107–116. ISSN: 0263-8223. DOI: <https://doi.org/10.1016/j.compstruct.2014.09.037>. URL: <http://www.sciencedirect.com/science/article/pii/S0263822314004851>.
- [201] Peng Qian et al. “A novel electrode-bipolar plate assembly for vanadium redox flow battery applications”. In: *Journal of Power Sources* 175.1 (2008), pp. 613–620. DOI: [10.1016/j.jpowsour.2007.09.006](https://doi.org/10.1016/j.jpowsour.2007.09.006). URL: <https://doi.org/10.1016%2Fj.jpowsour.2007.09.006>.
- [202] Duncan Guy Clark, Stephen Hampden Joseph, and Stewart Ernest Male. *Method for the fabrication of electrochemical cells*. US Patent 6,086,643. 2000.
- [203] L. F. Arenas, F. C. Walsh, and C. Ponce de León. “3D-Printing of Redox Flow Batteries for Energy Storage: A Rapid Prototype Laboratory Cell”. In: *ECS Journal of Solid State Science and Technology* 4.4 (2015), P3080–P3085. DOI: [10.1149/2.0141504jss](https://doi.org/10.1149/2.0141504jss). eprint: <http://jss.ecsdl.org/content/4/4/P3080.full.pdf+html>. URL: <http://jss.ecsdl.org/content/4/4/P3080.abstract>.
- [204] Susanta Mitra et al. “An investigation on changes in chemical properties of pure ethylene-propylene-diene rubber in aqueous acidic environments”. In: *Materials Chemistry and Physics* 98.2 (2006), pp. 248–255. ISSN: 0254-0584. DOI: <https://doi.org/10.1016/j.matchemphys.2005.09.028>. URL: <http://www.sciencedirect.com/science/article/pii/S0254058405006358>.
- [205] M Schulze et al. “Degradation of sealings for PEFC test cells during fuel cell operation”. In: *Journal of Power Sources* 127.1 (2004). Eighth Ulmer Electrochemische Tage, pp. 222–229. ISSN: 0378-7753. DOI: <https://doi.org/10.1016/j.jpowsour.2003.09.017>. URL: <http://www.sciencedirect.com/science/article/pii/S0378775303009558>.
- [206] Guo Li, Jinzhu Tan, and Jianming Gong. “Degradation of the elastomeric gasket material in a simulated and four accelerated proton exchange membrane fuel cell environments”. In: *Journal of Power Sources* 205 (2012), pp. 244–251. ISSN: 0378-7753. DOI: <https://doi.org/10.1016/j.jpowsour.2011.06.092>. URL: <http://www.sciencedirect.com/science/article/pii/S0378775311013292>.
- [207] Peng Liang et al. “Structure failure of the sealing in the assembly process for proton exchange membrane fuel cells”. In: *International Journal of Hydrogen Energy* 42.15 (2017), pp. 10217–10227. ISSN: 0360-3199. DOI: <https://doi.org/10.1016/j.ijhydene.2017.01.026>. URL: <http://www.sciencedirect.com/science/article/pii/S0360319917300472>.
- [208] Jinzhu Tan et al. “Chemical and mechanical stability of EPDM in a PEM fuel cell environment”. In: *Polymer Degradation and Stability* 94.11 (2009), pp. 2072–2078. ISSN: 0141-3910. DOI: <https://doi.org/10.1016/j.polydegradstab.2009.07.009>. URL: <http://www.sciencedirect.com/science/article/pii/S0141391009002547>.
- [209] Tong Cui, Y.J. Chao, and J.W. Van Zee. “Stress relaxation behavior of EPDM seals in polymer electrolyte membrane fuel cell environment”. In: *International Journal of Hydrogen Energy* 37.18 (2012). ICCE-2011, pp. 13478–13483. ISSN: 0360-3199. DOI: <https://doi.org/10.1016/j.ijhydene.2012.06.098>. URL: <http://www.sciencedirect.com/science/article/pii/S0360319912015169>.
- [210] Danick Reynard et al. “On-Site Purification of Copper-Contaminated Vanadium Electrolytes by using a Vanadium Redox Flow Battery”. In: *ChemSusChem* (2019).
- [211] In: *US2016/0149236A1, Proxima S.r.l., author=Angelo D’Anzi, year=2016, ()*.
- [212] Thomas A. Zawodzinski et al. “Water Uptake by and Transport Through Nafion® 117 Membranes”. In: *Journal of The Electrochemical Society* 140.4 (1993), pp. 1041–1047. DOI: [10.1149/1.2056194](https://doi.org/10.1149/1.2056194). eprint: <http://jes.ecsdl.org/content/140/4/1041.full.pdf+html>. URL: <http://jes.ecsdl.org/content/140/4/1041.abstract>.

- [213] T. Mohammadi, S.C. Chieng, and M. Skyllas Kazacos. “Water transport study across commercial ion exchange membranes in the vanadium redox flow battery”. In: *Journal of Membrane Science* 133.2 (1997), pp. 151–159. ISSN: 0376-7388. DOI: [https://doi.org/10.1016/S0376-7388\(97\)00092-6](https://doi.org/10.1016/S0376-7388(97)00092-6). URL: <http://www.sciencedirect.com/science/article/pii/S0376738897000926>.
- [214] Theresa Sukkar and Maria Skyllas-Kazacos. “Water transfer behaviour across cation exchange membranes in the vanadium redox battery”. In: *Journal of Membrane Science* 222.1 (2003), pp. 235–247. ISSN: 0376-7388. DOI: [https://doi.org/10.1016/S0376-7388\(03\)00309-0](https://doi.org/10.1016/S0376-7388(03)00309-0). URL: <http://www.sciencedirect.com/science/article/pii/S0376738803003090>.
- [215] Frank C Walsh. *A first course in electrochemical engineering*. Electrochemical consultancy, 1993.
- [216] Sara Corcuera and Maria Skyllas-Kazacos. “State-of-charge monitoring and electrolyte rebalancing methods for the vanadium redox flow battery”. In: *European Chemical Bulletin* 1.12 (2012), pp. 511–519.
- [217] Lawrence H Thaller. “Electrochemical cell for rebalancing redox flow system”. In: (1979).
- [218] Véronique Amstutz et al. “Renewable hydrogen generation from a dual-circuit redox flow battery”. In: *Energy Environ. Sci.* 7 (7 2014), pp. 2350–2358. DOI: [10.1039/C4EE00098F](https://doi.org/10.1039/C4EE00098F). URL: <http://dx.doi.org/10.1039/C4EE00098F>.
- [219] K.W. Knehr and E.C. Kumbur. “Open circuit voltage of vanadium redox flow batteries: Discrepancy between models and experiments”. In: *Electrochemistry Communications* 13.4 (2011), pp. 342–345. ISSN: 1388-2481. DOI: <https://doi.org/10.1016/j.elecom.2011.01.020>. URL: <http://www.sciencedirect.com/science/article/pii/S1388248111000336>.
- [220] Zhijiang Tang et al. “Monitoring the State of Charge of Operating Vanadium Redox Flow Batteries”. In: *ECS Transactions* 41.23 (2012), pp. 1–9. DOI: [10.1149/1.3697449](https://doi.org/10.1149/1.3697449). eprint: <http://ecst.ecsdl.org/content/41/23/1.full.pdf+html>. URL: <http://ecst.ecsdl.org/content/41/23/1.abstract>.
- [221] Maria Skyllas-Kazacos and Michael Kazacos. “State of charge monitoring methods for vanadium redox flow battery control”. In: *Journal of Power Sources* 196.20 (2011), pp. 8822–8827. ISSN: 0378-7753. DOI: <https://doi.org/10.1016/j.jpowsour.2011.06.080>. URL: <http://www.sciencedirect.com/science/article/pii/S0378775311013176>.
- [222] D. Noel Buckley et al. “Towards Optical Monitoring of Vanadium Redox Flow Batteries (VRFBs): An Investigation of the Underlying Spectroscopy”. In: *Journal of The Electrochemical Society* 161.4 (2014), A524–A534. DOI: [10.1149/2.023404jes](https://doi.org/10.1149/2.023404jes). eprint: <http://jes.ecsdl.org/content/161/4/A524.full.pdf+html>. URL: <http://jes.ecsdl.org/content/161/4/A524.abstract>.
- [223] Cattleya Petchsingh et al. “Spectroscopic Measurement of State of Charge in Vanadium Flow Batteries with an Analytical Model of VIV-VV Absorbance”. In: *Journal of The Electrochemical Society* 163.1 (2016), A5068–A5083. DOI: [10.1149/2.0091601jes](https://doi.org/10.1149/2.0091601jes). eprint: <http://jes.ecsdl.org/content/163/1/A5068.full.pdf+html>. URL: <http://jes.ecsdl.org/content/163/1/A5068.abstract>.
- [224] Wenhong Zhang, Le Liu, and Lin Liu. “An on-line spectroscopic monitoring system for the electrolytes in vanadium redox flow batteries”. In: *RSC Adv.* 5 (121 2015), pp. 100235–100243. DOI: [10.1039/C5RA21844F](https://doi.org/10.1039/C5RA21844F). URL: <http://dx.doi.org/10.1039/C5RA21844F>.
- [225] Le Liu et al. “Rapid detection of the positive side reactions in vanadium flow batteries”. In: *Applied Energy* 185 (2017), pp. 452–462. ISSN: 0306-2619. DOI: <https://doi.org/10.1016/j.apenergy.2016.10.141>. URL: <http://www.sciencedirect.com/science/article/pii/S0306261916314805>.

- [226] Le Liu et al. “State of charge monitoring for vanadium redox flow batteries by the transmission spectra of V(IV)/V(V) electrolytes”. In: *Journal of Applied Electrochemistry* 42.12 (2012), pp. 1025–1031. ISSN: 1572-8838. DOI: [10.1007/s10800-012-0477-2](https://doi.org/10.1007/s10800-012-0477-2). URL: <https://doi.org/10.1007/s10800-012-0477-2>.
- [227] S. Rudolph et al. “High resolution state of charge monitoring of vanadium electrolytes with IR optical sensor”. In: *Journal of Electroanalytical Chemistry* 694 (2013), pp. 17–22. ISSN: 1572-6657. DOI: <https://doi.org/10.1016/j.jelechem.2013.01.042>. URL: <http://www.sciencedirect.com/science/article/pii/S1572665713000763>.
- [228] Simon Ressel et al. “State of charge monitoring of vanadium redox flow batteries using half cell potentials and electrolyte density”. In: *Journal of Power Sources* 378 (2018), pp. 776–783. ISSN: 0378-7753. DOI: <https://doi.org/10.1016/j.jpowsour.2018.01.006>. URL: <http://www.sciencedirect.com/science/article/pii/S0378775318300065>.
- [229] Xiangrong Li et al. “Investigation of the use of electrolyte viscosity for online state-of-charge monitoring design in vanadium redox flow battery”. In: *Applied Energy* 211 (2018), pp. 1050–1059. ISSN: 0306-2619. DOI: <https://doi.org/10.1016/j.apenergy.2017.12.009>. URL: <http://www.sciencedirect.com/science/article/pii/S0306261917317221>.
- [230] Yi-Sin Chou et al. “A novel ultrasonic velocity sensing approach to monitoring state of charge of vanadium redox flow battery”. In: *Applied Energy* 182 (2016), pp. 253–259. ISSN: 0306-2619. DOI: <https://doi.org/10.1016/j.apenergy.2016.08.125>. URL: <http://www.sciencedirect.com/science/article/pii/S0306261916312259>.
- [231] Kittima Ngamsai and Amornchai Arpornwichanop. “Measuring the state of charge of the electrolyte solution in a vanadium redox flow battery using a four-pole cell device”. In: *Journal of Power Sources* 298 (2015), pp. 150–157. ISSN: 0378-7753. DOI: <https://doi.org/10.1016/j.jpowsour.2015.08.026>. URL: <http://www.sciencedirect.com/science/article/pii/S0378775315301804>.
- [232] Zhongbao Wei et al. “Real-time monitoring of capacity loss for vanadium redox flow battery”. In: *Journal of Power Sources* 390 (2018), pp. 261–269. ISSN: 0378-7753. DOI: <https://doi.org/10.1016/j.jpowsour.2018.04.063>. URL: <http://www.sciencedirect.com/science/article/pii/S0378775318304063>.
- [233] Zhongbao Wei et al. “Adaptive estimation of state of charge and capacity with online identified battery model for vanadium redox flow battery”. In: *Journal of Power Sources* 332 (2016), pp. 389–398. ISSN: 0378-7753. DOI: <https://doi.org/10.1016/j.jpowsour.2016.09.123>. URL: <http://www.sciencedirect.com/science/article/pii/S037877531631312X>.
- [234] B. Xiong et al. “State of Charge Estimation of Vanadium Redox Flow Battery Based on Sliding Mode Observer and Dynamic Model Including Capacity Fading Factor”. In: *IEEE Transactions on Sustainable Energy* 8.4 (2017), pp. 1658–1667. ISSN: 1949-3029. DOI: [10.1109/TSTE.2017.2699288](https://doi.org/10.1109/TSTE.2017.2699288).
- [235] Isabelle Kroner, Maik Becker, and Thomas Turek. “Monitoring the State of Charge of the Positive Electrolyte in a Vanadium Redox-Flow Battery with a Novel Amperometric Sensor”. In: *Batteries* 5.1 (2019). ISSN: 2313-0105. DOI: [10.3390/batteries5010005](https://doi.org/10.3390/batteries5010005). URL: <http://www.mdpi.com/2313-0105/5/1/5>.
- [236] Shi-Wei Luo, Shyong Lee, and Yiin-Kuen Fuh. “Micro-pillars enhanced all vanadium redox flow batteries and the effect of assembly torque on the electrochemical performance”. In: *Microsystem Technologies* 23.6 (2017), pp. 2065–2074. ISSN: 1432-1858. DOI: [10.1007/s00542-016-2964-6](https://doi.org/10.1007/s00542-016-2964-6). URL: <https://doi.org/10.1007/s00542-016-2964-6>.
- [237] Tong Cui, Y.J. Chao, and J.W. Van Zee. “Sealing force prediction of elastomeric seal material for PEM fuel cell under temperature cycling”. In: *International Journal of Hydrogen Energy* 39.3 (2014), pp. 1430–1438. ISSN: 0360-3199. DOI: <https://doi.org/10.1016/j.ijhydene.2013.10.086>. URL: <http://www.sciencedirect.com/science/article/pii/S0360319913025986>.

- [238] Jinzhu Tan et al. “Degradation of silicone rubber under compression in a simulated PEM fuel cell environment”. In: *Journal of Power Sources* 172.2 (2007), pp. 782–789. ISSN: 0378-7753. DOI: <https://doi.org/10.1016/j.jpowsour.2007.05.026>. URL: <http://www.sciencedirect.com/science/article/pii/S0378775307010154>.
- [239] URL: <http://www.sensorexpert.com/>.
- [240] Ao Tang, Jie Bao, and Maria Skyllas-Kazacos. “Studies on pressure losses and flow rate optimization in vanadium redox flow battery”. In: *Journal of Power Sources* 248 (2014), pp. 154–162. ISSN: 0378-7753. DOI: <https://doi.org/10.1016/j.jpowsour.2013.09.071>. URL: <http://www.sciencedirect.com/science/article/pii/S037877531301567X>.
- [241] Mark Griffiths, Carlos Ponce de León, and Frank C. Walsh. “Mass transport in the rectangular channel of a filter-press electrolyzer (the FM01-LC reactor)”. In: *AIChE Journal* 51.2 (2005), pp. 682–687. DOI: [10.1002/aic.10311](https://doi.org/10.1002/aic.10311). eprint: <https://aiche.onlinelibrary.wiley.com/doi/pdf/10.1002/aic.10311>. URL: <https://aiche.onlinelibrary.wiley.com/doi/abs/10.1002/aic.10311>.
- [242] URL: <http://www.portalehenkel.it/brands/prodotti/index.html?bid=10>.
- [243] A. Price. “A novel approach to utility-scale energy storage”. English. In: *Power Engineering Journal* 13 (3 1999), 122–129(7). ISSN: 0950-3366. URL: https://digital-library.theiet.org/content/journals/10.1049/pe_19990304.
- [244] Hideaki Nakahata et al. “Development of smart grid demonstration systems”. In: *SEI Technical Review* 76 (2013), p. 8.
- [245] Allen-Bradley . Rockwell Software. *Regole generali di cablaggio e messa a terra degli inverter a modulazione di ampiezza degli impulsi (PWM)*. URL: https://literature.rockwellautomation.com/idc/groups/literature/documents/in/drives-in001_-it-p.pdf.
- [246] *bericacavi.com*. URL: <http://www.bericacavi.com/index.php/4-schermati/92-fg7o-h2r-t-0-6-1-kv>.
- [247] *Lectures 32, 33, 34, 35 - Shielding, Padova, author=D. Desideri, year=2016/2017*.
- [248] *Datasheet NI 9207*.
- [249] *Datasheet NI 9209*.
- [250] *Datasheet NI 9216*.
- [251] *Datasheet NI 9263*.
- [252] Rick Bitter, Taqi Mohiuddin, and Matt Nawrocki. *LabVIEW: Advanced programming techniques*. Crc Press, 2006.
- [253] Bing-cai ZHANG et al. “data acquisition and signal analysis based on labview [J]”. In: *Instrument technique and sensor* 12 (2007), pp. 74–75.
- [254] LabVIEW Core. “Course Manual”. In: *National Instruments* (1).
- [255] I. M. Bayanov and R. Vanhaelst. “The numerical simulation of vanadium RedOx flow batteries”. In: *Journal of Mathematical Chemistry* 49.9 (2011), pp. 2013–2031. ISSN: 1572-8897. DOI: [10.1007/s10910-011-9872-x](https://doi.org/10.1007/s10910-011-9872-x). URL: <https://doi.org/10.1007/s10910-011-9872-x>.
- [256] Q. Xu and T.S. Zhao. “Fundamental models for flow batteries”. In: *Progress in Energy and Combustion Science* 49 (2015), pp. 40–58. ISSN: 0360-1285. DOI: <https://doi.org/10.1016/j.pecs.2015.02.001>. URL: <http://www.sciencedirect.com/science/article/pii/S036012851500012X>.
- [257] A.A. Shah, M.J. Watt-Smith, and F.C. Walsh. “A dynamic performance model for redox-flow batteries involving soluble species”. In: *Electrochimica Acta* 53.27 (2008), pp. 8087–8100. ISSN: 0013-4686. DOI: <https://doi.org/10.1016/j.electacta.2008.05.067>. URL: <http://www.sciencedirect.com/science/article/pii/S0013468608007214>.

- [258] A. A. Shah et al. “A Dynamic Unit Cell Model for the All-Vanadium Flow Battery”. In: *Journal of The Electrochemical Society* 158.6 (2011), A671–A677. DOI: [10.1149/1.3561426](https://doi.org/10.1149/1.3561426). eprint: <http://jes.ecsdl.org/content/158/6/A671.full.pdf+html>. URL: <http://jes.ecsdl.org/content/158/6/A671.abstract>.
- [259] A.A. Shah, H. Al-Fetlawi, and F.C. Walsh. “Dynamic modelling of hydrogen evolution effects in the all-vanadium redox flow battery”. In: *Electrochimica Acta* 55.3 (2010), pp. 1125–1139. ISSN: 0013-4686. DOI: <https://doi.org/10.1016/j.electacta.2009.10.022>. URL: <http://www.sciencedirect.com/science/article/pii/S001346860901295X>.
- [260] H. Al-Fetlawi, A.A. Shah, and F.C. Walsh. “Modelling the effects of oxygen evolution in the all-vanadium redox flow battery”. In: *Electrochimica Acta* 55.9 (2010), pp. 3192–3205. ISSN: 0013-4686. DOI: <https://doi.org/10.1016/j.electacta.2009.12.085>. URL: <http://www.sciencedirect.com/science/article/pii/S0013468610000344>.
- [261] H. Al-Fetlawi, A.A. Shah, and F.C. Walsh. “Non-isothermal modelling of the all-vanadium redox flow battery”. In: *Electrochimica Acta* 55.1 (2009), pp. 78–89. ISSN: 0013-4686. DOI: <https://doi.org/10.1016/j.electacta.2009.08.009>. URL: <http://www.sciencedirect.com/science/article/pii/S0013468609010524>.
- [262] Fernando F. Rivera et al. “The filter-press FM01-LC laboratory flow reactor and its applications”. In: *Electrochimica Acta* 163 (2015), pp. 338–354. ISSN: 0013-4686. DOI: <https://doi.org/10.1016/j.electacta.2015.02.179>. URL: <http://www.sciencedirect.com/science/article/pii/S0013468615005009>.
- [263] Tzayam Pérez et al. “Simulation of current distribution along a planar electrode under turbulent flow conditions in a laboratory filter-press flow cell”. In: *Electrochimica Acta* 154 (2015), pp. 352–360. ISSN: 0013-4686. DOI: <https://doi.org/10.1016/j.electacta.2014.11.166>. URL: <http://www.sciencedirect.com/science/article/pii/S0013468614023962>.
- [264] Roman Kodým et al. “Novel approach to mathematical modeling of the complex electrochemical systems with multiple phase interfaces”. In: *Electrochimica Acta* 179 (2015). Ubiquitus Electrochemistry, pp. 538–555. ISSN: 0013-4686. DOI: <https://doi.org/10.1016/j.electacta.2015.01.039>. URL: <http://www.sciencedirect.com/science/article/pii/S0013468615000596>.
- [265] Donald F Young et al. *A brief introduction to fluid mechanics*. John Wiley & Sons, 2010.
- [266] Maria Skyllas-Kazacos et al. “The Mechanism and Modelling of Shunt Current in the Vanadium Redox Flow Battery”. In: *ChemistrySelect* 1.10 (), pp. 2249–2256. DOI: [10.1002/slct.201600432](https://doi.org/10.1002/slct.201600432). eprint: <https://onlinelibrary.wiley.com/doi/pdf/10.1002/slct.201600432>. URL: <https://onlinelibrary.wiley.com/doi/abs/10.1002/slct.201600432>.
- [267] Y. S. Tsou. “Current Leakage Through Cascaded Cells”. In: *Transactions of The Electrochemical Society* 82.1 (1942), pp. 353–364. DOI: [10.1149/1.3071420](https://doi.org/10.1149/1.3071420). eprint: <http://jes.ecsdl.org/content/82/1/353.full.pdf+html>. URL: <http://jes.ecsdl.org/content/82/1/353.abstract>.
- [268] E. A. Kaminski and R. F. Savinell. “A Technique for Calculating Shunt Leakage and Cell Currents in Bipolar Stacks Having Divided or Undivided Cells”. In: *Journal of The Electrochemical Society* 130.5 (1983), pp. 1103–1107. DOI: [10.1149/1.2119891](https://doi.org/10.1149/1.2119891). eprint: <http://jes.ecsdl.org/content/130/5/1103.full.pdf+html>. URL: <http://jes.ecsdl.org/content/130/5/1103.abstract>.
- [269] S.K. Rangarajan and V. Yegnanarayanan. “Current losses in a bipolar cell—an analysis of the Tafel regime”. In: *Electrochimica Acta* 42.1 (1997), pp. 153–165. ISSN: 0013-4686. DOI: [https://doi.org/10.1016/0013-4686\(96\)00165-X](https://doi.org/10.1016/0013-4686(96)00165-X). URL: <http://www.sciencedirect.com/science/article/pii/S001346869600165X>.

- [270] H. S. Burney and R. E. White. “Predicting Shunt Currents in Stacks of Bipolar Plate Cells with Conducting Manifolds”. In: *Journal of The Electrochemical Society* 135.7 (1988), pp. 1609–1612. DOI: [10.1149/1.2096069](https://doi.org/10.1149/1.2096069). eprint: <http://jes.ecsdl.org/content/135/7/1609.full.pdf+html>. URL: <http://jes.ecsdl.org/content/135/7/1609.abstract>.
- [271] H. Fink and M. Remy. “Shunt currents in vanadium flow batteries: Measurement, modelling and implications for efficiency”. In: *Journal of Power Sources* 284 (2015), pp. 547–553. ISSN: 0378-7753. DOI: <https://doi.org/10.1016/j.jpowsour.2015.03.057>. URL: <http://www.sciencedirect.com/science/article/pii/S0378775315004735>.
- [272] I. Roušar and V. Cezner. “Experimental Determination and Calculation of Parasitic Currents in Bipolar Electrolyzers with Application to Chlorate Electrolyzer”. In: *Journal of The Electrochemical Society* 121.5 (1974), pp. 648–651. DOI: [10.1149/1.2401878](https://doi.org/10.1149/1.2401878). eprint: <http://jes.ecsdl.org/content/121/5/648.full.pdf+html>. URL: <http://jes.ecsdl.org/content/121/5/648.abstract>.
- [273] Harvey N. Seiger. “Leakage Current in Electrochemical Systems Having Common Electrolyte Paths: I. Experimental Measurements”. In: *Journal of The Electrochemical Society* 133.10 (1986), pp. 2002–2007. DOI: [10.1149/1.2108329](https://doi.org/10.1149/1.2108329). eprint: <http://jes.ecsdl.org/content/133/10/2002.full.pdf+html>. URL: <http://jes.ecsdl.org/content/133/10/2002.abstract>.
- [274] Ge Zhou, Lea-Der Chen, and James P. Seaba. “CFD prediction of shunt currents present in alkaline fuel cells”. In: *Journal of Power Sources* 196.20 (2011), pp. 8180–8187. ISSN: 0378-7753. DOI: <https://doi.org/10.1016/j.jpowsour.2011.04.029>. URL: <http://www.sciencedirect.com/science/article/pii/S0378775311008676>.
- [275] G.F. McLean et al. “An assessment of alkaline fuel cell technology”. In: *International Journal of Hydrogen Energy* 27.5 (2002), pp. 507–526. ISSN: 0360-3199. DOI: [https://doi.org/10.1016/S0360-3199\(01\)00181-1](https://doi.org/10.1016/S0360-3199(01)00181-1). URL: <http://www.sciencedirect.com/science/article/pii/S0360319901001811>.
- [276] Jeremy A. Schaeffer, Lea-Der Chen, and James P. Seaba. “Shunt current calculation of fuel cell stack using Simulink®”. In: *Journal of Power Sources* 182.2 (2008). Selected papers from the International Workshop on Degradation Issues in Fuel Cells, pp. 599–602. ISSN: 0378-7753. DOI: <https://doi.org/10.1016/j.jpowsour.2008.04.014>. URL: <http://www.sciencedirect.com/science/article/pii/S0378775308007234>.
- [277] Yong-Song Chen et al. “Modeling the effect of shunt current on the charge transfer efficiency of an all-vanadium redox flow battery”. In: *Journal of Power Sources* 390 (2018), pp. 168–175. ISSN: 0378-7753. DOI: <https://doi.org/10.1016/j.jpowsour.2018.04.042>. URL: <http://www.sciencedirect.com/science/article/pii/S0378775318303859>.
- [278] Feng Xing, Huamin Zhang, and Xiangkun Ma. “Shunt current loss of the vanadium redox flow battery”. In: *Journal of Power Sources* 196.24 (2011), pp. 10753–10757. ISSN: 0378-7753. DOI: <https://doi.org/10.1016/j.jpowsour.2011.08.033>. URL: <http://www.sciencedirect.com/science/article/pii/S0378775311015333>.
- [279] Cong Yin et al. “Numerical and experimental studies of stack shunt current for vanadium redox flow battery”. In: *Applied Energy* 151 (2015), pp. 237–248. ISSN: 0306-2619. DOI: <https://doi.org/10.1016/j.apenergy.2015.04.080>. URL: <http://www.sciencedirect.com/science/article/pii/S0306261915005437>.
- [280] S. König, M.R. Suriyah, and T. Leibfried. “Model based examination on influence of stack series connection and pipe diameters on efficiency of vanadium redox flow batteries under consideration of shunt currents”. In: *Journal of Power Sources* 281 (2015), pp. 272–284. ISSN: 0378-7753. DOI: <https://doi.org/10.1016/j.jpowsour.2015.01.119>. URL: <http://www.sciencedirect.com/science/article/pii/S0378775315001354>.

- [281] Qiang Ye et al. “Design trade-offs among shunt current, pumping loss and compactness in the piping system of a multi-stack vanadium flow battery”. In: *Journal of Power Sources* 296 (2015), pp. 352–364. ISSN: 0378-7753. DOI: <https://doi.org/10.1016/j.jpowsour.2015.06.138>. URL: <http://www.sciencedirect.com/science/article/pii/S0378775315300306>.
- [282] URL: <https://www.comsol.com/>.
- [283] Robert M. Darling et al. “The Influence of Electric Field on Crossover in Redox-Flow Batteries”. In: *Journal of The Electrochemical Society* 163.1 (2016), A5014–A5022. DOI: [10.1149/2.0031601jes](https://doi.org/10.1149/2.0031601jes). eprint: <http://jes.ecsdl.org/content/163/1/A5014.full.pdf+html>. URL: <http://jes.ecsdl.org/content/163/1/A5014.abstract>.
- [284] Jamie S. Lawton, Amanda Jones, and Thomas Zawodzinski. “Concentration Dependence of VO₂⁺ Crossover of Nafion for Vanadium Redox Flow Batteries”. In: *Journal of The Electrochemical Society* 160.4 (2013), A697–A702. DOI: [10.1149/2.004306jes](https://doi.org/10.1149/2.004306jes). eprint: <http://jes.ecsdl.org/content/160/4/A697.full.pdf+html>. URL: <http://jes.ecsdl.org/content/160/4/A697.abstract>.
- [285] E. Wiedemann, A. Heintz, and R.N. Lichtenthaler. “Transport properties of vanadium ions in cation exchange membranes:: Determination of diffusion coefficients using a dialysis cell”. In: *Journal of Membrane Science* 141.2 (1998), pp. 215–221. ISSN: 0376-7388. DOI: [https://doi.org/10.1016/S0376-7388\(97\)00308-6](https://doi.org/10.1016/S0376-7388(97)00308-6). URL: <http://www.sciencedirect.com/science/article/pii/S0376738897003086>.
- [286] Yasser Ashraf Gandomi, D.S. Aaron, and M.M. Mench. “Coupled Membrane Transport Parameters for Ionic Species in All-Vanadium Redox Flow Batteries”. In: *Electrochimica Acta* 218 (2016), pp. 174–190. ISSN: 0013-4686. DOI: <https://doi.org/10.1016/j.electacta.2016.09.087>. URL: <http://www.sciencedirect.com/science/article/pii/S0013468616319880>.
- [287] Xiao-Guang Yang et al. “Effects of the electric field on ion crossover in vanadium redox flow batteries”. In: *Applied Energy* 145 (2015), pp. 306–319. ISSN: 0306-2619. DOI: <https://doi.org/10.1016/j.apenergy.2015.02.038>. URL: <http://www.sciencedirect.com/science/article/pii/S0306261915002159>.
- [288] Ao Tang, Jie Bao, and Maria Skyllas-Kazacos. “Dynamic modelling of the effects of ion diffusion and side reactions on the capacity loss for vanadium redox flow battery”. In: *Journal of Power Sources* 196.24 (2011), pp. 10737–10747. ISSN: 0378-7753. DOI: <https://doi.org/10.1016/j.jpowsour.2011.09.003>. URL: <http://www.sciencedirect.com/science/article/pii/S0378775311017095>.
- [289] Seongyeon Won, Kyeongmin Oh, and Hyunchul Ju. “Numerical analysis of vanadium crossover effects in all-vanadium redox flow batteries”. In: *Electrochimica Acta* 177 (2015). International Conference on Electrochemical Energy Science and Technology (EEST2014), pp. 310–320. ISSN: 0013-4686. DOI: <https://doi.org/10.1016/j.electacta.2015.01.166>. URL: <http://www.sciencedirect.com/science/article/pii/S0013468615002121>.
- [290] Nataliya Roznyatovskaya et al. “Detection of capacity imbalance in vanadium electrolyte and its electrochemical regeneration for all-vanadium redox-flow batteries”. In: *Journal of Power Sources* 302 (2016), pp. 79–83. ISSN: 0378-7753. DOI: <https://doi.org/10.1016/j.jpowsour.2015.10.021>. URL: <http://www.sciencedirect.com/science/article/pii/S0378775315304092>.
- [291] Jingyu Xi et al. “Self-assembled polyelectrolyte multilayer modified Nafion membrane with suppressed vanadium ion crossover for vanadium redox flow batteries”. In: *J. Mater. Chem.* 18 (11 2008), pp. 1232–1238. DOI: [10.1039/B718526J](https://doi.org/10.1039/B718526J). URL: <http://dx.doi.org/10.1039/B718526J>.
- [292] Fabio J. Oldenburg, Thomas J. Schmidt, and Lorenz Gubler. “Tackling capacity fading in vanadium flow batteries with amphoteric membranes”. In: *Journal of Power Sources* 368 (2017), pp. 68–72. ISSN: 0378-7753. DOI: <https://doi.org/10.1016/j.jpowsour.2017.09.051>. URL: <http://www.sciencedirect.com/science/article/pii/S0378775317312703>.

- [293] L. Zeng et al. “Highly stable pyridinium-functionalized cross-linked anion exchange membranes for all vanadium redox flow batteries”. In: *Journal of Power Sources* 331 (2016), pp. 452–461. ISSN: 0378-7753. DOI: <https://doi.org/10.1016/j.jpowsour.2016.09.065>. URL: <http://www.sciencedirect.com/science/article/pii/S0378775316312277>.
- [294] Ao Tang, Jie Bao, and Maria Skyllas-Kazacos. “Thermal modelling of battery configuration and self-discharge reactions in vanadium redox flow battery”. In: *Journal of Power Sources* 216 (2012), pp. 489–501. ISSN: 0378-7753. DOI: <https://doi.org/10.1016/j.jpowsour.2012.06.052>. URL: <http://www.sciencedirect.com/science/article/pii/S037877531201052X>.
- [295] Yifeng Li, Maria Skyllas-Kazacos, and Jie Bao. “A dynamic plug flow reactor model for a vanadium redox flow battery cell”. In: *Journal of Power Sources* 311 (2016), pp. 57–67. ISSN: 0378-7753. DOI: <https://doi.org/10.1016/j.jpowsour.2016.02.018>. URL: <http://www.sciencedirect.com/science/article/pii/S0378775316301264>.
- [296] Yitao Yan et al. “Modelling and simulation of thermal behaviour of vanadium redox flow battery”. In: *Journal of Power Sources* 322 (2016), pp. 116–128. ISSN: 0378-7753. DOI: <https://doi.org/10.1016/j.jpowsour.2016.05.011>. URL: <http://www.sciencedirect.com/science/article/pii/S037877531630547X>.
- [297] Donghyeon Kim and Joonhyeon Jeon. “A high-temperature tolerance solution for positive electrolyte of vanadium redox flow batteries”. In: *Journal of Electroanalytical Chemistry* 801 (2017), pp. 92–97. ISSN: 1572-6657. DOI: <https://doi.org/10.1016/j.jelechem.2017.07.037>. URL: <http://www.sciencedirect.com/science/article/pii/S1572665717305222>.
- [298] Ke Wang et al. “Broad temperature adaptability of vanadium redox flow battery-Part 3: The effects of total vanadium concentration and sulfuric acid concentration”. In: *Electrochimica Acta* 259 (2018), pp. 11–19. ISSN: 0013-4686. DOI: <https://doi.org/10.1016/j.electacta.2017.10.148>. URL: <http://www.sciencedirect.com/science/article/pii/S0013468617322703>.
- [299] Daniela Oboroceanu et al. “Effects of Temperature and Composition on Catholyte Stability in Vanadium Flow Batteries: Measurement and Modeling”. In: *Journal of The Electrochemical Society* 164.9 (2017), A2101–A2109. DOI: [10.1149/2.1401709jes](https://doi.org/10.1149/2.1401709jes). eprint: <http://jes.ecsdl.org/content/164/9/A2101.full.pdf+html>. URL: <http://jes.ecsdl.org/content/164/9/A2101.abstract>.
- [300] M. Kazacos, M. Cheng, and M. Skyllas-Kazacos. “Vanadium redox cell electrolyte optimization studies”. In: *Journal of Applied Electrochemistry* 20.3 (1990), pp. 463–467. ISSN: 1572-8838. DOI: [10.1007/BF01076057](https://doi.org/10.1007/BF01076057). URL: <https://doi.org/10.1007/BF01076057>.
- [301] C. Zhang et al. “Effects of operating temperature on the performance of vanadium redox flow batteries”. In: *Applied Energy* 155 (2015), pp. 349–353. ISSN: 0306-2619. DOI: <https://doi.org/10.1016/j.apenergy.2015.06.002>. URL: <http://www.sciencedirect.com/science/article/pii/S0306261915007473>.
- [302] Seok Woo Lee et al. “An electrochemical system for efficiently harvesting low-grade heat energy”. In: *Nature communications* 5 (2014), p. 3942.
- [303] Danick Reynard et al. “Efficiency improvement of an all-vanadium redox flow battery by harvesting low-grade heat”. In: *Journal of Power Sources* 390 (2018), pp. 30–37. ISSN: 0378-7753. DOI: <https://doi.org/10.1016/j.jpowsour.2018.03.074>. URL: <http://www.sciencedirect.com/science/article/pii/S0378775318303252>.
- [304] Julian Marschewski et al. “3D-printed fluidic networks for high-power-density heat-managing miniaturized redox flow batteries”. In: *Energy Environ. Sci.* 10 (3 2017), pp. 780–787. DOI: [10.1039/C6EE03192G](https://doi.org/10.1039/C6EE03192G). URL: <http://dx.doi.org/10.1039/C6EE03192G>.
- [305] A. A. Andreev et al. “PowerCool: Simulation of Cooling and Powering of 3D MPSoCs with Integrated Flow Cell Arrays”. In: *IEEE Transactions on Computers* 67.1 (2018), pp. 73–85. ISSN: 0018-9340. DOI: [10.1109/TC.2017.2695179](https://doi.org/10.1109/TC.2017.2695179).

- [306] Ankur Bhattacharjee and Hiranmay Saha. “Development of an efficient thermal management system for Vanadium Redox Flow Battery under different charge-discharge conditions”. In: *Applied Energy* 230 (2018), pp. 1182–1192. ISSN: 0306-2619. DOI: <https://doi.org/10.1016/j.apenergy.2018.09.056>. URL: <http://www.sciencedirect.com/science/article/pii/S0306261918313424>.
- [307] Ankur Bhattacharjee et al. “Development and validation of a real time flow control integrated MPPT charger for solar PV applications of vanadium redox flow battery”. In: *Energy Conversion and Management* 171 (2018), pp. 1449–1462. ISSN: 0196-8904. DOI: <https://doi.org/10.1016/j.enconman.2018.06.088>. URL: <http://www.sciencedirect.com/science/article/pii/S0196890418306988>.
- [308] Ao Tang et al. “Investigation of the effect of shunt current on battery efficiency and stack temperature in vanadium redox flow battery”. In: *Journal of Power Sources* 242 (2013), pp. 349–356. ISSN: 0378-7753. DOI: <https://doi.org/10.1016/j.jpowsour.2013.05.079>. URL: <http://www.sciencedirect.com/science/article/pii/S0378775313008690>.
- [309] Binyu Xiong et al. “Thermal hydraulic behavior and efficiency analysis of an all-vanadium redox flow battery”. In: *Journal of Power Sources* 242 (2013), pp. 314–324. ISSN: 0378-7753. DOI: <https://doi.org/10.1016/j.jpowsour.2013.05.092>. URL: <http://www.sciencedirect.com/science/article/pii/S0378775313008823>.
- [310] AL Kraus and Avram Bar-Cohen. *Design and analysis of heat sinks*. Wiley, 1995.
- [311] Zhongbao Wei et al. “Dynamic thermal-hydraulic modeling and stack flow pattern analysis for all-vanadium redox flow battery”. In: *Journal of Power Sources* 260 (2014), pp. 89–99. ISSN: 0378-7753. DOI: <https://doi.org/10.1016/j.jpowsour.2014.02.108>. URL: <http://www.sciencedirect.com/science/article/pii/S0378775314003097>.
- [312] Zhongbao Wei, Jiyun Zhao, and Binyu Xiong. “Dynamic electro-thermal modeling of all-vanadium redox flow battery with forced cooling strategies”. In: *Applied Energy* 135 (2014), pp. 1–10. ISSN: 0306-2619. DOI: <https://doi.org/10.1016/j.apenergy.2014.08.062>. URL: <http://www.sciencedirect.com/science/article/pii/S0306261914008733>.
- [313] Andrea Trovò et al. “Standby thermal model of a vanadium redox flow battery stack with crossover and shunt-current effects”. In: *Applied Energy* 240 (2019), pp. 893–906. ISSN: 0306-2619. DOI: <https://doi.org/10.1016/j.apenergy.2019.02.067>. URL: <http://www.sciencedirect.com/science/article/pii/S0306261919303642>.
- [314] Dong-Jun Park et al. “Performance of the all-vanadium redox flow battery stack”. In: *Journal of Industrial and Engineering Chemistry* 45 (2017), pp. 387–390. ISSN: 1226-086X. DOI: <https://doi.org/10.1016/j.jiec.2016.10.007>. URL: <http://www.sciencedirect.com/science/article/pii/S1226086X16303860>.
- [315] David Reed et al. “Performance of a low cost interdigitated flow design on a 1 kW class all vanadium mixed acid redox flow battery”. In: *Journal of Power Sources* 306 (2016), pp. 24–31. ISSN: 0378-7753. DOI: <https://doi.org/10.1016/j.jpowsour.2015.11.089>. URL: <http://www.sciencedirect.com/science/article/pii/S0378775315305875>.
- [316] Ankur Bhattacharjee and Hiranmay Saha. “Design and experimental validation of a generalised electrical equivalent model of Vanadium Redox Flow Battery for interfacing with renewable energy sources”. In: *Journal of Energy Storage* 13 (2017), pp. 220–232. ISSN: 2352-152X. DOI: <https://doi.org/10.1016/j.est.2017.07.016>. URL: <http://www.sciencedirect.com/science/article/pii/S2352152X17302116>.
- [317] Massimo Guarnieri et al. “A selective hybrid stochastic strategy for fuel-cell multi-parameter identification”. In: *Journal of Power Sources* 332 (2016), pp. 249–264. ISSN: 0378-7753. DOI: <https://doi.org/10.1016/j.jpowsour.2016.09.131>. URL: <http://www.sciencedirect.com/science/article/pii/S0378775316313210>.
- [318] Yifeng Li et al. “Control of electrolyte flow rate for the vanadium redox flow battery by gain scheduling”. In: *Journal of Energy Storage* 14 (2017), pp. 125–133. ISSN: 2352-152X. DOI: <https://doi.org/10.1016/j.est.2017.10.005>. URL: <http://www.sciencedirect.com/science/article/pii/S2352152X1730316X>.

- [319] Tao Wang et al. “Dynamic control strategy for the electrolyte flow rate of vanadium redox flow batteries”. In: *Applied Energy* 227 (2018). Transformative Innovations for a Sustainable Future – Part III, pp. 613–623. ISSN: 0306-2619. DOI: <https://doi.org/10.1016/j.apenergy.2017.07.065>. URL: <http://www.sciencedirect.com/science/article/pii/S0306261917309376>.
- [320] Dong Kyu Kim et al. “Parametric study and flow rate optimization of all-vanadium redox flow batteries”. In: *Applied Energy* 228 (2018), pp. 891–901. ISSN: 0306-2619. DOI: <https://doi.org/10.1016/j.apenergy.2018.06.094>. URL: <http://www.sciencedirect.com/science/article/pii/S0306261918309620>.
- [321] Jiahui Fu et al. “Dynamic Flow Rate Control for Vanadium Redox Flow Batteries”. In: *Energy Procedia* 105 (2017). 8th International Conference on Applied Energy, ICAE2016, 8-11 October 2016, Beijing, China, pp. 4482–4491. ISSN: 1876-6102. DOI: <https://doi.org/10.1016/j.egypro.2017.03.952>. URL: <http://www.sciencedirect.com/science/article/pii/S1876610217310536>.
- [322] Jungmyung Kim and Heesung Park. “Experimental analysis of discharge characteristics in vanadium redox flow battery”. In: *Applied Energy* 206 (2017), pp. 451–457. ISSN: 0306-2619. DOI: <https://doi.org/10.1016/j.apenergy.2017.08.218>. URL: <http://www.sciencedirect.com/science/article/pii/S0306261917312527>.
- [323] Maik Becker et al. “Polarization curve measurements combined with potential probe sensing for determining current density distribution in vanadium redox-flow batteries”. In: *Journal of Power Sources* 307 (2016), pp. 826–833. ISSN: 0378-7753. DOI: <https://doi.org/10.1016/j.jpowsour.2016.01.011>. URL: <http://www.sciencedirect.com/science/article/pii/S0378775316300118>.
- [324] Jens N. Noack et al. “Aging Studies of Vanadium Redox Flow Batteries”. In: *ECS Transactions* 33.39 (2011), pp. 3–9. DOI: [10.1149/1.3589916](https://doi.org/10.1149/1.3589916). eprint: <http://ecst.ecsdl.org/content/33/39/3.full.pdf+html>. URL: <http://ecst.ecsdl.org/content/33/39/3.abstract>.
- [325] Francisco Díaz-González et al. “A review of energy storage technologies for wind power applications”. In: *Renewable and Sustainable Energy Reviews* 16.4 (2012), pp. 2154–2171. ISSN: 1364-0321. DOI: <https://doi.org/10.1016/j.rser.2012.01.029>. URL: <http://www.sciencedirect.com/science/article/pii/S1364032112000305>.
- [326] Alexandre Lucas and Stamatios Chondrogiannis. “Smart grid energy storage controller for frequency regulation and peak shaving, using a vanadium redox flow battery”. In: *International Journal of Electrical Power and Energy Systems* 80 (2016), pp. 26–36. ISSN: 0142-0615. DOI: <https://doi.org/10.1016/j.ijepes.2016.01.025>. URL: <http://www.sciencedirect.com/science/article/pii/S0142061516000375>.
- [327] Y. Hung et al. “Effects of current scan rate on the polarization curve of vanadium redox flow batteries”. In: *2017 International Energy and Sustainability Conference (IESC)*. 2017, pp. 1–4. DOI: [10.1109/IESC.2017.8167489](https://doi.org/10.1109/IESC.2017.8167489).
- [328] Massimo Guarnieri et al. “High current polarization tests on a 9 kW vanadium redox flow battery”. In: *Journal of Power Sources* 431 (2019), pp. 239–249. ISSN: 0378-7753. DOI: <https://doi.org/10.1016/j.jpowsour.2019.05.035>. URL: <http://www.sciencedirect.com/science/article/pii/S0378775319305907>.
- [329] Jen-Yu Chen et al. “Determining the Limiting Current Density of Vanadium Redox Flow Batteries”. In: *Energies* 7.9 (2014), pp. 5863–5873. ISSN: 1996-1073. DOI: [10.3390/en7095863](https://doi.org/10.3390/en7095863). URL: <https://www.mdpi.com/1996-1073/7/9/5863>.
- [330] Xiangkun Ma, Huamin Zhang, and Feng Xing. “A three-dimensional model for negative half cell of the vanadium redox flow battery”. In: *Electrochimica Acta* 58 (2011), pp. 238–246. ISSN: 0013-4686. DOI: <https://doi.org/10.1016/j.electacta.2011.09.042>. URL: <http://www.sciencedirect.com/science/article/pii/S001346861101423X>.

- [331] Ao Tang et al. “Thermal modelling and simulation of the all-vanadium redox flow battery”. In: *Journal of Power Sources* 203 (2012), pp. 165–176. ISSN: 0378-7753. DOI: <https://doi.org/10.1016/j.jpowsour.2011.11.079>. URL: <http://www.sciencedirect.com/science/article/pii/S0378775311023676>.
- [332] Yitao Yan, Maria Skyllas-Kazacos, and Jie Bao. “Effects of battery design, environmental temperature and electrolyte flowrate on thermal behaviour of a vanadium redox flow battery in different applications”. In: *Journal of Energy Storage* 11 (2017), pp. 104–118. ISSN: 2352-152X. DOI: <https://doi.org/10.1016/j.est.2017.01.007>. URL: <http://www.sciencedirect.com/science/article/pii/S2352152X16301293>.
- [333] M.R. Mohamed, P.K. Leung, and M.H. Sulaiman. “Performance characterization of a vanadium redox flow battery at different operating parameters under a standardized test-bed system”. In: *Applied Energy* 137 (2015), pp. 402–412. ISSN: 0306-2619. DOI: <https://doi.org/10.1016/j.apenergy.2014.10.042>. URL: <http://www.sciencedirect.com/science/article/pii/S0306261914010927>.
- [334] Jack P Holman. *Heat Transfer (McGraw-Hill Series in Mechanical Engineering)*. 2010.
- [335] Qiong Zheng et al. “Flow field design and optimization based on the mass transport polarization regulation in a flow-through type vanadium flow battery”. In: *Journal of Power Sources* 324 (2016), pp. 402–411. ISSN: 0378-7753. DOI: <https://doi.org/10.1016/j.jpowsour.2016.05.110>. URL: <http://www.sciencedirect.com/science/article/pii/S0378775316306644>.
- [336] Q. Xu, T.S. Zhao, and C. Zhang. “Performance of a vanadium redox flow battery with and without flow fields”. In: *Electrochimica Acta* 142 (2014), pp. 61–67. ISSN: 0013-4686. DOI: <https://doi.org/10.1016/j.electacta.2014.07.059>. URL: <http://www.sciencedirect.com/science/article/pii/S0013468614014510>.
- [337] Yu Zhang et al. “A comprehensive equivalent circuit model of all-vanadium redox flow battery for power system analysis”. In: *Journal of Power Sources* 290 (2015), pp. 14–24. ISSN: 0378-7753. DOI: <https://doi.org/10.1016/j.jpowsour.2015.04.169>. URL: <http://www.sciencedirect.com/science/article/pii/S037877531500837X>.
- [338] Yifeng Li et al. “Studies on optimal charging conditions for vanadium redox flow batteries”. In: *Journal of Energy Storage* 11 (2017), pp. 191–199. ISSN: 2352-152X. DOI: <https://doi.org/10.1016/j.est.2017.02.008>. URL: <http://www.sciencedirect.com/science/article/pii/S2352152X16301438>.
- [339] C. Blanc and A. Rufer. “Multiphysics and Energetic Modeling of a Vanadium Redox Flow Battery”. In: *2008 IEEE International Conference on Sustainable Energy Technologies*. 2008, pp. 696–701. DOI: [10.1109/ICSET.2008.4747096](https://doi.org/10.1109/ICSET.2008.4747096).
- [340] Bruce R Munson, Donald F Young, and Theodore H Okiishi. “Fundamentals of Fluid Mechanics, John Wiley & Sons”. In: *Inc., USA* (2006).
- [341] URL: [ASVStbbeGmbH&Co.KG, æKugelhahnC200, www.asv-stuebbe.de..](http://www.asv-stuebbe.de)
- [342] Michal Pavelka, Frank Wandschneider, and Petr Mazur. “Thermodynamic derivation of open circuit voltage in vanadium redox flow batteries”. In: *Journal of Power Sources* 293 (2015), pp. 400–408. ISSN: 0378-7753. DOI: <https://doi.org/10.1016/j.jpowsour.2015.05.049>. URL: <http://www.sciencedirect.com/science/article/pii/S0378775315009301>.
- [343] W.W. Yang et al. “Effect of various strategies of soc-dependent operating current on performance of a vanadium redox flow battery”. In: *Electrochimica Acta* 259 (2018), pp. 772–782. ISSN: 0013-4686. DOI: <https://doi.org/10.1016/j.electacta.2017.10.201>. URL: <http://www.sciencedirect.com/science/article/pii/S0013468617323472>.
- [344] Andrea Trovò, Francesco Picano, and Massimo Guarnieri. “Comparison of energy losses in a 9kW vanadium redox flow battery”. In: *Journal of Power Sources* 440 (2019), p. 227144. ISSN: 0378-7753. DOI: <https://doi.org/10.1016/j.jpowsour.2019.227144>. URL: <http://www.sciencedirect.com/science/article/pii/S0378775319311371>.
- [345] Massimo Guarnieri et al. “A Real Multitechnology Microgrid in Venice: A Design Review”. In: *IEEE Industrial Electronics Magazine* 12.3 (2018), pp. 19–31.

- [346] Ertan Agar et al. “Reducing capacity fade in vanadium redox flow batteries by altering charging and discharging currents”. In: *Journal of Power Sources* 246 (2014), pp. 767–774. ISSN: 0378-7753. DOI: <https://doi.org/10.1016/j.jpowsour.2013.08.023>. URL: <http://www.sciencedirect.com/science/article/pii/S0378775313013621>.
- [347] Rajagopalan Badrinarayanan et al. “Modelling and control of vanadium redox flow battery for profile based charging applications”. In: *Energy* 141 (2017), pp. 1479–1488. ISSN: 0360-5442. DOI: <https://doi.org/10.1016/j.energy.2017.11.082>. URL: <http://www.sciencedirect.com/science/article/pii/S0360544217319400>.
- [348] Rajagopalan Badrinarayanan et al. “Extended dynamic model for ion diffusion in all-vanadium redox flow battery including the effects of temperature and bulk electrolyte transfer”. In: *Journal of Power Sources* 270 (2014), pp. 576–586. ISSN: 0378-7753. DOI: <https://doi.org/10.1016/j.jpowsour.2014.07.128>. URL: <http://www.sciencedirect.com/science/article/pii/S0378775314011823>.
- [349] S. Rudolph et al. “Optimal electrolyte flow distribution in hydrodynamic circuit of vanadium redox flow battery”. In: *Journal of Electroanalytical Chemistry* 736 (2015), pp. 117–126. ISSN: 1572-6657. DOI: <https://doi.org/10.1016/j.jelechem.2014.11.004>. URL: <http://www.sciencedirect.com/science/article/pii/S1572665714004895>.
- [350] Q. Xu, T.S. Zhao, and C. Zhang. “Effects of SOC-dependent electrolyte viscosity on performance of vanadium redox flow batteries”. In: *Applied Energy* 130 (2014), pp. 139–147. ISSN: 0306-2619. DOI: <https://doi.org/10.1016/j.apenergy.2014.05.034>. URL: <http://www.sciencedirect.com/science/article/pii/S0306261914005297>.
- [351] W.W. Yang et al. “Effect of various strategies of soc-dependent operating current on performance of a vanadium redox flow battery”. In: *Electrochimica Acta* 259 (2018), pp. 772–782. ISSN: 0013-4686. DOI: <https://doi.org/10.1016/j.electacta.2017.10.201>. URL: <http://www.sciencedirect.com/science/article/pii/S0013468617323472>.
- [352] C.Y. Ling et al. “Pulsating electrolyte flow in a full vanadium redox battery”. In: *Journal of Power Sources* 294 (2015), pp. 305–311. ISSN: 0378-7753. DOI: <https://doi.org/10.1016/j.jpowsour.2015.06.020>. URL: <http://www.sciencedirect.com/science/article/pii/S037877531501054X>.
- [353] Xiangkun Ma et al. “An optimal strategy of electrolyte flow rate for vanadium redox flow battery”. In: *Journal of Power Sources* 203 (2012), pp. 153–158. ISSN: 0378-7753. DOI: <https://doi.org/10.1016/j.jpowsour.2011.11.036>. URL: <http://www.sciencedirect.com/science/article/pii/S037877531102283X>.
- [354] Wenyang Xiao and Lei Tan. “Control strategy optimization of electrolyte flow rate for all vanadium redox flow battery with consideration of pump”. In: *Renewable Energy* 133 (2019), pp. 1445–1454. ISSN: 0960-1481. DOI: <https://doi.org/10.1016/j.renene.2018.09.018>. URL: <http://www.sciencedirect.com/science/article/pii/S0960148118310814>.
- [355] S. König, M.R. Suriyah, and T. Leibfried. “Innovative model-based flow rate optimization for vanadium redox flow batteries”. In: *Journal of Power Sources* 333 (2016), pp. 134–144. ISSN: 0378-7753. DOI: <https://doi.org/10.1016/j.jpowsour.2016.09.147>. URL: <http://www.sciencedirect.com/science/article/pii/S0378775316313386>.
- [356] Y. Ashraf Gandomi et al. “Critical Review—Experimental Diagnostics and Material Characterization Techniques Used on Redox Flow Batteries”. In: *Journal of The Electrochemical Society* 165.5 (2018), A970–A1010. DOI: [10.1149/2.0601805jes](https://doi.org/10.1149/2.0601805jes). eprint: <http://jes.ecsdl.org/content/165/5/A970.full.pdf+html>. URL: <http://jes.ecsdl.org/content/165/5/A970.abstract>.
- [357] Yifeng Li et al. “Studies on dynamic responses and impedance of the vanadium redox flow battery”. In: *Applied Energy* 237 (2019), pp. 91–102. ISSN: 0306-2619. DOI: <https://doi.org/10.1016/j.apenergy.2019.01.015>. URL: <http://www.sciencedirect.com/science/article/pii/S0306261919300157>.

- [358] Jiahui Fu et al. “Flow-Rate Optimization and Economic Analysis of Vanadium Redox Flow Batteries in a Load-Shifting Application”. In: *Journal of Energy Engineering* 143.6 (2017), p. 04017064. DOI: [10.1061/\(ASCE\)EY.1943-7897.0000493](https://doi.org/10.1061/(ASCE)EY.1943-7897.0000493).
- [359] Leonardo J. Ontiveros and Pedro E. Mercado. “Modeling of a Vanadium Redox Flow Battery for power system dynamic studies”. In: *International Journal of Hydrogen Energy* 39.16 (2014), pp. 8720–8727. ISSN: 0360-3199. DOI: <https://doi.org/10.1016/j.ijhydene.2013.12.042>. URL: <http://www.sciencedirect.com/science/article/pii/S0360319913029765>.
- [360] Simon Ressel et al. “Performance of a vanadium redox flow battery with tubular cell design”. In: *Journal of Power Sources* 355 (2017), pp. 199–205. ISSN: 0378-7753. DOI: <https://doi.org/10.1016/j.jpowsour.2017.04.066>. URL: <http://www.sciencedirect.com/science/article/pii/S037877531730561X>.
- [361] M. Pugach, V. Vyshinsky, and A. Bischi. “Energy efficiency analysis for a kilo-watt class vanadium redox flow battery system”. In: *Applied Energy* 253 (2019), p. 113533. ISSN: 0306-2619. DOI: <https://doi.org/10.1016/j.apenergy.2019.113533>. URL: <http://www.sciencedirect.com/science/article/pii/S0306261919312073>.
- [362] Tao Wang et al. “Dynamic control strategy for the electrolyte flow rate of vanadium redox flow batteries”. In: *Applied Energy* 227 (2018). Transformative Innovations for a Sustainable Future – Part III, pp. 613–623. ISSN: 0306-2619. DOI: <https://doi.org/10.1016/j.apenergy.2017.07.065>. URL: <http://www.sciencedirect.com/science/article/pii/S0306261917309376>.
- [363] Binyu Xiong et al. “Thermal hydraulic behavior and efficiency analysis of an all-vanadium redox flow battery”. In: *Journal of Power Sources* 242 (2013), pp. 314–324. ISSN: 0378-7753. DOI: <https://doi.org/10.1016/j.jpowsour.2013.05.092>. URL: <http://www.sciencedirect.com/science/article/pii/S0378775313008823>.
- [364] Ao Tang, Jie Bao, and Maria Skyllas-Kazacos. “Studies on pressure losses and flow rate optimization in vanadium redox flow battery”. In: *Journal of Power Sources* 248 (2014), pp. 154–162. ISSN: 0378-7753. DOI: <https://doi.org/10.1016/j.jpowsour.2013.09.071>. URL: <http://www.sciencedirect.com/science/article/pii/S037877531301567X>.
- [365] Xiaoming Yan et al. “A novel long-side-chain sulfonated poly(2,6-dimethyl-1,4-phenylene oxide) membrane for vanadium redox flow battery”. In: *International Journal of Hydrogen Energy* 43.1 (2018), pp. 301–310. ISSN: 0360-3199. DOI: <https://doi.org/10.1016/j.ijhydene.2017.10.143>. URL: <http://www.sciencedirect.com/science/article/pii/S0360319917342180>.
- [366] “SGL carbon”. In: (). URL: <https://www.sglcarbon.com/en/markets-solutions/material/sigracell-bipolar-plates-and-end-plates/>.
- [367] Q. Wang et al. “Experimental study on the performance of a vanadium redox flow battery with non-uniformly compressed carbon felt electrode”. In: *Applied Energy* 213 (2018), pp. 293–305. ISSN: 0306-2619. DOI: <https://doi.org/10.1016/j.apenergy.2018.01.047>. URL: <http://www.sciencedirect.com/science/article/pii/S0306261918300540>.
- [368] D. Maggiolo, F. Picano, and M. Guarnieri. “Flow and dispersion in anisotropic porous media: A lattice-Boltzmann study”. In: *Physics of Fluids* 28.10 (2016), p. 102001. DOI: [10.1063/1.4963766](https://doi.org/10.1063/1.4963766). eprint: <https://doi.org/10.1063/1.4963766>. URL: <https://doi.org/10.1063/1.4963766>.
- [369] M. Dentz, M. Icardi, and J. J. Hidalgo. “Mechanisms of dispersion in a porous medium”. In: *Journal of Fluid Mechanics* 841 (2018), 851–882. DOI: [10.1017/jfm.2018.120](https://doi.org/10.1017/jfm.2018.120).
- [370] Jean-Philippe Bouchaud and Antoine Georges. “Anomalous diffusion in disordered media: Statistical mechanisms, models and physical applications”. In: *Physics Reports* 195.4 (1990), pp. 127–293. ISSN: 0370-1573. DOI: [https://doi.org/10.1016/0370-1573\(90\)90099-N](https://doi.org/10.1016/0370-1573(90)90099-N). URL: <http://www.sciencedirect.com/science/article/pii/037015739090099N>.

- [371] Andrea Trovò et al. “Thermal modeling of industrial-scale vanadium redox flow batteries in high-current operations”. In: *Journal of Power Sources* 424 (2019), pp. 204–214. ISSN: 0378-7753. DOI: <https://doi.org/10.1016/j.jpowsour.2019.03.080>. URL: <http://www.sciencedirect.com/science/article/pii/S0378775319303271>.
- [372] A. Trovò, F. Picano, and M. Guarnieri. “Maximizing Vanadium Redox Flow Battery Efficiency: Strategies of Flow Rate Control”. In: *2019 IEEE 28th International Symposium on Industrial Electronics (ISIE)*. 2019, pp. 1977–1982. DOI: [10.1109/ISIE.2019.8781152](https://doi.org/10.1109/ISIE.2019.8781152).
- [373] J. D. Boles et al. “Frequency support comparison for vanadium and lithium-ion BESSs using a converter-based grid emulator”. In: *2018 IEEE Applied Power Electronics Conference and Exposition (APEC)*. 2018, pp. 623–630. DOI: [10.1109/APEC.2018.8341077](https://doi.org/10.1109/APEC.2018.8341077).
- [374] Minghua Li and Takashi Hikiyama. “A Coupled Dynamical Model of Redox Flow Battery Based on Chemical Reaction, Fluid Flow, and Electrical Circuit”. In: *IEICE Trans. Fundam. Electron. Commun. Comput. Sci.* E91-A.7 (July 2008), pp. 1741–1747. ISSN: 0916-8508. DOI: [10.1093/ietfec/e91-a.7.1741](https://doi.org/10.1093/ietfec/e91-a.7.1741). URL: <http://dx.doi.org/10.1093/ietfec/e91-a.7.1741>.
- [375] A. Bhattacharjee, D. K. Mandal, and H. Saha. “Design of an optimized battery energy storage enabled Solar PV Pump for rural irrigation”. In: *2016 IEEE 1st International Conference on Power Electronics, Intelligent Control and Energy Systems (ICPEICES)*. 2016, pp. 1–6. DOI: [10.1109/ICPEICES.2016.7853237](https://doi.org/10.1109/ICPEICES.2016.7853237).
- [376] Chen Jizhong, Xu Ziqiang, and Li Bei. “Research on the characteristics of the vanadium redox-flow battery in power systems applications”. In: *Journal of Power Sources* 241 (2013), pp. 396–399. ISSN: 0378-7753. DOI: <https://doi.org/10.1016/j.jpowsour.2013.04.092>. URL: <http://www.sciencedirect.com/science/article/pii/S0378775313007003>.
- [377] V.K. Yu and D. Chen. “Peak power prediction of a vanadium redox flow battery”. In: *Journal of Power Sources* 268 (2014), pp. 261–268. ISSN: 0378-7753. DOI: <https://doi.org/10.1016/j.jpowsour.2014.06.053>. URL: <http://www.sciencedirect.com/science/article/pii/S0378775314009070>.
- [378] Zhongbao Wei et al. “An adaptive model for vanadium redox flow battery and its application for online peak power estimation”. In: *Journal of Power Sources* 344 (2017), pp. 195–207. ISSN: 0378-7753. DOI: <https://doi.org/10.1016/j.jpowsour.2017.01.102>. URL: <http://www.sciencedirect.com/science/article/pii/S037877531730112X>.
- [379] Mark E Orazem and Bernard Tribollet. *Electrochemical impedance spectroscopy*. John Wiley & Sons, 2017.
- [380] Asif Iqbal Zia and Subhas Chandra Mukhopadhyay. *Electrochemical sensing: carcinogens in beverages*. Springer, 2016.
- [381] Cornelia Breitung. “Impedance Spectroscopy”. In: *Old technique–New application. Lecturer Series at Fritz–haber–Institute Berlin Modern Methods in Heterogeneous Catalysis* (2012), p. 12.
- [382] Andreas Blidberg. *Correlation between different impedance measurement methods for battery cells*. 2012.
- [383] Bernard A Boukamp. “Electrochemical Impedance Spectroscopy”. In: *Nano-Electrocatalysis, U. Leiden* (2008), pp. 24–28.
- [384] I. Pine. “Research Instrumentation, EIS potentiostat/Bipotentiostat/Galvanostat User Guide”. In: (2018).
- [385] Petr Vyroubal and Tomáš Kazda. “Equivalent circuit model parameters extraction for lithium ion batteries using electrochemical impedance spectroscopy”. In: *Journal of Energy Storage* 15 (2018), pp. 23–31. ISSN: 2352-152X. DOI: <https://doi.org/10.1016/j.est.2017.10.019>. URL: <http://www.sciencedirect.com/science/article/pii/S2352152X17303493>.

- [386] Ricardo Monteiro et al. “Insights into all-vanadium redox flow battery: A case study on components and operational conditions”. In: *Electrochimica Acta* 267 (2018), pp. 80–93. ISSN: 0013-4686. DOI: <https://doi.org/10.1016/j.electacta.2018.02.054>. URL: <http://www.sciencedirect.com/science/article/pii/S0013468618303360>.
- [387] Portia Modiba, Mangaka Matoetoe, and Andrew M. Crouch. “Electrochemical impedance spectroscopy study of Ce(IV) with aminopolycarboxylate ligands for redox flow batteries applications”. In: *Journal of Power Sources* 205 (2012), pp. 1–9. ISSN: 0378-7753. DOI: <https://doi.org/10.1016/j.jpowsour.2012.01.004>. URL: <http://www.sciencedirect.com/science/article/pii/S0378775312000080>.
- [388] M.R. Mohamed et al. “Electrical circuit model of a vanadium redox flow battery using extended Kalman filter”. In: *Journal of Power Sources* 239 (2013), pp. 284–293. ISSN: 0378-7753. DOI: <https://doi.org/10.1016/j.jpowsour.2013.03.127>. URL: <http://www.sciencedirect.com/science/article/pii/S0378775313005211>.
- [389] Lei Su et al. “Orientated graphene oxide/Nafion ultra-thin layer coated composite membranes for vanadium redox flow battery”. In: *International Journal of Hydrogen Energy* 42.34 (2017), pp. 21806–21816. ISSN: 0360-3199. DOI: <https://doi.org/10.1016/j.ijhydene.2017.07.049>. URL: <http://www.sciencedirect.com/science/article/pii/S0360319917327866>.
- [390] M. Skyllas-Kazacos and J.F. McCann. “Chapter 10 - Vanadium redox flow batteries (VRBs) for medium- and large-scale energy storage”. In: *Advances in Batteries for Medium and Large-Scale Energy Storage*. Ed. by Chris Menictas, Maria Skyllas-Kazacos, and Tuti Mariana Lim. Woodhead Publishing Series in Energy. Woodhead Publishing, 2015, pp. 329–386. ISBN: 978-1-78242-013-2. DOI: <https://doi.org/10.1016/B978-1-78242-013-2.00010-8>. URL: <http://www.sciencedirect.com/science/article/pii/B9781782420132000108>.